

**Investigation of Flow Augmentation and
Dynamic Stall Control Devices as Performance
Enhancement of Lift-Driven Vertical Axis Wind
Turbine using High-Fidelity CFD Methods**

TAURISTA PERDANA SYAWITRI

**A thesis submitted in partial fulfilment of the requirements of
the University of the West of England, Bristol for the degree
of Doctor of Philosophy**

Faculty of Environment and Technology

Submitted:

August 2022

Declaration

This thesis is the author's PhD work at the Department of Engineering, Design and Mathematics, Faculty of Environment and Technology, University of the West of England (UWE) Bristol. It presents all the author's research works about the performance improvement of three-straight-bladed Vertical Axis Wind Turbine (VAWT) using dynamic stall passive flow control (i.e., Gurney flap (GF)) and flow augmentation device (i.e., straight plate upstream deflector (SUD)). This work mainly uses Computational Fluid Dynamics (CFD) to analyse the performance of VAWT and Taguchi Method for multiple parameter geometry optimisations of the Gurney flap.

All the works presented in this thesis have not been submitted for any other award or degree in the University of the West of England or other Universities or Institutions. Other sources of information or help from other parties used in this thesis have been acknowledged.

Acknowledgements

During the period of doctoral study, the author found that it was a remarkable experience not only doing research but also learning a lot of new things to support the research and improve the individual skill of the author. For their help, the author would like to thank to:

- Allah SWT, the source of knowledge, understanding and wisdom.
- The supervisor team, Prof. Yufeng Yao and Dr Budi Chandra, thank you for the guidance and persistent help.
- Jun Yao, for the help, comments and suggestions.
- Ministry of Education, Culture, Research and Technology and Indonesian Endowment Fund for Education (LPDP) of the Ministry of Finance of Indonesia, for financial support during my doctoral study.
- Parents, Family and Friends in Indonesia, for always supporting me and understanding that I had missed much memorable time with them.
- Friends in Bristol, thank you for all your help and kindness, making Bristol feels like home.
- Others who cannot be mentioned here.

Bristol, August 2022

Author

List of Publications including Journal and Conference Papers

Publications

Published journal papers:

- T. P. Syawitri**, Y. F. Yao, J. Yao and B. Chandra, The effect of gurney flap on flow characteristics of vertical axis wind turbine, **International Journal of Modern Physics B**, vol. 34, no. 14n16, Paper ID 2040107, 2020. (<https://doi.org/10.1142/S0217979220401074>).
- T. P. Syawitri**, Y. F. Yao, J. Yao and B. Chandra, Assessment of stress-blended eddy simulation model for accurate performance prediction of vertical axis wind turbine, **International Journal of Numerical Methods for Heat & Fluid Flow**, Vol. 31, Issues 2, pp. 655-673, 2020. (<https://doi.org/10.1108/HFF-09-2019-0689>).
- T. P. Syawitri**, Y. F. Yao, J. Yao and B. Chandra, Comparison study of URANS and hybrid RANS-LES models on predicting vertical axis wind turbine performance at low, medium and high tip speed ratio ranges, **Renewable Energy**, Vol. 168, pp. 247-269, 2021. (<https://doi.org/10.1016/j.renene.2020.12.045>).
- T. P. Syawitri**, Y. F. Yao, J. Yao and B. Chandra, Geometry optimisation of vertical axis wind turbine with Gurney flap for performance enhancement at low, medium and high ranges of tip speed ratios, **Sustainable Energy Technologies and Assessment**, Vol. 49, Paper ID 101779, 2022. (<https://doi.org/10.1016/j.seta.2021.101779>).
- T. P. Syawitri**, Y. F. Yao, J. Yao and B. Chandra, A review on the use of passive flow control devices as performance enhancement of lift-type vertical axis wind turbines, **Wiley Interdisciplinary Reviews: Energy and Environment**, Early View, Paper ID e435, 2022. (<https://doi.org/10.1002/wene.435>).
- T. P. Syawitri**, Y. F. Yao, J. Yao and B. Chandra, Optimisation of straight plate upstream deflector for the performance enhancement of vertical axis wind turbine at low, medium and high regimes of tip speed ratios. **Wind Engineering**, April 2022. (<https://doi.org/10.1177%2F0309524X221084980>).

Published Conference papers

- T. P. Syawitri**, Y. F. Yao, J. Yao and B. Chandra, A review of current technical development of vertical axis wind turbines and their braking system technology for low speed, urban and offshore areas application, **International Conference of**

Global Warming and Climate Change 2018 in Bangkok, Thailand, 4 – 5 October 2018, Paper ID 169.

T. P. Syawitri, Y. F. Yao, J. Yao and B. Chandra CFD Simulation of Three-Straight-Bladed Vertical Axis Wind Turbine at Low Speed Ratios, **International Conference of Global Warming and Climate Change 2018** in Bangkok, Thailand, 4 – 5 October 2018, Paper ID 170.

T. P. Syawitri, Y. F. Yao, J. Yao and B. Chandra, Assessment of stress-blended eddy simulation model for accurate prediction of three-straight-bladed vertical axis wind turbine performance, **54th 3AF International Conference on Applied Aerodynamics** in Paris, France, 25 – 27 March 2019, Paper ID FP51.

T. P. Syawitri, Y. F. Yao, J. Yao and B. Chandra, The Effect of Gurney Flap on Flow Characteristics of Vertical Axis Wind Turbine, **Eighth International Symposium on Physics of Fluids (ISPF8)** in Xian, China, June 10-13, 2019, Paper ID NMS-02.

T. P. Syawitri, Y. F. Yao, J. Yao and B. Chandra, Three-dimensional modification of Gurney flap to improve the lift-type vertical axis wind turbine performance, **UK Fluid Conference 2020-Rescheduled for 2021**, Online, September 8-10, 2021, Poster Presentation.

T. P. Syawitri, Y. F. Yao, J. Yao and B. Chandra, Drag reduction of lift-type vertical axis wind turbine with Gurney flap by means three-dimensional modification of Gurney flap, **56th 3AF International Conference on Applied Aerodynamics** in Toulouse, France, 28-30 March 2022, Paper ID FP10

Future conferences and journal publications:

T. P. Syawitri, Y. F. Yao, J. Yao and B. Chandra, Gurney flap and its shape modifications for performance enhancement of vertical axis wind turbine at low, medium and high ranges of tip speed ratios. **Under-preparation and to be submitted.**

T. P. Syawitri, Y. F. Yao, J. Yao and B. Chandra, A comparison study of Gurney flap and straight upstream deflector for performance enhancement of lift-driven vertical axis wind turbine. **Under-preparation and to be submitted.**

Abstract

This study performs an investigation of dynamic stall control (Gurney flap (GF)) and flow augmentation (straight upstream deflector (SUD)) devices to improve the performance of lift-driven Vertical Axis Wind Turbine (VAWT) as they can improve the VAWT power generation in all regimes of Tip Speed Ratios (*TSRs*). High-fidelity Computational Fluid Dynamics (CFD) method is applied to evaluate the performance and geometry optimisation. The accuracy and computational cost of Unsteady Reynolds Averaged Navier-Stokes (URANS) and hybrid RANS and Large Eddy Simulation (LES) turbulence models to predict the overall aerodynamic performance and flow-field characteristics of VAWT in all *TSR* regimes are compared, to identify the most suitable turbulence model with a reasonable computational cost for VAWT simulation in all *TSR* regimes.

Instead of using a single parameter variation optimisation at a time, multiple parameters geometry optimisation of GF using the Taguchi method is performed to understand the correlation between evaluated geometry parameters and optimal performance. Moreover, this study evaluates geometry optimisation of GF and SUD in VAWT configuration (i.e., considering rotational effects and blade-to-blade interaction) at all *TSR* regimes, rather than evaluate a single stationary aerofoil in a single *TSR* regime. Evaluation of combining GF and SUD is also delivered in this study. Additionally, 3D modifications of the Gurney flap to reduce the drag generation of VAWT with GF are evaluated to further improve the performance of VAWT.

The results show that URANS turbulence models are sufficient to predict the overall performance of a lift-driven VAWT in a single *TSR* regime evaluation. However, Hybrid RANS-LES turbulence models are necessary to investigate the aerodynamics and flow-field characteristics of lift-driven VAWT and all regimes of *TSRs* evaluation. Moreover, the GF and SUD indeed can increase the performance of lift-driven VAWT in all *TSR* regimes (up to 233.19% and 139.11% in low *TSR* regimes). As the *TSR* regime increases, both GF and SUD experience a decrease in the rate of C_{p-ave} improvement. Nevertheless, GF and SUD have different methods to improve the VAWT power generation for each *TSR* regime. Hence, it is proven that design optimisation and flow analysis of the GF and SUD need to be performed for each *TSR* regime. In addition, by adding the effect of rotating flow and blade-to-blade interaction, the optimum geometry design of GF is changed compared to the optimum design of a single stationary aerofoil.

It confirms that design optimisation needs to be performed in a VAWT configuration (i.e., including rotational effects and blade-to-blade interaction). Note that combining optimised GF and optimised SUD does not increase the power generation improvement of lift-driven VAWT further. Additionally, introducing 3D modifications of GF (i.e. slits or holes) in the blades of VAWT with GF further improves the power coefficient of lift-driven VAWT. The existence of slits can improve the power coefficient of VAWT with GF by 6.5%. Meanwhile, the holes can only improve the power coefficient of VAWT with GF by 0.28%. This value still needs further confirmation as it may be within the range of numerical simulation errors.

Nomenclatures

Symbols

A	: Rotor (turbine) swept area (m^2)
A_0 and A_s	: Model constants in Realisable k - ε turbulence model
c	: Chord length of the blade (m)
C_{a1} , C_{e1} , $C_{\theta t}$ and $C_{\gamma 3}$: Model constants in Transitional SST turbulence model
C_d	: Drag coefficient
C_{d1} and C_{d2}	: Model constants in Delayed-Detached Eddy Simulation
C_{dave}	: Averaged drag coefficient over one turbine revolution
C_{di}	: Instantaneous drag coefficient
C_{DES}	: Calibration constant used in the Detached Eddy Simulation
C_l	: Lift coefficient
C_{lave}	: Averaged lift coefficient over one turbine revolution
C_{li}	: Instantaneous lift coefficient
C_{lim}	: Coefficient of limit in Menter's production limiter
C_m	: Momentum coefficient
C_{mave}	: Averaged moment coefficient over one turbine revolution
C_{mi}	: Instantaneous moment coefficient
C_p	: Power coefficient
C_{pave}	: Averaged power coefficient over one turbine revolution
C_μ	: Coefficient of turbulence viscosity formulation
D_{rotor}	: Rotor (turbine) diameter (m)
$d\theta$: Azimuthal position increment ($^\circ$)
$E_{\gamma 1}$: Transition source in Transitional SST turbulence model
$E_{\gamma 2}$: Destruction/relaminarisation source in Transitional SST turbulence model
f_{DDES}	: Blending function used in the Delayed-Detached Eddy Simulation model
F_2	: Blending function in SST k - ω turbulence model
F_{DES}	: Blending function in Detached Eddy Simulation
F_{length}	: Empirical correlation that controls the length of the transition region in Transitional SST turbulence model

F_{onset}	: Functions that are used to trigger the intermittency production in Transitional SST turbulence model
F_{turb}	: Function to control the length of turbulence region in Transitional SST turbulence model
F_{wake}	: Function in Transitional SST turbulence model to ensures that the blending function is not active in the wake regions downstream of the body
$F_{\theta t}$: Blending function in Transitional SST turbulence model that is used to turn off the source term in the boundary layer
G_k	: Turbulence energy generation
$G_{k,cal}$: Modified turbulence energy generation
H	: Height of Gurney flap (m)
h_f	: Height of the flap of Gurney flap with slits (m)
h_g	: Height of the slit of Gurney flap with slits (m)
H_{rotor}	: Rotor (turbine) height (m)
I	: Observed performance indicator in Taguchi's method
I_i	: Value of observed performance indicator in each case for Taguchi's method
k	: Turbulent kinetic energy (m^2/s^2)
l	: Thickness of Gurney flap (m)
l_d	: Thickness of the deflector (m)
l_x	: Horizontal distance from the centre of the turbine (m) to straight upstream deflector (m)
l_y	: Vertical distance from the centre of the turbine to straight upstream deflector (m)
L	: Distance of the simulated model to the rotating axis (m)
L_t	: Turbulence length scale (m)
L_w	: Length of the wedge of Gurney flap (m)
L_{w1}	: Length of slope line 1 of curve gurney flap (m)
L_{w2}	: Length of slope line 2 of curve gurney flap (m)
\vec{k}	: Vector in z -direction
M	: Moment production of the turbine (N)
N	: Number of the blades

nc	: Total number of observed cases in Taguchi's method
$P_{\theta t}$: Source term Transitional SST turbulence model
$P_{\gamma 1}$: Transition source in Transitional SST turbulence model
$P_{\gamma 2}$: Destruction/relaminarisation source in Transitional SST turbulence model
R	: Radius of the turbine (m)
r_d	: Model constants in Delayed-Detached Eddy Simulation
Re	: Reynold number
Re_t	: Viscosity ratio
Re_{θ}	: Momentum-thickness Reynolds number
$Re_{\theta t}$: Transition onset momentum thickness Reynolds number
$\widetilde{Re_{\theta t}}$: Local transition onset momentum thickness Reynolds number
Re_{ω}	: Dissipation Reynolds number
Re_{Ω}	: Reynolds number based on angular velocity
R_k	: Model constant in SST k - ω turbulence model
s	: Distance of Gurney flap from trailing-edge (m)
S	: Shear strain rate (s^{-1})
S_a	: Surface area (m^2)
S_{ij}	: Strain rate components (s^{-1})
S/N	: Signal to noise (S/N) ratios
t	: Time scale that is present for dimensional reasons in Transitional SST turbulence model (s)
U_{eff}	: Effective velocity of the blade (m/s)
U_x	: x -velocity (m/s)
U_y	: y -velocity (m/s)
U_{∞}	: Incoming wind speed (m/s)
U^*	: Modified stream-wise mean velocity (m/s)
w	: Width of the deflector (m)
x, y and z	: The principal Cartesian directions
Y_k	: Dissipation term of the turbulence kinetic energy
y_w	: Distance to the next wall surface (m)
y^+	: Non-dimensional wall distance

Greek Symbols

$\alpha_1, \alpha_\infty^*$ and α_0^*	: Model constants in SST k - ω turbulence model
β_i	: Model constants in SST k - ω turbulence model
β^*	: Model constant in Detached Eddy Simulation
Δ_{max}	: Grid spacing (m)
Δ_x	: Grid spacing in the x -direction (m)
ε	: Turbulence energy dissipation rate of k - ε based turbulence model (m^2/s^3)
κ	: Karman constant
ρ	: Fluid density (kg/m^3)
θ	: Azimuthal angle position of the blade ($^\circ$)
θ_{BL}	: Momentum thickness in boundary layer transition (m)
θ_{GF}	: Mounting angle of Gurney flap ($^\circ$)
θ_{SUD}	: Inclination angle of straight upstream deflector ($^\circ$)
σ	: Turbine solidity
$\sigma_{\theta t}$: Model constants in Transitional SST turbulence model
Φ_2	: Set of constants in the transformed k - ε turbulence model
\varnothing_{hole}	: The diameter of the hole of Gurney flap (m)
φ	: Rotational angle ($^\circ$)
Γ	: Circulation (m^2/s)
δ	: Boundary layer thickness (m)
δ_{BL}	: Boundary layer transition thickness (m)
τ	: Stress tensor (N/m^2)
$\tau_{i,j}$: Turbulence stress tensors (N/m^2)
μ	: Dynamic viscosity ($Pa.s$)
μ_t	: Turbulence viscosity ($Pa.s$)
ν	: Kinematic viscosity (m^2/s)
ν_l	: Laminar kinematic viscosity (m^2/s)
ν_t	: Turbulence kinematic viscosity (m^2/s)
ω	: Turbulence energy dissipation rate of k - ω based turbulence model (m^2/s^3)
ω_r	: Rate of turbine rotation (rad/s)
γ	: Intermittency

ξ	: z-vorticity (s^{-1})
Ω	: Magnitude of the vorticity tensor (s^{-1})
$\widetilde{\Omega}_{ij}$: Modified vorticity tensor (s^{-1})

Abbreviations

2D	: Two-Dimensional
3D	: Three-Dimensional
AoA	: Angle of Attack
BEM	: Blade Element Momentum
CFD	: Computational Fluid Dynamics
CG	: C-grid
DDES	: Delayed-Detached Eddy Simulation
DES	: Detached Eddy Simulation
DMST	: Double Multiple Stream Tube
DNS	: Direct Numerical Simulation
DSV	: Dynamic Stall Vortex
DVAWT	: Darrieus Vertical Axis Wind Turbine
GF	: Gurney Flap
GIS	: Grid Induced Separation
HAWT	: Horizontal Axis Wind Turbine
IDDES	: Improved-Delayed-Detached Eddy Simulation
LB	: Larger-the-Better
LES	: Large Eddy Simulation
LHS	: Latin Hypercube Sample
MSD	: Modelled-Stress Depletion
NACA	: National Advisory Committee for Aeronautics
NB	: Nominal-the-Better
NS	: Navier-Stokes
ODGV	: Omnidirectional Guide Vane
OG	: O-grid
PISO	: Pressure Implicit with Splitting of Operators
PIV	: Particle Image Velocimetry
RANS	: Reynolds Averaged Navier-Stokes
RF	: Reduced Frequency

RKE	: Realisable $k-\varepsilon$
RMSE	: Root Mean Square Error
SA	: Spalart-Allmaras
SB	: Smaller-the-Better
SBES	: Stress-Blended Eddy Simulation
SDES	: Shielded-Detached Eddy Simulation
SGS	: Sub-grid Scale
SIMPLE	: Semi-Implicit Method for Pressure-Linked Equations
SIMPLEC	: Semi-Implicit Method for Pressure-Linked Equations Consistent
SST	: Shear-Stress Transport
SUD	: Straight Upstream Deflector
TSR	: Tip Speed Ratio
TSST	Transition Shear-Stress Transport
URANS	: Unsteady Reynolds Averaged Navier-Stokes (RANS)
VAWT	: Vertical Axis Wind Turbine
WMLES	: Wall-Modelled Large Eddy Simulation
VG	: Vortex Generator

Subscripts

i, j	: Component of vector
D	: Geometrical (in Angle of Attack)
D_{max}	: Maximum Geometrical (in Angle of Attack)
D, nor	: Non-dimensionalised Geometrical (in Angle of Attack)

List of Contents

Declaration	i
Acknowledgements	ii
List of Publications including Journal and Conference Papers.....	iii
Abstract	v
Nomenclatures.....	vii
List of Contents	xiii
List of Figures	xviii
List of Figures in Appendices	xxvii
List of Tables.....	xxx
List of Tables in Appendices.....	xxxii
1. Introduction.....	1
1.1 Study Background.....	1
1.2 Motivation, Aims and Objectives of the Research.....	2
1.3 Key Questions to Address	3
1.4 Thesis Structure.....	4
2. Literature Reviews.....	6
2.1 Overview of VAWTs	6
2.1.1 Types of VAWTs	6
2.1.2 VAWTs comparison with HAWTs.....	8
2.1.3 Flow characteristics around lift-driven VAWTs.....	9
2.2 Performance Enhancement of Lift-Driven VAWTs	14
2.2.1 Performance enhancement of lift-driven VAWTs by using blade modifications.....	15
2.2.2 Performance enhancement of lift-driven VAWTs by using flow augmentations	22
2.3 Experimental and site test studies of Lift-Driven VAWTs.....	31
2.4 Modelling VAWTs.....	35
2.3.1 Momentum theory-based models.....	35
2.3.2 Non-momentum theory-based models	36
2.5 Chapter Summary.....	42
2.5.1 Rationale for the present study performance enhancement approach	42

2.5.2	Rationale for the present state-of-the-art study of research methods	46
3.	Definitions and CFD Methodologies	48
3.1	Definitions of Fundamental Parameters of Lift-Driven VAWT	48
3.1.1	Solidity (σ)	48
3.1.2	Tip Speed Ratio (TSR)	48
3.1.3	Reduced Frequency (RF)	49
3.1.4	Geometrical Angle of Attack (AoA_D)	49
3.1.5	Power Coefficient (C_p)	49
3.2	CFD Procedures	50
3.2.1	Pre-processing	51
3.2.2	Solver	51
3.2.3	Post-processing	51
3.2.4	Other computational settings criteria	51
3.2.5	Domain sizes criteria	53
3.3	Design Procedures	54
3.4	Chapter Summary	57
4.	Two-Dimensional CFD Validation of Lift-Driven VAWT	59
4.1	VAWT Geometry	60
4.2	Simulation Domain and Grid Decomposition	62
4.2.1	Rectangular far-field sub-domain	63
4.2.2	Rotating core sub-domain	63
4.2.3	Control circle sub-domain	64
4.3	Computational Settings	65
4.4	Domain, Spatial and Temporal Convergence Studies	66
4.4.1	Domain size study	66
4.4.2	Spatial (grid) convergence study	68
4.4.3	Temporal (time) resolution study	69
4.5	Impact of Turbulence Models	70
4.5.1	Revolution convergence analysis	70
4.5.2	Revolution averaged of turbine power coefficient (C_{p-ave})	72
4.5.3	Turbine aerodynamics characteristics over one revolution	81
4.6	Chapter Summary and Further Works	94
4.6.1	Model independency	94

4.6.2	Model accuracy	95
4.6.3	Rationale for the choice of turbulence models.....	97
4.6.4	Further works	98
5.	2D CFD Simulation of Blade Shape Modifications for Performance Enhancement of Lift-Driven VAWT using Gurney Flap.....	99
5.1	VAWT with Gurney Flap.....	100
5.2	Model, Grid Generation and Numerical Setup.....	102
5.3	Geometries Optimisation using Taguchi Method	105
5.3.1	Results of optimisation.....	107
5.4	Results Comparison and Discussion	114
5.4.1	General effect of GF	114
5.4.2	Effect of the height of GF	121
5.4.3	Effect of the mounting angle of GF	127
5.4.4	Effect of the position from trailing-edge of GF	131
5.4.5	Effect of GF shape modification.....	138
5.4	Chapter Summary and Further Works	149
6.	2D CFD Simulation of Flow Augmentation Device for Performance Enhancement of Lift-Driven VAWT using Straight Upstream Deflector.....	152
6.1	VAWT with Straight Upstream Deflector	152
6.2	Model, Grid Generation and Numerical Setup.....	154
6.3	Results Comparison and Discussion	158
6.3.1	Effects of the location of upstream deflector	158
6.3.2	Effects of the width of upstream deflector.....	166
6.3.3	Effects of the inclination angle of upstream deflector	173
6.4	Chapter Summary and Further Works	178
7.	Performance Comparison between Gurney Flap, Straight Upstream Deflector and Combination of Gurney Flap and Straight Upstream Deflector for Performance Enhancement of Lift-Driven VAWT	180
7.1	Performance Comparison of GF and SUD as Performance Enhancement of VAWT	180
7.1.1	Low <i>TSRs</i> (representative <i>TSR</i> = 1.44).....	180
7.1.2	Medium <i>TSRs</i> (representative <i>TSR</i> = 2.64).....	184
7.1.3	High <i>TSRs</i> (representative <i>TSR</i> = 3.3)	188

7.2	Effect of Gurney Flap and Straight Upstream Deflector Combination on the Performance of VAWT	191
7.2.1	The geometry, model, grid generation and numerical setup.....	192
7.2.2	Comparison between VAWT with GF and SUD, VAWT with stand-alone GF, VAWT with stand-alone SUD and bare VAWT.....	192
7.5	Chapter Summary and Further Works	197
8.	3D CFD Validation of Lift-Driven VAWT	200
8.1	Model Description.....	200
8.2	3D Grid Discretisation	203
8.3	Grid Independence Study	206
8.4	3D Results	208
8.4.1	Validation of averaged power coefficient.....	208
8.4.2	Blade aerodynamics characteristics	210
8.5	Chapter Summary and Further Works	225
9.	Quasi-3D CFD Simulation of Modification of Gurney Flap for Drag Reduction of Lift-Driven VAWT with Gurney Flap.....	227
9.1	Geometric Models.....	228
9.1.1	VAWT with GF	228
9.1.2	3D Modifications of GF	228
9.2	Model, Grid Generation and Numerical Setup.....	230
9.3	Comparison between 2D and q3D Models of VAWT with GF.....	232
9.4	VAWT with 3D Modifications of GF.....	232
9.4.1	Moment coefficient comparison	232
9.4.2	Drag and lift coefficient comparisons.....	234
9.4.3	Flow-field comparison	240
9.5	Chapter Summary and Future Works.....	242
10.	Summary of Novelty and Contributions, Recommendations and Future Works	244
10.1	Summary of Novelty and Contribution of this Study Based on Answer to the Raised Key Questions	244
10.2	Recommendations and Future Works	254
	References.....	256
	Appendices.....	269
	Appendix A: Blade Shape Modification Devices Implemented in Lift-Driven VAWTs	269

Appendix B: Flow Augmentation Devices Implemented in Lift-Driven VAWTs.....	286
Appendix C: Previous Works of VAWTs using CFD Simulation.....	293
Appendix D: Detail of Implemented Turbulence Models in 2D CFD Validation Study	297
Appendix E: SBES Transition SST Sensitivity to Grid Topology	305
Appendix F: Evaluation of Range Values of the Height, Mounting Angle and Position from Trailing-edge of GF	313

List of Figures

Figure 1.1	Global Cumulative Installed Wind Capacity (Global Wind Energy Council, 2018).	1
Figure 2.1	Types of Vertical Axis Wind Turbines (Anon., 2017).....	7
Figure 2.2	(a) Illustration of the azimuthal position equals to 0, (b) Geometrical angle of attack, and (c) Reduced frequency distributions in different $TSRs$ of the case of Castelli, Englaro and Benini (2011).....	11
Figure 2.3	Typical lift coefficient distribution over angle of attack of static NACA 0021 in low Reynolds number (140000) (Holst et al., 2018).....	13
Figure 2.4	Comparison of power coefficient (C_p) distribution for different types of wind turbines (D’Ambrosio and Medaglia, 2010)	14
Figure 2.5	Configuration of wind tunnel test (Jin et al., 2015).....	33
Figure 2.6	Configuration of PIV test (Jin et al., 2015)	34
Figure 4.1	VAWT model based on Castelli, Englaro and Benini (2011), (a) 3D experimental and (b) 2D computational domain (all measurements are in mm)	61
Figure 4.2	Detailed computational domain and sub-domains	62
Figure 4.3	Grid details for the two main sub-domains	64
Figure 4.4	Detailed grid around the blade wall.....	65
Figure 4.5	Modified far-field sub-domain, (a) smaller domain ($20D_{rotor}$) and (b) larger domain ($80D_{rotor}$) (the drawing is not in scale).....	67
Figure 4.6	C_{mi} of the three different far-field sub-domain sizes over one turbine revolution.....	67
Figure 4.7	Comparison of C_{mi} of VAWT with different grids.....	69
Figure 4.8	C_{mi} of three different time steps over one turbine revolution.....	69
Figure 4.9	C_{m-ave} changes over turbine revolution for URANS turbulence models..	70
Figure 4.10	C_{m-ave} changes over turbine revolution for hybrid RANS-LES turbulence models.....	72
Figure 4.11	C_{p-ave} comparison of current CFD simulations using RANS turbulence models and the experimental and CFD using RKE results of Castelli, Englaro and Benini (2011)	73

Figure 4.12	Comparison of C_{p-ave} between current CFD simulation and the experiment and simulation of Castelli, Englaro and Benini (2011), as well as relative discrepancies to the experimental data in percentage.....	74
Figure 4.13	C_{p-ave} comparison of current CFD simulations using SST, DDES and IDDES turbulence models and Castelli, Englaro and Benini (2011) experimental results.....	76
Figure 4.14	Comparison of C_{p-ave} between current DDES and Transitional SST CFD simulations and the experimental results of Castelli, Englaro and Benini (2011), as well as relative discrepancies to the experimental data in percentage.....	77
Figure 4.15	C_{p-ave} comparison of current CFD simulation using SBES turbulence models based on SST $k-\omega$ and Transitional SST RANS turbulence models and Castelli, Englaro and Benini (2011) experimental results.....	78
Figure 4.16	Comparison of C_{p-ave} between current SBES and Transitional SST CFD simulations and the experimental results of Castelli, Englaro and Benini (2011), as well as relative discrepancies to the experimental data in percentage.....	79
Figure 4.17	Comparison of C_{mi} distribution of three URANS models (RKE, SST and TSST) in $TSR = 1.44$	82
Figure 4.18	Comparison of contour plots of z -vorticity indicating the flow separation process at important azimuthal positions in $TSR = 1.44$ (URANS models), (a) before vortex shedding and (b) after vortex shedding (not in scale) .	83
Figure 4.19	Comparison of C_{mi} distribution of three URANS models (RKE, SST and TSST) in $TSR = 2.64$	84
Figure 4.20	Comparison of contour plots of z -vorticity indicating the flow separation process at important azimuthal positions in $TSR = 2.64$ (URANS models), (a) before vortex shedding and (b) after vortex shedding (not in scale) .	85
Figure 4.21	Comparison of C_{mi} distribution of three URANS models (RKE, SST and TSST) in $TSR = 3.3$	87
Figure 4.22	Comparison of contour plots of z -vorticity indicating the flow separation process at important azimuthal positions in $TSR = 3.3$ (URANS models), (a) before shedding and (b) after shedding.....	88
Figure 4.23	C_{mi} comparison of four hybrid RANS-LES models (DDES, IDDES, SBES SST and SBES TSST) in $TSR = 1.44$	89

Figure 4.24	Comparison of contour plots of z -vorticity indicates the flow separation process at important azimuthal positions after vortex shedding in $TSR = 1.44$ (using hybrid RANS-LES models).....	90
Figure 4.25	C_{mi} comparison of four hybrid RANS-LES models (DDES, IDDES, SBES SST and SBES TSST) in $TSR = 2.64$	91
Figure 4.26	Comparison of contour plots of z -vorticity indicates the flow separation process at important azimuthal positions after vortex shedding in $TSR = 2.64$ (using hybrid RANS-LES models).....	92
Figure 4.27	C_{mi} comparison of four hybrid RANS-LES models (DDES, IDDES, SBES SST and SBES TSST) in $TSR = 3.3$	93
Figure 4.28	Comparison of contour plots of z -vorticity indicates the flow separation process at important azimuthal positions after vortex shedding in $TSR = 3.3$ (using hybrid RANS-LES models).....	94
Figure 5.1	Comparison between (a) clean NACA 0021 aerofoil and (b) NACA 0021 with GF and detailed geometric variation (the drawing is not in scale)	101
Figure 5.2	Detailed geometry of a GF with (a) wedged shape and (b) curved shape (the drawing is not in scale).....	102
Figure 5.3	Partition of control sub-domain with (a) original GF shape, (b) wedged GF and (c) curved GF (the drawing is not in scale)	103
Figure 5.4	Detailed mesh around (a) original GF shape, (b) wedged GF and (c) curved GF (the drawing is not in scale)	104
Figure 5.5	Comparison of the effect of varying combination of GF geometry parameters (a) mounting angle & height, (b) position from trailing-edge & mounting angle and (c) position from trailing-edge & height to the contour of C_{p-ave} in $TSR = 1.44$	111
Figure 5.6	Comparison of the effect of varying combination of GF geometry parameters (a) mounting angle & height, (b) position from trailing-edge & mounting angle and (c) position from trailing-edge & height to the contour of C_{p-ave} in $TSR = 2.64$	112
Figure 5.7	Comparison of the effect of varying combination of GF geometry parameters (a) mounting angle & height, (b) position from trailing-edge & mounting angle and (c) position from trailing-edge & height to the contour of C_{p-ave} in $TSR = 3.3$	113

Figure 5.8	Comparison of (a) C_{mi} , (b) C_{li} and (c) C_{di} over one rotation cycle of VAWT with GF (optimum geometries) and without GF in $TSR = 2.64$	116
Figure 5.9	Comparison of (a) velocity magnitude contours with super-imposed pathlines in the right graphs and (b) contours of z -vorticity between bare VAWT and VAWT with GF (optimum geometry) in $TSR = 2.64$, $\theta = 90^\circ$	117
Figure 5.10	C_{p-ave} comparison between the VAWT with GF ($H = 3\% c$, $\theta_{GF} = 90^\circ$ and $s = 0\% c$ from trailing-edge) and without GF in different TSR values..	119
Figure 5.11	C_{p-ave} increment in all tested $TSRs$ for a VAWT with GF ($H = 3\% c$, $\theta_{GF} = 90^\circ$ and $s = 0\% c$ from trailing-edge)	119
Figure 5.12	C_{mi} comparison of VAWT with GF ($H = 3\% c$, $\theta_{GF} = 90^\circ$ and $s = 0\% c$ from trailing-edge) and without GF in $TSR = 1.44$	120
Figure 5.13	C_{p-ave} comparison of VAWT with and without GF in various GF heights ($TSR = 2.64$).....	121
Figure 5.14	C_{mi} comparison from the VAWT with and without GF for various GF heights ($TSR = 2.64$).....	122
Figure 5.15	Comparison of streamlines coloured by z -vorticity contours of one selected blade (blade 1) in various heights of GF ($TSR = 2.64$, $\theta = 45^\circ$)	123
Figure 5.16	Comparison of x -velocity profiles in the wake region of one selected blade (blade 1) in various heights of GF ($TSR = 2.64$, $\theta = 45^\circ$)	124
Figure 5.17	Comparison of gauge pressure contours of one selected blade (blade 1) in various heights of GF ($TSR = 2.64$, $\theta = 45^\circ$).....	125
Figure 5.18	Comparison of C_{p-ave} improvement of VAWT with GF for various GF heights in different values of the TSR	126
Figure 5.19	Comparison of C_{p-ave} of VAWT with and without GF for various heights and mounting angles and a fixed position ($0\% c$ from trailing-edge) in $TSR = 2.64$	128
Figure 5.20	C_{mi} comparison of the VAWT with GF in various mounting angles for $TSR = 2.64$	129
Figure 5.21	Comparison of gauge pressure contours in various mounting angles of the GF ($TSR = 2.64$, $\theta = 120^\circ$)	130
Figure 5.22	Comparison of streamlines coloured by z -vorticity contours in various mounting angles of the GF ($TSR = 2.64$, $\theta = 120^\circ$)	131

Figure 5.23	C_{p-ave} comparison for a VAWT with and without GF in various GF positions from the trailing-edge ($H = 3\% c$ and $\theta_{GF} = 90^\circ$) for $TSR = 1.44$	132
Figure 5.24	C_{mi} comparison of VAWT with GF for various GF positions ($TSR = 1.44$)	133
Figure 5.25	C_{p-ave} comparison for a VAWT with and without GF in various GF positions from trailing-edge for $TSR = 2.64$ and $TSR = 3.3$ (GF height and mounting angle are fixed at $3\% c$ and 90° , respectively)	134
Figure 5.26	C_{mi} comparison of a VAWT with GF in various GF positions ($TSR = 2.64$)	134
Figure 5.27	Comparison of (a) streamlines coloured by z -vorticity contours (black regions show the vertical structures of the flow) and (b) contours of gauge pressure in various GF positions from the trailing edge ($TSR = 2.64$, $\theta = 45^\circ$)	135
Figure 5.28	Comparison of streamlines distribution of VAWT with GF at $s = 4\%$ of c from trailing-edge in different $TSRs$ ($\theta = 45^\circ$)	136
Figure 5.29	Comparison of x -velocity profile in the wake region of one selected blade (blade 1) of VAWT with GF mounted at $s = 4\% c$ from trailing-edge between $TSR = 2.64$ and $TSR = 1.44$ ($\theta = 45^\circ$)	137
Figure 5.30	Comparison of the effect of L_w/H to the C_{p-ave} of VAWT in different regimes of $TSRs$	139
Figure 5.31	Comparison of the effect of L_w/H on the C_{mi} in (a) $TSR = 1.44$ (low TSR) and (b) $TSR = 2.64$ (medium TSR)	140
Figure 5.32	Comparison of the effect of L_w/H on the C_{mi} in $TSR = 3.3$ (high TSR)	141
Figure 5.33	Comparison of the effect of L_w/H on the C_{li} of one selected blade (Blade 1) of the VAWT in (a) $TSR = 2.64$ and (b) $TSR = 3.3$	142
Figure 5.34	Comparison of streamlines between a bare VAWT and a VAWT with original GF, wedged and curved GFs in $TSR = 2.64$, $\theta = 45^\circ$, respectively	143
Figure 5.35	Comparison of contours of static pressure in $TSR = 1.44$ between VAWTs with original and wedged GFs ($\theta = 90^\circ$)	144
Figure 5.36	Comparison of contours of static pressure in $TSR = 2.64$ between VAWTs with original GF, wedged GF and curved GF ($\theta = 90^\circ$)	145
Figure 5.37	Illustration of curves of five curved GF cases	146

Figure 5.38	C_{mi} comparison of blade 1 of the VAWT with curved GF in various slope line ratios for (a) $TSR = 2.64$ and (b) $TSR = 3.3$	148
Figure 5.39	C_{mi} comparison of blade 1 of VAWT with curved GF in various vertical line ratios for $TSR = 2.64$	149
Figure 6.1	Detailed geometry of a VAWT with SUD, where l_x is a horizontal distance from the centre of the turbine (m), l_y is a vertical distance from the centre of the turbine (m), l_d is the thickness of the deflector (m) and w is the width of the deflector (m)	153
Figure 6.2	Comparison of the far-field sub-domain partition between bare VAWT and VAWT with SUD (four scenarios) (the drawing is not in scale)	157
Figure 6.3	Detailed grids within the far-field sub-domain	158
Figure 6.4	Sketches of four SUD locations (the deflector geometry is not in scale), (a) middle, (b) both upward and downward, (c) downward and (d) upward	159
Figure 6.5	C_{mi} comparison (three blades) between the bare VAWT and the VAWT with SUD at four different locations ($TSR = 2.64$).....	160
Figure 6.6	Comparison of streamline distributions coloured by velocity magnitude (m/s) of the flow around (a) bare VAWT and VAWT with SUD at (b) downward, (c) middle, (d) upward and (e) both upward and downward ($TSR = 2.64$, $\theta = 360^\circ$)	161
Figure 6.7	Comparison of mean pressure (Pa) contours of Blade 1 around the (a) bare VAWT and VAWT with SUD at (b) downward, (c) middle, (d) upward and (e) both upward and downward ($TSR = 2.64$, $\theta = 360^\circ$)	163
Figure 6.8	Comparison of pressure coefficient distribution of Blade 1 around the bare VAWT and VAWT with SUD at middle and “both upward and downward” ($TSR = 2.64$, $\theta = 360^\circ$).....	163
Figure 6.9	C_{mi} comparison between a bare VAWT and a VAWT with SUD (both upward and downward configuration) in (a) $TSR = 1.44$ and (b) $TSR = 2.64$	164
Figure 6.10	SUD with the width addition.....	167
Figure 6.11	C_{p-ave} comparison between the bare VAWT and the VAWT with SUD of “both upward and downward” configuration with four different width variations in the three TSR regimes	168

Figure 6.12	C_{p-ave} comparison between the bare VAWT and the VAWT with SUD of “both upward and downward” configuration with four different width variations in (a) $TSR = 1.44$, (b) $TSR = 2.64$ and (c) $TSR = 3.3$	169
Figure 6.13	Comparison of the velocity vectors, superimposed by contours coloured by velocity of the VAWT with SUD of different widths ($TSR = 2.64$, $\theta = 360^\circ$)	170
Figure 6.14	Comparison of velocity contours of VAWT with SUD of four different widths ($TSR = 2.64$, $\theta = 360^\circ$).....	171
Figure 6.15	C_{mi} comparison of the VAWT with SUD for four different widths (a) $TSR = 1.44$ and (b) $TSR = 2.64$	172
Figure 6.16	Inclination angle of the SUD (for both upward and downward configuration)	173
Figure 6.17	Comparison of the effect of inclination angle on the C_{mi} distribution of VAWT with SUD in (a) $TSR = 1.44$ and (b) $TSR = 2.64$	175
Figure 6.18	Comparison of streamlines around the VAWT with SUD at four different inclination angles ($TSR = 2.64$, $\theta = 360^\circ$).....	176
Figure 6.19	Comparison of velocity contours of the VAWT with SUD at four different inclination angles ($TSR = 2.64$, $\theta = 360^\circ$).....	177
Figure 7.1	C_{mi} comparison between bare VAWT, VAWT with GF and VAWT with SUD in $TSR = 1.44$	181
Figure 7.2	Contours of z -vorticity of (a) bare VAWT, (b) VAWT with GF and (c) VAWT with SUD in $TSR = 1.44$ ($\theta = 90^\circ$). The circles in white solid lines represent the rotating core sub-domain	182
Figure 7.3	Comparison of (a) C_{li} and (b) C_{di} between bare VAWT, VAWT with GF and VAWT with SUD in $TSR = 1.44$	183
Figure 7.4	C_{mi} comparison between bare VAWT, VAWT with GF and VAWT with SUD in $TSR = 2.64$ 185	
Figure 7.5	Comparison of streamlines coloured by the velocity magnitude (m/s) of the flow around (a) bare VAWT, (b) VAWT with GF, and (c) VAWT with SUD ($TSR = 2.64$, $\theta = 360^\circ$). The circles in dark solid lines represent the rotating core sub-domain.....	186
Figure 7.6	Comparison of (a) C_{li} and (b) C_{di} between bare VAWT, VAWT with GF and VAWT with SUD in $TSR = 2.64$	187

Figure 7.7	C_{mi} comparison between bare VAWT, VAWT with GF and VAWT with SUD in $TSR = 3.3$	189
Figure 7.8	Comparison of (a) C_{li} and (b) C_{di} between bare VAWT, VAWT with GF and VAWT with SUD in $TSR = 3.3$	190
Figure 7.9	C_{mi} comparison between bare VAWT, VAWT with GF, VAWT with SUD and VAWT with GF and SUD in (a) $TSR = 1.44$, (b) $TSR = 2.64$ and (c) $TSR = 3.3$	195
Figure 7.10	Comparison of z -vorticity (ζ) contours between VAWT with SUD and VAWT with GF and SUD in (a) $TSR = 1.44$, $\theta = 90^\circ$ (b) $TSR = 2.64$, $\theta = 90^\circ$ and (c) $TSR = 3.3$, $\theta = 135^\circ$. The circles in white solid lines represent the rotating core sub-domain	196
Figure 8.1	Main boundary conditions and dimensions of the 3D computational domain (the drawing is not in scale).....	201
Figure 8.2	3D computational domain and its sub-domains in detail (the drawing is not in scale).....	202
Figure 8.3	C_{mi} over the first 12 revolutions/cycles	203
Figure 8.4	Clustered grid around the tip of the blade	204
Figure 8.5	CutCell mesh around the far-field sub-domain	205
Figure 8.6	C_{mi} comparison of the 3D model with the different number of elements along the span-wise direction	206
Figure 8.7	C_{mi} comparison of the 3D model with various grids	207
Figure 8.8	Sketch of the important span-wise positions along rotating sub-domain	210
Figure 8.9	(a) Sketch of the important span-wise positions along rotating sub-domain) and (b) C_{mi} of blade 1 at various positions along the span-wise direction of the blade.....	211
Figure 8.10	Comparison of contour plots of z -vorticity at important azimuthal positions	216
Figure 8.11	Comparison of contour plots of z -vorticity ($\theta = 30^\circ$) at important span-wise positions, (a) sketch of the important span-wise positions along rotating sub-domain), (b) along the half of the blade and (c) after blade tip until the end of the rotating zone	219
Figure 8.12	Comparison of contour plots of z -vorticity ($\theta = 135^\circ$) at important span-wise positions, (a) sketch of the important span-wise positions along	

	rotating sub-domain), (b) along the half of the blade and (c) after blade tip until the end of the rotating zone.....	222
Figure 8.13	Comparison of contour plots of z -vorticity ($\theta = 240^\circ$) at important span-wise positions, (a) sketch of the important span-wise positions along rotating sub-domain), (b) along the half of the blade and (c) after blade tip until the end of the rotating zone.....	225
Figure 9.1	Detailed geometry of clean GF.....	228
Figure 9.2	Detailed geometry of GF and its modifications (not in scale).....	229
Figure 9.3.	Detailed grids of 3D modification of GF, (a) GF with slits and (b) GF with holes (the drawing is not in scale). The colour in the grids shows domain partition to help the grid generation process	231
Figure 9.4	Instantaneous moment coefficients comparison of q3D VAWT with clean GF, VAWT with slit GF and VAWT with holed GF.....	233
Figure 9.5	Comparison of C_{p-ave} between q3D VAWT with clean GF, VAWT with slit GF and VAWT with holed GF	233
Figure 9.6	Comparison of mean velocity contour in x - y cross-section between slit GF and holed GF at the middle of the slit or hole	235
Figure 9.7	Instantaneous drag coefficients comparison of one selected blade (blade 1) between q3D VAWT with clean GF, VAWT with slit GF and VAWT with holed GF	237
Figure 9.8	Instantaneous lift coefficients comparison of one selected blade (blade 1) between q3D VAWT with clean GF, VAWT with slit GF and VAWT with holed GF.	239
Figure 9.9	Geometrical angle of attack at $TSR = 2.64$ of Castelli, Englaro and Benini (2011) case.....	240
Figure 9.10	Comparison of an isosurface of Q criterion in the wake of the blade 1 (coloured by Q criterion) between 2.5D (a) VAWT with clean GF, (b) VAWT with slit GF and (c) VAWT with holed GF.....	241

List of Figures in Appendices

Figure A.1	NACA 0021 with optimum dimple location (Sobhani, Ghaffari and Maghrebi, 2017). Maghrebi, 2017)	270
Figure A.2	Aerofoil with GF (i.e. downward straight plate) and inward dimple on the pressure side near the trailing-edge (Shukla and Kaviti, 2017; Ismail and Vijayaraghavan, 2015)	271
Figure A.3	(a) Multiple counter-rotating vortex generators (Choudhry, Arjomandi and Kelso, 2016) and (b) Single counter-rotating micro vortex generator (Yan et al., 2019), deployed at the leading-edge of an aerofoil	272
Figure A.4	Drag coefficient and lift coefficient distributions of a NACA 0021 aerofoil with counter-rotating VGs at a pitching rate of 320 degree/s over evaluated AoA s. The darker dashed lines, after $AoA = 40^\circ$, shows the lift and drag behaviour of the aerofoil after the pitching process has stopped (Choudhry, Arjomandi and Kelso, 2016)	273
Figure A.5	Blades with opening modification at the pressure side (Chen et al., 2015)	274
Figure A.6	Three-straight-bladed Darrieus VAWT with J-shaped blade (Zamani et al., 2016).....	275
Figure A.7	Aerofoil with a slot (Belamadi et al., 2016)	276
Figure A.8	Aerofoil with λ slot along x -direction (Acarer, 2020).....	277
Figure A.9	The optimum geometric parameters of a slotted aerofoil (Acarer, 2020)	277
Figure A.10	Two-element aerofoil configuration, (a) S1210 two-element aerofoil (Chougule and Nielsen, 2014); (b) DU06-W200 two-element aerofoil (Chougule, Rosendahl and Nielsen, 2015) and (c) VAWT configuration with two-element aerofoil (Chougule, Rosendahl and Nielsen, 2015) .	279
Figure A.11	(a) Five-element aerofoil and (b) 3D isometric view of VAWT with five-element aerofoil (Srihari et al., 2019).....	280
Figure A.12	Blade of VAWT with leading-edge serrations (Wang and Zhuang, 2017)	281
Figure A.13	VAWT blade with a winglet at the tip (Zhang et al., 2019).....	282
Figure A.14	Illustration of flow behaviour around trailing-edge of aerofoil with GF (Liebeck, 1978).....	284

Figure A.15	Leading-edge micro-cylinder passive flow control (Choudhry, Arjomandi and Kelso, 2016).....	285
Figure B.1	Guide vane row with three arc plates (Takao et al., 2009).....	286
Figure B.2	Convergent duct configuration to increase wind velocity and direct the wind into the VAWT (Santoli et al., 2014)	287
Figure B.3	Diffuser application in lift-driven VAWTs, (a) two Selig 1223 wings diffuser (Letizia and Zanforlin, 2016) and (b) wind lens diffuser (Watanabe, Takahashi and Ohya, 2016).....	288
Figure B.4	VAWT model with curved plate (Stout et al., 2017)	289
Figure B.5	Straight plate upstream deflector application in lift-driven VAWTs (a) In the middle of two counter-rotating five-straight-bladed H-type VAWTs (Kim and Gharib, 2014; Kim and Gharib, 2013), (b) In the middle of two counter-rotating three-straight-bladed H-type VAWTs (Jin et al., 2018), and (c) downward of a single two-straight-bladed VAWT (Wong et al., 2018a; Wong et al., 2018b)	290
Figure B.6	A few omnidirectional-flow-augmentation devices to enhance the performance of lift-driven VAWTs, (a) Omni-Directional-Guide-Vane by Chong et al. (2013) (original) and Wong et al. (2014) (modified) and (b) Omnidirectional stator with NACA 0018 aerofoil profile by Nobile et al. (2014)	292
Figure E.1	Detailed computational domain and sub-domains of C-grid.....	306
Figure E.2	Grid details in two sub-domains of C-grid.....	307
Figure E.3	Grid around the blade wall in the C-grid.....	308
Figure E.4	C_{mi} comparison of VAWT with various grid resolutions for O-grids ...	309
Figure E.5	C_{mi} comparison of VAWT with various grid resolutions for C-grids ...	310
Figure E.6	C_{p-ave} comparison between the experiment, simulation of Castelli, Englaro and Benini (2011) and current CFD simulations (RKE) as well as relative errors in percentage (compared to experiment).....	311
Figure E.7	C_{p-ave} comparison between the experiment of Castelli, Englaro and Benini (2011) and current CFD simulation (SBES with TSST) as well as relative errors in percentage (compared to experiment).....	312
Figure E.8	C_{mi} comparison of blade 1 for one turbine revolution between O-grid and C-grid simulations	312

Figure F.1	C_{p-ave} comparison between VAWT with and without GF in various GF heights in all three regimes of $TSRs$	313
Figure F.2	C_{p-ave} comparison between VAWT with and without a GF for various GF mounting angles in all three regimes of $TSRs$	314
Figure F.3	C_{p-ave} comparison between VAWT with and without the GF in various GF positions from trailing-edge in all three regimes of $TSRs$	315

List of Tables

Table 2.1	Summary of blade shape modifications that have been integrated into lift-driven VAWTs	16
Table 2.2	Summary of flow augmentation devices that have been integrated into lift-driven VAWTs	24
Table 2.3	Summary of works of modelling VAWT using CFD simulations	39
Table 4.1	Main geometrical features of Castelli, Englaro and Benini (2011) model	62
Table 4.2	Details of the number of elements for each grid	68
Table 4.3	Comparison of 2D CFD simulation time using various turbulence models (2 CPUs @ 2.2 GHz, 128 GB RAM)	97
Table 5.1	Details of GF geometry parameters and levels of studies	107
Table 5.2	Matrix of case studies for each <i>TSR</i>	108
Table 5.3	C_{p-ave} values of all 27 cases in all <i>TSR</i> regimes (<i>bold and italic fonts</i> in yellow highlights are the optimum cases)	109
Table 5.4	Response table for Signal to Noise Ratios (i.e. the larger-is-better) of Taguchi analysis (<i>bold and italic fonts</i> in yellow highlights are the maximum values)	110
Table 5.5	C_{p-ave} comparison between bare VAWT, VAWT with original GF and VAWT with wedged shaped GF in different regimes of <i>TSRs</i> (<i>bold and italic fonts</i> in yellow highlights indicate the optimum C_{p-ave}).....	141
Table 5.6	Variation of slope line ratio of curved GF.....	146
Table 5.7	Variation of vertical line ratio of curved GF	146
Table 5.8	C_{p-ave} comparison between bare VAWT and VAWT with original GF, wedged GF and curved GF in various slope and/or vertical line ratios in different <i>TSR</i> regimes (<i>bold and italic fonts</i> in yellow highlights indicate the optimum C_{p-ave}).....	147
Table 6.1	Geometry specification of a base SUD	154
Table 6.2	Number of grid points along the width of the SUD	157
Table 6.3	Predicted C_{p-ave} values from four SUD locations compared to bare VAWT (<i>bold and italic fonts</i> in yellow highlights show the optimum cases)...	159

Table 6.4	Comparison of C_{p-ave} improvement due to a SUD of “both upward and downward” configuration in different $TSRs$ (bold and italic fonts in yellow highlights show the optimum cases).....	165
Table 6.5	Variations of the SUD’s inclination angle.....	173
Table 6.6	Comparison of the effect of inclination angle on the C_{p-ave} of VAWT with SUD (bold and italic fonts with yellow highlights show the optimum cases)	174
Table 7.1	Comparison of C_{l-ave} , C_{d-ave} and C_{l-ave}/C_{d-ave} over one turbine revolution between bare VAWT, VAWT with GF and VAWT with SUD in $TSR = 1.44$	184
Table 7.2	Comparison of C_{l-ave} , C_{d-ave} and C_{l-ave}/C_{d-ave} over one turbine revolution between bare VAWT, VAWT with GF and VAWT with SUD in $TSR = 2.64$	188
Table 7.3	Comparison of C_{l-ave} , C_{d-ave} and C_{l-ave}/C_{d-ave} over one turbine revolution between bare VAWT, VAWT with GF and VAWT with SUD in $TSR = 3.3$	189
Table 7.4	C_{p-ave} comparison between VAWT with GF and SUD, VAWT with GF, VAWT with SUD and bare VAWT	193
Table 8.1	Details of the number of elements for each grid and its C_{m-ave} prediction	208
Table 8.2	Comparison of experimental data of power coefficient (Castelli, Englaro and Benini, 2011; Castelli et al., 2010) and predicted averaged power coefficient of 2D and 3D models.....	212
Table 8.3	Comparison of averaged moment coefficient prediction between Elsakka (2020) and the present study at several locations along the span-wise direction of the blade	213
Table 9.1	Comparison of C_{d-ave} , C_{l-ave} and C_{l-ave}/C_{d-ave} between q3D VAWT with clean GF, VAWT with slit GF and VAWT with holed GF.....	234

List of Tables in Appendices

Table E.1	Detail of grid discretisation	306
-----------	-------------------------------------	-----

Chapter 1: Introduction

1.1 Study Background

Recently, the concern on global warming and climate change and the decline of fossil fuel sources has encouraged people to search and use renewable and clean energy sources (Ghasemian, Ashrafi and Sedaghat, 2017). Among all available sources, wind energy has become the most significant contributor to renewable energy growth in 2016 (BP PLC, 2017). As shown in Figure 1.1, the world's total installed wind capacity is about 539,581 MW, and it is continuing to increase in the future (Global Wind Energy Council, 2018).

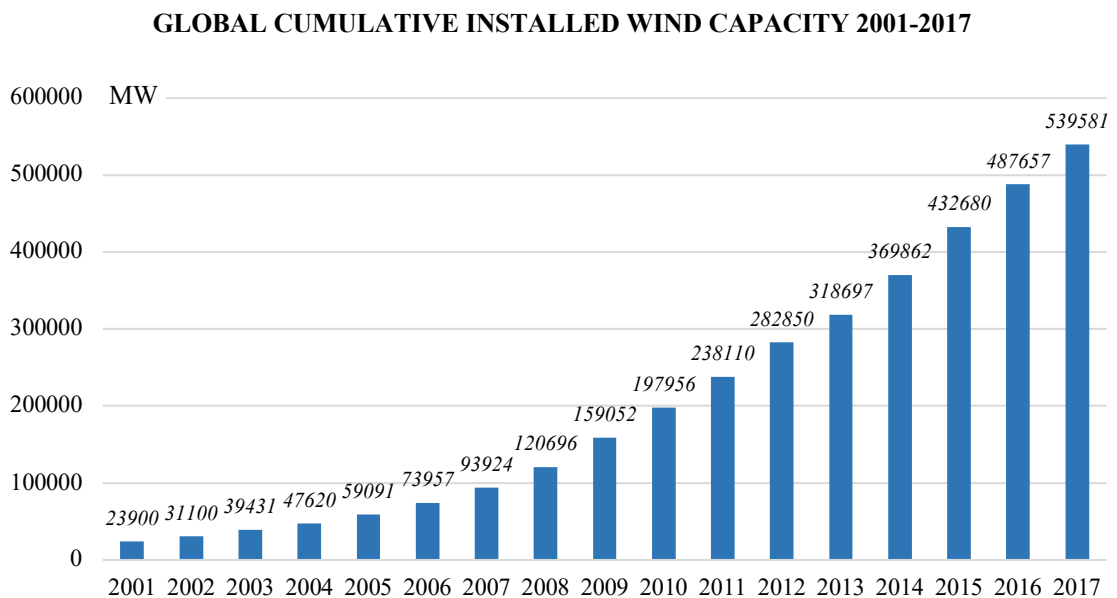


Figure 1.1 Global Cumulative Installed Wind Capacity (Global Wind Energy Council, 2018).

Since many years ago, humans have utilised wind energy in windmills for mechanical loads such as pumps and mills. Modern utilisation of wind energy is mostly for electricity generation by using wind turbines. Wind turbines have two main types, Horizontal Axis Wind Turbines (HAWTs) and Vertical Axis Wind Turbines (VAWTs). In the early 1990s, the researches in VAWTs were substantially reduced compared to researches in HAWTs as they have lower efficiency than HAWTs. Since then, HAWT technologies have become the leading wind turbine technology for onshore and high-speed wind systems (Crawford, 2012).

In recent years, the growing interest in utilising wind energy in low-speed wind regions, the high cost of the grid system and the concern of the wildlife damage have attracted people to apply wind turbines as power generation devices in low-speed wind and urban areas (Sranpat et al., 2017; Bhargav, Kishore and Laxman, 2016; Korprasertsak and Leephakpreeda, 2016; Bianchini, Ferrara and Ferrari, 2015). However, HAWT technologies are likely unsuitable for these areas mainly because of their lower economic feasibility in low-speed areas and lower stability, more easily affected by the wake and higher power loss in urban environments (Bhargav, Kishore and Laxman, 2016). Accordingly, VAWTs have been studied again as they give better performance than HAWTs for wind energy harvesting in these areas. Nevertheless, VAWTs current state of design development is still lagging behind HAWTs. To compete with HAWTs' power efficiency, complete knowledge of all the possible parameters influencing VAWT performance is crucial to allow system-level optimisation. Hence, research in VAWTs is still needed to prove whether VAWTs are worth investing in.

1.2 Motivation, Aims and Objectives of the Research

As mentioned above, to manage the increased energy demand and challenge of harvesting wind energy, especially in low-speed wind and urban areas, VAWTs have been investigated again as the potential technology to harvest wind energy in those mentioned areas. The design and performance of VAWTs that are still behind HAWTs are very appealing to be investigated. Hence, a small-scale straight-bladed VAWT is investigated as this type has more potential to be applied commercially.

The modelling approach is chosen as it is cheaper than the experimental method for evaluating the new design approach and geometry optimisation. Additionally, the modelling approach provides detailed information on the flow characteristics around the VAWT. Among several modelling approaches of a VAWT, Computational Fluid Dynamics (CFD) is selected due to its high-fidelity and reasonable computational cost compared to other modelling approaches.

The main aim of this study is to investigate the device that generate a higher performance improvement of lift-driven VAWT in all regimes of Tip Speed Ratio (*TSR*) operations (low, medium and high). Two main ways to improve the performance of a straight-bladed VAWT, i.e., using flow augmentation and dynamic stall control devices, are investigated. This study also evaluates the design optimisation to find the best design for each device. Furthermore, this study provides an in-depth understanding of the

aerodynamic flow-field and the characteristics behind improving the VAWT's performance caused by flow augmentation or a dynamic stall control device. Another aim of this study is to use the high-fidelity CFD method to predict the VAWT flow accurately and evaluate its performances for each regime of *TSRs*. Therefore, this study also performs in-depth evaluation of the choice of turbulence model. These mentioned aims are achieved by answering the following detailed objectives of the research.

- 1) **Building validated two-dimensional (2D) and three-dimensional (3D) VAWT CFD models** that can generate accurate predictions of the experiment result of the VAWT in all regimes of the *TSR*.
- 2) **Identifying the appropriate turbulence model** that can generate accurate prediction (overall performance and flow-field characteristics) in all regimes of *TSRs*. This study compares URANS and hybrid RANS-LES turbulence models to achieve this objective.
- 3) **Finding the best performance enhancement device** that can improve the performance of the VAWT across the *TSR* regimes. This study applies a dynamic stall control device (i.e., Gurney flap), a flow augmentation device (i.e., a straight upstream deflector) and integration of both devices into the VAWT configuration to fulfil this objective. This study also investigates the never previously applied blade shape modification device on a VAWT by applying 3D modifications of GF (i.e., adding slits and holes on GF).
- 4) **Improving the design optimisation** procedure by performing the design optimisation on the VAWT configuration (i.e., considering the rotational effects and blade-to-blade interaction) and in all *TSR* regimes. This study applies multiple parameter changes for GF optimisation by using the Taguchi Method (Qasemi and Azadani, 2020; Wang, Wang and Zhuang, 2018).

1.3 Key Questions to Address

Based on the background above and literature reviews, here are several key questions for guiding this study to answer the proposed aims of the project:

- 1) What are the domain sizes, and grid resolutions necessary to produce accurate simulation results?
- 2) What kind of turbulence models or their modified versions have minimum impact on physical results in all *TSR* regimes?

- 3) What are the accuracies of 2D and 3D VAWT CFD simulations on predicting experimental results?
- 4) What kind of blade modification and flow augmentation devices can effectively increase the inflow wind profile and improve the turbine's self-start behaviour and efficiency in all *TSR* regimes?
- 5) What is the appropriate optimisation method used to perform design optimisation? What is the optimum design of each enhancement device that can give an optimum improvement of VAWT performance in all *TSR* regimes?

1.4 Thesis Structure

The following paragraphs explain the ten chapters of this thesis.

Chapter 1 introduces the reason behind this study and the areas that will be contributed by this study. Following that, the goals of this study are explained to break down the contribution. Research questions also are presented to help this study fulfil the goals.

In **Chapter 2**, this study reviews the literature of this study critically. The first section explains the history, types, comparison of VAWTs with HAWTs and flow behaviour around VAWTs. Furthermore, the second section deliberates the types of performance enhancement that have been done and links to current research. Then, the methods of studied VAWTs, i.e., experimentally and numerically, are presented, including the benefits and drawbacks of several modelling VAWTs methods as this study is focused on numerical study. In the last section, the identified gap and potential future works are discussed.

Chapter 3 explains the methodologies used in the present study. This chapter also discusses all the parameters that are used in this study.

This study presents the model and validations of current 2D CFD model results against experimental data in **Chapter 4**. This chapter also discusses the investigation of the ability of chosen turbulence models to evaluate the performance of VAWT in all *TSR* regimes.

This study applies two methods to improve the performance of a VAWT, the first is by controlling the dynamic stall using blade shape modification. A Gurney flap (GF) is mounted around the trailing-edge of blades of a VAWT. The study of a VAWT with a GF is discussed in **Chapter 5**. The first section of this chapter explains the model and grid generation of a 2D VAWT with a GF. The method that is used for simultaneous

design optimisation is discussed in the next section. Then, the results of varying GF geometries and shapes in three *TSR* regimes, i.e., low *TSR* = 1.44, medium (optimum) *TSR* = 2.64 and high *TSR* = 3.3, is explained.

The second method of enhancing the performance of a VAWT is by using flow augmentation devices. In this present study, a straight plate deflector is positioned upstream of the VAWT in order to increase the performance of the VAWT. **Chapter 6** covers all the investigations of the use of a straight upstream deflector (SUD) to improve the performance of VAWTs by using 2D CFD simulations. Discussion about the model, grid generation and design optimisation can be found in this chapter. The last part of this chapter deliberates the effect of varying deflector parameters such as location, width and inclination angle to the performance enhancement of VAWT in all *TSR* regimes.

After finding the best design of GF and SUD for all *TSR* regimes, the comparison of GF and SUD performance to improve the performance of a VAWT for each *TSR* regime is further discussed in **Chapter 7**. This chapter also presents the study of a new attempt to combine a GF and a SUD to improve the performance of a VAWT.

To verify the CFD simulation results of a 2D VAWT model, a 3D VAWT model is investigated to improve the model accuracy in **Chapter 8**. This chapter explains in the first section the model and grid generation of the 3D VAWT. The results of the 3D VAWT model simulation and their comparison with the 2D model are discussed in the following section.

In order to further improve the performance of VAWTs, this study also introduces flow control device modification by modifying the GF mounted in the blades of the VAWT. 3D modifications of the GF are applied by adding slits and holes in the GF. **Chapter 9** presents all the evaluation of the use of GF with slits and GF with holes to improve the performance of a VAWT by performing quasi-3D CFD simulations. This chapter also discusses the comparison results of several aerodynamic characteristics such as lift coefficient, drag coefficient, moment coefficient and power coefficient between a VAWT with a clean GF, a VAWT with a slit GF and a VAWT with a holed GF.

Finally, this thesis is concluded in **Chapter 10**. The summary of the findings of this study is explained in this chapter. This chapter also deliberates the explanations about the novelty, contributions, recommendations, and future works related to this study.

Chapter 2: Literature Reviews

As described in Chapter 1, recently, VAWTs have attracted many researchers to study this topic again as there is more demand for electricity production based on wind energy in low-speed wind and urban areas due to the better overall performance of VAWTs in the low-speed wind and urban areas to HAWTs. However, as VAWTs have lower power generation compared to HAWTs and their design is less mature compared to HAWTs, it is worthy of understanding the flow behaviour around VAWTs and what mechanism can help to improve the performance of VAWTs so a comprehensive approach to designing a mechanism to improve the performance of VAWT can be achieved.

Therefore, Chapter 2 presents a review of the flow behaviour of VAWTs, the mechanisms that have been used to improve the performance of VAWTs and methods to analyse VAWTs. This chapter is divided into three sections to describe VAWTs and their characteristics. The first section discusses the history, type and comparison of VAWTs with HAWTs. As the present study focus on lift-driven VAWTs, this section also explains the flow behaviour around lift-driven VAWTs. After that, the type of performance enhancement approaches to improve the performance of lift-driven VAWTs is discussed in Section 2.2. Lastly, Section 2.3 deliberates VAWTs investigation methods, i.e., experimental and modelling methods.

2.1 Overview of VAWTs

2.1.1 *Types of VAWTs*

Based on their rotor blade design, VAWTs are classified into two types, namely drag-driven and lift-driven VAWTs. Drag-driven VAWTs use momentum transfer whilst lift-driven VAWTs utilise aerodynamic force to generate power (Sutherland, Berg and Ashwill, 2012). The blade shapes of drag-driven VAWTs are usually straight or concave cups that take advantage of the wind's drive forces to rotate the turbine. For lift-driven VAWTs, the interaction between wind and their aerofoil shaped blades will produce aerodynamic lift forces which rotate the turbine (Wong et al., 2017). Savonius rotors are the most common drag-driven VAWTs, whereas Darrieus rotors dominate lift-driven VAWTs (see Figure 2.1). In performance comparison, drag-driven VAWTs have better starting ability but lower efficiency than lift-driven VAWTs (Roy and Saha, 2013). Overall, due to their higher pressure coefficient, Darrieus Vertical Axis Wind Turbines

(DVAWTs) stand out among the other VAWTs (Jin et al., 2015). Moreover, as they give the highest power coefficient (C_p) compared to other types of VAWTs, these types of VAWTs commonly have been used as the starting point for further studies on the improvement of VAWT performance due to their capability in large-scale power production.

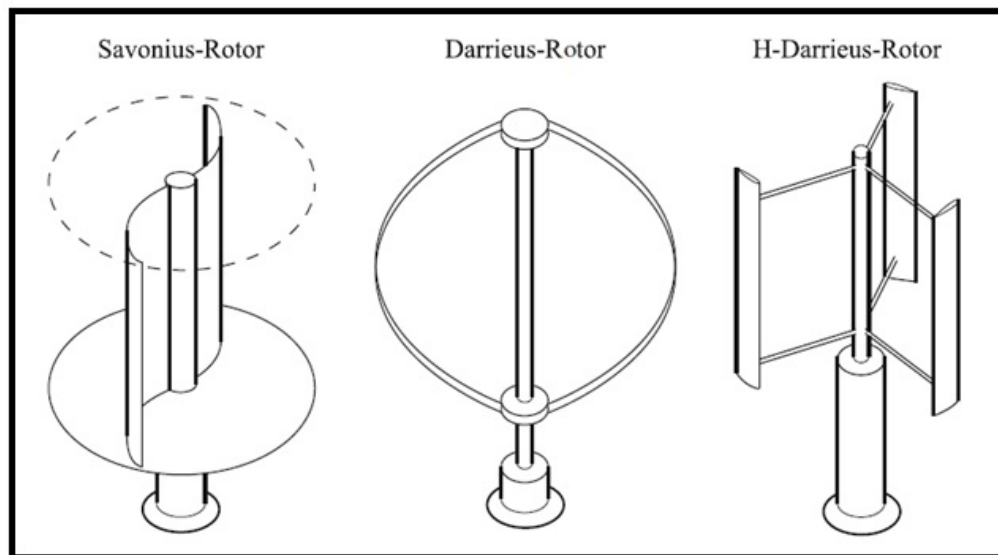


Figure 2.1 Types of Vertical Axis Wind Turbines (Anon., 2017).

There are several kinds of DVAWTs. The usual design is called "egg-beater" Darrieus VAWT. This DVAWT has blades with a shape similar to an egg-beater designed to avoid tremendous centrifugal stresses on the blades as this shape can centre the rotating mass not far from the axis (Sutherland, Berg and Ashwill, 2012). The other type is H-type or Giromill Darrieus VAWT. This type of VAWT has straight blades connected to the central tower with horizontal connection supports. H-type or Giromill Darrieus VAWT offer a more straightforward blade design compared to the previous type. However, it has several drawbacks such as a larger structure, it needs stronger blades, less efficiency and requires motors to start (Sutherland, Berg and Ashwill, 2012). Nevertheless, due to it being cheaper and easier to build, having a lighter tower structure and its generator being positioned on the ground; H-type DVAWTs are most commonly used to replace HAWTs for electricity generation where HAWTs are unsuitable. Hence, many studies have been done to improve H-type DVAWTs' efficiencies and self-starting abilities to be commercially competitive with HAWTs. Therefore, this study also utilises the H-type VAWT to evaluate the proposed modifications for performance improvement in VAWTs.

2.1.2 Comparison of VAWTs with HAWTs

The significant difference between VAWTs and HAWTs is their rotational axes' orientation relative to the wind direction. The HAWTs are parallel to the direction of the wind whilst the VAWTs are perpendicular to the direction of the wind (Crawford, 2012). VAWTs do not generally generate positive torque when the approaching wind stream sweeps the surface of their rotating blades. Hence, the negative torque that operates in the counter-direction can reduce the overall performance of the VAWTs. As a result, VAWTs generally produce a lower efficiency compared to HAWTs.

Moreover, in sizeable ground-based wind turbines, VAWTs have a lower economic feasibility compared to HAWTs. VAWTs have difficulty self-starting at low wind speeds compared to HAWTs which will start rotating independently, even in very light wind. Other downsides of VAWTs are that they are subject to cyclic loading and structural resonance, lack of reliable braking system and have higher operating costs (Zanforlin and Deluca, 2018; Crawford, 2012). Therefore, VAWTs were abandoned in the early 90s. Since then, the technology of HAWTs have evolved and generally matured. They became the leading technology in electricity generation based on wind energy, particularly for onshore and high wind systems.

On the other hand, due to the concern of high cost on the grid system, manufacturing and transportation and the increasing awareness of the importance of renewable energy also have triggered many researchers to evaluate the possibility of installing wind turbines near urban environments and low-speed wind areas (Sranpat et al., 2017; Korprasertak and Leephakpreeda, 2016; Bhargav, Kishore and Laxman, 2016; Bianchini et al., 2015). However, HAWTs are likely not suitable for near urban environments and low-speed wind areas.

HAWTs usually face low economic feasibility and operation time in low-speed wind areas because the wind speed does not allow the turbine always to generate excess electricity distributed to the national grid system (Akour et al., 2018). Alongside it, high costs in HAWT installation and maintenance are the reasons behind their low economic feasibility in low-speed wind areas. Hence, the electricity generated from the turbine will be very pricy and challenging to compete with fossil-fuel-generated electricity.

For the urban environment, the development of wind turbine utilisation in this area is challenging because the limited space and the wind profile in these areas are random with rapid fluctuation in terms of magnitude, direction, and high turbulence level. HAWTs are likely not suitable for this kind of wind profile as they generally only can be

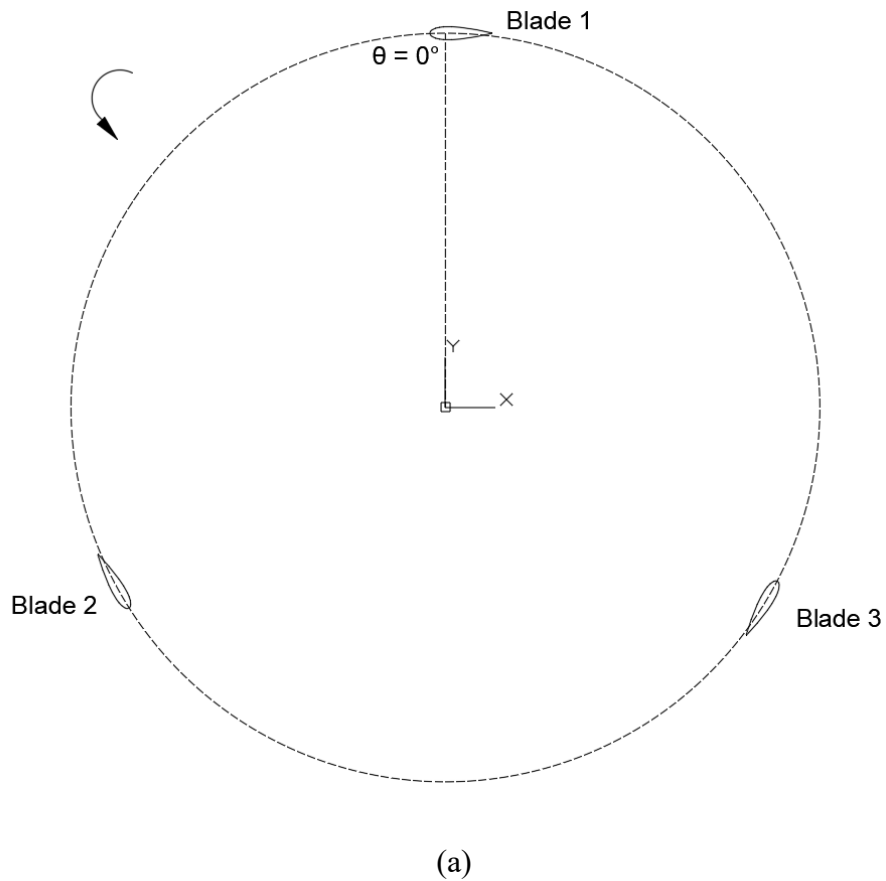
operated in a single wind direction. Hence, they need a yaw mechanism to change their facing direction to the wind, decreasing their reliability (Lee and Lim, 2015). In addition, as HAWTs are very sensitive to surrounding turbulence fluctuation and wake, they will primarily generate lower power in urban areas compared to open areas. Moreover, HAWTs have drawbacks in producing high noise pollution, which is not compatible with application near habitation areas. Their physical features also do not give an excellent aesthetical level to their surrounding areas. There is also a concern in public safety (Ahmed and Cameron, 2014; Ishugah et al., 2014). These concerns cause HAWTs to be moderately ineffectual in urban circumstances and facing resistance from residents.

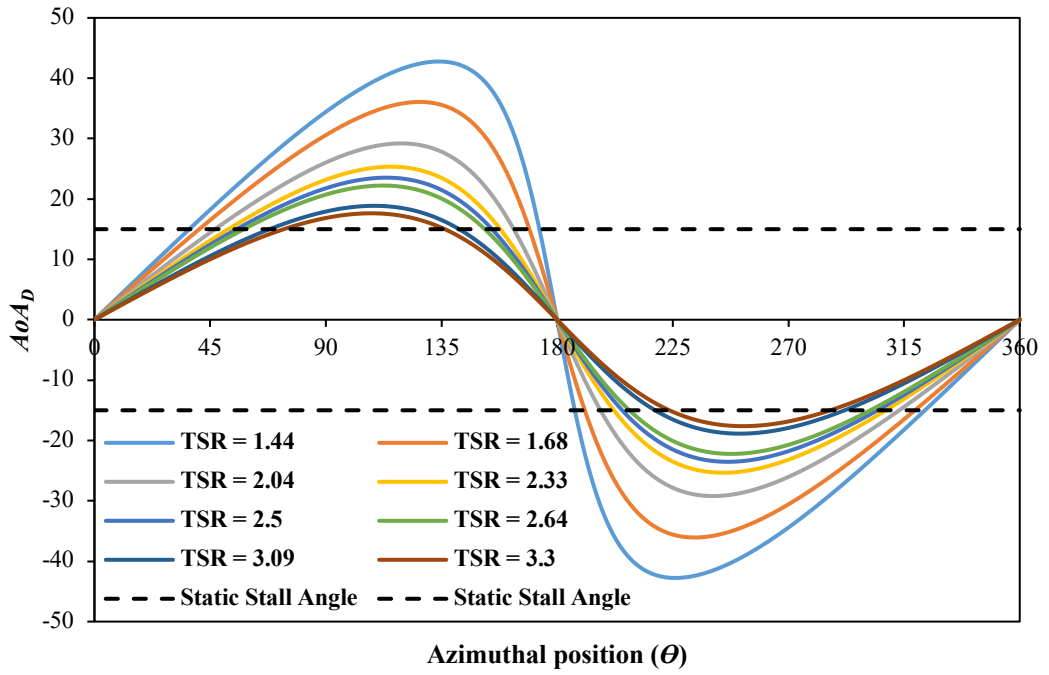
Whilst HAWTs face several problems in the low-speed wind and in urban areas, as mentioned above, VAWTs have generally better performance than HAWTs in these areas. In low-speed wind areas, VAWTs are competitive due to their easier maintenance (because the generator and the gearbox are installed near the ground), less noise, lower cut-in speed and the absence of a yaw mechanism (which can decrease the complexity of the system and increase turbine reliability) (Shires, 2013). Regarding urban environment areas, as HAWTs are relatively unsuitable to be applied in this area, VAWTs have mainly been utilised in urban and nearby territories for wind power generation. They have a moderately low environmental impact and produce more significant power outputs in high turbulence areas where unsteady and skewed wind conditions are present (Bhargav, Kishore and Laxman, 2016). Furthermore, there is no need for a yaw mechanism due to its ability to generate power from any direction; low cut-in wind speed, and relatively simple configuration to integrate with urban structures and foundations. These are among other benefits of VAWTs for urban environment applications.

2.1.3 Flow characteristics around lift-driven VAWTs

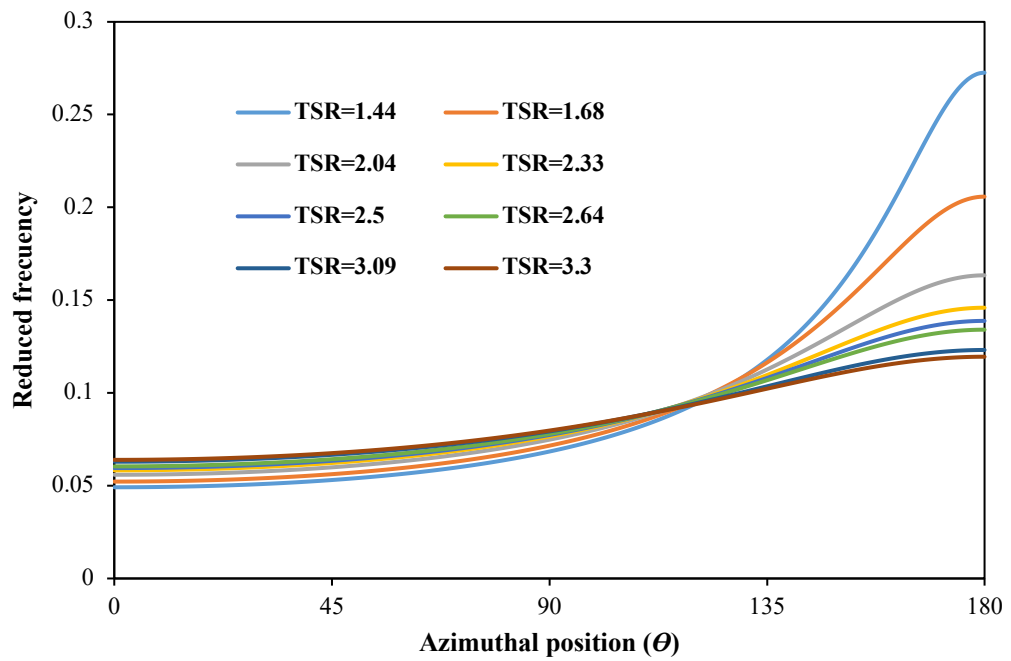
In general, flow around VAWTs has more complexity than flow surrounding HAWTs. When operating, VAWTs are subject to different flow behaviours and unsteadiness depending on the ratio between the tangential speed of the blade tip and the actual speed of the incoming wind, the *TSR*, its operation. Dynamic stall is mostly part of standard operating conditions. VAWTs have a parameter called the geometrical angle of attack (AoA_D), which varies in each rotation of the VAWT. The change in this parameter also varies as the *TSR* of the VAWT changes. Therefore, it can be utilised as a parameter to analyse the aerodynamic and flow behaviour of the VAWT. Figure 2.2 (b) and (c) illustrate the AoA_D variation and reduced frequency in different *TSR*, based on the

calculation of AoA_D of the blade NACA 0021 with chord length 85.8 mm that used in three-straight-bladed VAWT of Castelli, Englaro and Benini (2011) with wind speed U_∞ equal to 9 m/s. Noting that, in this case the zero azimuthal angle (θ) is the position of the blade 1 as depicted in Figure 2.2 (a). As shown in Figure 2.2 (b) and (c), the regime of VAWT operation can be divided into three regimes as follows.





(b)



(c)

Figure 2.2 (a) Illustration of the azimuthal position equals to 0, (b) Geometrical angle of attack, and (c) Reduced frequency distributions in different $TSRs$ of the case of Castelli, Englaro and Benini (2011).

2.1.3.1 Low regime of *TSR*

Malael, Dumitrescu and Cardos (2014) mentioned that low regime of *TSRs* falls under *TSR* equal to or lower than two. Based on the investigation using the straightforward motion of oscillating aerofoils (Wang et al., 2010), it has been found that in this *TSR* regime, the motion of aerofoils has both pitch and plunge components, and they have different peak positions in different values of *TSR*. As shown in Figure 2.2 (a), the blades of VAWTs can experience higher angles of attack (up to 27.7°) which is beyond the stall angles of a static aerofoil (normally 15° - 15°) for the most azimuthal positions in this *TSR* regime. This causes very small positive or sometimes even negative torque production, which leads to the poor self-starting ability of VAWT in low-speed wind or low *TSR* operation (Malael, Dumitrescu and Cardos, 2014).

It is known that flow surrounding VAWTs experiences a high-level unsteadiness. As shown in Figure 2.2 (b), the reduced frequency that can indicate the level of unsteadiness of the VAWT jumps to a higher value and shows a wider range of values in low regime of *TSRs*. Malael, Dumitrescu and Cardos (2014) categorised this level as the second level of unsteadiness related to an unsteady phenomenon called dynamic stall with drag reduction. Blades of a VAWT in low regime of *TSRs* will experience two types of dynamic stall. These two types of dynamic stall reflect different parts of the static lift characteristics in which the VAWT blade operating in low regime of *TSRs* presents a particular double peak characteristic, with two peak values one at low static angle of attack (around 10°) and the other at high static angle of attack (about 27°) (see Figure 2.3). The first is called dynamic lift stall. This stall results from the combination of the boundary layer's separation and the unsteady motion of the aerofoil (Wernert et al., 1996). This dynamic lift stall is very dependent on Reynolds number (Re). The second dynamic stall is the dynamic drag stall, which is independent of Re . This stall only exists when the blades are operating in a closed flow-field. The turbine's rotor will act as a force machine to move a separated air volume towards the blade radially. This term is used to describe the delay in the drop of the second static stall lift coefficient on the blade passing downwind of the turbine (azimuthal position $\geq 180^\circ$). Dynamic drag stall can generate a slight lift and significant drag reduction for a short period of time in low regime of *TSRs*, which is very important in the continuity of torque production that is directly related to the self-starting ability of VAWTs (Malael, Dumitrescu and Cardos, 2014).

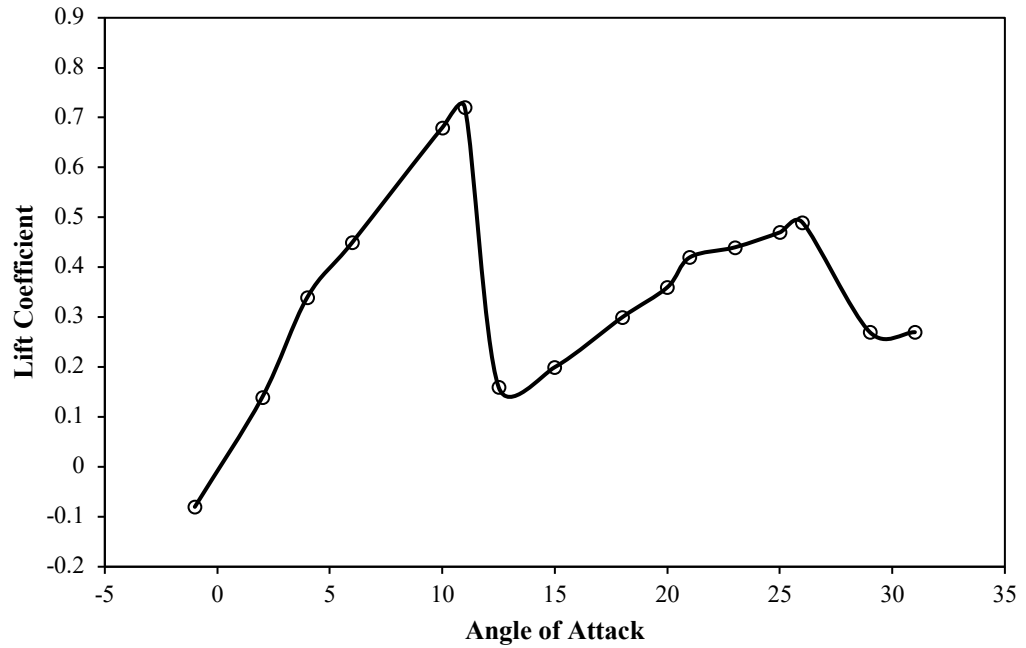


Figure 2.3 Typical lift coefficient distribution over angle of attack of static NACA 0021 in low Reynolds number (140000) (Holst et al., 2018).

2.1.3.2 Medium regime of *TSRs*

This regime is for *TSRs* higher than two until the optimum *TSR* for the particular geometry is reached (For Castelli, Englaro and Benini (2011) case $TSR = 2.64$). The relative wind speed and the angle of attack of VAWT blades in this *TSR* regime will experience a cyclic variation similar to a sinusoidal pitching blade in a stationary frame reference (Malael, Dumitrescu and Cardos, 2014). It also can be seen in Figure 2.2 (b) that in this *TSR* regime, the VAWT blades will have a small increase of AoA_D s beyond static stall angle compared to the low regime of *TSRs* (up to 10.3° higher than stall angles of the static aerofoil). As a result, the flow can be considered chiefly attached to blade surfaces and the level of flow unsteadiness of the VAWT will also decrease, which is called by Malael, Dumitrescu and Cardos (2014) as “first-level unsteadiness”. In this *TSR* regime, the optimum *TSR* operation is obtained due to the strong shed wake of the turbine and significant induction velocities (Dixon, 2008).

2.1.3.3 High regime of *TSRs*

A VAWT will have a smaller range beyond static stall in high regime of *TSRs* than low and medium regimes of *TSRs* (up to 5° higher than stall angles of static aerofoil). Even though the turbine can operate at the ranges of no static stall condition, the power

production will decrease due to the higher rotation of the turbine blades, compared to the incoming wind with the addition of high vibrations and drag and tip losses (Ragheb and Ragheb, 2011). Hence, a VAWT's loss in power production is not only because of the dynamic stall but also since the rotor can act as a solid wall obstruction due to high rotation speed (Bakırcı and Yılmaz, 2018).

2.2 Performance Enhancement of Lift-Driven VAWTs

As mentioned above, VAWTs are likely to be better for harvesting wind energy in low-speed wind and urban areas than HAWTs. However, to compete with HAWTs commercially, two main problems must be fixed so that VAWTs can be considered again as wind energy commercial harvesting technology.

- 1) Low efficiency. It is due to VAWT blades' inability to always generate positive torques in one full turbine rotation. On average, the efficiency of VAWTs falls between 30% and 40% (see Figure 2.4) (D'Ambrosio and Medaglia, 2010). It is still below the theoretical maximum efficiency achievable by HAWTs, called the Betz Limit (59%).

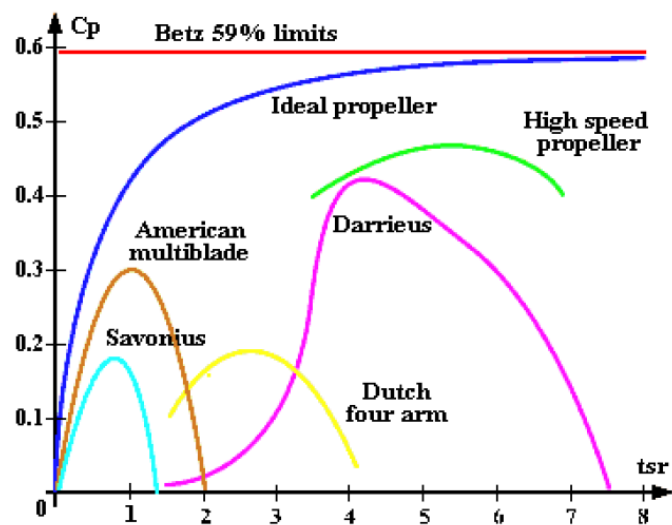


Figure 2.4 Comparison of power coefficient (C_p) distribution for different types of wind turbines (D'Ambrosio and Medaglia, 2010).

- 2) Low self-starting ability. As VAWTs operate at lower wind speeds, their incoming wind speed can be deficient in low regime of $TSRs$. Due to both static and dynamic stalls at most azimuthal positions, VAWTs are most likely to produce very low positive or even negative torque (Dixon, 2008). Hence, they will have difficulty rotating by themselves during starting point. As a result, they usually have a generator

or motor to drive the VAWTs to start the rotation until their operating point, i.e., the point at which VAWTs can spin freely. The addition of external power sources is not practical to adopt on a small VAWT system and is difficult to maintain.

Many studies have been done previously to address those problems mentioned above. Previous studies related to improving the efficiency and self-starting ability of lift-driven VAWTs will be discussed in the following sections. Their advantages and disadvantages will be underlined along with the possibility of future work.

2.2.1 Performance enhancement of lift-driven VAWTs by using blade modifications

Most studies for improving power efficiency and self-starting ability of lift-driven VAWTs were associated with dynamic stall control by using active or passive flow controls, or increasing incoming wind speed and focusing the direction of the incoming wind to the turbine by using flow augmentation devices. Active flow controls such as a synthetic jet (Xu et al., 2016; Yen and Ahmed, 2014) and flapping flaps (Yang et al., 2017) have been implemented in the blades of lift-driven VAWTs. These small additions influence flow separations and unsteady (fluctuating) aerodynamic loads to reduce the dynamic stall of turbine blades, and as a result, they can improve the power production of lift-driven VAWTs. However, the active flow controls are sometimes not practical for small-scale VAWTs, which are usually deployed in low-speed wind areas or urban environments. The need for an external power source to drive active flow control device(s) can introduce extra design and manufacturing complexity, reduce ‘net’ power production, increase maintenance cost and maintenance difficulty. In this regard, passive flow controls are superior. Primarily they do not need an external power source.

There are some studies on implementing passive flow control devices to ease the dynamic stall occurring on the blades of lift-driven VAWTs. It has been proven that this method can enhance the efficiency of VAWTs and improve self-starting ability by decreasing or even removing the negative torque production at low incoming wind speed (Bianchini et al., 2019; Sobhani, Ghaffari and Maghrebi, 2017; Wang and Zhuang, 2017; Zamani et al., 2016). The summary of passive flow control devices that have been integrated into the blades or aerofoils of lift-driven VAWTs is found in Table 2.1. The detailed discussion on the review of passive flow control devices (i.e., blade modification method) that have been implemented to improve the performance of lift-driven VAWTs, including their advantages and disadvantages, limitations of present work, and recommendations for future studies, can be found in Appendix A.

Table 2.1 Summary of blade shape modifications that have been integrated into lift-driven VAWTs.

No	Authors	Modifications	Figures	Description	Type of Aerofoil	Methodologies	Results
1	Sobhani, Ghaffari and Maghrebi (2017)	Inward dimple (cavity)	Fig. A.1	Half-circle cavity	NACA 0021	<ul style="list-style-type: none"> 2D CFD simulation (Fluent, $k-\omega$ SST) 2D full three-straight-bladed VAWT simulation (including rotational effects) 	Optimum output power 20% higher than clean blades
2	Ismail and Vijayaraghavan (2015)	Inward dimple (cavity) with GF	Fig. A.2	Half-circle cavity with GF addition near trailing-edge of aerofoil	NACA 0015	<ul style="list-style-type: none"> 2D CFD simulation (Comsol, $k-\omega$ SST) Single static aerofoil simulation 	Optimum average tangential force 35% higher than clean aerofoil
3	Choudhry, Arjomandi and Kelso (2016)	Vortex generator	Fig. A.3 (a)	Counter-rotating VGs are mounted, covering the entire span of the leading-edge aerofoil	NACA 0021	<ul style="list-style-type: none"> Experiment Single static aerofoil 	Drag 27% lower than clean aerofoil
4	Yan et al. (2019)	Vortex Generator	Fig. A.3 (b)	Single counter-rotating VG at leading-edge of aerofoil	NACA 0018	2D CFD simulation (single static aerofoil) for geometries evaluation (Fluent, $k-\omega$ SST)	Optimum power generation 50% higher than clean blades in high regime of $TSRs$

						3D three-bladed VAWT CFD simulation for confirming the improvement (Code Saturne, Large-eddy simulation (LES))	In low regime of <i>TSRs</i> , the power generation was lower than clean blades
5	Chen et al. (2015)	Opening Aerofoil	Fig. A.5	Open the trailing-edge part of the aerofoil	NACA 0015	2D CFD Simulation (Fluent, $k-\omega$ SST)	Optimum geometries could increase the average torque production around 66% higher than clean blades at the starting point (low regime of <i>TSRs</i>)
						2D Full Three-straight-bladed VAWT simulation (including rotational effects)	Worse C_p generation in a high regime of <i>TSRs</i> compared to the original configuration
6	Zamani, Maghrebi and Moshizi (2016); Zamani, Maghrebi and Varedi (2016)	J-shaped Aerofoil	Fig. A.6	Remove the trailing-edge part of the pressure side of the aerofoil	NACA 0015	2D CFD Simulation (single static aerofoil) for geometries evaluation (OpenFoam, $k-\omega$ SST)	Average power production two times higher than clean blades in the lowest <i>TSR</i>
						3D Three-bladed VAWT CFD Simulation for	Worse C_p generation in high regime of <i>TSRs</i>

	and Zamani, et al. (2016)					confirming the improvement (OpenFoam, $k-\omega$ SST)	compared to the original configuration
7	Mohamed et al. (2020)	y -direction Slotted Aerofoil	Fig. A.7	Generate a gap at the leading-edge of aerofoil along <i>the y</i> -direction	NACA 0018	2D CFD Simulation (single static aerofoil) for geometries evaluation (Fluent, $k-\epsilon$ realisable)	C_p could be up to two times higher than clean blades in TSR equal 2
						2D Three-bladed VAWT CFD Simulation for confirming the improvement (Fluent, $k-\epsilon$ realisable)	Worse C_p generation in a high regime of $TSRs$ compared to the original configuration. Optimum TSR was lower than clean blades
8	Acarer (2020)	x -direction Slotted Aerofoil	Fig. A.8	Generate a gap in the aerofoil along <i>the x</i> -direction	DU12-W262	2D CFD Simulation (single static aerofoil) for geometry evaluation (Fluent, Spalart-Allmaras)	Could improve the C_p ranging from 3.5% - 9.5 % in medium and high regimes of $TSRs$
						2D Three-bladed VAWT CFD Simulation for confirming the improvement (Fluent, Spalart-Allmaras)	Worse C_p generation in low regime of $TSRs$ compared to the original configuration. Optimum TSR was higher than clean blades

9	Chougule, Rosendahl and Nielsen (2015)	Double element aerofoil	Fig. A.10 (b) and A.10 (c)	Divided aerofoil into two parts: slat aerofoil and main aerofoil	DU06-W200	Experiment (single static aerofoil) for geometry evaluation	It could improve the maximum C_p by up to 90% compared to clean blades in low until medium values of wind speeds
						2D three-straight-bladed VAWT Double Multiple Stream Tube Method (DMST)	Worse C_p generation in high wind speeds compared to the original configuration
10	Srihari et al. (2019)	Five-elements aerofoils	Fig. A.11 (a) and A.11 (b)	Divided aerofoil into five parts: two slat aerofoils, main aerofoil and two slot aerofoils	DU06-W200	Experiment	Could produce positive torque in low regime of $TSRs$
						Three-straight-bladed VAWT	Generated similar C_p compared to original VAWT in a high regime of $TSRs$
							Worse C_p generation in medium and high regimes of $TSRs$
11	Wang and Zhuang (2017)	Leading-edge Serrations	Fig. A.12	Modify the blade by using serration at the leading-edge like the morphology of	NACA 0018	3D two-straight-bladed VAWT CFD Simulation (Star-CCM+, $k-\varepsilon$ realisable)	Increased the maximum lift coefficient by 25%
							The power performance increased

				humpback whales			by around 50.1% in low-speed wind
							Worse C_p generation in high wind speed
12	Zhang et al. (2019)	Winglet	Fig. A.13	Mounting winglet in the tip of the blade	NACA 0015	3D single blade isolated CFD simulation for geometries evaluation (Fluent, $k-\omega$ SST)	Could improve C_p up to 10.5% in medium regime of $TSRs$
						3D two-straight-bladed VAWT CFD Simulation for confirming the improvement (Fluent, $k-\omega$ SST)	No information of the performance in low and high regimes of $TSRs$
13	Yan, et al. (2020); Bianchini, et al. (2019); Zhu, et al. (2019); Malael, Bogateanu and Dumitrescu (2012)	Gurney flap	Fig. A.14	Mounting GF at the trailing-edge of aerofoil	NACA 00series (symmetric aerofoil)	All studies used 2D CFD simulation (single static aerofoil) for geometries evaluation (Fluent, URANS)	GF mostly could have a significant impact on C_p improvement in low and medium regimes of $TSRs$
						All studies applied 2D three-straight-bladed VAWT CFD Simulation for confirming the improvement (Fluent, URANS)	Whilst Bianchini et al. (2019) mentioned GF could produce better C_p for all regimes of $TSRs$, Yan et al. (2020) stated that GF could only

							improve C_p in low and medium $TSRs$
14	Choudhry, Arjomandi and Kelso (2016)	Leading-edge Micro-cylinder	Fig. A.15	Installing micro-cylinder in front of leading-edge of aerofoil	NACA 0021	Experiment	Delayed the unsteady flow separation around 25% in lower pitching rate
						NACA 0021 Aerofoil with pitching effect to include the rotational effects	5% delay on unsteady flow separation in higher pitching rate
							Decreased drag generation

Based on literature reviews shown in Table 2.1, it can be concluded that passive flow control devices can improve the performance of lift-type VAWTs by easing dynamic stall and as a result, the lift generation of lift-type VAWTs are improved. Conversely, the addition of passive flow control devices also increases the drag generation of the turbines. Hence, the geometry of passive flow control devices and their location on the blade of the turbines need to be considered carefully to ensure they can generate higher lift without adding too much drag so as to retain a higher lift-to-drag ratio. Additionally, most passive flow control devices (except for vortex generators and slotted aerofoils in x -direction) have performed well in enhancing the power generation of lift-type VAWTs in low incoming wind speed or low regime of TSR operation. However, in medium and high incoming wind speeds or medium and high regimes of TSR operation, their ability to improve the power generation of lift-type VAWTs decreases or even produces worse power generation than bare VAWTs. This is mainly based on the fact that when the incoming wind speed or regimes of TSR operation increases, the dynamic stall angle of lift-type VAWTs decreases. Hence, the ability of passive flow control to ease dynamic stall of lift-type VAWTs cannot be used effectively in medium and high incoming wind speeds or medium and high regimes of TSR operation. Lastly, most previous studies were performed merely for geometry optimisation using a single stationary aerofoil or in one regime of TSR operation. However, it is evident that the effect of the blade rotation on the power generation of the VAWT and the behaviours in different TSR regimes are significant. Thus, it is important to carry out geometric optimisation on real configurations (not just a single stationary aerofoil) of VAWTs in all regimes of $TSRs$ in future studies.

2.2.2 Performance enhancement of lift-driven VAWTs by using flow augmentations

As mentioned above, besides using dynamic stall control to enhance the power efficiency and self-starting ability of lift-driven VAWTs, flow augmentation devices have also been deployed in lift-driven VAWT configurations for the same purposes. These devices usually help lift-driven VAWTs to generate higher positive torques by guiding the wind to an optimum AoA of the VAWTs, increasing incoming wind speed and focusing the direction of the incoming wind to the turbine. Flow augmentation devices are divided into two types based on the flow's augmented direction, namely single directional flow augmentation and omnidirectional flow augmentation. Previous studies have shown the success of these devices to improve the performance of VAWTs. Hence,

the summary of flow augmentation devices that have been integrated into lift-driven VAWTs can be found in Table 2.2. The detail of the review of flow augmentation devices that have been implemented so far to improve the performance of VAWTs, including their advantages and disadvantages, limitations of present work and recommendations for future studies, is presented in Appendix B.

Table 2.2 Summary of flow augmentation devices that have been integrated into lift-driven VAWTs.

No	Authors	Flow Augmentation Methods	Figures	Description	Type of Aerofoil	Methodologies	Results
Single Directional Flow							
1	Takao et al. (2009)	Guide Vane Row and Tail Vane	Fig. B.1	Placed a guide vane row with three arc plates upstream of the VAWT and tail vanes as the yaw mechanism downstream of the VAWT	NACA4518	An experiment of three-straight-bladed VAWT	<p>Maximum of C_p of the turbine rose 1.5 times</p> <p>Generated lower power than the original turbine in low regime of $TSRs$ due to the radical change of the angle of airflow inlet causing by the guide vane row</p>
2	Santoli et al. (2014)	Convergent Duct	Fig. B.2	Covered VAWT with convergent duct	No information	<p>3D CFD of three-straight-bladed VAWT (Fluent, no information of turbulence model)</p> <p>Site test using a prototype</p>	<p>Venturi in the convergent duct configuration could increase the wind speed and direct the wind to the turbine</p> <p>Improved the power generation of the turbine by around 125% in low-speed wind and 30% at high wind speed</p>

							Very difficult to be applied in practice as the large duct size will need a strong support structure, thereby increasing the manufacturing and maintenance cost
3	Letizia and Zanforlin (2016)	Diffuser	Fig. B.3 (a)	Applied diffuser formed by two Selig 1223 wings with a zero AoA around the rotor hub of VAWT	NACA 0012	2D CFD-BEM methods with Dynamic stall model (no information of solver and turbulence model) of three-straight-bladed VAWT	Could improve the C_p by almost four times higher than the bare turbine
4	Watanabe, Takahashi and Ohya (2016)	Diffuser	Fig. B.3 (b)	Applied diffuser called wind lens around VAWT	NACA aerofoil series (no information about the series number)	An experiment of a two-straight-bladed VAWT	<p>The curved-surface-type diffuser generated higher power augmentation than the flat-panel-type diffuser</p> <p>Could improve the power generation up to 2.1 times than bare turbine</p> <p>Improved the power production in all TSR regimes</p>

							Very difficult to be applied in practice as the large diffuser size will need a strong support structure, thereby increasing the manufacturing and maintenance cost
5	Stout et al. (2017)	Curved Plate	Fig. B.4	Placed curved plate upstream of the VAWT	NACA 7715	2D CFD of three-straight-bladed VAWT for geometries optimisation (Fluent, $k-\epsilon$ RNG)	Curved plate at downward areas of the upstream of the turbine could improve the power generation up to around 2.2%
						An experiment of the optimum design prototype	Power production got worse than the bare turbine when curved plate placed at the upward areas
6	Kim and Gharib (2013) and Kim and Gharib (2014)	Straight Plate	Fig. B.5 (a)	Put straight plate deflector at the middle of upstream of two VAWTs that have different rotation directions.	No information	An experiment of commercial two-counter-rotating five-straight-bladed mini VAWT	Performance of the turbines improved due to the increase of local wind velocity caused by the proper position of the deflector
							The deflector caused worse performance than the original turbine if it is located inside the streamline of the flow

							Increased the maximum C_p by approximately three times and improved TSR by 26% compared to bare turbines
							Only limited for VAWT with high solidity and operated in low power coefficient and low Reynolds number regime (low regime of $TSRs$)
7	Jin et al. (2018)	Straight Plate	Fig. B.5 (b)	Positioned a straight plate deflector at the middle of upstream of two counter-rotating VAWTs	NACA 0021	3D CFD of two-counter-rotating three-straight-bladed VAWT (Fluent, $k-\omega$ SST)	Improvement of VAWT performance caused by the presence of a deflector is dependent on the geometry and the location of the deflector
							Could give improvement for the VAWT with lower solidity and higher TSR operation
8	Wong, et al. (2018a) and Wong, et al. (2018b)	Straight Plate	Fig. B.5 (c)	Placed straight plate in downward of the upstream region of VAWT	NACA 0021	3D CFD of two-straight-bladed VAWT (Fluent, $k-\omega$ SST)	Power improvement is very sensitive with the location of the deflector in x and y directions and the height and inclination angle of the deflector
							Could improve C_p by 33%

						An experiment of two-straight-bladed VAWT	Limited for VAWT with low solidity and low Re operation as the $TSRs$ only range between 0.2 and 1.2
Omnidirectional Flow							
9	Chong et al. (2013)	Omnidirectional Guide Vane (ODGV)	Fig. B.6 (a)	Placed guide vane called ODGV that surround VAWT	NACA 0015	2D CFD of single-straight-bladed VAWT for performance evaluation in different TSR value (Fluent, $k-\omega$ SST)	Self-starting behaviour of the turbine could be improved as the presence of ODGV could increase the inlet wind velocity and direct the wind to an optimum AoA
				ODGV has upper and lower ducts with four pairs of straight plate guide vanes surround VAWT			The rotational speed of the turbine could be enhanced by around 182%
				Each pair of the guide vanes has titled angle of 20° and 55°		An experiment of five-straight-bladed VAWT	Decreased the negative produced torque of the turbine and also the turbulence and rotational speed fluctuation Improved the power generation by 3.48 higher than the bare turbine in its optimum TSR

10	Wong et al. (2014)	ODGV	Fig. B.6 (a)	Same as Chong et al. (2013) but defined each guide vane into two segments and bent it at a 10° angle	NACA 0015	2D CFD of single-straight-bladed VAWT (Fluent, $k-\omega$ SST)	<p>Could enhance the C_p by around 31.65% and 147.1% compared to the original design of ODGV (Chong et al., 2013) and bare VAWT, respectively</p> <p>It could direct the flow in any direction as the vane surrounded the turbine</p> <p>The huge capital cost and potential on huge weight addition make this device is not compatible to be applied in VAWT commercially</p>
11	Nobile et al. (2014)	Omnidirectional Stator	Fig. B.6 (b)	Put stator around VAWT	NACA 0018	2D CFD of three-straight-bladed VAWT (CFX, $k-\omega$ SST)	<p>A conical surface profile could boost turbulence mixing and decrease the back pressure inside the stator whilst the presence of the blades concentrate the mass flow rate of the wind</p> <p>The stator design could increase and decrease the airflow at specific areas and help the turbine improve its generated positive torque</p>

				<p>The top and the bottom of the stator have a conical surface profile with eight straight vertical blades with a NACA0018 aerofoil profile in the middle</p>			<p>The average power coefficient and torque coefficient improved by 30-35% in the presence of this stator</p>
							<p>The considerable capital cost and potential of huge weight addition make this device unsuitable to be commercially applied in VAWTs</p>

Based on Table 2.2 above, it is proven that the flow augmentation devices are able to increase the performance of the lift-type VAWTs significantly in terms of self-starting ability and power coefficient value. Flow augmentation devices change the wind path to a better angle of attack of the blade and create a higher lift for the blade in lift-type VAWTs. These devices, including the diffuser, guide vanes, stator, shroud, plate, deflector, or duct, also reduce the negative torque at the second half revolution of the lift-type VAWTs. They work based on the basic principle of obtaining a higher mass flow rate for the wind stream by converging the wind flow from a larger flow area into a smaller area. With this Venturi effect, the wind velocity increases before interacting with the rotor blade and thus creates a higher positive torque on the VAWT. The increase of the wind flow enables a better self-start behaviour and higher efficiency. Overall, flow augmentation devices can improve the performance of lift-type VAWTs in all regimes of *TSRs*. However, similar to blade shape modification devices, most of their performance enhancement rate is reduced as the regime of *TSRs* increases. It is also noticeable that the most previous studies were performed merely for geometry optimisation using one *TSR* regime operation point. However, it is evident that the behaviours in different *TSR* regimes are significant. Thus, it is important to carry out geometric optimisation in all *TSR* regimes in future studies.

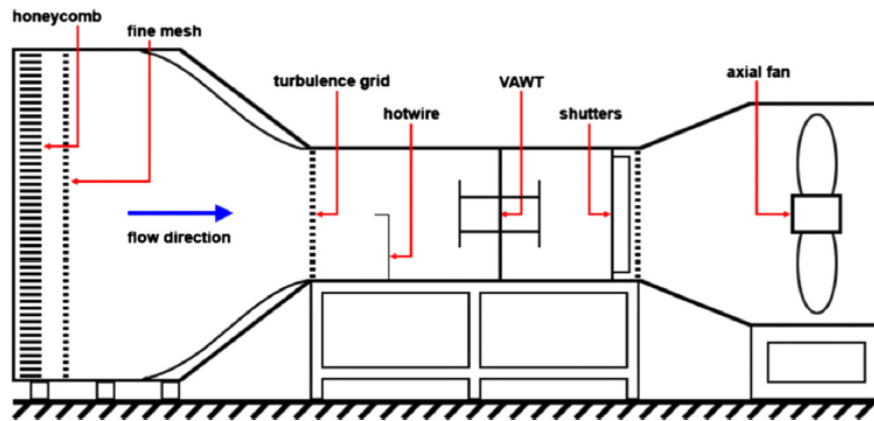
2.3 Experimental and site test studies of Lift-Driven VAWTs

The primary methodologies to investigate VAWTs using experimental methods are wind tunnel testing using particle image velocimetry (PIV) (Jin et al., 2015). These methodologies have been utilised to study the aerodynamic characteristics of VAWTs and evaluate devices that can improve the efficiency of VAWTs (Jin et al., 2015). Wind tunnel methodology (see Figure 2.5) is usually used to investigate VAWTs by evaluating the rotating speeds and torques corresponding to different wind speeds driven to the wind turbine by the wind from the wind tunnel. It can also be used to study the effect of surface roughness and attachments. Meanwhile, PIV methodology (see Figure 2.6) is utilised to observe the detailed flow across the turbine areas in a wind tunnel testing.

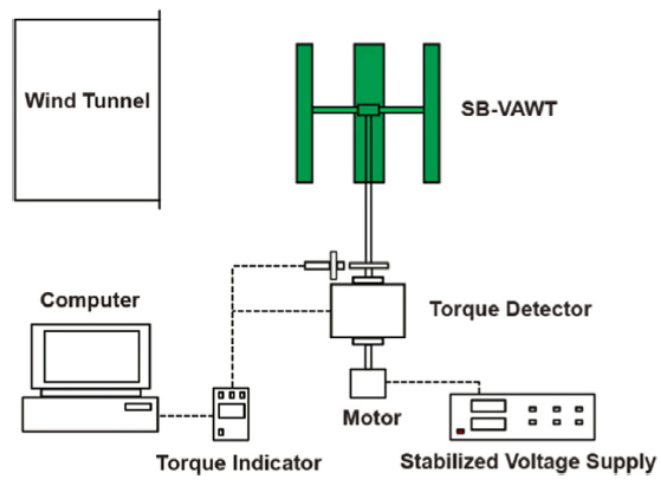
Note that, the precise values of measured variables in experimental studies are usually difficult to be determined. This is since experiments tend to have errors given by the instrumentations, data acquisition and environmental limitations (Stern et al., 1999). In a VAWT case, it is noticeable that the torque measurement device needs to be chosen carefully as a previous study by McLaren, Tullis and Ziada (2012) found that it was

impossible to measure the rotating speeds and torques if there is significant vibration from the tested VAWT. A study by Wong et al. (2018a) mentioned that the combined error of the torque transducer should be less than $\pm 0.1\%$ of the rated torque. The brake that was used to apply load to the rotor shaft must provide a smooth torque, repeatable measurements and precise load control. Moreover, the distance of the wind turbine from the blower that induces the wind must be sufficient (about 3 m) to ensure less wind speed fluctuation. A honeycomb can be also added in front of the blower to reduce these wind speed fluctuations (Kim and Gharib, 2013). Additionally, to check the spatial uniformity of the wind speed in the test section, it is very important to measure the wind speed over an area behind the blower.

For the PIV test, it is very important to choose the appropriate averaging method of the captured data so flow field image from the PIV test does not lead to the wrong analysis or conclusion. Ferreira, et al. (2009) applied a phase averaging method on the velocity field to visualise the dynamic stall on a VAWT. They focused on the strength and distribution of vortical structures, instead of individual point velocities, to reduce the number of the samples and the importance of the randomness of the vortical structures' location/shape. Ferreira, et al. (2009) found that there is a difference between the magnitude of the phase locked average leading-edge vortex and the average magnitude of the instantaneous vorticity as a result of the averaging at the contour limit. The differences between the values of circulation calculated by both methods indicates the uncertainty related to the low number of samples used. For an infinite number of samples, it is expected that both methods would converge to a single estimate. Hence, it is very important to have enough samples to obtain a relatively accurate result. Moreover, it is also necessary to perform an uncertainty analysis of the PIV measurements to understand the limitation of the PIV measurements. Study by Arpino et al. (2021) calculated this uncertainty based on the uncertainty propagation law. They mentioned that this uncertainty needs to be less than 1% to obtain a data with relatively good accuracy.



(a) Wind tunnel test



(b) Torque measurement system

Figure 2.5 Configuration of wind tunnel test (Jin et al., 2015).

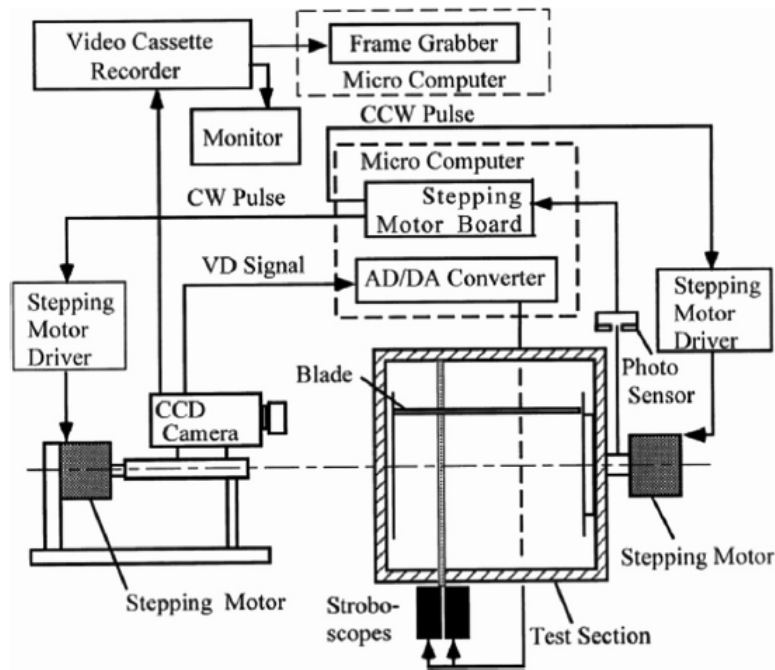


Figure 2.6 Configuration of PIV test (Jin et al., 2015).

Experimental studies of improving the power generation of a VAWT using flow augmentation devices and dynamic stall control devices have been done in previous years. For flow augmentation devices (see Section 2.2.2), Kim and Gharib (2013) and Kim and Gharib (2014) investigated the effect of placing a straight plate deflector (see Figure 2.23 (a)) in mid-section upstream of two five-straight-bladed VAWTs that have different rotational directions. A similar study by Wong et al. (2018a) and Wong et al. (2018b) evaluated the effect of placing a straight plate downward of the upstream region of the two-straight-bladed VAWT (see Figure B.5 (c) in Appendix B). Another study by Stout et al. (2017) performed an investigation of the effect of placing a curved plate deflector upstream of a three-straight-bladed VAWT (see Figure B.4 in Appendix B). Furthermore, Watanabe, Takahashi and Ohya (2016) applied a wind lens diffuser (see Figure B.3 (b) in Appendix B) around a two-straight-bladed VAWT. Lastly, Chong et al. (2013) studied the effect of using a type of guide vane called an ODGV surrounding a H-type VAWT to enhance performance of the VAWT (see Figure B.6 in Appendix B). For the site test, a study by Santoli et al. (2014) investigated the effect of covering a prototype of a commercial three-straight-bladed H-type VAWT with a convergent duct (see Figure B.2 in Appendix B).

Meanwhile, for dynamic stall control devices (i.e., passive flow control devices), it is rare to find experimental studies of the use of these devices as performance

enhancements of VAWTs. This is probably because these devices are mainly associated with blade shape modification, which significantly increase the VAWT model construction cost and difficulty. One study by Srihari et al. (2019) has investigated the effect on performance of the use of a five-element aerofoil on the blades of a three-straight-bladed VAWT (see Figure A.11 (a) and (b) in Appendix A).

2.4 Modelling VAWTs

The numerical modelling approach is prevalent in solving engineering problems due to several advantages compared to experimental and theoretical methods. Compared to an experimental study, a numerical study has advantages such as no experimental hazards and lower research costs in research based on multiple number of design (Shires, 2013). Moreover, if the model adjustment is needed, the numerical method model is generally easier to be modified than the experimental model (i.e., as long as no substantial new computer code is needed). Numerical models display detailed information about what has happened inside the devices. It also helps to evaluate new designs or models before they are applied in a real system. Compared to a theoretical study, a numerical study offers a faster time for problem-solving as long as the computer code is already given, and the computer source is adequate for the investigated case.

However, modelling the aerodynamic performance of a VAWT is very challenging due to the complexity of the flow and different behaviours in different *TSR* operation. Many studies have been done previously to address this problem. This section will discuss the current VAWT modelling approaches and briefly explain their abilities and limitations. Moreover, the reasoning behind the chosen method of this study will also be elaborated.

2.4.1 Momentum theory-based models

These models are usually based on the Blade Element Momentum method (BEM), widely utilised for analysing HAWTs. This BEM approach was modified for application to the VAWT. The first model is called the Single Streamtube Model, which was proposed by Templin (1974). Based on this model, several models to analyse the aerodynamic of VAWTs have been proposed. Among them, the Multiple Streamtubes Model by Wilson and Lissaman (1974) and Double-Multiple Streamtubes by Paraschivoiu (1988) are the most popular models to analyse the aerodynamic of VAWTs. These two models balance the force acting on the blades with the stream-wise change of

momentum generated by the wind turbine rotor. They produce a relatively good prediction of the overall performance of VAWTs (around 26% discrepancy compared to experimental data) with light rotor load in the low *TSR* regime. However, these models are not applicable for VAWTs with high solidity, operated in high regime of *TSRs*. Another approach based on momentum theory to model VAWTs is the Actuator Disc Theory Model. This model assumes the turbine's rotor is a permeable disk which allows the flow to pass through the rotor (Sørensen, 2012). This model also includes the influence of surface forces. The first application of this model to VAWTs was attempted by Newman (1983). After realising that classical Actuator Disc Theory is not suitable for analysing VAWTs, Newman (1986) applied Multiple Actuator Disc Theory to evaluate the performance of VAWTs. This Multiple Actuator Disc Theory assumes the turbine's rotor as multiple permeable discs rather than a single permeable disc like in classical Actuator Disc Theory. The distance of each permeable disk in Multiple Actuator Disc Theory is sufficient that the flow through each disc may be taken as one-dimensional flow.

The advantages of momentum theory-based models are that their time resolution is relatively quicker than the other approach, especially for 3D modelling. Therefore, it is suitable for the overall design process (Tchakoua et al., 2015). However, as they are usually based on one-dimensional simplified equations, these models require some measured data such as lift and drag coefficients on the employed aerofoil sections. They do not give any information around near-wake flow and cannot predict the wind speed variation across the rotor. Moreover, they have poor accuracy (up to 40% discrepancy compared to experimental data for moment prediction) when the aerofoil experiences dynamic stall due to inaccurate predictions for tip vortex and dynamic stall effects (Paraschivoiu and Delclaux, 1983).

2.4.2 Non-Momentum theory-based models

2.4.2.1 Vortex models

These models are based on vorticity equations. In vortex models, the blade element is treated as a lifting line representing the flow-field at areas more than one chord away from the aerofoil. As a result, pressure field values are not needed to calculate a velocity field. The vortex model was first proposed by Larsen (1975), which did not include the effect of the stall angle in the formulations. This was attended to by Strickland,

Webster and Nguyen (1979), who included aerodynamic stall into their vorticity equations.

Vortex models can be applied to VAWTs with high solidity and a wider range of *TSR* values than momentum theory-based models. Moreover, they can also generate information about the wake structure near the turbine (Claessens, 2006). Nevertheless, the excessive computational time compared to momentum theory-based or cascade models is the main drawback of these models. In some cases, they also experience convergence problems. Furthermore, the prediction accuracy depends on the potential flow model (Tchakoua et al., 2015). In addition, to avoid the excessive computational time compared to momentum theory-based or cascade models, they still depend on significant simplifications such as the wake modelled as potential flow and that the viscosity effect is only introduced by including an empirical force coefficient into the blade aerodynamics formulation.

2.4.2.2 *Cascade model*

This model was introduced by Hirsch and Mandal (1987), who suggested applying cascade principles, which are widely used for turbomachinery, for evaluating the performance of VAWTs. The Cascade model assumes the turbine's blade as a cascade by locating the blade in a planar surface with the blade interspaced equally to the turbine circumferential distance divided by the number of blades. Bernoulli's equation is used to establish the correlation between the wake velocity and free stream velocity, whilst a semi-empirical formulation is utilised in the relationship between the induced velocity and wake velocity. This model also includes the variation of local Reynolds number at the different azimuthal positions, zero-lift drag coefficient, finite aspect ratios and flow curvature effect (Islam, Ting and Fartaj, 2008).

The benefit of the Cascade model is its ability to generate a successful prediction of the performance of a VAWT for both low and high solidity turbines without any convergence problems in high regime of *TSRs* and high solidities (Islam, Ting and Fartaj, 2008). It also generates a better calculation of instantaneous blades forces compared to momentum theory-based models. Compared to momentum theory-based models, cascade model can reduce the discrepancy of numerical and experimental results up to 27%. Nevertheless, this model still needs a longer computational time than momentum theory-based models but is more reasonable than the Vortex models (Tchakoua et al., 2015).

2.4.2.3 *Computational Fluid Dynamics (CFD) model*

In this study, the CFD model solves the steady Reynolds Averaged Navier-Stokes (RANS) and Unsteady RANS (URANS) equations. Hence, all the mentioned CFD models in this study refer to CFD that solves RANS or URANS equations. Compared to those models mentioned above, CFD model offers a better aerodynamic prediction for VAWTs in terms of reliability and accuracy. Moreover, it can generate detailed flow visualisation near aerofoils. Therefore, it is possible to evaluate dynamic stall and wake flow around the blades of VAWTs. It can also reduce the time of the design process and overall cost design, making it an attractive solution for performance optimisation (Tchakoua et al., 2015). However, the performance of the RANS/URANS model is greatly dependent on the choice of turbulence models, computational settings and domain and mesh qualities. Hence, it will usually need more extensive computing power and computational time for suitably addressing these three mentioned aspects.

As mentioned above, one major challenge in CFD simulations of VAWTs is to model turbulent flow around the rotating blades and the wake-turbulence interactions. Hence, several turbulence models have been used to simulate the VAWT model. The majority of turbulence models can capture the time-averaged mean flow properties with a steady RANS approach, whilst the large-scale flow unsteadiness can be reproduced using URANS simulations. Both are sufficient for most engineering applications. However, the RANS model does not capture the small-scale turbulence fluctuations, which are essential for understanding the underlying flow physics. This affects the accuracy of CFD predictions for VAWT performance.

Therefore, to improve the accuracy of predictions for VAWT performance, the Large Eddy Simulation (LES) approach can be used, although the use of the turbulence model is still limited due to the high computational cost compared to RANS/URANS turbulence models. Another alternative to improve numerical predictions' accuracy for VAWT performance with lower computational cost compared to LES is implementing hybrid RANS-LES turbulence models. These models still utilise the RANS turbulence model in the near-wall region to model small eddies whilst switching to LES to more accurately simulate large eddies in the intermediate and the far flow-fields, including the separated shear layer and wake region. The summary of the CFD simulation of VAWTs performed in the previous studies can be found in Table 2.3. The detail of the review of the simulation of VAWTs performed in the previous studies, including the advantages

and disadvantages of each turbulence model implemented in the simulation of VAWTs so far, is discussed in Appendix C.

Table 2.3 Summary of works of modelling VAWT using CFD simulations.

No	Authors	Features	Advantages	Limitations
1	Ferreira et al. (2010)	2D URANS one-equation Spalart-Allmaras (SA)	Lowest computational cost in 2D URANS turbulence models	Underestimates the generation and shedding of vorticity at the leading-edge in the stall zone
				Excludes 3D effects
				Limited to high aspect ratio
2	Mohamed, Ali and Hafiz (2015), Trivellato and Castelli (2014), Castelli, Englaro and Benini (2011), Castelli et al. (2010), Ferreira et al. (2010)	2D URANS two-equation $k-\varepsilon$	Moderate computational cost in 2D URANS turbulence models	Underestimates the generation and shedding of vorticity at the leading-edge in the stall zone
			Predicts the trend line of C_p over TSR correctly	Overestimates C_p in all regimes of $TSRs$
				In lower regime of $TSRs$, C_p is overestimated by a factor of 2 compared to test data
			Predicts the optimum TSR correctly	Excludes 3D effects
Limited to high aspect ratios				
3	Wang, et al. (2018), Arab, et al. (2017), Lam and Peng (2016), Almohammadi, et al. (2015)	2D URANS two-equation $k-\omega$ SST	Moderate computational cost in 2D URANS turbulence models	Underestimates the generation and shedding of vorticity at the leading-edge in the stall zone
			Reduces the overestimation of C_p by 50% in low $TSRs$ and 35% in medium and high regimes of $TSRs$ compared to the $k-\varepsilon$ turbulence model	Excludes 3D effects
				Limited to high aspect ratio

4	Rezaeiha, Montazeri and Blocken (2018), Bangga, et al. (2017), Lanzafame, Mauro and Messina (2013)	2D URANS four-equation Transition SST	Moderate to high computational cost in 2D URANS turbulence models	Higher computational cost compared to two-equation URANS.
				Similar overestimations of C_p with two-equation URANS in high regime of $TSRs$
			Reduces the overestimation of C_p prediction in low and medium regimes of $TSRs$ by two-equation URANS	Excludes 3D effects Limited to high aspect ratio
5	Lei, et al. (2017), Lam and Peng (2016)	Quasi-3D (q3D) or 3D URANS	Higher fidelity compared to 2D URANS	Higher computational cost compared to 2D URANS
			Lower overestimation of C_p in low regime of $TSRs$ compared to 2D URANS	Similar overestimation of C_p with 2D URANS in medium and high $TSRs$.
				Underestimates 3D vortex structures around the blades
6	Lei, et al. (2017), Lam and Peng (2016), Peng and Lam (2016), Ferreira, et al. (2010)	Hybrid RANS-LES	Higher fidelity compared to URANS	Higher computational cost compared to URANS
			Reduces the discrepancy of C_p prediction up to around 16% in high regime of $TSRs$	
			Reduces the discrepancy of C_p prediction until less than 10% in low and medium regimes of $TSRs$	Very sensitive to grid resolution
Can predict richer vortex structures compared to URANS in a higher azimuthal position				

			when dynamic stall occurs	
7	Posa and Balaras (2018), Elkhoury, Kiwata and Aoun (2015), Ghasemian and Nejat (2015), Li et al. (2013)	q3D or 3D LES	<p>Highest fidelity compared to URANS and Hybrid RANS-LES</p> <p>Can predict richer vortex structures compared to URANS in a higher azimuthal position when dynamic stall occurs</p> <p>Reduces the discrepancy of C_p and C_m prediction of CFD simulations compared to the experimental data caused by URANS simulation in all TSR regimes</p>	Highest computational cost compared to URANS and Hybrid RANS-LES

As presented in Table 2.3, the choice of turbulence model is critical to generate relatively good accuracy of the result of modelling VAWT using CFD simulation. URANS turbulence models can capture the overall performance evaluation of VAWT, such as power coefficient distribution over TSR value and the optimum value of TSR . However, they have poor accuracy in low regime of $TSRs$ and cannot capture detailed flow-field around VAWT. Nevertheless, they have the advantage of relatively low computational cost compared to LES and hybrid RANS-LES turbulence models. On the other hand, LES and hybrid RANS-LES turbulence models can improve the disadvantages of URANS turbulence models as they have good accuracy in all regimes of $TSRs$ and capture more detailed flow-field around VAWT. However, the computational cost of these two types of turbulence models, particularly LES, is much higher compared to URANS turbulence models. Hence, it is very important to choose the appropriate turbulence models for VAWT evaluation depend on the operation condition of VAWT and the type of evaluation (i.e., overall performance or detailed flow-field for further evaluation in noise and vibration).

2.5 Chapter Summary

2.5.1 Rationale for the present study performance enhancement approach

It is clear that to compete with HAWTs, lift-driven VAWTs need to improve their performance, especially their efficiency and self-starting ability. As mentioned above, these improvements can be made by using flow control devices to control the dynamic stall or flow augmentation devices to increase wind speed and direct the wind toward the blades of VAWTs. In the dynamic stall control method, passive flow controls seem to be more practical than active flow controls as they do not require any external power source system. It also suggests that passive flow controls are mainly implemented to the blades of lift-driven VAWTs to ease the dynamic stall usually experienced by these VAWTs at low and medium *TSRs*. As a result, the modified lift-driven VAWTs can escape from the dead band zone due to suppressing negative torque production. Hence, their self-starting ability can be improved.

Based on the summary in Table 2.1, whilst other passive flow controls have limitations that can only improve the turbine's performance in several regimes of *TSRs*, the use of a GF in the blades of lift-driven VAWTs suggests that a GF could generate better performance than clean blades for all *TSR* regimes (low, medium and high) even though the performance improvement decreased in high regime of *TSRs*. Regardless of this, several studies have been done on the use of a GF to improve the performance of lift-driven VAWTs. There are some limitations on these studies.

- 1) Firstly, most research presented has merely focused on the outcome of the power coefficient increase (e.g., the work of Liebeck (1978)), rather than further analysing and explaining the underlying flow physics and characteristics. They mainly explain power coefficient and moment coefficient distributions of the results only during the peak *TSR* value (Bianchini et al., 2019). There is no explanation about the flow behaviour in high regime of *TSRs*. In addition, there is no statement about how the GF can improve the self-starting ability in low regime of *TSRs*. It is essential to understand flow behaviour which leads to the torque production and power improvement in low regime of *TSRs* as this is the region where VAWT needs self-starting ability to avoid the addition of external power sources.
- 2) Secondly, it is well known that the blade rotational effects and blade-to-blade interactions significantly impact the performance of a VAWT. Moreover, it is also known that a VAWT can be operated in typically three different regimes of *TSRs* namely, low, medium and high *TSRs*. Within each *TSR* regime it is known that flow

behaviour around the VAWT will behave quite differently (Malael, Dumitrescu and Cardos, 2014). Consequently, it is crucial to conduct the VAWT optimisation (i.e., considering blade rotational effects and blade-to-blade interaction) for these three regimes of *TSRs* (low, medium and high *TSRs*) so that the GF geometry can be adjusted accordingly to generate the optimum solution for VAWT performance improvement in all *TSR* regimes. Nevertheless, previous studies on using a GF on a VAWT have primarily focused on performing geometric optimisation for a single stationary aerofoil and in a single region of *TSRs* (Bianchini et al., 2019; Malael, Bogateanu and Dumitrescu, 2012). Although there is a study that performed geometric optimisation of a VAWT configuration and across all regimes of *TSRs* (Yan, Avital and Williams, 2019), it only focused on how the geometric parameters (i.e., height and mounting angle) behave in different *TSR* regimes without evaluating the optimum value for each *TSR* regime and the reason behind it. This shows that geometric optimisation of a GF on a VAWT configuration and for all regimes of *TSRs* still needs further evaluation.

- 3) Thirdly, due to the constraint of key parameters in the GF geometric evaluation, previous studies were often limited to merely focussing on the height (H) and mounting angle (θ_{GF}) optimisations (Bianchini et al., 2019; Yan, Avital and Williams, 2019; Malael, Bogateanu and Dumitrescu, 2012). On the other hand, in the aerodynamic community, the evaluation of other GF geometric parameters for aerofoil modification has been widely performed, including GF position from the trailing-edge (s) (Jain, Sitaram and Krishnaswamy, 2015) and GF shape modifications (e.g., straight, curve or wedge) (Mohammadi, Doosttalab and Doosttalab, 2012). It was found that these parameters also have significant effects on aerofoil performance. However, it is unclear on their effectiveness for rotating multiple blades such as a VAWT.
- 4) Fourthly, all the previous studies (Bianchini et al., 2019; Yan, Avital and Williams, 2019; Malael, Bogateanu and Dumitrescu, 2012) performed geometric optimisation merely for one single parameter variation at a time. Hence, there is no information about which GF parameter gives the highest or the lowest impact on the performance improvement of VAWT.
- 5) Lastly, 3D GF modifications such as a GF with slits and a GF with holes (Meyer et al., 2006) proved that they could reduce the drag generation of an aerofoil with GF for aircraft applications by about 12%. The slitted GF is usually called riblets, defined

as a passive flow control device inspired by drag reduction of structures found in nature such as sharkskin (Martin and Bhushan, 2016a) and bird beaks (Martin and Bhushan, 2016b). The flight test evaluation of riblet effectiveness at high Reynolds numbers and Mach numbers in the range of 0.30-0.70 has given strong support to the wind tunnel correlations of drag reduction. Maximum skin friction drag reduction of about 6% has been observed in both fuselage tests (under nearly zero pressure gradient conditions) and wing tests including adverse pressure gradient (Viswanath, 2002). In actual flight applications, Szodruch (1991) found that by covering the 70% of the aircraft surface with riblets, a total drag reduction of a little less than 2% in the Mach number range of 0.77-0.79 can be achieved based on the assessment of the fuel burn saving.

Nevertheless, riblets have better performance reducing drag generation at low Reynolds numbers rather than high Reynolds numbers (Spalart and McLean, 2011; Han et al., 2003). Hence, they are very attractive to apply to the VAWT blades as VAWTs mostly operate at low incoming wind speed. Previous studies on a stationary aerofoil found that riblets reduce the drag generation by around 16% on a typical symmetric aerofoil, whilst 4-6% drag reduction was found for an asymmetric aerofoil (Sundaram, Viswanath and Rudrakumar, 1996). In the case of wind turbines, Chamorro, Arndt and Sotiropoulos (2013) have investigated an asymmetric stationary aerofoil, which is usually used for large HAWT blades. The riblets addition resulted in a maximum drag reduction of approximately 6% for the nominal operational range. However, the real potential of riblets for drag reduction in full-scale wind turbine configurations (including the rotational effects) is still not yet investigated.

Regarding the use of flow augmentation devices, the upstream deflector has superior effectiveness, as it can improve the performance of a VAWT whilst operating in all regimes of *TSRs*. They also have the advantage of having a simpler design than any other omnidirectional flow augmentation device. Whilst the curved plate upstream deflector only gave a small performance increase (Stout et al., 2017), a SUD could generate a better performance improvement and has been widely applied on drag-driven VAWTs (Wong et al., 2017). However, there are still few studies on the SUD application on lift-driven VAWTs (see Section B.1.5 in Appendix B). Moreover, these few studies also have some limitations that need to be addressed.

- 1) There is no investigation about the optimum location of a SUD upstream of a VAWT. All previous studies (see Section B.1.5 in Appendix B) only chose one specific location upstream for the VAWT (i.e., downward, upward or middle) without performing parametric studies about the optimum position of the deflector. Those previous studies mostly choose one particular site for the VAWT (i.e., downward, upward or middle) other than studying the effect of other location parameters such as distances from the turbines in x and y directions.
- 2) Most previous studies (see Section B.1.5 in Appendix B) only evaluated a SUD and performed geometric optimisation in a single TSR region. As mentioned above, it is known that flow around a VAWT behaves quite differently depending on the regime of TSR considered. A previous study has evaluated geometric optimisations for all regimes of $TSRs$ (Kim and Gharib, 2013). However, there is no explanation about the effect of $TSRs$ on the geometric optimisations and the SUD's performance enhancement of the VAWT.
- 3) Lastly, there is a lack of investigation into the use of an upstream deflector on a single lift-driven VAWT with high solidity.

Therefore, this study will address all those limitations identified in previous studies of GF application to VAWTs by performing the optimisation of GF geometry for a VAWT configuration with consideration of the rotational effects and broader GF parameters (i.e., height, mounting angle, position and shapes (straight, curve and wedge)) in all three TSR regimes. The Taguchi method (Qasemi and Azadani, 2020; Wang, Wang and Zhuang, 2018) is adopted to simultaneously optimise different GF geometric parameters (i.e., height, mounting angle and position from trailing-edge). After finding the optimum height, mounting angle and position from trailing-edge values at all regimes of $TSRs$ using Taguchi's method, the effect of a shape change based on these optimum geometric parameters is evaluated. To the author's knowledge, this is the first work to be attempted for multiple parameter GF optimisation applied to a VAWT configuration as previous optimisations (Bianchini et al., 2019; Yan, Avital and Williams, 2019; Malael, Bogateanu and Dumitrescu, 2012) were for varying one parameter at a time. Furthermore, 3D modifications using a slit or holed flap will also be investigated for a VAWT configuration (i.e. considering rotational effects and blade-to-blade interactions) as it is mentioned in the previous study of a single stationary aerofoil that these 3D modifications of a GF can decrease the drag generation caused by the GF (Meyer et al., 2006).

Meanwhile, this study will cover all the shortcomings mentioned above by including the effect of the deflector location for a SUD application in the VAWT's study. This study will also perform geometric optimisation of the SUD in all three *TSR* regimes. A three-straight-bladed VAWT configuration is adopted to accommodate higher solidity.

In addition to GF and SUD evaluations as performance enhancements of a VAWT, this study will also compare the capability of GFs and SUDs to improve the performance of lift-driven VAWTs in each *TSR* regime. Moreover, this study will also attempt to combine dynamic stall control devices (i.e., the GF) and flow augmentation devices (i.e., SUD) as performance enhancement of lift-driven VAWT. The evaluation of this new combination device and comparison with bare VAWT, VAWT with a stand-alone GF and VAWT with a stand-alone SUD is also performed in each *TSR* regime, so the best choice of device to improve the performance of the VAWT in each regime can be determined.

2.5.2 Rationale for the present state-of-the-art study of research methods

As mentioned above, numerical studies have several advantages compared to experimental studies. These include no experimental hazards, lower research costs in large-scale research, easier to be modified, displays detailed information, and help to develop new designs or models. Therefore, this study utilises a numerical method to evaluate the performance enhancement devices of lift-driven VAWTs and analyse the flow around VAWTs. Note that, among all available numerical methods, this study uses CFD simulations to generate better predictions than other methods. Although such simulations have higher computational demand, it is reasonable to utilise CFD simulations rather than other numerical methods as this present study will evaluate the overall performance of VAWTs and investigate flow behaviour around the blades of the VAWTs.

It is also noticeable that the choice of turbulence model is critical to generate relatively good accuracy of the result of modelling VAWT using CFD simulations. As mentioned in Section C.1 in Appendix C, URANS turbulence models can capture the overall performance evaluation of a VAWT, such as the power coefficient distribution over *TSR* values and the optimum value of the *TSR*. However, they have poor accuracy in low regime of *TSRs* and cannot capture detailed flow-fields around the VAWT. On the other hand, LES and hybrid RANS-LES turbulence models can improve these disadvantages of URANS turbulence models. Hence, before evaluating the performance

enhancement devices of a VAWT, this study compares the effect of several RANS/URANS and hybrid RANS-LES based turbulence models on the accuracy of numerical prediction of the performance of the VAWT and flow around the VAWT. This evaluation includes a relatively new hybrid RANS-LES turbulence model called stress-blended eddy simulation (SBES) (Menter, 2018). The LES turbulence model is not applied as it will generate unreasonable computational costs and a very long computational time. The turbulence model that gives higher average accuracy across all three regimes of *TSRs* is chosen for evaluating the performance enhancement devices of the VAWT.

Due to the consideration of computational cost and the fact that the same method has been applied in the previous studies (Yan et al., 2020, Rezaeiha, Montazeri and Blocken, 2019; Zamani, Maghrebi and Moshizi, 2016, Zamani et al., 2016), a 2D model VAWT is adopted for the turbulence study and other numerical setups (i.e. size of domain, spatial convergence, temporal resolution and resolution convergence) evaluations and the design optimisation of the Gurney flap and straight upstream deflector. After finding the optimum design of the performance enhancement device, a quasi-3D (q3D) VAWT model is adopted to include the 3D effects into the evaluation of the performance improvement rate of a VAWT induced by the enhancement device, i.e., a GF. A q3D VAWT model is also applied to evaluate the effect of 3D modifications of the GF on the performance of the VAWT with GF.

Chapter 3: Definitions and CFD Methodologies

This chapter discusses fundamental parameters used to discuss the performance and flow behaviour of lift-driven VAWTs. From here on in this thesis, the acronym CFD (computational fluid dynamics) will apply to the RANS and URANS cases only. This chapter will also explain the CFD method and equations inside the chosen turbulence models.

3.1 Definitions of Fundamental Parameters of Lift-Driven VAWTs

3.1.1 Solidity (σ)

Solidity is fundamental in designing a VAWT as it is related to the lift and drag production of the VAWT's blades. The solidity of VAWT is calculated by:

$$\sigma = \frac{Nc}{R} \quad (3.1)$$

where N is the number of the blades, c (m) is the blade's chord length, and R (m) is the radius of the turbine calculated from the centre of the turbine to the connecting point of the arm in the blade.

3.1.2 Tip Speed Ratio (TSR)

The *TSR* is the most important factor in designing any wind turbine. It is the ratio between the wind speed and the speed of the tips of the wind turbine blades as written in the equation (3.2). In a VAWT, the *TSR* has an essential role as it determines the operational region of the VAWT and give an insight into the expected flow phenomena around the VAWT.

$$TSR = \frac{\omega_r R}{U_\infty} \quad (3.2)$$

where ω_r is the turbine rotation rate (*rad/s*) and U_∞ is the incoming freestream wind speed (*m/s*).

3.1.3 Reduced Frequency (RF)

This parameter is used to determine the unsteadiness of the VAWT. It can be estimated using the equation below.

$$RF = \frac{\omega_r c}{2U_{eff}} = \frac{c}{2R} \quad (3.3)$$

where U_{eff} (m/s) is the effective velocity of the blade. When the tip speed of the blade is greater than the incoming wind speed, the reduced frequency equation can be simplified to a function of the blade chord and the radius of the turbine. Reduced frequency is also be expressed in terms of the TSR by

$$RF = \left(\frac{c}{2R}\right) \frac{TSR}{\sqrt{TSR^2 + 2TSR \cos\theta + 1}} \quad (3.4)$$

where θ is the azimuthal angle of the blade of the VAWT.

3.1.4 Geometrical Angle of Attack (AoA_D)

The geometrical angle of attack is the angle of attack (AoA) measured from a VAWT blade as it rotates. It is expressed by:

$$\tan(AoA_D) = \frac{U_\infty \sin\theta}{\omega_r r + U_\infty \cos\theta} = \frac{\sin\theta}{TSR + \cos\theta} \quad (3.5)$$

Note that as the turbine rotates, this angle of attack will continually change. This parameter also can be expressed using a non-dimensionalised parameter, as depicted in the equation below.

$$AoA_{D,nor} = \frac{AoA_D}{AoA_{D,max}} \quad (3.6)$$

where $AoA_{D,max}$ is the maximum geometric angle of attack of the VAWT blade.

3.1.5 Power coefficient (C_p)

It is very common to evaluate the design of a VAWT by the mean of its power coefficient. In theory, the C_p of the wind turbine can be expressed as a product between

the TSR and moment coefficient (C_m) of the wind turbine, as depicted in the equation below.

$$C_p = TSR \times C_m \quad (3.7)$$

where C_m is calculated by

$$C_m = \frac{M}{\frac{1}{2}\rho U_\infty^2 AL} \quad (3.8)$$

where M (N) is the moment production of the turbine, ρ (kg/m^3) is the fluid density, A (m^2) is the wind turbine's rotor swept area and L (m) is the distance of the blade to the rotating axis. L is set to be the same as the rotor radius for 2D CFD.

Note that in order to determine the C_m of each blade of the turbine, the M will be the moment production of each blade. In case of the C_m of one azimuthal position, i.e., instantaneous moment coefficient (C_{mi}), the M is the moment production of the turbine or each blade in one azimuthal position. Therefore, for the overall power coefficient evaluation, the averaged power coefficient (C_{p-ave}) over one turbine revolution (i.e., 360° rotating angle) is utilised. This C_{p-ave} can be calculated using equation (3.7) with the C_m now being the average moment coefficient (C_{m-ave}) over one turbine revolution. This C_{m-ave} is determined by averaging the C_{mi} value over one turbine revolution.

3.2 CFD Procedures

In this study, ANSYS Fluent v19 (Ansys, 2020) is chosen for CFD simulations due to its broad, physical modelling capability to model flow, turbulence, heat transfer and reactions. Its wide choice of turbulence models and more straightforward application are also amongst other benefits. Moreover, its capabilities to directly import geometry from CAD and accept a large number of mesh extension types can help avoid the complexity of the pre-processing step. Although, ANSYS Fluent may not be the best CFD code available, it still offers respectable accuracy and is easy to access at UWE Bristol. Additionally, for simulating two different domains (i.e., rotating and non-rotating domains) like VAWTs, ANSYS Fluent offers several benefits such as broader options of how to connect these two domains, a relatively straight forward method to combine two different types of mesh and uncomplicated approach of how to assign the connection of two domains by using an option of domain-to-domain interface.

CFD procedures contain three steps, namely, pre-processing, solving and post-processing, which are explained below.

3.2.1 Pre-processing

Pre-processing starts with the problem definition of the simulation problem. After that, geometry and mesh generations are performed. In this study, the CAD is utilised to create a 3D turbine blades. After that, the file is imported to ANSYS Geometry to generate other sub-domains such as the turbine rotor and far-field sub-domains. Mesh generation, domain and boundary layer definition are performed in ANSYS Mesh. A structured mesh is chosen as it will give relatively smaller element numbers than unstructured or hybrid meshes. Note that grid non-orthogonality or skewness increase needs to be controlled in the structured mesh as it can cause unphysical solutions due to the transformation of the governing equations (Tu, Yeoh and Liu, 2013).

3.2.2 Solving

In this step, fluid material properties, the flow physics model, and boundary conditions are solved. This study uses ANSYS Fluent to solve the defined model. As this study evaluates RANS/URANS turbulence models, i.e., $k-\epsilon$ realisable (RKE), Shear-Stress Transport $k-\omega$ (SST) and Transition SST (TSST), and hybrid-RANS turbulence models, i.e., Delayed-Detached Eddy Simulation (DDES), Improved DDES (IDDES), and SBES based on shear-Stress Transport $k-\omega$ and Transition SST, the extended explanation of these turbulence models are given in Appendix D.

3.2.3 Post-processing

The simulation results can be interpreted in many ways, such as contour plots, vector plots, streamlines and data curves. This study mainly uses ANSYS CFD-Post and Tecplot 360 to analyse the results.

3.2.4 Other computational settings criteria

Besides turbulence models, the proper choice of other computational settings is also crucial in VAWT simulation using CFD. Therefore, the following sections will explain several important guidelines for choosing the proper computational settings and criteria for better accuracy of VAWT simulation using CFD.

3.2.4.1 Azimuthal increment

In wind turbine simulations, relation of time step with the turbine revolution called azimuthal increment ($d\theta$) is widely used. $d\theta$ is the total number of degrees of turbine rotation every time step. For VAWTs, it is suggested that the minimum required $d\theta$ is dependent on the TSR operation and solidity. Lower TSR and solidity values will require lower $d\theta$. It was argued that at least $d\theta = 0.1^\circ$ is needed for low regime of $TSRs$ and solidity, whilst for medium and high regimes of $TSRs$ and high solidities it can go up until $d\theta = 0.5^\circ$ (Rezaeiha, Montazeri and Blocken, 2019). Nevertheless, other studies also mentioned (Elkhoury et al., 2019; Delafin et al., 2017; Castelli, Englaro and Benini, 2011) that the use of $d\theta = 1^\circ$ is enough to generate good prediction. They found that decreasing $d\theta$ lower than 1° generated similar results.

3.2.4.2 Revolution convergence

In VAWT simulation, it is essential to obtain a statistically converged flow-field before collecting data samples. Hence, several studies have suggested some required number of turbine revolutions to run before collecting the data. It was usually defined by analysing the time history of the C_m or C_p . In their previous URANS simulations, Castelli, Englaro and Benini (2011) started the data sampling whilst the C_m variation between two neighbouring revolutions is less than 1%. Another study using the Transitional SST turbulence model (Rezaeiha, Montazeri and Blocken, 2019) has found that the changes of the average C_m and C_p over one turbine revolution could be below 0.1% and 0.2%, respectively, after 20 revolutions, and the cumulated differences of these two values would be low to 1.06% and 2.41%, respectively, between 20 and 100 revolutions.

3.2.4.3 Solver type

The operation of VAWTs is usually associated with low-speed wind (i.e., low Mach number). Therefore, the effect of compressibility can be neglected. Consequently, the pressure-based solver type is more applicable as the pressure is mostly not related to the density. Balduzzi et al. (2016) found that the pressure-based approach could produce a more stable and faster convergence rate than the density-based one. Due to the requirement of very low residuals and short time steps for ensuring accurate solution, the density-based approach cannot be applied for VAWT simulation associated with extensive and unsteady simulations (Balduzzi et al., 2016).

3.2.4.4 Pressure-Velocity coupling methods

The pressure-based solver type offers four types of pressure-velocity coupling methods called Semi-Implicit Method for Pressure-Linked Equations (SIMPLE), SIMPLE-Consistent (SIMPLEC), Pressure Implicit with Splitting of Operators (PISO) and Coupled. Whilst the three first mentioned methods are based on semi-implicit solution methods, the later method solves Navier-Stokes equations directly using implicit discretisation of pressure in the momentum equation. A coupled method offers benefits in terms of robustness and convergence, particularly with large time steps or with a poor-quality mesh (Peyret, 1996).

Previous work found that PISO generated the worst accuracy compared to SIMPLE and Coupled as it gave a false detection of stall onset (Balduzzi et al., 2016). Furthermore, for finer time steps, SIMPLE and Coupled methods produce similar results. However, the SIMPLE method could not generate an accurate prediction for a larger time step, whilst the Coupled method could still produce a good prediction with only slight differences than the finer time step (Balduzzi et al., 2016). Hence, it was decided to choose the SIMPLE or Coupled method for the velocity-pressure coupling method in CFD simulation of VAWTs.

3.2.4.5 The number of iterations in each time step

The complex nature of VAWT simulation affects the inability of the simulation to always reach the residual criteria of each parameter. Choosing the correct number of iterations in each time step is a common solution to address this problem. Previous work suggested that 40 iterations in each time step could bring down the turbulent kinetic energy residuals until order 10^{-4} whilst the order of all other residuals could reach 10^{-5} (Balduzzi et al., 2016).

3.2.5 Domain size criteria

It is crucial to position the outer boundaries of the domain far enough from the wind turbine to ensure that the outer boundaries do not influence the result of the CFD simulations. This section discusses the guides for setting the distance of the inlet and outlet boundaries from the model of the wind turbine. In addition, the guide of the size of the VAWT rotating core domain model is also explained. For this study, the details of the chosen domain size are explained in Chapter 4, Section 4.2.1.

3.2.5.1 *Distance to the inlet*

It is known that wind turbines will experience decelerated velocities at the downstream compared to upstream. The region where this happens is called the induction field upstream. Hence, the computational domain should have enough distance upstream in order to accommodate this induction field. A study by Rezaeiha, Montazeri and Blocken (2018) suggested that it is needed at least 15 times the turbine diameter (D_{rotor}) distance from the turbine centre to the inlet to generate accurate prediction at all values of the *TSRs* and solidities. Other studies by Balduzzi et al. (2016) and Wang et al. (2018) argued that the inlet boundaries should be placed 40 turbine diameters away from the centre to avoid the influences of the boundary conditions. This difference is probably due to the use of different types of VAWT whilst the first-mentioned study evaluated a two-straight-bladed VAWT, the later study investigated a three-straight-bladed VAWT. In addition, the different inlet wind speeds and different type of aerofoil could be other reasons.

3.2.5.2 *Distance to the outlet*

To make sure that the wake downstream has developed sufficiently, the outlet of the computational domain should have enough distance from the turbine. Previous work mentioned that $10D_{rotor}$ distance from the turbine centre to the domain outlet is sufficient to produce accurate results in all values of *TSRs* and solidities (Rezaeiha, Montazeri and Blocken, 2018). However, a different study mentioned that this distance should be at least $40D_{rotor}$ (Wang et al., 2018). Again, this difference may be due to the similar reason mentioned on the distance to the inlet section.

3.2.5.3 *Diameter of rotating domain*

CFD simulation of VAWTs usually sets a rotating sub-domain that includes the turbines or blades inside the sub-domain to simulate the turbine rotation. As mentioned in the previous study, this region can be set between $1.5D_{rotor}$ to $2D_{rotor}$ to avoid unwanted disturbances produced by the sliding interface (Balduzzi et al., 2016; Rezaeiha, Montazeri and Blocken, 2018).

3.3 **Design Procedures**

This study will investigate the use of flow augmentation devices and passive flow control devices to improve the performance of lift-driven VAWT by using CFD

simulation. Hence, before performing the design evaluation, it is vital to ensure that the CFD model is accurate enough to predict the performance, aerodynamic characteristics and flow-field characteristics of lift-driven VAWT.

Step 1 Literature review studies.

- Identify the current technologies and problems in performance enhancement of lift-driven VAWTs, i.e., flow augmentation devices and flow control devices.
- Identify the type of flow augmentation and flow control devices that have straightforward design and better performances, need further design improvement, and can be applied in all *TSR* regimes, i.e., straight upstream deflector for flow augmentation device and Gurney flap for flow control device.
- Identify the gap that needs to be fulfilled in the future study in the design of a straight upstream deflector and a Gurney flap as performance enhancement of a lift-driven VAWT.
- Identify the CFD accuracy and limitation in modelling lift-driven VAWT.

Step 2 Evaluate the CFD capability in modelling lift-driven VAWT

- Identify previous experimental data that have been used to validate the CFD model of lift-driven VAWT in previous studies, i.e., study of Castelli, Englaro and Benini (2011).
- Identify numerical setups inside ANSYS Fluent that significantly influence the simulation results based on previous studies.
- Build a 2D model of the chosen lift-driven VAWT (Castelli, Englaro and Benini, 2011).
- Perform domain, spatial convergence, temporal resolution, and revolution convergence studies of the current 2D VAWT model.
- Evaluate the accuracy of the 2D VAWT model in predicting the experimental results (Castelli, Englaro and Benini, 2011) based on the choice of turbulence model. Three URANS turbulence models (RKE, SST and TSST) and four hybrid RANS-LES turbulence models (DDES, IDDES, SBES with $k-\omega$ SST and SBES with Transitional SST) are investigated to evaluate which

turbulence model generates better prediction in the VAWT performance (C_p) and flow characteristics in all *TSR* regimes (low, medium and high) with reasonable simulation time.

Step 3 Gurney flap and straight upstream deflector optimisation design

- Choose the base geometry based on previous studies, i.e., the Gurney flap is based on a study by Mohammadi, Doosttalab and Doosttalab (2012) and the straight upstream deflector is based on a study by Kim and Gharib (2013).
- Build the 2D VAWT model with Gurney flap and 2D VAWT model with straight upstream deflector.
- Evaluate the effect of geometric variation of the Gurney flap (height, mounting angle and position from trailing-edge) using the Taguchi Method (see Chapter 5, Section 5.3 for further explanation and the reason behind choosing this method) in the improvement of VAWT performance for each regime of *TSRs* (low, medium and high)
- Evaluate the effect of geometric variation of the straight upstream deflector (position, width and inclination angle) in improving VAWT performance for each regime of *TSRs* (low, medium and high).
- Choose the optimum geometry for the Gurney flap and straight upstream deflector that can generate relatively better performance of the modified VAWT compared to bare VAWT in all *TSR* regimes.

Step 4 Comparison of the performance enhancement devices to the improvement rate of the VAWT performance for each *TSR* regime

- Compare the rate of VAWT performance enhancement between the optimum design of the Gurney flap and the straight upstream deflector for each *TSR* regime.
- Combine the optimum design Gurney flap and straight upstream deflector as a potential performance enhancement device of VAWT.
- Compare the rate of VAWT performance enhancement of Gurney flap and straight upstream deflector combination with stand-alone Gurney flap and stand-alone straight upstream deflector in each *TSR* regime.
- Chose the device that generates the highest performance improvement of VAWT in each *TSR* regime.

Step 5 Evaluate the 3D VAWT model

- Build a 3D VAWT model based on a previous study (Castelli, Englaro and Benini, 2011).
- Evaluate the spatial convergence of the 3D VAWT model.
- Validate the CFD simulation result of the 3D VAWT model with experimental results of Castelli, Englaro and Benini (2011).
- Build the q3D VAWT with Gurney flap model.
- Compare the results of the 2D VAWT with Gurney flap and the q3D VAWT with Gurney flap.
- Modify the q3D VAWT with the Gurney flap by introducing slits and holes around the flap.
- Evaluate the effect of slits and holes on the rate of VAWT performance enhancement and compare to the original shape of the Gurney flap.

3.4 Chapter Summary

The procedure of modelling using CFD simulation is explained above. It is noticeable that the turbulence models, azimuthal increment, revolution convergence, solver type, pressure-velocity coupling method, number of iterations in each time step and domain model have a significant effect on the model accuracy. Moreover, URANS turbulence models have relatively good accuracy in predicting the overall performance of VAWT, whilst their ability to predict the flow characteristics still needs to be investigated. Therefore, in the next chapter, this study will compare three highly recommended URANS turbulence models called $k-\varepsilon$ realisable, $k-\omega$ SST and Transitional SST to predict overall performance and flow characteristics of the VAWT. Furthermore, to improve the accuracy of the CFD model, the chosen URANS turbulence models are also compared with four hybrid RANS-LES turbulence models called DDES, IDDED, SBES with $k-\omega$ SST and SBES with Transitional SST to evaluate which model that can generate better overall performance and flow characteristics of VAWT in all regimes of $TSRs$. Note that before doing turbulence model studies, this study will also perform domain, spatial convergence, temporal resolution and revolution convergence studies. Other numerical setups such as solver type, pressure-velocity coupling method and the number of iterations in each time step are adopted from previous studies (Elkhoury et al., 2019; Rezaeiha, Montazeri and Blocken, 2018; Delafin et al., 2017; Balduzzi et al., 2016;

Castelli, Englaro and Benini, 2011) which are explained in Chapter 4. The adopted optimisation method for the Gurney flap, i.e., the Taguchi method, will be explained in Chapter 5, where the details of the Gurney flap study are discussed.

Chapter 4: Two-Dimensional CFD Validation of Lift-Driven VAWT

Flow behaviour around lift-driven VAWTs has different characteristics depending on its value of TSR operation (see Chapter 2, Section 2.1.3). Hence, it is crucial to choose VAWT model parameters and models, particularly its turbulence model, to generate accurate predictions in all values of $TSRs$. Based on the discussion in Chapter 2, Section 2.4.2.3, it can be observed that hybrid RANS-LES models offer better accuracy in predicting the performance of VAWT compared to URANS models. The hybrid RANS-LES models also offer relatively lower computational cost compared to LES models. Even though there are some reports on the use of hybrid RANS-LES models for CFD simulation of VAWT flows, there has been no comprehensive investigation to assess the capability of hybrid RANS-LES models for predicting VAWTs performance compared to URANS models for all regimes of TSR operation. Mostly, previous studies only compare one hybrid RANS-LES turbulence model with a few URANS turbulence models or even only one URANS turbulence model. They did not provide a direct comparison between several hybrid RANS-LES turbulence models. Moreover, they usually only compared the C_p predictions rather than the blade instantaneous moment coefficients and the details of blade aerodynamics. In addition, they did not present the effects of turbulence models on the accuracy of predicting VAWT performance in all three TSR operational regimes and the reason(s) behind them.

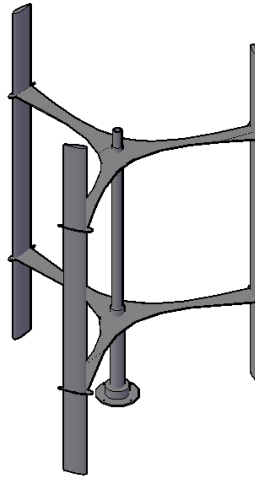
Therefore, in this chapter, a comparison study is performed for the accuracy of VAWT simulation of three different hybrid RANS-LES models, namely DDES, IDDES and a relatively new hybrid RANS-LES model: the stress-blended eddy simulation SBES, along with three URANS turbulence models, namely $k-\varepsilon$ realisable with enhanced wall treatment, $k-\omega$ SST and Transitional SST models in all three TSR operational regimes. This chapter starts with an explanation of the adopted VAWT geometry (see Section 4.1). Then, the domain and grid decomposition are discussed in Section 4.2. Furthermore, Section 4.3 will deliberate the computational settings that are used in this study. Although this study is focused on the choice of turbulence models (hybrid RANS-LES and URANS turbulence models), the effect of domain size, grid convergence and timestep independence are also evaluated before studying the effect of the turbulence model to ensure that the model is independent of the change in these parameters (see Section 4.4).

Due to the importance of obtaining a statistically converged flow-field before collecting data samples in VAWT simulations, the comparison of revolution

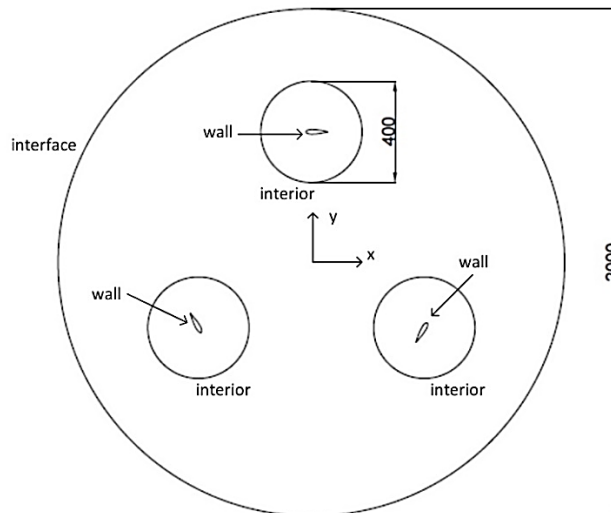
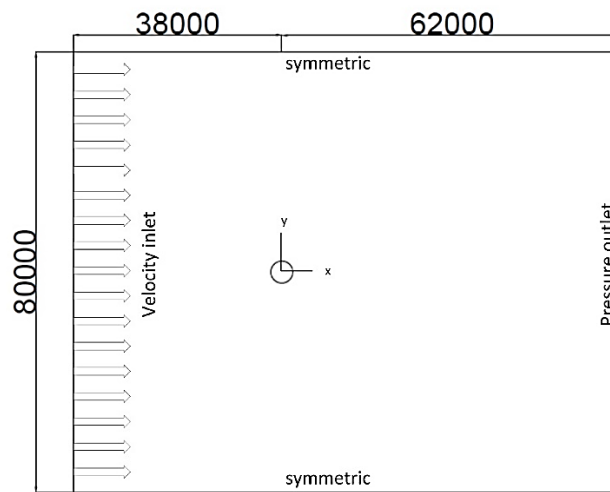
convergences between hybrid RANS-LES and URANS turbulence models is undertaken before investigating the effect of turbulence models on the prediction of VAWT performance. This evaluation is discussed in Section 4.5. Moreover, in Section 4.5, the power coefficient results of the CFD simulations are also compared with the results of the wind tunnel experiments by Castelli, Englaro and Benini (2011) and analyses undertaken in all three *TSR* operational regimes. The distribution of instantaneous moment coefficients and blade aerodynamics are only compared within the results of CFD simulations as Castelli, Englaro and Benini (2011) only provided experimental results of the power coefficient. The detailed comparison of this study will help to understand the performance of the hybrid RANS-LES model in VAWT simulations compared to the URANS turbulence model, in particular the new SBES hybrid RANS-LES turbulence model, in all three *TSR* operational regimes. Lastly, the summary and further work of the following chapter are presented in Section 4.6.

4.1 VAWT Geometry

The study is based on experimental and numerical studies by Castelli, Englaro and Benini (2011), which have been widely used as validation cases in many numerical studies of VAWTs (Rezaeiha, Montazeri and Blocken, 2019; Ghazalla, Mohamed and Hafiz, 2019; Wang et al., 2018; Sobhani, Ghaffari and Maghrebi, 2017). The experiment considered a three-straight-bladed Darrieus VAWT equipped with NACA 0021 aerofoils for *TSRs* ranging between 1.44 and 3.3, as shown in Figure 4.1. The trailing-edge of each blade is defined as a straight wall with a finite thickness of 0.3792 mm. The turbine aspect ratio is 1.4. The free stream velocity (U_∞) is set to be 9 m/s. The turbine rotational speed (ω_r (rad/s)) is calculated based on Equation (3.2). The main geometrical features and the operational parameters of the test VAWT (both numerical and experimental models) can be found in Table 4.1. Note that Castelli, Englaro and Benini (2011) have also compared the results of their three-dimensional experiment with two-dimensional CFD simulations regarding the power coefficient. They argued that the differences between the results of the 3D experiment and 2D CFD were mainly caused by the combined effects of finite blade length and spoke drag.



(a)



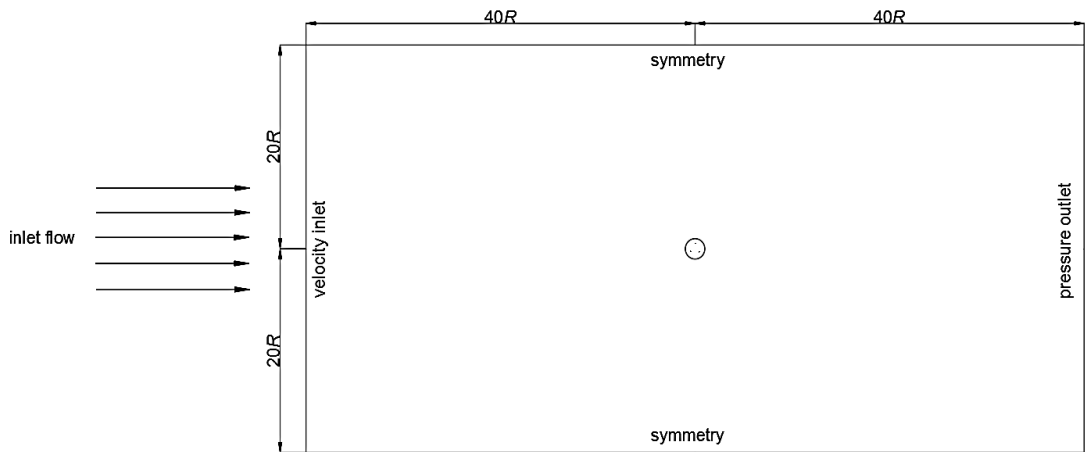
(b)

Figure 4.1 VAWT model based on Castelli, Englaro and Benini (2011), (a) 3D experimental and (b) 2D computational domain (all measurements are in *mm*).

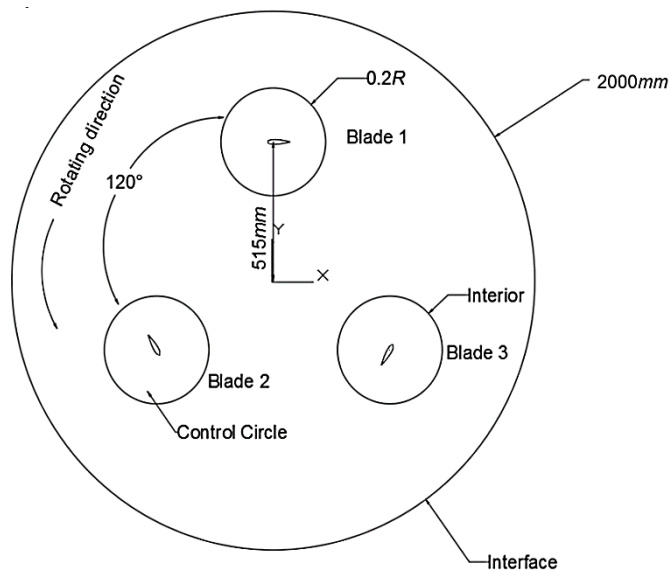
Table 4.1 Main geometrical features of Castelli, Englaro and Benini (2011) model.

Parameters	Simulation	Experiment
VAWT diameter ($D_{rotor} (mm)$)	1030	1030
Blade height ($H_{rotor} (mm)$)	1000 (for 2D simulation)	1456.4
VAWT swept area ($A_s (m^2)$)	1.03 (for 2D CFD VAWT simulation, A_s is equal to the D_{rotor} multiply by the H_{rotor} (i.e., 1 m))	1.236
Number of blades ($N (-)$)	3	3
Blade profile	NACA 0021	NACA 0021
Chord length ($c (mm)$)	85.8	85.8
Spoke-blade connection	0.25c	0.5c
solidity ($\sigma (-)$)	0.5	0.5

4.2 Simulation Domain and Grid Decomposition



(a) Overall computational domain



(b) Rotating core sub-domain

Figure 4.2 Detailed computational domain and sub-domains.

Figure 4.2 illustrates a 2D computational domain consisting of a rotating core with three turbine blades placed inside it and a rectangular far-field sub-domain surrounding the rotating core. The current CFD mesh uses a hybrid mesh type and has 117,353 elements and 174 elements around each blade surface with refined meshes towards both the leading and trailing-edge regions, respectively. In order to have a good quality mesh, the skewness is kept under 0.85 and the maximum change in grid spacing is less than 20% (i.e., maximum change between two neighbouring meshes is around 1.2).

4.2.1 Rectangular far-field sub-domain

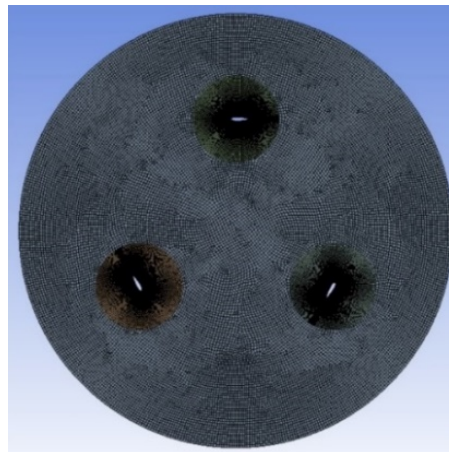
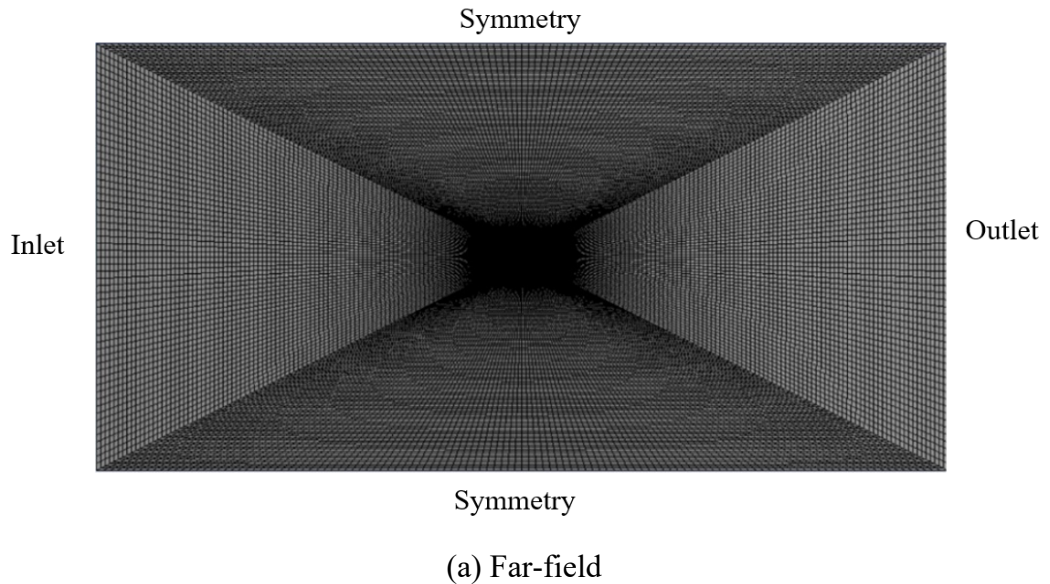
A rectangular domain is used for the far-field. As suggested by Wang et al. (2018), both inlet and outlet planes are placed at 40 rotor diameters away from the centre, whilst the outer domain boundaries are placed at 20 rotor diameters away from the centre of the turbine rotational axis, so numerical boundary conditions will have negligible influences on simulation results. Noting that, this study also evaluates the effect of the location of these boundaries, which will be explained in Section 4.4.1. The inlet and outlet are set as velocity inlet and pressure outlet conditions, respectively. Meanwhile, symmetry boundary conditions are used for the side boundaries to ensure that a zero flux of all quantities across the side boundaries. It is also to reduce the possible influences of the domain dimensions on the flow-field (Lanzafame, et al. 2020). A structured grid with quadrilateral elements is generated for this non-rotating domain (see Figure 4.3 (a)). This domain has overall 34,200 elements.

4.2.2 Rotating core sub-domain

The circular rotating core is treated as the fluid region representing the VAWT revolution. As mentioned in the previous studies (Rezaeiha, Montazeri and Blocken, 2018; Balduzzi et al., 2016), the size of the rotating core needs to be at least around 1.5-2 times that of turbine diameter to avoid unwanted disturbances produced by the sliding interface. In this study, the size of the rotating core is the same as those well-validated studies, which is 2000 mm (about 1.94 times of turbine diameter).

Together with meshes inside, the domain rotates in an anticlockwise direction around the turbine rotational axis at a given angular velocity. The mesh moves at the prescribed speed for this simulation. Therefore, the mesh motion is only applied in this sub-domain. In general, mesh topologies and even sizes could be different between the far-field domain and the rotating core sub-domain. Thus, to ensure the continuity of fluid

flow across the interface, a sliding boundary condition is set at the interface between these two domains, together with data interpolations of the same or higher order than the numerical scheme. The rotating core sub-domain uses dominant quadrilateral elements (see Figure 4.3 (b)) with a total number of 20,513 elements.



(b) Rotating core

Figure 4.3 Grid details for the two main sub-domains.

4.2.3 Control circle sub-domain

Three control circles with embedded blades are placed inside the rotating core, separated by a 120° angular distance to each other. Each control circle has a radius of 200 mm, in which a structured O-type grid discretisation around the blade is produced. The total elements in each control circle are 20880. The control circle boundary is set as 'interior' to ensure the continuity of the fluid flow. Blade surfaces are defined as rotating

walls with reference to the rotation centre, i.e., the main rod of the spoke-blade-connection on each blade, to ensure it rotates together with the rotating core sub-domain.

The grid discretisation in this sub-domain uses structured quadrilateral elements with fine grids in the near-wall region (Figure 4.4). When applying the turbulence model to solve the near-wall region, the first element must be placed inside the viscous sublayer. Hence, the normal distance of the first element to the wall must be pre-defined to satisfy the criteria of the non-dimensional wall distance of $y^+ < 1$ (for the SST turbulence model). As the wall function is not applicable for flows that experience flow separation like flow around the blade of VAWT, it is important to maintain a y^+ value lower than unity to properly resolve the laminar sublayer region near the wall (Bangga et al., 2017). Note that LES criteria in the far-field region are applied when generating grids for DDES and IDDES turbulence models. For Wall-Modelled LES (WMLLES) approach, the element size in the x -direction (Δ_x) should be less than or equal to half of the boundary layer thickness whilst the near-wall grid points need to maintain the y^+ value in the y -direction (i.e., $y^+ = 1$). Hence, this study has two grid types. The first grid type is the one used for DDES and IDDES turbulence models, which has a higher number of elements to accommodate the LES criteria in the far-field region and the second grid type is the one used for URANS turbulence models in the rest of the flow domain.

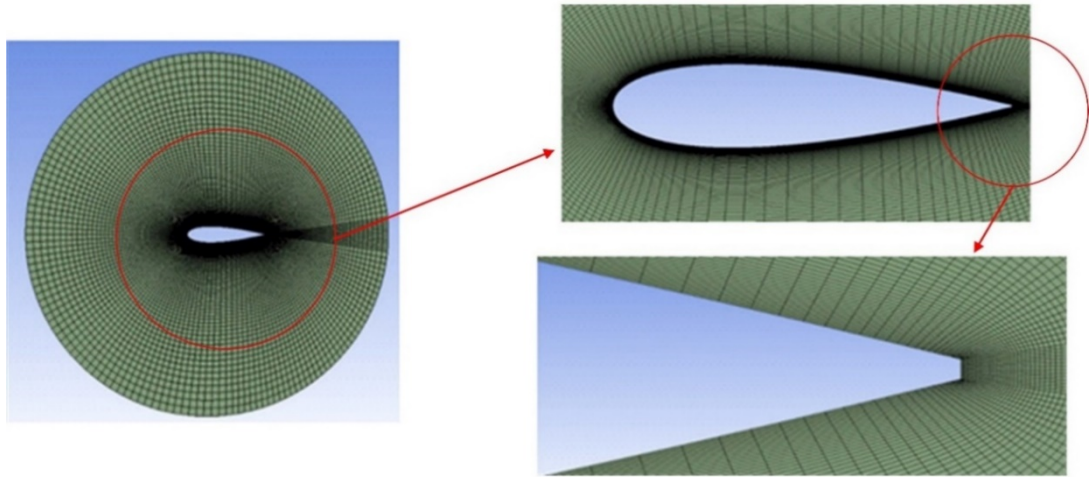


Figure 4.4 Detailed grid around the blade wall.

4.3 Computational Settings

In this study, the incompressible URANS equations are solved using a coupled numerical scheme for pressure-velocity coupling and a second-order scheme for temporal

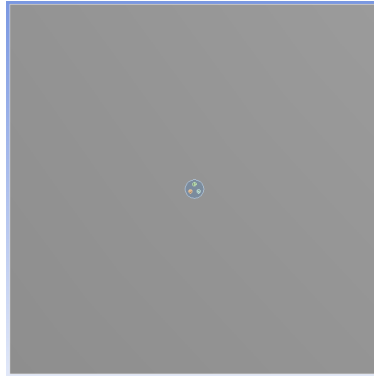
and spatial discretisation. In hybrid RANS-LES simulations, computational settings remain the same as URANS simulation except for momentum spatial discretisation where Bounded Central Differencing is applied as the requirement of the hybrid RANS-LES model. All residual convergence criteria for the inner loop are set to be equal to or less than 10^{-6} .

As mentioned in Chapter 3, Section 3.2.4.5, it is difficult for all parameters to reach the same residual criteria simultaneously during the simulation due to the complex nature of VAWT. In order to overcome this issue, a previous study suggested that applying 40 inner loop iterations in each time step could reduce the turbulence kinetic energy residuals by order of 10^{-4} (Balduzzi et al., 2016). Hence, 40 inner loop iterations per time step are applied in the simulations. Note that for the initialization procedure, this study uses hybrid initialization, which is a collection of recipes and boundary interpolation methods (Ansys, 2020). A Laplace equation is solved during the initialization to produce a velocity field that conforms to complex domain geometries and a pressure field that smoothly connects high and low-pressure values in the computational domain (Ansys, 2020).

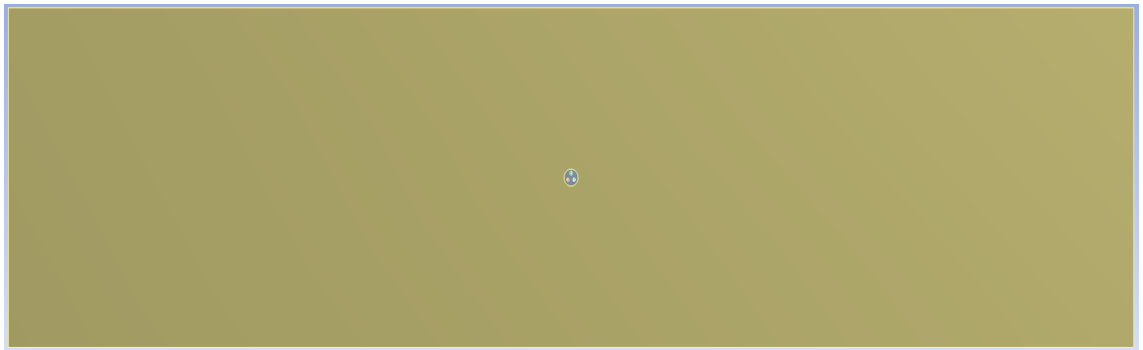
4.4 Domain, Spatial and Temporal Convergence Studies

4.4.1 Domain size study

As mentioned in Chapter 3, Section 3.2.5, it is essential to build the boundaries of the domain far enough from the simulated model to ensure that the boundaries do not significantly affect the simulation results. This study also performs domain size evaluation to ensure that the far-field sub-domain is large enough to accommodate the mentioned criteria. Three different sizes of far-field sub-domain are evaluated. The base far-field sub-domain is adopted from a study by Wang et al. (2018) as it was already proven that numerical boundary conditions have negligible influences on simulation results. The inlet and outlet planes are placed 40 rotor diameters away, whilst the side boundaries are placed 20 rotor diameters away from the centre of the turbine rotational axis. Then, this base far-field domain is modified by changing the inlet and outlet position to the 20 (smaller domain) and 80 (larger domain) rotor diameter away from the centre of the turbine rotational axis, respectively (see Figure 4.5 (a) and (b), respectively).



(a)



(b)

Figure 4.5 Modified far-field sub-domain, (a) smaller domain ($20D_{rotor}$) and (b) larger domain ($80D_{rotor}$) (the drawing is not in scale).

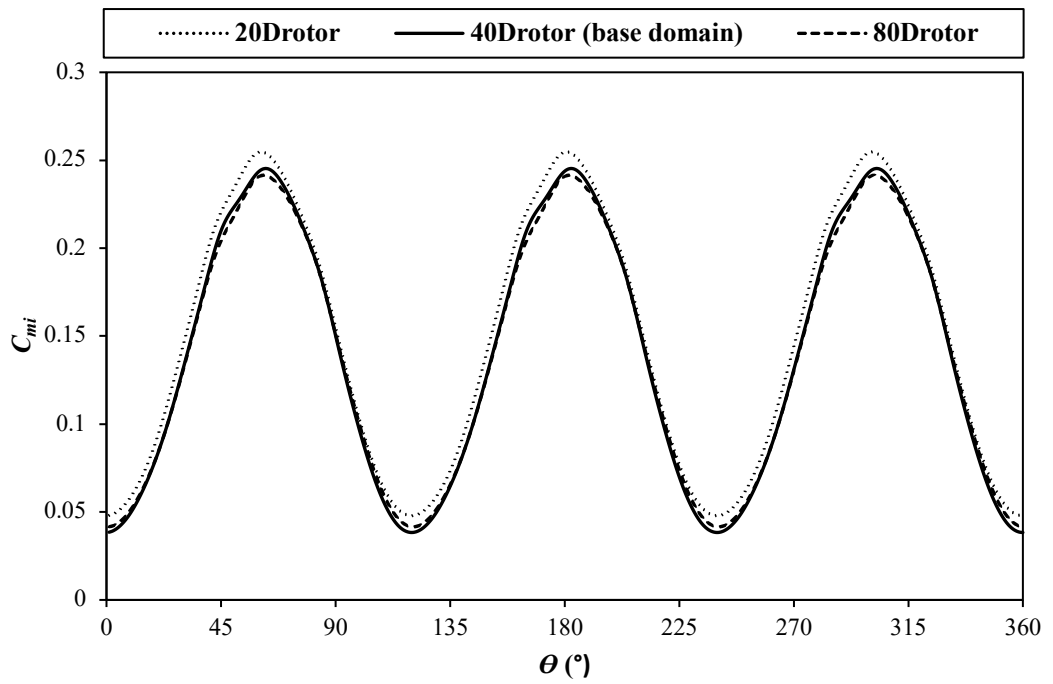


Figure 4.6 C_{mi} of the three different far-field sub-domain sizes over one turbine revolution.

Figure 4.6 depicts the comparison of C_{mi} of the turbine over one revolution in $TSR = 2.64$ (using the RKE turbulence model) between three different far-field domain sizes. The C_{mi} value here is extracted after the difference between the latest revolution and the previous revolution is less than 1%. The calculation of each C_m is defined by equation (3.8). It is shown that increasing the domain size from the base domain does not significantly change the C_{mi} distribution. The C_{p-ave} value demonstrates only a 0.1% difference between the base and larger domains. On the other hand, decreasing the far-field sub-domain size give a relatively higher effect on the C_{mi} distribution. For the smaller domain, the C_{p-ave} value changes about 5.5% compared to the base domain. Therefore, the base domain is chosen for the rest of the simulation.

4.4.2 Spatial (grid) convergence study

Simulations for a case study of $TSR = 2.5$ were performed on coarse, medium and fine successive grids (see Table 4.2) for a grid convergence study using the RKE turbulence model. The influence of element sizes around the blade is considered with 87, 174 and 348 grid elements, respectively, for each simulation.

Table 4.2 Details of the number of elements for each grid.

Grid	Type of grid	Total Elements	Elements around blade wall	Trailing-edge elements
Coarse	Structured grid	86033	87	7
Medium		117353	174	14
Fine		179993	348	28

Figure 4.7 illustrates the comparison of C_{mi} using different grids. C_m is chosen as most of VAWT studies compared C_m or C_p in their grid convergence study (Rezaeiha, Montazeri and Blocken, 2019; Ghazalla, Mohamed and Hafiz, 2019; Wang et al., 2018; Sobhani, Ghaffari and Maghrebi, 2017; Castelli, Englaro and Benini, 2011) and the available experimental data of the evaluated VAWT is only C_p (Castelli, Englaro and Benini, 2011). The curves representing the moment coefficient at varying azimuthal positions have shown little difference between medium and fine grid results, whilst the coarse grid could not produce satisfying instantaneous moment coefficients. Moreover, the relative discrepancy C_{p-ave} between the medium and fine grids is less than 0.02%. Therefore, the medium grid is chosen for the rest of the simulations.

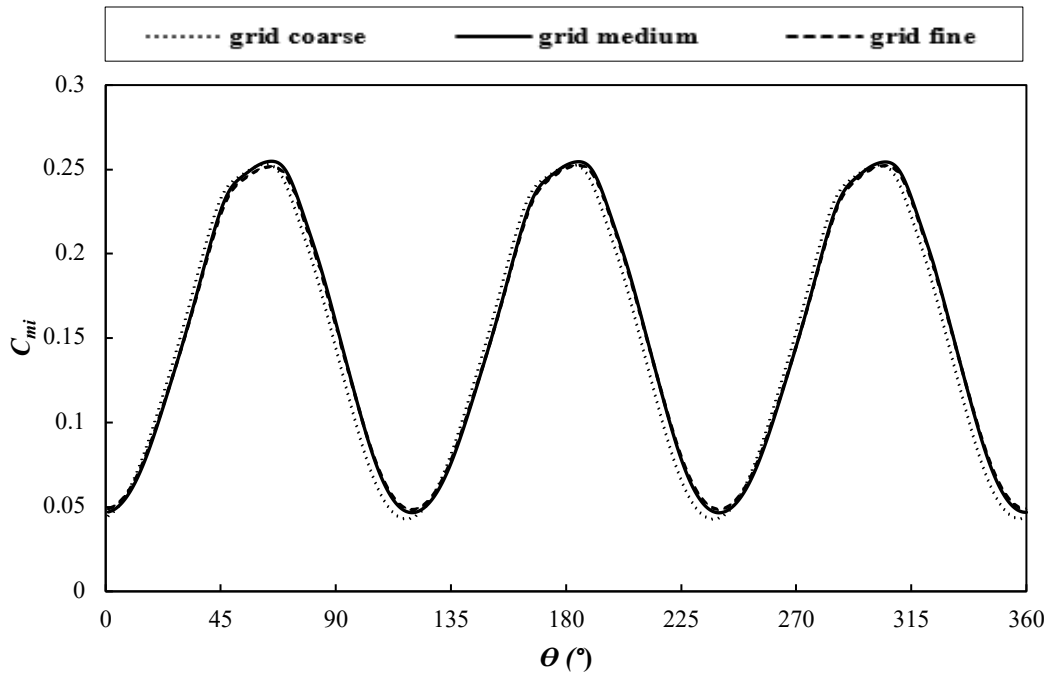


Figure 4.7 Comparison of C_{mi} of VAWT with different grids.

4.4.3 Temporal resolution study

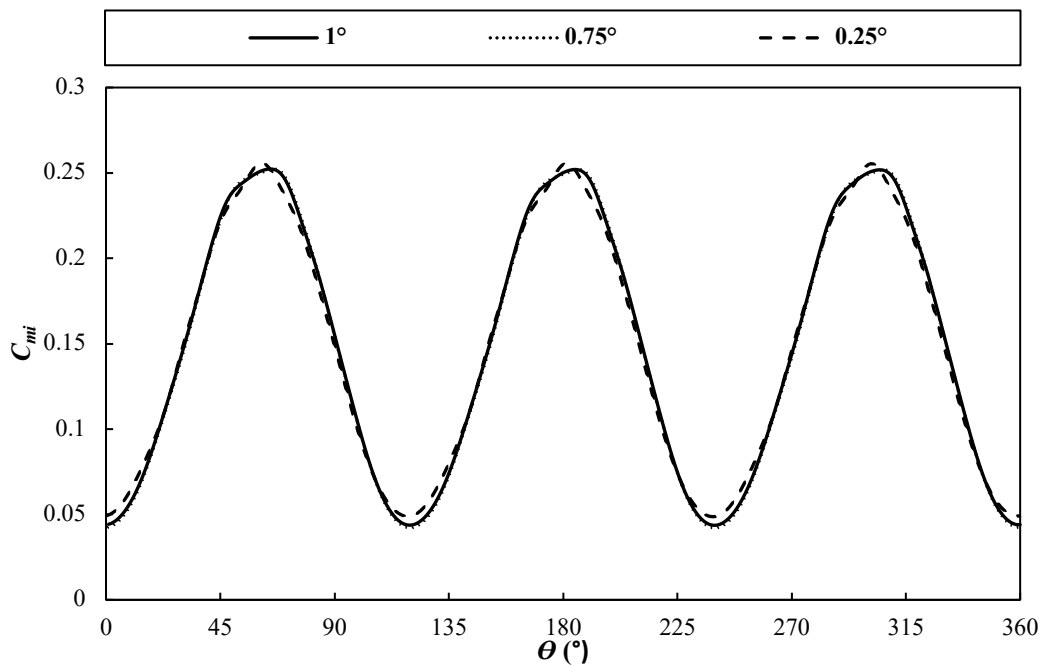


Figure 4.8 C_{mi} of three different time steps over one turbine revolution.

McMullen, Jameson and Alonso (2001) stated that the rate of rotation and the number of blades significantly affect the periodicity of relative motion of the rotating blades, which is the main contributor to the unsteadiness of VAWTs. Castelli, Englaro

and Benini (2011) have considered this effect by defining a small time step as the rotor's lapse time making a 1° rotation. They also found that any further reduction of time step did not improve the accuracy of the simulation results. The current simulation repeats the time independence study with three different time-step settings corresponding to three different time-lapses for 1° , 0.75° and 0.25° rotations, respectively, to confirm their findings.

The C_{mi} over one complete turbine revolution of three different time-steps in $TSR = 2.5$ is illustrated in Figure 4.8. It was found that there were no significant differences in C_{mi} between three different time steps. In addition, C_{p-ave} between 1° and 0.25° time steps shows a slight difference of only 0.44%. Hence, for the rest of the simulations, the time step equals the rotor's lapse making a 1° rotation is chosen.

4.5 Impact of Turbulence Models

4.5.1 Revolution convergence analysis

In VAWT simulations, it is important to obtain a statistically converged flow-field before collecting data samples. Hence, several studies have suggested some required number of turbine revolutions to run before collecting the data. It was usually defined by analysing the time history of the moment coefficient or power coefficient.

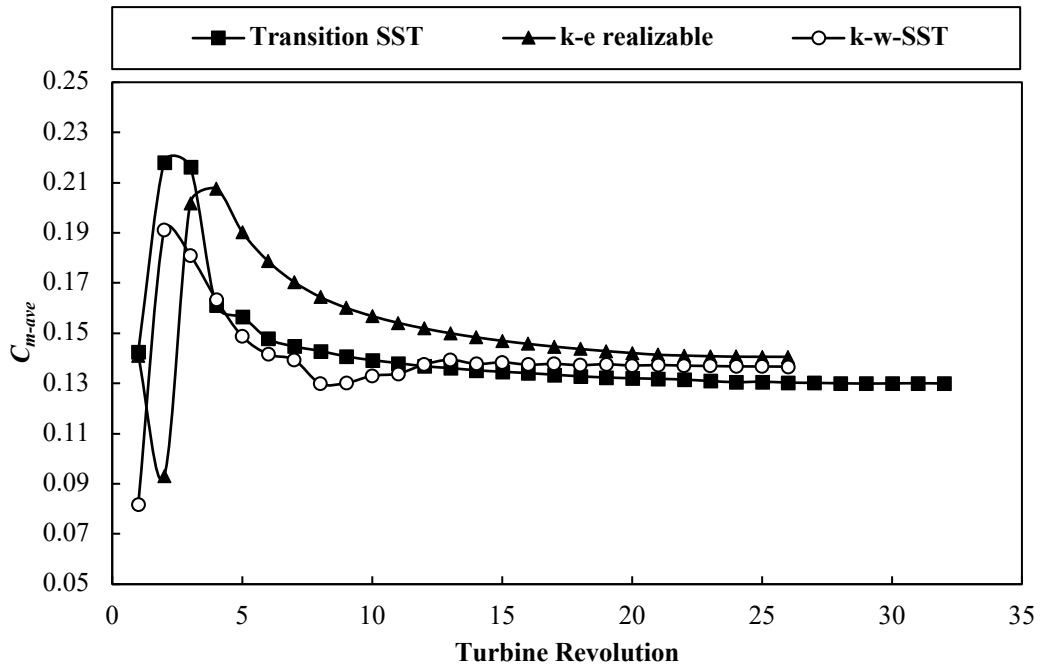


Figure 4.9 C_{m-ave} changes over turbine revolution for URANS turbulence models.

In the previous URANS simulation, Castelli, Englaro and Benini (2011) started the data sampling whilst the C_{m-ave} variations of the turbine between two neighbouring revolutions is less than 1%. Another study using the TSST turbulence model (Rezaeiha, Montazeri and Blocken, 2018) has found that the changes of C_{m-ave} and C_{p-ave} could be below 0.1% and 0.2%, respectively after 20 revolutions, and the cumulated differences of these two values were as low as 1.06% and 2.41%, respectively, between 20 and 100 revolutions. Therefore, this study will start the data retrieval using these examples after the C_{m-ave} variations fall under 0.1%.

Noting that, in this study, the y^+ value has been kept between 1 and 1.1 during the simulation. The mass imbalance can be negligible as it is only about 0.00005% difference between inlet and outlet mass. Moreover, the residual of all other parameters in this study can reach the order of 10^{-6} except the residual of turbulence kinetic energy which can only reach the order of 10^{-4} . This is understandable as it was mentioned above (see Chapter 3, Section 3.2.4.5) that due to the complex nature of VAWT simulation, it is difficult to always reach the residual criteria of each parameter simultaneously (Balduzzi et al., 2016).

In the case of URANS turbulence models, this study finds that the C_{m-ave} dropped less than 0.1% compared to the previous revolution after 23 revolutions (see Figure 4.9) for both RKE and SST turbulence models, confirming that a good convergence has been achieved. Hence, for the case of these two-equation URANS turbulence models, the data retrieval can be done at the 24th revolution. On the other hand, the four-equation URANS turbulence model, i.e., TSST needs 27 revolutions before the C_{m-ave} dropped less than 0.1%. Therefore, the data can be collected at the 28th revolution for this turbulence model. TSST turbulence model takes longer to achieve statistically steady C_{m-ave} than two-equations URANS turbulence models, probably due to the addition of two more equations for the intermittency and momentum thickness Reynolds number.

For hybrid RANS-LES turbulence models, all four tested turbulence models need 34 revolutions before the C_{m-ave} dropped less than 0.1% (see Figure 4.10). Compared to the URANS, hybrid RANS-LES turbulence models took more revolutions to reach convergence status. It is probably because URANS turbulence models mainly solve the mean flow and those large flow motions in the near field and use ensemble averaging solution in the far-field (Salim, Ong and Cheah, 2013). In contrast, the hybrid RANS-LES turbulence model utilises the LES model in the far-field, which can resolve the flow

fluctuations to some extent, and as a result, it will take a longer time to achieve statistically converged flow-field for both near and far-fields.

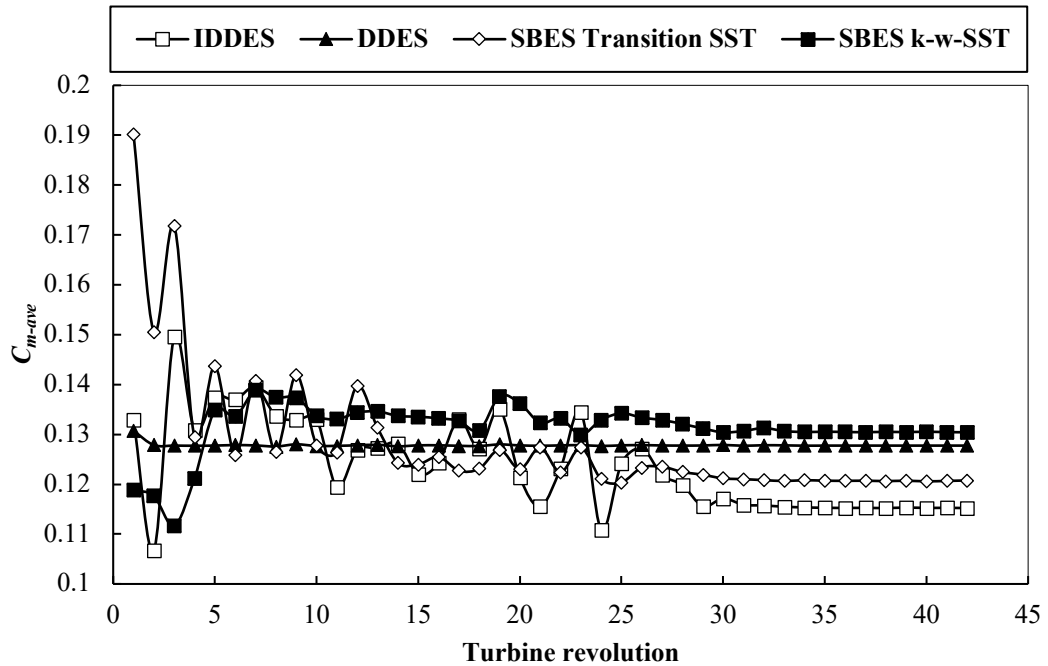


Figure 4.10 C_{m-ave} changes over turbine revolution for hybrid RANS-LES turbulence models.

4.5.2 Revolution averaged turbine power coefficient (C_{p-ave})

4.5.2.1 URANS turbulence models

Figure 4.11 shows the revolution C_{p-ave} prediction of current CFD simulations using two-equation URANS turbulence models (RKE and SST) and a four-equation URANS turbulence model (i.e., TSST), compared with the experimental and the CFD simulation results of Castelli, Englaro and Benini (2011) using the RKE model. The current CFD simulations successfully generate the C_{p-ave} curve in a similar trend to the previous study's experimental and CFD simulation results. It is also able to capture the optimum $TSR = 2.64$, which gives the maximum C_{p-ave} . In addition, the current CFD results give better C_{p-ave} predictions in all three TSR regimes than the CFD predictions of Castelli, Englaro and Benini (2011), even for the same turbulence model (i.e., RKE). This might be due to the grid quality improvement, smaller time steps, higher order of residual convergence criterion, and the number of iterations. Further investigation about the reason behind this improvement needs to be performed in the future study.

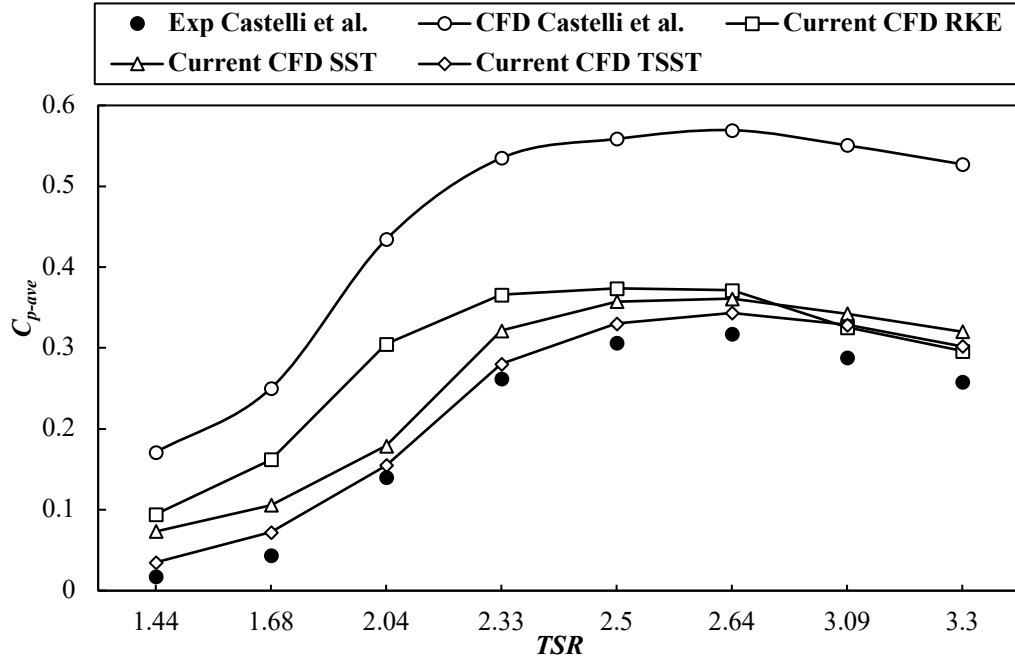


Figure 4.11 C_{p-ave} comparison of current CFD simulations using RANS turbulence models and the experimental and CFD using RKE results of Castelli, Englaro and Benini (2011).

From Figure 4.12, it can be observed that the two-equation URANS turbulence models (RKE and SST) still overestimate the experimental C_p across the three tested TSR regimes. Compared to medium and high regimes of $TSRs$, these turbulence models generate significant discrepancies in low regime of $TSRs$ (<2). This is understandable as flow around VAWTs will experience a high level of unsteadiness in low TSR regime compared to medium and high regimes of $TSRs$ (>2). This behaviour is caused by a higher AoA_D frequently experienced by VAWT blades, even beyond the static stall $AoAs$, in low regime of $TSRs$ compared to medium and high regimes of $TSRs$ (Ma et al., 2018). This condition can trigger dynamic stall with drag reduction called dynamic drag stall at high AoA . Moreover, flow around blades could experience the large viscous region in low $TSRs$ regimes due to low Re number effects (Lei et al., 2017). Hence, the RKE model generally produces a massive discrepancy (in this case is about 441% compared to experimental data in the lowest value of TSR) as it has a reputation for generating poor flow prediction accuracy with prominent separation and over-prediction of turbulence kinetic energy (Wilcox, 2006). In addition, it also performs poorly in low Re number due to the need to generate viscous corrections to reproduce the law of the wall for flow with low Re number (Wilcox, 2006). Even though the SST model results still give a

significantly large discrepancy of the C_{p-ave} value of experimental data, this turbulence model generates better predictions than the RKE model. As mentioned by Wilcox, the $k-\omega$ model can give a more accurate prediction of the C_{p-ave} value of experimental data for flow with separation and with the absence of viscous correction, it can produce better predictions than the $k-\epsilon$ model in flow with low Re number (Wilcox, 2006). In cases of medium and high regimes of $TSRs$, the flow around VAWTs will have lower-level unsteadiness as the blades experience dynamic stall with lift increases in low AoA , similar to a sinusoidal pitching aerofoil (Malael, Dumitrescu and Cardos, 2014). Therefore, although the flow still separates, it is relatively easier for these two turbulence models to generate more accurate predictions than for cases in low regime of $TSRs$.

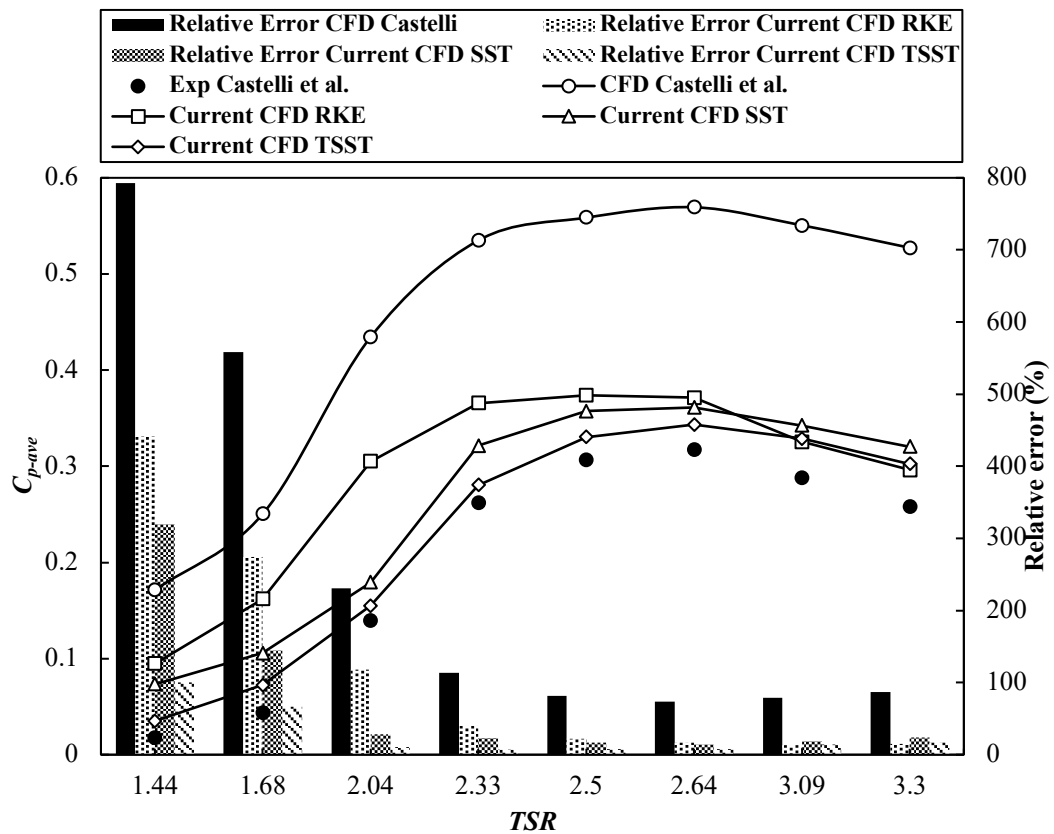


Figure 4.12 Comparison of C_{p-ave} between current CFD simulation and the experiment and simulation of Castelli, Englaro and Benini (2011), as well as relative discrepancies to the experimental data in percentage.

During the evaluation of the flow type around VAWTs, the flow is assumed to be predominantly laminar, as the estimated Reynolds number based on the free stream velocity and the blade chord, Re_{U_∞} is about 51000. However, when the VAWT simulation

is carried out using a laminar viscous model, the results are far from the experiment and the instantaneous moment coefficient distribution. For this reason, it can be concluded that the flow does not retain the laminar flow characteristics. As the blades are rotating, the generated rotating speed will facilitate the development of flow turbulence. The Reynolds number based on the angular velocity (Re_Ω) (see Equation (4.1)) indicates that the flow is already in turbulent status even in the lowest TSR , i.e. $Re_\Omega = 449460$ in $TSR = 1.44$, $Re_\Omega = 815760$, in $TSR = 2.64$ and $Re_\Omega = 1019700$ in $TSR = 3.3$, respectively. Note that the flow is categorised as turbulent flow if Re_Ω is more than 60, according to a previous study (Childs, 2011).

$$Re_\Omega = \frac{\rho \omega_r R^2}{\mu} \quad (4.1)$$

Hence, the VAWT blades will experience laminar-to-turbulent flow transition from the incoming background flow to the zone of rotating flow (Rezaeiha, Montazeri and Blocken, 2019).

The averaging process in RKE and SST turbulence model equations does not accommodate the description of transitional flows where both nonlinear and linear breakdowns from laminar to turbulent effects are relevant (Menter, Langtry and Volker, 2006). The averaging method of these two models ignores the effects of linear growth of the disturbance, and as a result, there is difficulty in applying these two models to the transition process (Menter, Langtry and Volker, 2006). To overcome this, the TSST turbulence model is applied for the current CFD simulation. As described in Appendix D, section D.1.3, this model has two additional transport equations, one for intermittency (γ) (see Equation (D.8)) and the other for the transition onset criteria in term of momentum-thickness Reynolds number (Re_θ) (see Equation (D.9)), with the SST $k-\omega$ transport equations. The two additional equations are applied to enable the SST $k-\omega$ model to predict the transition onset and length (Langtry and Menter, 2009). Turbulence production limiters are also included in this model to eliminate an excessive turbulence kinetic energy prediction in the stagnation region. As illustrated in Figure 4.12, this model can significantly decrease discrepancies in all regimes of $TSRs$. These results suggest that the VAWT blades indeed experience transition flow.

4.5.2.2 Hybrid RANS-LES turbulence models

To further decrease the CFD prediction discrepancy, it is recognised that the use of LES or Direct Numerical Simulation (DNS) is preferable. However, the high computing time and cost demands make these two methods hardly used in VAWT CFD simulation. Hence, in order to reach a similar result as LES with less computing time and simulation demands, hybrid RANS-LES turbulence models are preferred to be used in VAWT CFD simulations.

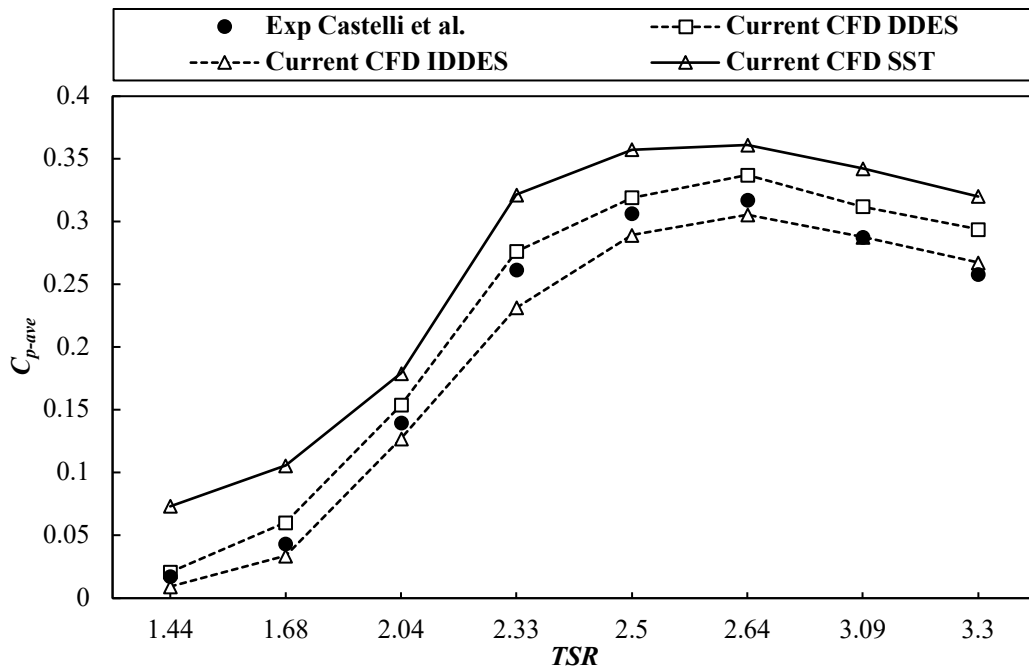


Figure 4.13 C_{p-ave} comparison of current CFD simulations using SST, DDES and IDDES turbulence models and Castelli, Englaro and Benini (2011) experimental results.

Figure 4.13 illustrates the C_{p-ave} prediction of current CFD simulations using hybrid RANS-LES turbulence models called DDES and IDDES, compared with current CFD URANS SST $k-\omega$ simulation and the experimental results from Castelli, Englaro and Benini (2011). It is seen that these turbulence models generate a similar trend to the experiment results. The DDES model decreases the simulation discrepancy in all $TSRs$ regimes (see Figure 4.14) compared to the SST model. This is expected as this turbulence model is based on the SST model, so it will inherit the ability of SST to give good accuracy in flow with separation and low Re number (Wilcox, 2006). In addition, the LES mode will decrease the discrepancy caused by the RANS turbulence model. This mode can fix the problem of incorrect calculation of the momentum transport in the far-field of

the RANS turbulence model (due to the isotropic treatment of turbulence from the RANS averaging method) by solving the large eddies in the far-field using the LES model. The incorrect calculation of momentum transport in the far-field can generate unwanted greater intermittency (Warhaft, 2000) (For example, turbulent heat fluxes caused by RANS simplification do not affect the mean temperature, whilst the turbulence fluctuations may produce a significant change of properties in space and instantaneous properties in time (McDonough, 2007)). For IDDES, whilst all URANS turbulence models and DDES overestimate the C_{p-ave} in all TSR regimes, this model underestimates C_{p-ave} except for the prediction in $TSR = 3.3$. Nonetheless, this model can generate a relatively smaller discrepancy than the DDES model (in comparison, the IDDES model generates an average discrepancy across all $TSRs$ of around 9% whilst the DDES model gives about 13.5%).

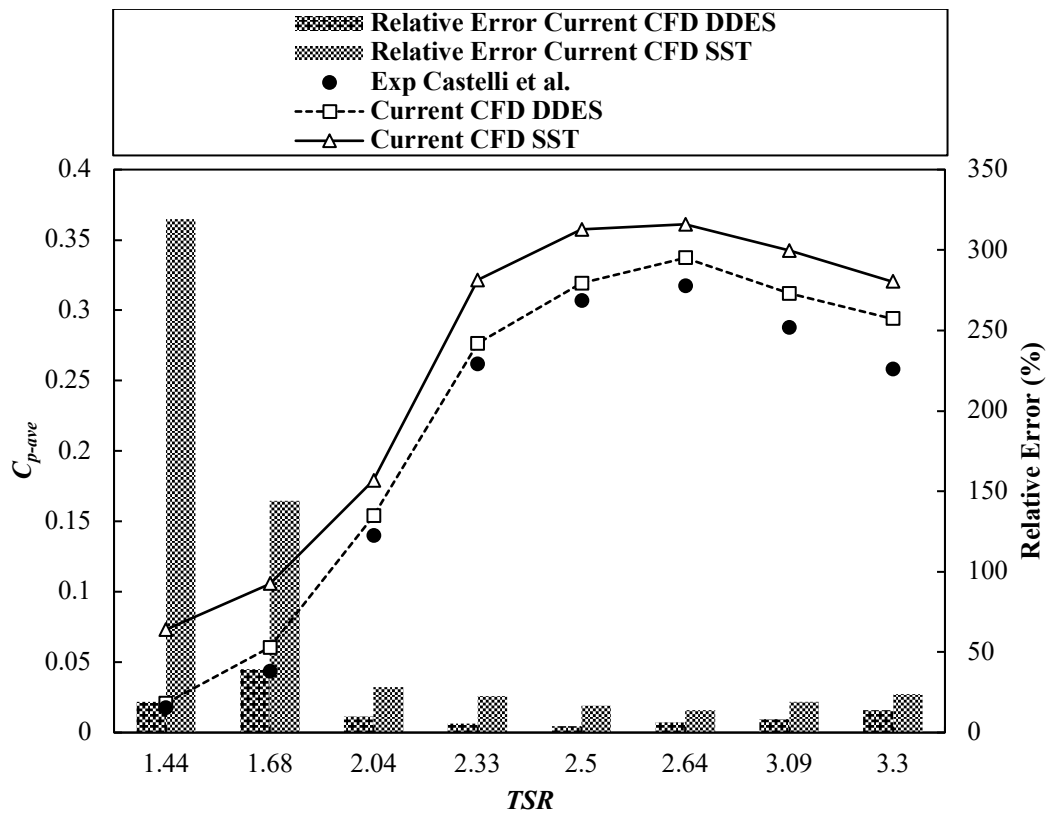


Figure 4.14 Comparison of C_{p-ave} between current DDES and Transitional SST CFD simulations and the experimental results of Castelli, Englaro and Benini (2011), as well as relative discrepancies to the experimental data in percentage.

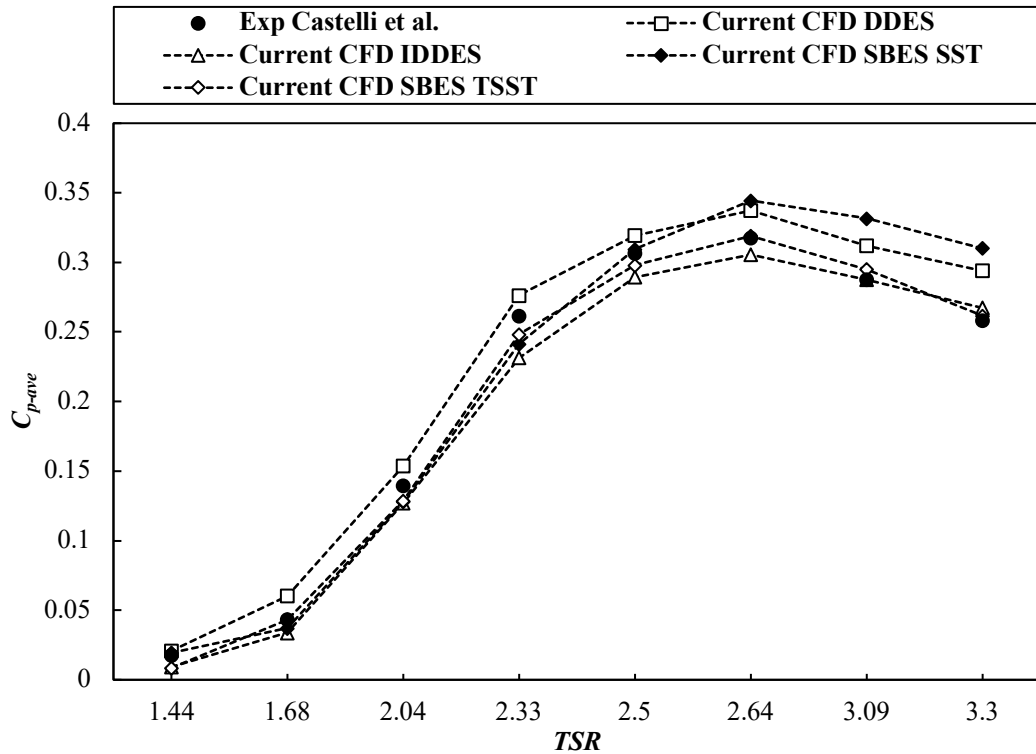


Figure 4.15 C_{p-ave} comparison of current CFD simulation using SBES turbulence models based on SST $k-\omega$ and Transitional SST RANS turbulence models and Castelli, Englaro and Benini (2011) experimental results.

Despite producing better results, these two models (DDES and IDDES) have some complexities during the grid generation. Like other standard DES methods, DDES and IDDES have the grid requirement of the LES method in the far-field that can still add a tremendous amount of computational time and cost. Moreover, due to the zonal method changing from RANS to LES mode, DES is very sensitive to the local grid size, mainly in the “grey area” where the model changes from RANS to LES mode, which can introduce a problem called modelled-stress depletion (MSD) (Spalart et al., 2006). It occurs because when the grid is gradually refined or the geometric features demand a fine wall-parallel grid or a boundary layer thickens and near flow separation (leading to the ambiguous grid, i.e. the grid should be still treated as RANS or URANS region but due to the size of the grid, it is already treated as LES region or in another way), the modelled Reynolds stress terms will produce "unreal" stress in order to restore the balance due to eddy viscosity reduction caused by the DES limiter activation. MSD can lead to an "unreal" separation called GIS (Spalart et al., 2006). Even though this problem has been fixed in the DDES and IDDES models, it can still appear in extreme grids (for example:

grid with refinement in all directions (x , y and z) and separations that the VAWT flow experiences.

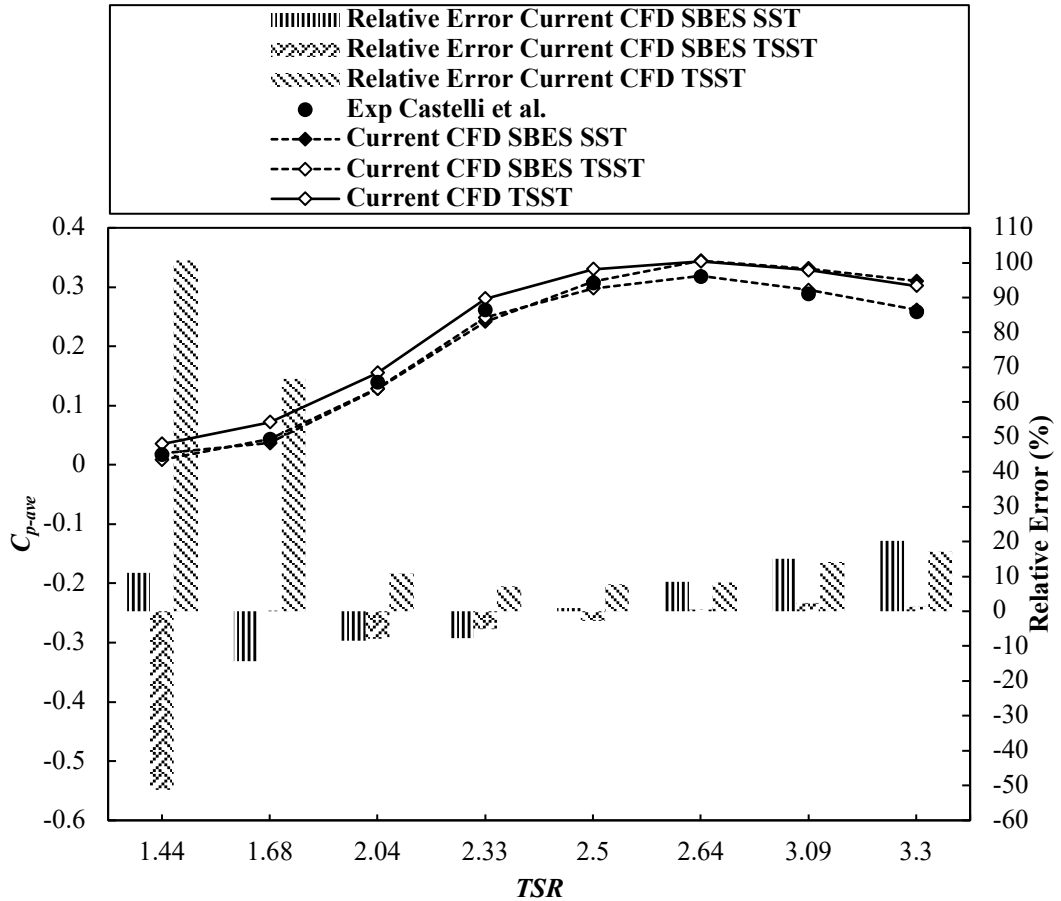


Figure 4.16 Comparison of C_{p-ave} between current SBES and Transitional SST CFD simulations and the experimental results of Castelli, Englaro and Benini (2011), as well as relative discrepancies to the experimental data in percentage.

A relatively new hybrid RANS-LES model called SBES is applied in the current CFD simulation (Menter, 2018) to overcome the grid development difficulty. As mentioned above, this turbulence model allows a RANS-LES "transition" even on a coarser grid which other DES models cannot. Based on Figure 4.15, the SBES turbulence model can reproduce the trend line of experiment results and generate relatively similar results with DDES and IDDES for both SST and TSST based SBES turbulence models. Moreover, the SBES TSST turbulence model performs better than its SST version in all $TSRs$ values except for the $TSR = 1.44$ and $TSR = 2.5$ (see Figure 4.16). It might be due to the fact that the flow in these $TSRs$ has a very low Re number and the transition

behaviour is not as strong as in higher $TSRs$. Hence, the SST version of SBES performs better than its TSST version. In addition, compared to the TSST turbulence model (the best model for URANS model in current CFD simulations), the SBES SST produces a more significant discrepancy in $TSR \geq 2.64$ (see Figure 4.16). Again, this might be caused by transition flow becoming stronger in higher $TSRs$ compared to lower $TSRs$ and therefore the TSST turbulence model is more suitable than the SBES SST. Overall, the SBES TSST turbulence model generates the smallest discrepancy (e.g., on average, discrepancy across all TSR regimes is around 8.9%) compared to all RANS and hybrid RANS-LES turbulence models.

Whilst using an appropriate turbulence model can improve the CFD predictions, simulation results still exhibit some differences compared to experimental results in all values of $TSRs$. It is likely because the experimental measurements of Castelli, Englaro and Benini (2011) are 3D data. As mentioned above (see Section 4.1), this difference is mainly caused by the combined effects of finite blade length and spoke drag. Castelli, Englaro and Benini (2011) also mentioned that the correction due to wind tunnel blockage was not applied in their study. Moreover, the experimental power coefficient curves were representative of average-stationary rotor behaviour, not the instantaneous one (Castelli et al., 2010). These two experimental setups can be considered as the uncertainty of the experimental data.

The 2D wind turbine simulation usually represents the mid-plane of a turbine with high aspect ratio, where the 3D tip effects are small (Rezaeiha, Kalkman and Blocken, 2017). Hence, the result of 2D VAWT simulation is only acceptable for VAWT with high aspect ratio. Nevertheless, it is worth note that the primary purpose of this 2D simulation study is to compare various turbulence models and assess their capability in predicting the power coefficient of VAWT quantitatively and visualising the flow around VAWT qualitatively. Whilst a full 3D simulation is preferable to capture more defined flow separation, a previous study using a hybrid LES-RANS model (DDES) showed that 2D simulation could produce similar results as 3D simulation of turbulent flow separation on the blade (Lanzafame et al., 2020), as long as the spatial and temporal discretisations are fine enough to resolve the high vorticity gradients near the blades.

4.5.3 Turbine aerodynamics characteristics over one revolution

4.5.3.1 URANS turbulence models

The detailed comparison of C_{p-ave} prediction of three different URANS turbulence models already showed that whilst the TSST model was superior in low to medium $TSRs$, its performance in high regime of $TSRs$ mainly was the same as from the RKE and SST models. Hence, further investigation to understanding these differences is discussed for each TSR regime in this section.

1) Low TSR regime (Representative $TSR = 1.44$)

Figure 4.17 displays the prediction of instantaneous moment coefficient C_{mi} , i.e., C_m value in every time step (1°), distribution of blade 1 during one revolution (360° rotation). It shows that SST and TSST models produce lower maximum C_{mi} and earlier and greater first fall of C_{mi} (around azimuthal angle (θ) = 57°) compared to the RKE model, indicating these models predict earlier and stronger flow separation. It can also be seen that in all three models, the C_{mi} distribution is constantly fluctuating with greater and similar magnitude predicted by SST and TSST models compared to the RKE results. This fluctuation demonstrates a strong flow separation at almost all azimuthal angles when the VAWT is operated in low TSR regime because the blade is mostly operated in a stall condition. Furthermore, even though SST and TSST models give a similar prediction, overall, the TSST model predicts a lower value of C_{mi} , resulting in a lower value of C_{p-ave} . Hence, the TSST model can give the smallest discrepancy of the prediction of C_{p-ave} from experimental data in this TSR .

To confirm those aforementioned behaviours, Figure 4.18 illustrates the contour plots of z -vorticity (ξ_z) at several important azimuthal angles of blade 1 to understand the prediction of the unsteady separation process of each model. ξ_z is calculated by taking the curl of the velocity vector (\vec{U}) (see Equation (4.2)).

$$\xi_z = \vec{k} \left(\frac{\partial U_y}{\partial x} - \frac{\partial U_x}{\partial y} \right), \quad (4.2)$$

where U_y is the y -velocity component and U_x is the x -velocity component. Noting that, Equation (4.2) contains the vorticity component in the z -direction.

It can be seen that from $\theta = 0^\circ$ to 45° , there is a development of trailing and leading-edges vortices with three URANS models predicting similar growth behaviour of

these vortices (see Figure 4.18 (a)). However, when the flow starts to experience a dynamic stall (the vortex shedding starts at a location around $\theta = 50^\circ$, for $Re_\Omega = 61800$), RKE and SST models predict a later strong vortex shedding development on the leading-edge with no flow vortex shedding of the trailing-edge vortex compared to TSST. As shown in Figure 4.18 (b), at $\theta = 75^\circ$, TSST already predicts strong leading and trailing-edge vortex shedding, leading to the development of dynamic stall and roll up trailing-edge vortices. In addition, as the degree of azimuthal angle increases, SST and TSST give similar vortex development with larger vortex shedding far from the wall compared to RKE. Hence the dynamic stall and vortex shedding are responsible for the fluctuations as a function of angle and turbulence model.

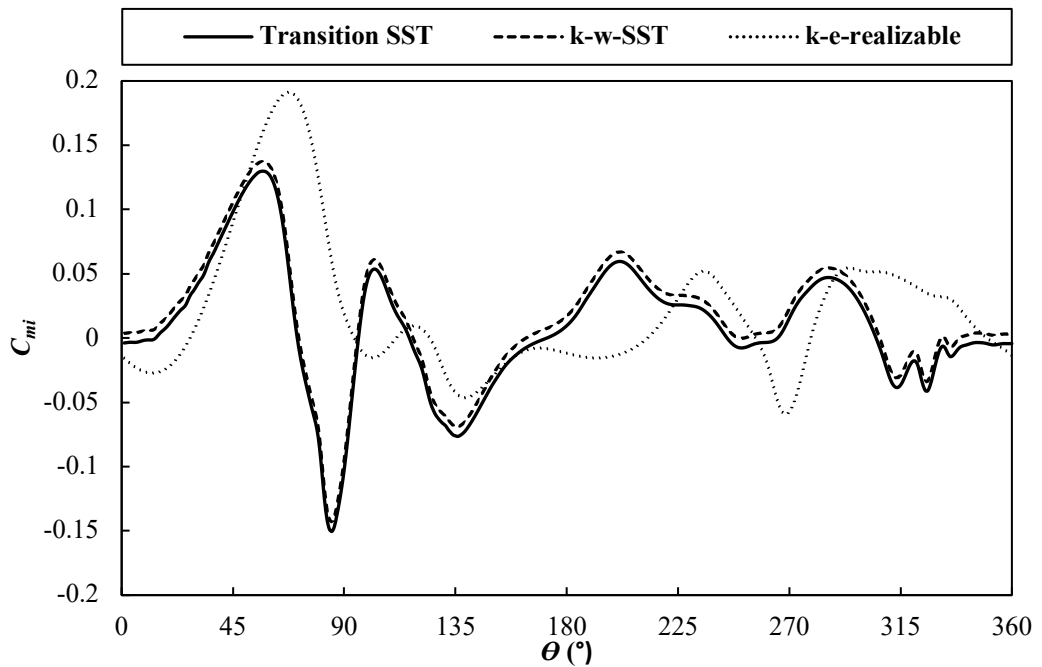
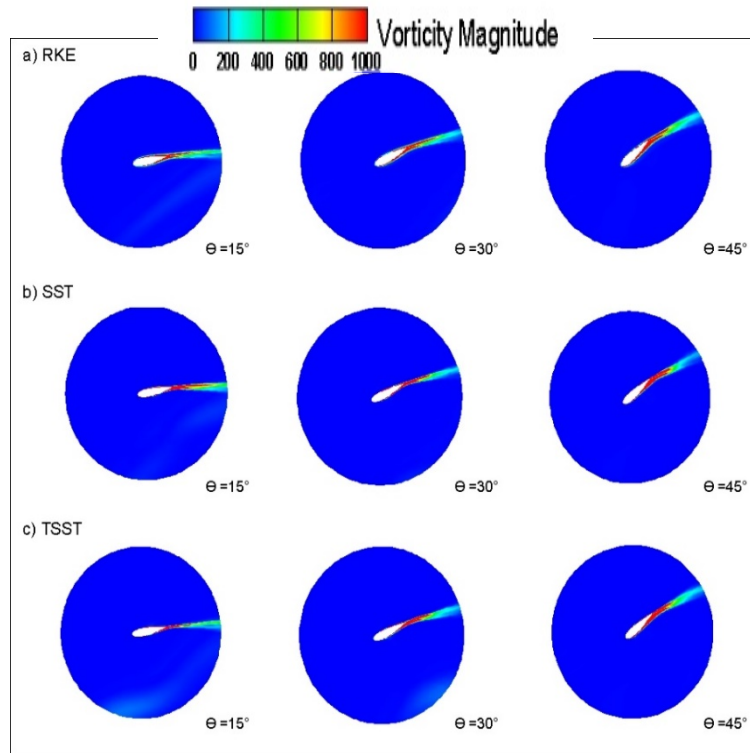
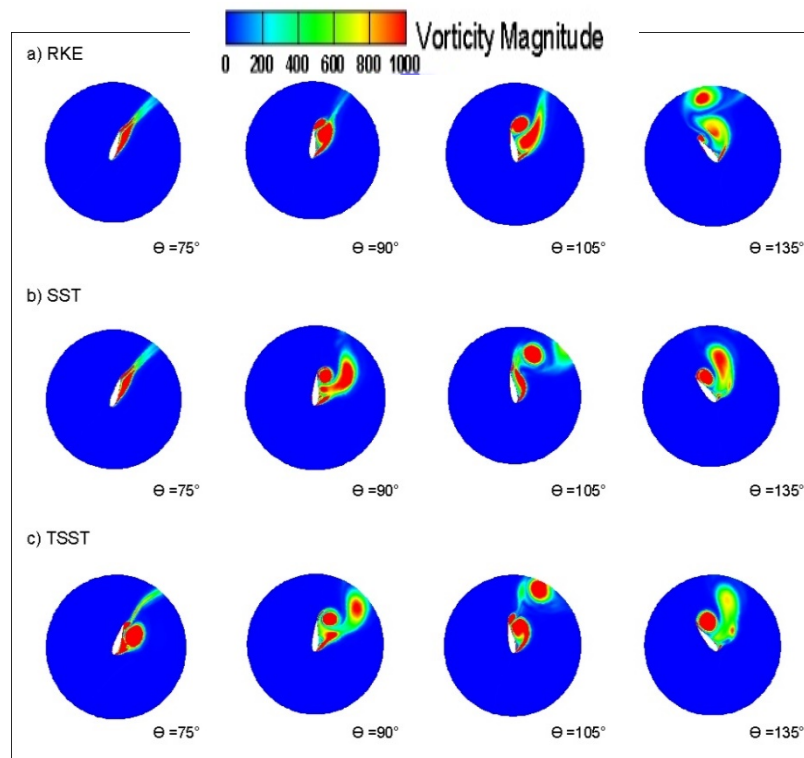


Figure 4.17 Comparison of C_{mi} distribution of three URANS models (RKE, SST and TSST) in $TSR = 1.44$.



(a)



(b)

Figure 4.18 Comparison of contour plots of z-vorticity indicating the flow separation process at important azimuthal positions in $TSR = 1.44$ (URANS models), (a) before vortex shedding and (b) after vortex shedding (not in scale).

2) *Medium TSR regime (Representative TSR = 2.64)*

C_{mi} distribution shows a smaller fluctuation for optimum TSR (as indicated in Castelli, Englaro and Benini (2011)), indicating that flow separation strength is reduced in this TSR due to a smaller positional range where the blade experiences dynamic stall. As illustrated in Figure 4.19, the TSST model predicts an earlier and steeper fall of C_{mi} ($\theta = 90^\circ$), indicating that this model predicts earlier and stronger separation than other URANS models in the optimum value of TSR . Figure 4.19 also demonstrates that the RKE model does not generate a negative value during the fall of C_{mi} , showing that this model does not predict strong separation, unlike SST and TSST models. In addition, from $\theta = 135^\circ$ to 260° where dynamic stall occurred, TSST and SST models produce fluctuation of C_{mi} , suggesting the process of vortex shedding at these azimuthal angles. As the TSST model generates a larger drop of C_{mi} during the dynamic stall, this model predicts lower power generation compared to other URANS models and as a result, it gives a closer C_{p-ave} value to the experiment result.

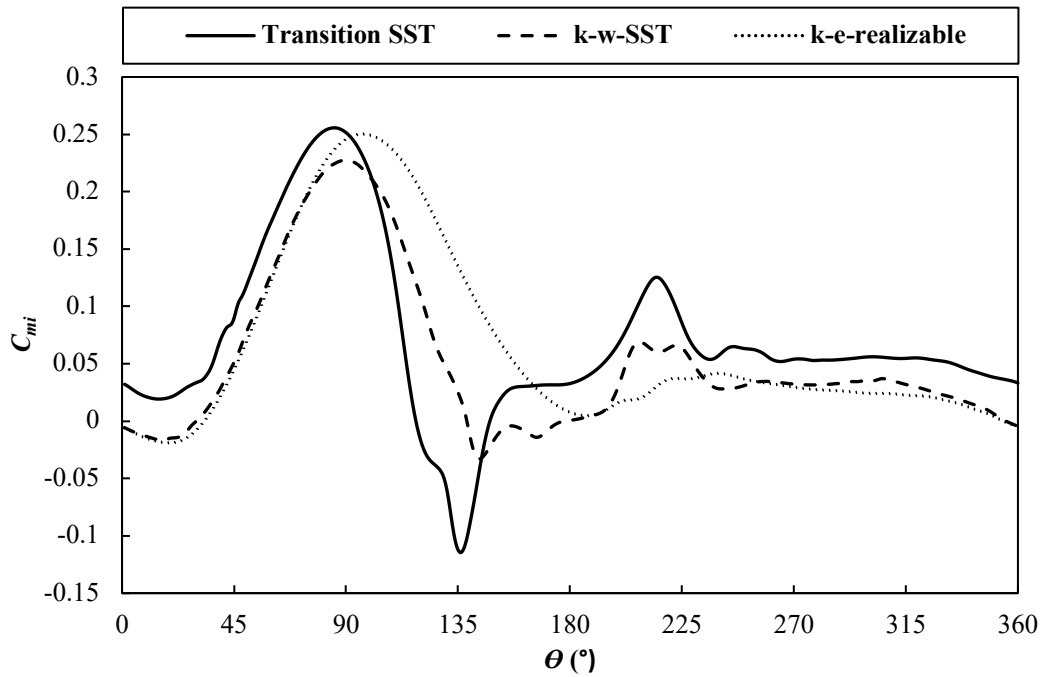
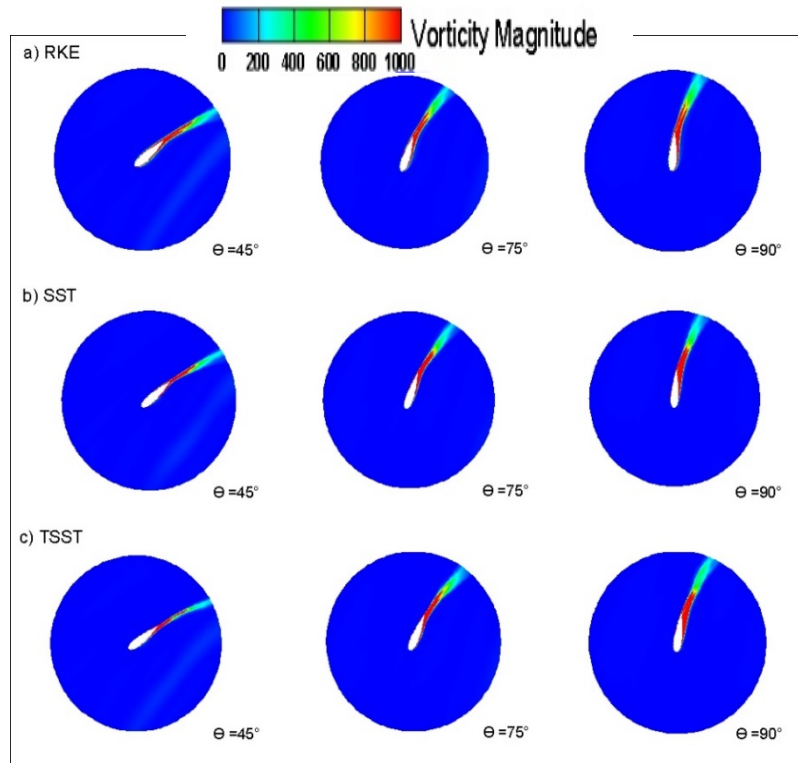
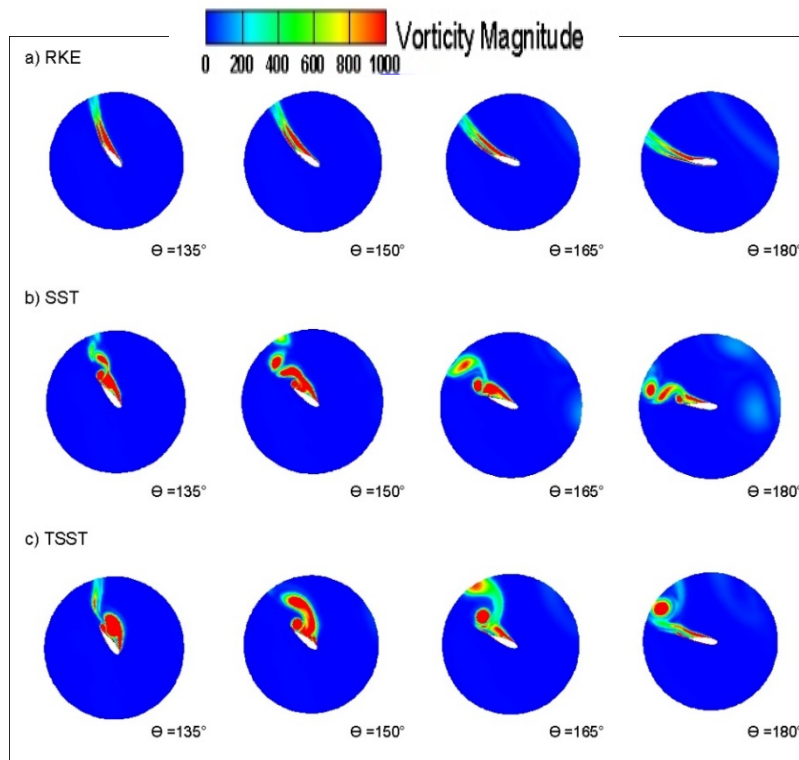


Figure 4.19 Comparison of C_{mi} distribution of three URANS models (RKE, SST and TSST) in $TSR = 2.64$.



(a)



(b)

Figure 4.20 Comparison of contour plots of z-vorticity indicating the flow separation process at important azimuthal positions in $TSR = 2.64$ (URANS models), (a) before vortex shedding and (b) after vortex shedding (not in scale).

It is essential to understand the flow behaviour associated with the results above. Figure 4.20 (a) shows the development of trailing-edge and leading-edge vortices with three URANS models predicting similar behaviour of this vortex growth from $\theta = 0^\circ$ to 90° . This result is identical to the lower *TSR* results, which means that the RKE model can generate a similar prediction with SST and TSST models when the dynamic stall has still not occurred (the vortex shedding starts at a location around $\theta = 95^\circ$, for $Re_\Omega = 215270$). At $\theta = 135^\circ$ (when the dynamic stall already occurs and vortex shedding appears), the RKE model only suggests that there is a small vortex shed at the trailing-edge generating secondary trailing-edge vortices, without leading-edge vortex shedding (see Figure 4.20 (b)). On the other hand, SST and TSST models predict strong vortex shedding at both trailing-edge and leading-edge, indicating the presence of a dynamic stall, trailing-edge roll up, and secondary vortices that match earlier work. These vortex shedding are associated with the fluctuation of C_{mi} in the region where dynamic stall occurred. Note that the TSST model generates stronger shedding compared to the SST model. Hence, the TSST model produces a larger fluctuation of C_{mi} , as illustrated in Figure 4.19.

3) *High TSR regime (Representative TSR = 3.3)*

As mentioned above, VAWTs experience a smaller range of attack angles in high regime of *TSRs* than in low and medium regimes of *TSRs*. Even though the turbine operates in the region of no static stall condition, the power production will decrease due to the higher rotation of the turbine compared to the incoming wind with the addition of high vibration, high drag and high tip losses (Ragheb and Ragheb, 2011). The loss in power production is confirmed by the optimum value of C_{mi} prediction of all three URANS models in high *TSR* falling under the optimum *TSR*. It is noted that all three URANS models produce a similar trend line for C_{mi} with a slight difference over one turbine revolution (see Figure 4.21). Nevertheless, the TSST model predicts the lowest values of C_{mi} and earlier fall of C_{mi} compared to RKE and SST models. Hence, TSST still gives the lowest value of C_{p-ave} prediction (about 15% in average), although it is still quite similar to RKE and SST predictions (about 18% in average).

It also can be observed that these URANS models predict that the C_{mi} distribution does not have a significant fluctuation, indicating that there is no intense vortex shedding in high regime of *TSRs*. This phenomenon can be verified by Figure 4.22. As illustrated, in this *TSR*, after developing trailing and leading-edge vortices from $\theta = 0^\circ$ to 90° , there

is only a tiny vortex at the trailing-edge where the vortex is not detached from the blade (the vortex shedding starts at a location of around $\theta = 110^\circ$, for $Re_\rho = 311575$). This shows that in high regime of $TSRs$, VAWT loss in power production is not mainly because of the dynamic stall but because the rotor acts as a solid wall obstruction due to high rotation speed (Bakırcı and Yılmaz, 2018). It is worth mentioning that all URANS models also predict similar vortex growth in this TSR regime resulting in similar prediction in power generation.

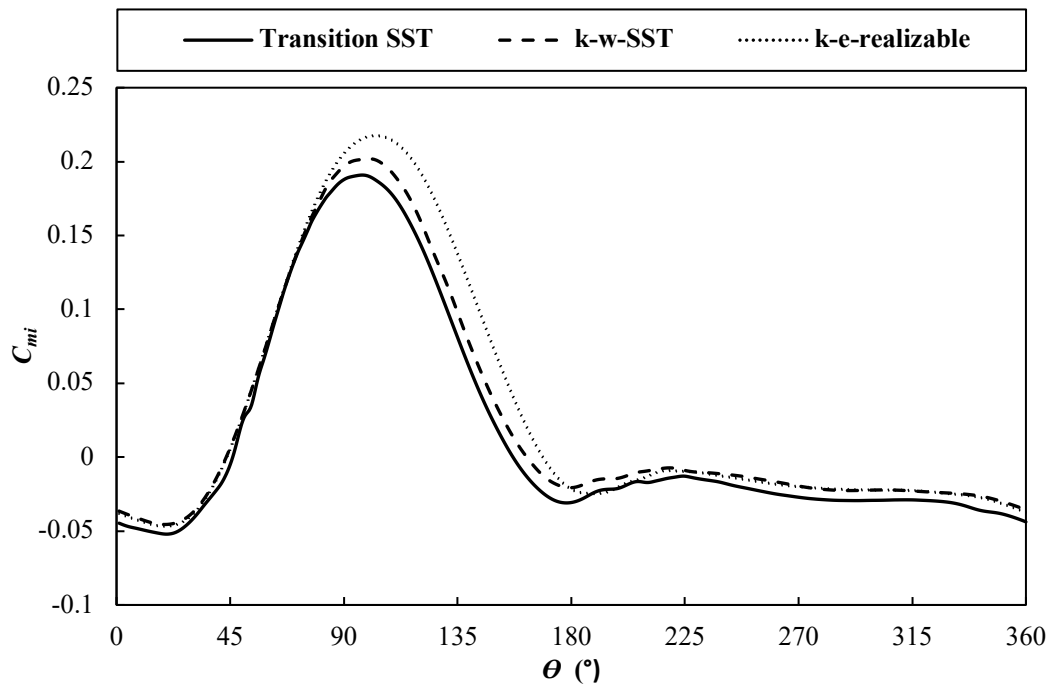
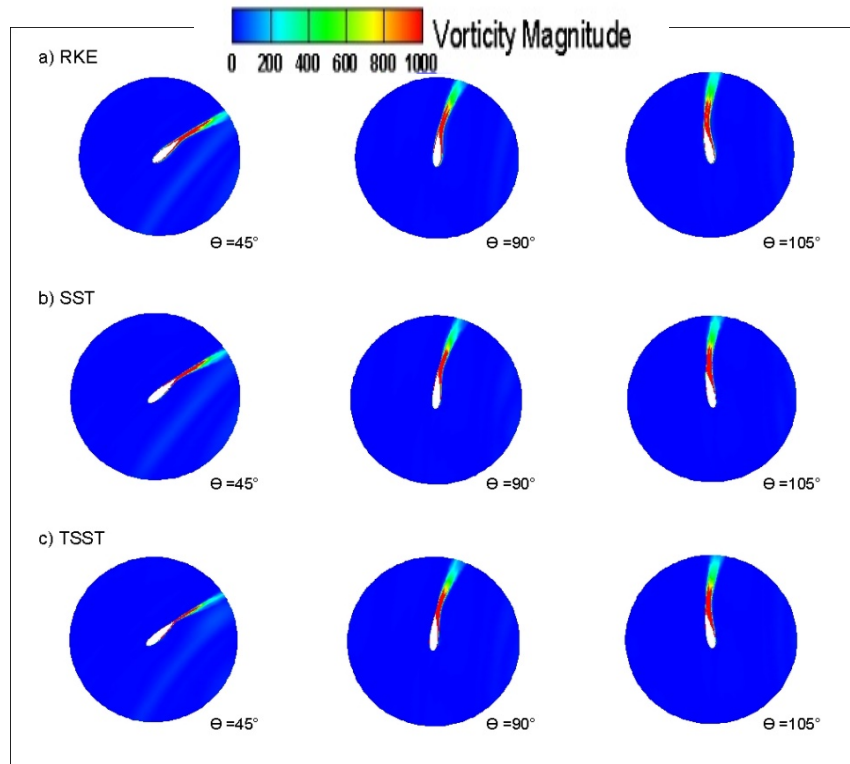
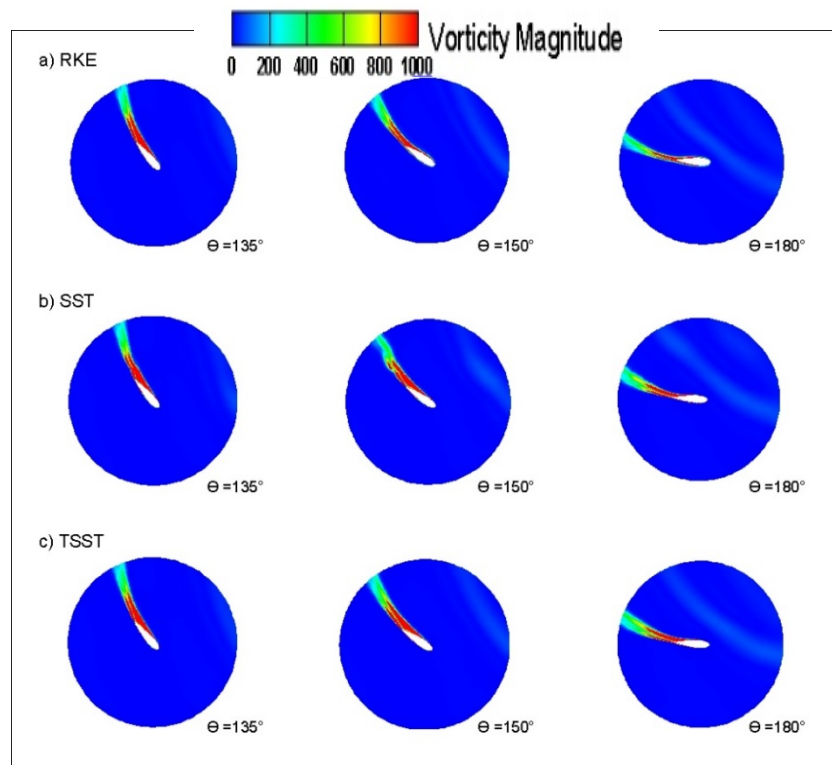


Figure 4.21 Comparison of C_{mi} distribution of three URANS models (RKE, SST and TSST) in $TSR = 3.3$.



(a)



(b)

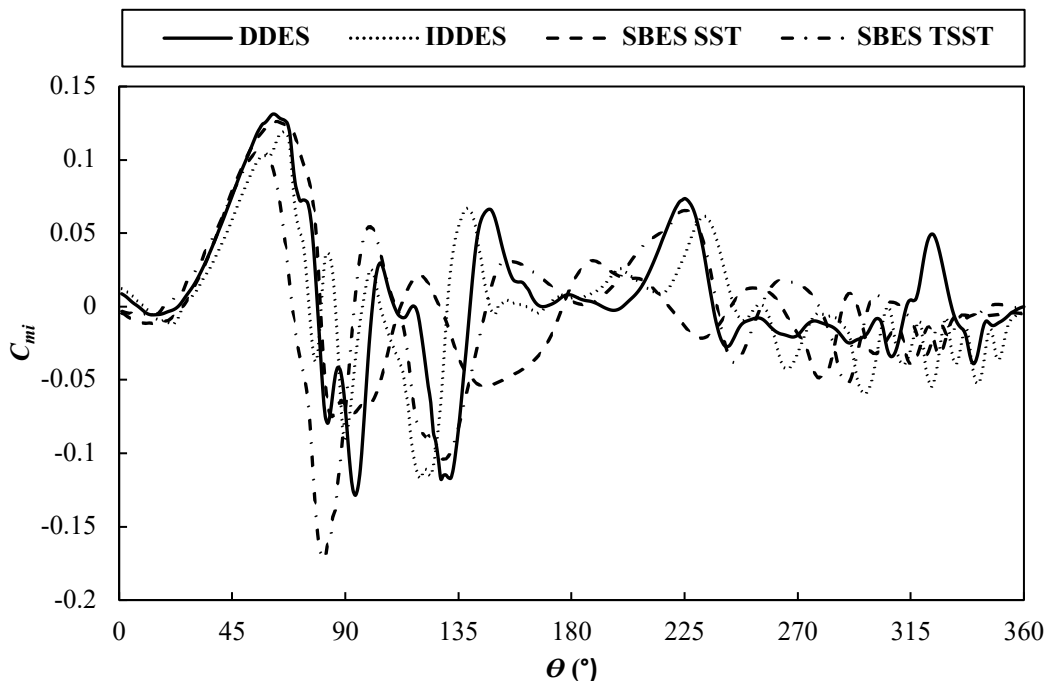
Figure 4.22 Comparison of contour plots of z-vorticity indicating the flow separation process at important azimuthal positions in $TSR = 3.3$ (URANS models), (a) before shedding and (b) after shedding.

4.5.3.2 Hybrid RANS-LES turbulence models

The detailed comparison of C_{p-ave} prediction of four different hybrid RANS-LES turbulence models shows that they can reduce the inaccurate prediction of URANS turbulence models in all TSR regimes. Therefore, further investigation to understand these differences is discussed for each TSR regime in this section.

1) Low TSR regime (Representative $TSR = 1.44$)

Figure 4.23 presents the prediction of C_{mi} distribution of four hybrid RANS-LES turbulence models in $TSR = 1.44$. It is noticed that SBES TSST predicts the earliest and steepest fall of the C_{mi} value compared to other hybrid RANS-LES models. This indicates that this model predicts the earlier start of the dynamic stall. Furthermore, it also generates the lowest peak value of C_{mi} . Hence, this model predicts the lowest value of C_{p-ave} other than URANS models and other hybrid RANS-LES models. This prediction can be further analysed by investigating their vorticity prediction. As presented in Figure 4.24, the SBES TSST model predicts stronger vortex shedding at $\theta = 75^\circ$ resulting in more substantial detached flow away from the near field of the blade, whilst other hybrid RANS-LES models (especially DDES and IDDES) still generate attached flow towards the near field of the blade.



(b)

Figure 4.23 C_{mi} comparison of four hybrid RANS-LES models (DDES, IDDES, SBES SST and SBES TSST) in $TSR = 1.44$.

Furthermore, all hybrid RANS-LES models produce more substantial C_{mi} distribution fluctuations than the URANS models in low regime of $TSRs$ (see Figure 4.23). This shows that hybrid RANS-LES models can predict stronger vortex shedding (i.e., stronger dynamic stall) than URANS models, thereby generating a smaller C_{p-ave} prediction discrepancy than the experimental data. Vorticity visualisation shows that hybrid RANS-LES models can generate clearer detached flow away from the near field of the blade compared to URANS models (see Figure 4.24). Nevertheless, further validation of this flow-field behaviour is still needed by performing an experimental study.

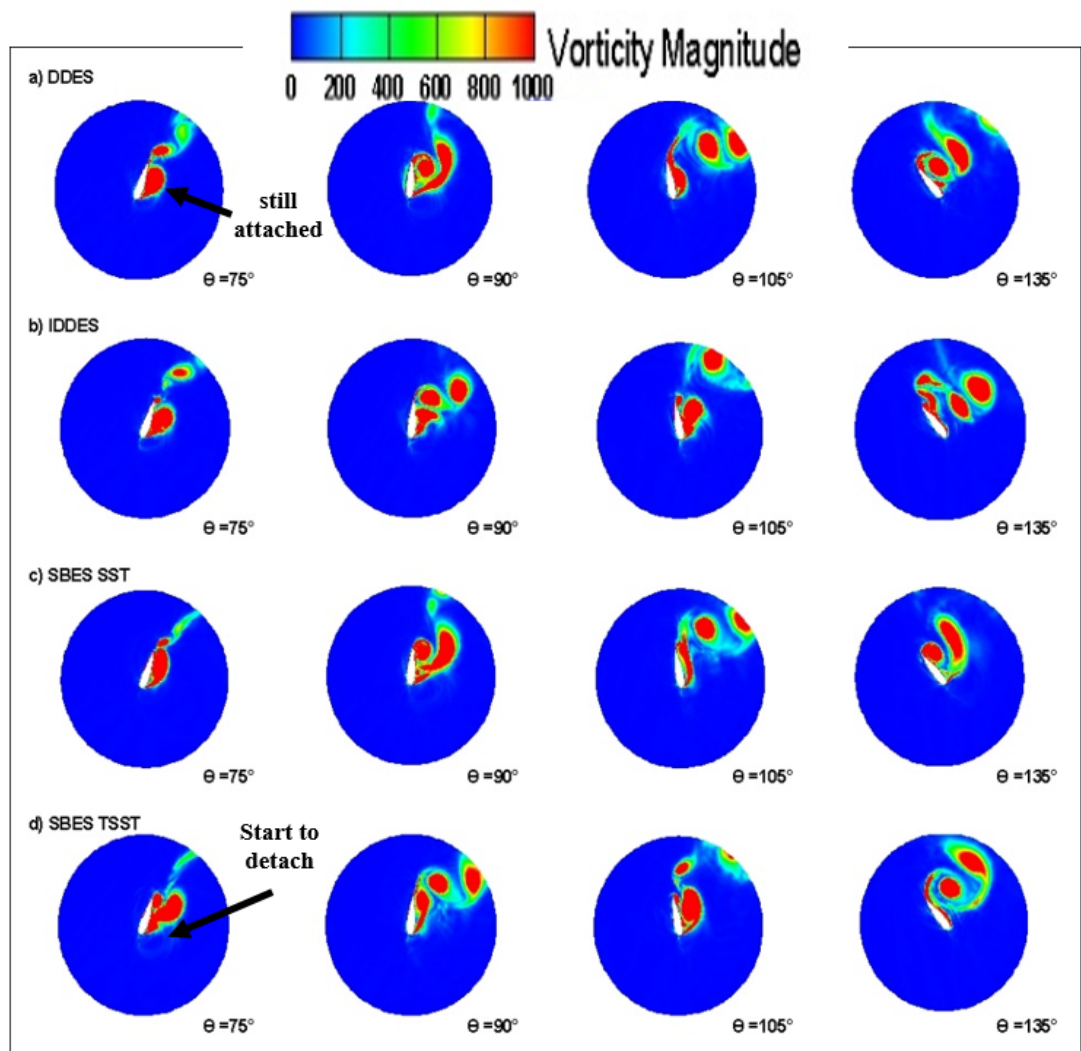


Figure 4.24 Comparison of contour plots of z -vorticity indicates the flow separation process at important azimuthal positions after vortex shedding in $TSR = 1.44$ (using hybrid RANS-LES models).

2) *Medium TSR regime (Representative TSR = 2.64)*

In medium regime of $TSRs$, hybrid RANS-LES models still give different predictions than URANS models but not as severe as in low regime of $TSRs$. Regarding prediction of C_{mi} distribution, IDDES and DDES models show the more substantial fluctuation of C_{mi} distribution than SBES models after the significant drop of C_{mi} region (after around $\theta = 135^\circ$) as displayed in Figure 4.25. Furthermore, hybrid RANS-LES models generate a similar peak value of C_{mi} except for IDDES models. SBES TSST model presents the latest significant fall of C_{mi} but weakest fluctuation in dynamic stall than other hybrid RANS-LES models (i.e., proved by smaller vortex shedding after around $\theta = 135^\circ$ (see Figure 4.26)). In addition, it predicts a slower significant fall of C_{mi} compared to DDES and IDDES models. As a result, the SBES TSST model generates C_{p-ave} lower than DDES and SBES SST models but higher than the IDDES model. Nevertheless, it gives the closest prediction of C_{p-ave} to the experimental result.

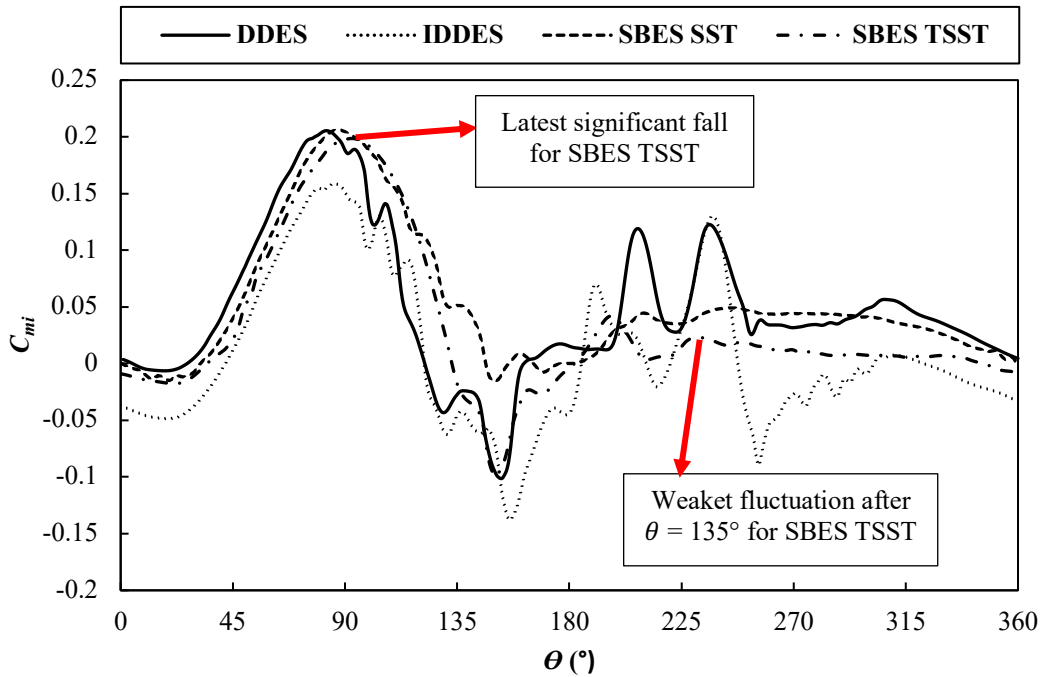


Figure 4.25 C_{mi} comparison of four hybrid RANS-LES models (DDES, IDDES, SBES SST and SBES TSST) in $TSR = 2.64$.

It is noticed that hybrid RANS-LES models show a slight fluctuation of C_{mi} in the region of significant fall of C_{mi} (around $\theta = 90^\circ$ - 135°) compared to URANS models. This indicates that hybrid RANS-LES models can predict stronger vortex shedding in this region than URANS models. This ability is confirmed by the prediction of vortex growth

of hybrid RANS LES models that demonstrates stronger shedding of vortices than URANS models at $\theta = 135^\circ$.

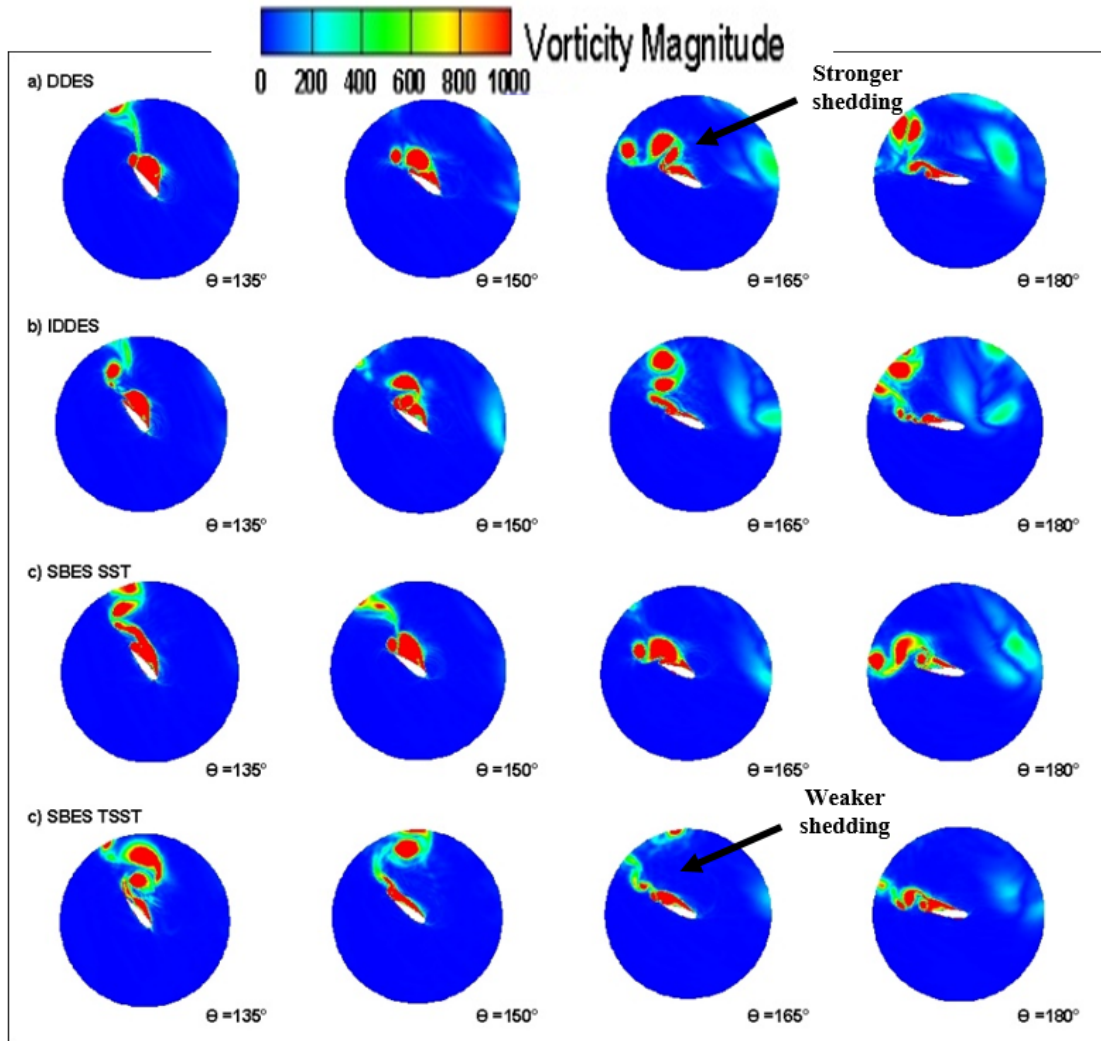


Figure 4.26 Comparison of contour plots of z-vorticity indicates the flow separation process at important azimuthal positions after vortex shedding in $TSR = 2.64$ (using hybrid RANS-LES models).

3) High TSR regime (Representative $TSR = 3.3$)

As mentioned before, in high regime of $TSRs$, URANS models have difficulty generating accurate prediction even with the TSST model due to generation of strong vortex shedding in the region of high azimuthal angle was not determined. In this regard, hybrid RANS-LES models show a promising result to address this problem. Compared to URANS models, whilst these models produce a relatively smooth distribution of C_{mi} after $\theta = 180^\circ$, the prediction of C_{mi} distributions by hybrid RANS-LES models demonstrate slight fluctuations in this region (see Figure 4.27). This shows that hybrid

RANS-LES models predict the presence of vortex shedding in this region. Vorticity visualisation of hybrid RANS-LES models in this region confirms that flow detachment indicates vortex shedding, which triggers a stronger dynamic stall (see Figure 4.28).

Figure 4.27 illustrates that the SBES TSST model predicts the earliest significant drop and the lowest peak value of C_{mi} with a similar drop rate compared to other hybrid RANS-LES models. Therefore, the SBES TSST model can produce the lowest C_{p-ave} and it has the closest data match to the experimental data. The SBES models also produce weaker fluctuation at the significant drop region than DDES and IDDES models indicating that SBES models predict weaker vortex shedding at this region than DDES and IDDES models. This is validated by the prediction of the flow behaviour of the SBES TSST model that presents weaker leading-edge vortex shedding and smaller detached flow at $\theta = 135^\circ$ (see Figure 4.28).

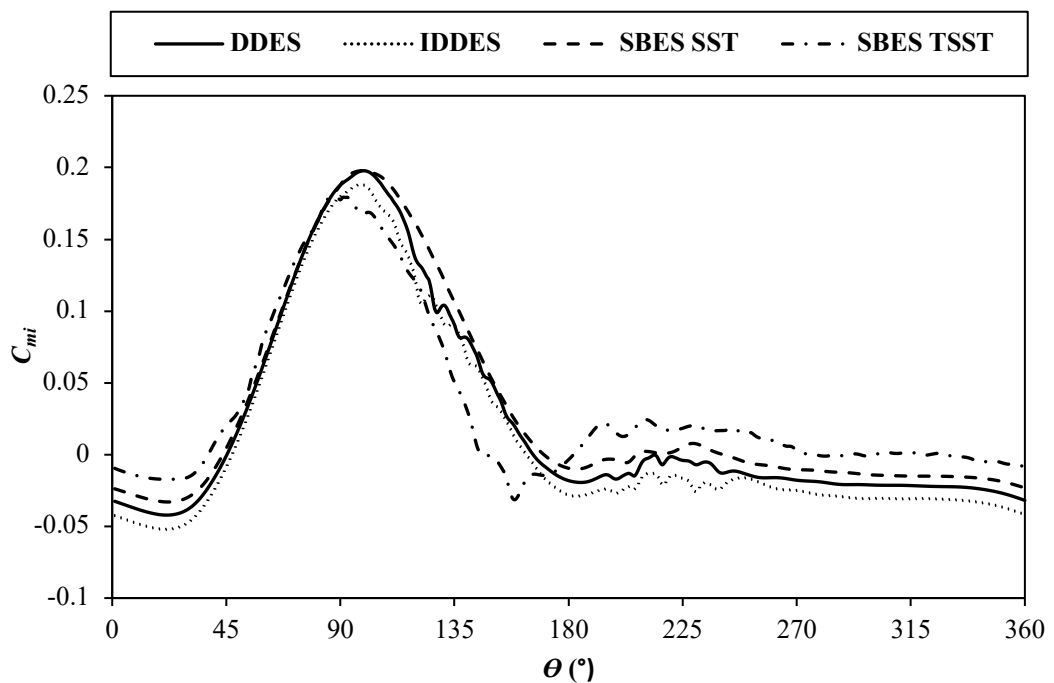


Figure 4.27 C_{mi} comparison of four hybrid RANS-LES models (DDES, IDDES, SBES SST and SBES TSST) in $TSR = 3.3$.

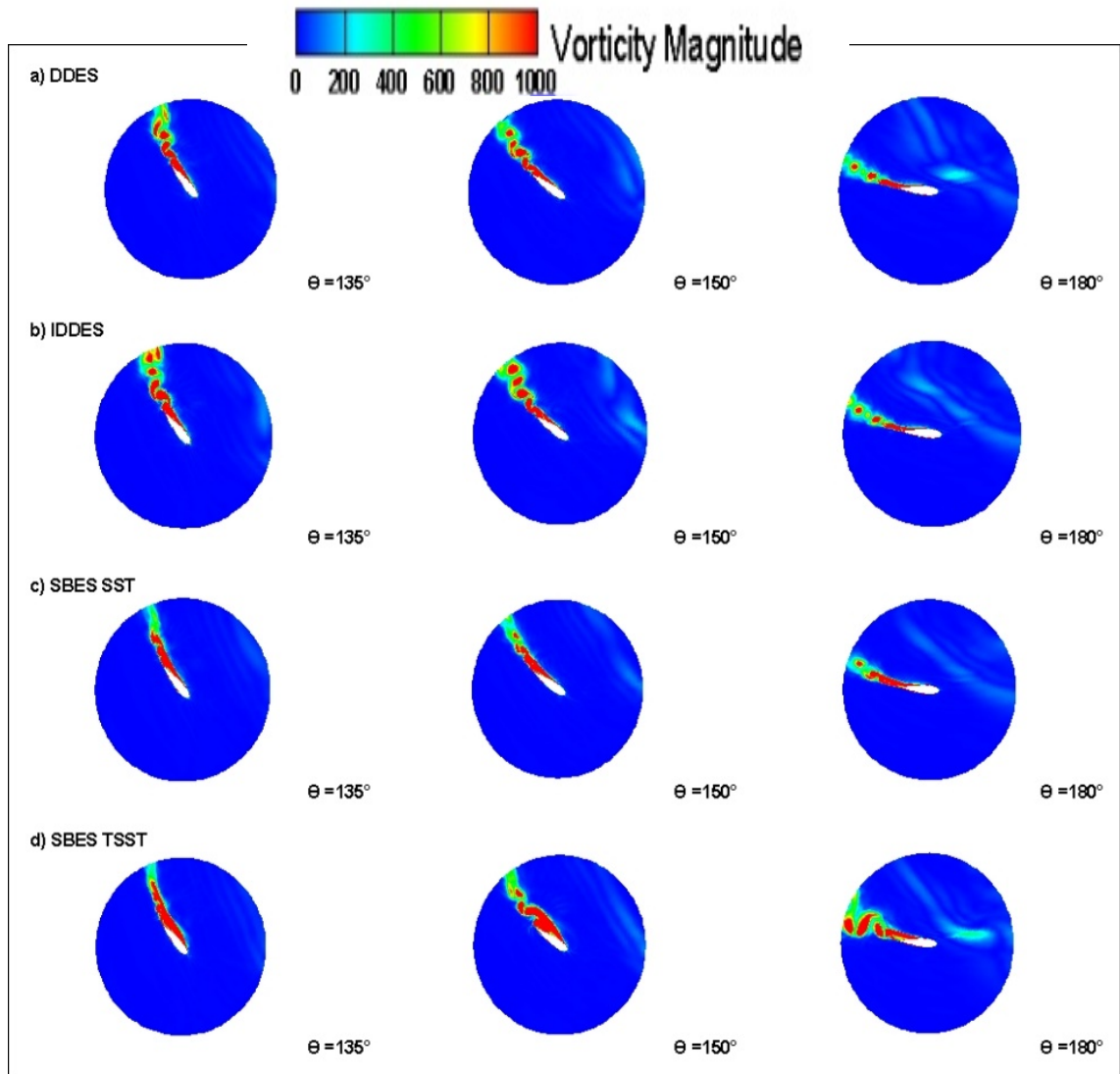


Figure 4.28 Comparison of contour plots of z -vorticity indicates the flow separation process at important azimuthal positions after vortex shedding in $TSR = 3.3$ (using hybrid RANS-LES models).

4.6 Chapter Summary and Further Work

4.6.1 Model independence

Based on the explanation above, a domain size with both inlet and outlet placed 40 diameters away from the centre of the turbine's rotational axis is sufficient to ensure that there is no significant effect of numerical boundary conditions on the numerical results. In addition, 174 grid points around the 2D VAWT blade are sufficient to achieve a reasonable prediction of the VAWT experimental result of the C_{p-ave} with 88.5 mm length of the blade's chord. Furthermore, 1° azimuthal increment, i.e., the time step of the

unsteady simulation, is also sufficient to generate good accuracy of the prediction of experiment result of C_{p-ave} of VAWT. Note that the rest of the simulation adopts a C-grid. It generates better accuracy in the simulation results and provides an easier modification to accommodate the domain change caused by the presence of the Gurney flap and straight upstream deflector in future work.

Regarding the revolution convergence, it is noticeable that revolution convergence depends on the choice of turbulence model. URANS turbulence models can achieve faster revolution convergence than hybrid RANS-LES turbulence models as URANS turbulence models mainly solve the mean flow and use an ensemble averaging solution in the far-field (Salim, Ong and Cheah, 2013). Meanwhile, the hybrid RANS-LES turbulence model utilises the LES model in the far-field, which can better resolve the flow fluctuations, and as a result, it takes a longer time to achieve a statistically converged flow-field for both near and far-fields. In URANS turbulence models, RKE and SST are the fastest turbulence models to achieve revolution convergence with 23 revolutions, whilst TSST needs 27 revolutions to reach revolution convergence. On the other hand, in hybrid RANS-LES turbulence models, all four tested turbulence models need 34 revolutions to achieve the revolution convergence. Hence, the simulation data is retrieved in the 24th revolution for RKE and SST, 28th revolution for TSST and 35th revolution for hybrid RANS-LES turbulence models.

4.6.2 Model accuracy

Evaluation of three unsteady RANS turbulence models (i.e., RKE, SST and TSST) and four hybrid RANS-LES models (i.e., DDES, IDDES, SBES with SST $k-\omega$ and SBES with Transition SST) on predicting the performance of three-straight-bladed VAWT is discussed and compared to the experiment of Castelli, Englaro and Benini (2011). The 2D CFD model is chosen to decrease the computational cost as this study focuses on evaluating the ability of the different turbulence models to predict the flow characteristics around the VAWT. Moreover, it was mentioned in the previous studies that the 2D computational model of VAWT could give a reasonable overall prediction on the performance and flow-field around a rotor.

The results show that, in general, the two-equation turbulence models produce relatively large discrepancies compared to the experiment data, especially in low and medium regimes of $TSRs$ (in which most VAWTs operate). Concerning the revolution averaged turbine power coefficient, the RKE and SST turbulence models generate around

400% and 15% discrepancy compared to the experimental data in low and medium regimes of *TSRs*, respectively. These discrepancies can be reduced further by using four-equation turbulence models, such as the TSST model, which can decrease the discrepancies in low and medium regimes *TSRs* to about 100% and 8%, respectively. Nevertheless, all RANS turbulence models give a similar discrepancy in high regime of *TSRs* (about 17%). The ability of the TSST model to reduce the discrepancy in low and medium *TSRs* is benefitted by its capability to predict stronger dynamic stall, trailing-edge roll up and secondary vortices showed by the presence of vortex shedding at both trailing-edge and leading-edge.

Considering the relatively low accuracy of RANS turbulence models to predict the performance and flow behaviour of VAWTs and the demanding need for computer resources for LES, this study examines hybrid RANS-LES turbulence models in order to analyse their capability to predict the performance and flow behaviour of VAWTs with relatively low to moderate increase in computational resources. This study demonstrates that all four hybrid RANS-LES turbulence models (DDES, IDDES, SBES with SST and SBES with TSST) can generate a small discrepancy of C_{p-ave} prediction in all *TSR* regimes. In low regime of *TSRs*, hybrid RANS-LES models can reduce the discrepancies by almost 60% on average compared to the TSST model. In medium and high regimes of *TSRs*, the discrepancy reduction varies. Whilst DDES, IDDES and SBES with SST models still generate relatively similar discrepancies compared to the TSST model (between 5-7% compared to experimental data), SBES with TSST model can produce further results discrepancy reduction in medium regime of *TSRs* (around 2.2% compared to experimental data). The SBES with TSST model joined by the IDDES model also produces a small discrepancy (about 2%) in high regime of *TSRs* compared to DDES and SBES with SST models (approximately 15%). Hence, SBES with TSST model generates overall the best accuracy in all *TSR* regimes compared to URANS and other hybrid RANS-LES turbulence models. Note that hybrid RANS-LES turbulence models are better in predicting dynamic stall behaviour than RANS turbulence models, as indicated by further vortex shedding away from the near blade wall. In addition, they can also predict weak trailing-edge roll up in high regime of *TSRs* whilst RANS turbulence models only show weak shedding on the vortex around trailing-edge. Therefore, hybrid RANS-LES turbulence models (particularly IDDES and SBES with TSST) can generate lower discrepancy in high regime of *TSRs*.

4.6.3 Rationale for the choice of turbulence models

Even though the SBES with TSST model generates the most accurate results compared to other evaluated models in all regimes of *TSRs*, additional simulation time compared to URANS models needs to be considered (see Table 4.3) in the application, and the time overhead is primarily due to stricter grid requirements (e.g., grid quality). The choice of turbulence model also depends on evaluating the VAWT's operational conditions at both design and off-design points over a wider regime of *TSRs*. Due to the longer simulation time of hybrid RANS-LES turbulence models and more complex grid generation (for example, the SBES with TSST model can increase the simulation time by about 25% compared to TSST turbulence models), URANS models are still the best choice for overall performance evaluation and results produced are reasonable in terms of accuracy for a specific *TSR* regime. Note that the Transitional SST turbulence model is recommended for low to medium regimes of *TSRs* as it generates a good accuracy in these *TSR* regimes due to better prediction of the development of dynamic stall compared to the RKE and SST models. Compared to the RKE and SST models, the TSST model gives a similar prediction on flow separation in high regime of *TSRs* resulting in identical accuracy of C_{p-ave} prediction (about 17% differences compared to the experimental data). However, this model will increase simulation time by around 34% and 27% compared to RKE and SST models, respectively. Therefore, beyond the optimum *TSR* value, the RKE or SST turbulence model is acceptable as it produces relatively similar results as the TSST model at a shorter simulation time.

Table 4.3 Comparison of 2D CFD simulation time using various turbulence models (2 CPUs @ 2.2 GHz, 128 GB RAM).

Turbulence model	Total simulation times (hours)
RKE	35.604
SST	37.26
TSST	47.628
DDES	260.304
IDDES	261.664
SBES SST	56.304
SBES TSST	59.296

Nevertheless, this study recommends hybrid RANS-LES models if the analysis further examines the flow behaviour (such as wake development) or noise production and

is performed in all *TSR* regimes. However, the DDES or IDDES turbulence models can increase simulation time by around 4.5 times compared to the TSST turbulence model. Meanwhile, the SBES with TSST turbulence model can produce similar accurate predictions as DDES and IDDES turbulence models in all *TSR* regimes in average, about 20% in low regime of *TSR*, 2.2% in medium regime of *TSR* and 2% in high regime of *TSR* values compared to the experimental data, respectively) with reasonable simulation time increase (about 24.5% longer than TSST turbulence model) and grid complexity.

4.6.4 Further work

This chapter has discussed the validation of the 2D VAWT model. After finding the model that is relatively independent of the change of numerical parameters such as domain size and shape, grid, and time step and the suitable choice of turbulence models, this study further investigates the application of Gurney flap as dynamic stall control to improve the VAWT performance. The 2D validated VAWT model is modified by adding a Gurney flap around the blades' trailing-edges. Therefore, the following chapter will discuss the design optimisation and result comparison of a VAWT with a GF.

Chapter 5: 2D CFD Simulation of Blade Shape Modifications for Performance Enhancement of Lift-Driven VAWT using Gurney Flap

Among passive flow controls by blade shape modifications, the GF is very attractive to be applied as a dynamic stall control in VAWTs due to its simple geometry modification, low cost in production and better performance, especially in low *TSRs*. Recent studies (see the detailed reviews in Appendix A, Section A.7.2) found that a GF could significantly improve the lift coefficient whilst having a minor impact on the drag coefficient, resulting in considerable VAWT power coefficient improvement. The GF could also improve the self-starting ability of a VAWT, which reduces the external power source needed to rotate the turbine initially in a very low incoming wind speed or low *TSR* (Bianchini et al., 2019). Furthermore, overall, the GF could improve the performance of bare VAWT compared to other passive flow controls in all regimes of *TSRs* (see summary in Table 2.1).

Based on the discussion in Chapter 2, Section 2.5.1, the geometric optimisation of a GF on a VAWT configuration and all regimes of *TSRs* still needs further investigation. Moreover, the investigation of the effect of the GF position from trailing-edge (*s*) and GF shape modification (e.g., straight, curve or wedge) to the performance of rotating multiple blades such as a lift-driven VAWT is necessary as previous studies (Jain, Sitaram and Krishnaswamy, 2015; Mohammadi, Doosttalab and Doosttalab, 2012) only focussed on a single stationary aerofoil. Additionally, all previous studies (Yan et al., 2020; Yan, Avital and Williams, 2019; Bianchini et al., 2019) performed geometric optimisation merely for one parameter variation at a time. Hence, there is no information about which GF parameter has the highest or the lowest impact on the performance improvement of a VAWT.

Therefore, to cover all of the shortcomings above, optimisation of a GF geometry for a VAWT configuration (i.e., considering the rotational effects and blade-to-blade interaction) and for all regimes of *TSRs* with broader GF parameters is undertaken in this chapter. Section 5.1 explains the VAWT geometry with a GF. In addition to GF height (*H*) and mounting angle (θ_{GF}) as previously studied (Yan et al., 2020; Yan, Avital and Williams, 2019; Bianchini et al., 2019), the GF position from the trailing-edge is also evaluated, together with the effect of shape changes from an original shape (rectangular) to wedged and curved GFs. The model, grid generation and numerical setup of the CFD simulation can be found in Section 5.2. Note that only one *TSR* is chosen as a

representative value for each regime of *TSRs*, i.e., $TSR = 1.44$ for low *TSRs*, $TSR = 2.64$ for medium *TSRs* and $TSR = 3.3$ for high *TSRs*, due to the VAWT behaving quite similarly in the same *TSR* regime (Rezaeiha, Montazeri and Blocken, 2018). Furthermore, Section 5.3 describes the method and the results of geometric optimisation. The Taguchi method (Qasemi and Azadani, 2020; Wang, Wang and Zhuang, 2018) is adopted to simultaneously optimise different GF geometric parameters (i.e., height, mounting angle and position from trailing-edge).

Furthermore, the explanation of the effect of each geometric variation (i.e., height, mounting angle and position from trailing-edge) on the improvement of the VAWT performance for each *TSR* regime is presented in Section 5.4. The explanation of how a GF can improve the self-starting ability in low regime of *TSRs* also is found in this section. Lastly, in Section 5.5 are presented the chapter summary and further work in the following chapter.

5.1 VAWT with Gurney Flap

This study modifies a bare VAWT model by mounting a GF at the trailing-edge of a NACA 0021 aerofoil. The original GF has a rectangular shape with a fixed thickness (t) (0.33% of aerofoil chord) and other parameters such as a height (H), a mounting angle (θ_{GF}) and a distance (s) from the trailing-edge are varied for geometry optimisation studies (see Figure 5.1). Noting that, in this study, the mounting angle is measured from the end point of the suction side of the aerofoil to the upper surface of the GF (see Figure 5.1 (b)). This study adopts the GF thickness from a previous study by Mohammadi, Doosttalab and Doosttalab (2012). In addition to the original GF shape (rectangular), this study also investigates other GF shape modifications, namely wedge and curve shapes, as shown in Figure 5.2. Based on the study by Mohammadi, Doosttalab and Doosttalab (2012), this investigation varies a length of the geometry of these two shapes to height ratio (L_w/H) for optimisation.

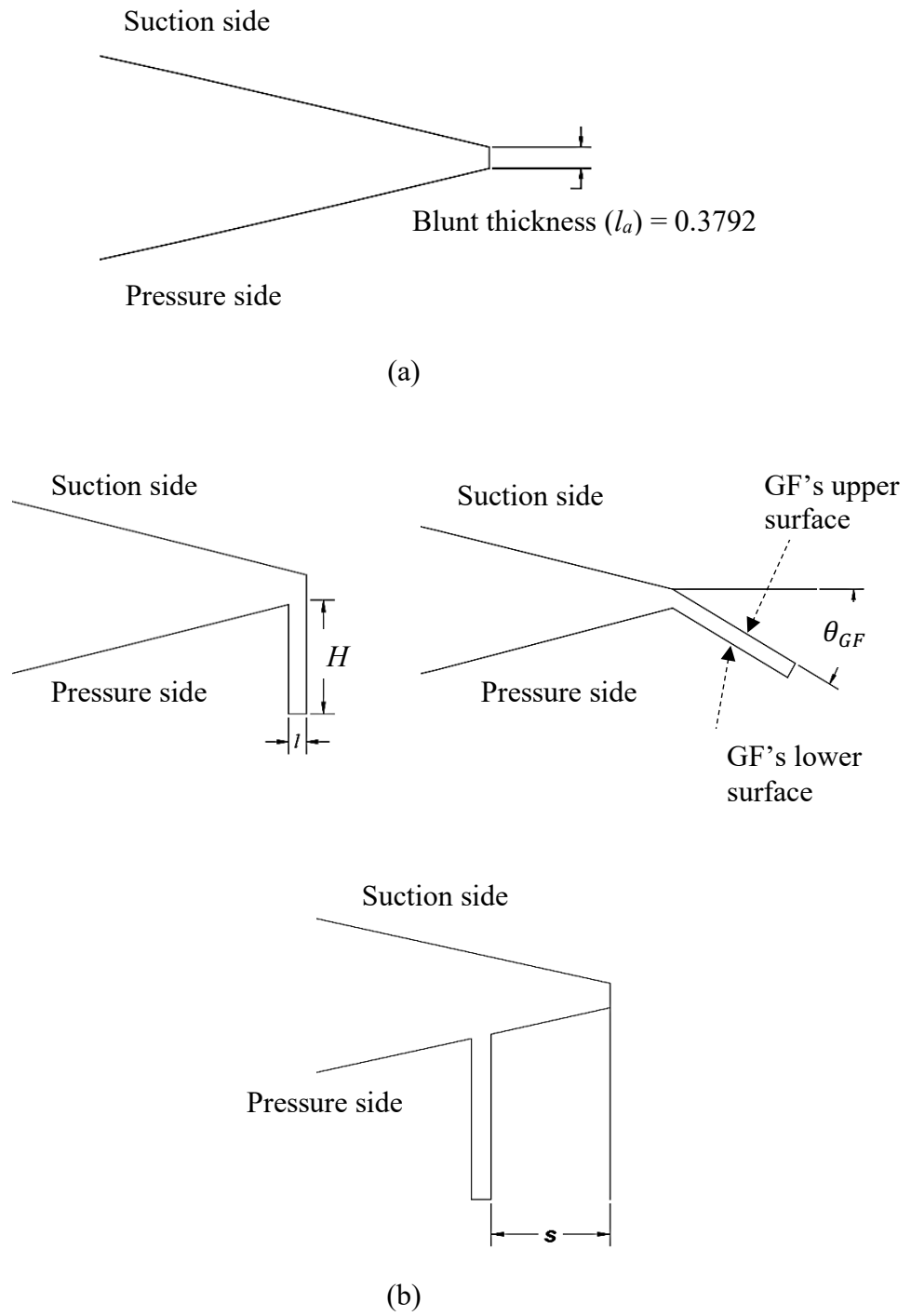


Figure 5.1 Comparison between (a) clean NACA 0021 aerofoil and (b) NACA 0021 with GF and detailed geometric variation (the drawing is not in scale).

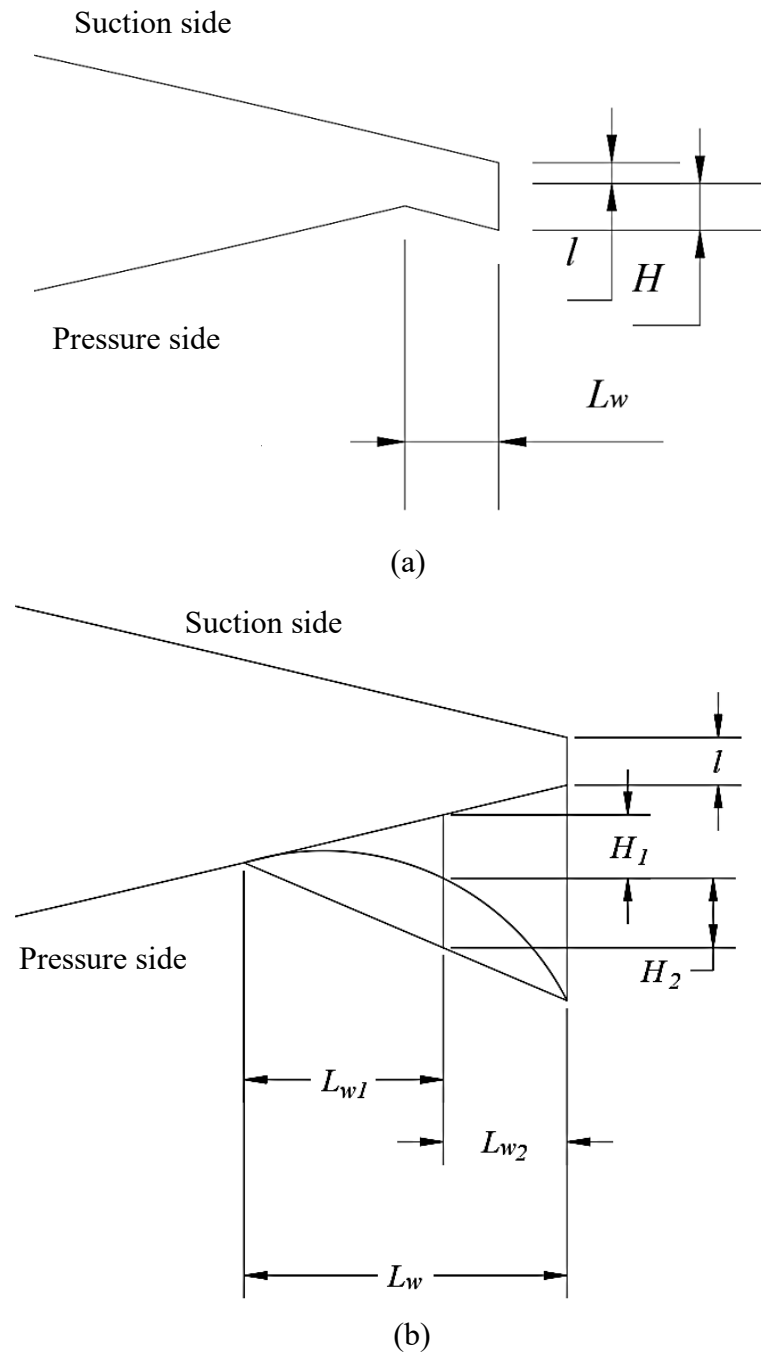
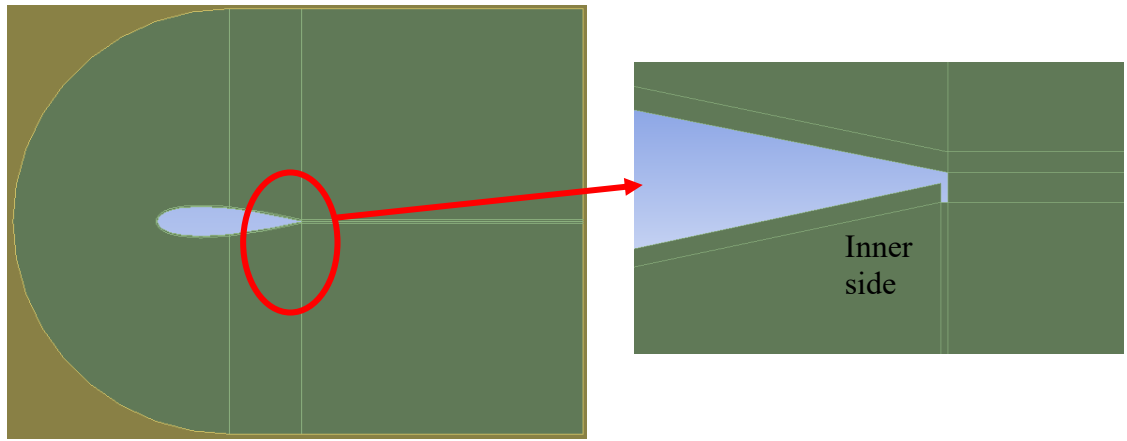


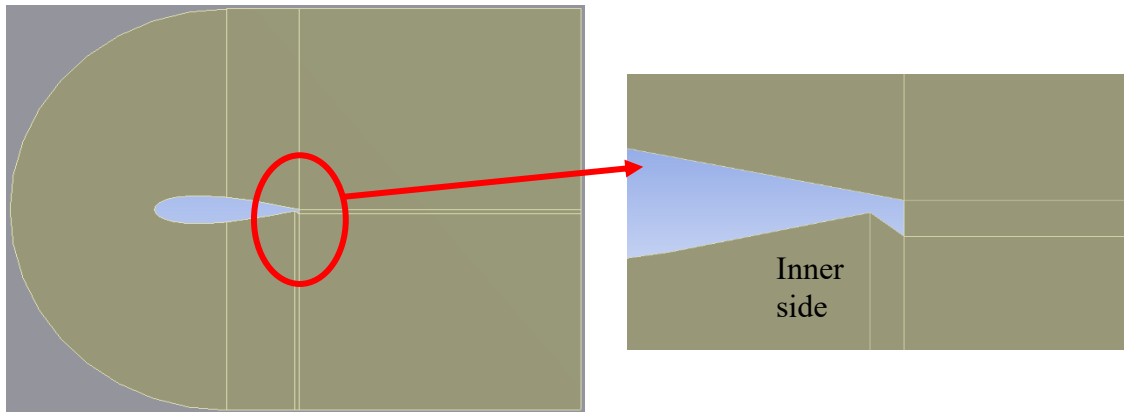
Figure 5.2 Detailed geometry of a GF with (a) wedged shape and (b) curved shape (the drawing is not in scale).

5.2 Model, Grid Generation and Numerical Setup

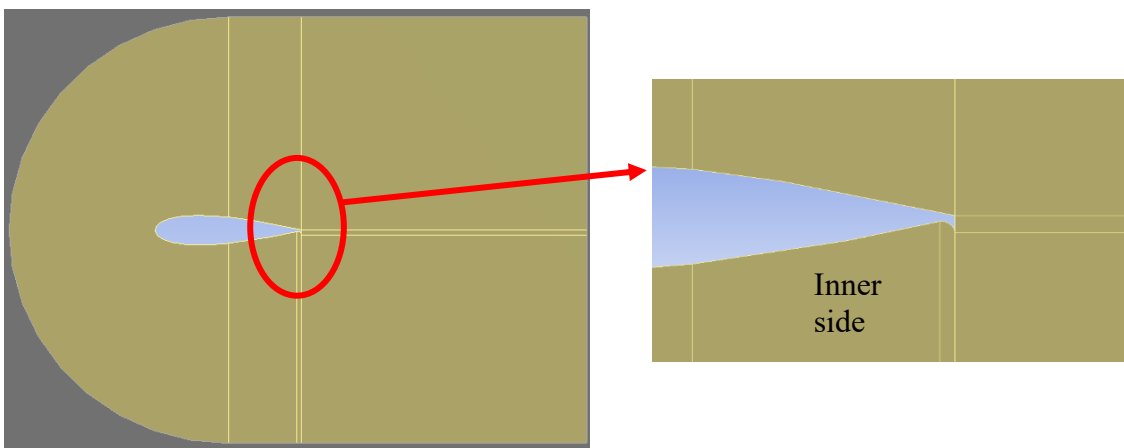
This 2D VAWT with GF study implements all models and numerical setups used in 2D validation studies (see Chapter 4). As mentioned in Appendix E, the C-grid can generate better accuracy compared to the O-grid for the SBES turbulence model. Hence, the C-grid is adopted. This C-grid can also produce quality structured grids for blades equipped with the GF geometry.



(a)



(b)



(c)

Figure 5.3 Partition of control sub-domain with (a) original GF shape, (b) wedged GF and (c) curved GF (the drawing is not in scale).

edge of the aerofoil (i.e., $2.71 \times 10^{-5} m$). The control sub-domain is divided into several parts to accommodate this grid generation, as illustrated in Figure 5.3. Figure 5.4 shows the detailed grids around the GF.

5.3 Geometries Optimisation using Taguchi Method

To investigate the effect of various GF geometric parameters on the VAWT performance (e.g., the power coefficient), the design of numerical experiments can be a powerful tool due to the possibility of studying the effect of multiple parameters simultaneously. However, the study of all the possible parameters combined can be quite challenging because it needs a complete factorial design which is not feasible for investigation with a large number of parameters, and the time and resources can be very demanding. Hence, this study adopts a fractional design investigation based on the Taguchi method (Qasemi and Azadani, 2020; Wang, Wang and Zhuang, 2018; Cavazzuti, 2012).

The Taguchi method is an optimisation method that Taguchi developed in order to improve the quality of manufactured goods. This method can largely reduce the computational cost as it allows the optimisation design to be performed on a fractional design rather than a complete factorial design (Qasemi and Azadani, 2020). It is more suitable for investigating the sensitivity of each parameter to the goal of the design (Zou et al., 2019). It also has two robust characteristics of “uniformity and decentralisation, orderliness and comparable”. “Orderliness and comparable” can ensure that the experimental results comparison is convenient, whilst “uniformity and decentralisation” can establish uniformly scattered sample points over the domain (Zou et al., 2019). These two robust characteristics are the advantages of the Taguchi method compared to other fractional design methods such as the Latin Hypercube Sample (LHS). Compared to LHS, the Taguchi method performs optimisation processes using predominantly orthogonal arrays instead of optimisation algorithms. Hence, the Taguchi method does not need to perform a design of simulation model and can achieve an obvious separation of the parameters through arrays (Kemmler et al., 2015). Meanwhile, in LHS, a design of simulation model is necessary and usually only sensitive design parameters are considered. Therefore, LHS suffers from the optimum case not usually being technically feasible, whilst the Taguchi method can set parameter dimension in production engineering points of view due to the low number of tests it requires (Kemmler et al., 2015).

The main principle of the Taguchi method is based on a so-called quality loss function, expressed by the deviation of the parameter from its target value (Cavazzuti, 2012). Note that the parameters are divided into control and noise parameters in the Taguchi method. The control parameters determine the optimum condition, whilst noise parameters show the deviation of the system from its target value and the Taguchi method does not control these noise parameters. The influence of the noise parameters on the system performance determines the optimisation and the signal to noise (S/N) ratio calculates this influence. In the Taguchi method, there are three kinds of S/N ratio functions, namely the larger-the-better (LB), the nominal-the-better (NB) and the smaller-the-better (SB) respectively. The choice of the S/N ratio function depends on the target value of the evaluation.

After determining the control and noise parameters, the matrix of numerical experiments in the Taguchi method's approach can be designed based on orthogonal arrays of the control and noise parameters. This matrix guides the numerical experiments until each test cycle obtains the results. Then, the S/N ratio determines the optimum value of each control parameter. As this study aims to generate higher power output, the larger-the-better S/N ratio function to maximise the target value of power output is applied. This LB S/N ratio can be obtained by using the following Equation (5.1) (Cavazzuti, 2012):

$$S/N = -10 \log \left(\frac{1}{nc} \sum_{i=1}^{nc} \frac{1}{I_i^2} \right) \quad (5.1)$$

where nc is the total number of observed cases, I_i is the value of the observed performance indicator of each case (in the present study, this value is the VAWT averaged power coefficient obtained from the CFD simulations), and i is the index of the simulation case.

As mentioned above, this study will evaluate the effect of three GF geometric parameters on the VAWT performance, including GF height, mounting angle and position from trailing-edge. Therefore, before applying the Taguchi method, precursor studies are carried out to evaluate the effects of GF height, mounting angle, and position from trailing-edge variations to identify appropriate regions, thus avoiding an unnecessarily large number of test cases during the optimisation stage (see Appendix F). During these precursor studies, only one parameter is varied at a time, while the other two parameters are fixed based on the optimum values of previous studies (Yan et al., 2020; Jain, Sitaram and Krishnaswamy, 2015).

5.3.1 Results of optimisation

Following the GF geometric variants described above, a case study matrix is proposed based on the Taguchi method. As this study aims to optimise three different geometrical parameters of GF (i.e., height, mounting angle and position from trailing-edge) with each parameter having three different values (see Table 5.1), a 3×3 matrix with a total of 27 cases (see Table 5.2) is formed. Note that as VAWT performance has different behaviours in different *TSR* regimes, this investigation is performed in all three *TSR* regimes with *TSR* = 1.44 representing low *TSRs*, and *TSRs* = 2.64 and 3.3 for medium and high *TSRs*, respectively. Therefore, this study investigates 81 cases in total (i.e., each *TSR* has 27 cases).

Table 5.3 shows the predicted C_{p-ave} of 27 cases for each pre-defined *TSR*. The results indicate that the optimum C_{p-ave} has shown difference in improvement rate in each *TSR* compared to the bare VAWT. By choosing certain geometric parameters, the C_{p-ave} variation can be around 233.19% higher than a bare VAWT in low regime of *TSRs*. Meanwhile, this increment reduces to 69.94% and 41.36%, respectively, in medium and high regimes of *TSRs*. Moreover, the optimum geometry differs between low regime of *TSRs* and medium and high regimes of *TSRs*. Based on the mean *S/N* ratio tabulated in Table 5.4, in medium and high regimes of *TSRs*, level 2 gives the largest mean *S/N* ratio for the GF height and mounting angle, whilst for position from trailing-edge, it is obtained at level 1. It means that the optimum GF geometry in these *TSR* regimes is a GF configuration with $H = 3\% c$, $\theta_{GF} = 90^\circ$ and $s = 0\% c$. However, there is a change in optimum geometric parameter for the position from the trailing-edge in low regime of *TSRs*. The mean *S/N* ratio for the *s* parameter reaches its maximum value at level 2 in low regime of *TSRs* with the same optimum level for the other two parameters. Hence, the optimum GF geometry is a GF configuration with $H = 3\% c$, $\theta_{GF} = 90^\circ$ and $s = 4\% c$ in low regime of *TSRs*. The possible reason behind this behaviour will be explained later in Section 5.4.4.

Table 5.1 Details of GF geometry parameters and levels of studies.

Parameter	Level		
	1	2	3
H	2% c	3% c	4% c
θ_{GF}	60°	90°	135°
S	0% c	4% c	7% c

Table 5.2 Matrix of case studies for each *TSR*.

Run	<i>H</i> (% <i>c</i>)	θ_{GF} (°)	<i>s</i> (% <i>c</i> from trailing-edge)
1	2	60	0
2	2	60	4
3	2	60	7
4	2	90	0
5	2	90	4
6	2	90	7
7	2	135	0
8	2	135	4
9	2	135	7
10	3	60	0
11	3	60	4
12	3	60	7
13	3	90	0
14	3	90	4
15	3	90	7
16	3	135	0
17	3	135	4
18	3	135	7
19	4	60	0
20	4	60	4
21	4	60	7
22	4	90	0
23	4	90	4
24	4	90	7
25	4	135	0
26	4	135	4
27	4	135	7

Table 5.3 C_{p-ave} values of all 27 cases in all TSR regimes (***bold and italic fonts*** in yellow highlights are the optimum cases).

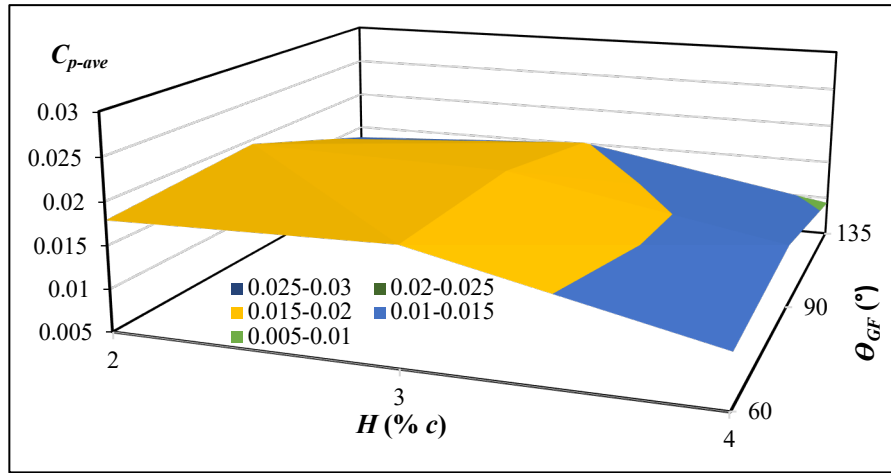
Run	$TSR = 1.44$		$TSR = 2.64$		$TSR = 3.3$	
	C_{p-ave}	C_{p-ave} increment (%)	C_{p-ave}	C_{p-ave} increment (%)	C_{p-ave}	C_{p-ave} increment (%)
1	0.0179	110.38	0.3693	16.33	0.2940	12.37
2	0.0189	122.09	0.3198	0.75	0.2327	-11.06
3	0.0108	27.54	0.3124	-1.59	0.2265	-13.43
4	0.0185	117.25	0.5394	69.93	0.3624	38.51
5	0.0267	213.58	0.4873	53.51	0.3020	15.40
6	0.0133	56.20	0.4756	49.84	0.2937	12.23
7	0.0112	31.48	0.4019	26.62	0.2176	-16.84
8	0.0189	122.53	0.3587	13.00	0.1692	-35.33
9	0.0096	13.00	0.3493	10.03	0.1641	-37.28
10	0.0194	128.36	0.4474	40.95	0.3075	17.51
11	0.0205	141.49	0.3904	22.97	0.2449	-6.40
12	0.0110	29.20	0.3810	20.03	0.2389	-8.68
13	0.0196	130.94	0.5394	69.94	0.3699	41.36
14	0.0283	233.19	0.4980	56.88	0.3470	32.63
15	0.0163	91.24	0.4866	53.31	0.3301	26.14
16	0.0126	47.85	0.4065	28.07	0.2295	-12.30
17	0.0232	172.49	0.3584	12.92	0.1806	-30.97
18	0.0115	35.14	0.3490	9.96	0.1749	-33.15
19	0.0135	58.27	0.3286	3.51	0.1835	-29.88
20	0.0147	73.28	0.2878	-9.34	0.1241	-52.59
21	0.0089	4.54	0.2809	-11.50	0.1205	-53.95
22	0.0152	78.43	0.5193	63.61	0.2663	1.76
23	0.0214	151.74	0.4766	50.16	0.1943	-25.72
24	0.0124	46.22	0.4653	46.57	0.1888	-27.85
25	0.0093	9.33	0.3319	4.56	0.1133	-56.70
26	0.0151	77.18	0.2855	-10.05	0.0879	-66.39
27	0.0078	-8.68	0.2776	-12.53	0.0850	-67.50

It is noticeable that the significance of each parameter on the predicted C_{p-ave} of the VAWT behaves differently in a different regime of $TSRs$. According to the deviation (denoted Δ thereafter) of S/N ratio and the parameter rank by Taguchi analysis (see Table 5.4), the position from the trailing-edge in low regime of $TSRs$ has the most significant effect on the C_{p-ave} of VAWT, followed by the mounting angle and the height of GF. Note that, Δ = the highest average response characteristic value minus the lowest average

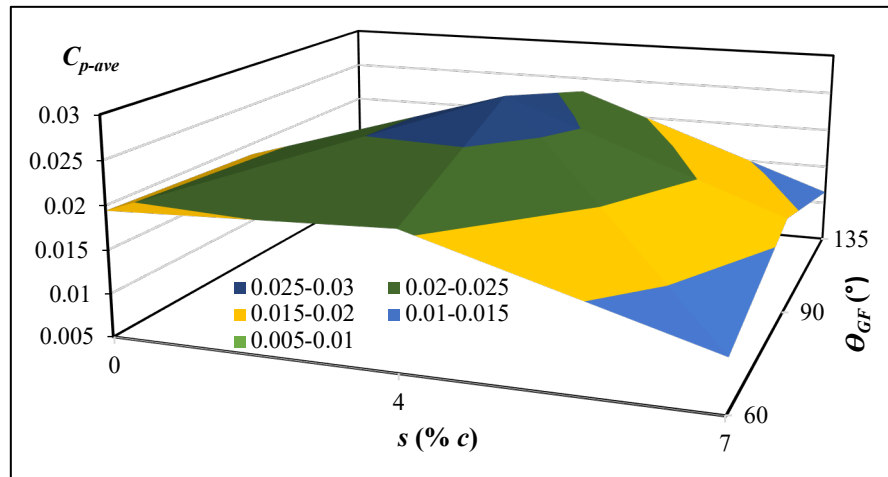
response characteristic value for specific factor levels. Figure 5.5 shows that changing the position of the GF gives a higher change in C_{p-ave} represented by the contour plot, compared to the changing of the other two parameters. In addition, varying both the position of the GF and the mounting angle of the GF can change the C_{p-ave} contour value significantly compared to varying the position and the height of GF or the mounting angle and the height of GF combined. It seems reasonable as the change of GF position in low regime of $TSRs$ has a considerable effect on the improvement of C_{p-ave} (see Figure F.3 in Appendix F). The averaged moment coefficient (C_{m-ave}) in low regime of $TSRs$ indicates that changing the position of the GF can increase this value around 32.22%. Meanwhile, changing the height and mounting angle of GF can only increase the C_{m-ave} values by 14.03% and 18.37%, respectively.

Table 5.4 Response table for Signal to Noise Ratios (i.e., the larger-is-better) of Taguchi analysis (*bold and italic fonts* in yellow highlights are the maximum values).

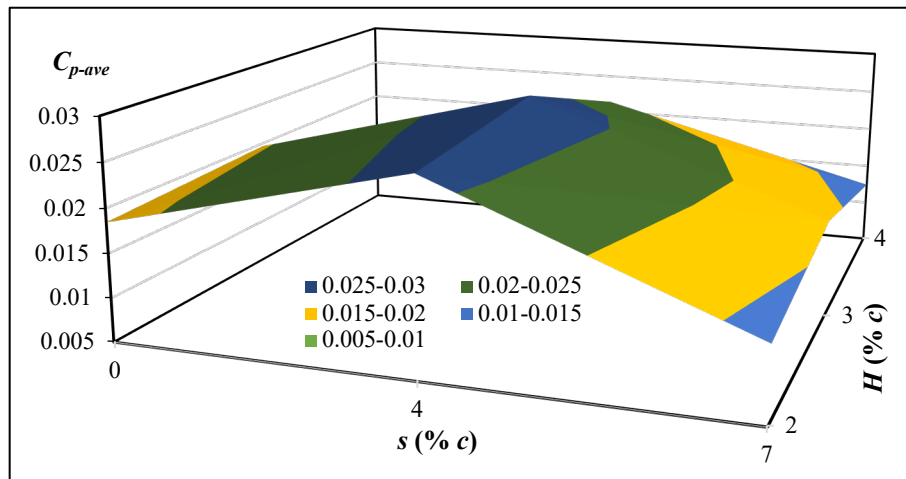
Level	<i>TSR = 1.44</i>			<i>TSR = 2.64</i>			<i>TSR = 3.3</i>		
	Parameter			Parameter			Parameter		
	<i>H</i>	<i>θ_{GF}</i>	<i>s</i>	<i>H</i>	<i>θ_{GF}</i>	<i>S</i>	<i>H</i>	<i>θ_{GF}</i>	<i>s</i>
1	-36.25	-36.78	-36.66	-8.076	-9.301	-7.448	-12.27	-13.59	-12.17
2	-35.33	-34.77	-33.81	-7.454	-6.056	-8.481	-11.68	-10.84	-14.25
3	-38.03	-38.07	-39.14	-9.098	-9.270	-8.698	-16.99	-16.51	-14.52
Delta	2.69	3.30	5.33	1.645	3.245	1.250	5.30	5.68	2.36
Rank	3	2	1	2	1	3	2	1	3



(a)

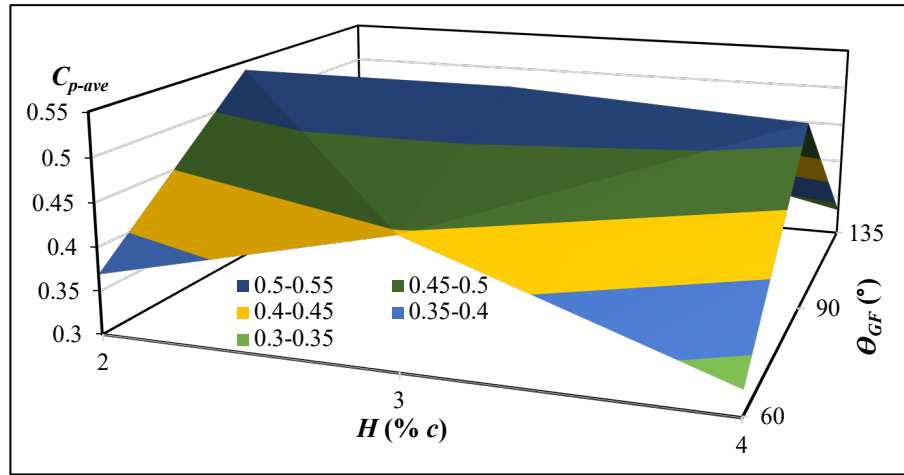


(b)

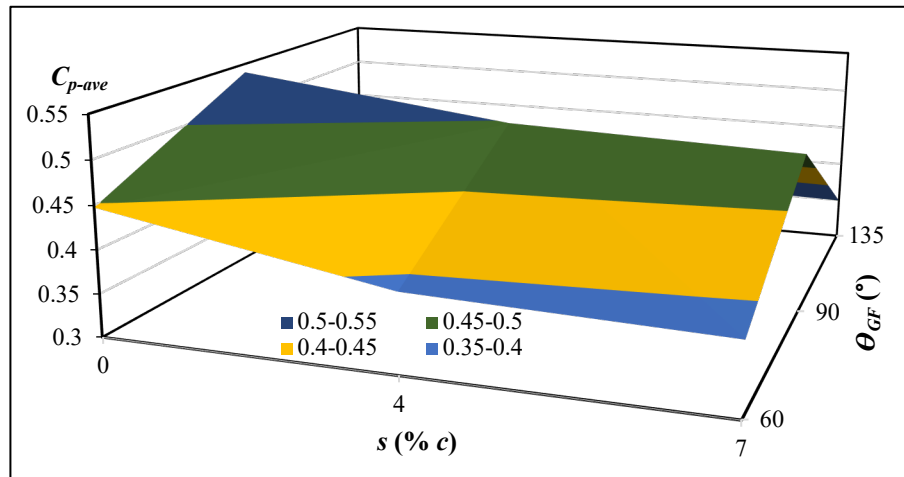


(c)

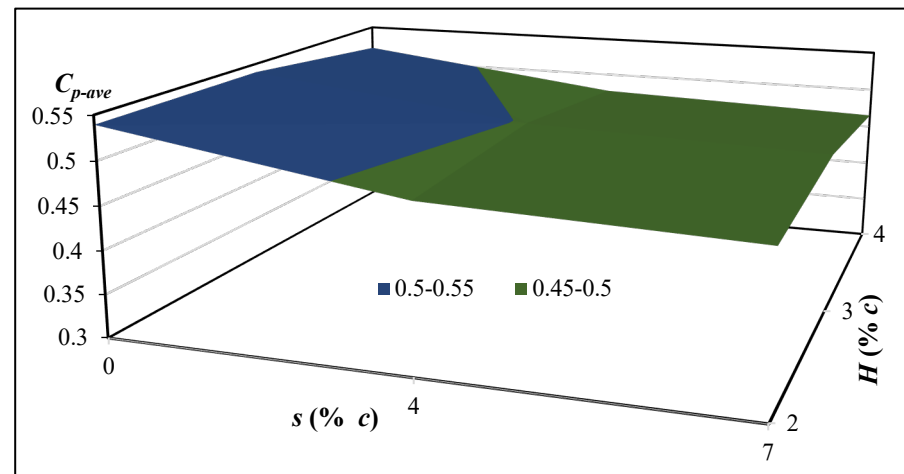
Figure 5.5 Comparison of the effect of varying combination of GF geometry parameters (a) mounting angle & height, (b) position from trailing-edge & mounting angle and (c) position from trailing-edge & height to the contour of C_{p-ave} in $TSR = 1.44$.



(a)

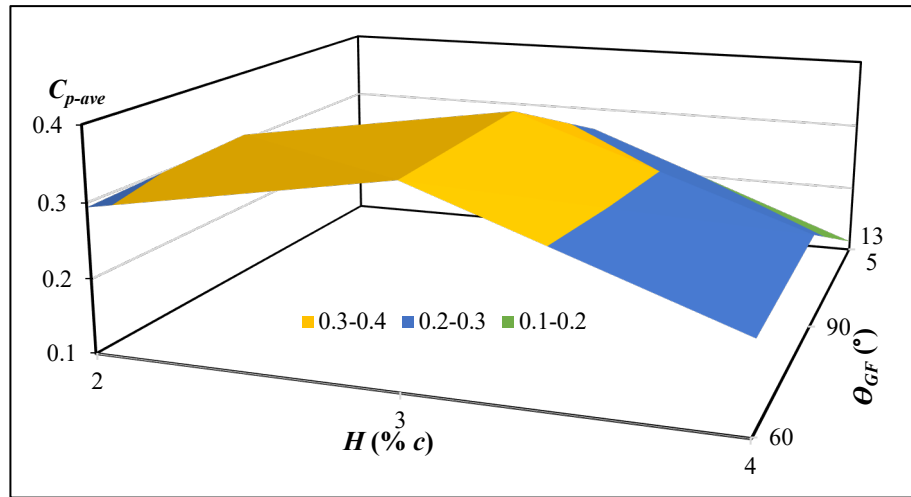


(b)

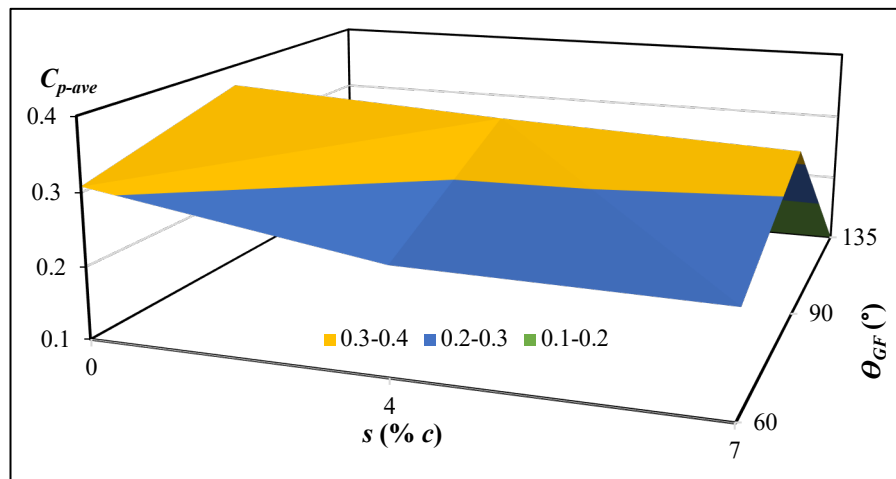


(c)

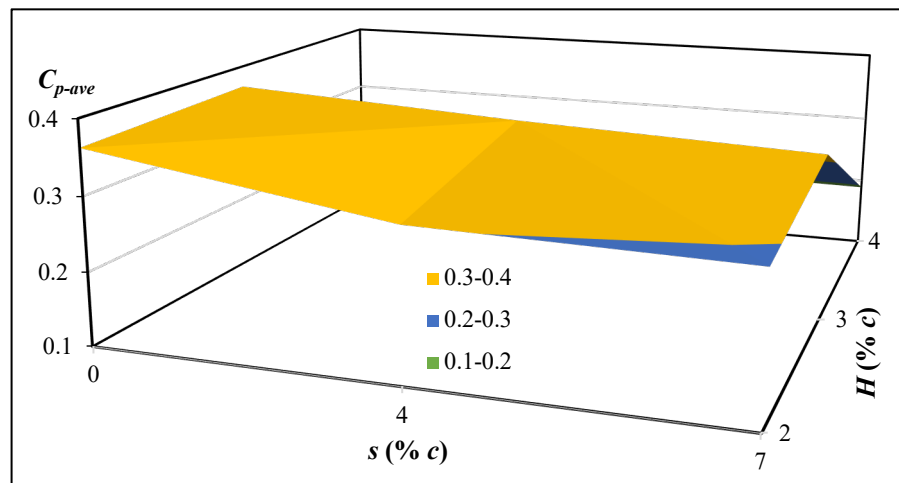
Figure 5.6 Comparison of the effect of varying combination of GF geometry parameters (a) mounting angle & height, (b) position from trailing-edge & mounting angle and (c) position from trailing-edge & height to the contour of C_{p-ave} in $TSR = 2.64$.



(a)



(b)



(c)

Figure 5.7 Comparison of the effect of varying combination of GF geometry parameters (a) mounting angle & height, (b) position from trailing-edge & mounting angle and (c) position from trailing-edge & height to the contour of C_{p-ave} in $TSR = 3.3$.

However, the most significant parameter in medium and high regimes of *TSRs* is the mounting angle, followed by the height and GF position. As illustrated in Figures 5.6 and 5.7, changing the mounting angle of GF can produce more remarkable changes in C_{p-ave} contour values compared to the changing of height or position of the GF. Same as those in low regime of *TSRs* by combining two influential parameters (here they are the mounting angle and the height of GF), the C_{p-ave} contour value is altered significantly compared to any other two parameters in combination. The reason that the mounting angle of the GF has more effect on the change of C_{p-ave} value compared to the height of GF in all *TSR* regimes is likely because the chosen variation of the height of GF does not generate immense change in moment production of VAWT, as the performance of VAWT with GF is already very close to its optimum value. For example, in medium regimes of *TSRs*, changing the height from 2% c to 3% c only alters the moment production by 0.01%. Meanwhile, altering the mounting angle from 60° to 90° can change the moment production by 53.6%. Furthermore, the contours of z -vorticity show that changing the height can only slightly change the flow behaviour around the aerofoil, whilst it is significantly altered if the mounting angle is modified (see later in Figures 5.13 and 5.22, respectively).

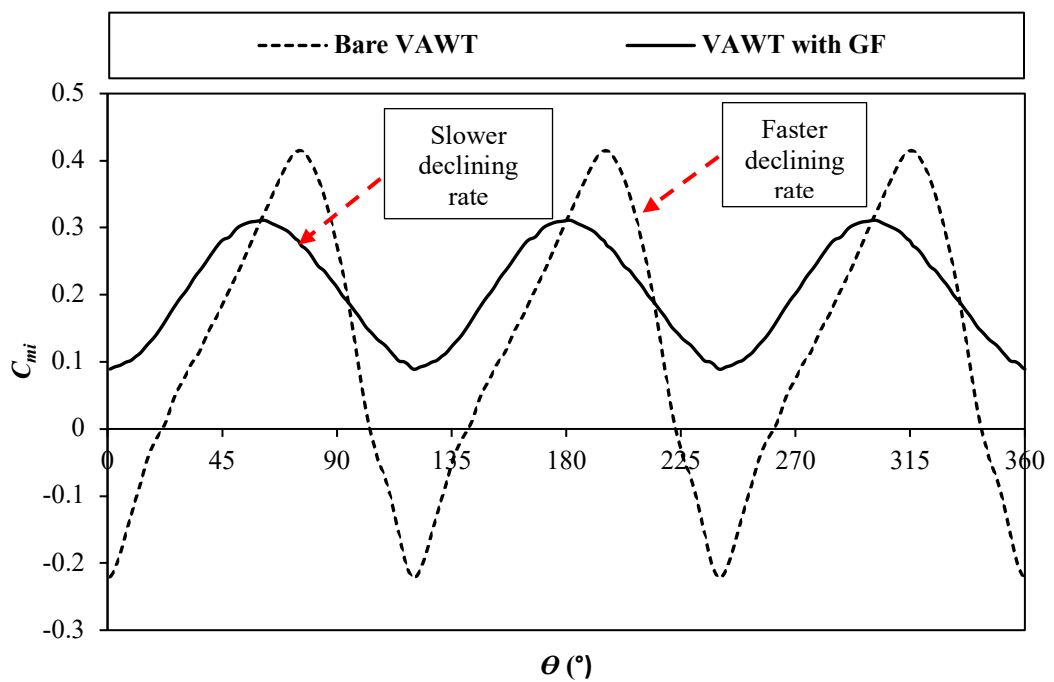
5.4 Results Comparison

5.4.1 General Effect of GFs

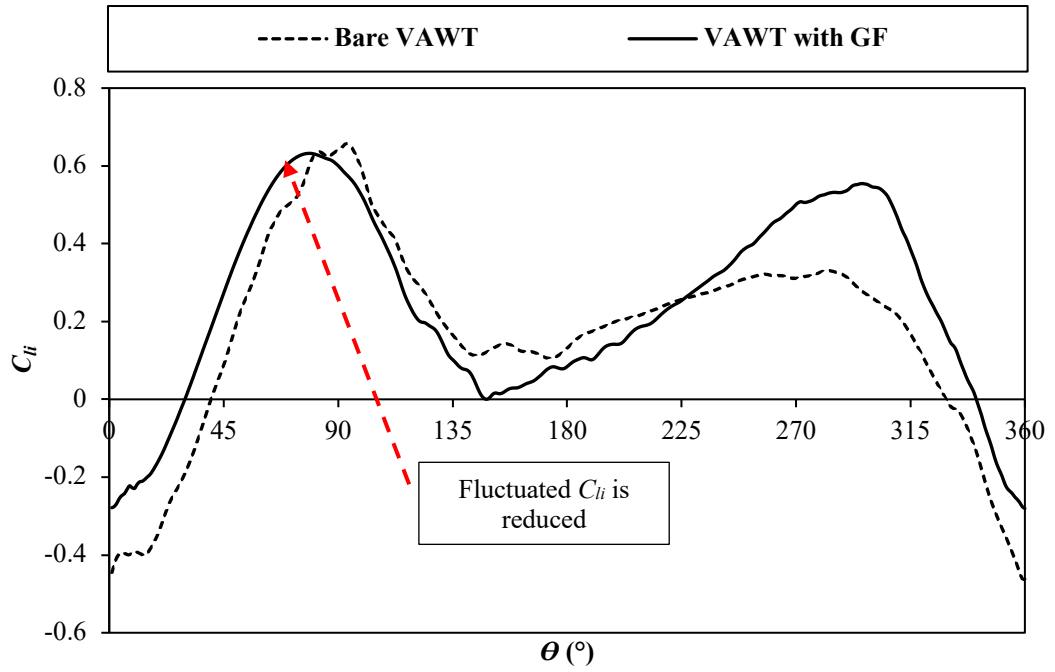
As shown in Figures F.1-F.3 in Appendix F, the introduction of a GF can generally increase the power coefficient of a VAWT, and it is mainly due to the ability of the GF to mitigate the negative moment coefficient production, as illustrated in Figure 5.8 (a). Moreover, the presence of the GF can ease the deep stall of turbine blades, which is evident by a slower declining rate in the C_{mi} curves after reaching its maximum peak, as seen in Figure 5.8 (a).

In order to further understand the effect of the VAWT blades mounted with GFs on turbine performance, the instantaneous lift coefficient (C_{li}) and drag coefficient (C_{di}) of one selected blade (blade 1) over one rotation cycle are depicted in Figure 5.8 (b) and Figure 5.8 (c), respectively. Noting that, these drag and lift coefficients calculations are based on the geometrical angle of attack that is experienced by Blade 1, therefore, the effect of the interaction between the downward blade and the wake of upward blade on the change of geometrical angle of attack is neglected. It shows that the introduction of a GF can reduce the fluctuation amplitude of C_{li} and delay the sudden increase of C_{di} at an

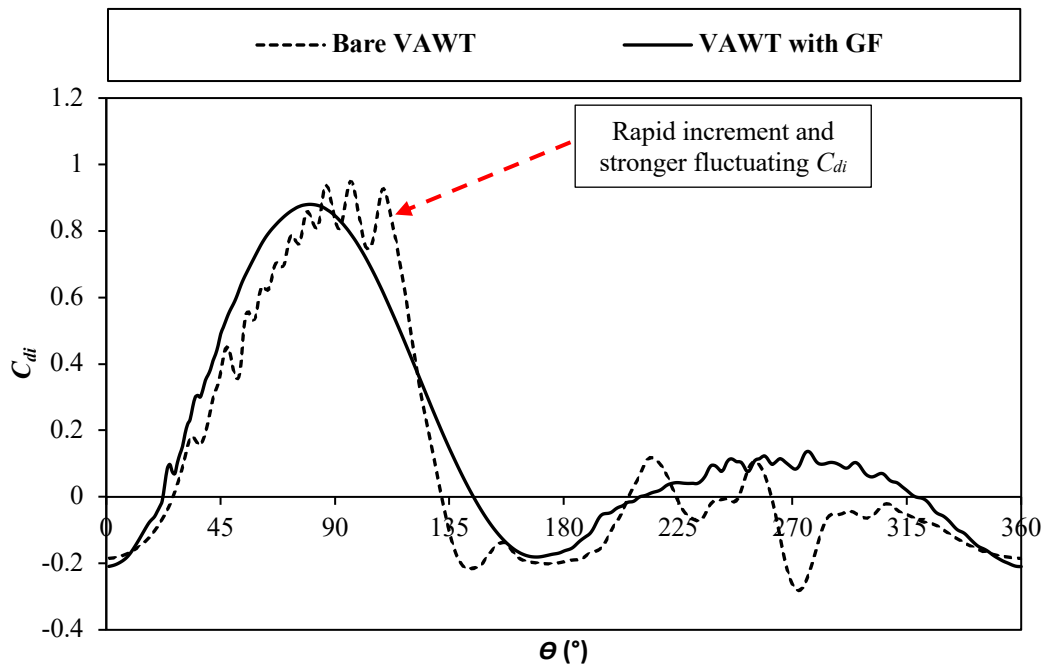
azimuthal position of about 90° . It confirms that the GF can ease the deep stall of turbine blades. The unsteady behaviour of C_{li} and the rapid increment of C_{di} also suggest that the VAWT will start to experience the stall between azimuthal positions of 60° - 100° approximately. Furthermore, it can be seen that there are negative drag coefficients production along the change of azimuthal positions of the blade of VAWT. This negative drag coefficient means that there is a reduction in the drag force production of the blade of VAWT. This reduction can accelerate the wind turbine rotation which is beneficial especially for wind turbine that operated at relatively low wind speed area (Karhadkar et al., 2018).



(a)

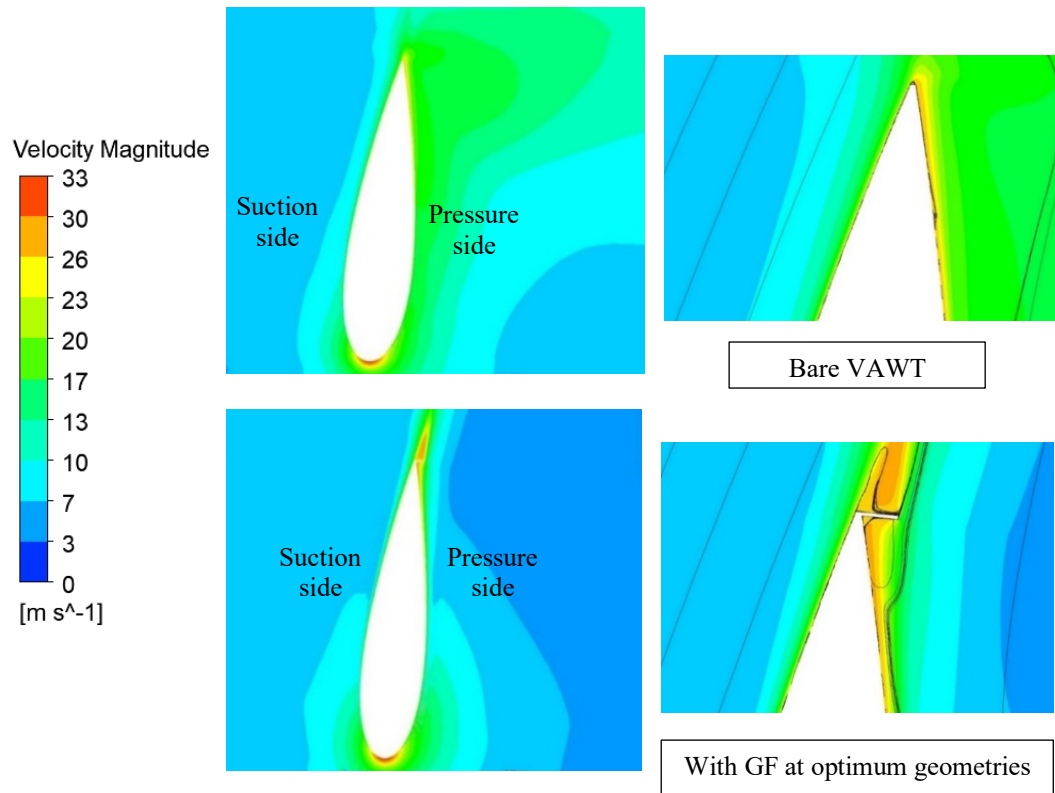


(b)

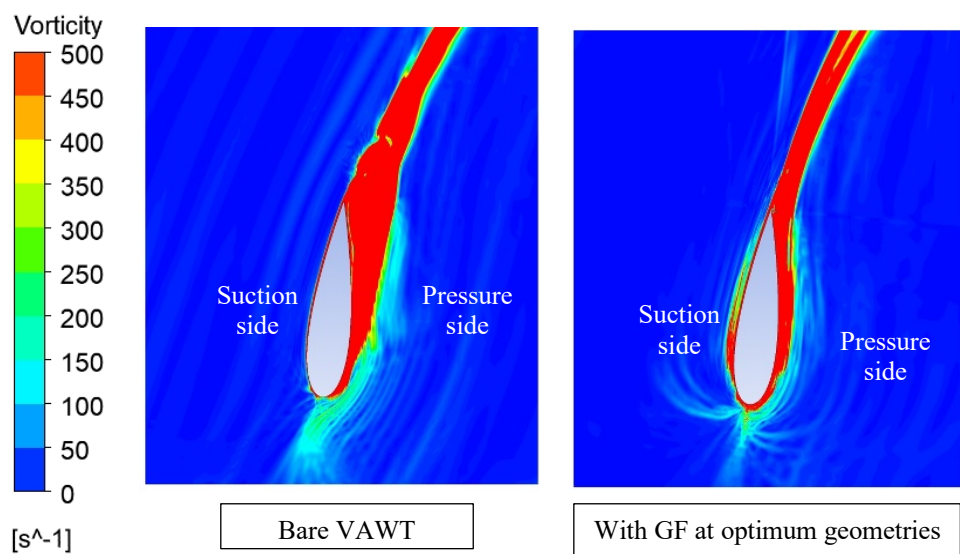


(c)

Figure 5.8 Comparison of (a) C_{mi} , (b) C_{li} and (c) C_{di} over one rotation cycle of VAWT with GF (optimum geometries) and without GF in $TSR = 2.64$.



(a)



(b)

Figure 5.9 Comparison of (a) velocity magnitude contours with super-imposed pathlines in the right graphs and (b) contours of z-vorticity between bare VAWT and VAWT with GF (optimum geometry) in $TSR = 2.64$, $\theta = 90^\circ$.

Further investigation on the velocity magnitude contours with super-imposed pathlines (see Figure 5.9 (a)) reveals that the GF addition can certainly introduce vortices

downstream, which can influence the flow and pressure fields near the trailing-edge. Moreover, as shown in Figure 5.9 (a), contours of velocity magnitude suggest that whilst the GF reduce slightly the velocity magnitude over the suction surface, it can significantly decrease the velocity magnitude on the pressure surface (indicated by large dark blue region near the trailing-edge). As a result, less flow separation can be seen (shown by less vortex shedding in Figure 5.9 (b)) and the total circulation of the blade will be increased (consistent with the enhanced lift coefficient). For example, the calculation of circulation (Γ) by taking surface area (S_a) integral of z-vorticity (ξ_z) (see Equation (5.2)) of the blades shows that the addition of the GF (optimum geometries) can improve the total circulation of the blades of VAWT by about 108% compared to the bare VAWT in $TSR = 2.64$ ($\theta = 90^\circ$). Therefore, the lift enhancement will lead to more power generation using the GF mounted on the blades.

$$\Gamma = \oint \xi_z \cdot dS_a \quad (5.2)$$

where $\xi_z = \nabla \times \vec{U} = \vec{k} \left(\frac{\partial U_y}{\partial x} - \frac{\partial U_x}{\partial y} \right)$ with U_y is the y-velocity component and U_x is the x-velocity component.

For the case studies in the other two TSR regimes, i.e., both high and low regimes of $TSRs$, the addition of a GF also positively influences the increment of VAWT performance (see Figure 5.10). It confirms that the GF can be applied to improve the VAWT performance in all regimes of $TSRs$. However, note that the degree of improvement varies with each TSR regime. For example, as shown in Figure 5.11, a GF with a height equal to 3% c , 90° mounting angle and mounted at the trailing-edge of the blade, the GF is likely to have a significant influence on the increment of C_{p-ave} in low regime of $TSRs$ (around 130.94% performance increment compared to bare VAWT in the lowest value of TSR). In medium regime of $TSRs$, the improvement of C_{p-ave} of VAWT in the presence of GF is lower compared to low regime of $TSRs$ (about 69.94% of the optimum TSR value of a bare VAWT), whilst in high regime of $TSRs$, GF can still enhance the C_{p-ave} (approximately 41.36% in the highest value of TSR), but not as significant as those in low and medium regimes of $TSRs$. This phenomenon is most likely caused by the different values of angle of attack during operation and beyond static stall AoA_Ds of the aerofoil in those $TSRs$. As Malael, Dumitrescu and Cardos (2014) mentioned, the range of AoA_Ds in operation and beyond static stall AoA_Ds in low regime of $TSRs$ is more widely attained than at medium and high regimes of $TSRs$. Hence, the benefit of having

a GF to increase the maximum lift and reducing the dynamic stall of VAWT can be utilized effectively in this TSR regime, compared to medium and high regimes of $TSRs$.

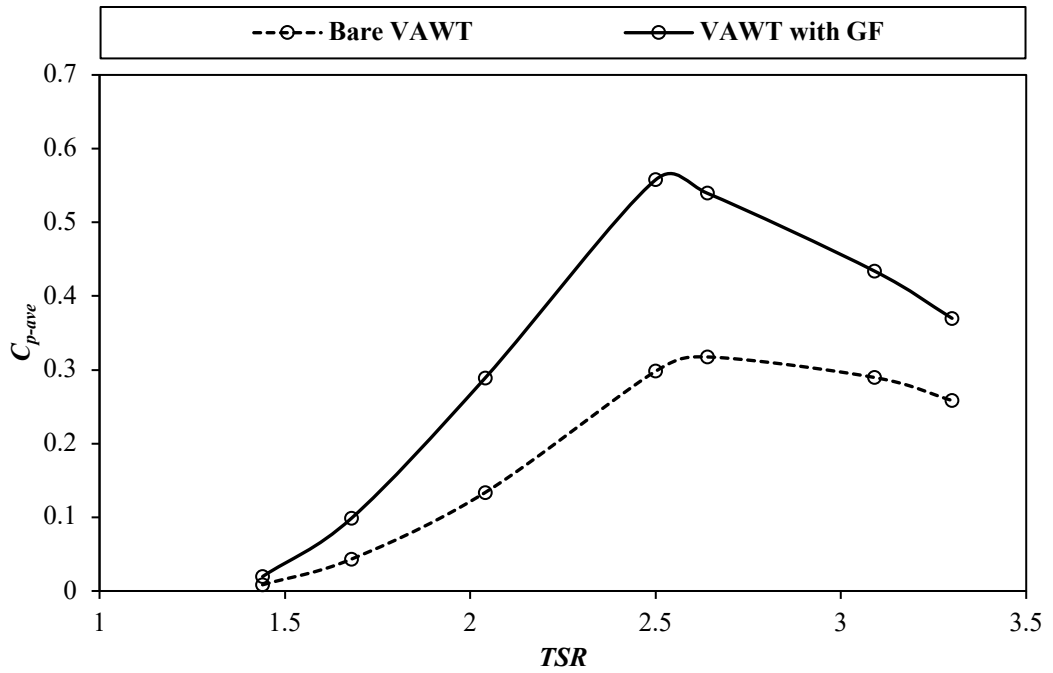


Figure 5.10 C_{p-ave} comparison between the VAWT with GF ($H = 3\% c$, $\theta_{GF} = 90^\circ$ and $s = 0\% c$ from trailing-edge) and without GF in different TSR values.

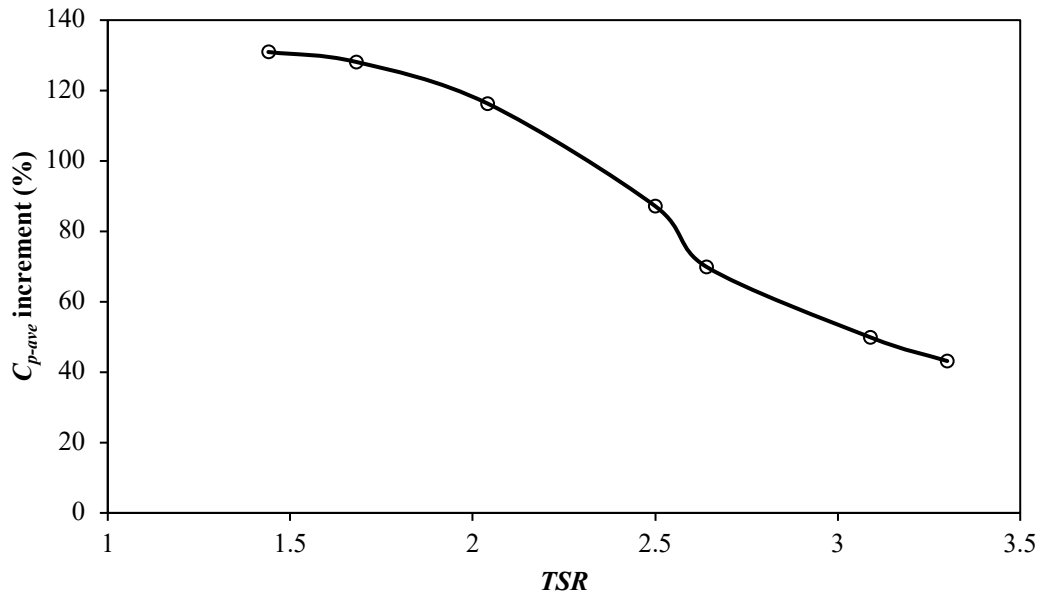


Figure 5.11 C_{p-ave} increment in all tested $TSRs$ for a VAWT with GF ($H = 3\% c$, $\theta_{GF} = 90^\circ$ and $s = 0\% c$ from trailing-edge).

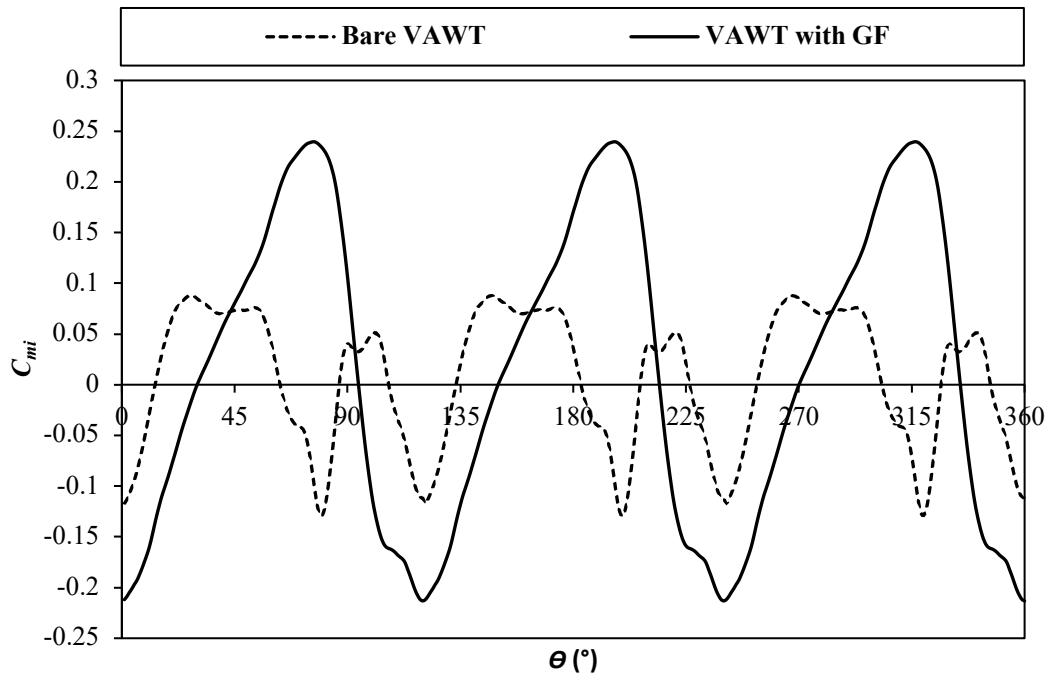


Figure 5.12 C_{mi} comparison of VAWT with GF ($H = 3\% c$, $\theta_{GF} = 90^\circ$ and $s = 0\% c$ from trailing-edge) and without GF in $TSR = 1.44$.

It is also noticeable that the presence of the GF moves an optimum TSR to a lower value compared to the bare VAWT (e.g., from $TSR = 2.64$ to $TSR = 2.50$). It is rather desirable as the VAWT can produce an optimum power output in lower TSR , as a higher TSR expresses the higher tangential speed at the blade trailing-edge resulting in a large and undesirable centrifugal force. Consequently, the VAWT will produce a higher noise level and need structurally stronger blades to balance the larger centrifugal force. Therefore, the GF also helps the VAWT to produce optimum power with a lower noise level and strength requirements of the blade structure.

The use of the GF to significantly improve the VAWT power generation in the low TSR regime is desirable as it can also enhance the self-starting ability of the VAWT. It is widely known that in the low TSR regime, the VAWT tends to experience dynamic stalls and, therefore, produces a substantial amount of negative moment that prevents the VAWT from rotating by itself. As a result, the VAWT that operates in low regime of $TSRs$ often needs additional external power to rotate the turbines before producing a positive moment for power generation. The addition of the GF can reduce the number of positive/negative moment production pairs as indicated with only one negative peak of C_{mi} distribution in every 120° azimuthal position, as seen in Figure 5.12. It shows that the GF can ease dynamic stall in low regime of $TSRs$. Adding a GF can decrease the number

of negative peak C_{mi} regions compared to the bare VAWT. It also enhances the optimum value of C_{mi} significantly. Thus, the presence of the GF improves the moment production of the VAWT in low regime of $TSRs$ and demonstrates that the GF can broadly elevate the self-starting ability in this TSR regime.

5.4.2 Effect of the height of GF

Figure 5.13 shows the change of C_{p-ave} as the effect of variation of GF height with a fixed mounting angle (90°) and a fixed position (0% c from trailing-edge) in $TSR = 2.64$. In general, the VAWT C_{p-ave} rises with the increase of the GF height, with a maximum C_{p-ave} achieved for a GF height of 3% c . Increasing GF height will lose its capability to increase the C_{p-ave} further. Compared to a single stationary aerofoil with an optimum GF height of 2% c (Yan, Avital and Williams, 2019), this optimum GF height is slightly higher, possibly due to the rotational effects and the wake-blade interactions. Nevertheless, this observation confirms that those findings from a single stationary aerofoil with GF are not applicable to the rotating wind turbine blade scenarios.

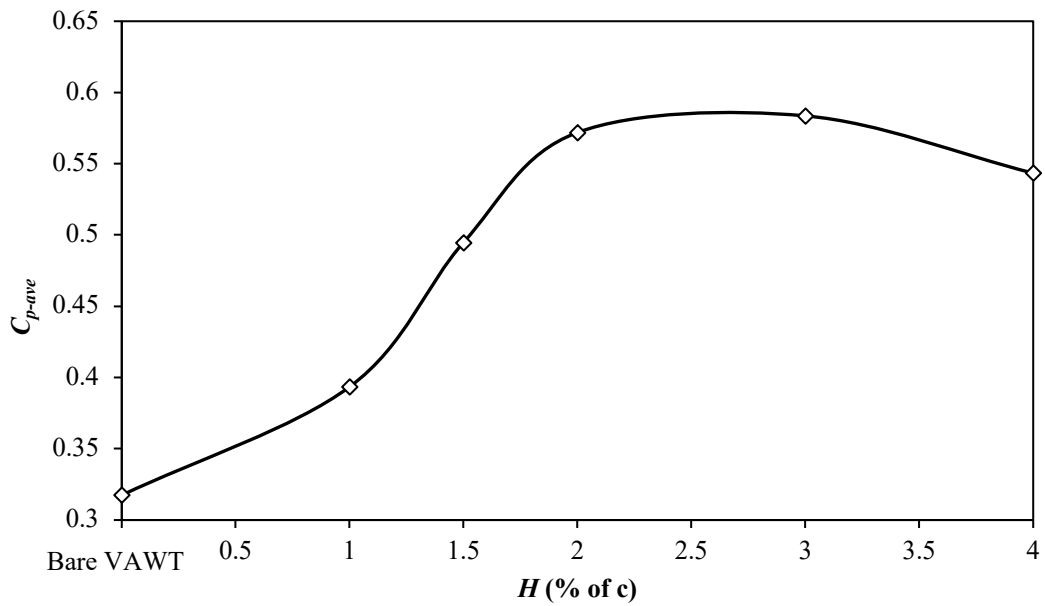


Figure 5.13 C_{p-ave} comparison of VAWT with and without GF in various GF heights ($TSR = 2.64$).

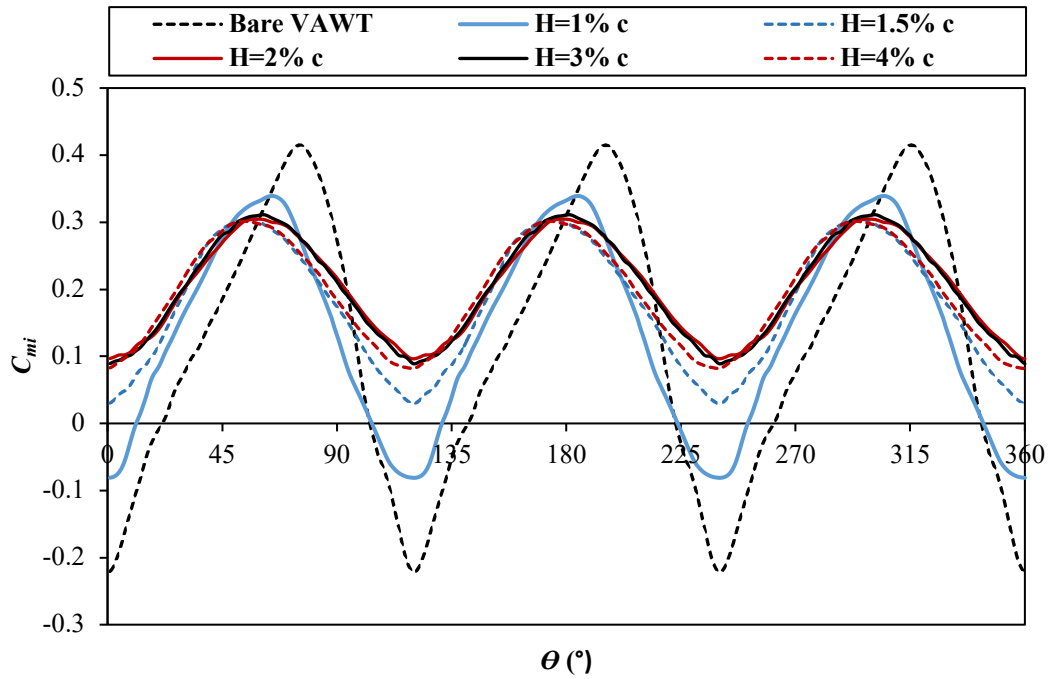
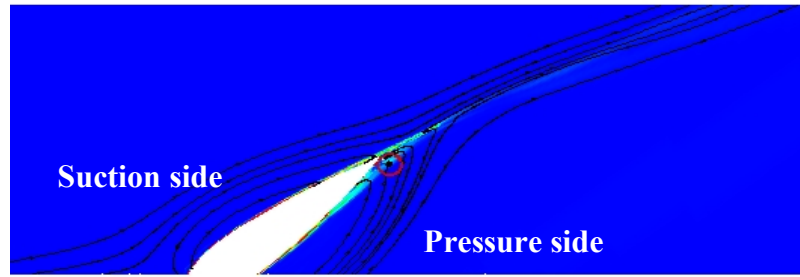
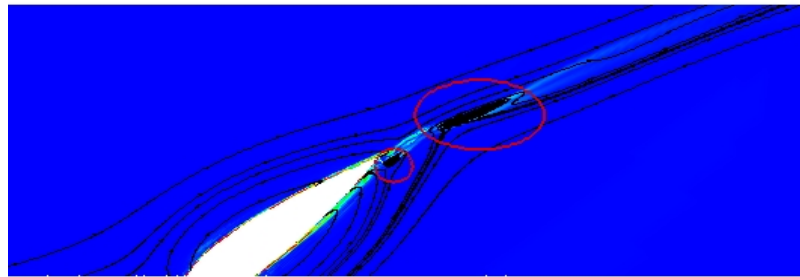


Figure 5.14 C_{mi} comparison from the VAWT with and without GF for various GF heights ($TSR = 2.64$).

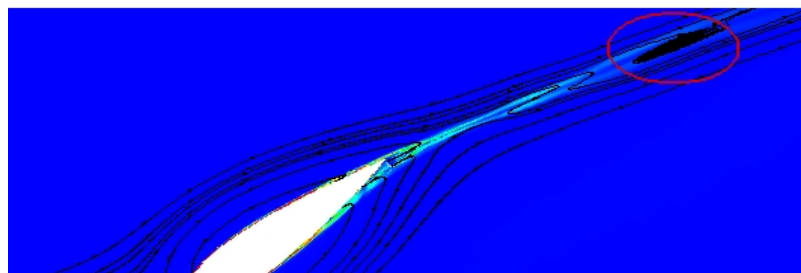
Figure 5.14 illustrates the instantaneous moment coefficients over one turbine revolution from simulations of different GF heights. The C_{mi} distribution demonstrates that a GF addition with a height equal to or higher than $1.5\% c$ can remove the negative C_{mi} . As the height of the GF increases, the values of C_{mi} moves forward to positive values and the average value of C_{mi} increases (For example, averaged C_{mi} increases from 0.1409 for a GF with $H = 1\% c$ to 0.2043 for a GF with $H = 3\% c$), resulting in an increased power output at an optimum GF height of $3\% c$. After this optimum height, even if there is no negative C_{mi} production, the values of C_{mi} shift down to the lower values compared to $H = 3\% c$ and thus, the average value of C_{mi} decreases (averaged C_{mi} declines from 0.2043 for GF with $H = 3\% c$ to 0.1967 for GF with $H = 4\% c$). It indicates that when a GF height is greater than $3\% c$, the GF addition starts to reduce the moment production of the turbine. In Figure 5.14, the GF with $H = 4\% c$ has a slight decrease of the minimum value of C_{mi} compared to the GF with optimum height and, as a result, decreases the improvement of VAWT performance.



$$H = 2\% c$$



$$H = 3\% c$$



$$H = 4\% c$$

Vorticity Magnitude

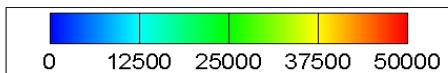


Figure 5.15 Comparison of streamlines coloured by z -vorticity contours of one selected blade (blade 1) in various heights of GF ($TSR = 2.64$, $\theta = 45^\circ$).

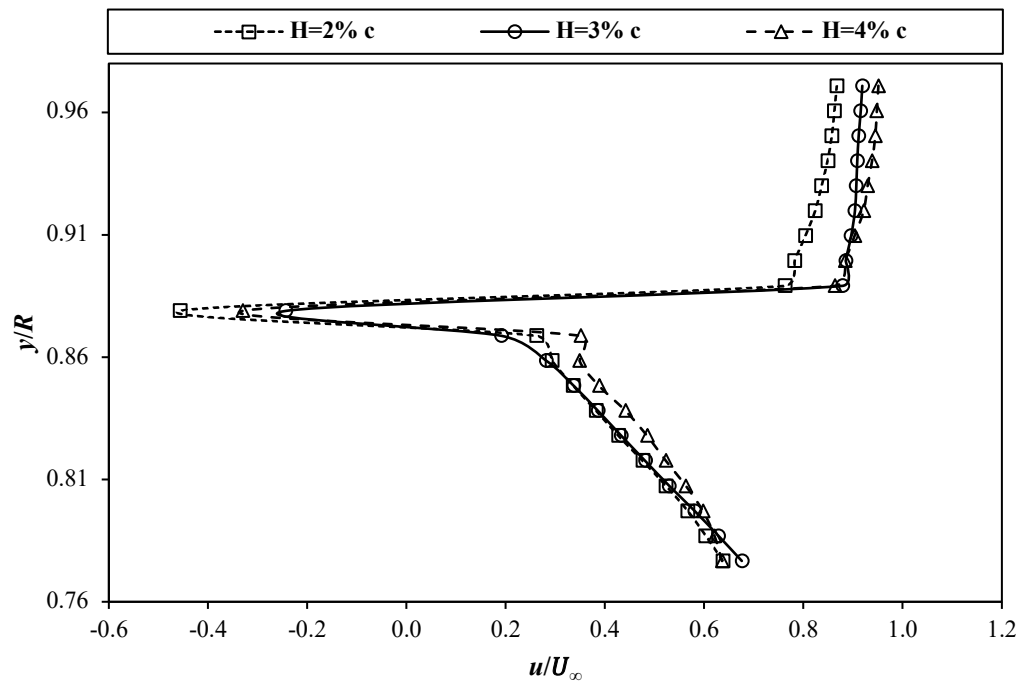
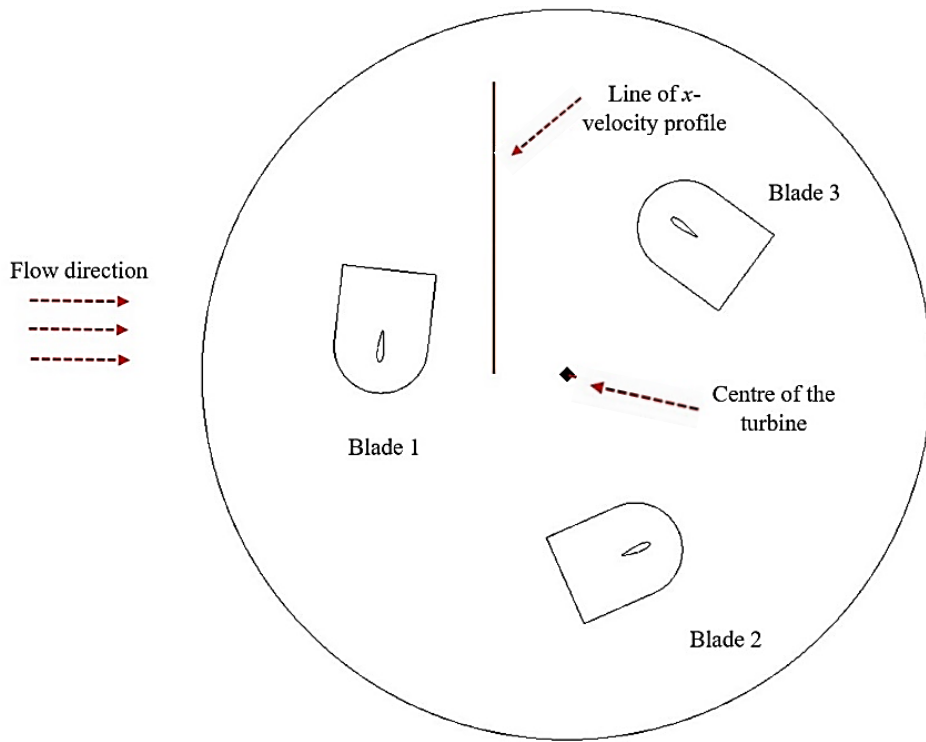


Figure 5.16 Comparison of x -velocity profiles in the wake region of one selected blade (blade 1) in various heights of GF ($TSR = 2.64$, $\theta = 45^\circ$).

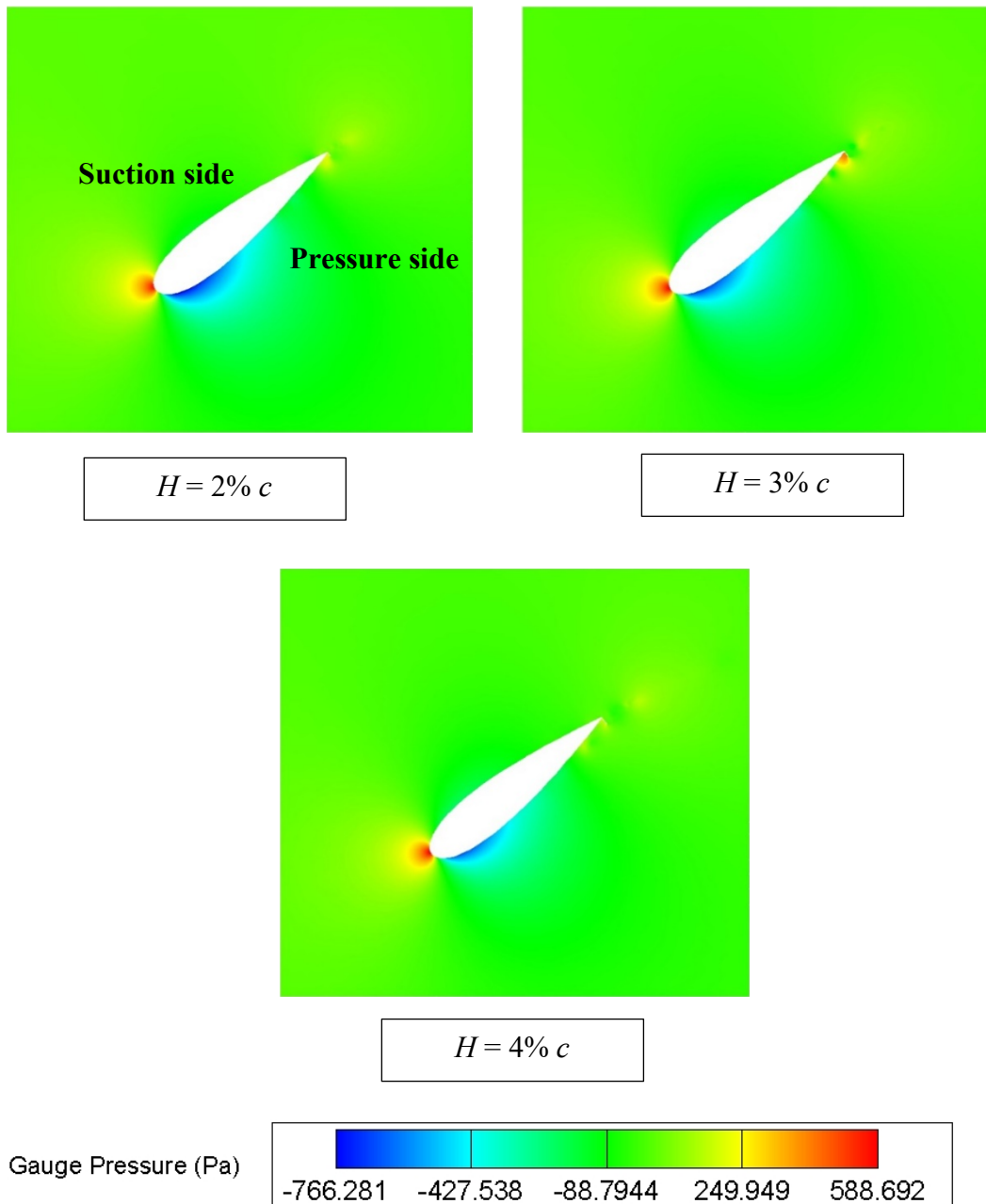


Figure 5.17 Comparison of gauge pressure contours of one selected blade (blade 1) in various heights of GF ($TSR = 2.64$, $\theta = 45^\circ$).

Further investigation of streamlines coloured by z -vorticity contours (see Figure 5.15) at the azimuthal position = 45° (i.e., where there is a significant difference of C_{mi} between the GF with three different heights) indicates that a GF with $H = 3\% c$ generates two counter-rotating vortices in the near wake of the GF, while a GF with $H = 2\% c$ and $4\% c$ only generates one vortex in the same wake region (see, e.g. red circles in Figure 5.15). These two counter-rotating vortices downstream of the GF lead the GF with $H = 3\% c$ to have smaller momentum deficits in the wake region (as shown by narrower x -

velocity variation in Figure 5.16). Hence, the highest increment of lift force generation can be achieved by the GF with $H = 3\% c$. In addition, the gauge pressure contours demonstrate that there is no significant difference in pressure distributions at the leading-edge of the blade, showing that the GF indeed does not affect the flow around the leading-edge of the blade (see Figure 5.17). On the other hand, a noticeable difference can be seen around the trailing-edge of the blade (in particular at the pressure side of the blade) when the height of the GF is altered. Compared to a GF with $H = 2\% c$ and $4\% c$, the GF with $H = 3\% c$ has shown higher variations in the gauge pressure contours around the trailing-edge of the blade (see, e.g., colour differences between the suction and pressure sides of the blade). This suggests that the GF with $H = 3\% c$ can produce the highest difference in gauge pressure compared to other two heights, resulting in the largest moment production. As a result, the GF with $H = 3\% c$ can produce the greatest improvement of the power coefficient of VAWT.

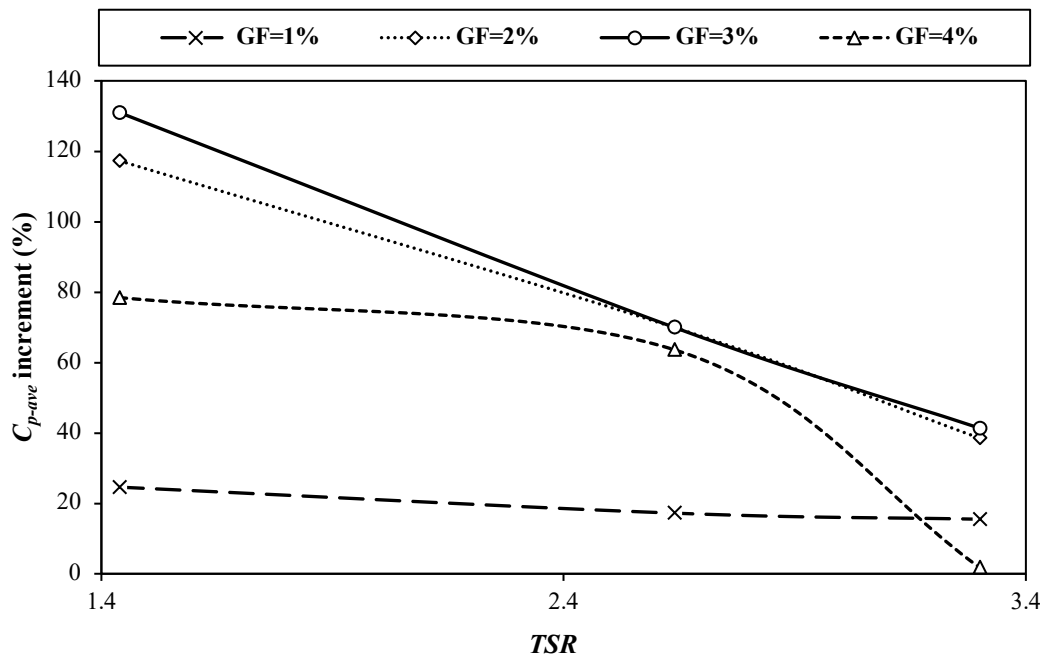


Figure 5.18 Comparison of C_{p-ave} improvement of VAWT with GF for various GF heights in different values of the TSR .

Concerning the effect of the GF height on the VAWT performance improvement in different TSR regimes, the effect of the GF on the improvement of the VAWT power coefficient has shown similar trends in all three regimes of low, medium and high $TSRs$ (see Figure F.1 in Appendix F). As the GF height increases, the C_{p-ave} increases until it reaches an optimum value for a GF with $H = 3\% c$. After that, the C_{p-ave} decreases,

indicating that GF height increment cannot further enhance the C_{p-ave} of VAWT. For all tested GF heights, it is observed that GF generates the highest C_{p-ave} increment in low regime of $TSRs$, followed by medium and high regimes of $TSRs$ (e.g., see Figure 5.18). It indicates that at those choices of GF height, the presence of the GF has the strongest capability to improve the VAWT performance in low regime of $TSRs$. Nevertheless, it has been observed in high regime of $TSRs$ that whilst a GF with a height of less than or equals to $3\% c$ experiences a similar rate of decrease of the C_{p-ave} enhancement, a GF with a height greater than $3\% c$ (e.g., $4\% c$) experiences a significant reduction in C_{p-ave} improvement. It is probably because the decrease in lift to drag ratio as the GF height increases could be more prominent in this TSR regime. In $TSR = 2.64$ (medium regime of $TSRs$), the averaged lift to drag ratio is reduced by about 0.004 whilst GF height increases from $3\% c$ to $4\% c$. Meanwhile, in $TSR = 3.3$ (high regime of $TSRs$), this value decreases significantly by about 0.0128. As explained above, the GF cannot optimally enhance its ability to reduce the VAWT dynamic stall in high regime of $TSRs$. In this TSR regime, the values of AoA beyond the static stall angle becomes smaller, compared to both low and medium regimes of $TSRs$. Hence, the GF contribution to lift improvement reduces (in $TSR = 3.3$, averaged lift decreases from 0.243 to 0.242 whilst the GF height increases from $3\% c$ to $4\% c$) whilst the drag rises (in $TSR = 3.3$, averaged drag increases from 0.1309 to 0.1315 whilst GF height increases from $3\% c$ to $4\% c$), resulting in a lower lift to drag ratio. Nevertheless, it still can improve the performance of bare VAWT by about 1.75%.

5.4.3 *Effect of the mounting angle of GF*

Figure 5.19 illustrates the effect of variation of GF mounting angle and height at a fixed position ($0\% c$ from trailing-edge) on the VAWT C_{p-ave} in $TSR = 2.64$. There are similar tendencies of C_{p-ave} variations between different GF heights as those GF mounting angle values change. It means that the VAWT C_{p-ave} increases with the increase in the GF mounting angle until reaching its optimum value at $\theta_{GF} = 90^\circ$. Beyond this angle, the ability of the GF to improve the VAWT C_{p-ave} starts to reduce. Nevertheless, the VAWT with a GF height lower than $1.5\% c$ and a mounting angle larger than 90° (it is 135° in this case) will produce a C_{p-ave} value lower than that of a bare VAWT. This finding suggests that a GF with a shorter height and smaller mounting angle towards the lower surface of the blade will not improve the performance of VAWT.

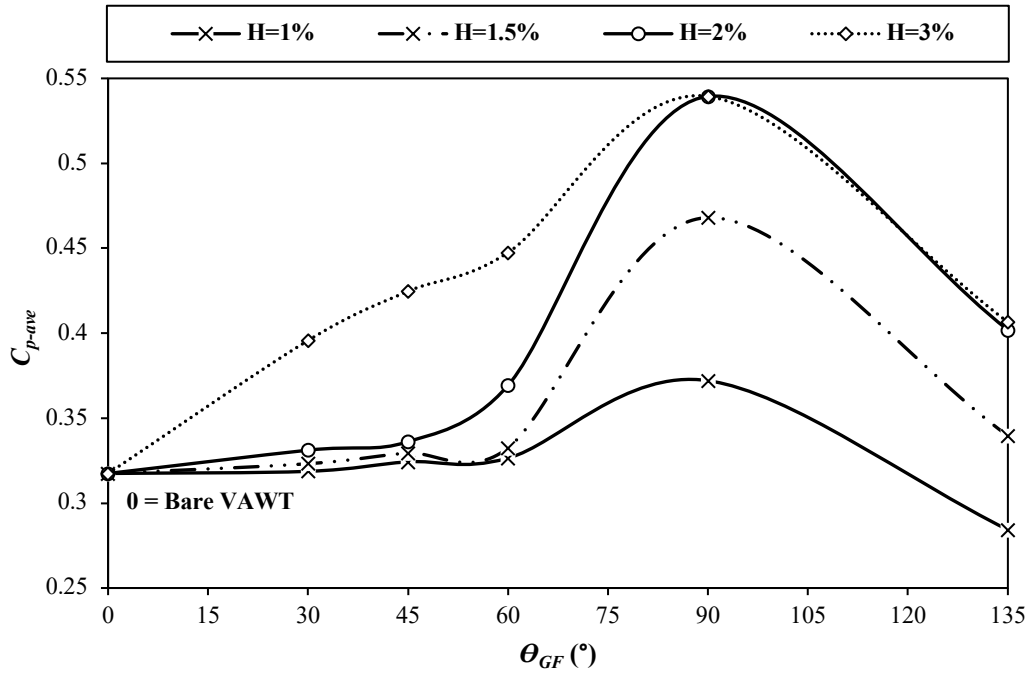


Figure 5.19 Comparison of C_{p-ave} of VAWT with and without GF for various heights and mounting angles and a fixed position (0% c from trailing-edge) in $TSR = 2.64$.

Further investigation of C_{mi} distribution shows that GF at trailing-edge with a height equals to 3% c and mounting angles between 60° and 90° or an angle of $\theta_{GF} = 90^\circ$ can remove the negative moment production of VAWT, resulting in the highest positive moment production, for $TSR = 2.64$ (see Figure 5.20). The gauge pressure contours (see Figure 5.21) at $\theta = 120^\circ$ (i.e. where there are significant C_{mi} differences between a GF with $\theta_{GF} = 60^\circ, 90^\circ$ and 135°) demonstrate that compared to a GF with the other two mounting angles, the GF with $\theta_{GF} = 90^\circ$ produces significantly higher gauge pressure at the trailing-edge of the blade (as indicated by the yellow colour shading domination at the trailing-edge of the pressure side of the blade). This leads to a better C_{m-ave} increment for GF with $\theta_{GF} = 90^\circ$ than other two mounting angles, resulting in higher C_{p-ave} value.

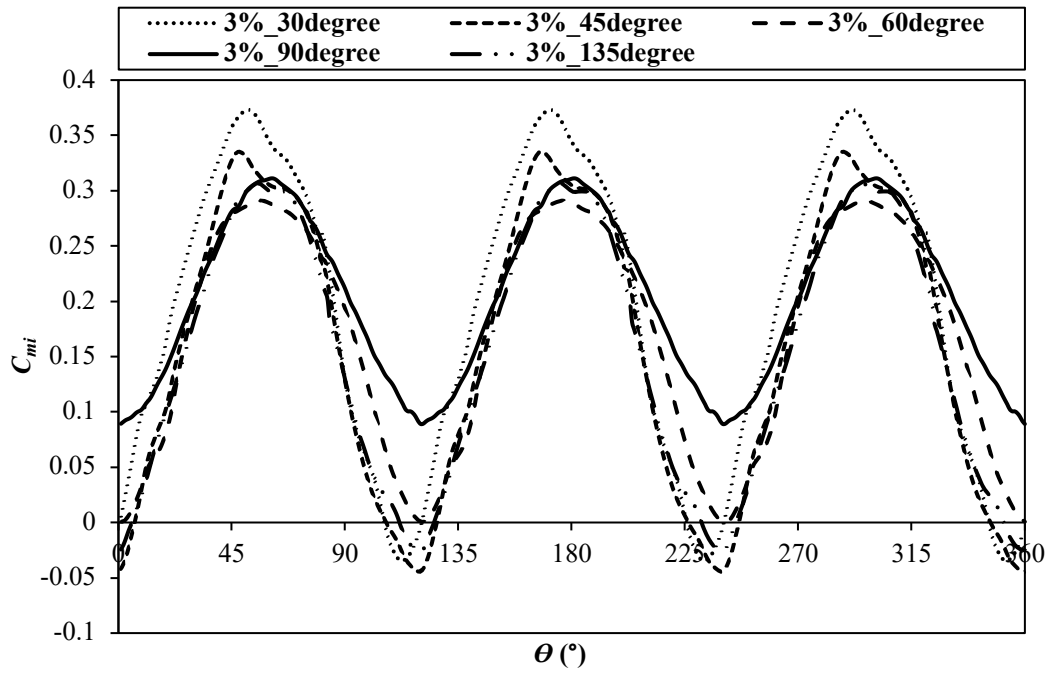


Figure 5.20 C_{mi} comparison of the VAWT with GF in various mounting angles for $TSR = 2.64$.

Moreover, C_{mi} distribution for $\theta_{GF} = 90^\circ$ implies the slowest rate of decrease of C_{mi} and the longest delay in the fall of C_{mi} (see Figure 5.20), indicating that GF mounting angle of $\theta_{GF} = 90^\circ$ has the best ability to reduce the dynamic stall experienced by VAWT, and in the meantime increases its lift production. It is further confirmed by the streamlines coloured by z -vorticity contours at $\theta = 120^\circ$. At this azimuthal position, the GF with $\theta_{GF} = 90^\circ$ generates a small region of reverse flow at the leading-edge of the pressure side of the blade compared to the GFs at the other two mounting angles, whilst relatively weaker or even almost invisible vortex shedding behind the trailing-edge of the blade is produced (see Figure 5.22). On the other hand, GFs with $\theta_{GF} = 60^\circ$ and 135° induce larger regions of reverse flow at the leading-edge of the pressure side of the blade. This region is quite large, ranging from the leading-edge up to the trailing-edge. It causes stronger vortex shedding behind the trailing edge of the blade with increased drag, compared to the GF with $\theta_{GF} = 90^\circ$ (see Figure 5.22). Hence, a GF with 90° mounting angle can generate the highest C_{m-ave} improvement in the VAWT, leading to the highest C_{p-ave} value compared to a GF with other two mounting angles. This is in an agreement with a previous study that mentioned that stronger vortex shedding could increase the drag generation and as a result, reduce the lift to drag ratio and lead to performance decrease (Nedić and Vassilicos, 2015). In relation to the effect of GF mounting angle in different regimes of

TSRs, it has been shown in Figure F.2 in Appendix F that the change of *TSR* regime does not affect the trend of C_{p-ave} variation caused by the change of GF mounting angle. In all regimes of *TSRs*, the VAWT produces the highest C_{p-ave} at $\theta_{GF} = 90^\circ$, indicating that this optimum mounting angle can be applied in all regimes of *TSRs*.

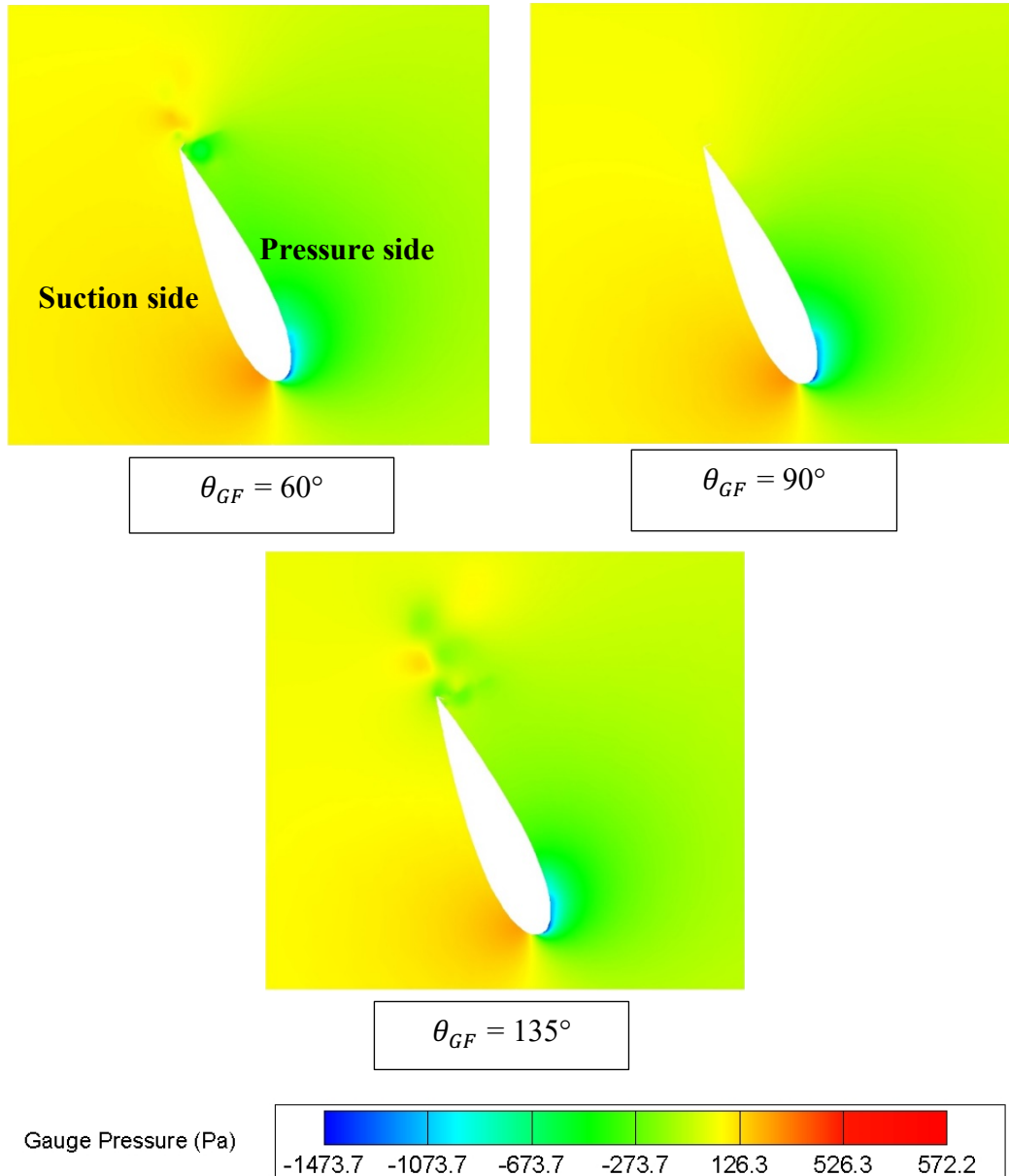


Figure 5.21 Comparison of gauge pressure contours in various mounting angles of the GF ($TSR = 2.64$, $\theta = 120^\circ$).

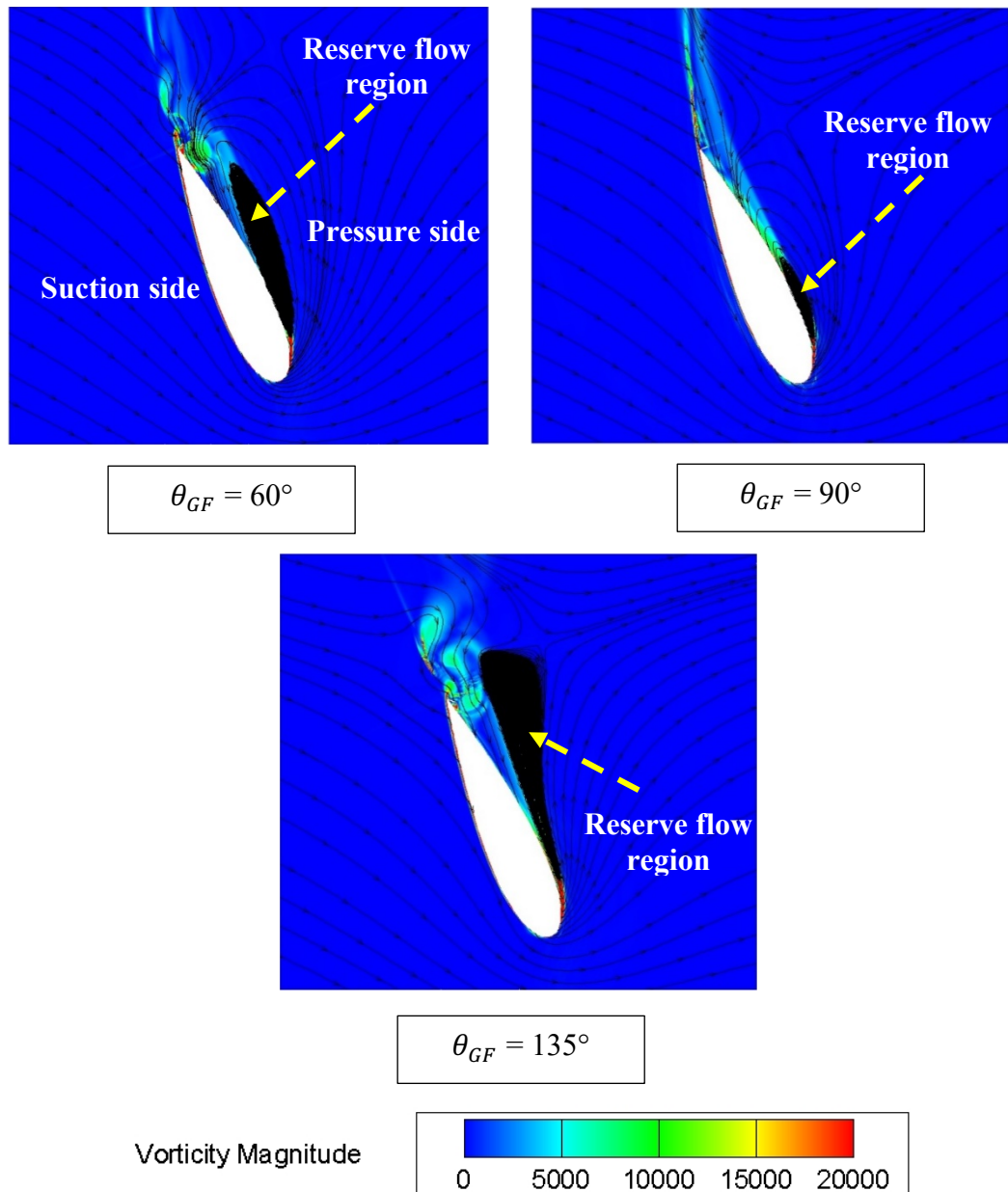


Figure 5.22 Comparison of streamlines coloured by z-vorticity contours in various mounting angles of the GF ($TSR = 2.64$, $\theta = 120^\circ$).

5.4.4 Effect of the position from trailing-edge of the GF

As illustrated in Figure F.3 in Appendix F, the GF position will have different effects on the performance of the VAWT with GF in different regimes of $TSRs$. Noting that, GF height and mounting angle are fixed to $H = 3\% c$ and $\theta_{GF} = 90^\circ$, respectively. In low regime of $TSRs$, a GF position from the trailing-edge less than $4\% c$ can improve the C_{p-ave} production, compared to a GF at trailing-edge (see Figure 5.23). If the GF is moved further than $4\% c$ from the trailing-edge, the C_{p-ave} generation starts to decrease, although

it is still higher than the bare VAWT. Moving the GF position towards the leading-edge will likely reduce or even remove the ability of the GF to improve the VAWT performance. Figure 5.24 shows that by mounting the GF further away from the trailing-edge ($0\% c \leq s \leq 4\% c$), the GF can further decrease the negative moment production of VAWT, which can improve the power generation VAWT. After $s > 4\% c$, this ability starts to be weakened, and optimum moment production has shown to be lower than those whilst $s \leq 4\% c$. Therefore, the C_{p-ave} generation for a GF position $> 4\% c$ is lower than that for a GF position less than $4\% c$.

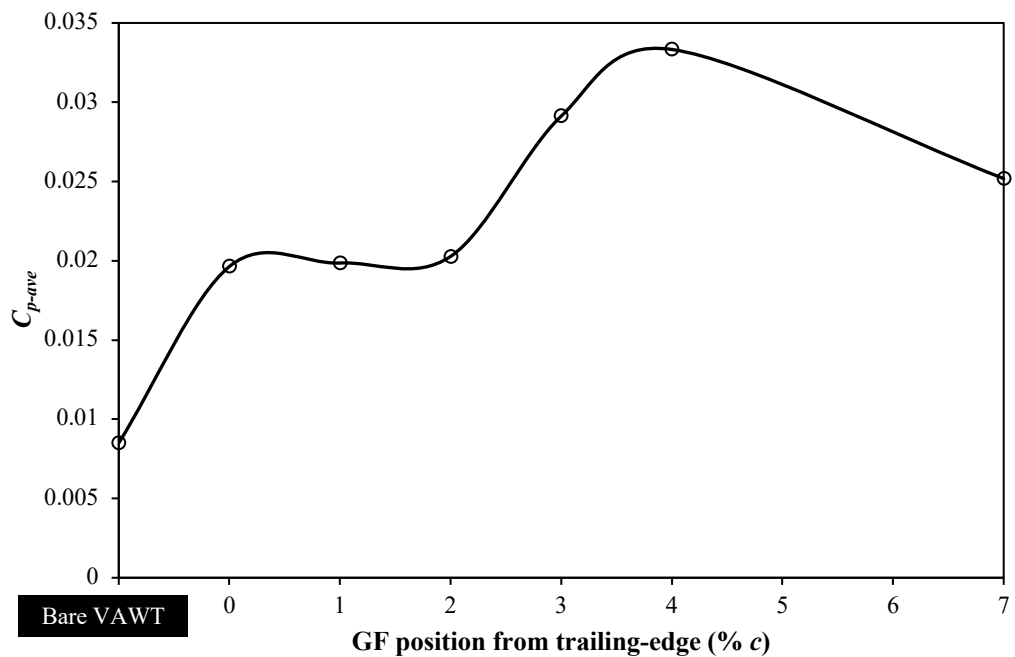


Figure 5.23 C_{p-ave} comparison for a VAWT with and without GF in various GF positions from the trailing-edge ($H = 3\% c$ and $\theta_{GF} = 90^\circ$) for $TSR = 1.44$.

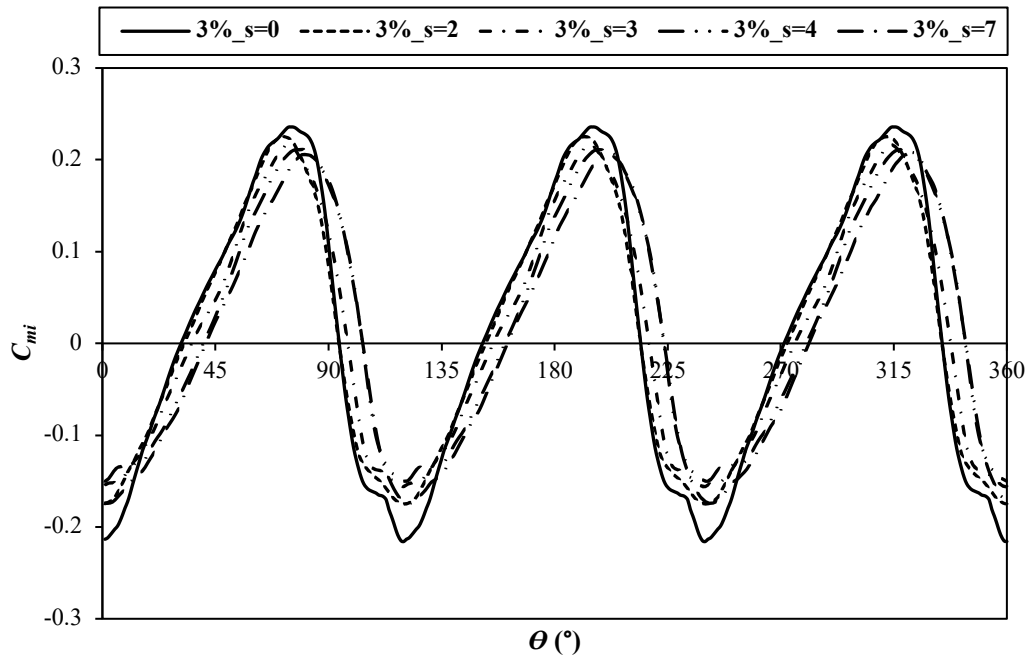


Figure 5.24 C_{mi} comparison of VAWT with GF for various GF positions ($TSR = 1.44$).

Meanwhile, in medium and high regimes of $TSRs$, changing the GF position further away from the trailing-edge does not positively influence the improvement of C_{p-ave} of bare VAWT (see Figure 5.25). The C_{p-ave} continuously decreases compared to the C_{p-ave} of VAWT with GF at the trailing-edge. The C_{mi} distribution in $TSR = 2.64$, as shown in Figure 5.26, suggests a significant drop of optimum C_{mi} when the GF position is shifted from the trailing-edge (and thus a loss in produced power). The C_{mi} distribution also shows the same behaviours mentioned above for all tested GF positions. Furthermore, the GF still maintains its ability to remove negative moments, which can improve the VAWT performance. Nevertheless, as the GF moves upstream towards the leading-edge, the C_{mi} minimum value drops to a lower value. This is probably due the fact that changing the GF position further away from the trailing-edge ($s = 4\% c$) generates more vortices both upstream and downstream of the flap (see Figure 5.27 (a)). This is supported by the gauge pressure contours which indicate that moving the GF position towards the leading-edge of the blade can introduce a lower pressure region upstream and downstream of the GF (e.g., see green shaded colour in the front of and behind the GF in Figure 5.27 (b)), triggering the formation of more vortices. Accordingly, the C_{m-ave} production of the VAWT with GF at $s = 4\% c$ is lower than that of the VAWT with GF at the trailing-edge. Therefore, placing the GF further away from the trailing-

edge only reduces the C_{p-ave} value of the VAWT with GF, although the C_{p-ave} of a VAWT with GF is still better than the bare VAWT until $s = 7\% c$.

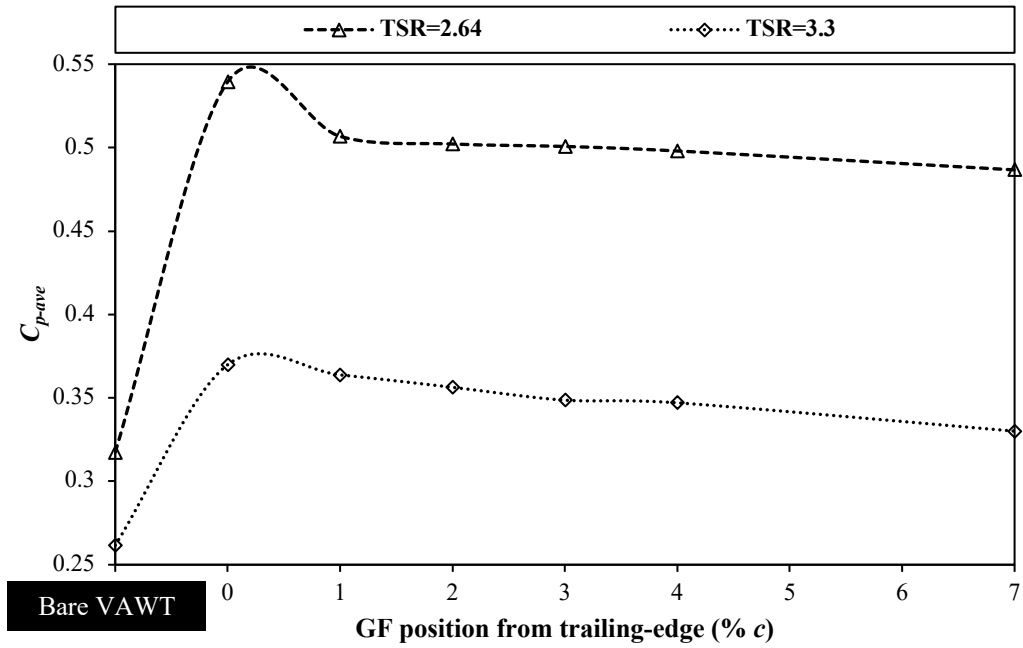


Figure 5.25 C_{p-ave} comparison for a VAWT with and without GF in various GF positions from trailing-edge for $TSR = 2.64$ and $TSR = 3.3$ (GF height and mounting angle are fixed at $3\% c$ and 90° , respectively).

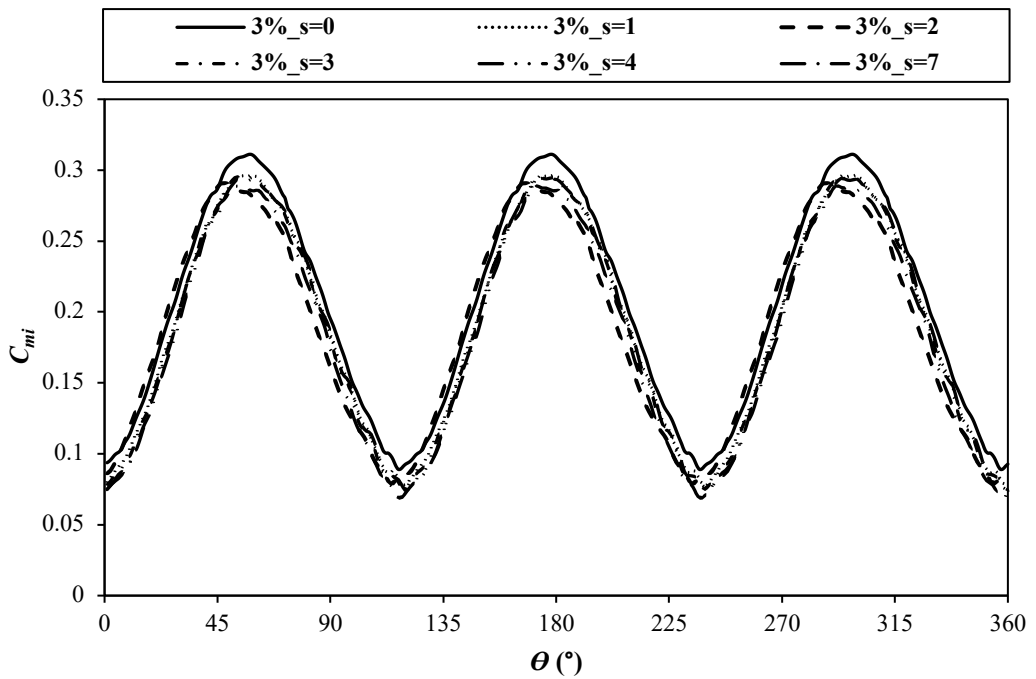
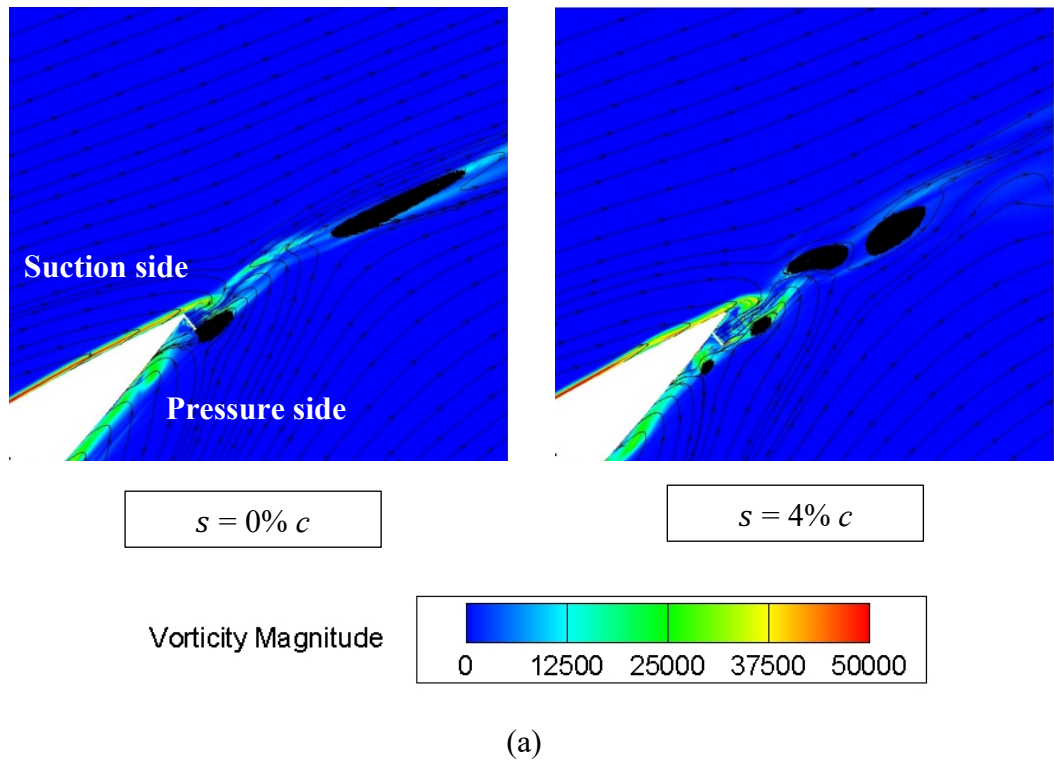
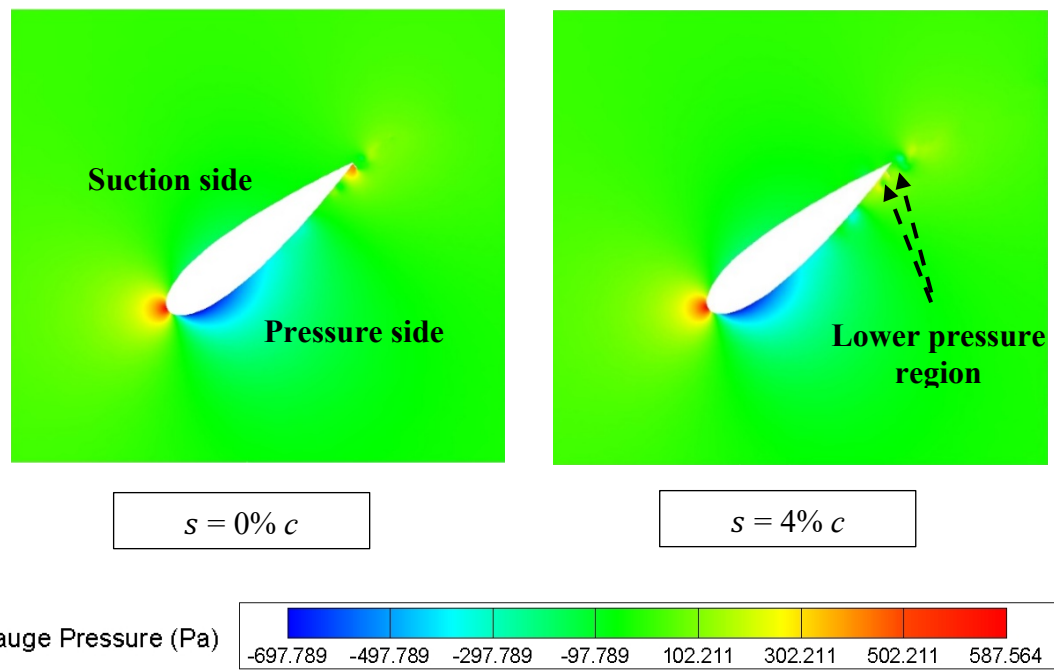


Figure 5.26 C_{mi} comparison of a VAWT with GF in various GF positions ($TSR = 2.64$).



(a)



(b)

Figure 5.27 Comparison of (a) streamlines coloured by z -vorticity contours (black regions show the vortical structures of the flow) and (b) contours of gauge pressure in various GF positions from the trailing edge ($TSR = 2.64$, $\theta = 45^\circ$).

The observed difference in the GF position's effect on the C_{p-ave} improvement between the low regime of $TSRs$, and medium and high regimes of $TSRs$ can be explained by the streamline distributions at $\theta = 45^\circ$ as illustrated in Figure 5.28. It demonstrates that at $TSR = 2.64$, the GF positioned from trailing-edge at $s = 4\% c$ can separate the second vortex, which is located further from the GF, from the newly formed vortices. These newly formed vortices can reduce flow turning over the leeward of the GF, leading to considerable momentum deficits in the wake region (as shown by wider x -velocity variation in Figure 5.29), and as a result, it reduces the lift force generation. On the other hand, in $TSR = 1.44$, these newly formed vortices do not appear and there are still two strong counter-rotating vortices downstream of the GF, which better reduce momentum deficits in the wake region (as shown by narrower x -velocity variation in Figure 5.29). Hence, the increment of lift force generation still can be achieved.

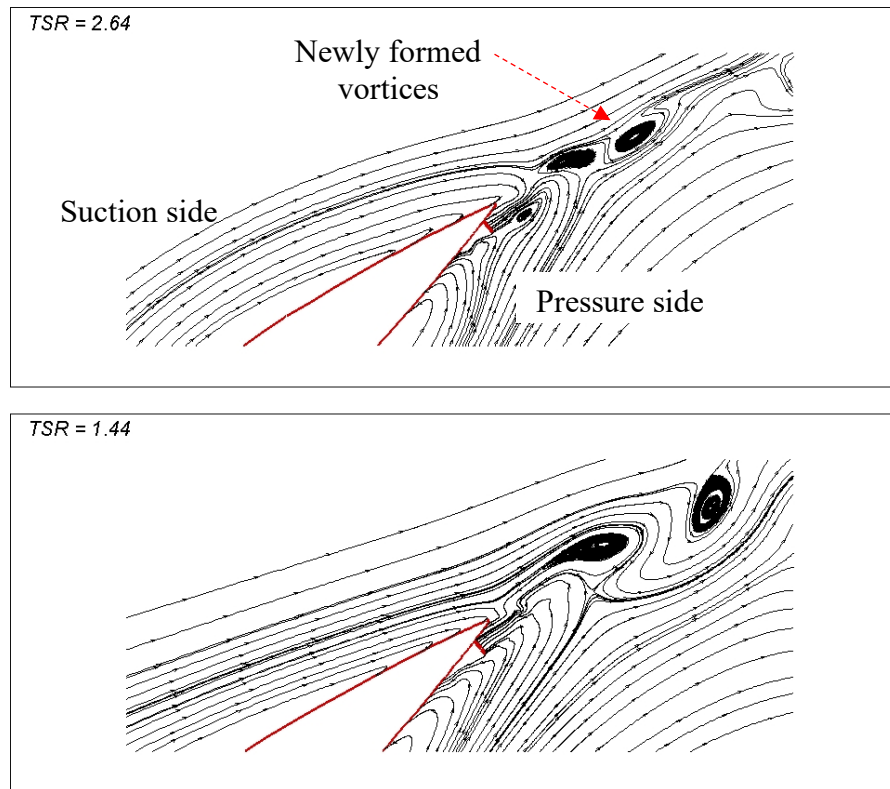


Figure 5.28 Comparison of streamlines distribution of VAWT with GF at $s = 4\%$ of c from trailing-edge in different $TSRs$ ($\theta = 45^\circ$).

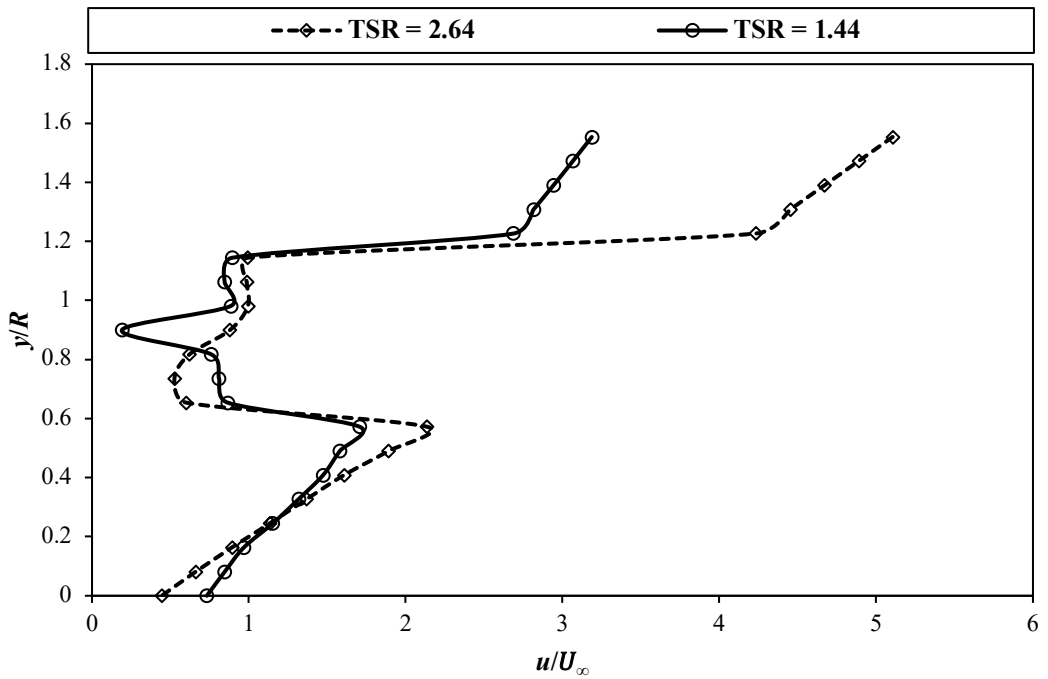
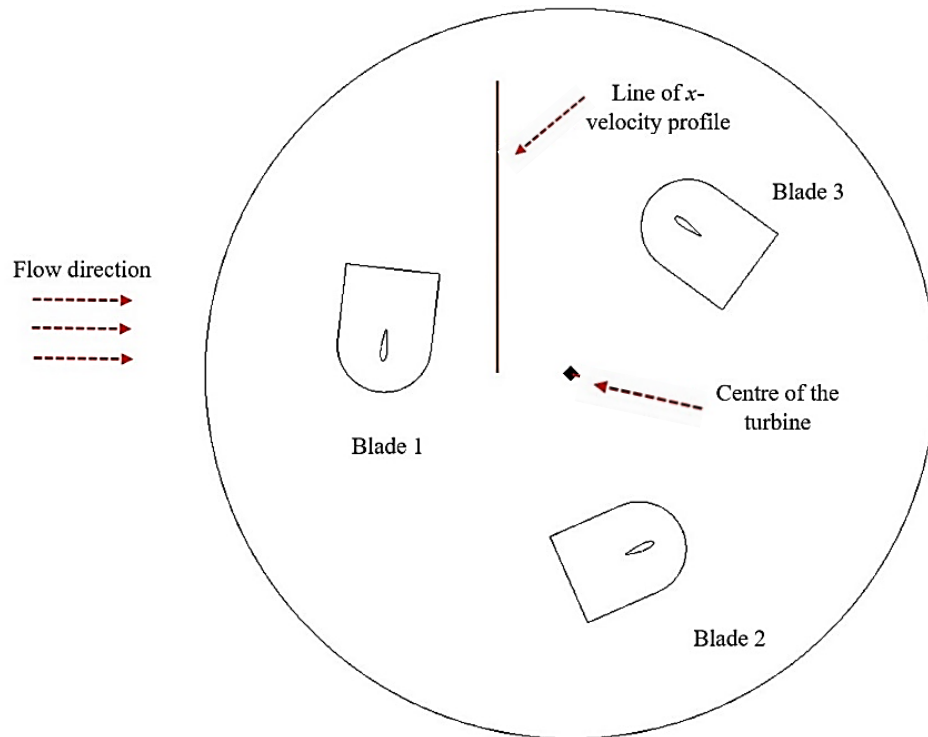


Figure 5.29 Comparison of x -velocity profile in the wake region of one selected blade (blade 1) of VAWT with GF mounted at $s = 4\% c$ from trailing-edge between $TSR = 2.64$ and $TSR = 1.44$ ($\theta = 45^\circ$).

5.4.5 Effect of GF shape modification

5.4.5.1 Effect of the wedged shape

Mohammadi, Doosttalab and Doosttalab (2012) found that changing the original GF shape to be wedged and curved could produce better lift improvement of a single stationary aerofoil that has been used for HAWT application (see Figure 5.2). The wedged and curved GFs can generate better optimum lift to drag ratio compared to that of the original GF by around 3% and 1.7%, respectively, due to the modified GF shape removing the separation bubble upstream at the trailing-edge of the GF that often occurs in an aerofoil with original GF shape (Mohammadi, Doosttalab and Doosttalab, 2012). Hence, the drag production decreases, resulting in an improved lift to drag ratio. Nevertheless, these modifications are not yet applied to rotating multiple blades such as in a VAWT. Therefore, it is worthwhile to investigate these modifications on a VAWT configuration.

In this study, both the wedged and curved GF types are mounted to the blades of a three-straight-bladed VAWT. The simulation is applied to a 2D VAWT configuration. This study evaluates the effect of the GF shape modifications from original (rectangular) to wedge and curve based on the performance improvement of VAWT in all three *TSR* regimes. The original GF is the optimum GF geometry at medium and high regimes of *TSRs* with $H = 3\% c$, $\theta_{GF} = 90^\circ$ and $s = 0\% c$ from the trailing-edge, resulting from previous optimisation studies (see Section 5.3). The wedged GF is varied by changing the L_w/H value, depicting the ratio between the length (L_w) and height of the wedge (see Figure 5.2). Note that the height of the GF will be kept the same ($H = 3\% c$). L_w/H ratios of 1, 2 and 3 are studied and compared to the original GF.

Figure 5.30 depicts the effect of L_w/H variation on the C_{p-ave} of VAWT in three different *TSR* regimes. As the L_w/H ratio increases, the VAWT C_{p-ave} generation rises in low and medium regimes of *TSRs*, whilst the L_w/H ratio increment has shown an adverse effect on the VAWT C_{p-ave} generation in high regime of *TSRs*. Based on the moment coefficient distribution shown in Figure 5.31, as the L_w/H increases, the value of C_{mi} increases to the higher value in $TSR = 1.44$ and $TSR = 2.64$, resulting in higher C_{p-ave} . On the other hand, the value of C_{mi} decreases as the L_w/H increases in $TSR = 3.3$ (see Figure 5.32), leading to lower VAWT C_{p-ave} . In addition, the significant drop of C_{mi} in low and medium regimes of *TSRs* happens at higher azimuthal degree positions as L_w/H increases (for example, in low regime of *TSRs*, the significant drop of C_{mi} value is at θ around 82° for $L_w/H = 3$, whilst for $L_w/H = 1$, the C_{mi} experiences a significant drop at about $\theta = 85^\circ$). It indicates that as the L_w/H increase, the VAWT primary stall can be delayed by

improving the VAWT lift generation and delaying the first drop of C_{li} in low and medium regimes of $TSRs$ as predicted in Figure 5.33 (a). However, the significant drop of C_{mi} in high regime of $TSRs$ appears earlier as L_w/H increases (for $L_w/H=1$, the significant drop of C_{mi} starts at $\theta = 55^\circ$ whilst it starts at $\theta = 53^\circ$ for $L_w/H = 3$), showing that the rise of L_w/H in this TSR regime will trigger earlier primary stall and lead to lower lift generation of VAWT (see Figure 5.33 (b)).

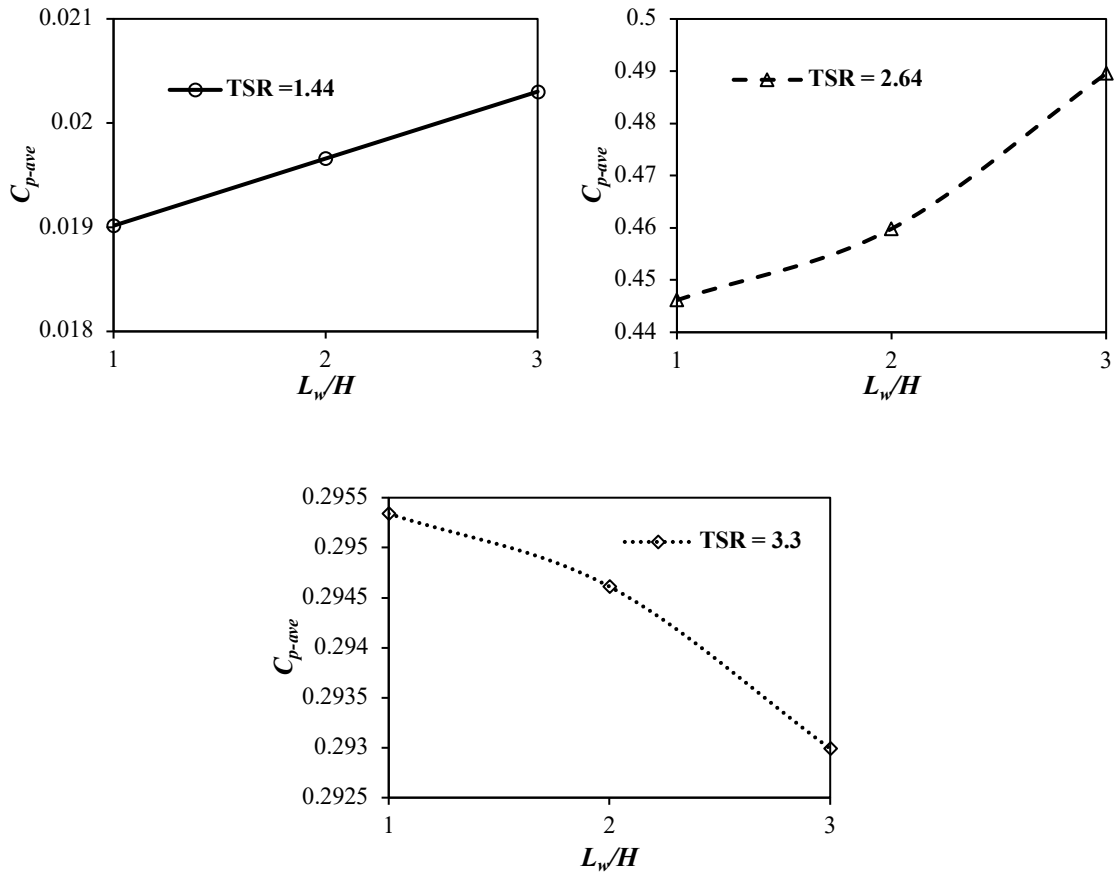
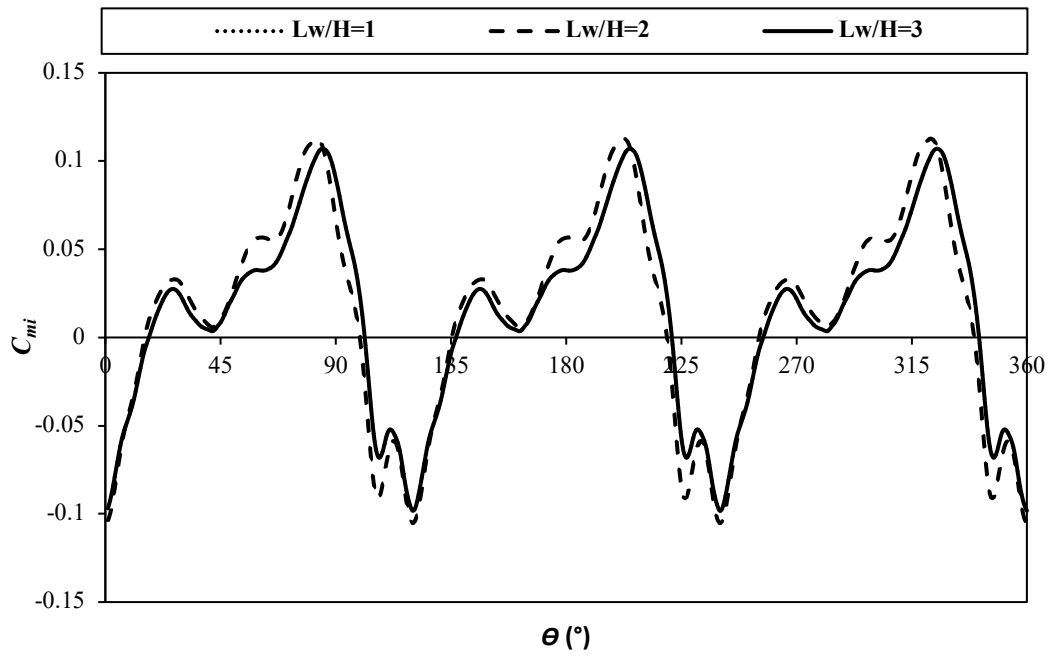
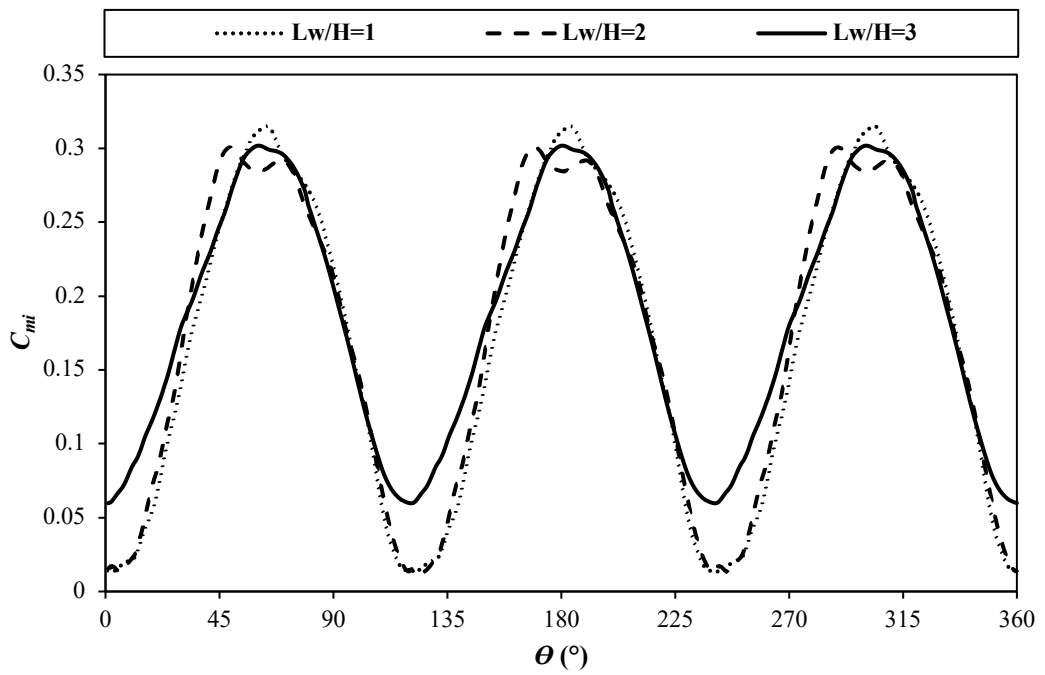


Figure 5.30 Comparison of the effect of L_w/H to the C_{p-ave} of VAWT in different regimes of $TSRs$.



(a)



(b)

Figure 5.31 Comparison of the effect of L_w/H on the C_{mi} in (a) $TSR = 1.44$ (low TSR) and (b) $TSR = 2.64$ (medium TSR).

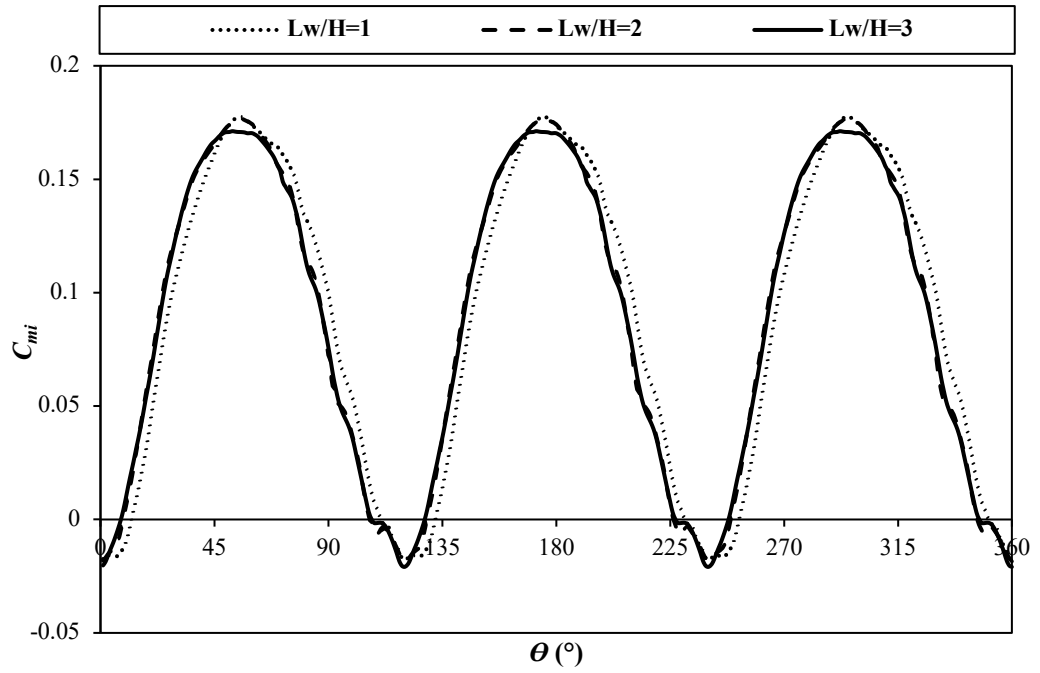
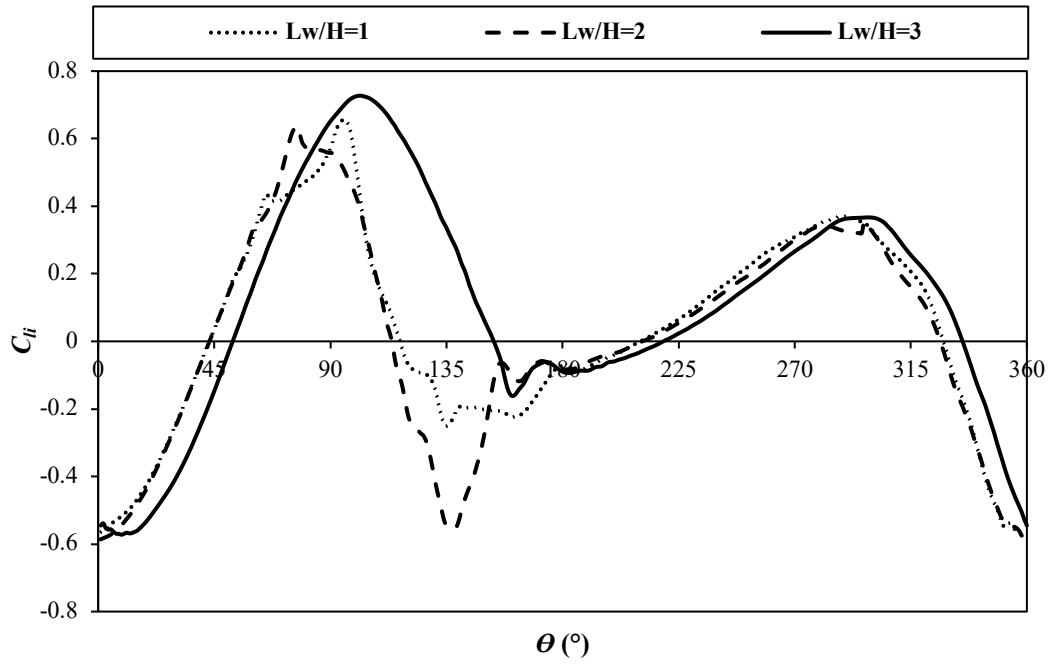


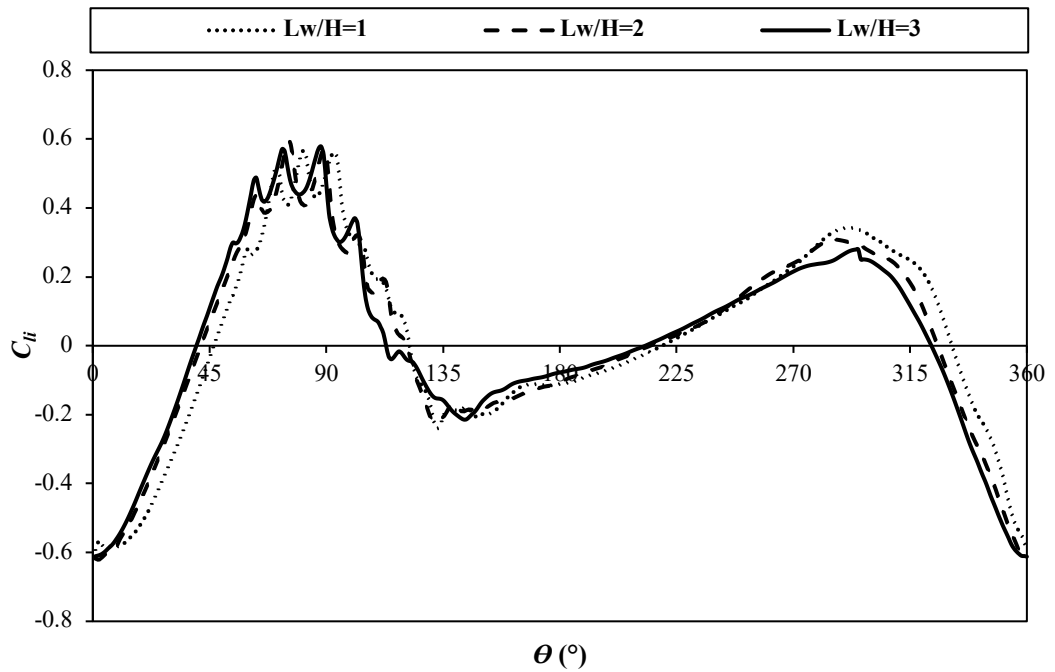
Figure 5.32 Comparison of the effect of L_w/H on the C_{mi} in $TSR = 3.3$ (high TSR).

Table 5.5 C_{p-ave} comparison between bare VAWT, VAWT with original GF and VAWT with wedged shaped GF in different regimes of $TSRs$ (**bold and italic fonts** in yellow highlights indicate the optimum C_{p-ave}).

Case	C_{p-ave}		
	$TSR = 1.44$	$TSR = 2.64$	$TSR = 3.3$
Bare VAWT	0.008502	0.317431	0.261656
Original GF $H=3\%$	0.019634	<i>0.53943</i>	<i>0.369864</i>
$L_w/H=1$	0.019015	0.446151	0.29534
$L_w/H=2$	0.019659	0.459811	0.294611
$L_w/H=3$	<i>0.020302</i>	0.489528	0.29299



(a)



(b)

Figure 5.33 Comparison of the effect of L_w/H on the C_{li} of one selected blade (Blade 1) of the VAWT in (a) $TSR = 2.64$ and (b) $TSR = 3.3$.

As for the overall performance, although a VAWT with wedged shaped GF can generate slightly better C_{p-ave} values than the bare VAWT (as seen in Table 5.5), it can only produce a better optimum improvement of C_{p-ave} value above that of the VAWT with

original GF in low regime of $TSRs$. In medium and high regimes of $TSRs$, changing the original GF shape to a wedge shape does not produce a better performance. It is in good agreement with the study of Mohammadi, Doosttalab and Doosttalab (2012), which stated that if the GF height is relatively high (e.g., larger than $1\% c$), the wedged GF could not generate a better enhancement of lift coefficient compared to original GF shape. In the present study, the adopted original GF shape already has quite a large height ($H = 3\% c$). Therefore, it is interesting to see if the GF shape modifications of this already optimised GF geometry can further improve the performance of VAWT.

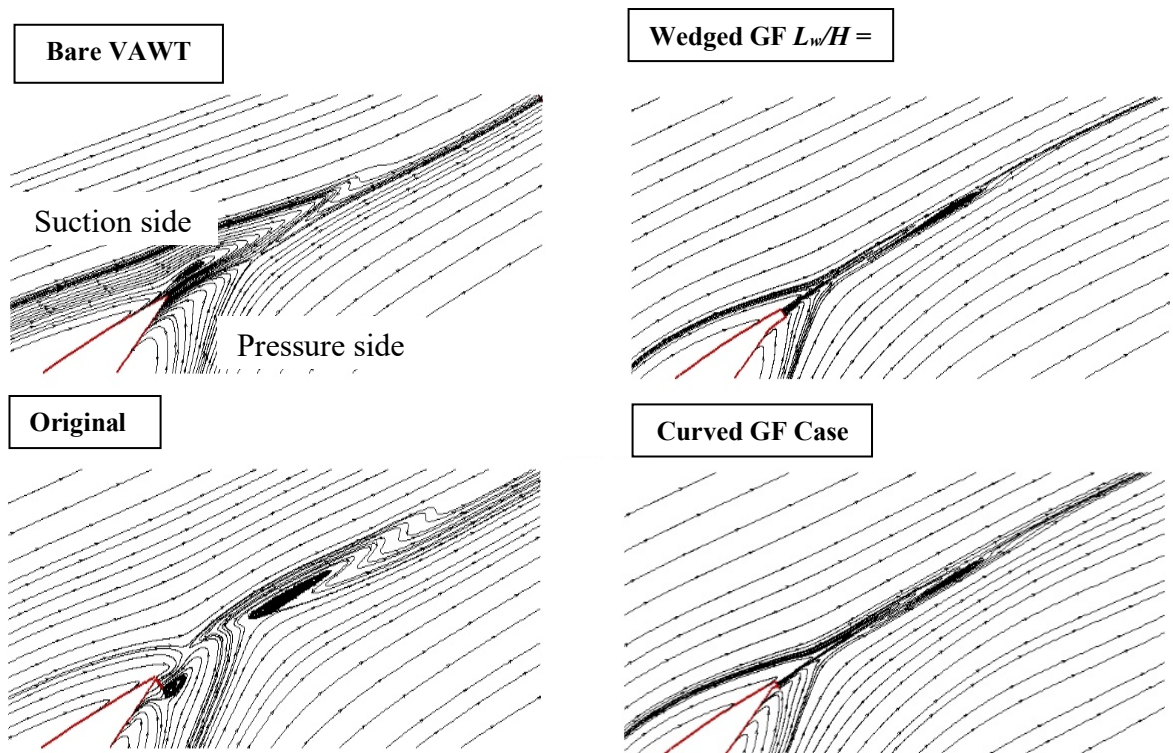


Figure 5.34 Comparison of streamlines between a bare VAWT and a VAWT with original GF, wedged and curved GFs in $TSR = 2.64$, $\theta = 45^\circ$, respectively.

Based on streamline distributions shown in Figure 5.34, it is noticeable that the wedged GF removes one of the counter-rotating vortices downstream of the GF, compared to the original GF. The VAWT with wedged GF generates similar vortices as the bare VAWT, but these vortex locations are further downstream of the VAWT blades. Consequently, a wedged GF loses its ability to decrease the wake momentum deficits resulting from counter-rotating vortices downstream of the flap. It is also noticeable that there is no vortex generation upstream of the flap, even for the original GF. Therefore, the ability of a wedged GF to reduce the separation bubble at the upstream of the flap

(similar to that demonstrated in a single stationary aerofoil case (Mohammadi, Doosttalab and Doosttalab, 2012)) is no longer applicable for rotating blades. Hence, as the dynamic stall for a VAWT with GF in medium and high regimes of $TSRs$ is relatively mild compared to that in low regime of $TSRs$, a wedged GF cannot further increase the performance of VAWT compared to the original GF at medium and high regimes of $TSRs$.

Nevertheless, different performance behaviours happen in low regime of $TSRs$. In this TSR regime, adding a wedged GF on the blades of VAWT can successfully improve the C_{p-ave} enhancement, compared to VAWT with the original GF shape if the L_w/H ratio is equal to or larger than 2 (see Table 5.5). The flow visualisation of the static pressure displayed in Figure 5.35 indicates that the wedged GF in this regime of $TSRs$ can significantly reduce the pressure on the pressure side whilst maintaining similar pressure on the suction side of the blades, compared to the original GF shape. Meanwhile, the wedged GF in medium regime of $TSRs$ decreases the pressure gradient (see Figure 5.36), as it seems to slightly raise the pressure on the suction side with only slightly pressure decrease on the pressure side near the trailing-edge. Therefore, the higher value in pressure gradient caused by a wedged GF in low regime of $TSRs$ can further improve the lift and moment generations and enhance the power generation of VAWT by 3% compared to VAWT with the original GF shape.

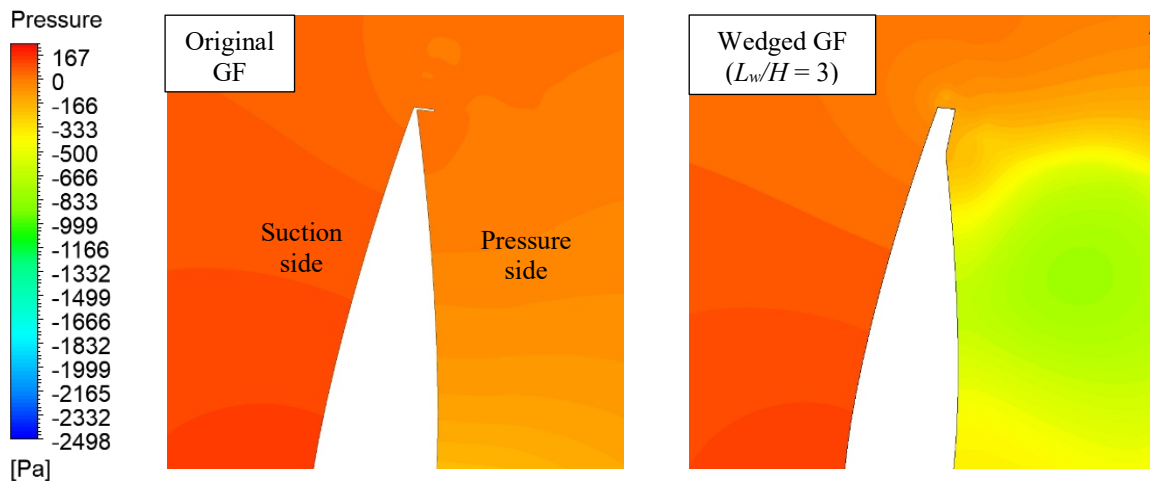


Figure 5.35 Comparison of contours of static pressure in $TSR = 1.44$ between VAWTs with original and wedged GFs ($\theta = 90^\circ$).

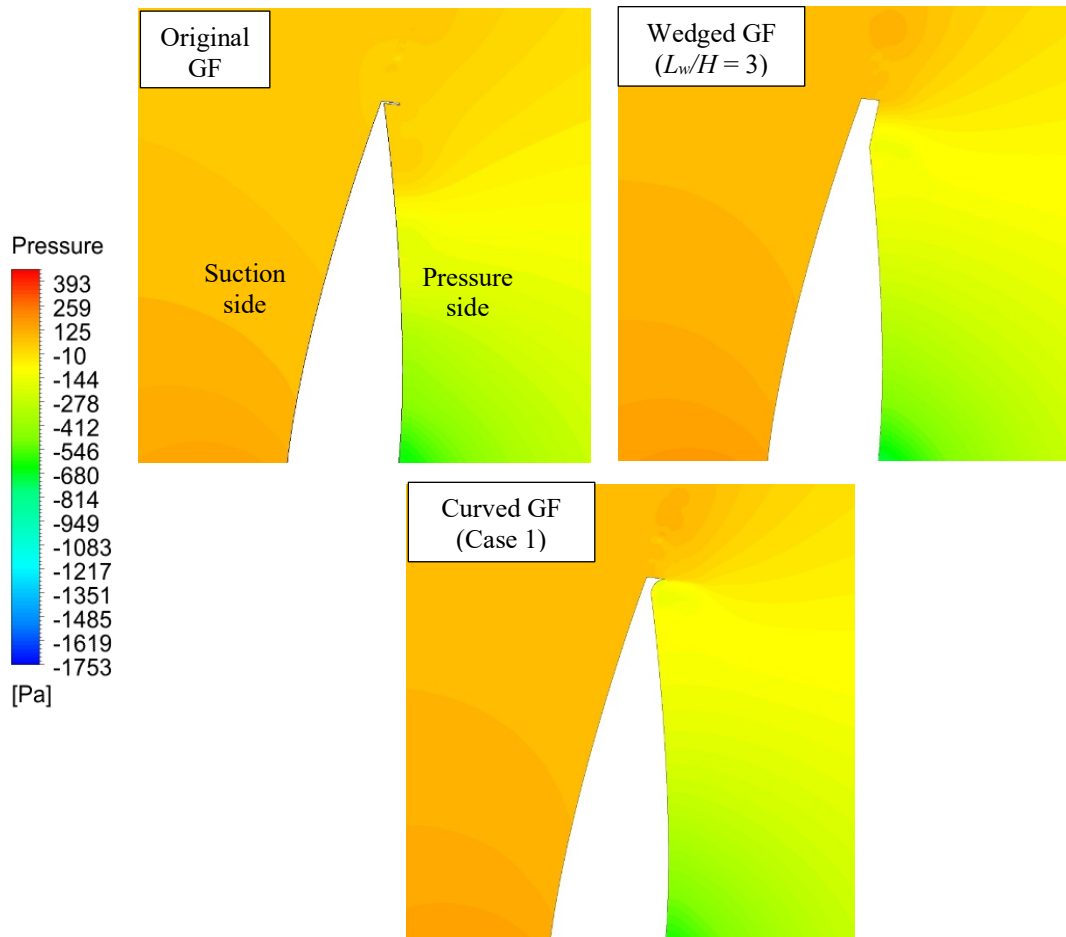


Figure 5.36 Comparison of contours of static pressure in $TSR = 2.64$ between VAWTs with original GF, wedged GF and curved GF ($\theta = 90^\circ$).

5.4.5.2 Effect of the curved shape

The effect of a curved GF on the performance of a VAWT is also investigated and compared to the original GF shape. The curved GF is a modification of the wedged GF by incorporating curves instead of straight lines, as shown in Figure 5.2. The original GF shape is a GF with optimum geometry in medium and high regimes of $TSRs$ ($H = 3\% c$, $\theta_{GF} = 90^\circ$ and $s = 0\% c$ from trailing-edge). Both the slope line ratio (L_{w1}/L_{w2}) and vertical line ratio (H_1/H_2) are applied to determine the curve, similar to that suggested by Mohammadi, Doosttalab and Doosttalab (2012) (referred to Case 1 thereafter). Then, the slope line and vertical line ratios are varied (see Tables 5.6 and 5.7, respectively, and illustration in Figure 5.37) to find out whether or not there is any effect of changing these values on the VAWT performance enhancement.

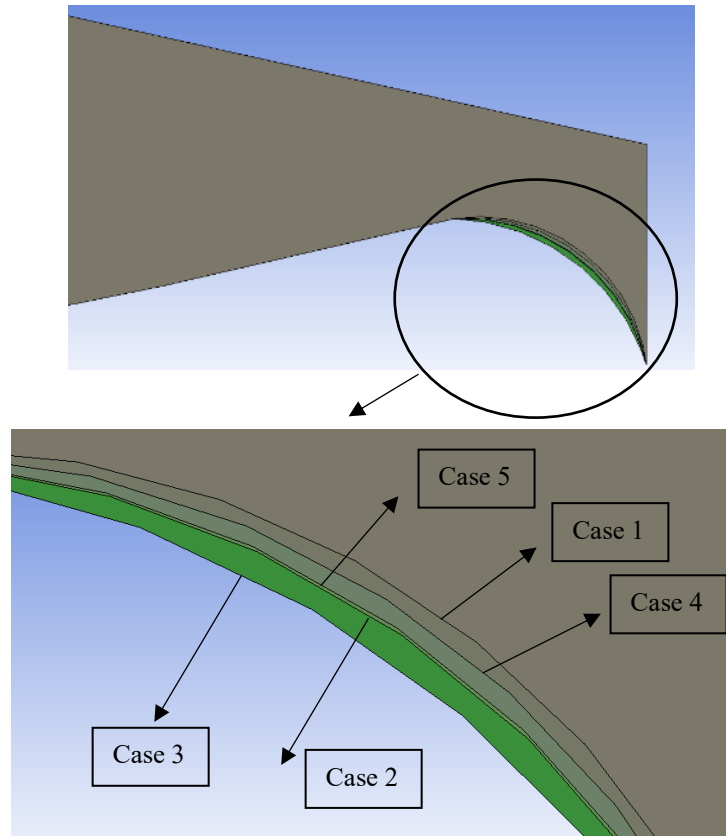


Figure 5.37 Illustration of curves of five curved GF cases.

Table 5.6 Variation of slope line ratio of curved GF.

Case	Slope Line Ratio (multiple by L_w value)		Vertical Line Ratio (multiply by H value)	
	L_{w1}	L_{w2}	H_1	H_2
1	0.605	0.395	0.465	0.535
2	0.5	0.5	0.465	0.535
3	0.395	0.605	0.465	0.535

Table 5.7 Variation of vertical line ratio of curved GF.

Case	Slope Line Ratio (multiple by L_w value)		Vertical Line Ratio (multiply by H value)	
	L_{w1}	L_{w2}	H_1	H_2
1	0.605	0.395	0.465	0.535
4	0.605	0.395	0.5	0.5
5	0.605	0.395	0.535	0.465

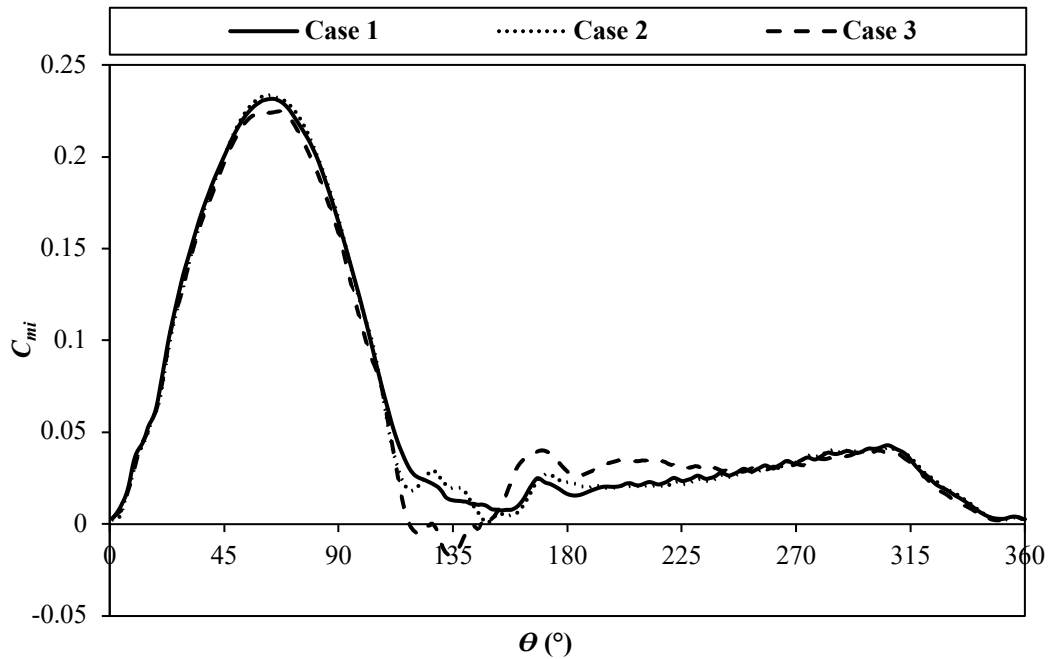
Table 5.8 shows that the C_{p-ave} value produced by the VAWT with curved GF of all pre-defined configurations is still higher than the bare VAWT in all TSR regimes. However, the curved GF cannot further enhance the VAWT C_{p-ave} compared with the original and wedged GFs in all TSR regimes. For instance, the modification of the original GF shape to a wedged GF reduces the pressure gradient, which decreases the C_{p-ave} improvement of VAWT in $TSR = 2.64$. This pressure gradient decrease is slightly worsened in the case of curved GF, as shown in Figure 5.36. The pressure decrease at the pressure side are quite similar with wedged GF. However, the pressure increase is slightly higher at the suction side of the blades. Moreover, although a curved GF still can introduce a similar pattern of vortices downstream of the VAWT as can the wedged GF, the location of these vortices moves further downstream than with the wedged GF (see Figure 5.34). As a result, these vortices have less effect on the change in the wake flow downstream of the VAWT blades. Therefore, the lift enhancement reduces, leading to the slight power improvement of the VAWT.

Table 5.8 C_{p-ave} comparison between bare VAWT and VAWT with original GF, wedged GF and curved GF in various slope and/or vertical line ratios in different TSR regimes (**bold and italic fonts** in yellow highlights indicate the optimum C_{p-ave}).

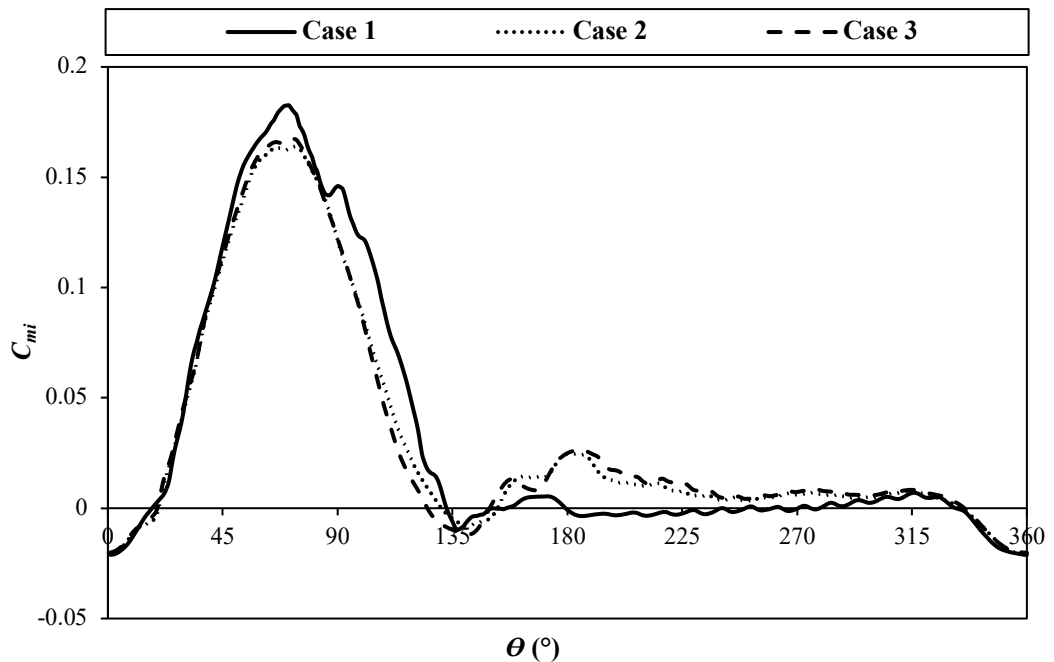
Case	C_{p-ave}		
	$TSR = 1.44$	$TSR = 2.64$	$TSR = 3.3$
Bare VAWT	0.008502	0.317431	0.261656
GF $H=3\%$	0.019634	<i>0.539430</i>	<i>0.369864</i>
Wedged GF $L_w/H=3$	<i>0.020302</i>	0.489528	0.292990
1	0.010400	0.487365	0.275683
2	0.010350	0.484461	0.270924
3	0.009351	0.474845	0.273705
4	0.010259	0.485884	0.272123
5	0.008920	0.359286	0.264291

Regarding the effect of the changes in slope line and vertical line ratios, the Table 5.8 data shows that the curved GF with both original slope line ratio and vertical line ratio (i.e., Case 1) can improve the VAWT performance by producing the highest C_{p-ave} value, compared to other curved GF geometries. In changing the slope line ratio, Case 3 has produced the lowest C_{p-ave} value compared to Cases 1 and 2 except at high regime of $TSRs$. The C_{mi} distribution of one selected blade (blade 1) in Figure 5.38 (a) demonstrates that at $TSR = 2.64$, Case 3 generates the lowest minimum moment, compared to other

cases. It also experiences negative moments after the stall whilst the other two cases do not experience the same downfall. Despite that Case 3 produces higher moments after the downfall (at $\theta = 150^\circ$ - 240°). The initial poor performance of Case 3 with the lowest optimum C_{mi} compared to other cases outweighs this great benefit.



(a)



(b)

Figure 5.38 C_{mi} comparison of blade 1 of the VAWT with curved GF in various slope line ratios for (a) $TSR = 2.64$ and (b) $TSR = 3.3$.

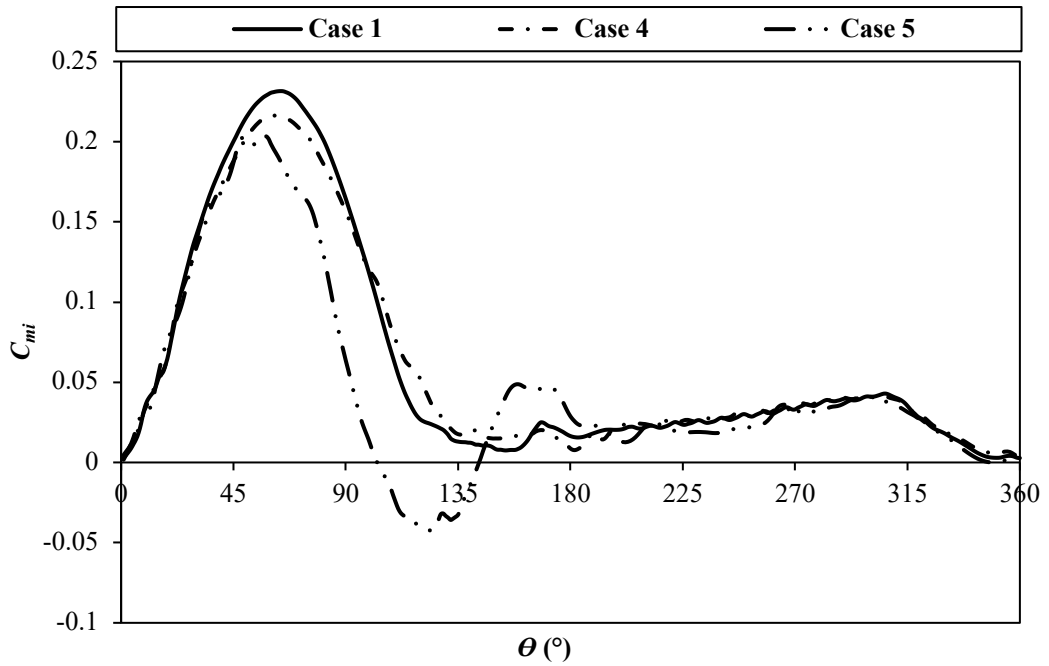


Figure 5.39 C_{mi} comparison of blade 1 of VAWT with curved GF in various vertical line ratios for $TSR = 2.64$.

On the contrary, the predicted optimum C_{mi} of Case 3 in $TSR = 3.3$ outperforms Case 2 but is still lower than Case 1. Furthermore, Case 3 can create the larger moment after the downfall (at azimuthal after 165°) compared to Cases 1 & 2 (see Figure 5.38 (b)). Hence, Case 3 can produce a higher C_{p-ave} value than Case 2 in high regime of $TSRs$. When changing the vertical line, Case 5, which has the lowest H_1/H_2 ratio, generates the lowest C_{p-ave} value compared to other cases (e.g., Cases 1 and 4) in all TSR regimes. For example, the C_{mi} distribution of blade 1 in $TSR = 2.64$ shows that Case 5 encounters an earlier downfall of moment production and has the lowest minimum C_{mi} compared to Cases 1 and 4. Case 5 also falls into negative moment generation, whilst Cases 1 and 4 do not have negative moment generation (see Figure 5.39). It indicates that Case 5 experiences the earliest and strongest stall, which leads to the lowest C_{p-ave} generation.

5.5. Chapter Summary and Further Work

The effect of the GF and its geometric modification and optimisation for the VAWT performance enhancement in all TSR regimes have been studied by hybrid RANS-LES CFD simulations subjected to the chosen ranges of values of studied parameters. GF geometry optimisation needs to be done for a practical VAWT configuration, particularly rotating multiple blades, rather than for a single stationary aerofoil. This study

finds that the VAWT equipped with GF will have an optimum height of $H = 3\% c$, compared to a single stationary aerofoil with GF, which usually has an optimum height of $H = 2\% c$. It is probably due to the rotational effects hindering the vortex generation upstream of the flap for a VAWT with GF (see Figure 5.34).

Overall, a VAWT equipped with a GF can improve the performance compared to a bare VAWT in all TSR regimes. It confirms that a GF can be applied as a passive device to improve the performance of a VAWT for all $TSRs$ regimes. Nevertheless, the degree of the VAWT performance improvement caused by GF addition differs for each TSR regime. The GF has shown the most significant effect in low regime of $TSRs$ (e.g., the C_{p-ave} increment can be up to 233.19% compared to a bare VAWT). It also can improve the self-starting ability in this regime of $TSRs$ as the GF can decrease negative moment production of the VAWT and reduce the moment fluctuation, meaning that the GF can ease the dynamic stall in this TSR regime. Meanwhile, the level of VAWT performance improvement starts to decrease in medium regime of $TSRs$ (e.g., C_{p-ave} increases up to 69.94% in $TSR = 2.64$, compared to a bare VAWT) and in high $TSRs$, this rate is further reduced (e.g., C_{p-ave} increases up to 41.36% in $TSR = 3.3$, compared to the bare VAWT). It is possible because the range of AoA_Ds operation and beyond static stall AoA_Ds (AoA_Ds that are higher than stall $AoAs$ of the static aerofoil) acting on the blades becomes wider with the decrease of $TSRs$. Hence, the benefit of a VAWT with GF in increasing the maximum lift and reducing the dynamic stall of VAWT can be utilised more effectively in low regime of $TSRs$.

Regarding geometric optimisation, it is essential to evaluate in all TSR regimes. Whilst the GF has the same optimum height and mounting angle (i.e., $H = 3\% c$ and $\theta_{GF} = 90^\circ$) in all TSR regimes, there is still a difference in optimum position from the trailing-edge between low regime of $TSRs$ and medium and high regime of $TSRs$. In low regime of $TSRs$, the C_{p-ave} value reaches its optimum value whilst the GF has optimum height and mounting angle and is located at $s = 4\% c$. Meanwhile, moving the position of the GF towards the leading-edge of the blade reduces the C_{p-ave} generation in medium and high regimes of $TSRs$. Hence, the optimum position of the GF in medium and high regimes of $TSRs$ is at the trailing-edge of the blade (i.e., $s = 0\% c$). The flow visualisation shows that whilst changing the position of the GF in low regime of $TSRs$ can introduce stronger counter-rotating vortices downstream of the flap, this behaviour does not happen in the other two higher TSR regimes.

Furthermore, the modifications of the original GF shape into wedge and curve shapes generally do not further improve the performance of a VAWT equipped with the original GF for most *TSR* regimes. This is most likely because the height of the GF is already high, so the advantages of wedged and curved GFs to suppress the vortex generation upstream of the flap is no longer valid in the VAWT configuration whereas it does so for a single stationary aerofoil. The VAWT with original GF does not induce this type of vortex behaviour. Nonetheless, a VAWT with wedged or curved GFs can still generate a better C_{p-ave} value compared to the bare VAWT. It shows the importance of performing a design evaluation of a performance enhancement device of a VAWT in VAWT configuration by considering rotation effects and blade-to-blade interaction. Additionally, it also shows that as long as the other three parameters (i.e., height, mounting angle and position from trailing-edge) are already at their optimum values, modifying the shape of GF does not significantly affect the improvement rate C_{p-ave} of the VAWT.

In conclusion, to generate a relatively higher average performance enhancement in all *TSR* regimes, the optimal GF geometry will have a height of $3\% c$, a mounting angle of 90° and be positioned at the trailing-edge of the blade. A VAWT equipped with this GF geometry can produce an optimum C_{p-ave} enhancement in medium and high regimes of *TSRs* (i.e., 69.94% and 41.36%, respectively) and still retain significant C_{p-ave} improvement in low regime of *TSRs* (i.e., 130.94%).

After analysing the use of the GF as a passive flow control device to improve the performance of VAWT by controlling its dynamic stall, this study will evaluate the use of a straight plate deflector upstream of the VAWT as a flow augmentation device to enhance the performance of the VAWT by increasing the incoming wind speed and controlling the direction of the wind. These deflector studies are discussed in the following chapter.

Chapter 6: 2D CFD Simulation of Flow Augmentation Device for Performance Enhancement of Lift-Driven VAWT using Straight Upstream Deflector

As discussed in Chapter 2, Section 2.5.1, among flow augmentation devices, a SUD has superior effectiveness, as it can improve the performance of the VAWT whilst it operates in all *TSR* regimes. The SUD has also benefited from a simple design and is lightweight. Although the use of SUDs as performance enhancement devices for a VAWT has been investigated in previous studies (see Appendix B, Section B.1.5), there are several limitations in those studies that need to be addressed (see Chapter 2, Section 2.5.1).

Therefore, this chapter will address all those limitations identified in those previous studies (see Chapter 2, Section 2.5.1) by including the location effect and performing geometric optimisation of SUDs in all *TSR* regimes. Sections 6.1 and 6.2 discuss the model and how the location and SUD geometries change. This investigation evaluates a VAWT with SUD for three *TSR* regimes: low, medium and high, with each *TSR* regime represented by one *TSR* value (e.g., low *TSR* = 1.44, medium *TSR* = 2.64 (optimum *TSR*), and high *TSR* = 3.3). The investigation of SUDs starts with evaluating the effect of the SUD location upstream of a three-straight-bladed VAWT, which is the 2D model that has been validated in Chapter 4. Following this, this study also evaluates other geometric studies such as the deflector's width and inclination angle. All these investigations are performed in each *TSR* regime. Then, in this study the SUD's effect on the performance enhancement of a VAWT is analysed for each *TSR* regime based on C_{p-ave} value. As a result, the best SUD design in all *TSR* regimes can be achieved. Section 6.3 covers all these discussions of the results analysis. This chapter is closed with the chapter summary and further work in the following chapter.

6.1 VAWT with Straight Upstream Deflector

This study investigates the effect of a SUD as a VAWT performance enhancer by placing a straight plate deflector upstream of a 2D plane cutting through the middle of a three-straight-bladed VAWT model. All turbine geometric values are the same as in the bare VAWT model. This investigation adopts a baseline SUD geometry (see Table 6.1 and Figure 6.1, respectively) from a previous study of Kim and Gharib (2013) with the same range of Reynolds number investigated.

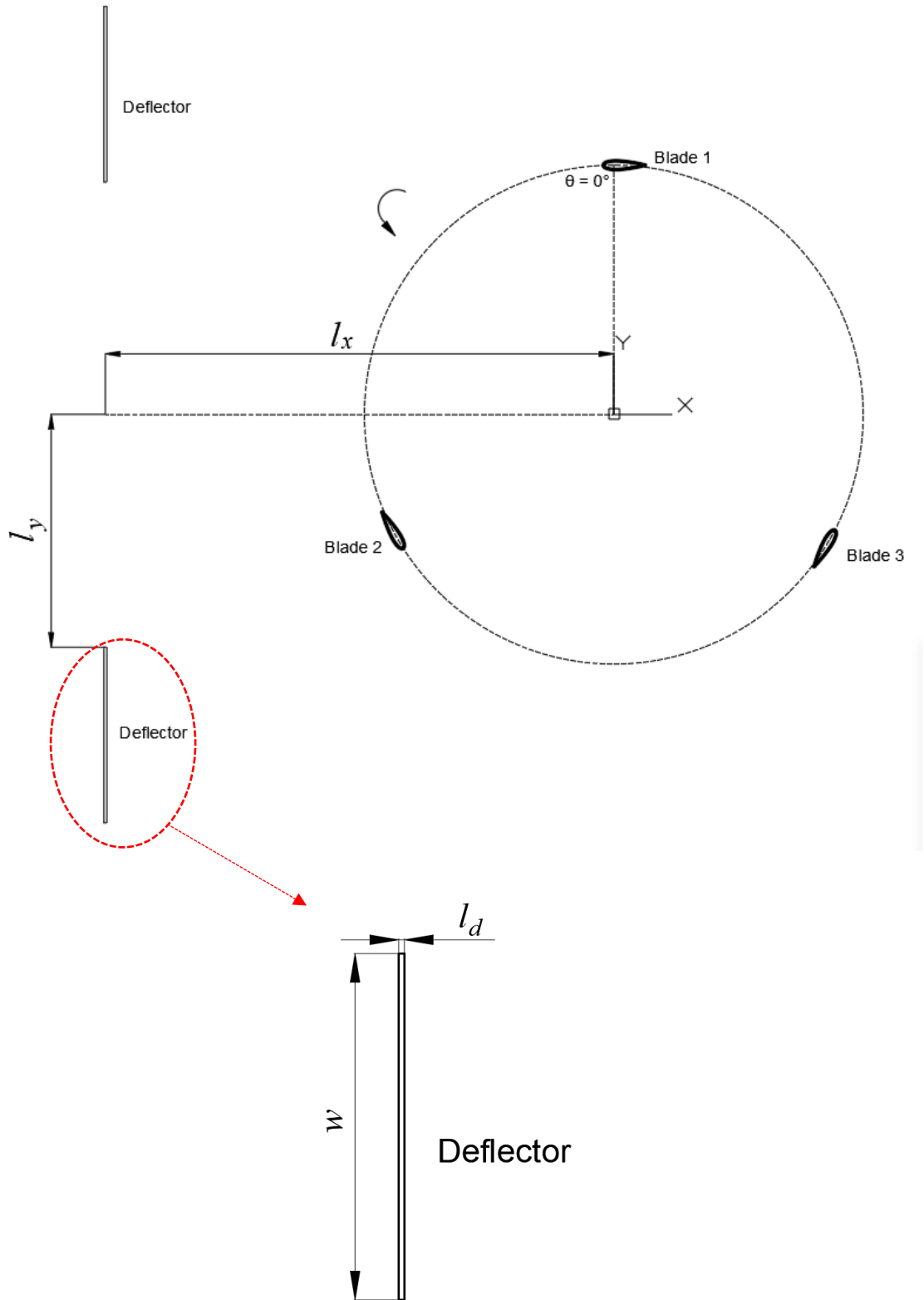


Figure 6.1 Detailed geometry of a VAWT with SUD, where l_x is a horizontal distance from the centre of the turbine (m), l_y is a vertical distance from the centre of the turbine (m), l_d is the thickness of the deflector (m) and w is the width of the deflector (m).

Table 6.1 Geometry specification of a base SUD.

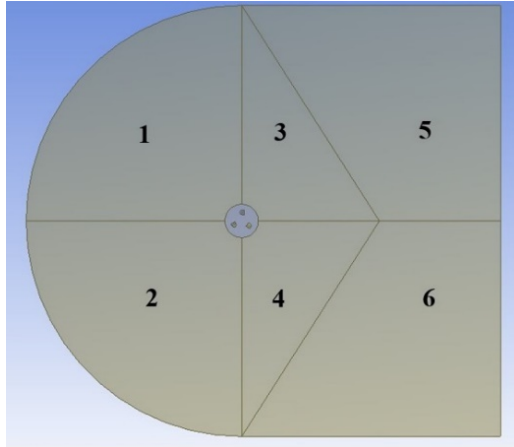
Parameter	Measurement	
l_x	$1.02 D_{rotor}$	1050 mm
l_y	$0.47 D_{rotor}$	480.25 mm
l_d	6 mm	6 mm
w	$0.34 D_{rotor}$	346.5 mm

For design optimisation, three parameters, namely location, width and inclination angle of the SUD, are considered. First, this study investigates the effect of four SUD locations upstream of the VAWT (i.e., upward, middle, downward, and “both upward and downward”) on the C_{p-ave} of the VAWT. After identifying the SUD location with the best performance, this study continues to evaluate the effects of the width and inclination angle of the SUD on the C_{p-ave} production of the VAWT. Noting that all these investigations are performed in all TSR regimes with $TSR = 1.44$ representing low $TSRs$ whilst medium and high $TSRs$ are represented by $TSR = 2.64$ and $TSR = 3.3$, respectively.

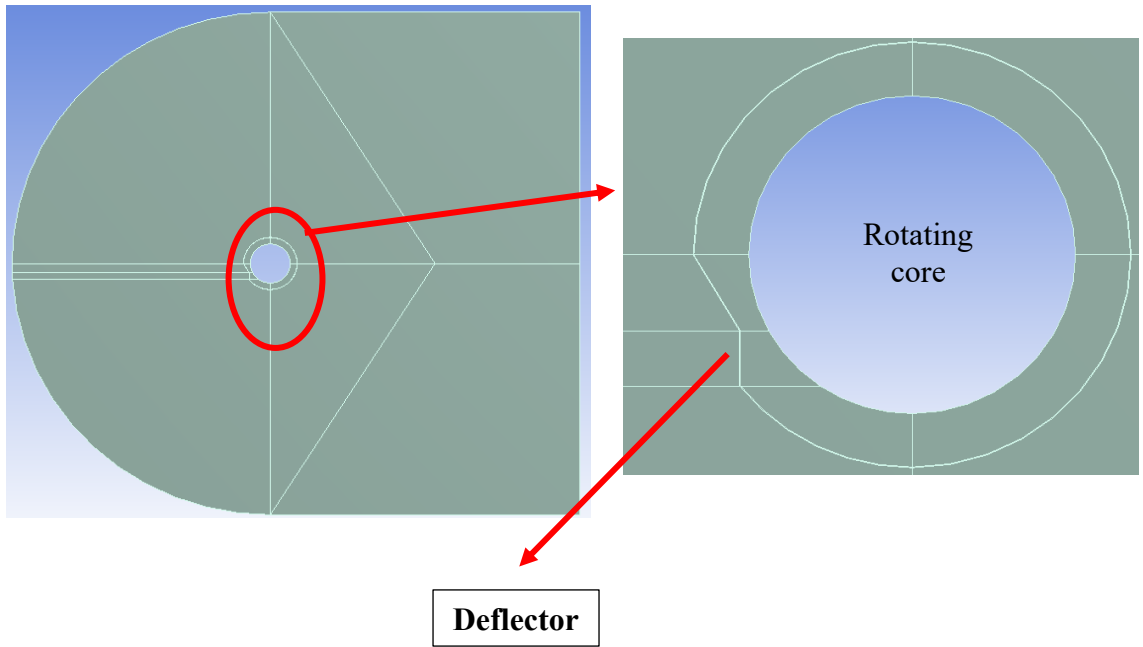
6.2 Model, Grid Generation and Numerical Setup

This 2D VAWT with SUD model implements the same models and numerical setup used in the 2D validation studies (see Chapter 4). Similar to the VAWT with GF, the C-grid is adopted in this study to generate a better accuracy than the O-grid for the SBES turbulence model (see Appendix E, Section E.1). Note that the grid in the rotating core, including near the blade wall, remains the same as the validated 2D VAWT model.

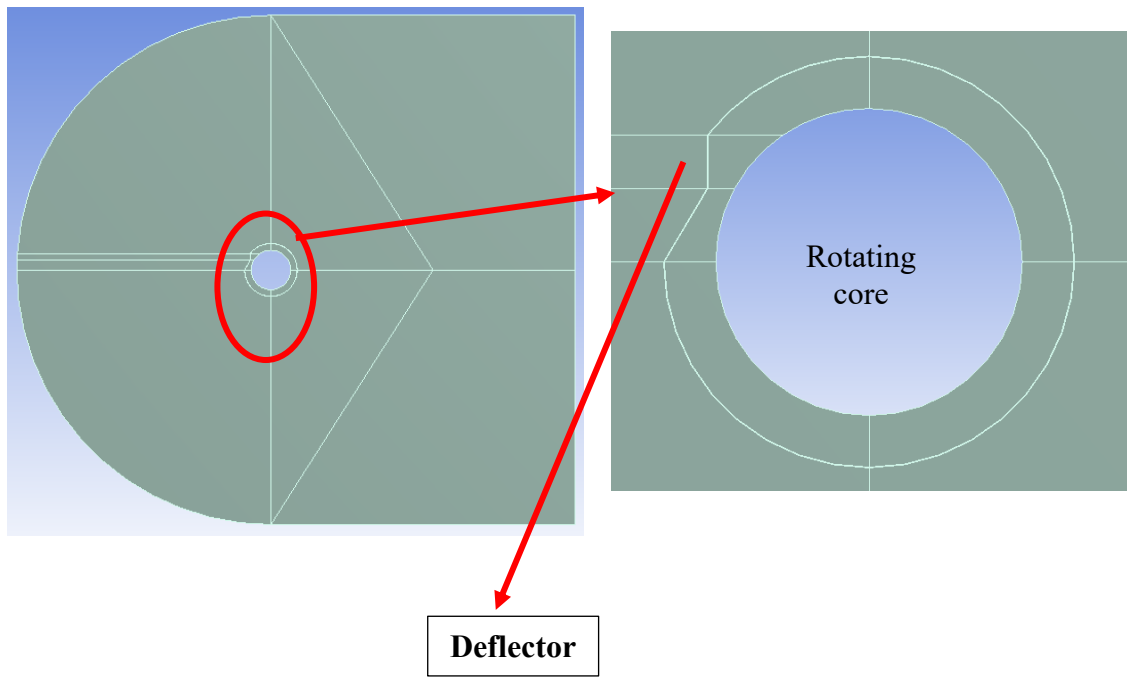
The SUD is located in the far-field sub-domain, surrounding the rotating core sub-domain. Hence, there is a slightly different approach to generating grids in this domain between the bare VAWT and the VAWT with SUD (see Figure 6.2). Structured grids are generated within the far-field sub-domain (see Figure 6.3 (a)). Figure 6.3 (b) shows the detailed grids around the deflector. Around the deflector, 50 elements are generated along with the thickness of the deflector. Along the width of the deflector, 200 elements are created for the base SUD. The number of elements increases with the increase of the width of the SUD (see Table 6.2). The elements are distributed along with the deflector's thickness and width by using finer elements to accommodate the near-wall y^+ criteria (e.g., $y^+ < 1$ for Transitional SST turbulence model).



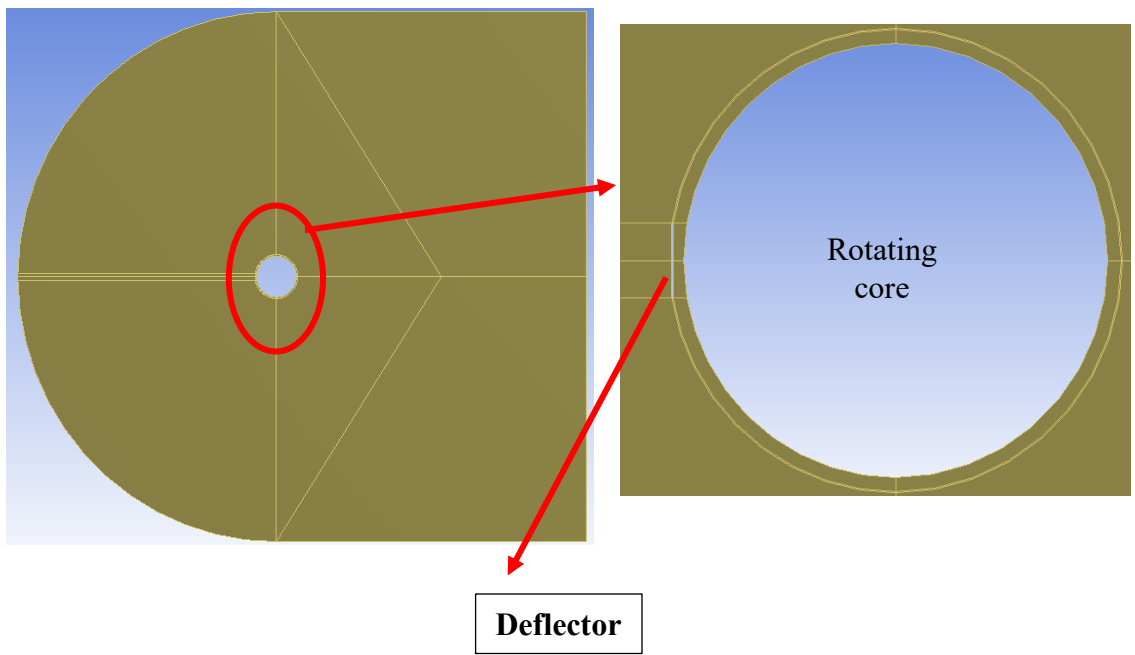
(a) Bare VAWT



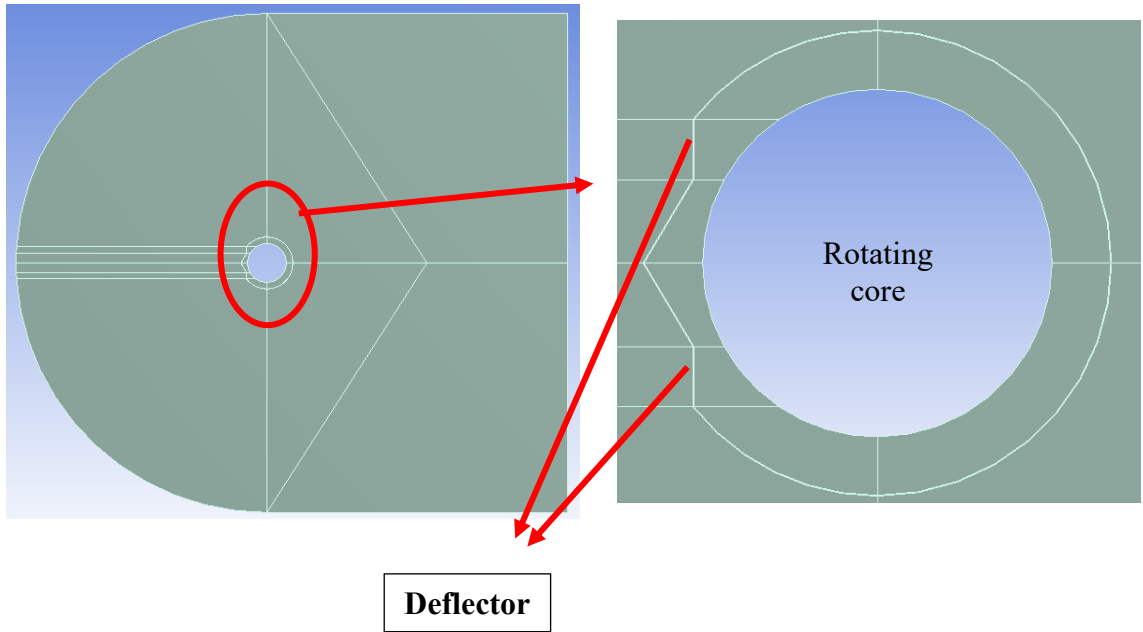
(b) VAWT with a downward SUD



(c) VAWT with an upward SUD



(d) VAWT with a middle SUD

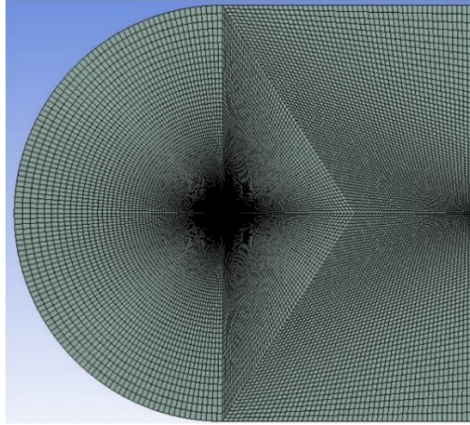


(e) VAWT with both upward and downward SUD

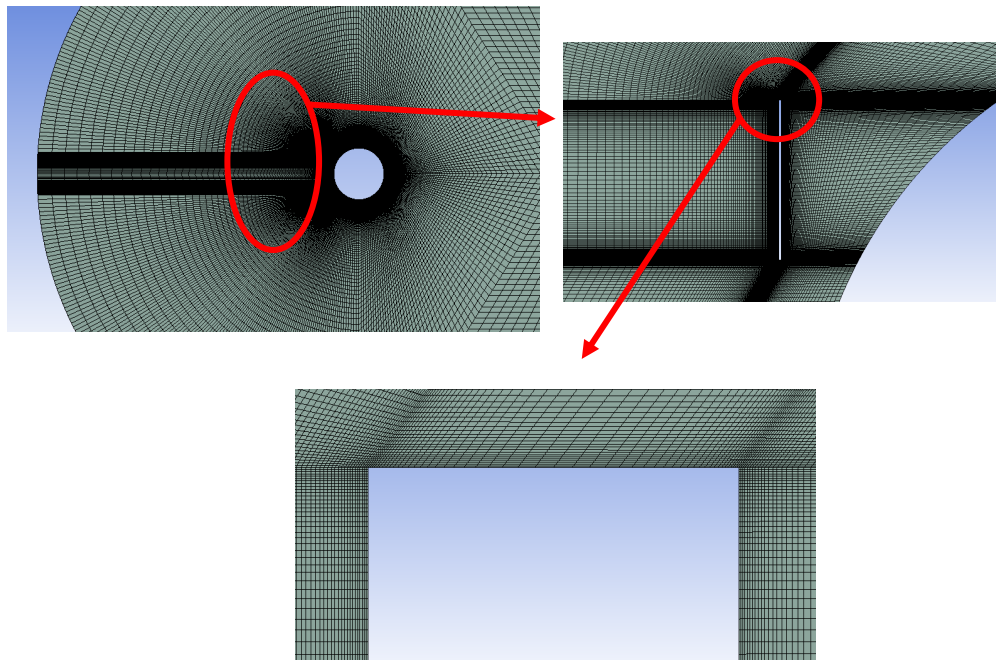
Figure 6.2 Comparison of the far-field sub-domain partition between bare VAWT and VAWT with SUD (four scenarios) (the drawing is not in scale).

Table 6.2 Number of grid points along the width of the SUD.

Cases	Number of Grid points along the Width of the SUD
w_0 (base geometry)	200
w_1 (25% of w_0 increment)	250
w_2 (50% of w_0 increment)	300
w_3 (75% of w_0 increment)	350



(a) Detailed grids in the far-field sub-domain of a bare VAWT



(b) Detailed grids in the near-wall region of SUD

Figure 6.3 Detailed grids within the far-field sub-domain.

6.3 Results comparison

6.3.1 Effect of the location of the upstream deflector

The effect of the SUD location on the performance of the VAWT is investigated considering four deflector locations upstream of the VAWT, i.e., upward, downward, middle and “both upward and downward” (as shown in Figure 6.4). Table 6.3 shows that all four SUD locations can improve the C_{p-ave} value compared to the bare VAWT in all TSR regimes. Moreover, locating the SUD upstream “both upward and downward” of the VAWT can achieve the best C_{p-ave} improvement in all TSR regimes. The downward positioned SUD generates the least C_{p-ave} improvement.

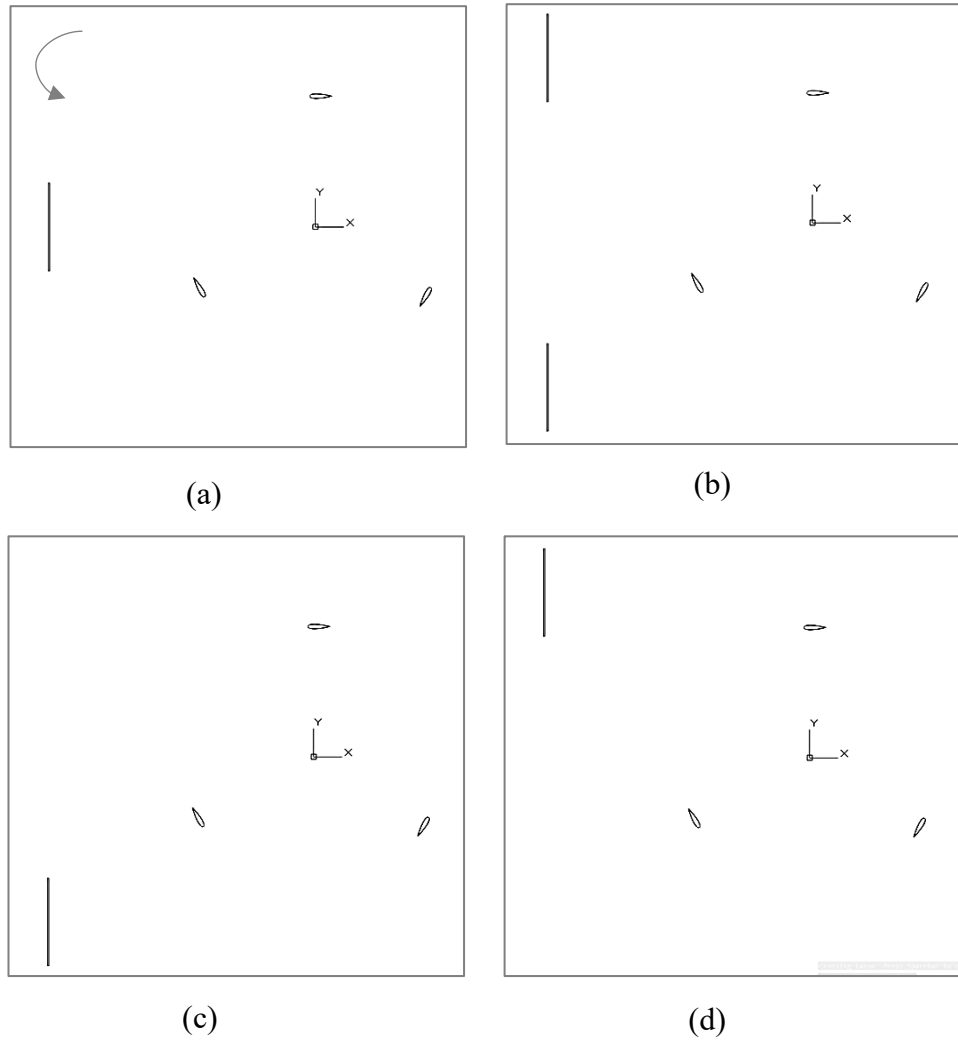


Figure 6.4 Sketches of four SUD locations (the deflector geometry is not in scale), (a) middle, (b) both upward and downward, (c) downward and (d) upward.

Table 6.3 Predicted C_{p-ave} values from four SUD locations compared to bare VAWT (**bold** and *italic fonts* in yellow highlights show the optimum cases).

Position	C_{p-ave}		
	<i>TSR = 1.44</i>	<i>TSR = 2.64</i>	<i>TSR = 3.3</i>
Bare VAWT	0.008502	0.317431	0.261656
Downward	0.008950	0.320839	0.271715
Middle	0.015753	0.364896	0.297980
Upward	0.018643	0.402920	0.386776
Both	<i>0.019274</i>	<i>0.484587</i>	<i>0.399071</i>

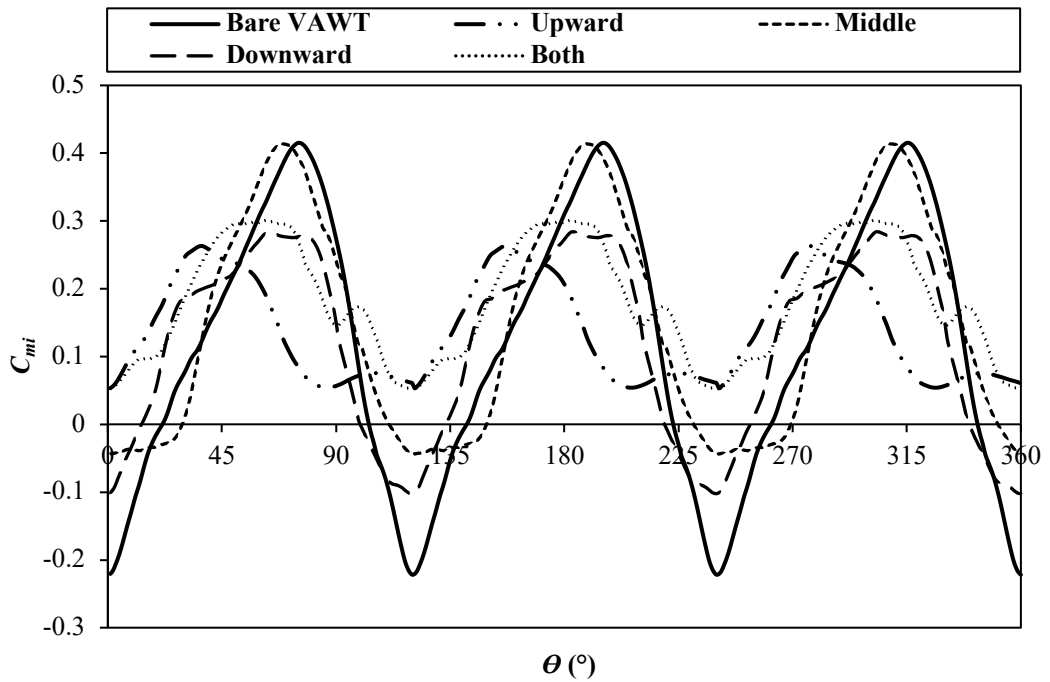
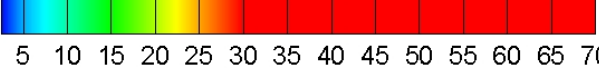


Figure 6.5 C_{mi} comparison (three blades) between the bare VAWT and the VAWT with SUD at four different locations ($TSR = 2.64$).

Figure 6.5 depicts the effect of the SUD location on the C_{mi} distribution of the VAWT in $TSR = 2.64$. It shows that only the upward and “both upward and downward” configurations can remove the negative moment production of the VAWT. Meanwhile, for the middle and downward configurations, the negative moment is still generated by the VAWT. It is also noticeable that all four configurations decrease the optimum moment coefficient of the VAWT. Nevertheless, it is noticeable that all four SUD locations investigated can improve the average value of the moment coefficient compared to the bare VAWT. For example, a VAWT with SUD of “both upward and downward” configuration can improve the C_{m-ave} of bare VAWT from 0.12024 to 0.18356 in $TSR = 2.64$. Hence, the VAWT with four SUD locations can produce better C_{p-ave} values (up to max 52.7% in $TSR = 2.64$ when applying “both upward and downward” SUD) compared to the bare VAWT.

Velocity magnitude (m/s)



5 10 15 20 25 30 35 40 45 50 55 60 65 70

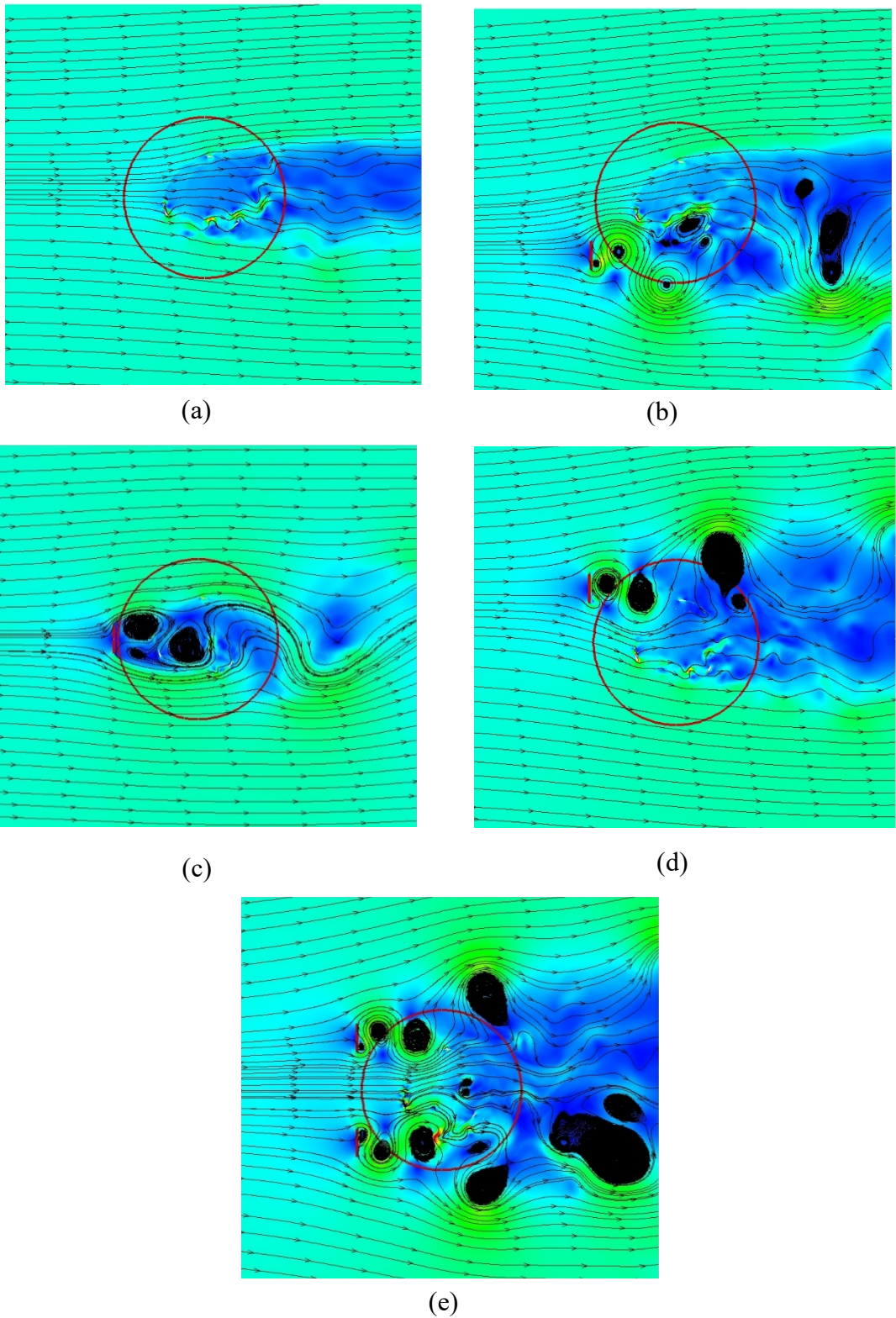


Figure 6.6 Comparison of streamline distributions coloured by velocity magnitude (m/s) of the flow around (a) bare VAWT and VAWT with SUD at (b) downward, (c) middle, (d) upward and (e) both upward and downward ($TSR = 2.64$, $\theta = 360^\circ$).

Further investigation of flow streamlines indicates that placing a SUD both upward and downward upstream of the VAWT can induce a larger vortex upstream of the VAWT compared to the other three configurations (i.e., upward, middle and downward arrangements) (see Figure 6.6). It leads to stronger wake flow, resulting in greater augmented wind speed and direction change downstream of the deflector where the VAWT is located. In the “both upward and downward” configuration, the VAWT blades can avoid the near-wake region of the deflector whilst they are rotating. Meanwhile, for the other three (upward, middle and downward) configurations, at least one blade will enter the near-wake region of the deflector whilst the blades are rotating. Therefore, the “both upward and downward” configuration can generate a higher power coefficient than the other three configurations. This finding is in good agreement with the previous study (Kim and Gharib, 2013) by placing a VAWT outside the near-wake region of the deflector, enabling the increased power from the VAWT. Moreover, the “both upward and downward” configuration is observed to be better in directing the incoming wind towards the VAWT than the upward, middle, and downward configurations (see Figure 6.6). Since the “both upward and downward” configuration introduces a nozzle-like effect upstream of the VAWTs, there is a decrease in the flow areas upstream of the VAWT due to a gap between two deflectors. Apart from accelerating local wind speed, this effect can also help to re-direct the wind towards the turbines.

Additionally, based on Figures 6.6 (b) and 6.6 (c), both downward and middle configurations can induce strong vortex flow motions between the blades of the VAWT, compared to the upward and “both upward and downward” configurations, which do not generate these kind of vortex flow motions (see Figures 6.6 (d) and 6.6 (e), respectively). This is possibly the main reason behind the reduced C_{p-ave} improvement from these two former configurations. Furthermore, based on the mean pressure contours depicted in Figures 6.7 (b) and 6.7 (c), the downward and middle configurations can reduce the pressure on the pressure side but still maintain similar pressure around the leading-edge of the blade. In addition, the upward and “both upward and downward” configurations can also reduce the pressure around the leading-edge of the blade significantly (see Figures 6.7 (d) and 6.7 (e), respectively). Hence, the pressure gradient will increase accordingly (see Figure 6.8), resulting in higher lift and power production.

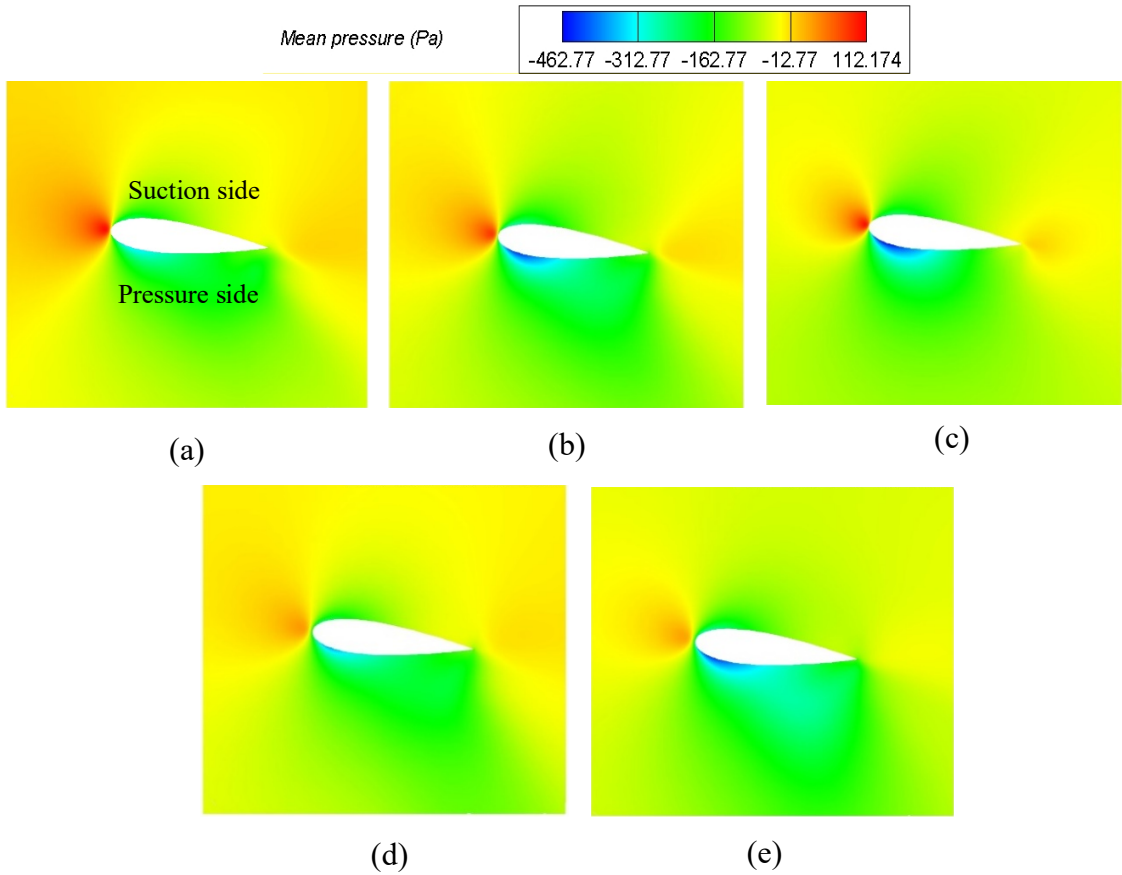


Figure 6.7 Comparison of mean pressure (Pa) contours of Blade 1 around the (a) bare VAWT and VAWT with SUD at (b) downward, (c) middle, (d) upward and (e) both upward and downward ($TSR = 2.64$, $\theta = 360^\circ$).

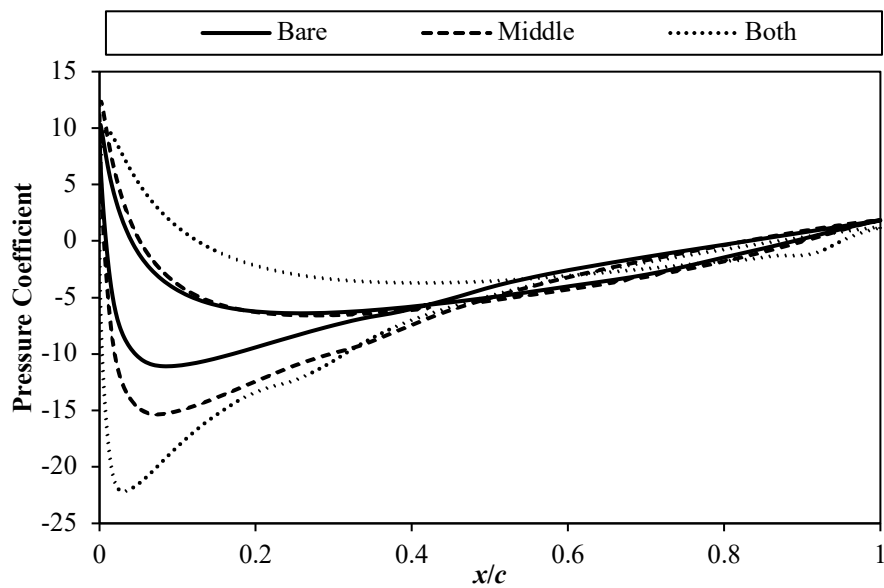
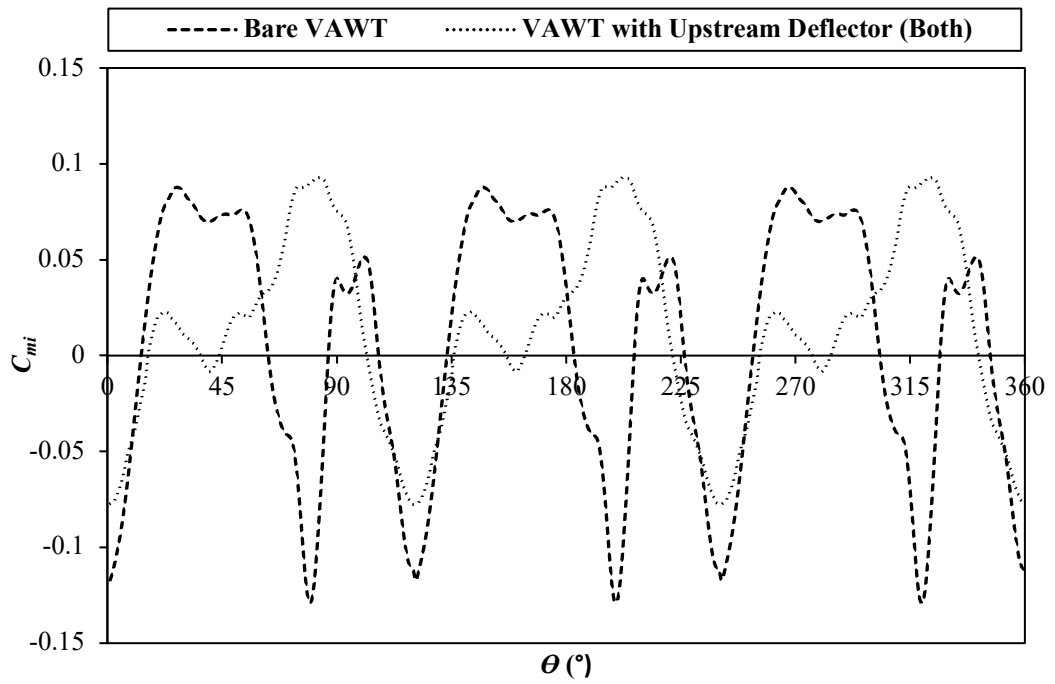
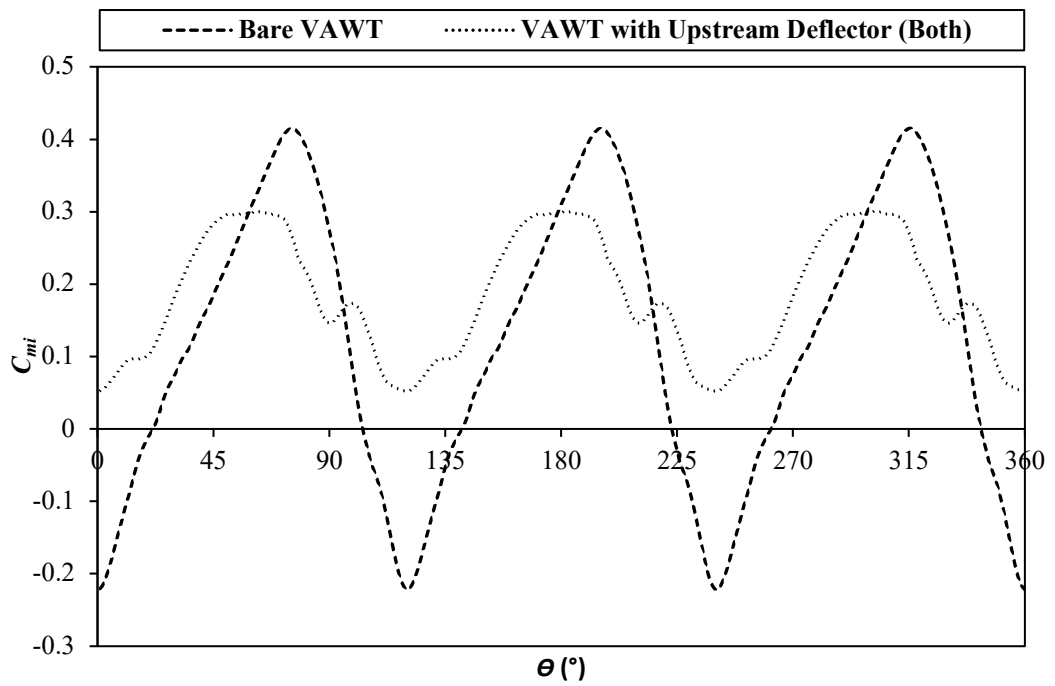


Figure 6.8 Comparison of pressure coefficient distribution of Blade 1 around the bare VAWT and VAWT with SUD at middle and both upward and downward ($TSR = 2.64$, $\theta = 360^\circ$).



(a)



(b)

Figure 6.9 C_{mi} comparison between a bare VAWT and a VAWT with SUD (both upward and downward configuration) in (a) $TSR = 1.44$ and (b) $TSR = 2.64$.

It is also found that the existence of a SUD upstream of the VAWT can improve the C_{p-ave} of the VAWT in all TSR regimes. However, the level of C_{p-ave} improvement varies in each regime. The SUD can generate better improvement in low regime of $TSRs$

compared to medium and high regimes of $TSRs$. For example, in the case of the “both upward and downward” configuration, a SUD can improve the C_{p-ave} value by around 126.7% in low regime of $TSRs$ compared to the bare VAWT, whilst in medium and high regimes of $TSRs$, the C_{p-ave} value can only be enhanced by approximately 52.7% and 52.5%, respectively. Note that the level of the C_{p-ave} improvement reduces significantly until $TSR = 2.5$ (see Table 6.4). After that, the C_{p-ave} improvement continues to decrease but only slightly less than 0.1% compared to lower value of TSR in $2.64 \leq TSR \leq 3.3$. The other three configurations studied also has similar behaviours. It suggests that the augmented wind speed mainly causes this behaviour, and is more beneficial in low regime of $TSRs$ than medium and high regimes of $TSRs$. In low regime of $TSRs$, the turbine rotation speed is relatively slow, so that the turbine usually needs external power to start the rotation until the turbine can self-rotate to produce positive power production. The higher incoming wind speed induced by the SUD will help the turbine rotate faster after the rotational starting point. It is clear that the SUD can sometimes help the turbine self-rotate without any external power and significantly improve power production afterwards. However, in medium and high regimes of $TSRs$, the turbine rotational speed is already high. The higher rotational speed caused by higher incoming wind speed can induce the blockage effect to the flow with the addition of higher structural vibration and drag and tip losses in the case of 3D VAWT configurations. Therefore, in these TSR regimes, the benefit of the SUD would be less significant compared to the start-up stage of the VAWT.

Figure 6.9 illustrates the C_{mi} distributions of a bare VAWT compared with a VAWT with SUD (i.e., both upward and downward configuration) in different TSR regimes. The C_{mi} distributions in $TSR = 1.44$ indicate that adding a deflector upstream of the VAWT can reduce the negative moment production of VAWT whilst still maintaining the optimum value of the positive moment. However, in $TSR = 2.64$, even though the SUD can remove the negative moment production of VAWT, it also reduces the optimum moment value of the VAWT. It means that the SUD can help the VAWT produce higher moment increases in low regime of $TSRs$ than medium and high regimes of $TSRs$. Nevertheless, the SUD in $TSR = 1.44$ can reduce the fluctuations of the moment production whilst in $TSR = 2.64$, it increases the fluctuations of the moment production. The higher drag and lift possibly cause this as the turbine rotational speed increases in higher regimes of $TSRs$. This increase in the turbine rotational speed can cause the turbine acts as a solid wall obstruction. Therefore, the upstream deflector (all location

configurations) is proven as a device to improve the power generation of a VAWT in all *TSR* regimes, regardless of its lower effectiveness in medium and high regimes of *TSRs*.

Table 6.4 Comparison of C_{p-ave} improvement due to a SUD of “both upward and downward” configuration in different *TSRs* (**bold** and *italic fonts* in yellow highlights show the optimum cases).

<i>TSR</i>	C_{p-ave}		
	Bare VAWT	VAWT with SUD	Improvement (%)
1.44	0.00850	0.01927	126.7
1.68	0.04332	0.07742	78.7
2.04	0.13346	0.23207	73.9
2.33	0.25302	0.41826	65.3
2.5	0.29798	0.45696	53.4
2.64	0.31743	0.48459	52.7
3.09	0.28968	0.44194	52.6
3.3	0.26166	0.39907	52.5

The ability of the SUD to reduce negative moment production and ease its fluctuations in low regime of *TSRs* can help the VAWT improve its self-starting ability, which is very important in this *TSR* regime. The SUD can also reduce the cut-in wind speed in the lowest *TSR* operation ($TSR = 1.44$). Evaluating the C_{p-ave} value of the bare VAWT in $TSR = 1.44$ (i.e., by reducing the incoming wind speed from 9 m/s to a cut-in wind speed until VAWT starts to generate a negative averaged moment in $TSR = 1.44$) shows that the bare VAWT starts to generate a negative averaged moment (thus, it cannot produce power) in an incoming wind speed of $U_{\infty} = 4.3$ m/s. The presence of the SUD upstream of the VAWT can reduce this cut-in wind speed to $U_{\infty} = 3.5$ m/s. It means that the VAWT with SUD can start to produce power at lower incoming wind speed, resulting in a better self-starting ability.

6.3.2 Effects of the width of the upstream deflector

After obtaining the optimum location to place the deflector upstream of the VAWT, this study investigates the effect of the width of the upstream deflector on the performance of the VAWT. The width of the upstream deflector increases from the base SUD of the “both upward and downward” configuration by increasing the width of the deflector on both ends (i.e., upward and downward) simultaneously. Note that this width

addition is extended from the top and bottom ends of the deflector so that the centre of the deflector remains unchanged (see Figure 6.10). As a result, the gap between two deflectors in both upward and downward configuration decreases as the width of the deflectors increases. By modifying the width of the deflectors using this approach, the effect of reducing of the gap between the two deflectors can be also investigated.

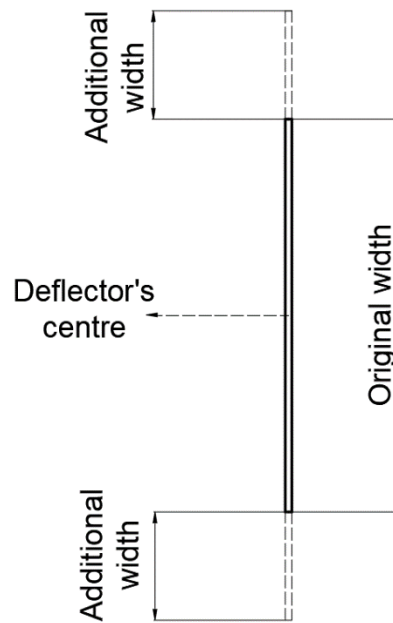


Figure 6.10 SUD with the width addition.

The simulation evaluates three width variations (w_1 , w_2 and w_3). The detail of these width variations compared with the base width (w_0) is tabulated in Table 6.2. Additional width at each deflector's end is half of the width increment w_0 as the width is extended from the centre of the deflector. For example, the width increment is 25% of w_0 for the case of w_1 . It means that the width is extended 12.5% of w_0 at each side of the deflector. Figure 6.11 illustrates the effect of width variations on the C_{p-ave} production of the VAWT with SUD. The results have shown that all width variations investigated can produce better C_{p-ave} than the bare VAWT in all TSR regimes. In each TSR regime, the increase of deflector width can improve the C_{p-ave} of the VAWT until reaching an optimum value of C_{p-ave} improvement at $w = 50\%$ of w_0 .

Compared to the original width, the SUD with $w = 50\%$ of w_0 can further improve C_{p-ave} by 5.5%, 1.2% and 1.7% in low, medium and high regimes of $TSRs$, respectively. Further increase of the deflector width will reduce the C_{p-ave} value of the VAWT by 3.63%, 1.26% and 0.65% in low, medium and high regimes of $TSRs$,

respectively, compared to the optimum width (see Figure 6.12). The higher power generation of the VAWT by the increase of deflector width can be due to the decreased gap between the two deflectors as the width of the deflector increases. Based on the law of mass conservation, the flow velocity will rise at the outlet if the outlet area decreases. Hence, the local incoming wind speed increases as the gap between two deflectors decrease (as shown in Figure 6.13). The velocity vector and mean velocity contours have shown velocity increase inside the gap between two deflectors as this gap decreases.

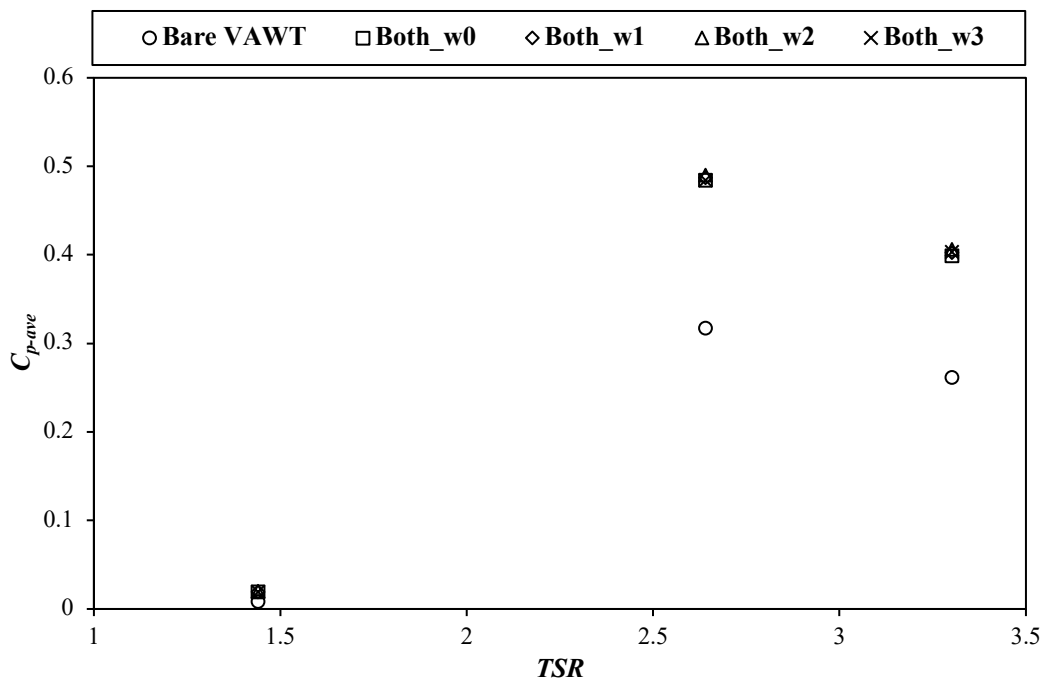
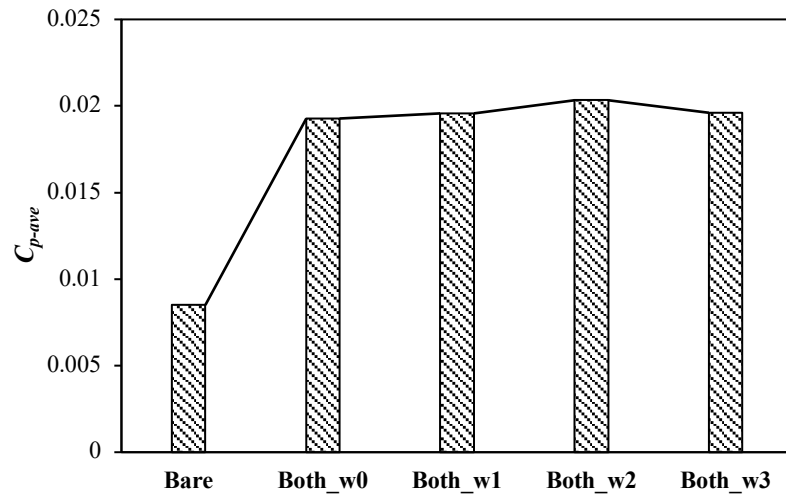
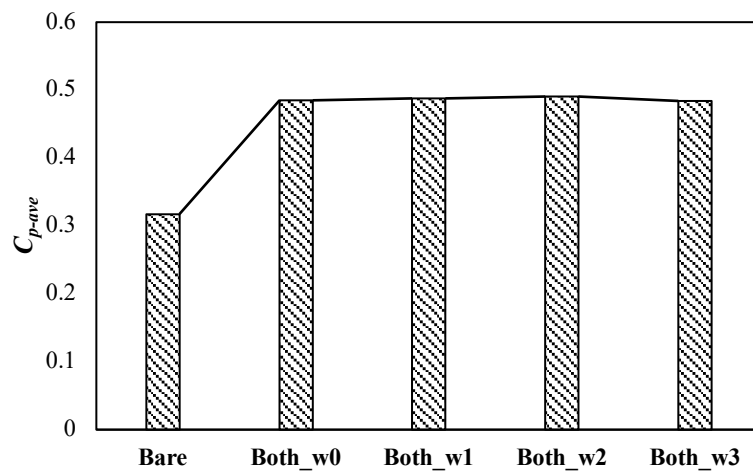


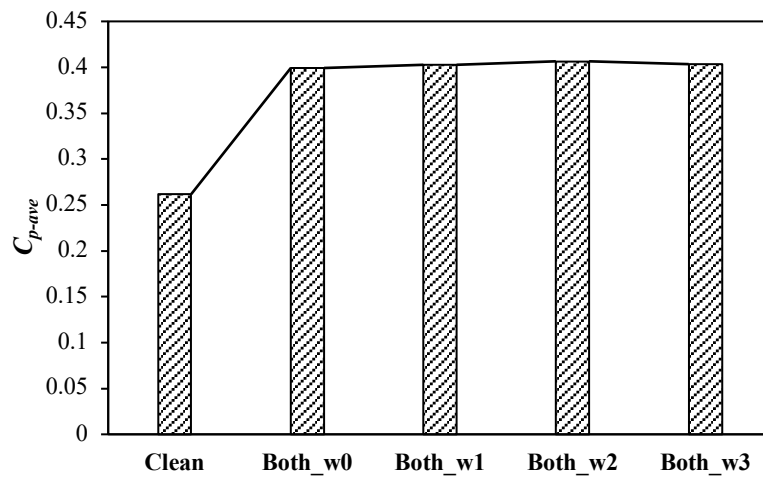
Figure 6.11 C_{p-ave} comparison between the bare VAWT and the VAWT with SUD of “both upward and downward” configuration with four different width variations in the three TSR regimes.



(a)



(b)



(c)

Figure 6.12 C_{p-ave} comparison between the bare VAWT and the VAWT with SUD of “both upward and downward” configuration with four different width variations in (a) $TSR = 1.44$, (b) $TSR = 2.64$ and (c) $TSR = 3.3$.

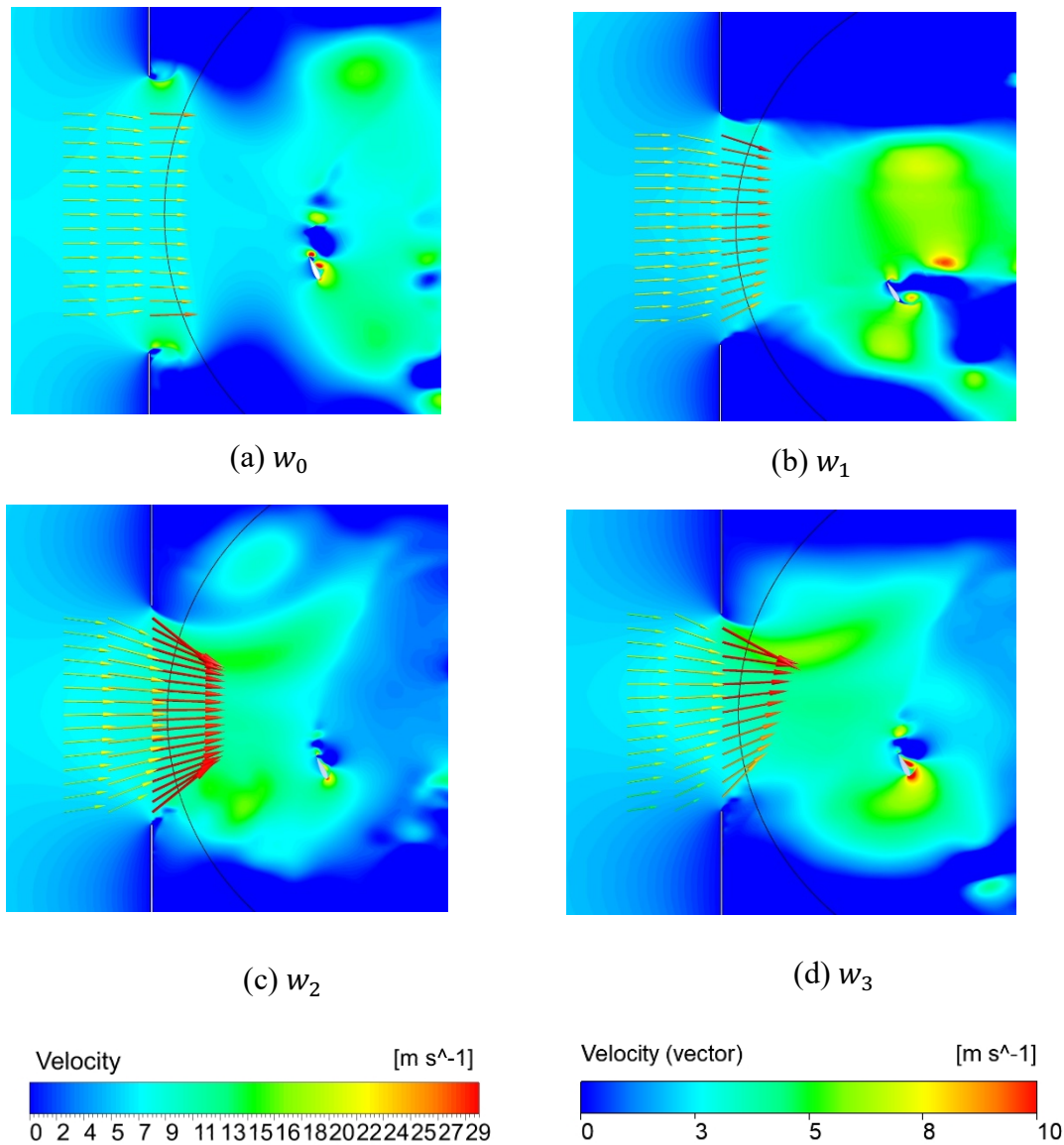


Figure 6.13 Comparison of the velocity vectors, superimposed by contours coloured by velocity of the VAWT with SUD of different widths ($TSR = 2.64$, $\theta = 360^\circ$).

However, once w is greater than 50% of w_0 , this incoming velocity improvement reduces. This is probably because the deflector width increase leads to a larger wake behind the deflector (see Figure 6.14). This larger wake affects the ability of the deflector to improve the VAWT performance as the velocity of the flow is not fully recovered before entering the turbine areas. Hence, this adverse effect can reduce the benefit of the SUD in the “both upward and downward” configuration because of the smaller gap between the two deflectors. Also, this is likely because there is an insignificant change in the C_{p-ave} value as the deflector width increases. The optimum width, w_2 , can only

increase the C_{p-ave} value by about 5.5%, 1.3% and 1.7% compared to the baseline SUD in low, medium and high regimes of $TSRs$, respectively.

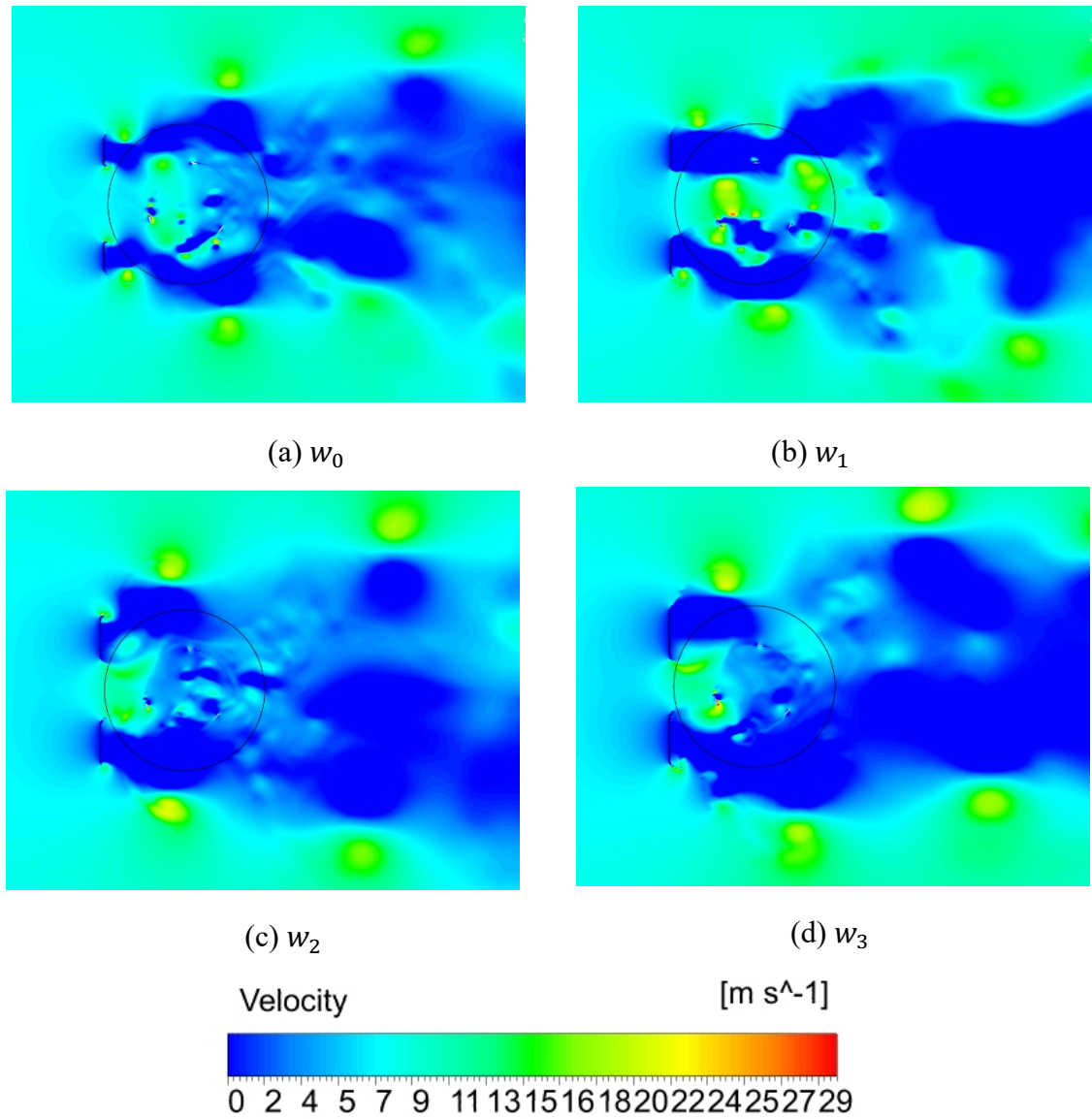
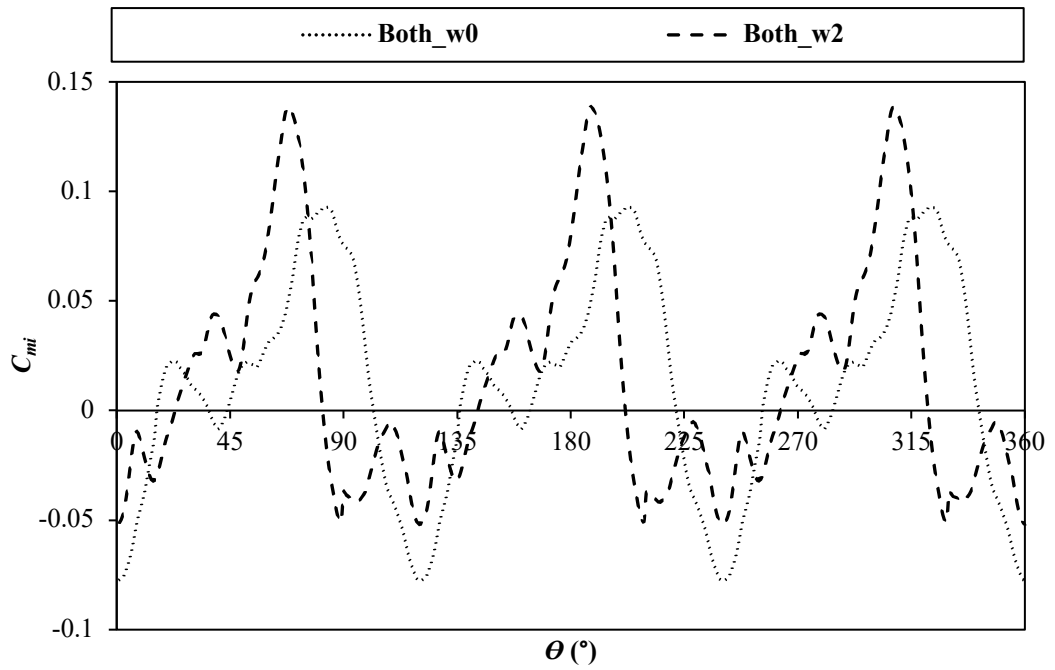


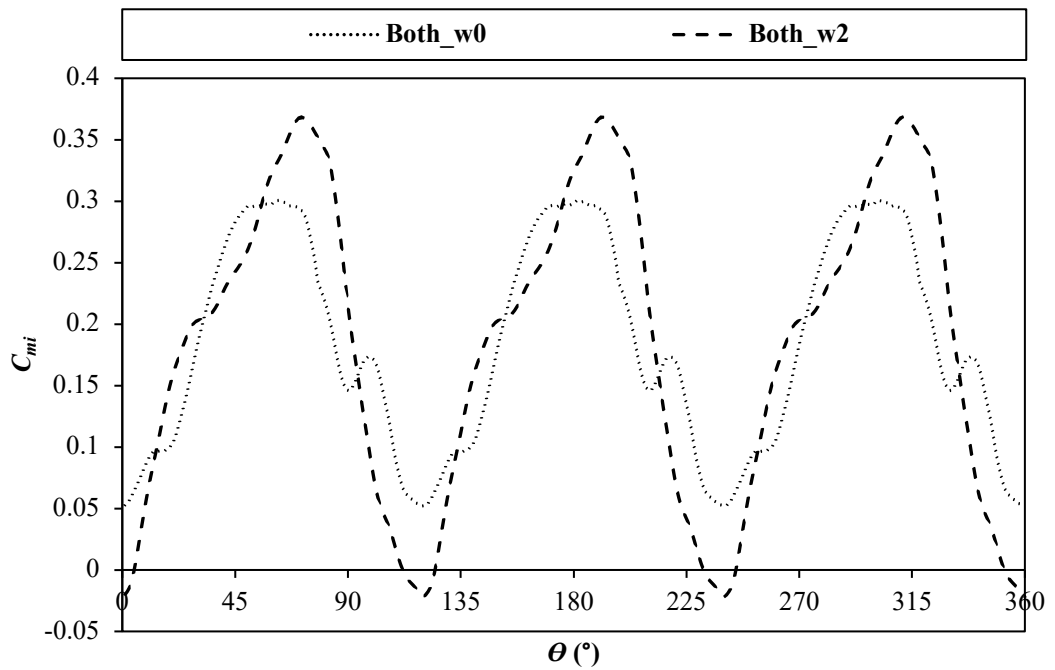
Figure 6.14 Comparison of velocity contours of VAWT with SUD of four different widths ($TSR = 2.64$, $\theta = 360^\circ$).

Furthermore, the increase of deflector width has a more significant effect on the C_{p-ave} improvement in low regime of $TSRs$ compared to medium and high regimes of $TSRs$. The C_{mi} distributions shown in Figure 6.15 demonstrate that in low regime of $TSRs$, the change of width can improve the positive moment production and reduce the negative moment production. However, in medium regime of $TSRs$, the change of width can enhance the positive moment production, but it also increases the negative moment

production. Hence, the increment of the width of the SUD cannot work effectively outside low TSR regime.



(a)



(b)

Figure 6.15 C_{mi} comparison of the VAWT with SUD for four different widths (a) $TSR = 1.44$ and (b) $TSR = 2.64$.

6.3.3 Effects of the inclination angle of upstream deflector

Following the investigation of the width variations of the deflector, the simulation continues with investigating the effect of inclination angle (θ_{SUD}) on the performance enhancement of the VAWT (see Figure 6.16). The motivation behind this investigation comes from a convergence duct or nozzle configuration that can avoid the sudden change of flow, especially around the deflector gap, created by vertically arranged deflectors. By introducing an inclination angle, it is anticipated that the incoming flow speed can gradually increase before passing through the gap between the deflectors compared to the original SUD configuration. Table 6.5 tabulates the proposed angle variations.

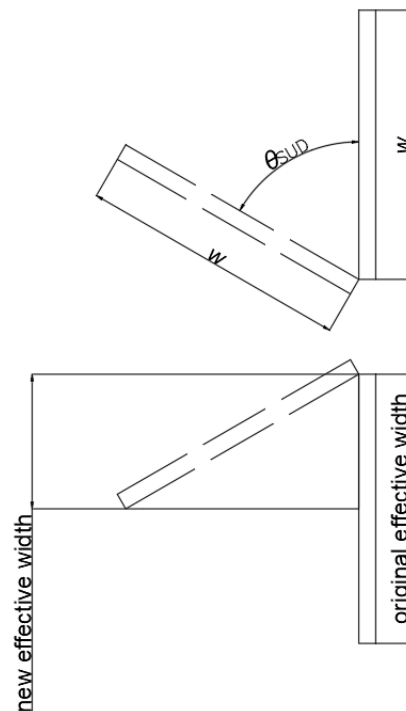


Figure 6.16 Inclination angle of the SUD (for both upward and downward configuration).

Table 6.5 Variations of the SUD's inclination angle.

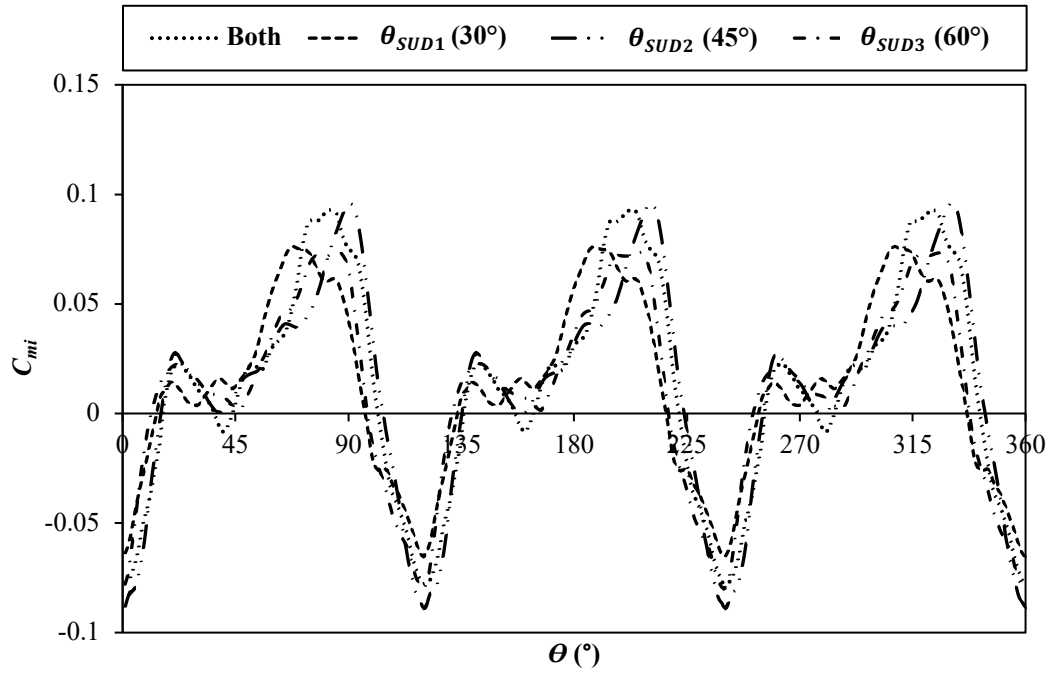
Case	Angle
θ_{SUD0} (base geometry)	0°
θ_{SUD1}	30°
θ_{SUD2}	45°
θ_{SUD3}	60°

Table 6.6 gives the effect of θ_{SUD} on the C_{p-ave} value of the VAWT in all TSR regimes. Interestingly, introducing three θ_{SUD} angles reduces the C_{p-ave} of the VAWT in all TSR regimes rather than increasing it as initially anticipated. It is because adding an inclination angle will reduce the deflector's effective width (i.e., the frontal area) (see Figure 6.16) whilst the deflector is tilted. Section 6.3.2 has shown that increasing the width of the deflector can enhance the C_{p-ave} value of the VAWT, whilst reducing it will decrease the C_{p-ave} value of the VAWT. To further confirm this, the VAWT with SUD using a reduced width of $0.5w$ is studied. The C_{p-ave} value of the VAWT with this thin SUD decreases to 0.4126 compared to the VAWT with base geometry of SUD in $TSR = 2.64$ ($C_{p-ave} = 0.48459$), in agreement with those findings discussed above.

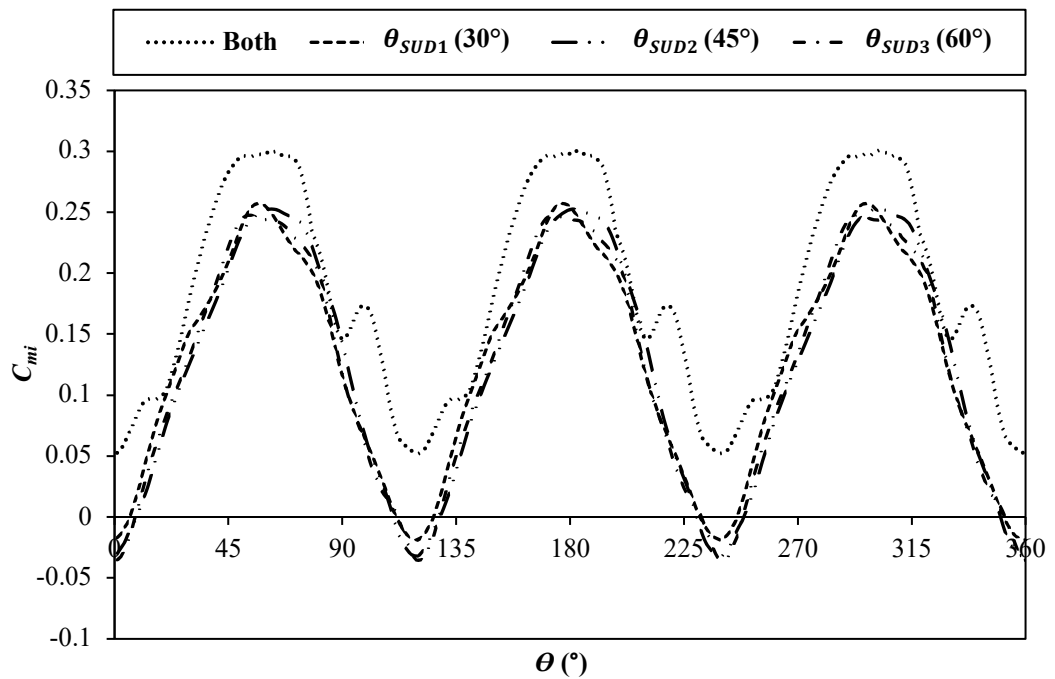
Table 6.6 Comparison of the effect of inclination angle on the C_{p-ave} of VAWT with SUD (**bold** and *italic fonts* with yellow highlights show the optimum cases).

Case	C_{p-ave}		
	<i>TSR = 1.44</i>	<i>TSR = 2.64</i>	<i>TSR = 3.3</i>
Bare VAWT	0.00850	0.31743	0.26166
θ_{SUD0} (base geometry)	0.01927	0.48459	0.39907
θ_{SUD1}	0.01883	0.33771	0.29914
θ_{SUD2}	0.01745	0.32929	0.28589
θ_{SUD3}	0.01530	0.32699	0.28561

Further investigation shows that based on the C_{mi} distributions in $TSR = 2.64$ (see Figure 6.17), tilting the deflectors can reintroduce the negative moment production of the VAWT and decrease its positive moment generation. Hence, the averaged moment reduces, resulting in lower power generation. Introducing a deflector inclination angle also decreases the ability of the deflectors to guide the wind towards the turbine blades. Figure 6.18 shows that the wind starts to "shift" away from the turbine's blades as the deflectors are tilted. The wake region behind the deflector is also shifted away from the blades of the turbine (see Figure 6.19). This wake region can be drifted further away from the blades as the inclination angle increases. It means that the blades of the turbine are no longer entirely located behind the wake region of the upstream deflectors. Hence, the effect of augmentation of the SUD on the wind speed reduces. As shown in Figure 6.19, the velocity of the tilted deflectors is relatively lower than that of the non-tilted deflectors inside the blades of VAWT.



(a)



(b)

Figure 6.17 Comparison of the effect of inclination angle on the C_{mi} distribution of VAWT with SUD in (a) $TSR = 1.44$ and (b) $TSR = 2.64$.

However, the inclination angle can re-generate smooth C_{mi} distributions following the reduction of its fluctuation distributions caused by the existence of the deflectors. The streamlines illustrated in Figure 6.18 demonstrate that the tilted deflectors

can decrease the vortex generation behind the deflectors, reducing the flow unsteadiness. However, this benefit cannot assist the tilted deflectors to further improve the performance of VAWT as it changes the primary purposes of adding a deflector in upstream of VAWT (i.e., to enhance the local wind speed and to re-direct the wind towards the blades of turbines).

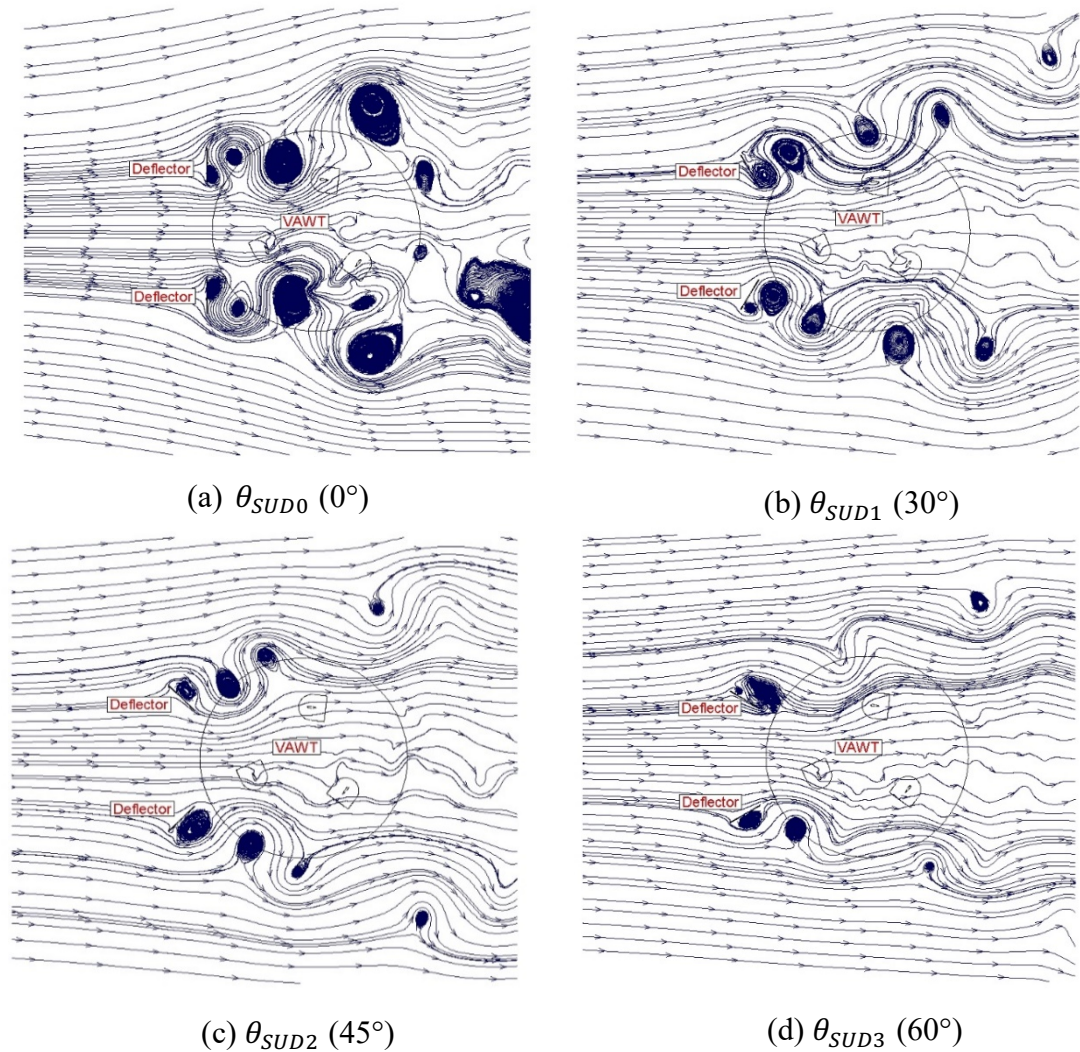


Figure 6.18 Comparison of streamlines around the VAWT with SUD at four different inclination angles ($TSR = 2.64$, $\theta = 360^\circ$).

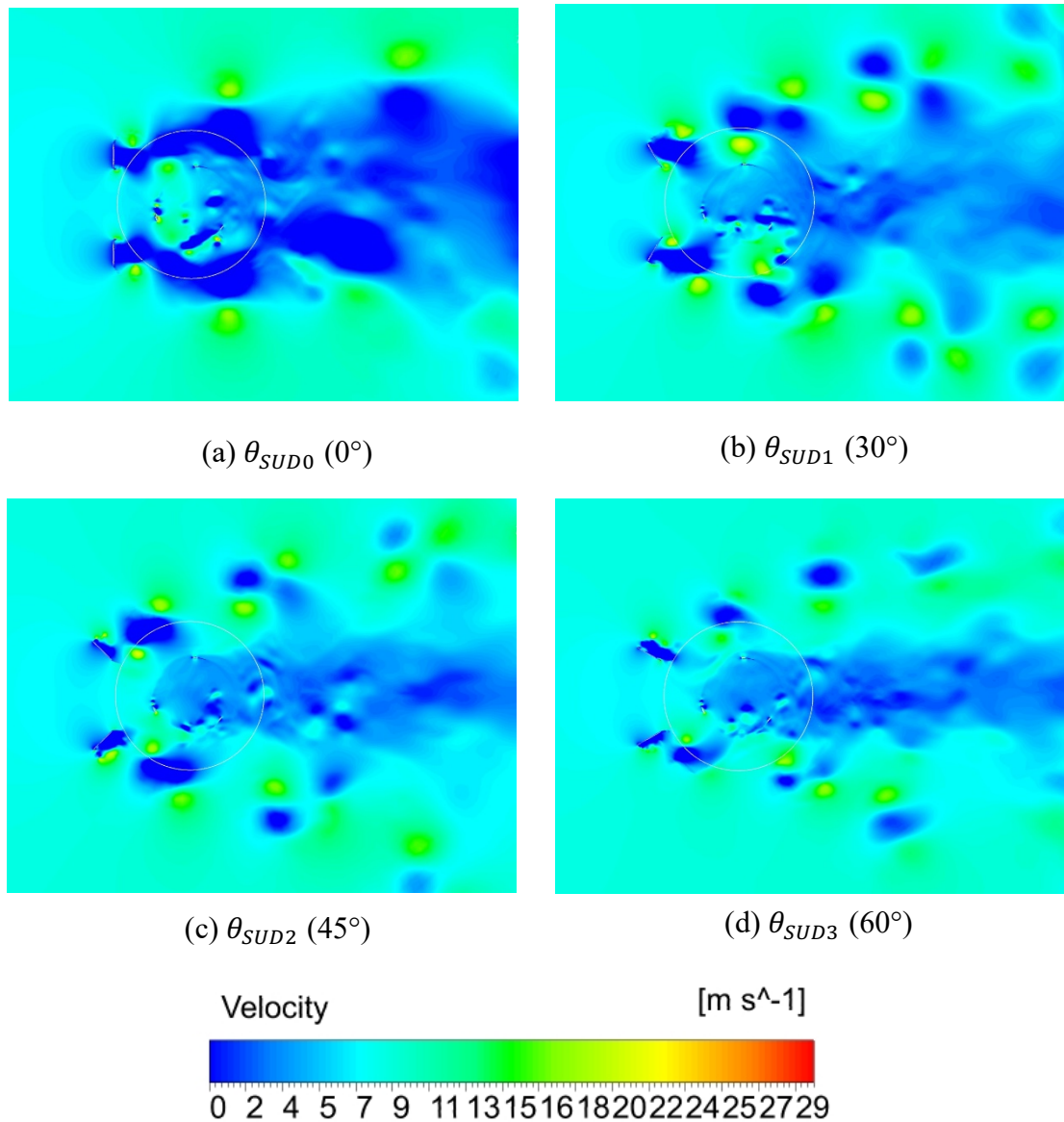


Figure 6.19 Comparison of velocity contours of the VAWT with SUD at four different inclination angles ($TSR = 2.64$, $\theta = 360^\circ$).

From Table 6.6, it can be seen that in medium ($TSR = 2.64$) and high ($TSR = 3.3$) TSR regimes, tilting the deflectors has a worse effect on the decrease of the C_{p-ave} value than in low regime of $TSRs$ ($TSR = 1.44$). In fact, in medium and high regimes of $TSRs$, a deflector with an inclination angle can reduce the C_{p-ave} almost down to the value of the bare VAWT. Compared to the base geometry of the SUD, a SUD with optimum inclination angle can decrease C_{p-ave} improvement significantly by about 87.8% and 72.7% in medium and high regimes of $TSRs$, respectively. Meanwhile, in low regime of $TSRs$, the decrease of the C_{p-ave} value is not that significant (only around 4.1% compared

to the base geometry of SUD). The C_{mi} distribution suggests that tilting the deflectors can increase negative moment production in all TSR regimes (see Figure 6.17). However, whilst it can weaken the positive moment production in other TSR regimes, tilting the deflectors can generally improve the positive moment production in low regime of $TSRs$. Therefore, the decrease of averaged moment production, which reduces the VAWT's power generation in low regime of $TSRs$, is found not as strong as those in medium and high regimes of $TSRs$.

6.4 Chapter Summary and Further Work

The effect of a straight plate upstream deflector on the performance enhancement of a VAWT is studied and based on results obtained, it can be concluded that the addition of a deflector upstream of the VAWT can improve the VAWT performance in all TSR regimes. It is mainly because the existence of an upstream deflector can enhance the incoming wind speed and help direct the wind towards the blades of the turbine. However, the ability of the SUD to improve the performance of the VAWT varies for each TSR regime. In low regime of $TSRs$, the C_{p-ave} enhancement can be up to 126.7%, whilst in medium and high regimes of $TSRs$ this enhancement is around 52.7% and 52.5%, respectively. It is because, in low regime of $TSRs$, the enhancement of rotational speed has a more significant benefit to help the turbine reduce negative moment production, which can lead to the improvement of self-starting ability and increase power generation. However, the higher rotational speed can also introduce a blockage effect and higher drag in medium and high regimes of $TSRs$, resulting in less improvement in power generation of the VAWT.

Furthermore, it is essential to place the SUD at the correct location upstream of the VAWT. Based on C_{p-ave} value evaluation, placing deflectors at “both upward and downward” positions upstream of the VAWT can generate the best improvement of power generation in all TSR regimes compared to the other three studied configurations (i.e., upward, middle and downward). The gap between the two deflectors in the “both upward and downward” configuration introduces a converged duct/nozzle flow effect, further enhancing the incoming wind speed. Adding deflectors at “both upward and downward” locations can also direct the wind towards the turbines of VAWT, resulting in a higher mass flow rate of wind directed to the blades of the turbine. Moreover, compared to the other three SUD configurations (i.e., upward, middle and downward), the blades of the VAWT in “both upward and downward” configuration can largely

mitigate the upstream deflector wake by not directly impinging onto the downstream blades when they are rotating. Thus, this configuration is better to improve the C_{p-ave} value of the VAWT.

After identifying the best configuration of the SUD, further parametric studies have been performed, focussing on the width and inclination angle of the SUD. It is found that the increase in the deflector width has a slightly positive effect on the increase of the C_{p-ave} value of the VAWT as long as the positive influence of a narrower gap between the two deflectors can withstand the impact of a larger wake region caused by a wider deflector. The SUD with optimum width (150% of w_0) can further enhance the C_{p-ave} improvement by 5.5%, 1.2% and 1.7% in low, medium and high regimes of $TSRs$, respectively. On the other hand, adding an inclination angle to the SUD reduces the C_{p-ave} improvement of a SUD without inclination angle. Surprisingly, whilst tilting deflectors can reduce the vortex generation behind the straight (vertical) deflector to reduce flow unsteadiness, the reduction in effective width can decrease the C_{p-ave} value of the VAWT. The tilting deflectors can also re-direct the incoming wind away from the blades of the turbine, causing a reduction of the ability of the deflectors to direct the wind to the blades of VAWT. Therefore, “both upward and downward” configuration with original (vertical arranged) geometry is more acceptable as a SUD design to improve the performance of the VAWT. If the drawback of adding the weight caused by the width increase can be overcome (e.g., using lighter materials such as composite), the width of the deflector can be increased to 150% of w_0 to gain further performance improvement.

Nevertheless, it is critical to compare the ability of the GF and the SUD to improve the performance of the VAWT in each TSR regime. Accordingly, the next chapter discusses the comparison between the GF and the SUD of their capability to enhance the performance of the VAWT in each TSR regime. Moreover, a new attempt to combine the GF and SUD simultaneously to improve the performance of the VAWT in each TSR regime is also investigated in the following chapter.

Chapter 7: Comparison between a Gurney Flap, Straight Upstream Deflector and a Combination of Gurney Flap and Straight Upstream Deflector for Performance Enhancement of a Lift-Driven VAWT

In the previous two chapters, it has been discussed that a Gurney flap and a straight upstream deflector can improve the performance of a VAWT's mean averaged power coefficient over one turbine revolution in all regimes of *TSRs*. It is critical to understand the comparison of the rate of C_{p-ave} improvement of the VAWT caused by the GF and SUD and the method by which the GF and SUD improve the C_{p-ave} of the VAWT in each *TSR* regime, so the best choice of device to improve the VAWT C_{p-ave} in each *TSR* regime can be determined.

Hence, this chapter presents a cross-comparison of performance enhancement of VAWT by using GF and SUD. Note that the used GF and SUD for this comparison is GF at the trailing-edge with $H = 3\% c$ and $\theta_{GF} = 90^\circ$ and SUD with "both upward and downward" configuration (base geometry (see Table 6.1)), respectively. Cross comparison of the stand-alone GF and stand-alone SUD's performance in improving the C_{p-ave} of VAWT in low, medium and high regimes of *TSRs* can be found in Section 7.1.

This chapter has also covered the evaluation of the combination of GF and SUD as performance enhancement device of lift-driven VAWT. As mentioned in Chapters 5 and 6, both dynamic stall control and flow augmentation devices positively influence the increment of C_{p-ave} of the VAWT in all *TSR* regimes. However, the attempt to combine dynamic stall control devices and flow augmentation devices as performance enhancement of lift-driven VAWT has not been done in previous VAWT studies. The evaluation of this new combination device and comparison with bare VAWT, VAWT with stand-alone GF and VAWT with stand-alone SUD are performed in all *TSR* regimes and presented in Section 7.2. Lastly, Section 7.3 discussed the summary of this chapter and further works of the following chapter.

7.1 Performance Comparison of GF and SUD as Performance Enhancement of VAWT

7.1.1 Low regime of *TSRs* (representative *TSR* = 1.44)

In this *TSR* regime, a VAWT with GF produces slightly better performance enhancement compared to VAWT with SUD. The increase of C_{p-ave} is approximately

130.94% using GF, whilst it is about 118.77% using SUD for the same incoming wind conditions. C_{mi} distributions over azimuthal position (see Figure 7.1) show that even though GF can significantly improve the positive moment production of VAWT, it also has larger negative moment production. Meanwhile, SUD can largely reduce the negative moment production of VAWT, but the peaks of the positive moment are shifted backwards and have almost the same maximum as bare VAWT. GF can help VAWT reduce the number of pairs of positive and negative peaks of C_{mi} distributions from six observed in bare VAWT to three observed in VAWT with GF, whilst SUD does not clearly show this kind of reduction. The vorticity contours in Figure 7.2 show that GF has dramatically reduced the vortex shedding around the rotor area of VAWT, but SUD has not. SUD instead increases the vortex shedding around the rotor area of VAWT (see Figure 7.2 (c)). It is known that dynamic stall is associated with large recirculation area and multiple vortex shedding (Rocchio et al., 2020). Hence, GF ability to reduce the vortex shedding shows that indeed GF can ease the dynamic stall of VAWT.

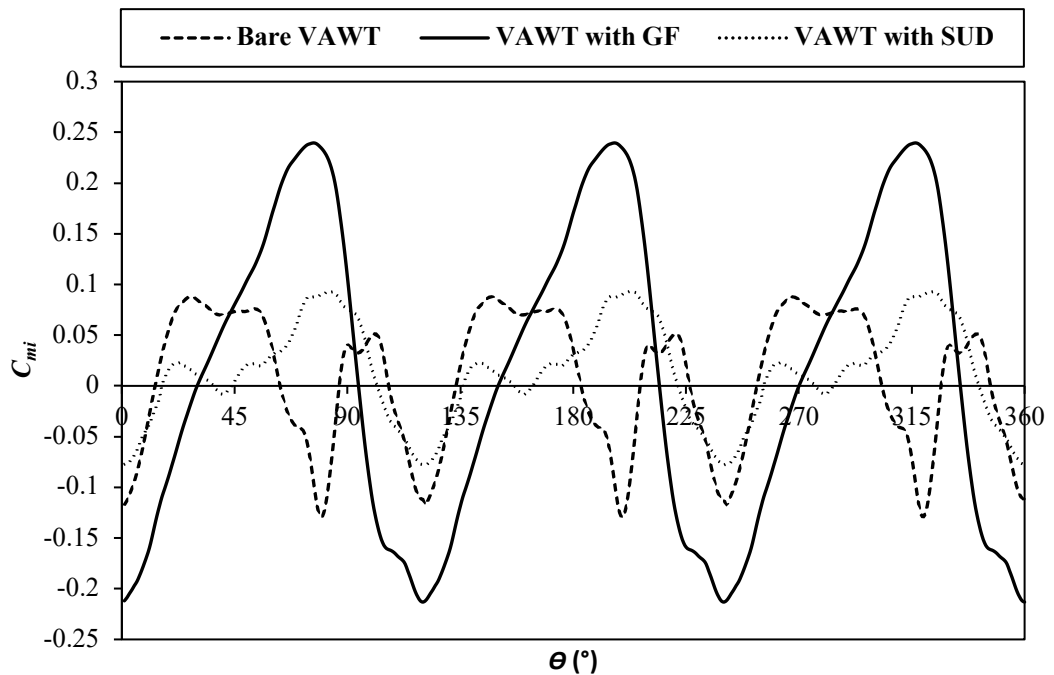


Figure 7.1 C_{mi} comparison between bare VAWT, VAWT with GF and VAWT with SUD in $TSR = 1.44$.

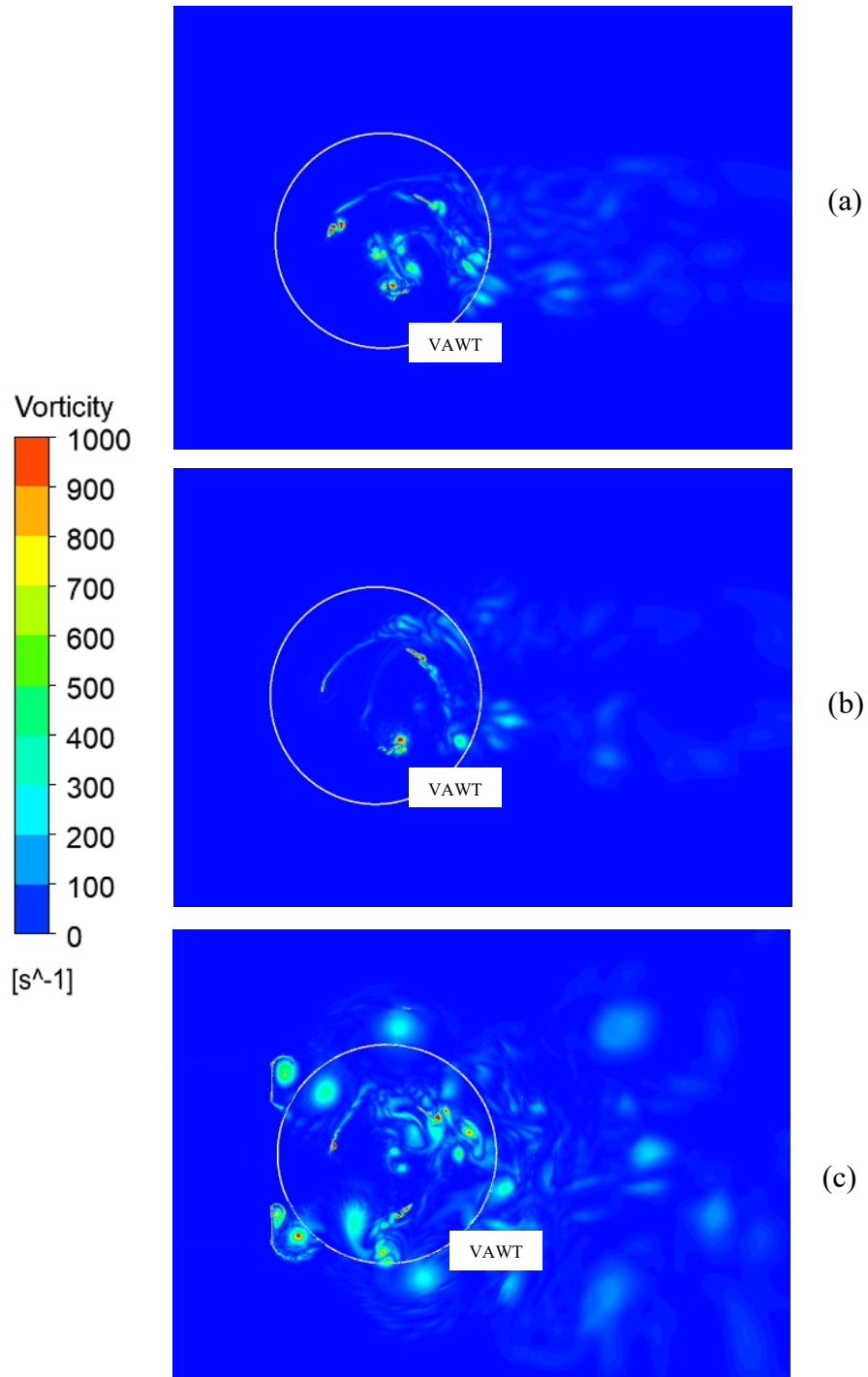
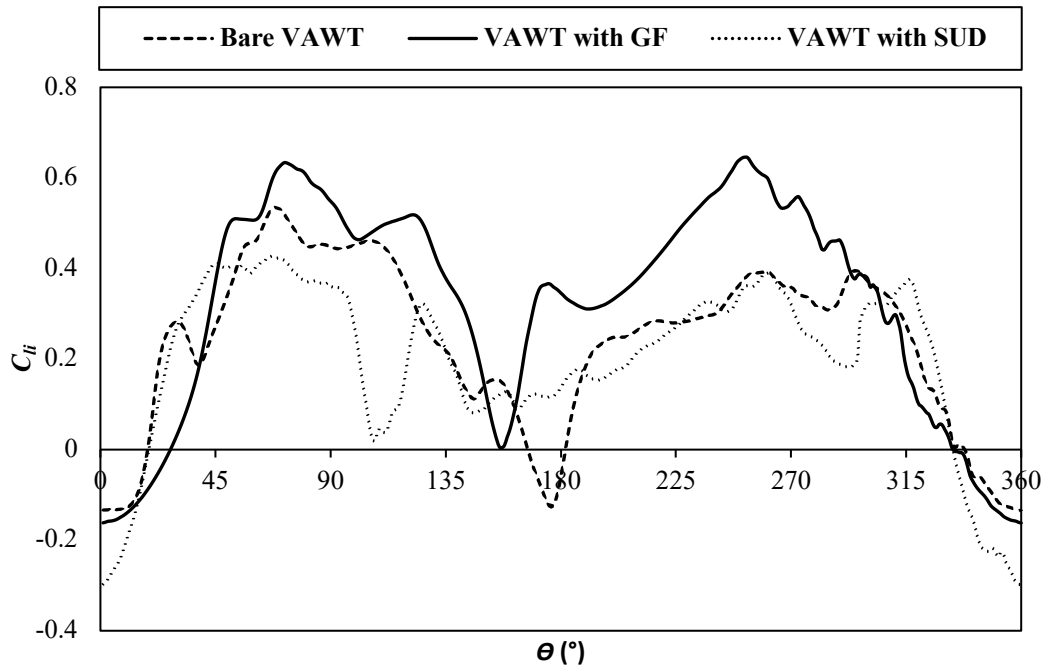
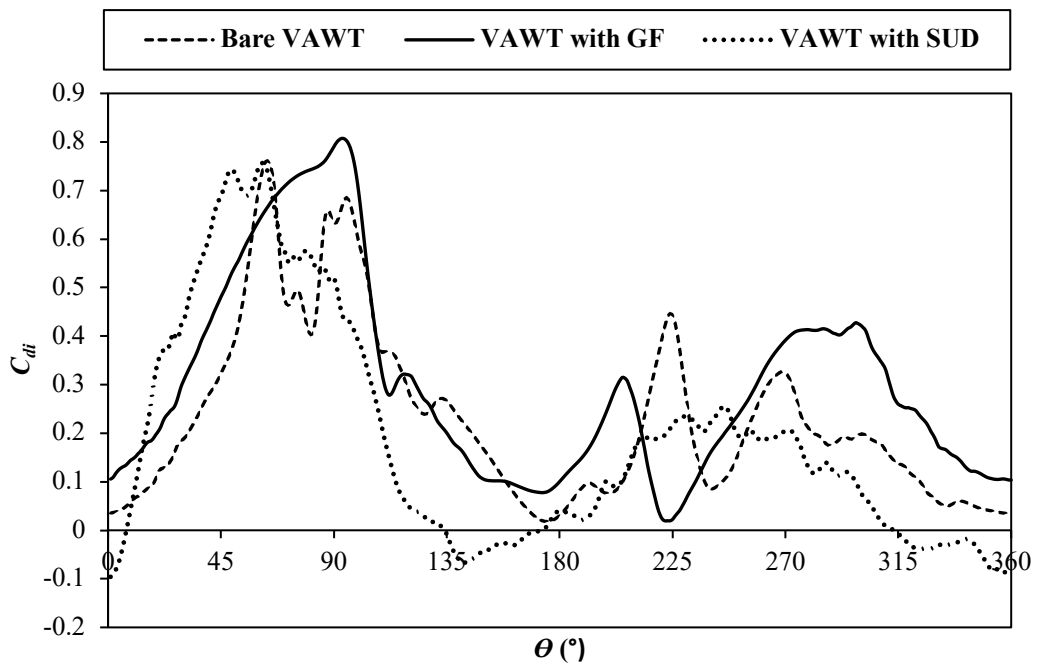


Figure 7.2 Contours of z -vorticity of (a) bare VAWT, (b) VAWT with GF and (c) VAWT with SUD in $TSR = 1.44$ ($\theta = 90^\circ$). The circles in white solid lines represent the rotating core sub-domain.



(a)



(b)

Figure 7.3 Comparison of (a) C_{li} and (b) C_{di} between bare VAWT, VAWT with GF and VAWT with SUD in $TSR = 1.44$.

The correlations between the VAWT performance improvements and lift and drag characteristics modifications due to the introduction of GF and SUD are examined. Figure 7.3 shows the instantaneous lift coefficient and drag coefficient distributions of

Blade 1 and Table 7.1 gives averaged C_l (i.e., C_{l-ave}) and C_d (i.e., C_{d-ave}) over one turbine revolution of Blade 1. Results indicate that the GF can significantly increase the instantaneous lift force and produce larger drag force simultaneously. It may be due to the GF on the VAWT blades that can cause a larger drag force than bare VAWT blades. On the other hand, the SUD largely reduces the drag generation and reduces the lift force generation, compared to the bare VAWT, and it is possibly due to larger and stronger vortex generation in the VAWT rotor area (see Figure 7.2 (c)). Based on these results, the GF can increase the VAWT lift generation by easing the dynamic stall, whilst the SUD can improve the incoming wind speed to largely reduce the drag force in low regime of $TSRs$.

Table 7.1 Comparison of C_{l-ave} , C_{d-ave} and C_{l-ave}/C_{d-ave} over one turbine revolution between bare VAWT, VAWT with GF and VAWT with SUD in $TSR = 1.44$.

Case	C_{l-ave}	C_{d-ave}	C_{l-ave}/C_{d-ave}
Bare VAWT	0.2373	0.2314	1.0255
VAWT with GF	0.3220	0.3006	1.0713
VAWT with SUD	0.1960	0.1877	1.0442

7.1.2 Medium regime of $TSRs$ (representative $TSR = 2.64$)

In medium regime of $TSRs$, GF produces better improvement of C_{p-ave} generation of VAWT (i.e., C_{p-ave} improves about 69.94%) compared to SUD (i.e., C_{p-ave} improves about 52.6%). Compared to low regime of $TSRs$, the ability of GF or SUD to improve the C_{p-ave} value of VAWT in medium regime of $TSRs$ significantly decreases to almost a half of its respective value. The C_{mi} distributions (see Figure 7.4) demonstrate that in medium regime of $TSRs$, both GF and SUD are capable of removing the negative moment production of VAWT. However, the maximum positive moment production also decreases due to the existence of GF or SUD.

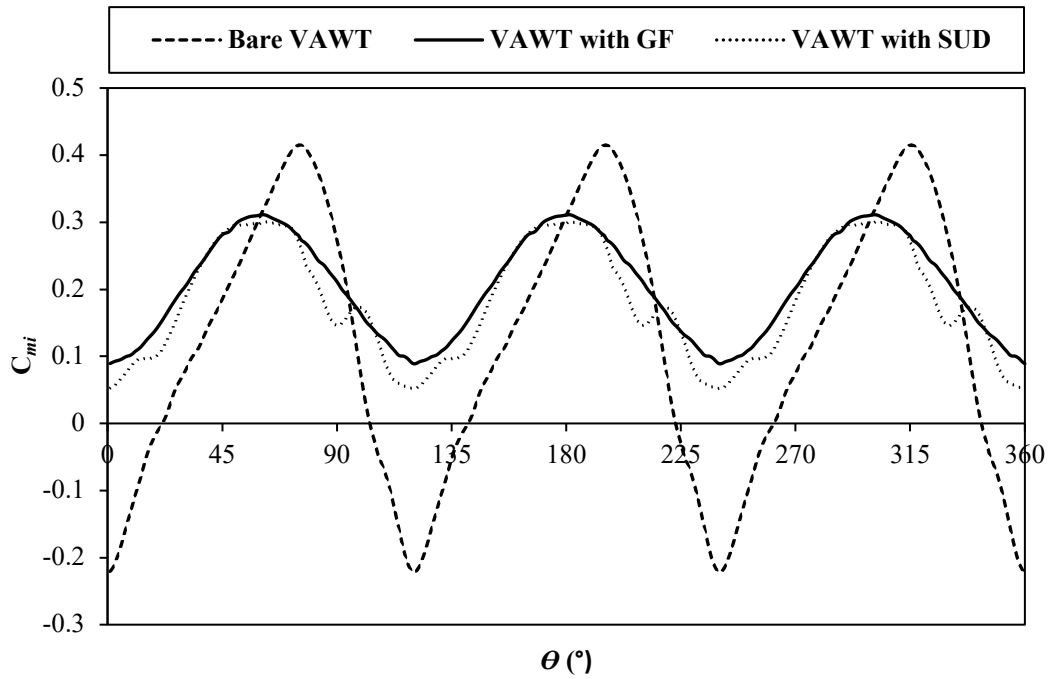


Figure 7.4 C_{mi} comparison between bare VAWT, VAWT with GF and VAWT with SUD in $TSR = 2.64$.

Furthermore, Figure 7.4 shows no significant differences in C_{mi} distributions between the modified VAWTs with GF and SUD. It confirms that in medium regime of $TSRs$, the ability of GF to reduce the dynamic stall of VAWT is not as effective as that in low regime of $TSRs$ (e.g., GF can halve the number of pair of positive/negative peaks of C_{mi} fluctuation in low regime of $TSRs$ as seen in Figure 7.1). The addition of SUD in the VAWT configuration introduces small secondary peaks in C_{mi} distributions, indicating that the existence of SUD will increase the flow unsteadiness. It is possibly due to SUD can induce strong wake vortices travelling through the rotor area of VAWT, whilst GF does not induce this kind of behaviour (see Figure 7.5).

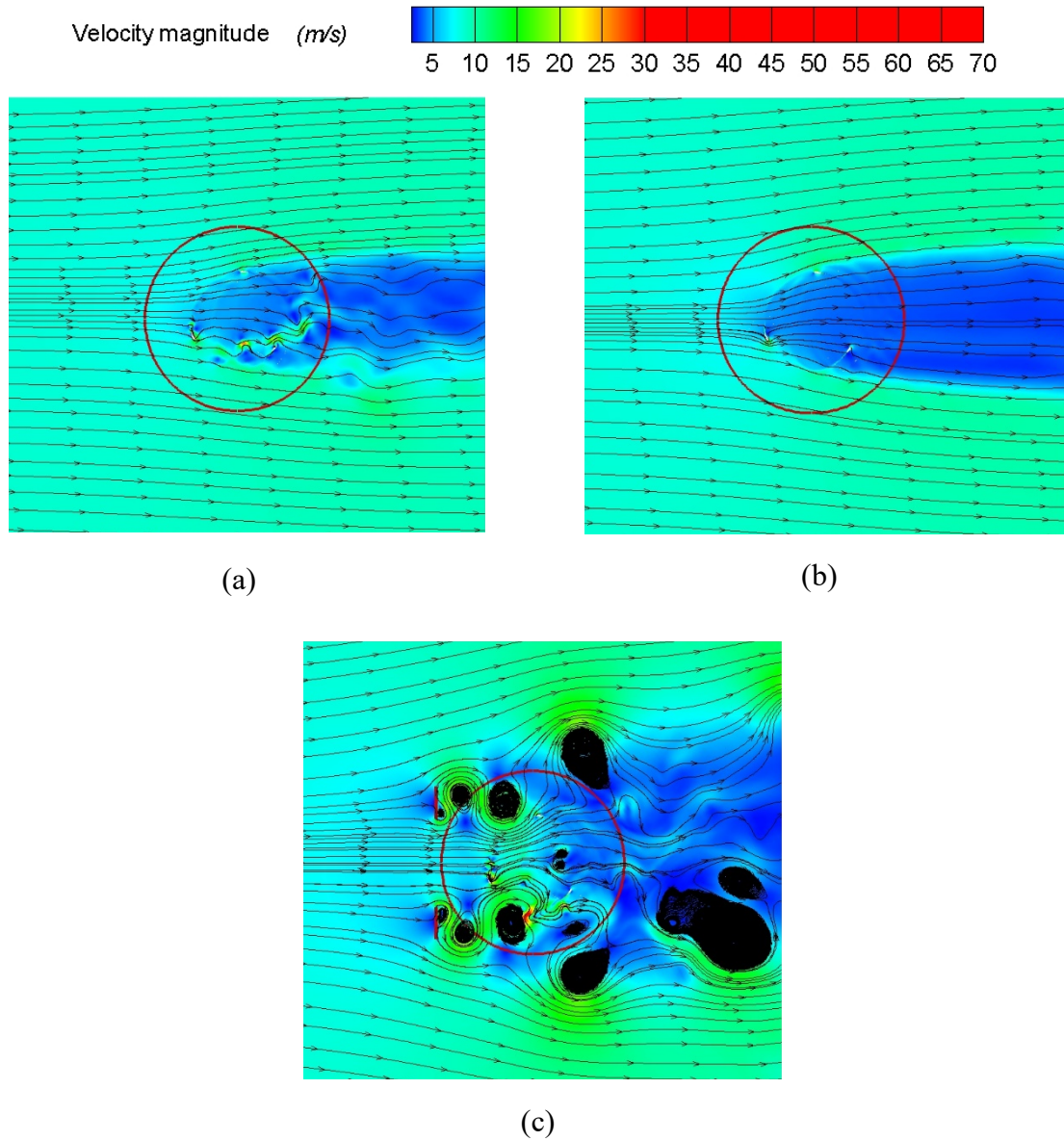
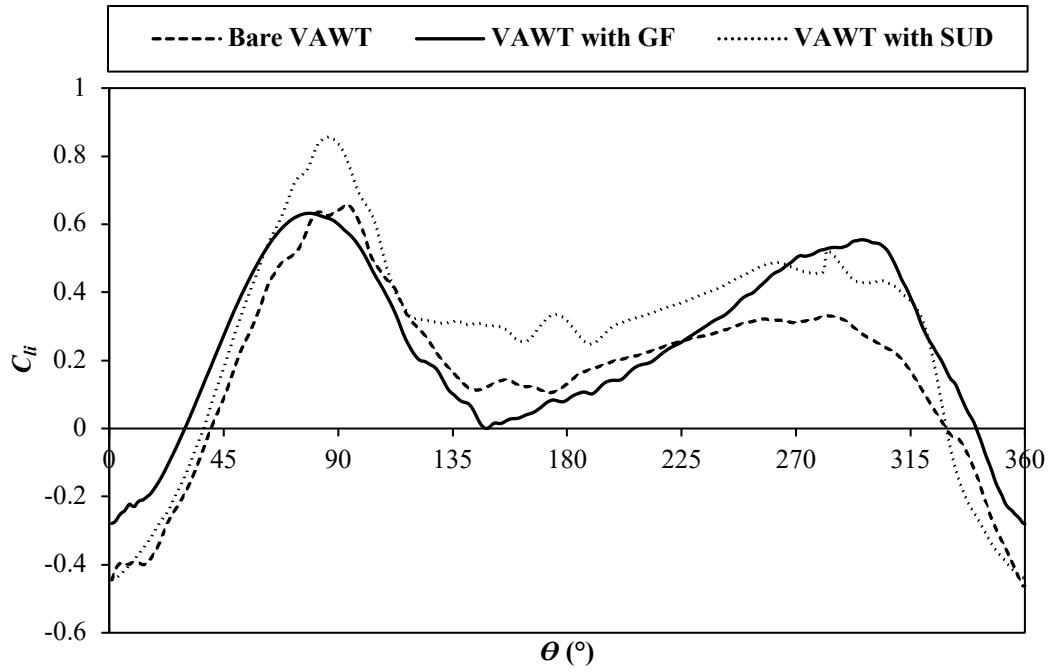
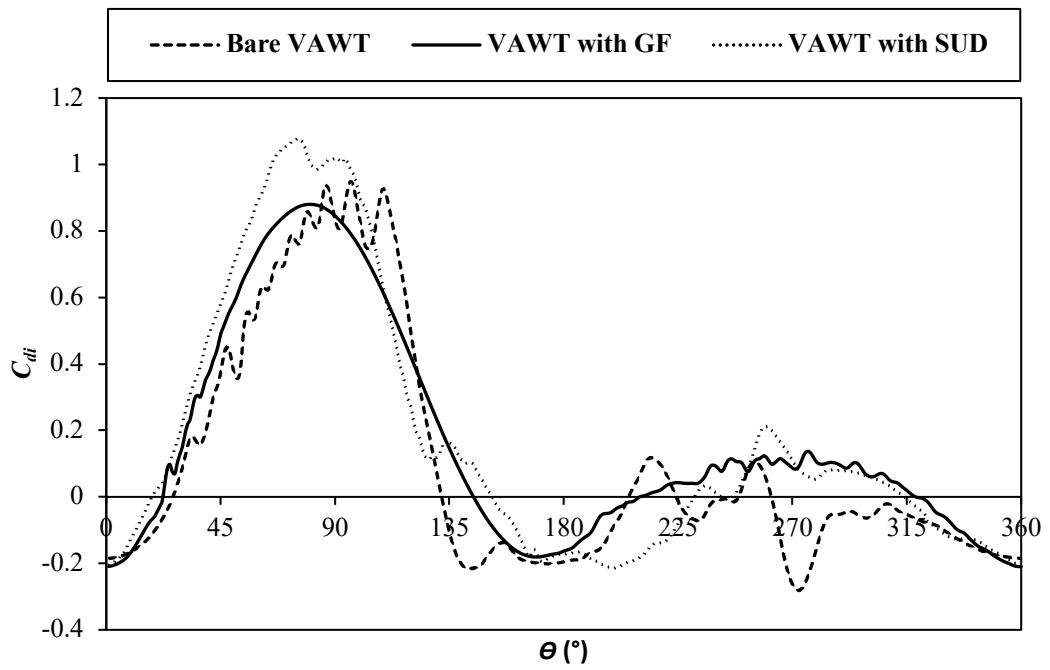


Figure 7.5 Comparison of streamlines coloured by the velocity magnitude (m/s) of the flow around (a) bare VAWT, (b) VAWT with GF, and (c) VAWT with SUD ($TSR = 2.64$, $\theta = 360^\circ$). The circles in dark solid lines represent the rotating core sub-domain.



(a)



(b)

Figure 7.6 Comparison of (a) C_{li} and (b) C_{di} between bare VAWT, VAWT with GF and VAWT with SUD in $TSR = 2.64$.

Table 7.2 Comparison of C_{l-ave} , C_{d-ave} and C_{l-ave}/C_{d-ave} over one turbine revolution between bare VAWT, VAWT with GF and VAWT with SUD in $TSR = 2.64$.

Case	C_{l-ave}	C_{d-ave}	C_{l-ave}/C_{d-ave}
Bare VAWT	0.2175	0.0973	2.2360
VAWT with GF	0.3657	0.1614	2.2663
VAWT with SUD	0.3829	0.1697	2.2563

The ratio of C_{l-ave}/C_{d-ave} in Table 7.2 shows that GF produces a slightly higher ratio than SUD, indicating that VAWT with GF can generate more power than SUD. GF can reduce the amplitude of C_{li} and C_{di} variations of bare VAWT (see Figure 7.6), showing that GF can ease the dynamic stall of VAWT in medium regime of $TSRs$. The C_{di} distributions shown in Figure 7.6 (b) and the C_{d-ave} value in Table 7.2 confirm that both GF and SUD increase the drag force generation compared to bare VAWT, indicating that SUD no longer can decrease the drag force as it does in low regime of $TSRs$. In this TSR regime, the rotational speed is already sufficiently high. The further wind speed increment due to SUD will have a negligible effect on the higher rotational turbine speed. In addition, this can cause the blockage effect (e.g., the rotor can act as an obstructed solid wall due to high rotational speed) to the flow with higher vibrations and drag losses (Bakırcı and Yılmaz, 2018). Nevertheless, there are considerable improvements of lift force by both GF and SUD (see Figure 7.6 (a)) compared to bare VAWT, which will suppress the adverse effects from the increment of drag force. Therefore, GF and SUD can still achieve higher ratios of C_{l-ave}/C_{d-ave} (see Table 7.2), resulting in the improvement of the C_{p-ave} value of VAWT.

7.1.3 High regime of $TSRs$ (representative $TSR = 3.3$)

In high regime of $TSRs$, GF has significantly reduced the ability to improve the power generation of VAWT compared to that in medium regime of $TSRs$ (e.g., the C_{p-ave} improvement is now reduced to about 41.36%). However, this does not happen for SUD, as it continues to produce a similar amount of C_{p-ave} improvement compared to that in medium regime of $TSRs$ (e.g., the C_{p-ave} improvement is about 52.5%). Figure 7.7 depicts a comparison of C_{mi} distributions, and it shows that the GF can eliminate the negative moment production whilst the positive moment production maintains quite similar to bare VAWT. However, VAWT with SUD behaves differently regarding its C_{mi} distributions, which significantly improves positive moment production compared to bare VAWT and

slightly improves the negative moment. Hence, the average value of moment production of the VAWT with SUD is larger than for a VAWT with GF and for the bare VAWT, and this is the cause of a higher C_{p-ave} value for the VAWT with SUD in a higher TSR regimes.

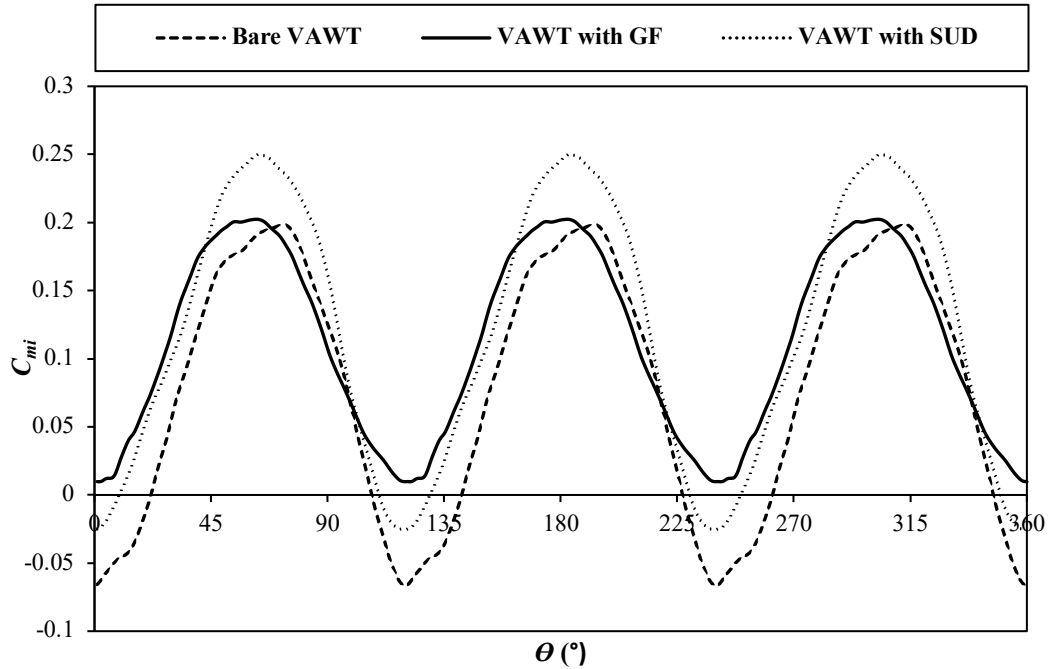
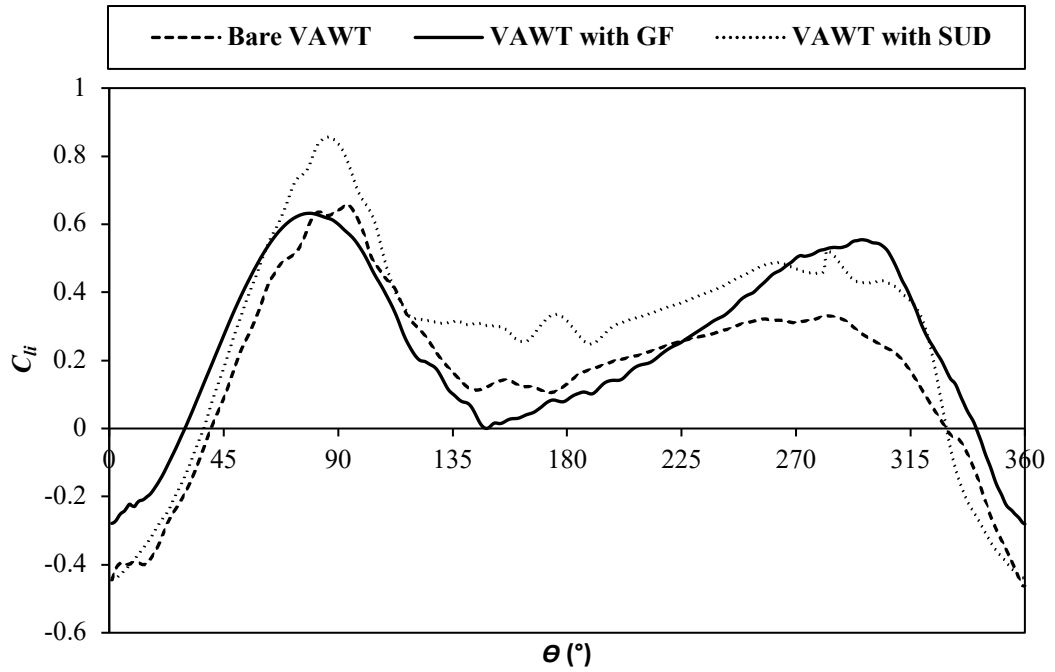


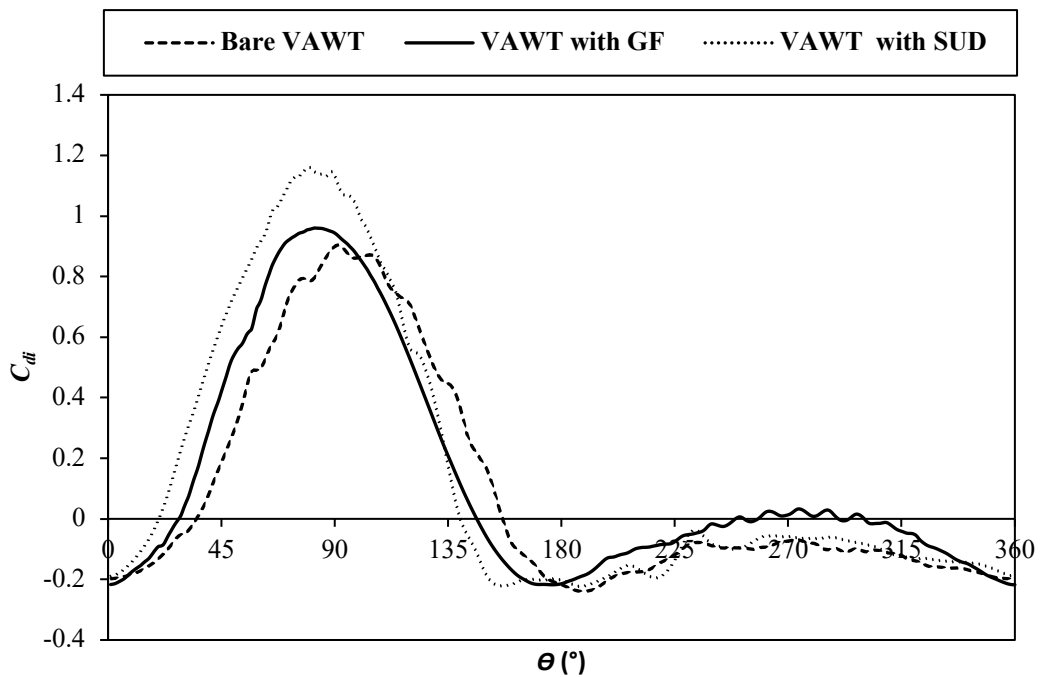
Figure 7.7 C_{mi} comparison between bare VAWT, VAWT with GF and VAWT with SUD in $TSR = 3.3$.

Table 7.3 Comparison of C_{l-ave} , C_{d-ave} and C_{l-ave}/C_{d-ave} over one turbine revolution between bare VAWT, VAWT with GF and VAWT with SUD in $TSR = 3.3$.

Case	C_{l-ave}	C_{d-ave}	C_{l-ave}/C_{d-ave}
Bare VAWT	0.1730	0.0937	1.8460
VAWT with GF	0.2430	0.1309	1.8561
VAWT with SUD	0.2802	0.1507	1.8597



(a)



(b)

Figure 7.8 Comparison of (a) C_{li} and (b) C_{di} between bare VAWT, VAWT with GF and VAWT with SUD in $TSR = 3.3$.

The C_{di} distributions in Figure 7.8 (b) and the C_{d-ave} value in Table 7.3 show that both SUD and GF can significantly increase the drag production of VAWT. Of which, SUD generates higher drag generation, possibly related to its blockage effects and higher

drag losses caused by the increase of turbine rotating speed in high regime of *TSRs*, similar to that in medium regime of *TSRs* discussed earlier (Bakırcı and Yılmaz, 2018). The C_{li} distributions and the C_{l-ave} value (see Figure 7.8 (a) and Table 7.3, respectively) illustrate that SUD produces the highest lift generation compared to VAWT with GF and bare VAWT in this high *TSR* regime, and overall SUD generates the highest C_{l-ave}/C_{d-ave} ratio. It confirms that in high regime of *TSRs*, it is more effective to improve the power generation of VAWT by improving the wind speed and directing the wind towards the frontal turbine area via SUD rather than controlling its dynamic stall via GF. It is possibly due to the fact that in high regime of *TSRs*, the flow around the VAWT has the lowest level of flow unsteadiness. This is mainly due to the smaller values beyond the static stall *AoAs* in high regime of *TSRs*, compared to low and medium regimes of *TSR*. This means that the dynamic stall is not as significant as that in low and medium regimes of *TSRs* (Malael, Dumitrescu and Cardos, 2014). Hence, the capability of GF to reduce the dynamic stall of VAWT will not have full effectiveness in this regard. Moreover, the additional drag generation caused by GF makes its performance enhancement in high regime of *TSRs* not as good as in low and medium regimes of *TSRs*.

7.2 Effect of Gurney Flap and Straight Upstream Deflector Combination on the Performance of VAWT

From the discussions above, it is clear that the performance of the VAWT in terms of power generation can be improved by using either flow augmentation devices (e.g., a SUD) and/or dynamic stall control devices (e.g., a GF) in all *TSR* regimes. These two devices can also improve the self-starting ability of a VAWT in low regime of *TSRs*. In particular, SUD can improve the power generation of VAWT by increasing the incoming wind speed and guiding the wind towards the rotor area of the turbines. Meanwhile, GF can ease the dynamic stall of VAWT so that to enhance its power generation. However, SUD will induce higher flow unsteadiness than bare VAWT and VAWT with GF, as it generates stronger wake vortices and GF will increase the drag production of VAWT compared to bare VAWT in all *TSR* regimes. Hence, it is worthwhile to examine the combined effect of both flow augmentation device and dynamic stall control device to improve the performance of VAWT, particularly in high regime of *TSRs*. Based on the results of a stand-alone device study, SUD can increase the lift generation of VAWT to improve the lift-to-drag ratio, whilst GF can reduce the flow unsteadiness induced by SUD.

Therefore, in this section, a study of combining GF and SUD to improve the performance of VAWT is carried out and results are compared with VAWT with a stand-alone GF or SUD, respectively. Same as previous studies, all three TSR regimes in low (representative $TSR = 1.44$), medium (representative $TSR = 2.64$) and high (representative $TSR = 3.3$) are considered to identify optimal performance enhancement in each TSR regime.

7.2.1 The geometry, model, grid generation and numerical setup

GF used in this combination device has a GF's optimum geometry design in medium and high regimes of $TSRs$ (i.e., GF with 3% c of height and 90° mounting angle mounted at the end of trailing-edge of VAWT's blade). Furthermore, this combination device implements SUD with base geometry (see Table 6.1) located both in upward and downward of VAWT's upstream (see Figure 6.4 (b)).

This 2D VAWT with SUD and GF study implements all models and numerical setups used in validated 2D VAWT (see Chapter 4). Similar to VAWT with stand-alone GF and VAWT with stand-alone SUD, the C-grid is adopted in this study (see Appendix E, Section E.1). The grids in the rotating core are adopted from 2D VAWT with the GF model (see Figure 5.3 (a) and 5.4 (a)). In the far-field sub-domain, the grids follow VAWT with SUD with both configuration models (see Figure 6.2 (b) and 6.3).

7.2.2 Comparison between VAWT with GF and SUD, VAWT with stand-alone GF, VAWT with stand-alone SUD and bare VAWT

Table 7.4 gives the comparison between VAWT with both GF and SUD, VAWT with a stand-alone GF and VAWT with a stand-alone SUD, respectively, in terms of the predicted C_{p-ave} of VAWT. Unexpectedly, combining a GF and SUD does not produce a higher C_{p-ave} than merely using either a GF or a SUD as performance enhancements of the VAWT in all TSR regimes. However, the GF and SUD combination still improves the C_{p-ave} of the bare VAWT in all TSR regimes.

Table 7.4 C_{p-ave} comparison between VAWT with GF and SUD, VAWT with GF, VAWT with SUD and bare VAWT.

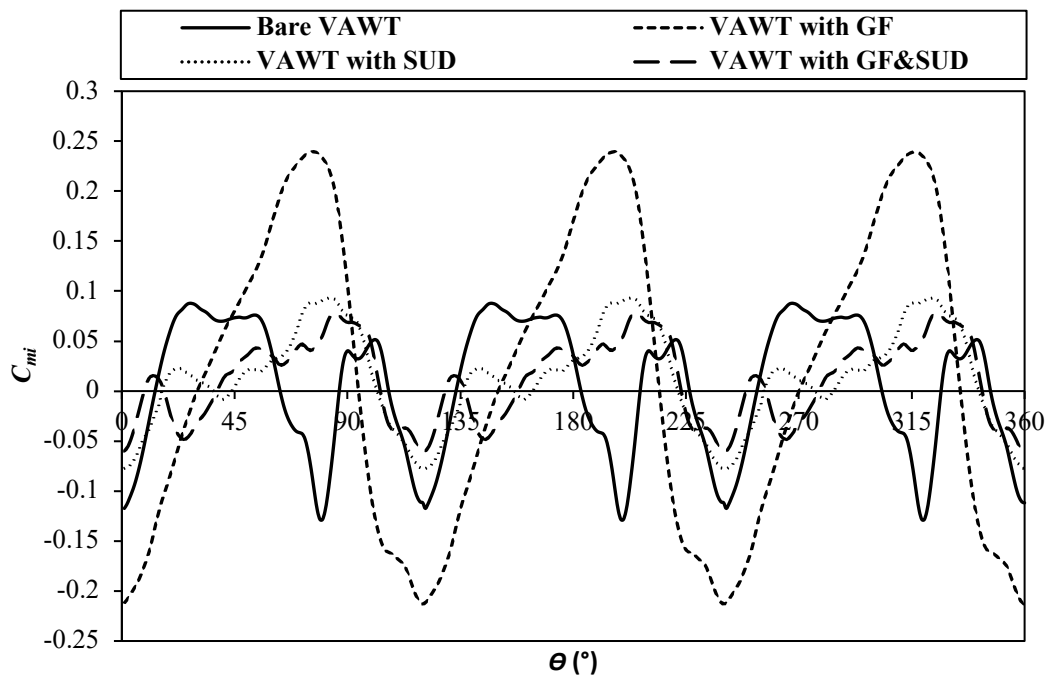
TSR	C_{p-ave}			
	Bare VAWT	GF	SUD	GF & SUD
1.44	0.0085	0.0196	0.0193	0.0157
2.64	0.3174	0.5394	0.4846	0.3791
3.3	0.2617	0.3699	0.3991	0.3461

Figure 7.9 illustrates the effect of VAWT with GF and SUD combination on the C_{mi} distributions compared to VAWT with a stand-alone GF or SUD in all TSR regimes. Overall, it shows that SUD has stronger influences on the change of flow characteristics than GF, as the C_{mi} distributions of VAWT with GF and SUD inherit similar behaviours of VAWT with a stand-alone SUD. The vorticity contours in Figure 7.10 further confirm that VAWT with GF and SUD induces similar or even stronger vortices compared to VAWT with a stand-alone SUD. Therefore, combining flow augmentation devices such as SUD with dynamic stall control devices such as GF will not improve the performance of VAWT compared to VAWT with a stand-alone GF or SUD.

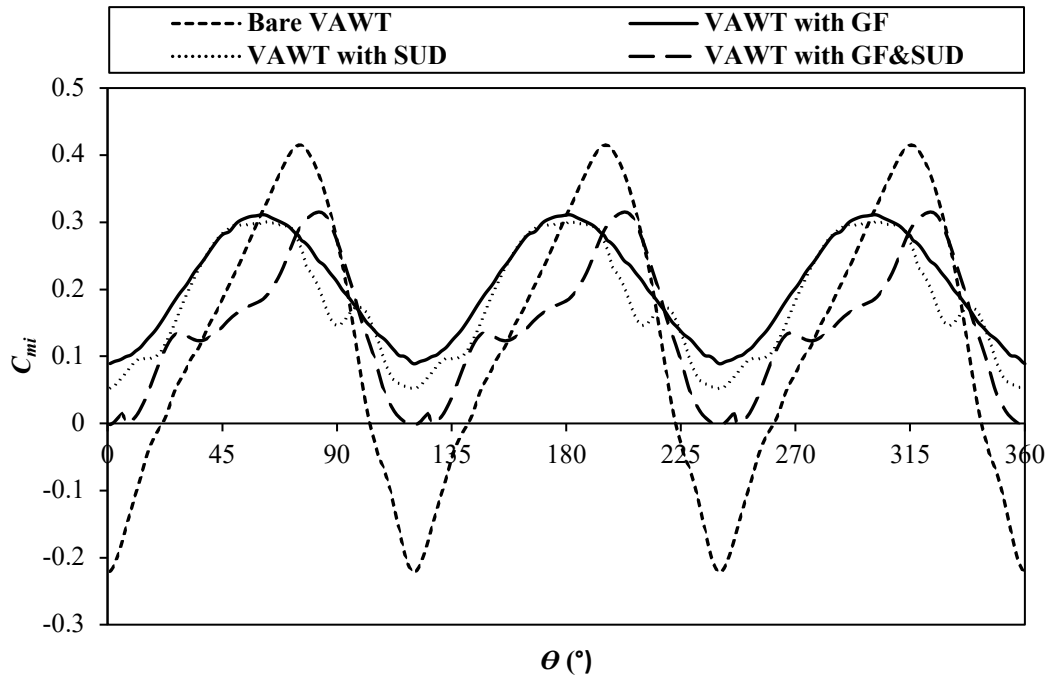
In low regime of $TSRs$, the combination of GF and SUD can improve the C_{p-ave} of bare VAWT by 84.49%, which is about 35.31% and 28.68% lower than a stand-alone GF and a stand-alone SUD, respectively. It is because that such a combination generates the highest decrease in negative moment production, compared to a stand-alone GF and/or a stand-alone SUD (see Figure 7.9 (a)). It indicates that GF addition can further decrease the negative moment production of VAWT. However, as discussed earlier in Section 7.1.1, GF will produce a high drag force of VAWT. Therefore, the higher turbine rotation speed caused by higher incoming wind speed (as a result of placing SUD in upstream of VAWT) will have a higher drag force on the GF. Hence, GF addition will significantly increase the drag whilst having a tiny lift force improvement. Moreover, combining GF with SUD can introduce stronger vortices generated and propagated downstream in the rotor area of VAWT, compared with a stand-alone SUD (see Figure 7.10 (a)). As a result, VAWT with GF and SUD produces the lowest peak values of positive moment generation, leading to the lowest value of C_{p-ave} improvement.

Meanwhile, a combination of GF and SUD generates the worst C_{p-ave} improvement in medium regime of $TSRs$, compared to both low and high regimes of $TSRs$. It can only increase the C_{p-ave} of bare VAWT by about 19.43%. It is significantly lower compared to a stand-alone GF and a stand-alone SUD that can improve the C_{p-ave}

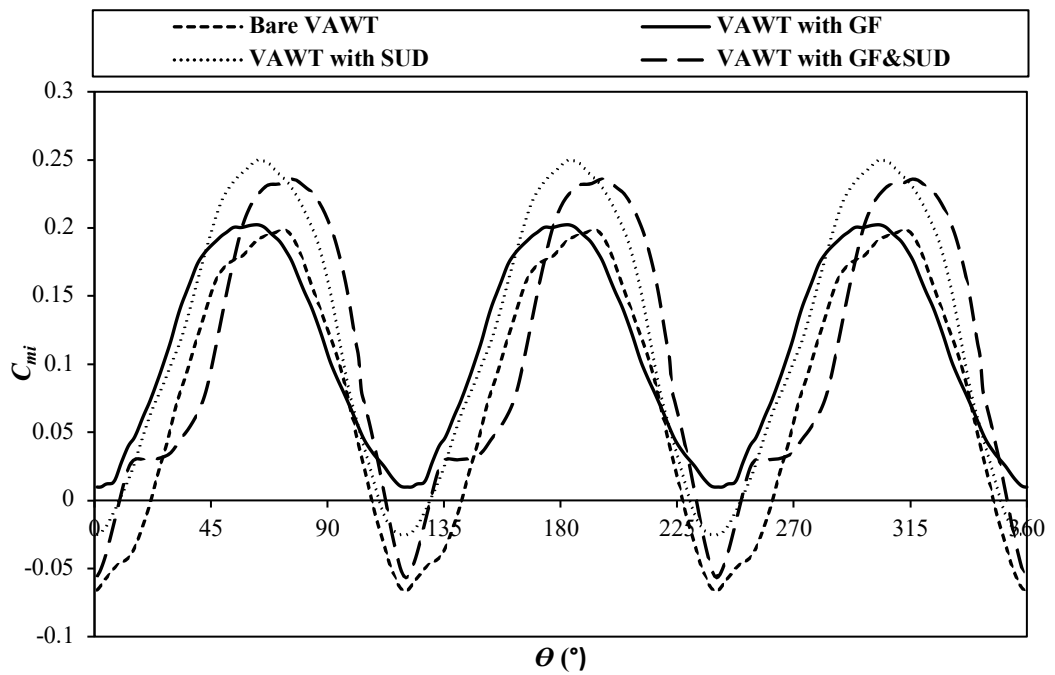
of bare VAWT by 69.94% and 52.6%, respectively. VAWT with GF and SUD combination generates a similar peak value of positive moment production (i.e., around 0.3) with VAWT with a stand-alone GF and VAWT with a stand-alone SUD. However, this combination can reintroduce the negative moment production of VAWT in medium regime of $TSRs$ (see Figure 7.9 (b)). The C_{mi} distributions are also more vibrant compared to VAWT with a stand-alone SUD. Similar to those cases in low regime of $TSRs$, GF addition will generate higher drag force, and whilst the rotational speed increases in medium regime of $TSRs$, the drag generation will also increase compared to that in low regime of $TSRs$. The vortex generation is also higher than VAWT with a stand-alone SUD (see Figure 7.10 (b)). In the meantime, the lift force improvement is not so significant, as the turbine rotational speed is already high. Hence, there is only a small improvement in the averaged C_m value, resulting in low improvement of C_{p-ave} .



(a)



(b)



(c)

Figure 7.9 C_{mi} comparison between bare VAWT, VAWT with GF, VAWT with SUD and VAWT with GF and SUD in (a) $TSR = 1.44$, (b) $TSR = 2.64$ and (c) $TSR = 3.3$.

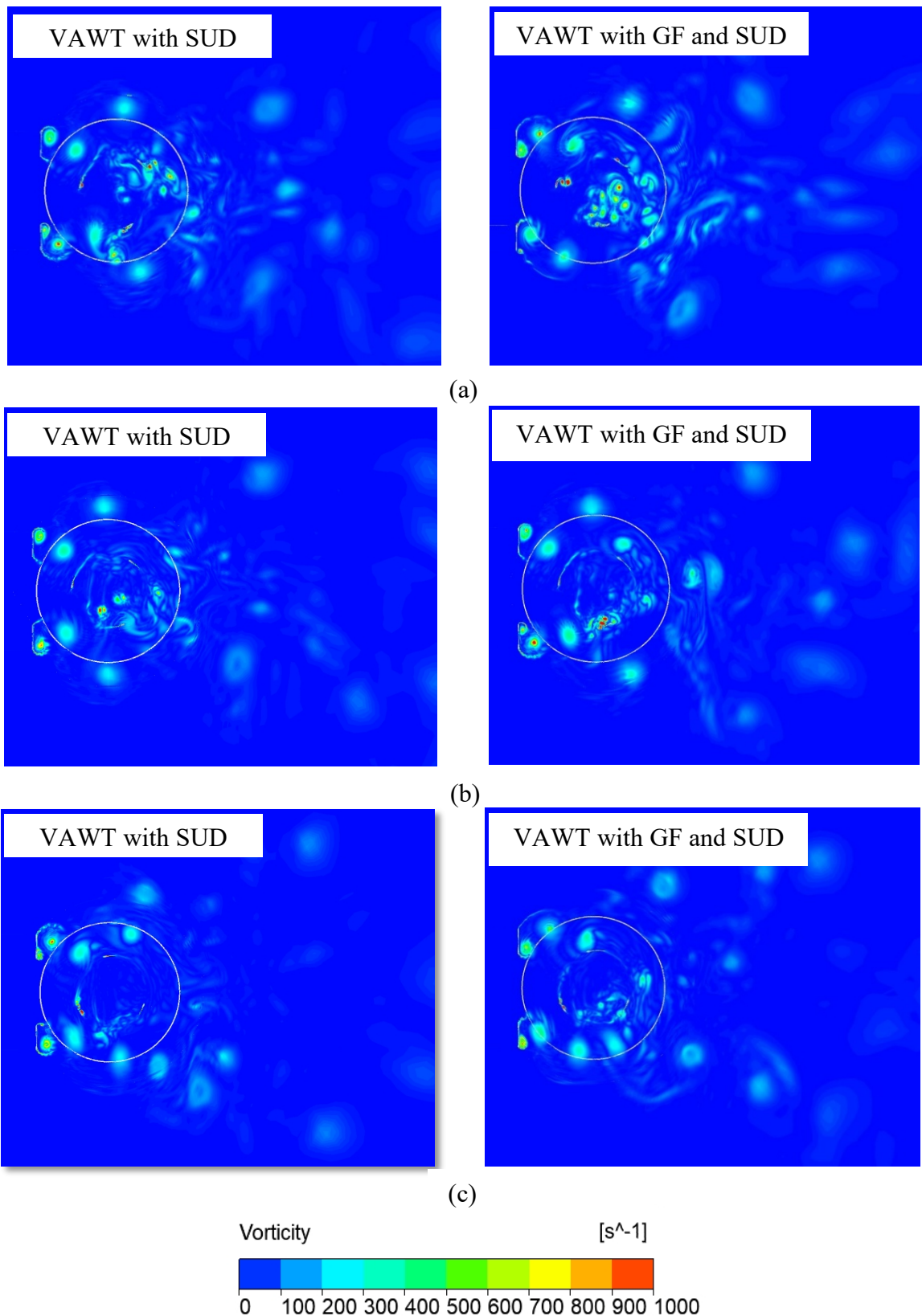


Figure 7.10 Comparison of z -vorticity (ζ) contours between VAWT with SUD and VAWT with GF and SUD in (a) $TSR = 1.44$, $\theta = 90^\circ$ (b) $TSR = 2.64$, $\theta = 90^\circ$ and (c) $TSR = 3.3$, $\theta = 135^\circ$. The circles in white solid lines represent the rotating core sub-domain.

For high regime of $TSRs$, C_{p-ave} improvement of VAWT with GF and SUD also reduces compared to VAWT with a stand-alone GF and VAWT with a stand-alone SUD. However, this reduction is the lowest compared to those obtained in low and medium regimes of $TSRs$. In high regime of $TSRs$, VAWT with GF and SUD combination can still generate C_{p-ave} improvement of about 32.29%, which is 30% and 9% lower than C_{p-ave} improvement of VAWT with a stand-alone SUD and VAWT with a stand-alone GF, respectively.

The C_{mi} distributions seen in Figure 7.9 (c) demonstrate that the combination of GF and SUD still can enhance the positive moment generation of bare VAWT. Nonetheless, such an improvement of positive moment generation is lower than VAWT with a stand-alone SUD. Furthermore, the GF and SUD combination can only slightly reduce the negative moment production of bare VAWT. It generates the lowest reduction of negative moment production compared to a stand-alone GF and a stand-alone SUD. Hence, similar to those cases in low and medium regimes of $TSRs$, the VAWT with GF and SUD combination do not positively influence the C_{p-ave} improvement of VAWT. In this scenario, GF can no longer ease the dynamic stall of VAWT as it does in a stand-alone GF case, and the ability of GF to ease the dynamic stall of VAWT is also not as effective as that in high regime of $TSRs$. Furthermore, GF will introduce more drag force as the rotational speed increases (compared to bare VAWT) due to the increase of incoming wind speed caused by SUD. It is confirmed by the C_{mi} distributions showing that the GF and SUD combination introduces a small amplitude fluctuation in the C_{mi} distributions. Moreover, the vorticity contours show that the GF and SUD combination induces stronger vortices generation than a stand-alone SUD (see Figure 7.10 (c)). Therefore, the combination of GF and SUD will lead to the smallest C_{p-ave} improvement compared to a stand-alone GF and a stand-alone SUD in high regime of $TSRs$.

7.3 Chapter Summary and Further Works

A comparison study between the use of dynamic stall control device (GF) and flow augmentation device (SUD) as performance enhancement of VAWT in all TSR regimes has been performed by CFD numerical simulations. In addition, a new attempt by combining GF and SUD is also carried out. The results are compared with a stand-alone GF and a stand-alone SUD. It is found that a stand-alone GF can generate a better improvement of the C_{p-ave} of VAWT in low and medium regimes of $TSRs$, whilst a stand-alone SUD can improve the C_{p-ave} of VAWT higher than that of a stand-alone GF in high

regime of *TSRs*. Both GF and SUD have shown the reduced capability to enhance the C_{p-ave} of VAWT as the *TSR* regime increases from low to high. Compared to SUD, GF has a higher loss of its ability to enhance the C_{p-ave} of VAWT in high regime of *TSRs* (e.g., compared to medium regime of *TSRs*, VAWT with GF loses this ability by about 28% whilst VAWT with SUD only loses around 0.3%). It indicates that the GF is more suitable to be used as the VAWT performance enhancement device in low and medium regimes of *TSRs* due to stronger dynamic stalls in these two *TSR* regimes than in high *TSR* regime. Therefore, the ability of GF to control dynamic stalls can be utilised more effectively in low and medium regimes of *TSRs*. On the other hand, SUD is a better choice for performance enhancement of VAWT in high regime of *TSRs* because in this *TSR* regime, the flow is relatively stable (i.e., experience weaker dynamic stall and has a very low level of flow unsteadiness compared to other two *TSR* regimes) so that the dynamic stall control device is not fully functioning at this regime. Hence, to improve the performance enhancement of VAWT, it is more crucial to increase the incoming wind speed and guide the wind towards the rotor area of VAWT to improve the rotational speed of the turbines.

Furthermore, results from an investigation of combining the GF and SUD to apply flow augmentation device and dynamic stall control device simultaneously have shown that this combination cannot enhance the improvement of C_{p-ave} achieved by a stand-alone GF or a stand-alone SUD in all *TSR* regimes. Compared to VAWT with GF or VAWT with SUD, VAWT with GF and SUD combination generates the lowest C_{p-ave} improvement of VAWT in all *TSR* regimes. It is due to stronger vortex generation introduced by combination GF and SUD as SUD alone mainly changes the flow characteristics. Meanwhile, the GF loses its ability to ease the dynamic stall of VAWT and introduces a higher drag force. It further confirms that GF is more suitable as a performance enhancement device for VAWT in low and medium regimes of *TSRs*, whilst SUD is a better choice for improving VAWT performance in high regime of *TSRs*.

Note that all the works above use a 2D CFD model, which is usually more relevant in the centre area of the turbine and turbine with a high aspect ratio. Hence, it is essential to evaluate those performance improvements above in a 3D CFD model to account the effect of the flow around the tip of the blade of VAWT. Thus, in the following two chapters, a 3D model of VAWT will be investigated. In addition, as GF generates the best improvement of C_{p-ave} in the optimum *TSR*, 3D model VAWT with GF will also be

studied. An attempt to reduce the drag production caused by GF is also performed by doing 3D modifications of GF (i.e., by introducing slits and holes in GF).

Chapter 8: 3D CFD Validation of Lift-Driven VAWT

Although the 2D VAWT model would be sufficient to predict the performance and aerodynamic flow characteristics, it still overestimates the 3D experimental results and has limitations for a VAWT with a high aspect ratio as the 3D and blade tip effects are neglected in 2D studies. In addition, performance enhancements caused by the addition of devices such as a GF or SUD probably are not as high as those shown in the 2D model if the 3D and blade tip effects are included. Therefore, to verify these factors, this chapter presents the validation of CFD simulation using a 3D VAWT model.

This chapter consists of five sections. In the first section is explained the 3D model used in this study. Then, the grid discretisation and grid independence study are detailed in the second and third sections, respectively. The result of the power coefficient prediction of the 3D model is validated using 3D experimental results and compared with the numerical results of the 2D model in the fourth section. This section also presents the blade aerodynamic characteristics of the VAWT predicted by the 3D model. Lastly, the chapter summary and further work are discussed in the fifth section.

8.1 Model Description

For the 3D study, the numerical specifications of the validated 2D model with C-grid against the 3D experimental result of Castelli, Englaro and Benini (2011) (see Chapter 4, Section 4.6) are adopted. Due to the symmetrical condition in the mid-span section of VAWT, this 3D study only models the upper half of the rotor blades. Meanwhile, the turbine mid-span plane is considered as the symmetric boundary. This approach is utilised to reduce computational costs (Howell et al., 2010). Figure 8.1 illustrates the detail of the shape and dimensions of the 3D domain and the location of inlet, outlet, and symmetric boundary conditions. Note that, the dimensions of the mid-span plane of the 3D model are the same as the baseline of 2D domain size (see Chapter 4, Section 4.6.1). The height of the 3D domain is about 31 times that of the turbine rotor's radius, i.e., around 11 turbine heights. This height is large enough for the 3D model based on previous studies [Elsakka, 2020], and only half of the rotor is modelled in this study through applying symmetry boundary conditions.

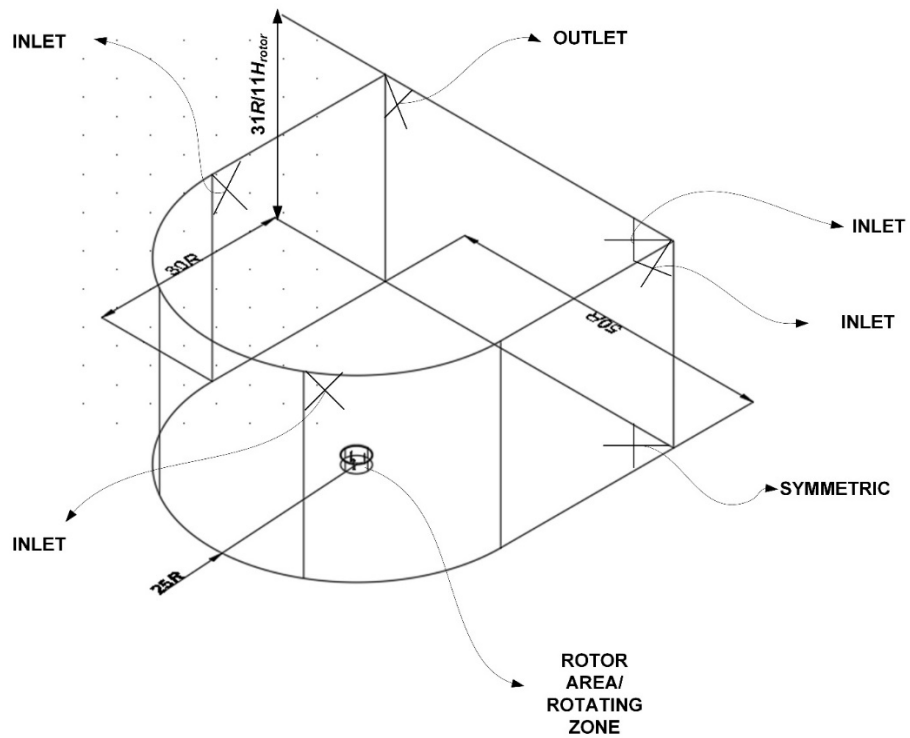
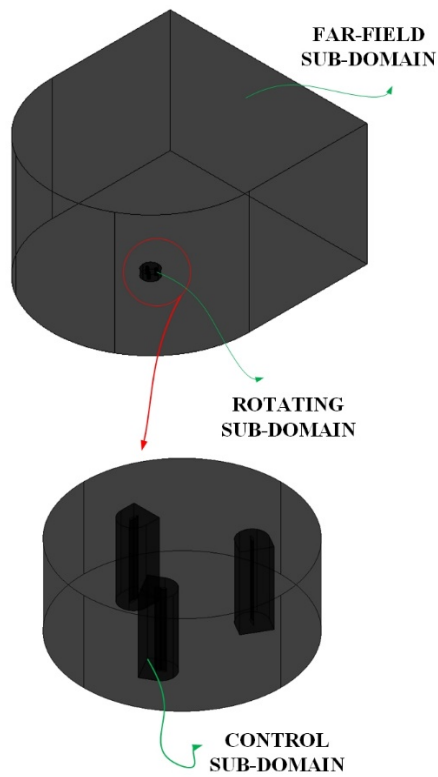
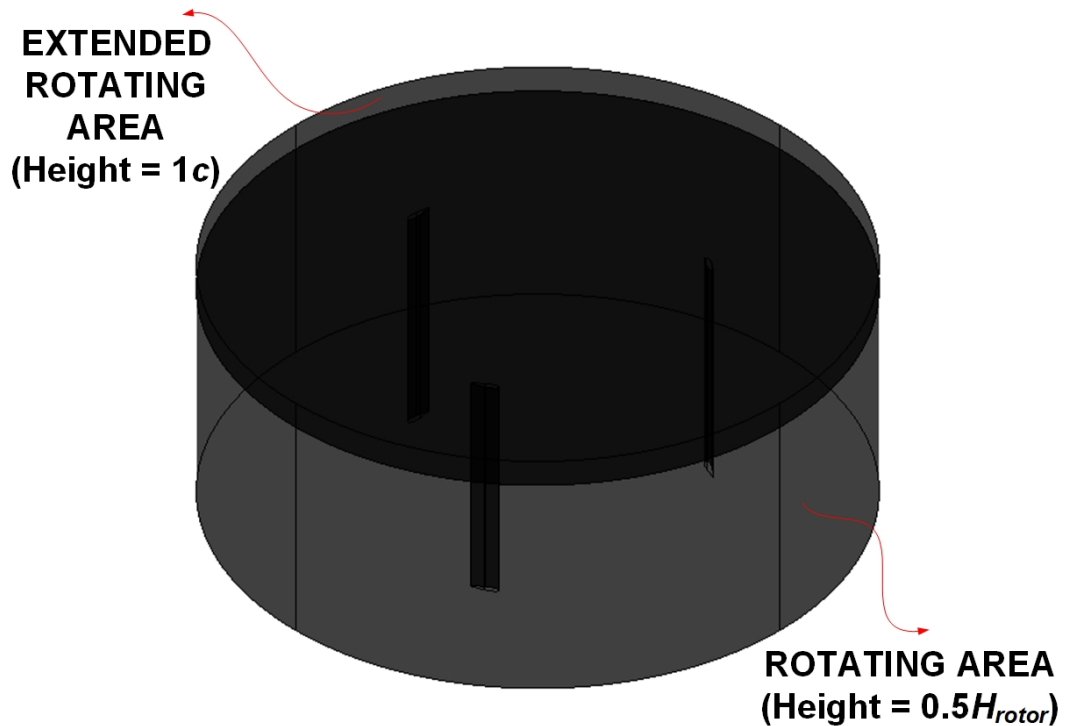


Figure 8.1 Main boundary conditions and dimensions of the 3D computational domain (the drawing is not in scale).



(a) The detail of sub-domains in the 3D model (the drawing is not in scale).



(b) Rotating sub-domain with extended height

Figure 8.2 3D computational domain and its sub-domains in detail (the drawing is not in scale).

The boundary conditions and domain discretisation settings of the 2D model, as explained in Chapter 4, Section 4.6.1, are adopted for the 3D model. Similar to the 2D domain, the 3D domain is divided into three sub-domains (see Figure 8.2 (a)), which represent the region around each blade (i.e., control sub-domain), the region around the rotor (i.e., rotating sub-domain) and the surrounding region (i.e., far-field sub-domain). A "fluid to fluid" non-conformal mesh interface is applied to connect these two sub-domains between the rotating and far-field sub-domains. Meanwhile, the boundaries between the three control and rotating sub-domains are treated as interior to ensure the continuity of the fluid flow. In order to ensure that the model accommodates the tip of the blade correctly, the height of the rotating zone is extended to around one chord blade (0.0858 m) away from the tip of the blade (see Figure 8.2 (b)). This extended height is enough to accommodate the vortex development around the blade's tip, as a previous study with a similar Reynolds number showed that the maximum vortex size is about 0.04 m above the blade's tip with 0.06 m chord length (Hofemann et al., 2008).

Based on the 2D model turbulence model study (see Chapter 4, Section 4.5), SBES with TSST turbulence model is adopted for the 3D model as it generates the

smallest discrepancy of power coefficient prediction compared to other turbulence models. Due to enormous computational cost, this 3D model is only evaluated in the optimum TSR value of the baseline model of VAWT (i.e., $TSR = 2.64$). In order to reduce the computational cost, this 3D study starts the data sampling whilst the averaged C_m over one turbine revolution variations between two neighbouring revolutions is less than 1%, following the studies by Castelli, Englaro and Benini (2011). The C_{m-ave} drops less than 1% compared to the previous revolution after 10 revolutions for the 3D model using the SBES Transition SST turbulence model (see Figure 8.3). Therefore, this 3D study collects data from the 11th revolution.

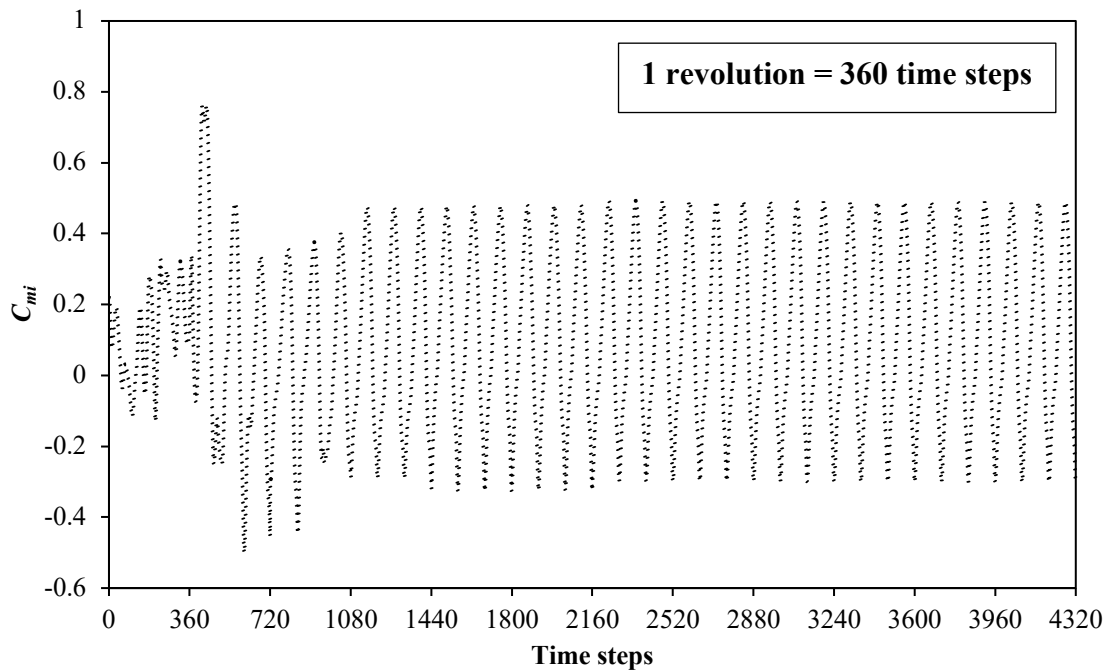


Figure 8.3 C_{mi} over the first 12 revolutions/cycles.

8.2 3D Grid Discretisation

For grid discretisation, the 3D model adopts validated grid discretisation of the 2D model in the rotating and control sub-domains (see Chapter 4, Section 4.6.1) with 174 elements around the blade cross-section. In the span-wise direction, the 3D model has 30 elements along with the half blade height. Meanwhile, the extended height of the rotating zone is divided into ten elements in the span-wise direction. Note that, the grids are clustered near the tip of the blade (see Figure 8.4).

In order to reduce the total number of elements and computational cost, grid discretisation of the 3D far-field sub-domain is different from the 2D model. As the far-field sub-domain is large, this study decides to have relatively large elements in this sub-

domain. Fine grids around the rotor zone and along the turbine wake zone are required to have good accuracy of CFD results. Meanwhile, a relatively large element size can be applied elsewhere to reduce the total number of cells and hence the computational cost. Therefore, this study applies CutCell meshing technique (AnsysInc, 2010) in the far-field sub-domain to reduce the total number of elements and computational cost. This technique assists grid discretisation by building predominantly a Cartesian grid. This grid mainly consists of hexahedral elements with a good aspect ratio everywhere in the subjected domain. Moreover, the CutCell meshing technique can maintain a high growth rate without producing any high skewed elements.

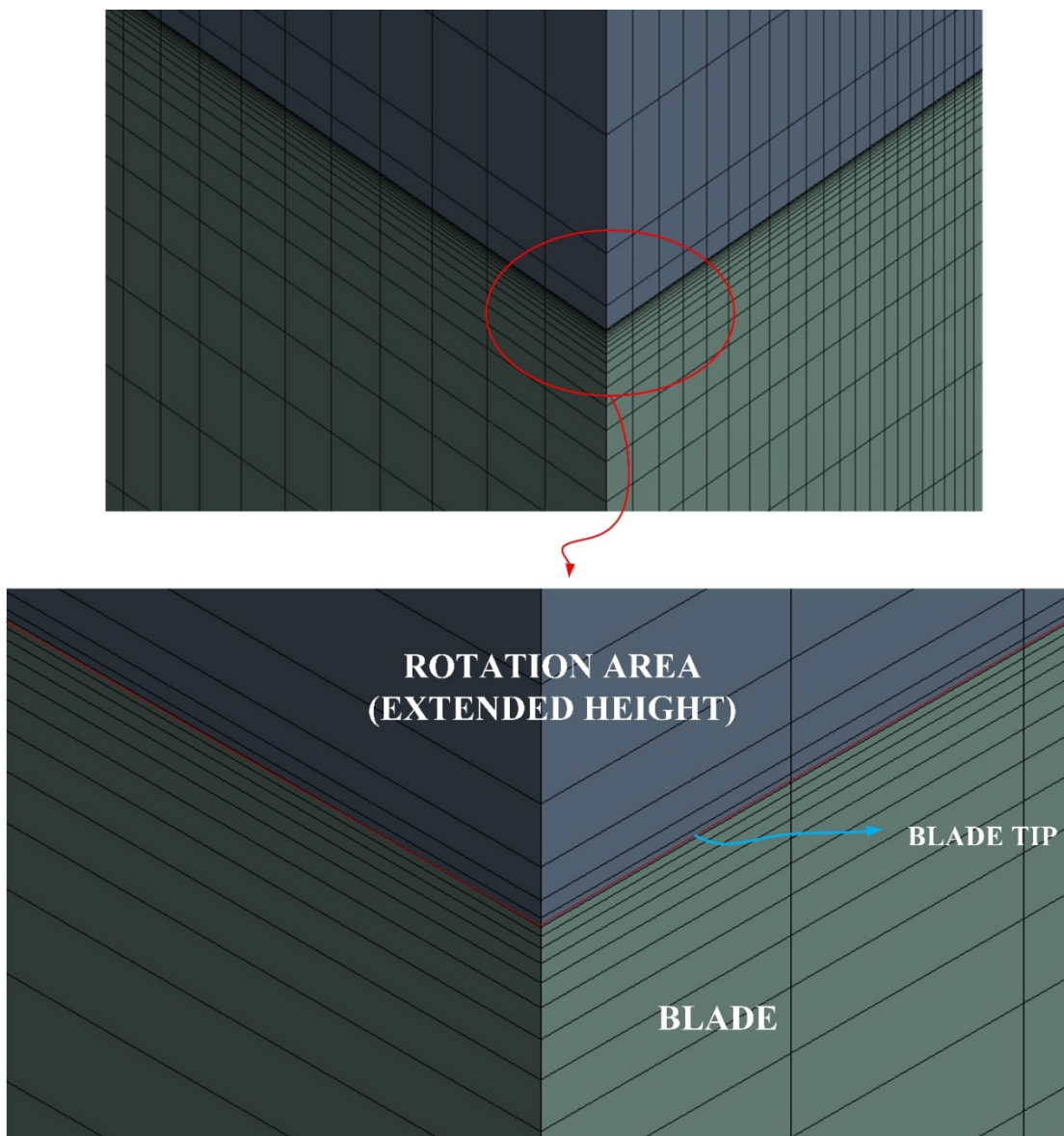


Figure 8.4 Clustered grid around the tip of the blade.

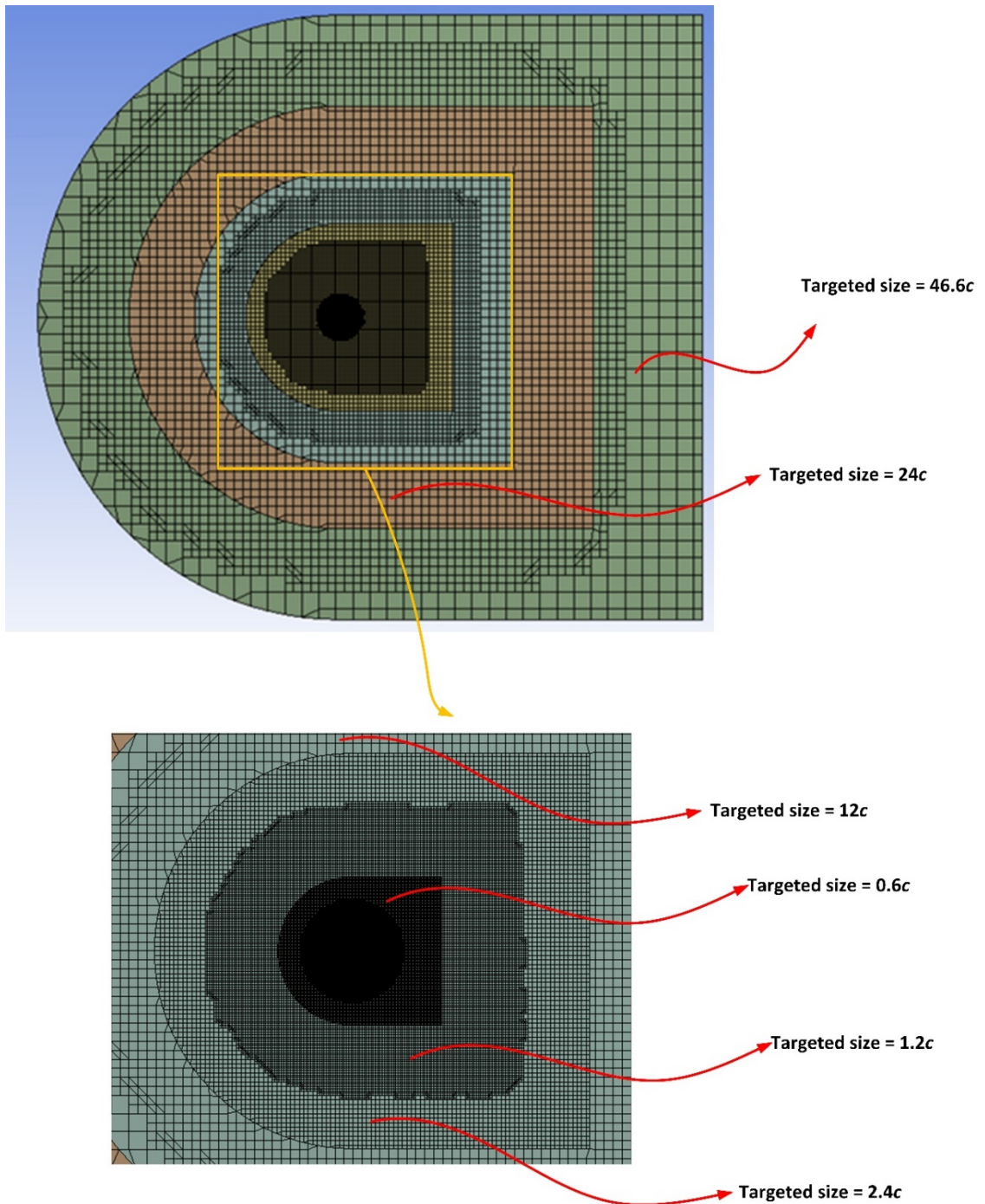


Figure 8.5 CutCell mesh around the far-field sub-domain.

This study adopts different sizing controls for Cutcell meshing to generate relatively finer grids near the rotor and wake regions. As shown in Figure 8.5, the CutCell meshing technique helps the grid generation process distribute the elements with different sizes more flexibly than the structured meshing technique. Hence, the total number of elements can be reduced in the far-field sub-domain. Nevertheless, it is crucial to keep in mind that the structured meshing technique offers a higher degree of control that is more

beneficial in generating grids around turbine blades due to the fine grid requirement in this area.

8.3 Grid Independence Study

As mentioned above, this 3D study adopts grid discretisation of the 2D model in the rotating and control sub-domains (see Chapter 4, Section 4.6.1) to ensure grid independence in x and y directions. Additionally, to achieve grid independence in span-wise direction (z -direction), this 3D study performs grid independence study by considering three different total numbers of elements (i.e., 35, 40 and 45 elements) along the span-wise direction. The results depicted in Figure 8.6 indicate no significant change in C_{mi} distribution between these three different grids. Furthermore, the difference of C_{m-ave} between grid with 35 elements and 40 elements along the span-wise direction is about 7.28%, whilst 1.48% C_{m-ave} difference is found between grid with 40 elements and 45 elements along the span-wise direction. Therefore, this 3D study adopts 40 elements along the span-wise direction for the rest of the study.

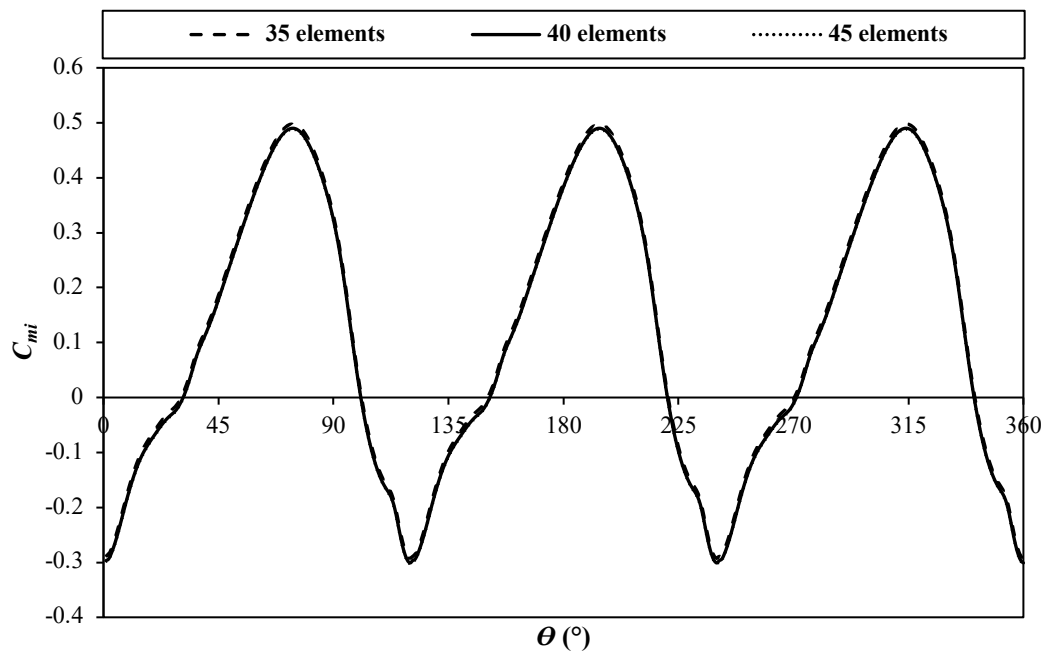


Figure 8.6 C_{mi} comparison of the 3D model with the different number of elements along the span-wise direction.

Moreover, due to the change of grid discretisation in the far-field sub-domain, this study also evaluates three different grids by changing the total number of elements to

ensure grid independence in the far-field sub-domain. The baseline grid has 5598471 elements. Two more grids are also generated to evaluate the effect of grid refinement on the computational results. These two grids are constructed by refining the baseline grid with two cell number ratios around 1.3 and 1.66 compared to the baseline grid (see Table 8.1). Note that, the number of elements along the blade cross-section (174 elements), the blade in span-wise direction (30 elements) and the extended height of rotating sub-domain (10 elements) are kept the same in these three constructed grids (i.e., baseline, finer and finest grids).

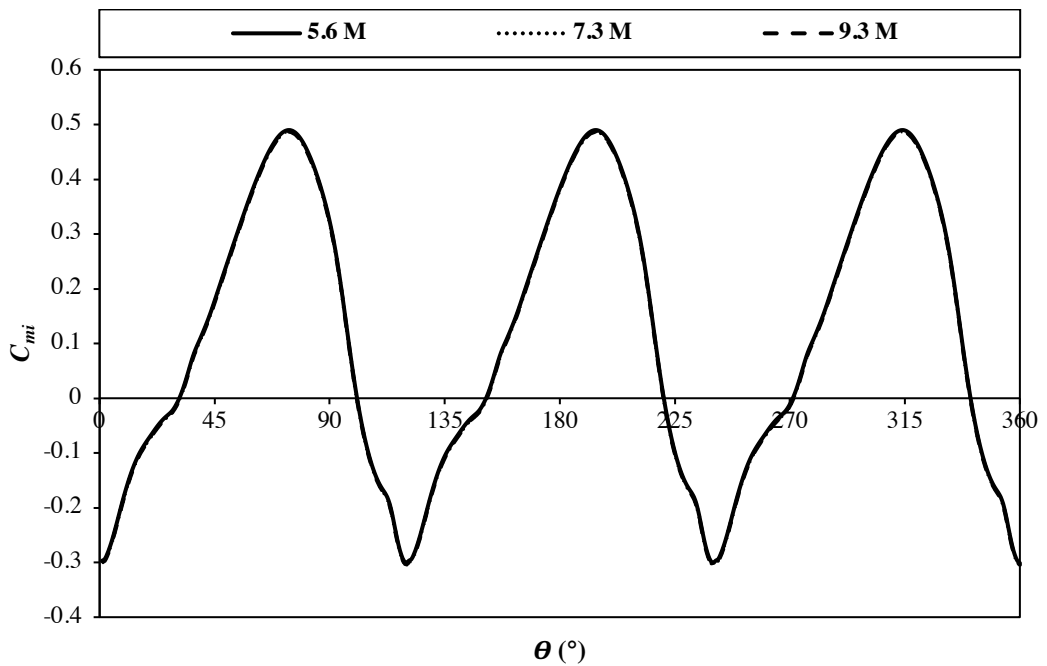


Figure 8.7 C_{mi} comparison of the 3D model with various grids.

Figure 8.7 shows the effect of the mesh refinement on the prediction of instantaneous moment coefficient. Based on simulations using SBES with Transition SST turbulence model, it can be seen that the 3D model results are relatively less sensitive to the grid refinement. The comparison of averaged moment coefficient indicates that although the grid is refined almost twice the baseline grid, the difference of C_{m-ave} is only about 2.91% (see Table 8.1). Hence, the baseline grid is chosen for further 3D studies.

Table 8.1 Details of the number of elements for each grid and its C_{m-ave} prediction.

Grid	The ratio between the number of cells relative to baseline grid	C_{m-ave}	% difference of C_{m-ave}
Baseline Grid	1	0.11124	–
5.6 M			
Finer Grid	≈ 1.3	0.10876	2.23
7.3 M			
Finest Grid	≈ 1.66	0.10700	2.91
9.3 M			

8.4 3D Results

8.4.1 Validation of averaged power coefficient

Table 8.2 shows the comparison of averaged power coefficient between experimental results of Castelli, Englaro and Benini (2011) and Castelli et al. (2010), several CFD results of the 2D model (Chapter 4 results; Wang et al., 2018; Castelli, Englaro and Benini, 2011) and CFD results of 3D model (i.e., results in this Chapter) at several span-wise positions along the half blade of the rotor (see Figure 8.8). It can be observed that at mid-span plane, 3D model result under-predicts the C_{p-ave} of experimental data whilst 2D model result slightly over-predicts it. The prediction of the C_{p-ave} of the 2D model is in agreement with other previous works (Wang et al., 2018; Castelli, Englaro and Benini, 2011). Understandably, the 3D model result under-predicts the C_{p-ave} of experimental data as the 2D model prediction of C_{p-ave} is already very close to the experimental data (about 0.47% discrepancy).

Compared to experimental data, the 3D model result under-predicts the C_{p-ave} by 7.47721% in the mid-span plane. As the measured position gets closer to the blade tip, the deviation between predicted 3D model C_{p-ave} and experimental data increases with the maximum discrepancy at 17.51727% at the blade tip. This tendency is in agreement with the study by Elsakka (2020) (see Table 8.3). Elsakka (2020) suggested that the deviation between predicted 3D model C_{m-ave} and the experimental data rises closer to the blade tip. Note that, the C_{m-ave} deviation between the 3D model and the experimental data in Elsakka (2020) case is higher than the present study in a similar span-wise position. It is understandable as the turbine's aspect ratio in Elsakka (2020) study is lower than the present study. Therefore, the tip effect is higher in Elsakka (2020) study compared to the

present study, resulting in higher differences of the C_{m-ave} value between mid-span and position closer to the blade tip of the blade.

On average, the 3D model result under-predicts the C_{p-ave} of experimental data by around 13.13468%. It means that using SBES with TSST turbulence model for 3D models only decreases CFD modelling accuracy in C_{p-ave} prediction. It is probably due to the fact that the ability of SBES with TSST turbulence model to generate a very close value of C_{p-ave} to the experimental result in the 2D model is mainly contributed by the accuracy of numerical predictions. This accuracy is related to the level of governing equations (RANS or hybrid RANS-LES or LES), numerical treatments (low or high schemes) and other models (e.g., turbulence models). It is mentioned in the previous study of Alam, Thompson and Walters (2017) that DES based hybrid RANS-LES turbulence models can over-predict the pressure decrease and the size of flow separation region in separated turbulent flow case. Hence the C_{m-ave} prediction of SBES with TSST turbulence model can be much lower than other investigated turbulence models, resulting in closer C_{p-ave} prediction to the experimental result in 2D CFD model. As a result, when this SBES with TSST turbulence model with the same parameters and settings as the 2D model is applied in the 3D model (which is closer to the experimental model), the accuracy of C_{p-ave} prediction of the CFD modelling is altered. Accordingly, further study in the future is needed to adjust this turbulence model to generate good accuracy in the 3D model.

Understanding that the accuracy of CFD modelling to predict C_{p-ave} value is reduced by implementing SBES with TSST turbulence model in 3D model, this study performs other simulations by applying URANS turbulence model (i.e., SST turbulence model) in 3D model. This turbulence model is chosen because it generates a low discrepancy in the 2D model, i.e., 13.77542%, in the evaluated TSR value ($TSR = 2.64$). Accordingly, there is still a reasonable discrepancy to be reduced for 3D model implementation. The result of the 3D model with SST turbulence model indicates that this model still over-predicts the C_{p-ave} of experimental result. However, the discrepancy decreases to 1.16629%. Consequently, the SST turbulence model has a good capability for C_{p-ave} prediction of the 3D CFD model in $TSR = 2.64$. Note that, the 3D model with SST turbulence model still inherits the lacking capability of the SST turbulence model to predict dynamic stall, trailing-edge roll up, and secondary vortices in the 2D model. For this reason, further experimental study to provide blade aerodynamic characteristics such as vorticity contour is necessary to validate the prediction of flow characteristics around the evaluated VAWT model.

Nonetheless, the discrepancy of C_{p-ave} between experimental and 3D model (using SBES with TSST turbulence model) results, i.e. 13.13468%, is still reasonable as previous studies of the 3D VAWT model using hybrid RANS-LES turbulence model have reported that the maximum discrepancy is between 9-16% (Su et al., 2019; Lei et al., 2017). Note that, the experimental study by Castelli et al. (2010) measured the rotor torque to calculate the C_p value of VAWT. Hence, it is believable that the experimental data is an averaged C_p value rather than a C_p value at a specific position along the span-wise direction of the blade.

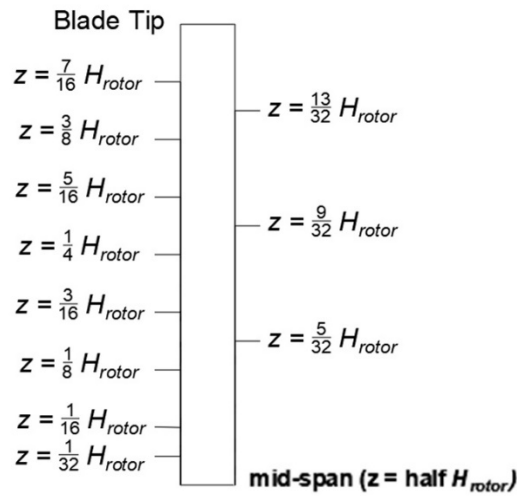
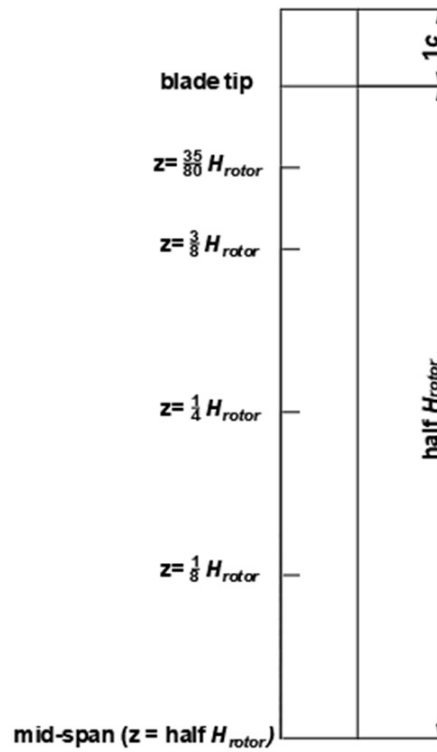


Figure 8.8 Sketch of the important span-wise positions along rotating sub-domain.

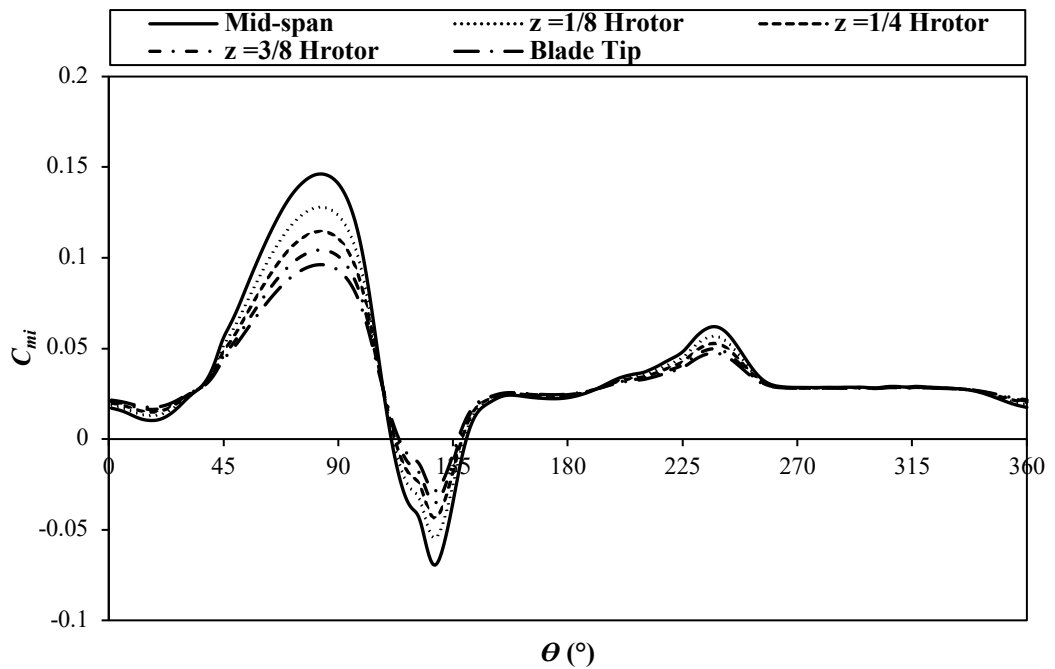
8.4.2 Blade aerodynamics characteristics

Figure 8.9 illustrates the instantaneous moment coefficient over one turbine revolution of blade 1 at several positions along the span-wise direction of the blade. It can be seen that the difference of instantaneous moment coefficient value along the span-wise direction of the blade is quite visible at $\theta = 45^\circ$ - 150° and $\theta = 210^\circ$ - 270° . At other azimuthal positions, the deviation of instantaneous moment coefficient along the span-wise direction of the blade is minimal. This behaviour is likely because the blade of VAWT experiences a large excursion of the angle of attack resulting in unsteady flow separation and possibly dynamic stall of the blade at $\theta = 45^\circ$ - 150° (Rezaeiha, Montazeri and Blocken, 2019). At $\theta = 210^\circ$ - 270° , the blade of VAWT interacts with the shed vortices from the blades further upstream (Rezaeiha, Montazeri and Blocken, 2019). Hence, at those azimuthal positions, the moment generation of the blade would be more affected by the blade tip, causing a significant deviation of the instantaneous moment

coefficient between different positions along the span-wise direction of the blade (see Figure 8.9).



(a)



(b)

Figure 8.9 (a) Sketch of the important span-wise positions along rotating sub-domain) and (b) C_{mi} of blade 1 at various positions along the span-wise direction of the blade.

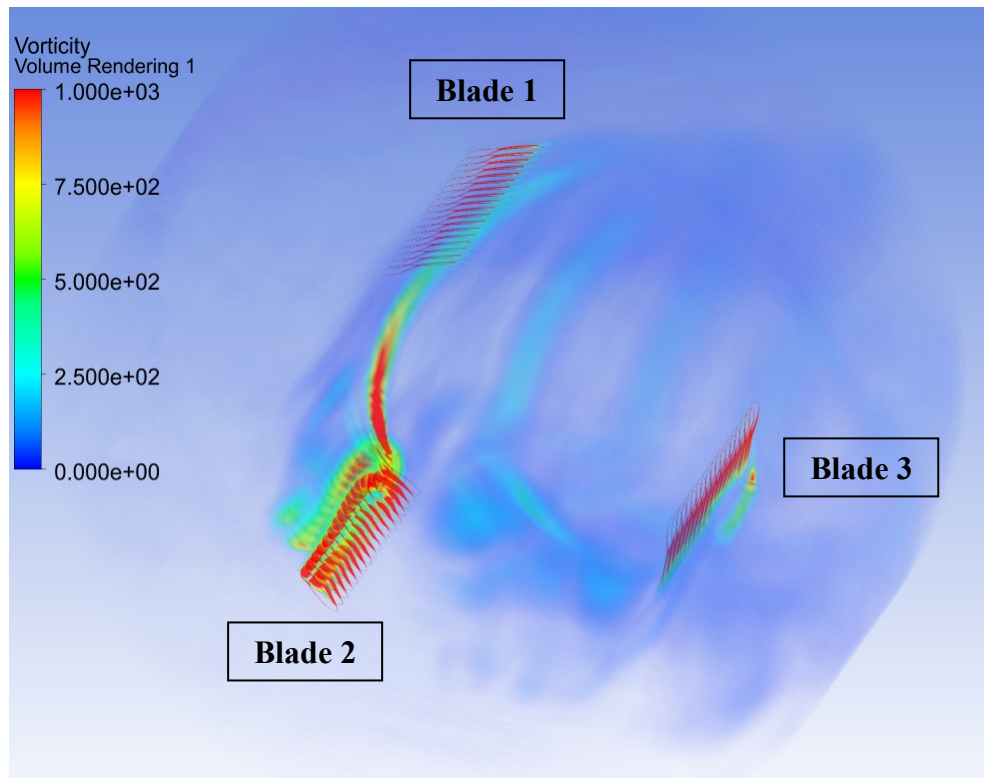
Table 8.2 Comparison of experimental data of power coefficient (Castelli, Englaro and Benini, 2011; Castelli et al., 2010) and predicted averaged power coefficient of 2D and 3D models.

Case	Turbulence Model	Span-wise location	C_{p-ave}	%difference with experiment	%difference with mid-span
Experiment (Castelli, Englaro and Benini, 2011; Castelli et al., 2010))	–	–	0.31741	–	–
2D CFD (Castelli, Englaro and Benini, 2011))	RKE	Mid-span	0.56937	79.37765	–
2D CFD (Wang et al., 2018))	RKE	Mid-span	0.30364	4.34027	–
2D CFD (Wang et al., 2018))	SST	Mid-span	0.37407	17.85093	–
2D CFD (present study)	RKE	Mid-span	0.37133	16.98658	–
2D CFD (present study)	SST	Mid-span	0.36114	13.77542	–
2D CFD (present study)	SBES with TSST	Mid-span	0.31892	0.47425	–
3D CFD (present study)	SBES with TSST	Mid-span	0.29368	7.47721	–
		$z = 1/32 H_{rotor}$	0.29039	8.51446	1.12107
		$z = 1/16 H_{rotor}$	0.28737	9.46516	2.14861
		$z = 1/8 H_{rotor}$	0.28203	11.14694	3.96630
		$z = 5/32 H_{rotor}$	0.27966	11.89430	4.77406
		$z = 3/16 H_{rotor}$	0.27746	12.58823	5.52406
		$z = 1/4 H_{rotor}$	0.27349	13.83716	6.87393

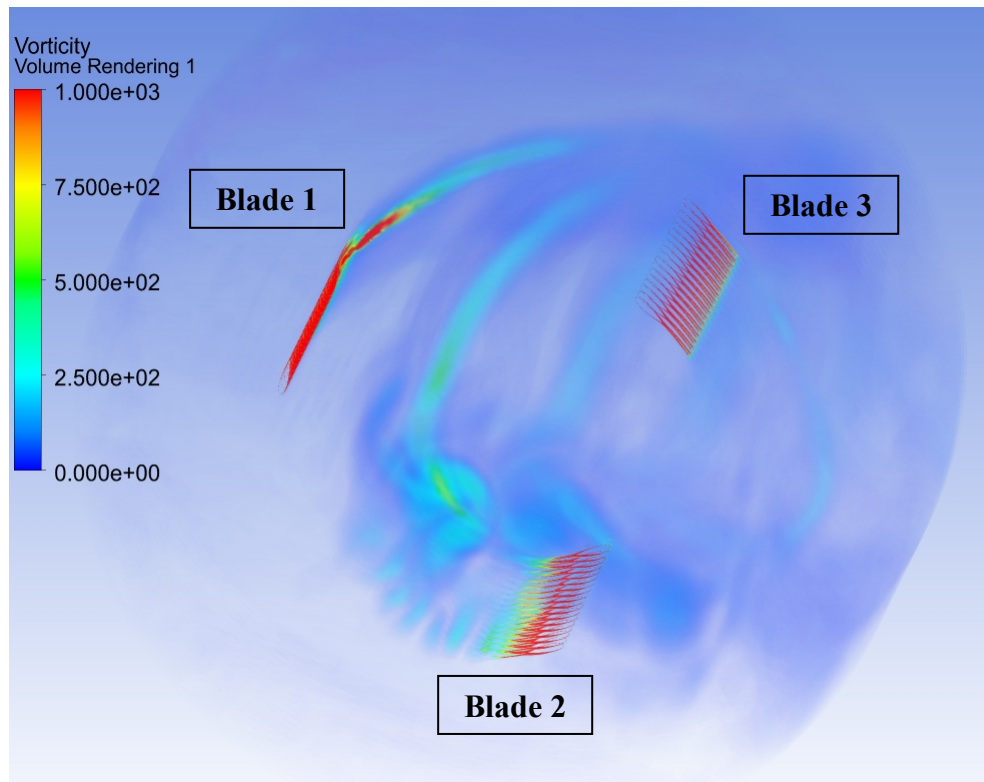
		$z = 9/32 H_{rotor}$	0.27170	14.40114	7.48349
		$z = 5/16 H_{rotor}$	0.27002	14.92985	8.05492
		$z = 3/8 H_{rotor}$	0.26696	15.89387	9.09685
		$z = 13/32 H_{rotor}$	0.26557	16.33453	9.57312
		$z = 7/16 H_{rotor}$	0.26424	16.75070	10.02292
		Blade tip	0.26181	17.51727	10.85144
		Averaged 3D	0.27572	13.13468	6.11467

Table 8.3 Comparison of averaged moment coefficient prediction between Elsakka (2020) and the present study at several locations along the span-wise direction of the blade.

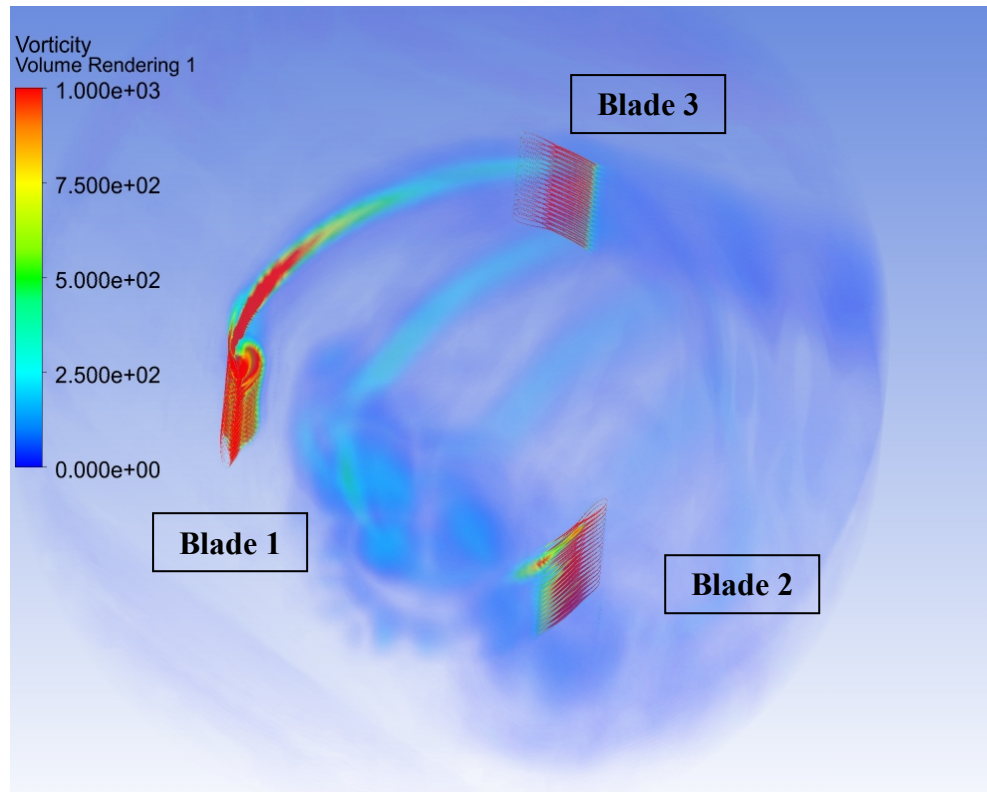
Case	r (m)	H_{rotor} (m)	Aspect Ratio	Turbulence Model	Span-wise location	C_{m-ave}	% Difference with Mid-span
Elsakka, 2020	0.850	1.2000	1.41176	SST	Mid-span	0.09400	–
					$z = 3/8 H_{rotor}$	0.07300	22.34043
					$z = 13/32 H_{rotor}$	0.06600	29.78723
				TSST	Mid-span	0.09100	–
					$z = 3/8 H_{rotor}$	0.05600	38.46154
					$z = 13/32 H_{rotor}$	0.05100	43.95604
Present study	0.515	1.4564	2.82796	SBES with TSST	Mid-span	0.11124	–
					$z = 3/8 H_{rotor}$	0.10112	9.09685
					$z = 13/32 H_{rotor}$	0.10059	9.57312



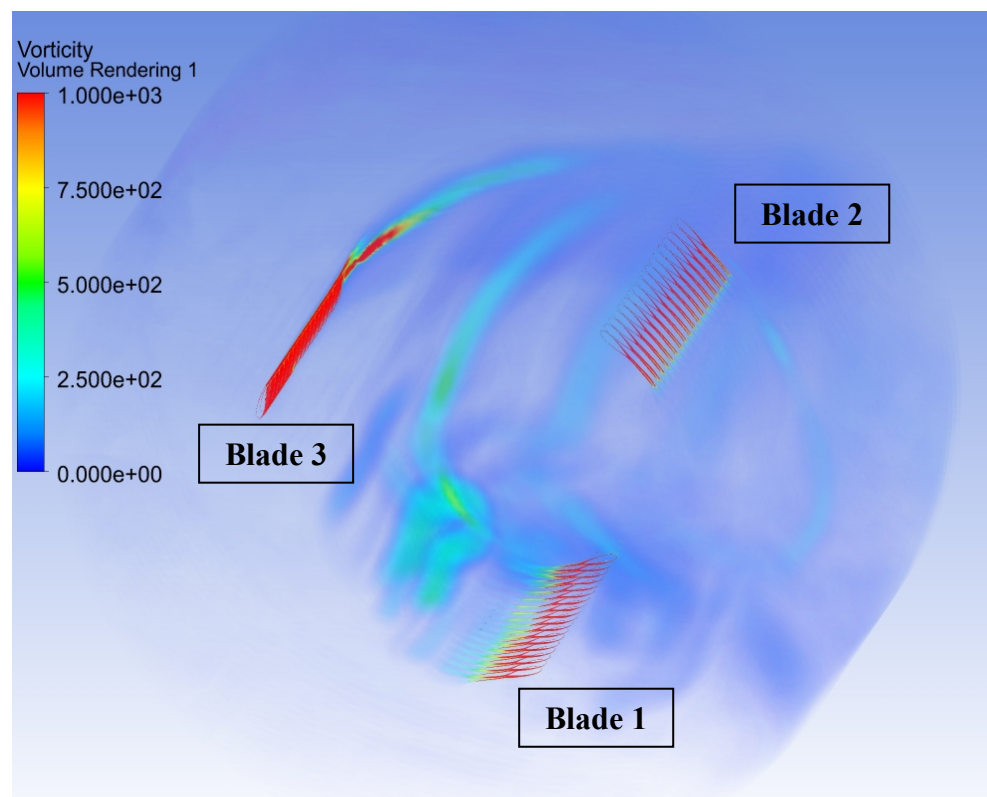
(a) $\theta = 30^\circ$



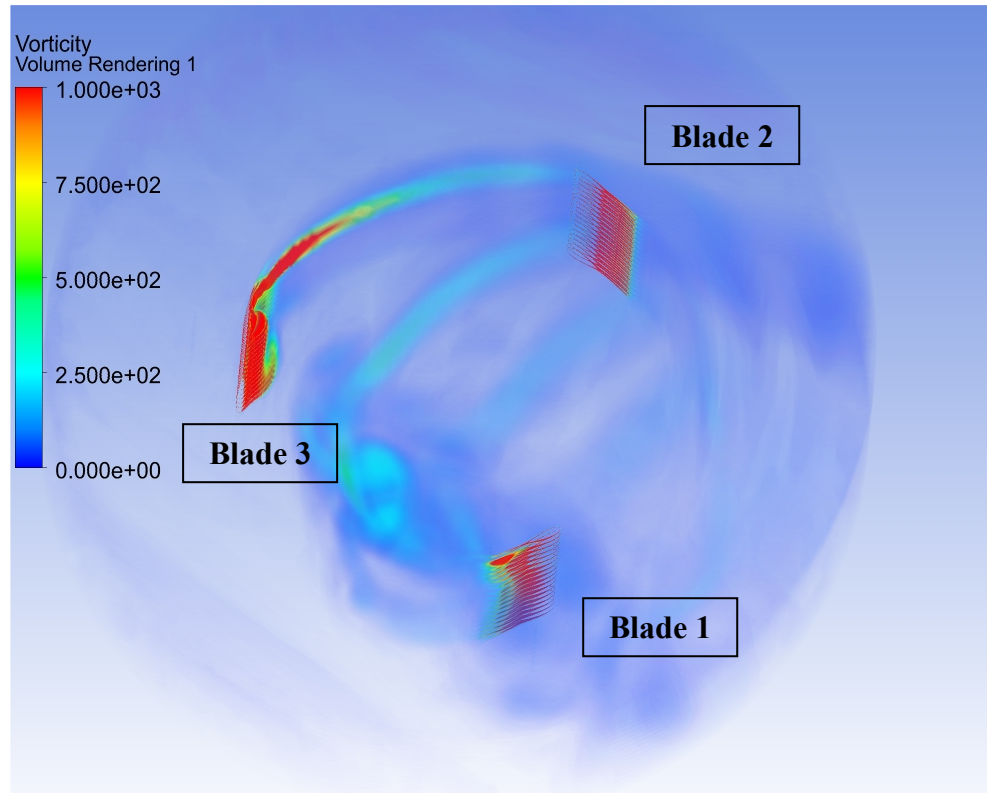
(b) $\theta = 90^\circ$



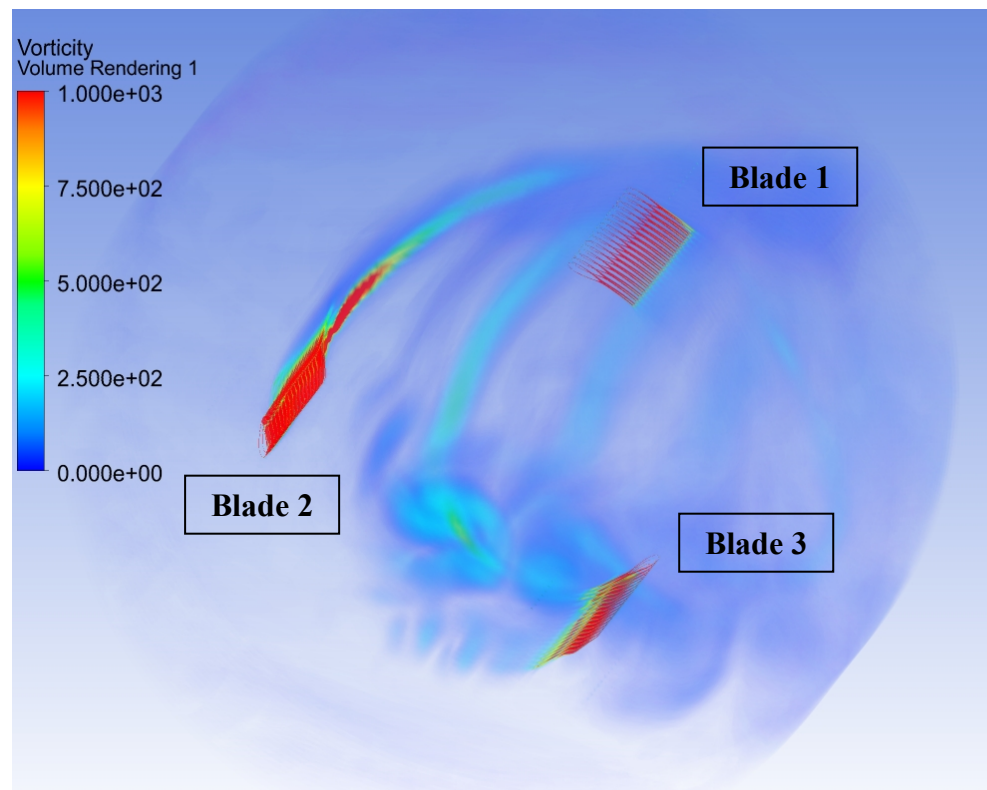
(c) $\theta = 135^\circ$



(d) $\theta = 210^\circ$



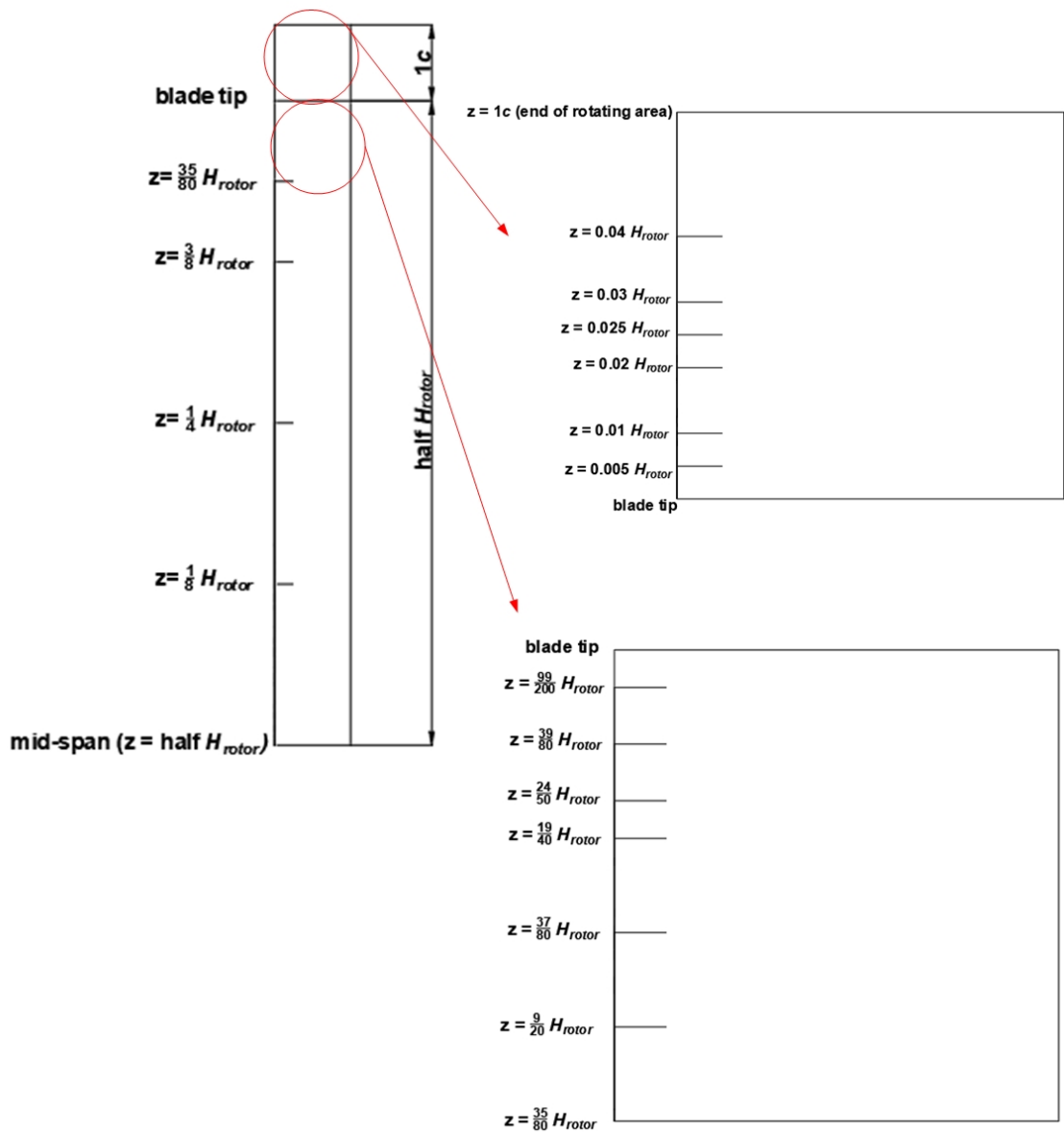
(e) $\theta = 240^\circ$



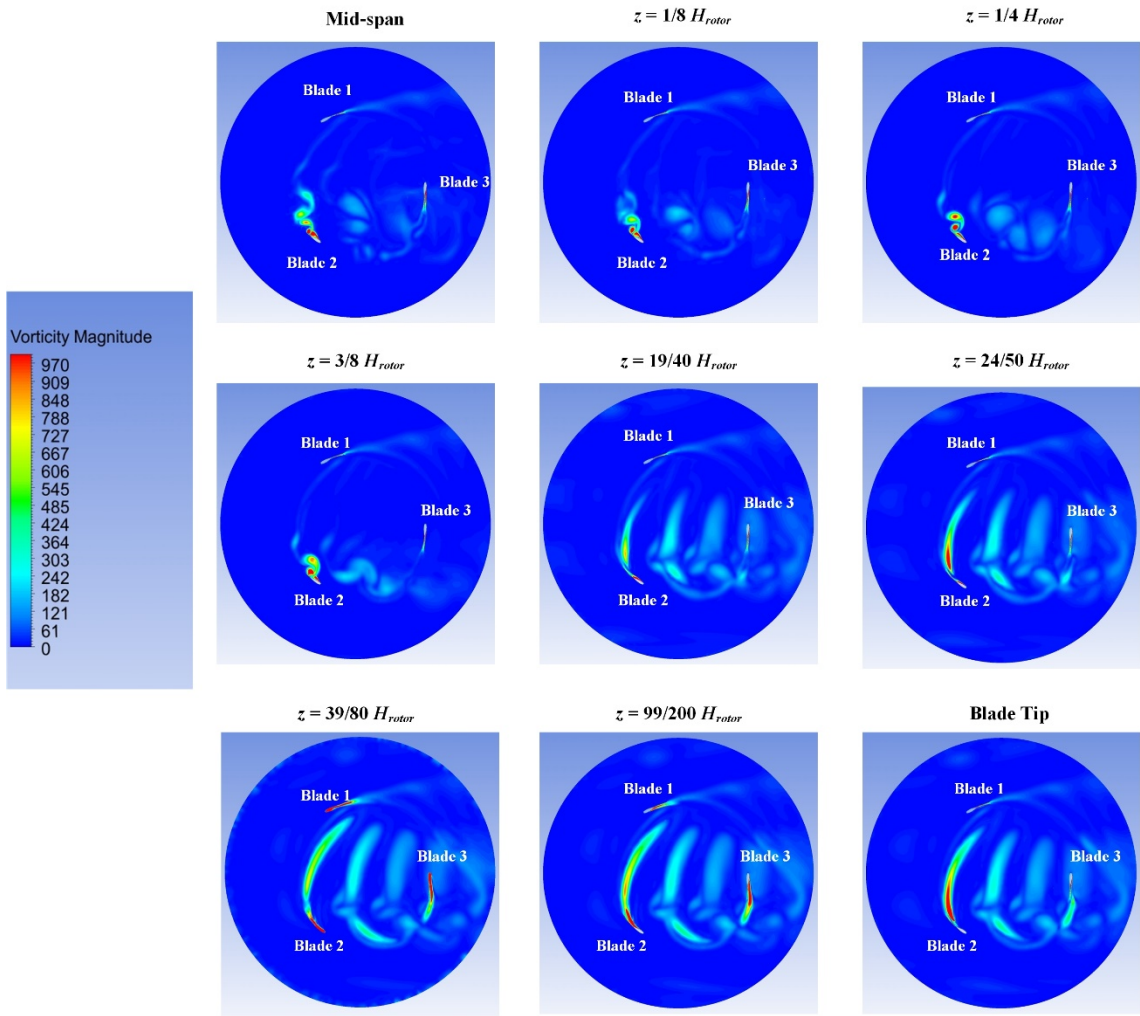
(f) $\theta = 345^\circ$

Figure 8.10 Comparison of contour plots of z -vorticity at important azimuthal positions.

Figure 8.10 illustrates the contour plots of z -vorticity at several important azimuthal positions of the blade to confirm those aforementioned behaviours. Note that, the azimuthal positions shown in Figure 8.10 are the azimuthal positions of blade 1. It is clearly shown that at the azimuthal positions outside $\theta = 45^\circ$ - 150° and $\theta = 210^\circ$ - 270° , the blades of VAWT only experiences weaker trailing-edge vortex shedding (see blade 1 in Figure 8.10 (a) and (f)). The behaviour of vortex shedding is also quite similar along the span-wise of the blade (e.g., see blade 1 in Figure 8.11 (b)). In addition, weak blade tip vortex shedding only starts to appear near the blade's tip ($0.005 H_{rotor}$ from the blade tip). These indicate the weak effect of blade tip outside $\theta = 45^\circ$ - 150° and $\theta = 210^\circ$ - 270° .



(a)



(b)

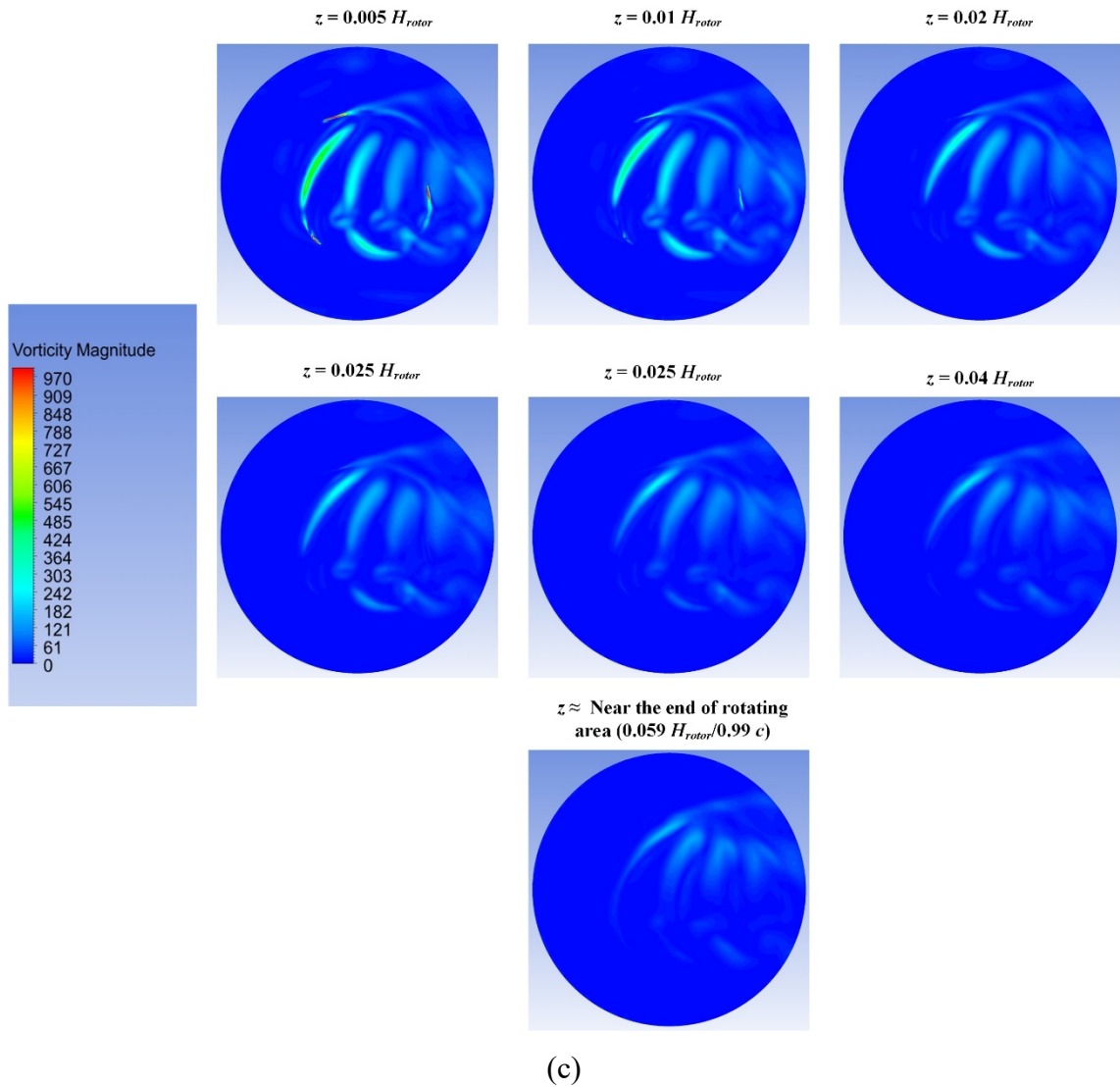
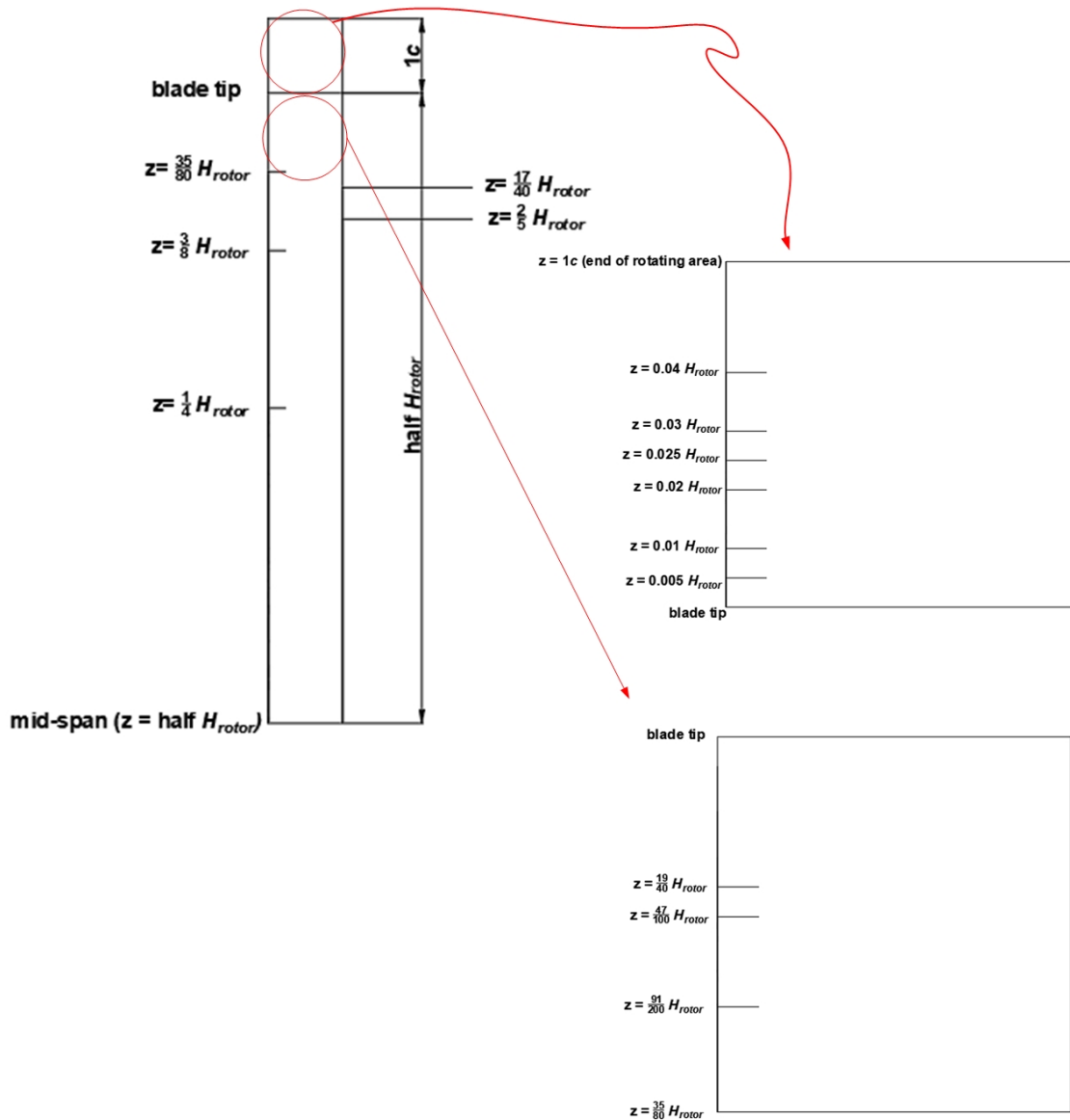


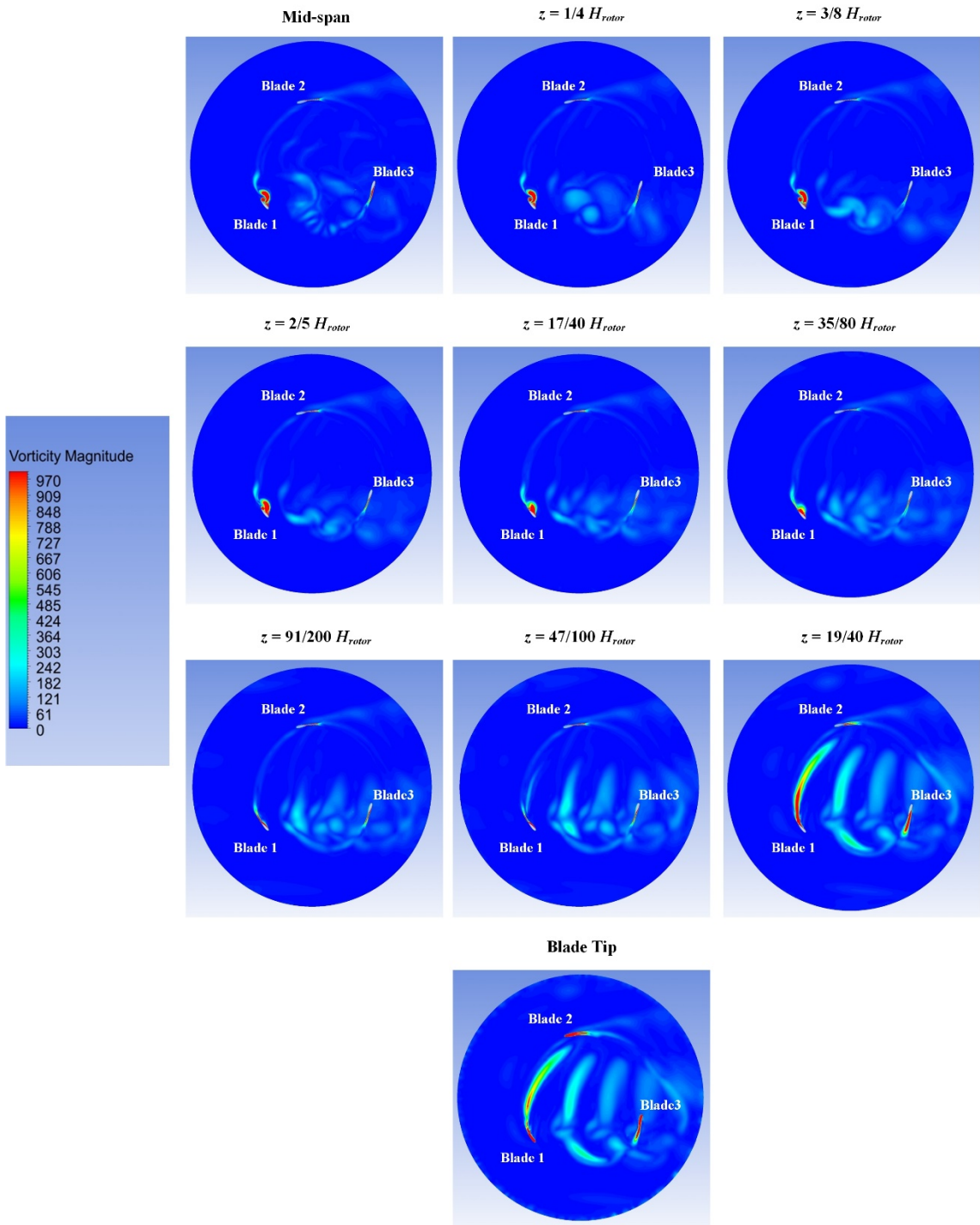
Figure 8.11 Comparison of contour plots of z -vorticity ($\theta = 30^\circ$) at important span-wise positions, (a) sketch of the important span-wise positions along rotating sub-domain), (b) along the half of the blade and (c) after blade tip until the end of the rotating zone.

Meanwhile, the blades of VAWT starts to experience stronger trailing-edge vortex shedding with the addition of leading-edge vortex shedding leading to the development of dynamic stall and roll up trailing-edge vortices (e.g., see blade 1 in Figure 8.10 (b) and (c)) at $\theta = 45^\circ$ - 150° . In contrast with the vortex shedding behaviour outside $\theta = 45^\circ$ - 150° and $\theta = 210^\circ$ - 270° , the vortex shedding behaviour shows significant change along span-wise of the blade at $\theta = 45^\circ$ - 150° , indicating the more substantial effect of the blade tip.

For example, at $\theta = 135^\circ$, the vortex shedding behaviour is quite similar until the middle of the half blade ($z = 1/4 H_{rotor}$). After that, the dynamic stall vortex starts to shed away towards the blade's trailing-edge and later merge with a roll-up trailing-edge vortex (see Figure 8.12 (b)). At $z = 91/200 H_{rotor}$, this merged vortex begins to wash away from the blade. Then, it merges with blade tip vortex (which starts to appear at $z = 47/100 H_{rotor}$ (i.e., $0.3 H_{rotor}$ from the blade tip)) at $z = 19/40 H_{rotor}$ (i.e., $0.25 H_{rotor}$ from the blade tip). Note that, the blade tip vortex at this azimuthal position is much stronger than at $\theta = 30^\circ$.



(a)



(b)

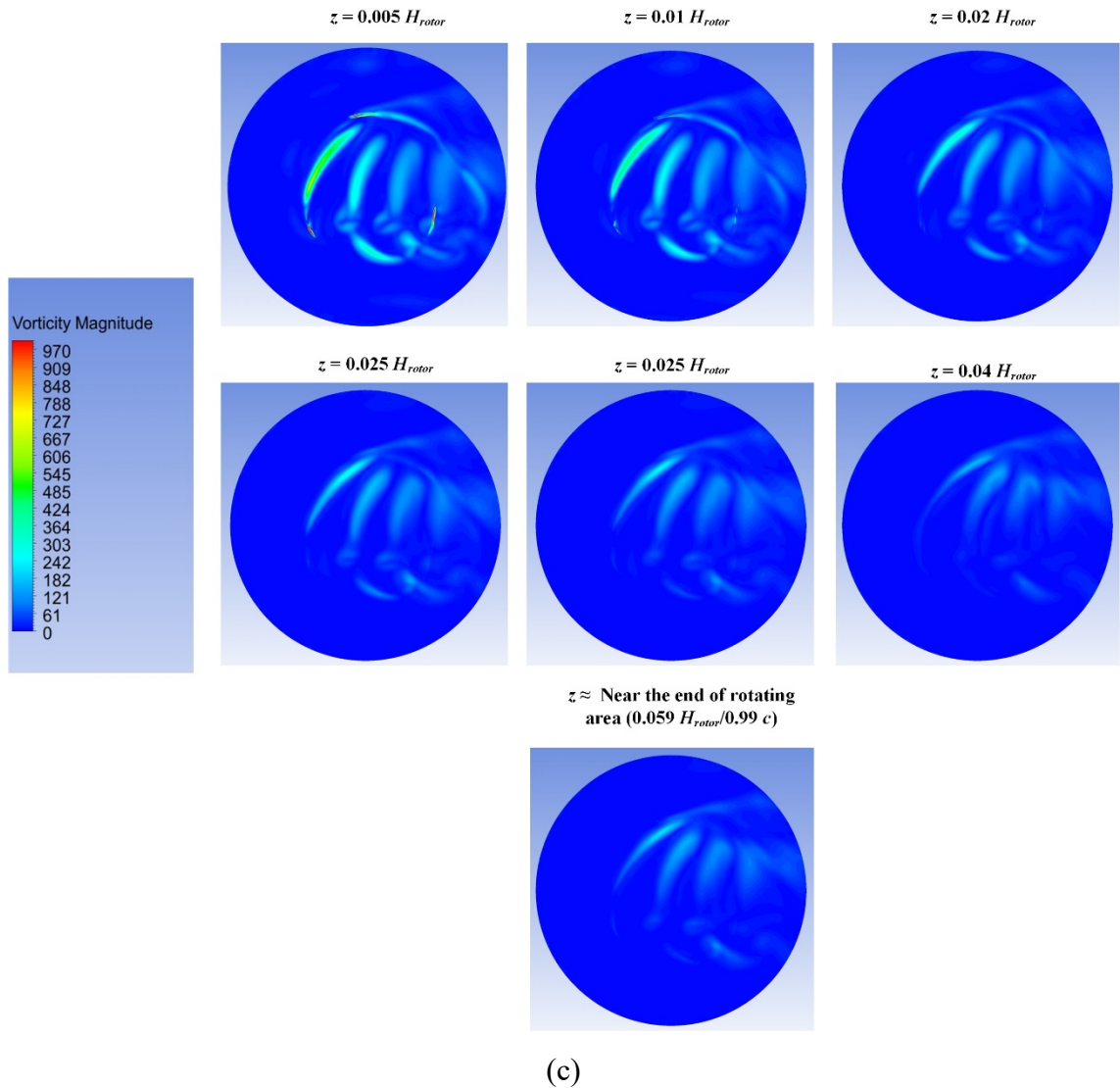
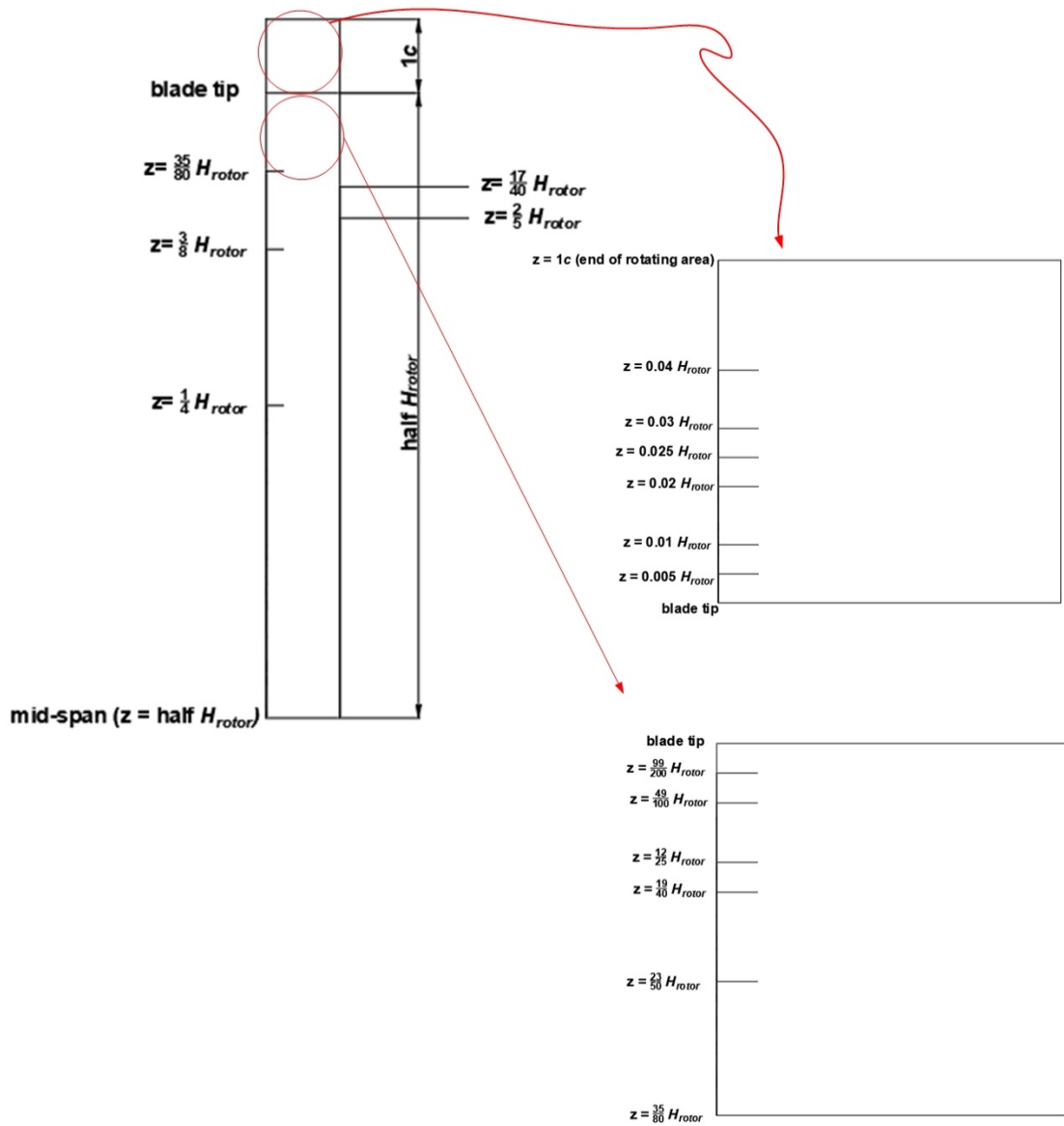


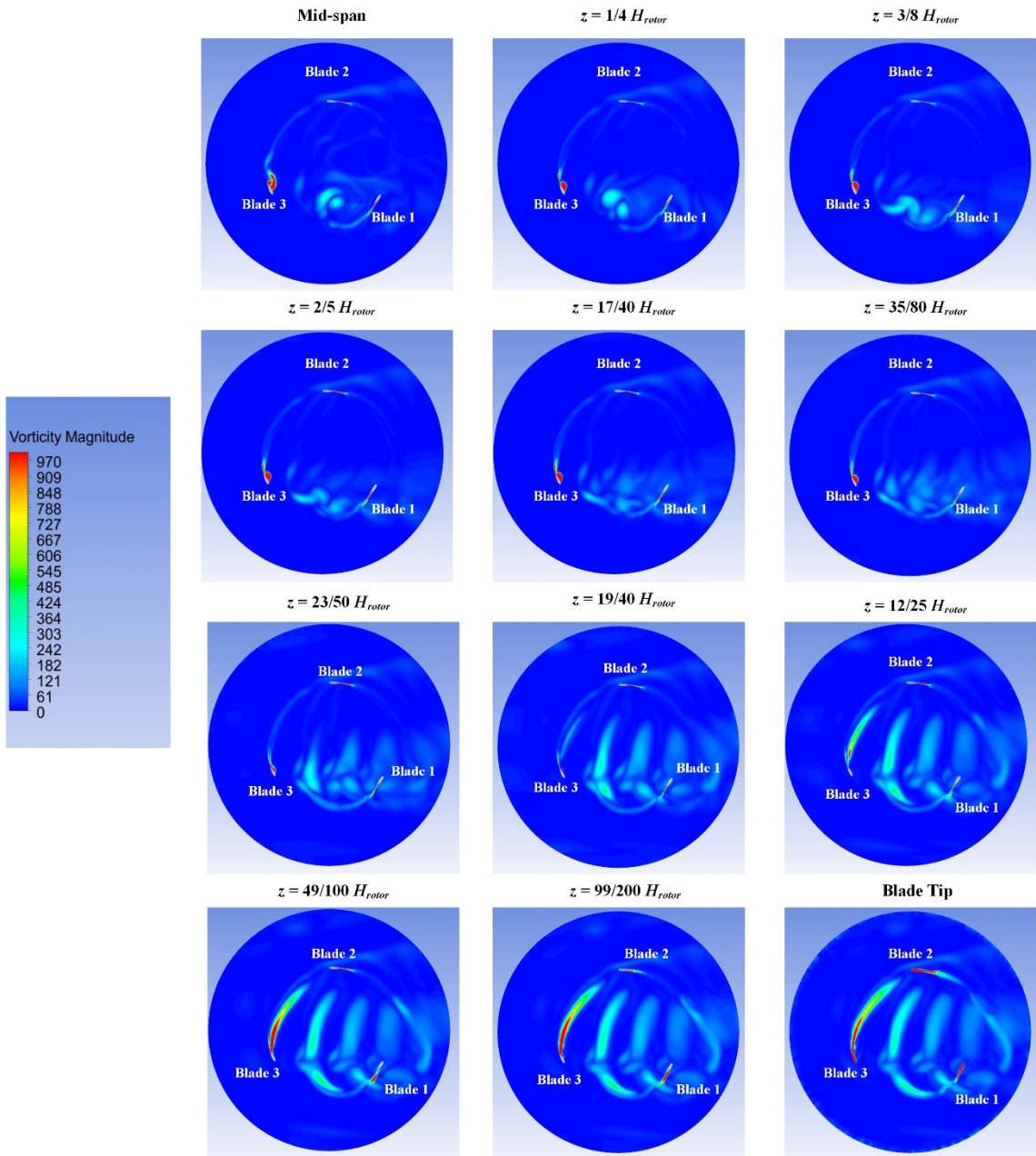
Figure 8.12 Comparison of contour plots of z -vorticity ($\theta = 135^\circ$) at important span-wise positions, (a) sketch of the important span-wise positions along rotating sub-domain), (b) along the half of the blade and (c) after blade tip until the end of the rotating zone.

As mentioned above, at $\theta = 210^\circ$ - 270° , the blade of VAWT interacts with the shed vortices from the blades further upstream. For example, at $\theta = 240^\circ$, the VAWT blade exposes to shed vortices from blades further upstream (see blade 1 in Figure 8.10 (d) and (e)). In addition, the trailing-edge vortex is also developed around the blade. The trailing-edge vortex starts to shed away from the blade and merge with shed vortices from blades further upstream as the position is getting closer to the blade tip (see blade 1 in Figure 8.13 (b)). At $z = 23/50 H_{rotor}$ (i.e., $0.04 H_{rotor}$ from the blade tip), the shed vortices are getting stronger due to the blade tip effect. Then, a secondary vortex near the trailing-

edge of the blade appears at $z = 12/25 H_{rotor}$ (i.e., $0.02 H_{rotor}$ from the blade tip). This secondary vortex starts to merge with the trailing-edge vortex leading to the development of blade tip vortex at $z = 49/100$ (i.e., $0.01 H_{rotor}$ from the blade tip).



(a)



(b)

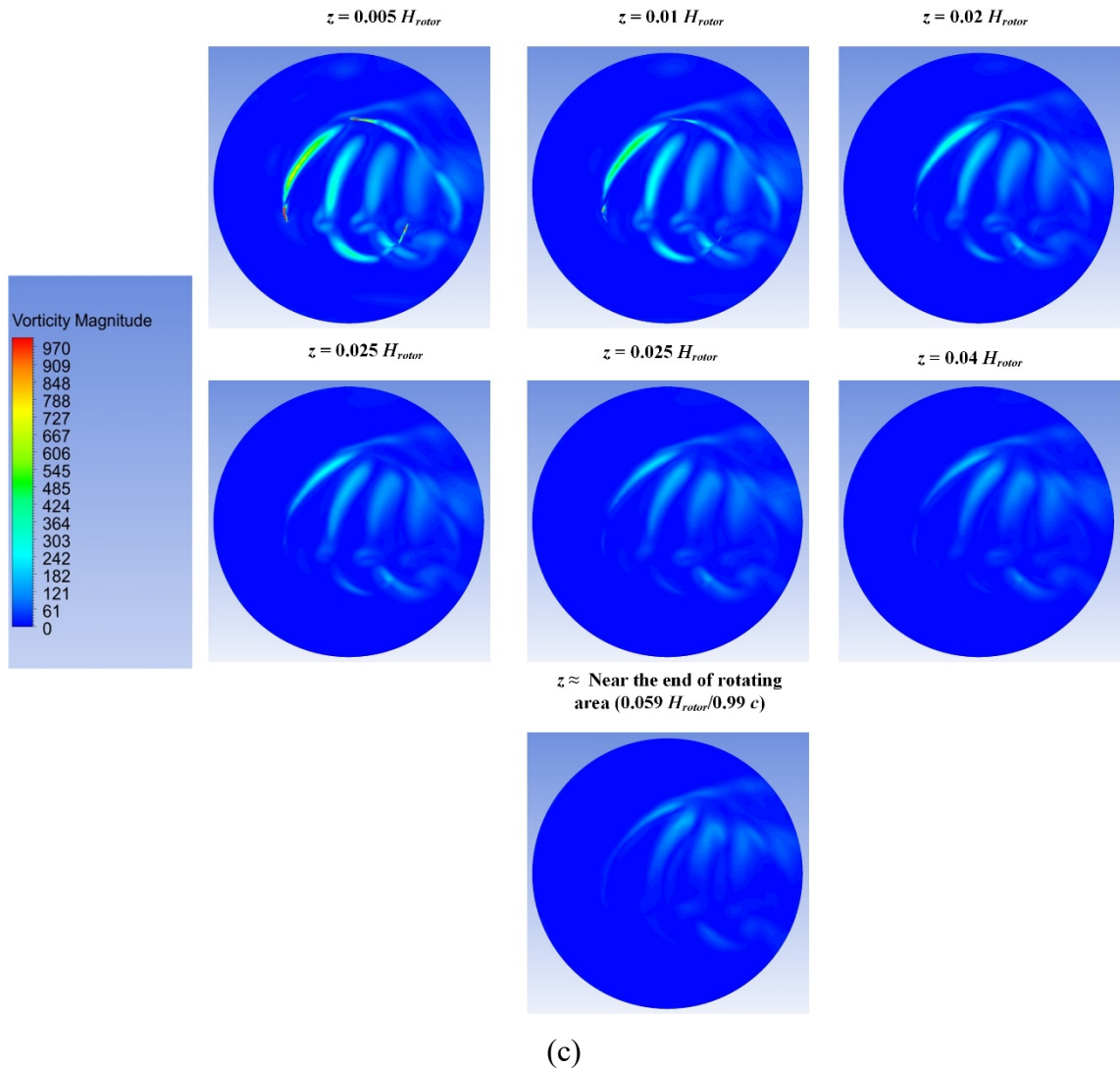


Figure 8.13 Comparison of contour plots of z -vorticity ($\theta = 240^\circ$) at important span-wise positions, (a) sketch of the important span-wise positions along rotating sub-domain), (b) along the half of the blade and (c) after blade tip until the end of the rotating zone.

Regarding flow behaviour away from the blade tip, it can be observed that the blade tip vortex tends to wash away quickly from the blade at all azimuthal positions (see Figures 8.11 (c), 8.12 (c) and 8.13 (c)). The blade tip vortex also sheds away from the blade with a similar pattern at all azimuthal positions, indicating that the flow behaviour is quite similar after the blade tip regardless of azimuthal positions.

8.5 Chapter Summary and Further Works

The discussion about 3D VAWT model validation is presented in this chapter. The 3D model result is relatively less sensitive with the grid refinement. The C_{p-ave}

prediction of the 3D model using the SBES TSST turbulence model under-predicts the experimental data of Castelli, Englaro and Benini (2011) and Castelli et al. (2010). On average, the 3D model under-predicts the experimental data by around 13.13468%, which is still reasonable as previous studies of the 3D VAWT model using hybrid RANS-LES turbulence model reported the maximum discrepancy is between 9-16% (Su et al., 2019; Lei et al., 2017). Hence, the 3D model has been verified numerically.

Furthermore, the C_{mi} distribution shows that there is a visible difference of C_{mi} prediction of the 3D model as the position changes along the span-wise direction of the blade at $\theta = 45^\circ$ - 150° and $\theta = 210^\circ$ - 270° . Note that, the blade of VAWT experiences a large excursion of the angle of attack resulting in unsteady flow separation and possibly dynamic stall of the blade and interacts with the shed vortices from the blades further upstream at these azimuthal positions. The vorticity contour indicates that the blade tip effect is much stronger at these azimuthal positions than other azimuthal positions. In addition, the vorticity contour in the region after the blade tip shows that the blade tip vortex sheds quickly and there is no significant difference in flow behaviour in this region regardless of the azimuthal position of the blade.

After performing the 3D model validation and understanding the 3D flow behaviour of VAWT, this study will be continued in the next Chapter to evaluate the use of riblets to improve the performance of VAWT. In this study, riblets are developed by introducing gaps or holes along the span-wise direction of the blade with GF. The purpose of riblets is to reduce the increment of drag generation caused by the original GF (without gap or hole), so the drag to lift ratio can be increased. Hence, the performance enhancement of VAWT can be improved. Quasi 3D CFD simulation is applied to reduce the computational cost of full 3D CFD simulation.

Chapter 9: Quasi-3D CFD Simulation of 3D Modification of Gurney Flap to Reduce the Drag Generation of Lift-Driven VAWT

As mentioned in Chapter 5, a GF can enhance the VAWT power coefficient up to 2.3 times that of the clean VAWT in its lowest *TSR* operation. In higher *TSR* regimes, GF ability to improve the power coefficient of VAWT decreases, but it still can enhance the power coefficient of VAWT (see Chapter 5, Section 5.3.4). Nevertheless, the addition of GF can also increase the drag production of VAWT, especially in higher rotational speed (i.e., medium and high regimes of *TSRs*). This drag increment can reduce the lift-to-drag ratio improvement of VAWT, therefore, decrease the power generation improvement of VAWT.

On the other hand, other flow control devices called riblets are known for their ability to reduce drag generation (see Chapter 2, Section 2.5.1). As mentioned in Chapter 2, Section 2.5.1, riblets have the potential to be applied in VAWT as they have better performance to reduce drag generation at low Reynolds number compared to high Reynolds number (Spalart and McLean, 2011; Han et al., 2003). Note that, GF can be modified into riblets by introducing 3D modifications such as slits to introduce several vacant areas around the flap so the flow can go through these vacant areas. These 3D modifications of GF can reduce the drag generation caused by the GF up to 12% at a single stationary aerofoil for wings application (Meyer et al., 2006). The slits act as wake stabilisers to reduce the wake instability (Meyer et al., 2006). However, the real potential of riblets for drag reduction in full-scale wind turbine configurations (including the rotational effect and blade-to-blade interaction) is still not yet investigated.

Therefore, to understand the potential of riblets applied in the blades of VAWT, this chapter evaluates the effect of 3D modifications of GF, i.e., slits and holes, on the performance improvement of lift-driven VAWT. Quasi-3D CFD simulation is applied to reduce the enormous computational cost of running a full 3D CFD simulation. This chapter will consist of five sections. The first section explains the geometry of clean GF and its 3D modifications. The model, grid generation and numerical setup of the CFD simulation can be found in section 9.2. Then, the averaged power coefficient prediction comparison between 2D and q3D models VAWT with GF is discussed in section 9.3. Furthermore, the discussion of the effect of 3D modifications GF on the performance of lift-driven VAWT with GF is deliberated in section 9.4. Lastly, the summary of this chapter is discussed in the fifth section.

9.1 Geometries Models

9.1.1 VAWT with GF

In this study, a bare VAWT model is modified by mounting GF in the trailing-edge of NACA 0021 aerofoil. All turbine geometries are kept the same as the clean model. The clean GF has a rectangular shape, with the main geometrical features can be seen in Figure 9.1. The chosen thickness is adopted from the study by Mohammadi, Doosttalab and Doosttalab (2012). The other geometrical features, i.e., height (H), mounting angle (θ_{GF}) and position from trailing-edge (s), are chosen from the previous optimisation study of GF (see Chapter 5).

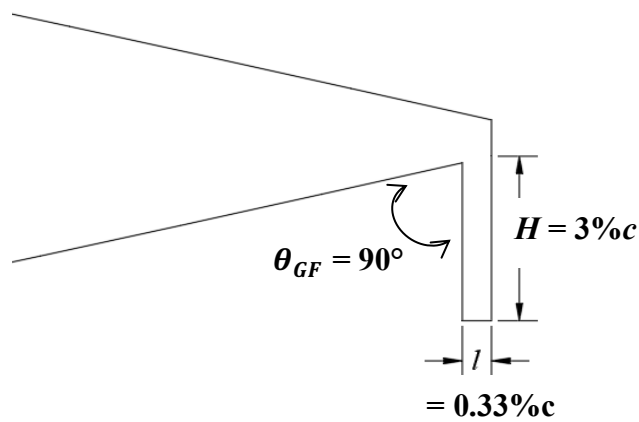
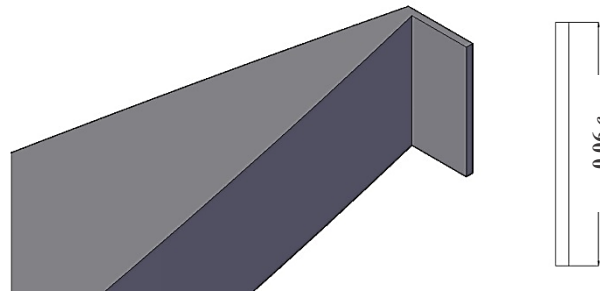


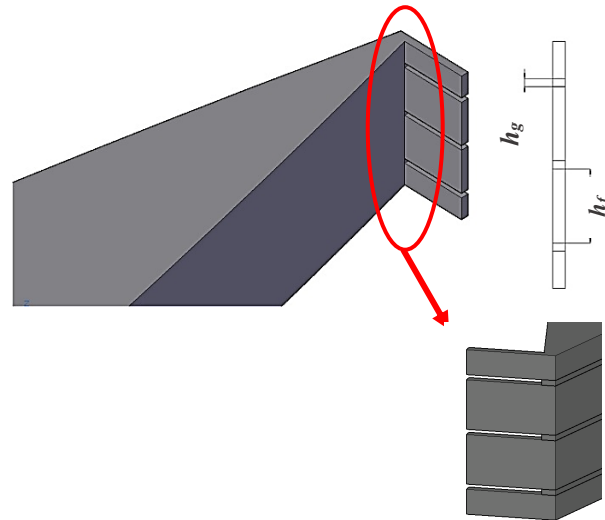
Figure 9.1 Detailed geometry of clean GF.

9.1.2 3D modifications of GF

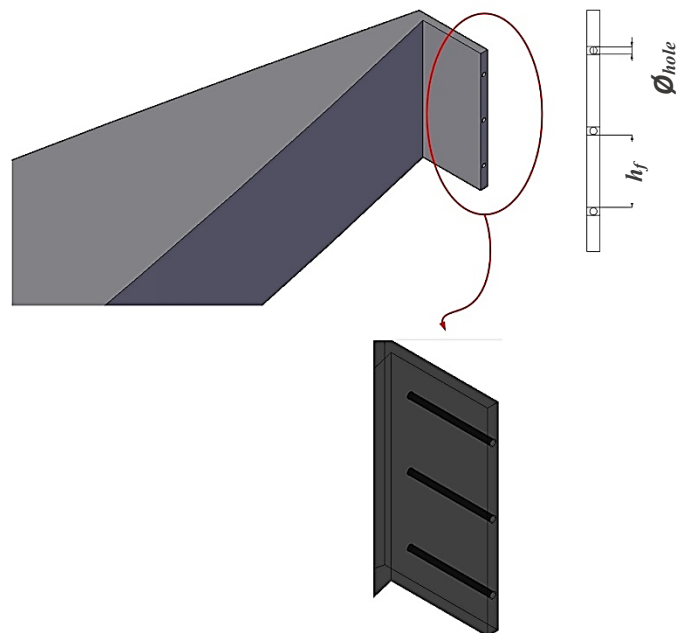
3D modifications called slits and holes are introduced in GF with the aim to reduce the drag generation caused by GF. For the GF with slits, the height of the slit (h_g) is $0.2\%c$ whilst the height of the flap (h_f) is $1.8\%c$ (see Figure 9.2 (b)). Meanwhile, the flap of GF with holes has the exact height of the flap of GF with slits, and the hole diameter (ϕ_{hole}) is the same as the height of the slits (see Figure 9.2 (c)). All these dimensions are adopted from a study by Meyer et al. (2006) who investigated the effect of slit and holed GF on the performance of stationary aerofoil for wings application.



(a) Clean GF



(b) GF with slits



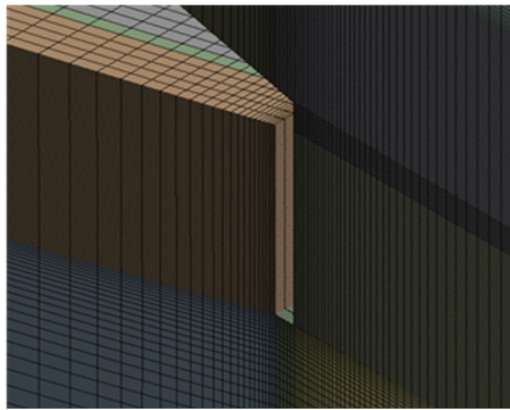
(c) GF with holes

Figure 9.2 Detailed geometry of GF and its modifications (not in scale).

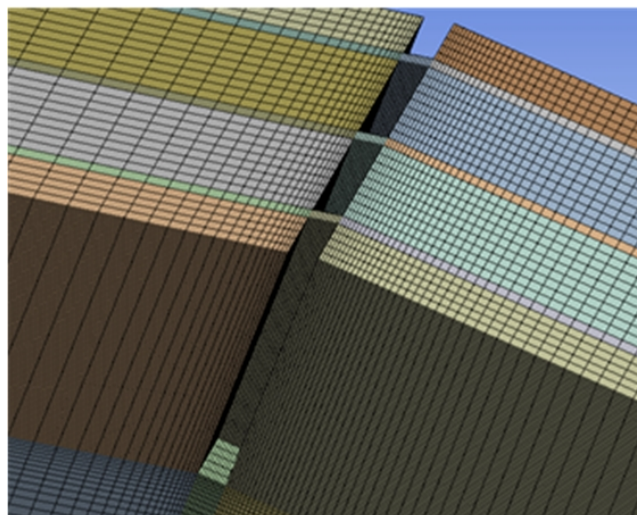
9.2 Model, Grid Generation and Numerical Setup

This study adopts q3D CFD simulation to reduce the enormous computational cost of running a full 3D CFD simulation. The computational domain is extended about $6\% c$ (see Figure 9.2 (a)) in the span-wise direction to accommodate three flaps and three slits or holes of GF with 3D modifications (see Figure 2 (b) and (c), respectively). A pair of periodic translational conditions were enforced on the top and bottom boundaries of span-wise direction.

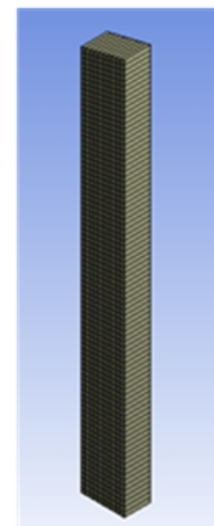
All models and numerical setup used in 2D validation studies are implemented in this q3D VAWT with 3D modifications of GF studies (see Chapter 4). As mentioned in Chapter 4, the C-grid can generate better accuracy compared to O-grid for the SBES turbulence model. Hence, the C-grid is adopted. This C-grid can also produce quality structure grids for blades quipped with GF geometry.



Detail around the trailing-edge of the blade

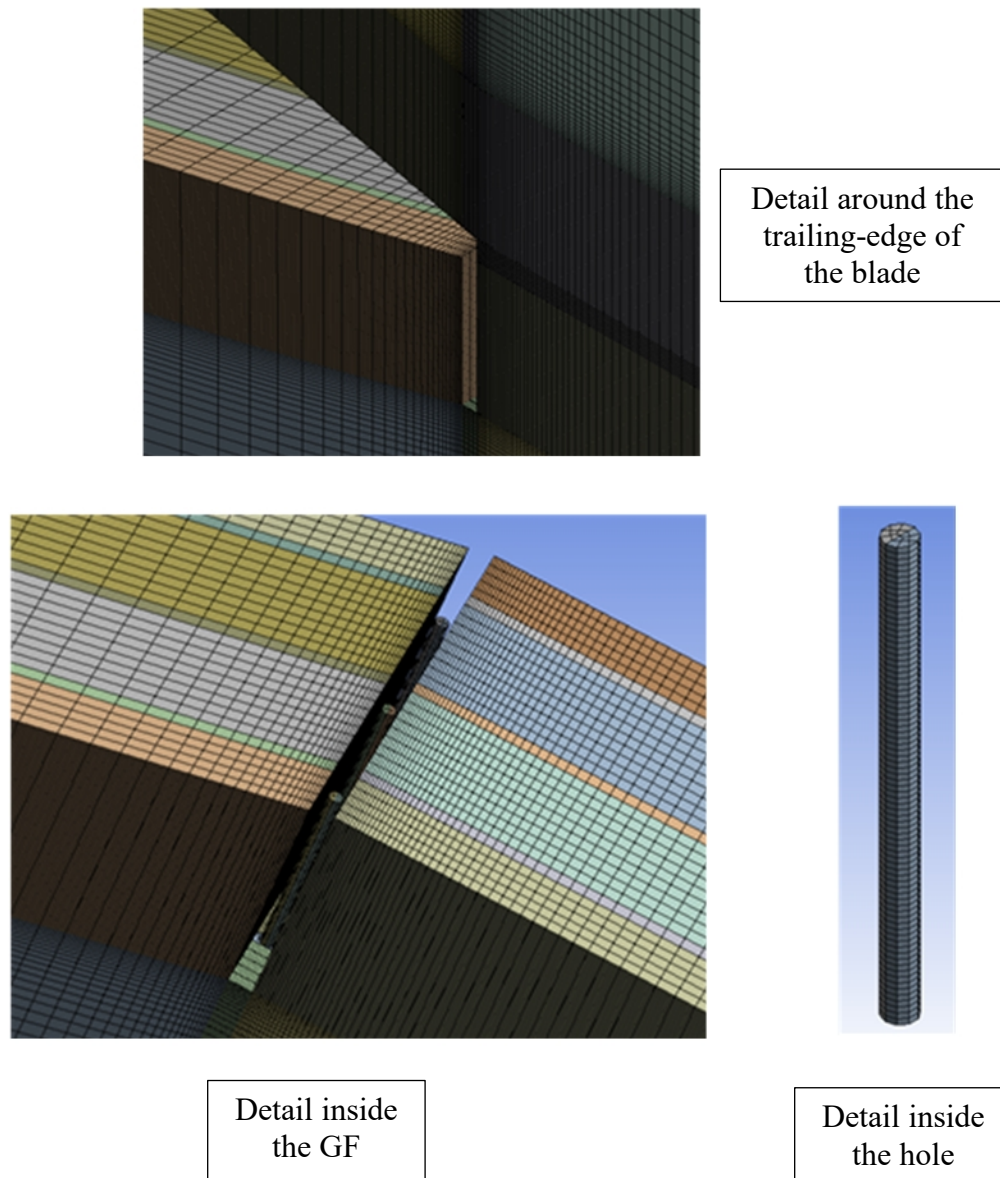


Detail inside the GF



Detail inside the slit

(a)



(b)

Figure 9.3. Detailed grids of 3D modification of GF, (a) GF with slits and (b) GF with holes (the drawing is not in scale). The colour of grids shows the domain partition used in the grid generation process.

For the grid discretisation, this study adopts the grid discretisation of 2D CFD simulation of VAWT with GF (see Chapter 5, Section 5.2) at the cross-section of the computational domain. The flap is divided into nine grids in the span-wise direction whilst one grid is placed in the slit for GF with slits (see Figure 9.3 (a)). For GF with holes, nine grids are also implemented along the span-wise direction of the flap and 16 unstructured grids are distributed around the holes (see Figure 9.3 (b)).

9.3 Comparison between 2D and q3D Models of VAWT with GF

Before applying the 3D modifications of GF (i.e., slits and holes) to the VAWT with GF, this study compares the results of CFD simulation of 2D and q3D models of VAWT with GF. Note that, the q3D model of VAWT with GF is extended from the 2D model of VAWT with GF by 6% c (same as the q3D model of VAWT with 3D modifications of GF). Hence, the grid discretisation in the cross-section of the computational domain is the same as the 2D model. Along the span-wise direction, 30 grids are allocated along with the height of the computational domain. The results show that the q3D model predicts lower C_{p-ave} compared to the 2D model. Whilst the 2D model predicts the C_{p-ave} of VAWT with GF about 0.5394, the q3D model predicts the C_{p-ave} value about 5% lower (0.5124). This result is reasonable as a previous study also found that the difference of C_{p-ave} prediction between 2D and 2.5D models of VAWT can be around 8% (Li et al., 2013).

9.4 VAWT with 3D Modifications of GF

9.4.1 Moment coefficient comparison

Understanding the capability of 3D modifications of GF by adding slits and holes in the GF to reduce the drag generation with a slight reduction of lift production of a single stationary aerofoil (Meyer et al., 2006), this study applies slits and holes in the blades of VAWT with GF where rotational effects and blade-to-blade interaction are presented. Note that, this study only evaluates these 3D modifications of GF at optimum TSR value of bare VAWT ($TSR = 2.64$). Figure 9.4 depicts the comparison of instantaneous moment coefficient distributions over one turbine revolution between q3D VAWT with clean GF, VAWT with slit GF and VAWT with holed GF. It can be seen that the 3D modifications of GF do not significantly change the trend line of C_{mi} distribution. Nevertheless, the existence of slits and holes can increase the C_{mi} 's optimum value of VAWT with clean GF. Whilst slit GF can relatively maintain the minimum value of C_{mi} , the holed GF slightly reduce the minimum value of C_{mi} . Therefore, GF with slits has a better capability to improve the averaged value of the moment coefficient of VAWT with clean GF (i.e., from 0.1941 to 0.2067) than GF with holes. The VAWT with later modification of GF can only generate a slight improvement of moment coefficient compared to VAWT with clean GF (i.e., from 0.1941 to 0.1947). As a result, both GF with slits and GF with holes can improve the C_{p-ave} improvement of VAWT with clean GF by about 6.50% and 0.28%, respectively (see Figure 9.5).

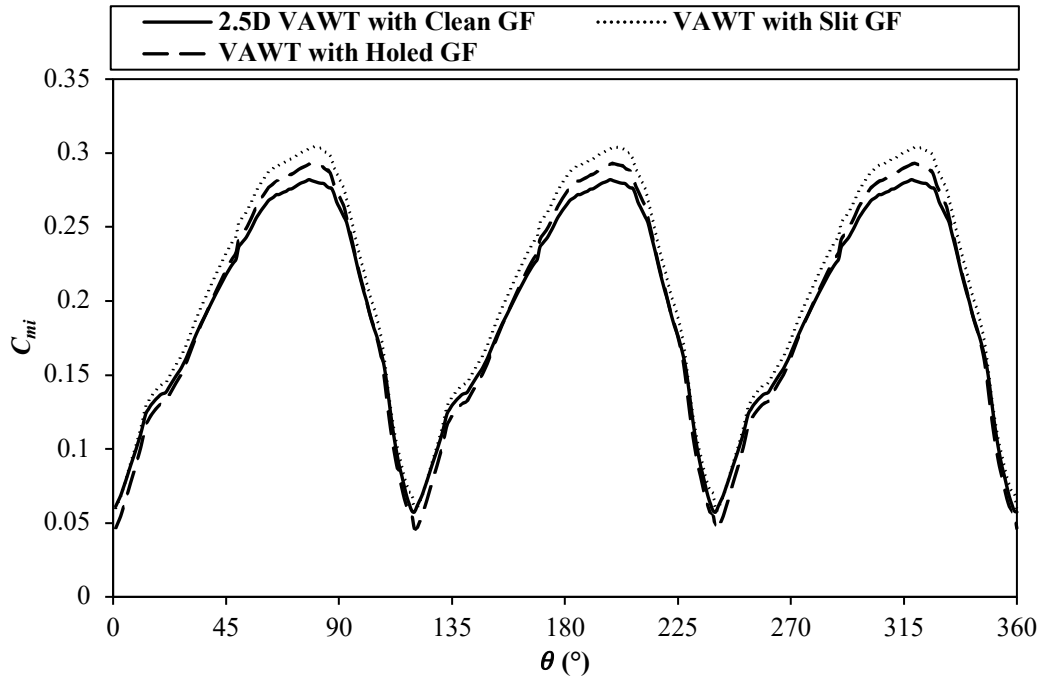


Figure 9.4 Instantaneous moment coefficients comparison of q3D VAWT with clean GF, VAWT with slit GF and VAWT with holed GF.

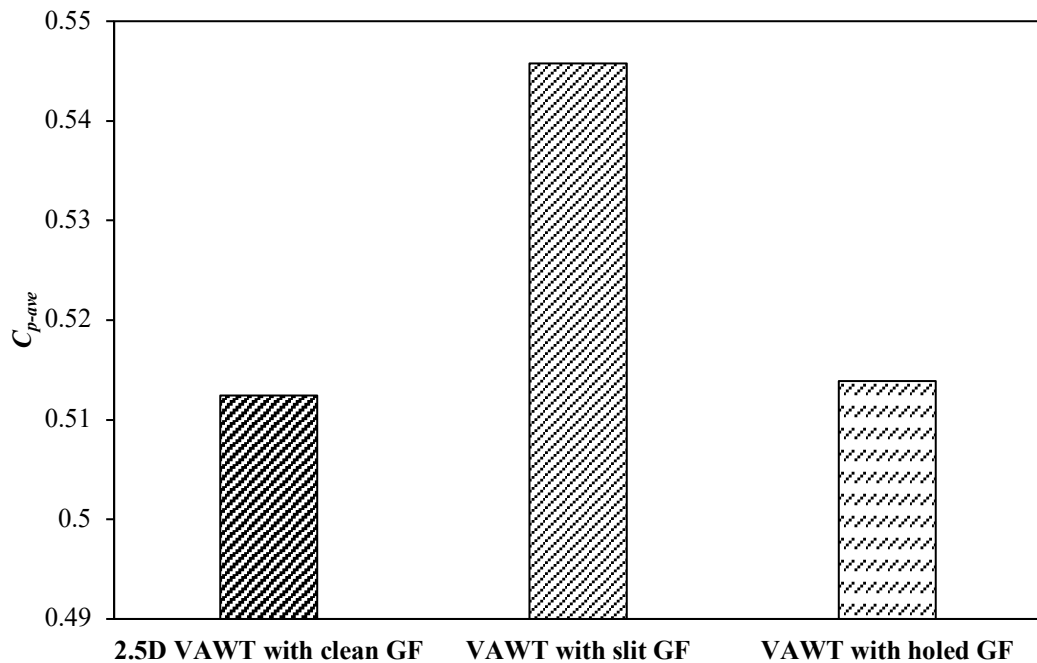


Figure 9.5 Comparison of C_{p-ave} between q3D VAWT with clean GF, VAWT with slit GF and VAWT with holed GF.

9.4.2 Drag and lift coefficients comparison

Table 9.1 shows the comparison of averaged drag coefficient, averaged lift coefficient and C_{l-ave}/C_{d-ave} over one turbine revolution between VAWT with original GF,

VAWT with slit GF and VAWT with holed GF. It can be seen that the introduction of slits and holes in the GF indeed can reduce the drag generation of VAWT with GF. The GF with slits can reduce a significant amount of the drag generation of VAWT with clean GF (8%) compared to the GF with holes (only about 0.29%).

Table 9.1 Comparison of C_{d-ave} , C_{l-ave} and C_{l-ave}/C_{d-ave} between q3D VAWT with clean GF, VAWT with slit GF and VAWT with holed GF.

Turbines	C_{d-ave}	C_{l-ave}	C_{l-ave}/C_{d-ave}	%Increment or Decrement		
				C_{d-ave}	C_{l-ave}	C_{l-ave}/C_{d-ave}
2.5 VAWT with Clean GF	0.12849	0.23339	1.81642	-	-	-
VAWT with Slit GF	0.11821	0.22872	1.93488	Decrease ~ 8%	Decrease ~ 2%	Increase ~ 6.5%
VAWT with Holed GF	0.12812	0.23337	1.82148	Decrease ~ 0.29%	Decrease ~ 0.01%	Increase ~ 0.28%

Although slits and holes can reduce the drag generation of VAWT with GF, they both can also slightly cut down the lift generation of VAWT with GF. The existence of slits and holes in the GF can slightly reduce lift generation of VAWT by 2% and 0.01%, respectively. It is understandable as the air flow through the slits and the air flow inside the holes reduces the effective surface of GF. The reduction of lift generation caused by holes is relatively lower than slits due to the larger effective surface of GF in GF with holes compared to GF with slits. Nonetheless, the drag reduction is still higher than the lift decrease, and as a result, the lift-to-drag ratio of VAWT with GF increases, leading to the further improvement of VAWT's performance. As shown in Table 9.1, the slits and holes can improve the lift-to-drag ratio of VAWT with GF by 6.5% and 0.28%, respectively. However, the improvement of C_{p-ave} in VAWT with holed GF compared to VAWT with clean GF is still questionable as the percentage of the improvement is still under the range of the numerical accuracy of CFD simulation. Hence, experimental study is necessary to confirm the ability of both of VAWT with slit GF and VAWT with holed GF to improve the performance of VAWT with clean GF.

It is noticeable that GF with holes does not significantly affect the C_{l-ave} and C_{d-ave} of VAWT with clean GF. It is due to the arrangement of the holes as a cavity, so only a tiny of air flow goes inside the holes. The contour of averaged velocity indicates that the flow's average velocity through the holes is relatively low compared to the slits (see Figure 9.6). Hence, the holes cannot really change the characteristics of the flow,

resulting in a very small improvement of the C_{p-ave} compared to VAWT with clean GF. Nevertheless, it seems that the air velocity inside the hole is relatively high for air inside a hole. This is probably due to the blade rotating effect and the interaction between blades as the blade is entering the wake region of upward blade during rotation.

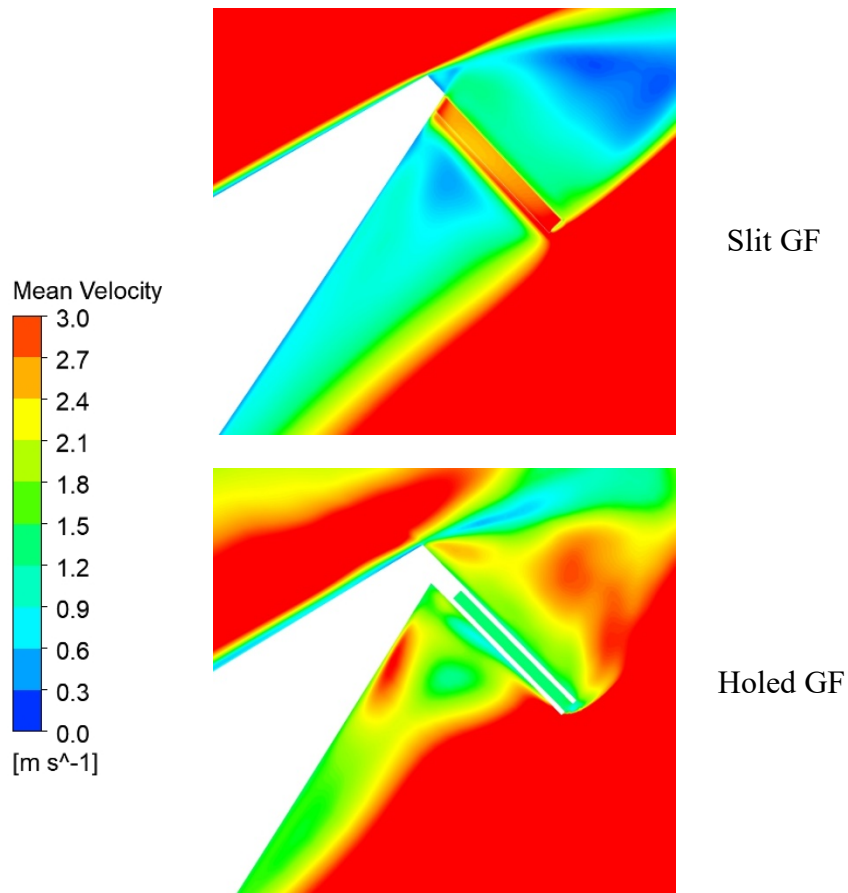
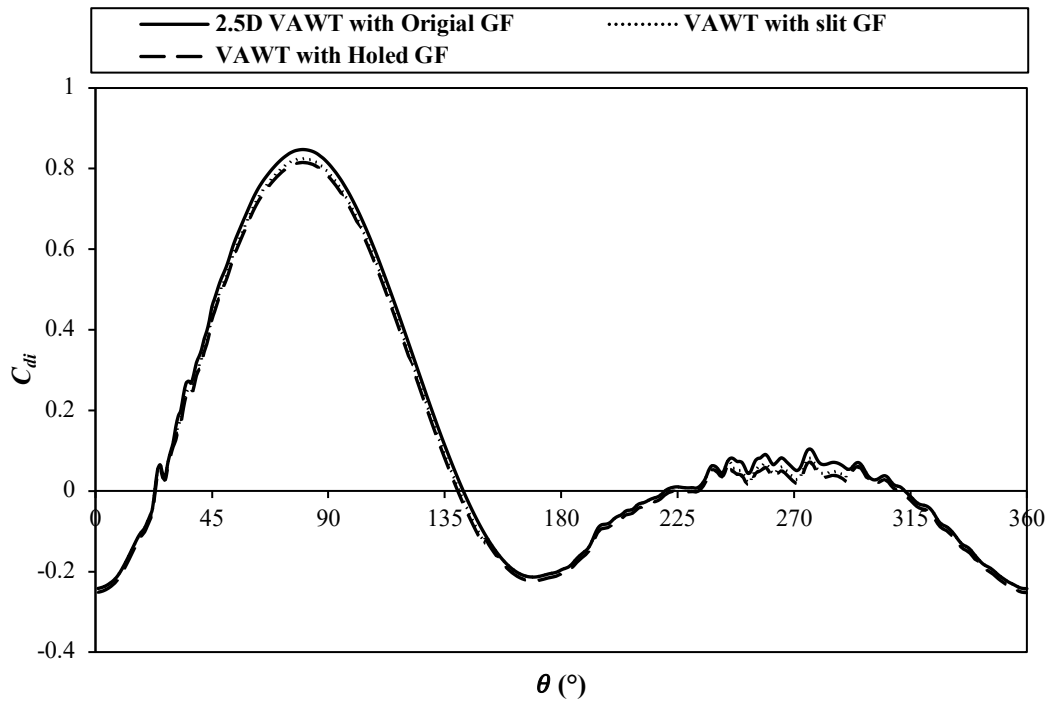
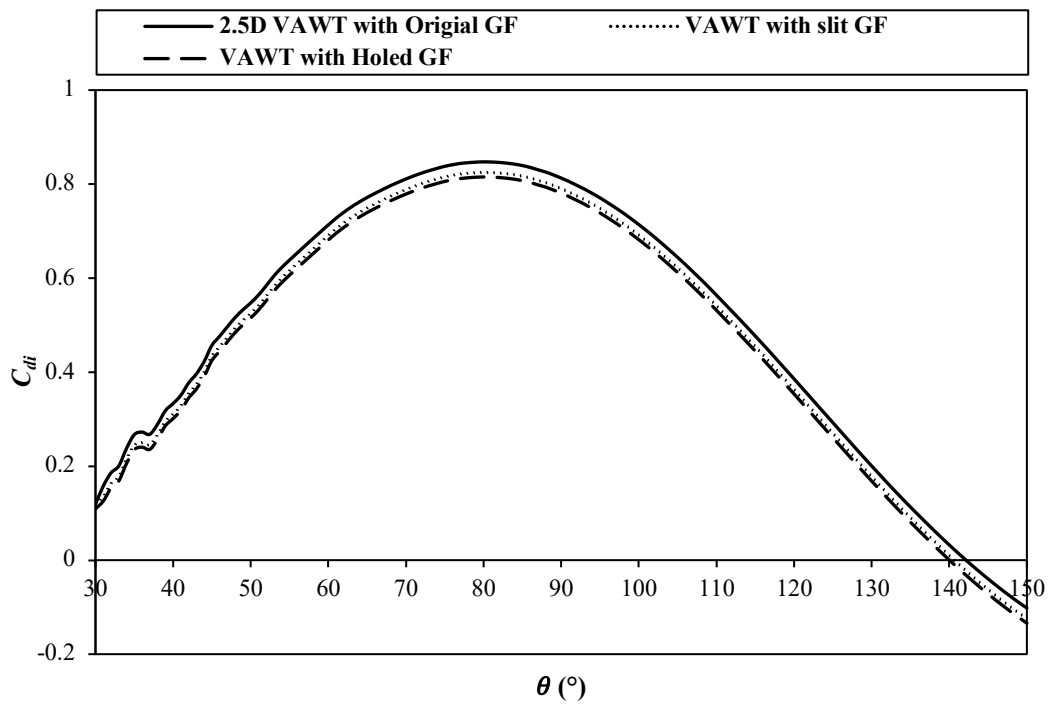


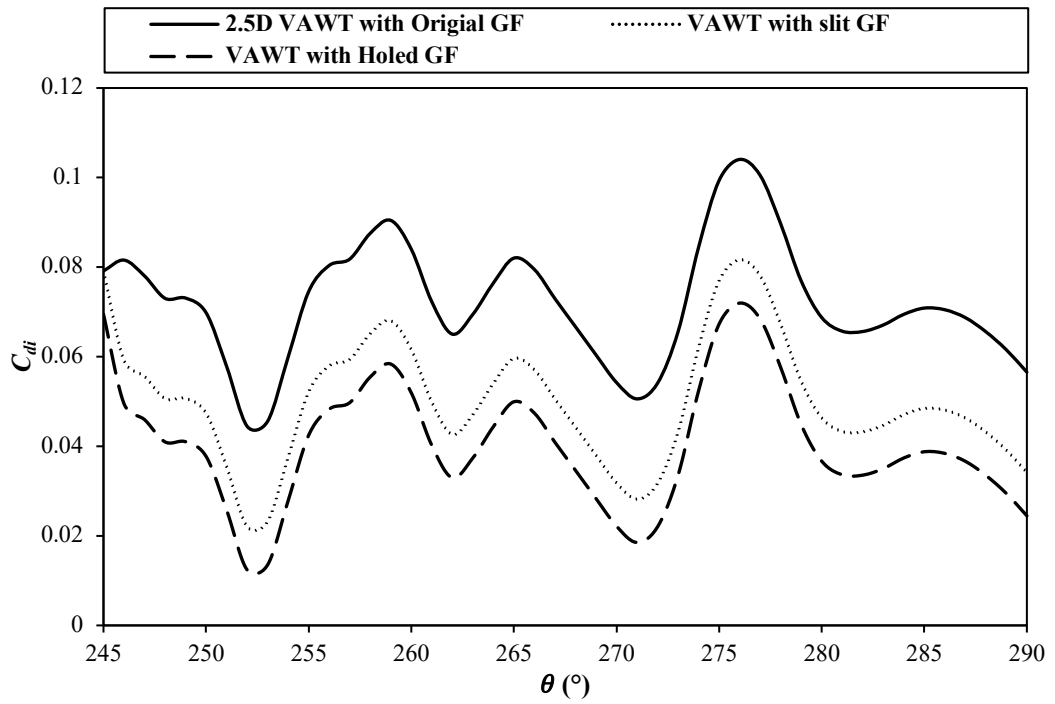
Figure 9.6 Comparison of mean velocity contour in x - y cross-section between slit GF and holed GF at the middle of the slit or hole.



(a) One turbine revolution

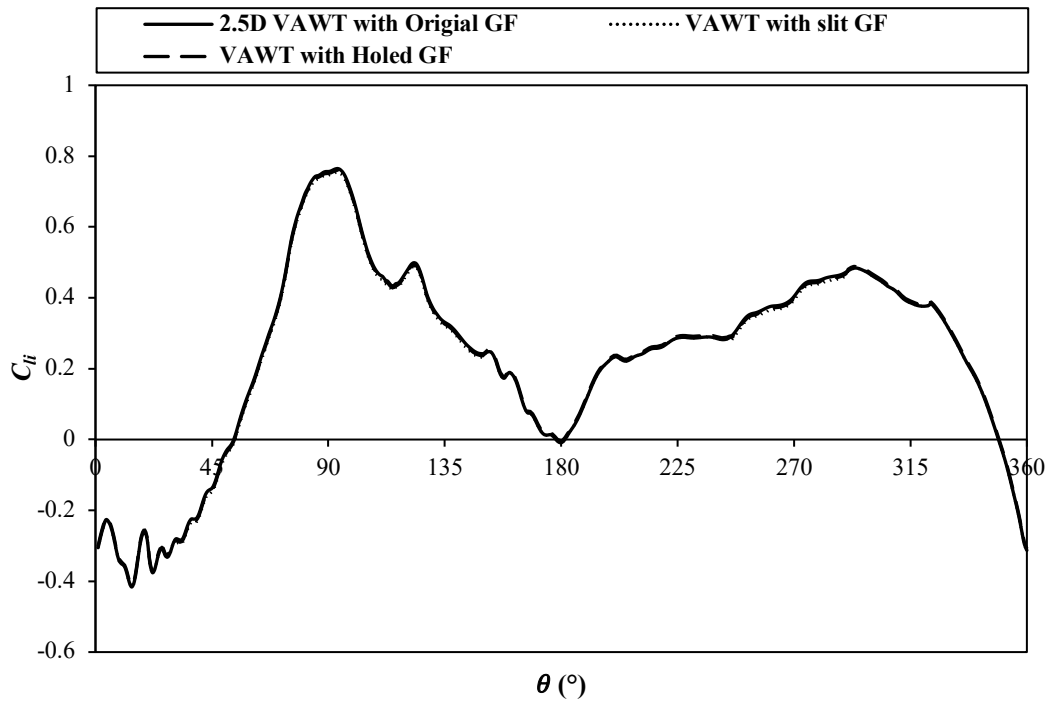


(b) At $\theta = 30-150^\circ$

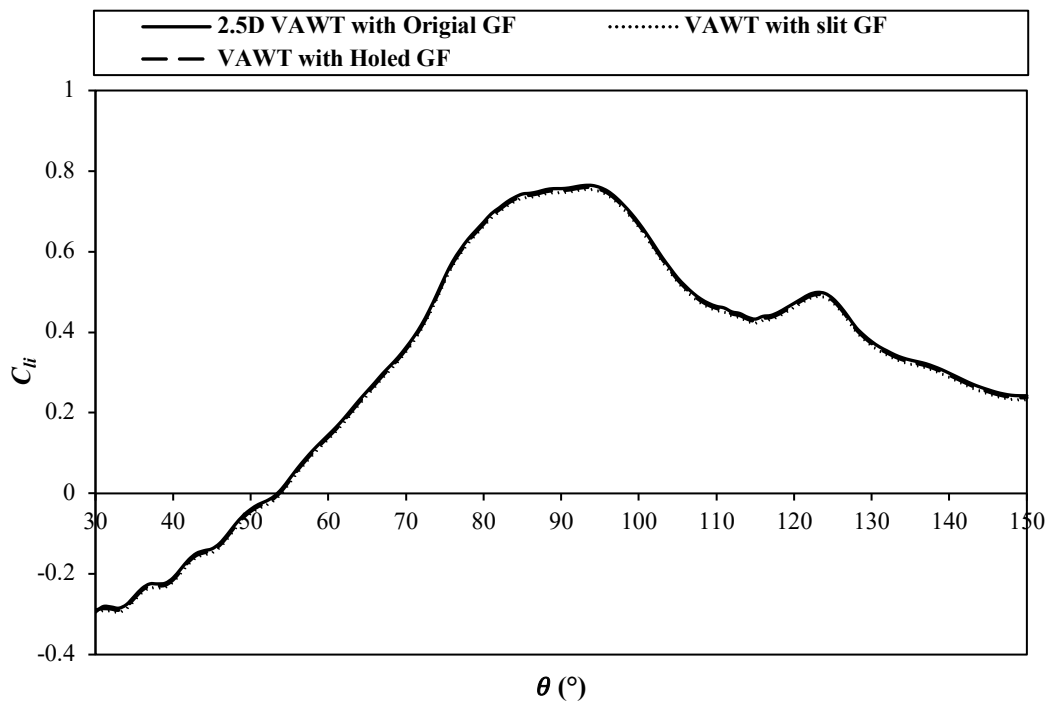


(c) At $\theta = 245-290^\circ$

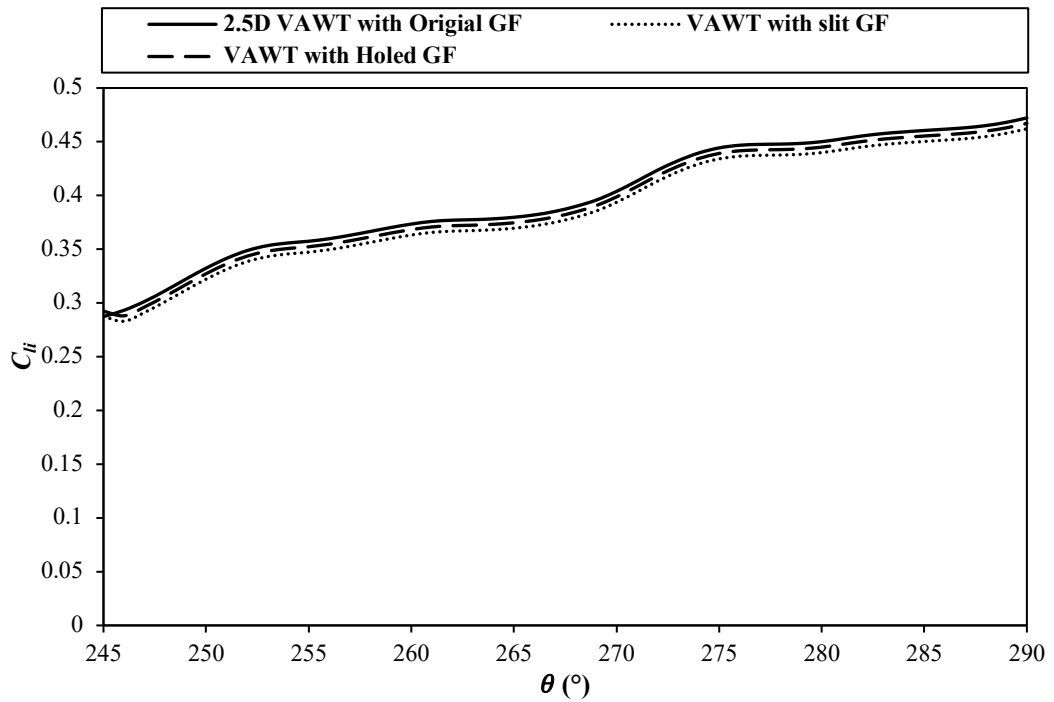
Figure 9.7 Instantaneous drag coefficients comparison of one selected blade (blade 1) between q3D VAWT with clean GF, VAWT with slit GF and VAWT with holed GF.



(a) One turbine revolution



(b) At $\theta = 30-150^\circ$



(c) At $\theta = 245-290^\circ$

Figure 9.8 Instantaneous lift coefficients comparison of one selected blade (blade 1) between q3D VAWT with clean GF, VAWT with slit GF and VAWT with holed GF.

Further investigation of the C_{di} and C_{li} coefficient distributions over one turbine revolution indicate that slits and holes have a different impact on drag and lift generation at a different azimuthal position of the blade of VAWT with GF. It can be observed in Figures 9.7 and 9.8 that slits and holes have a significant impact on the drag and lift generation of VAWT with GF at $\theta = 30-150^\circ$ and $\theta = 245-290^\circ$. At these azimuthal positions, the blade of VAWT experiences mostly low geometrical angle of attacks (AoA_D s) i.e., lower than stationary stall angle of attacks (see Figure 9.9). Note that, AoA_D (see Equation 3.5) is the angle of attack seen by the blade of VAWT as it rotates and will always change as the turbine rotates (i.e., changes the azimuthal position). The behaviour of slits and holes that do not significantly impact the C_{li} and C_{di} values at a high geometrical angle of attacks is in agreement with a previous study which mentioned that slits and holes could not anymore reduce drag at high angle of attack due to the wake of aerofoil becomes strongly asymmetrical (Meyer et al., 2006).

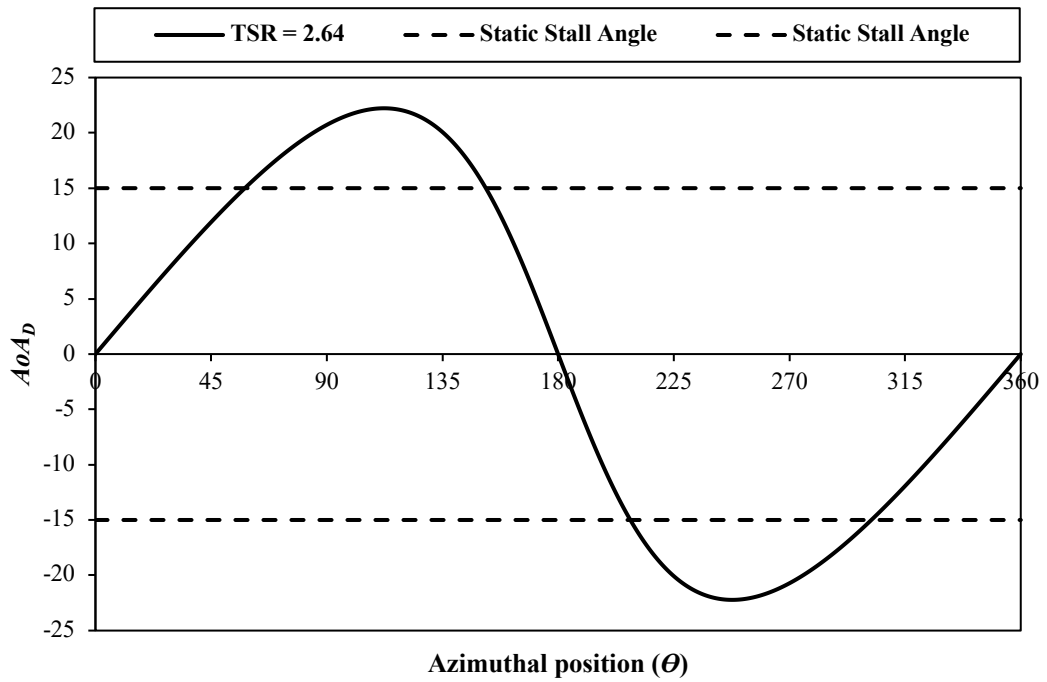
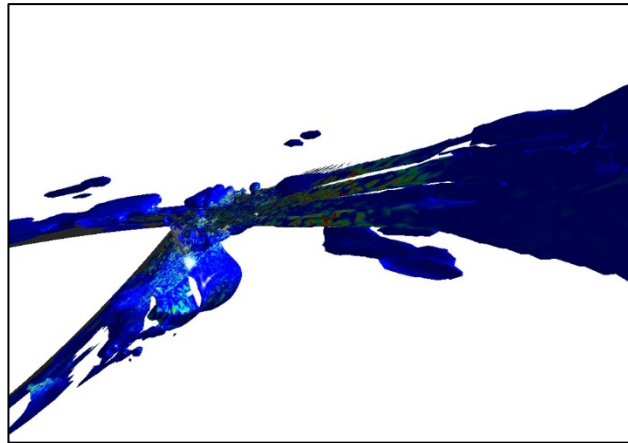


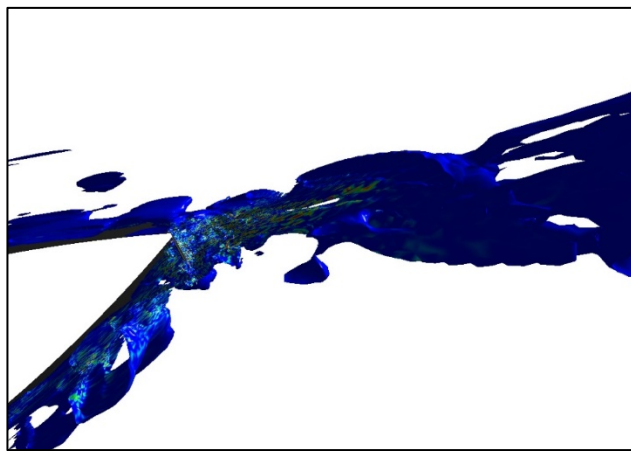
Figure 9.9 Geometrical angle of attack at $TSR = 2.64$ of Castelli, Englaro and Benini (2011) case.

9.4.3 Flow-field comparison

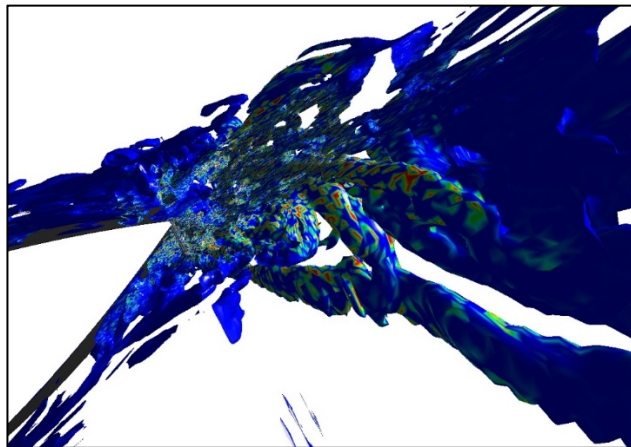
To understand how slits and holes can reduce the drag generation of VAWT with GF, the isosurface plots of Q criterion of blade 1 coloured by Q criterion at $\theta = 45^\circ$ where slits and holes have a significant impact on the drag and lift generation of VAWT with GF are depicted in Figure 9.10. It can be observed that compared to clean GF, GF with slits and GF with holes generate smaller structures of vortices with irregular orientation near the wake-field. Whilst the existence of slits can also trigger these vortices to interact and dissipate faster than vortices generated by clean GF, the GF with holes does not have this capability, resulting in lower levels of alteration of the flow characteristics of GF with holes. Regardless, this change behaviour of vortices is the reason behind the ability of GF with slits and GF with holes to reduce the drag generation of VAWT with GF.



(a)



(b)



(c)

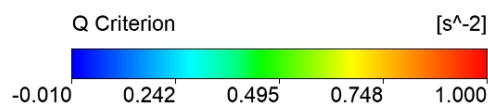


Figure 9.10 Comparison of an isosurface of Q criterion in the wake of the blade 1 (coloured by Q criterion) between 2.5D (a) VAWT with clean GF, (b) VAWT with slit GF and (c) VAWT with holed GF.

9.5 Chapter Summary and Future Work

The evaluation of the introduction of slits and holes in the GF to reduce the drag generation of three-straight-bladed VAWT with GF has been carried out. It can be concluded that indeed the slits and holes can reduce the drag generation of VAWT with GF with a slight reduction in lift generation due to the air flow through the slits and the air flow inside the holes reduce the effective surface of GF. The drag reduction is triggered by the ability of slits and holes to generate smaller structures of vortices with random orientation, which for VAWT with slit GF tend to interact and dissipate faster. Note that, the slits and holes have a significant impact on the drag and lift generation of VAWT with GF at $\theta = 30-150^\circ$ and $\theta = 245-290^\circ$ where the blade of VAWT experiences mostly low geometrical angle of attacks.

The existence of slits and holes can reduce the averaged drag coefficient of VAWT with GF by 8% and 0.29%, respectively. Nonetheless, slits and holes can also decrease the lift generation of VAWT with GF. Whilst slits decrease the averaged lift coefficient of VAWT with GF by 2%, holes reduce the averaged lift coefficient of VAWT with GF with a lower rate, i.e., 0.01%. Therefore, the lift-to-drag ratio of VAWT with slit GF and VAWT with holed GF are higher than VAWT with clean GF. This improvement leads to power coefficient improvement of VAWT with GF by around 6.5% for GF with slits and 0.28% GF with holes. However, as mentioned above, the improvement of C_{p-ave} in VAWT with holed GF compared to VAWT with clean GF is still questionable as the percentage of the improvement is still under the range of the numerical accuracy of CFD simulation. Hence, experimental study is necessary to confirm the ability of both of VAWT with slit GF and VAWT with holed GF to improve the performance of VAWT with clean GF.

The low capability of GF with holes to improve the C_{p-ave} improvement of VAWT with clean GF shows that the arrangement of the holes in the present study is not effective to change the flow behaviour and characteristics around the blade of VAWT with clean GF. It is due to the holes in the present study are introduced not in the direction of the incoming wind. As a result, the holes act as a cavity, and the flow cannot really go through them. Therefore, it is necessary to evaluate other arrangements of the holes in the future study, particularly creating the holes in the direction of the incoming wind.

It is also worth note that this evaluation of the application GF with slits and GF with holes in the blades of VAWT is only performed in the optimum TSR value of clean VAWT (i.e., $TSR = 2.64$). It means that this study only evaluated these modifications of the GF in one TSR regime, i.e., medium regime of $TSRs$. Therefore, the investigation of

the use of a GF with slits and a GF with holes in the VAWT blades in other *TSR* regimes (i.e., low and high regimes of *TSRs*) needs to be performed in the future study due to the different behaviour of the flow around the VAWT in a different *TSR* regime. By evaluating these modifications of the GF in other *TSR* regimes, the effectiveness of adding slits and holes to the GF to improve the performance of a VAWT with GF can be confirmed in all *TSR* regimes.

Chapter 10: Summary of Novelty and Contributions, Recommendations and Future Works

Evaluation of performance enhancement devices of lift-driven VAWTs in all *TSR* regimes using high-fidelity CFD has been discussed above. It is noticeable that high-fidelity CFD is necessary to accurately predict lift-driven VAWT performance and its aerodynamics and flow characteristics. High-fidelity CFD is also required for the evaluation of VAWT performance in all *TSR* regimes. URANS turbulence models are sufficient to predict the overall performance of lift-driven VAWTs in a single *TSR* regime. However, Hybrid RANS-LES turbulence models are necessary to investigate the aerodynamics and flow-field characteristics of lift-driven VAWTs and all *TSR* regimes.

Furthermore, the investigation of performance enhancement devices of lift-driven VAWTs shows that the Gurney flap and the straight upstream deflector increase the performance of lift-driven VAWTs in all *TSR* regimes. Nevertheless, the GF and the SUD utilise different approaches to improve the power generation of VAWTs in all *TSR* regimes. Hence, it is proven that design optimisation and flow analysis of GFs and SUDs need to be performed for each regime. In addition, adding the effect of a rotational flow and blade-to-blade interaction, the optimum geometric design of a GF is changed compared to the optimum design of a single stationary aerofoil. It confirms that design optimisation needs to be performed for a VAWT configuration (i.e., including rotational effects and blade-to-blade interaction). Moreover, combining an optimised GF and an optimised SUD does not further increase the power generation improvement of lift-driven VAWTs. The detailed summary of this study is discussed below based on the raised key questions in Chapter 1, Section 1.3.

10.1 Summary of Novelty and Contribution of this Study Based on Answer to the Raised Key Questions

1) *What are domain sizes, grid resolutions necessary to produce accurate simulation results?*

Based on the current study, the accuracy of CFD modelling of VAWTs is indeed sensitive to the domain sizes, spatial resolution, temporal resolution and revolution convergence. The following summaries are drawn based on the current study:

- Placing the inlet and outlet boundaries around $40D_{rotor}$ from the turbine rotational centre is necessary to avoid the effect of the outer numerical boundaries influencing the numerical results. A mesh with 174 elements around the blade is sufficient to generate great accuracy for flow with the Reynolds number based on the chord length (equalling 51480). Regarding the temporal resolution, it needs to be at least equal to 1° azimuthal increment of the rotation of the turbine, as further reduction of the azimuthal increment to 0.25° only changes the numerical C_{p-ave} by 0.44% compared to 1° azimuthal increment.
- For revolution convergence, it depends on the choice of turbulence model. The URANS turbulence models achieve faster revolution convergence than hybrid RANS-LES turbulence models due to the extended solving of flow fluctuations further from the wall. Two-equation URANS turbulence models achieve resolution convergence after 23 revolutions, whilst the four-equation URANS turbulence model needs 27 revolutions to achieve resolution convergence. On the other hand, hybrid RANS-LES turbulence models need at least 34 revolutions to achieve resolution convergence.

2) ***What kind of turbulence models or their modified versions can have minimum impact on the physical results in all TSR regimes?***

It is widely known that the accuracy of CFD predictions is highly affected by the choice of turbulence model. Due to higher computational cost, most of the previous CFD simulations of VAWTs are based on URANS turbulence models, particularly two-equation turbulence models such as $k-\epsilon$ realisable and $k-\omega$ SST. However, URANS turbulence models cannot predict the correct aerodynamic and flow-field characteristics during dynamic stall, which extensively happens in VAWTs. Therefore, an LES study is needed to improve the prediction of these characteristics. Nevertheless, LES significantly increases the computational cost compared to URANS turbulence models, which is not practical for design optimisation. Hence, hybrid RANS-LES is the better choice to improve the accuracy of CFD predictions with a lower increase of computational cost. In order to evaluate the ability of a hybrid RANS-LES model to predict the performance, aerodynamics and flow-field characteristics of a VAWT, this study compares three URANS turbulence models and four hybrid

RANS-LES turbulence models on their accuracies and abilities. This evaluation gives a better understanding of the capability of hybrid RANS-LES turbulence models in CFD modelling of VAWTs and to what extent they increase the computational cost compared to URANS turbulence models. It has never been done before as the previous study only focused on comparing URANS turbulence models (Rezaeiha, Montazeri and Blocken, 2019). The evaluation is performed at each TSR regime to understand each turbulence model's performance and its relation to different flow behaviour of the VAWT. The following summary of this evaluation can be found below.

- The current model can decrease the significant discrepancy (i.e., the difference between the simulation and experiment results) of C_{p-ave} prediction of the Castelli, Englaro and Benini (2011) model. All the compared turbulence models (RKE, SST, TSST, DDES, IDDES, SBES with $k-\omega$ SST and SBES with transition SST) can predict the trend-line of C_{p-ave} distribution over the evaluated $TSRs$ values. They can also predict the optimum value of TSR , i.e., $TSR = 2.64$.
- Two-equation URANS turbulence models (RKE and SST) produce the largest discrepancy of C_{p-ave} prediction in all TSR regimes compared to other evaluated turbulence models. The discrepancy is quite large in low regime of $TSRs$ (400%), whilst in medium regime of $TSRs$, the discrepancy is about 15%. The four-equation URANS turbulence models (TSST) reduce the discrepancy in low and medium regimes of $TSRs$ to about 100% and 8%, respectively, due to their capability to predict stronger dynamic stall, trailing-edge roll up and secondary vortices shown by the presence of vortex shedding at both the trailing-edge and the leading-edge. All URANS turbulence models have a similar capability to predict C_{p-ave} in a high regime of $TSRs$ (the discrepancy is about 17%).
- All the compared hybrid RANS-LES turbulence models generate smaller discrepancies than the URANS turbulence models in all TSR regimes. They can reduce the discrepancy to a similar value of about 60% in low regime of $TSRs$. Among the four compared hybrid RANS-LES turbulence models, SBES with TSST turbulence model generates the lowest discrepancy in the medium TSR regime (around 2.2% compared to experimental data). The SBES with TSST turbulence model and IDDES turbulence model can

produce a smaller discrepancy (about 2%) in high TSR regimes than DDES and SBES with SST $k-\omega$ models (approximately 15%). This better capability of hybrid RANS-LES turbulence models to predict the VAWT C_{p-ave} is caused by their better prediction of dynamic stall behaviour of the VAWT compared to using RANS turbulence models as indicated by further vortex shedding away from the near blade wall. In addition, they can also predict weak trailing-edge roll-up in high regime of $TSRs$ whilst URANS turbulence models only show weak shedding of the vortex around the trailing-edge. Overall, SBES with the TSST model generates the best accuracy in all TSR regimes compared to URANS and other hybrid RANS-LES turbulence models.

- The choice of turbulence model depends on the computational resources and the VAWT's operational conditions that need to be evaluated in both design and off-design points over a wider regime of $TSRs$. Due to the longer simulation time of hybrid RANS-LES turbulence models and more complex grid generation, URANS models are still the best choice for overall performance evaluation and the results produced are pretty reasonable (can be about 100%, 8% and 17% in low, medium and high regimes of $TSRs$, respectively) in terms of accuracy in a specific TSR regime. The TSST turbulence model is recommended for low to medium $TSRs$ regimes due to better accuracy at these regimes compared to using the RKE and SST models. Beyond the optimum TSR value, using RKE or SST turbulence models is acceptable as they produce relatively similar discrepancy of C_{p-ave} prediction as the TSST model results but in a shorter simulation time. For further analysis of the flow behaviour (such as wake development) or noise production and performance analysis in all TSR regimes, hybrid RANS-LES type of models are recommended, in particular, the SBES with transitional SST turbulence model as it produces accurate predictions in all TSR regimes (compared to experimental data, the discrepancies are approximately 20%, 2% and 2.2% in low, medium and high regimes of $TSRs$, respectively) with reasonable simulation time increment (about 24.5% longer than TSST turbulence model) and grid complexity. This study does not recommend the DDES or IDDES turbulence model as it can increase simulation time by around 4.5 times compared to the TSST turbulence model.

3) ***What is the accuracy comparison between 2D and 3D CFD simulations of the VAWT model for predicting experimental results?***

Having understood the limitations of the 2D model, this study also evaluates the 3D model of the bare VAWT using the most accurate turbulence model based on the turbulence model evaluation in Chapter 4. As discussed in Chapter 8, the findings of this evaluation are that:

- The 3D model under-predicts the C_{p-ave} compared to experimental data whilst the 2D model slightly over-predicts it at the mid-span plane using the SBES with TSST turbulence model. Note that, the prediction of the C_{p-ave} of the 2D model using URANS turbulence models is in agreement with other previous works (Wang et al., 2018; Castelli, Englaro and Benini, 2011). The 3D model result under-predicts the C_{p-ave} by 7.4% in the mid-span plane compared to experimental data. As the measured position gets closer to the blade tip, the deviation between predicted 3D model C_{p-ave} and experimental data increases with the maximum discrepancy at 17.52% at the blade tip.
- On average, the 3D model under-predicts the C_{p-ave} compared with experimental data by around 13.13468%, showing that the SBES with TSST turbulence model for 3D models only decreases CFD modelling accuracy in the C_{p-ave} prediction. This is probably due to the fact that the ability of the SBES with TSST turbulence model to generate a very close value of C_{p-ave} to the experimental result in the 2D model is mainly affected by the accuracy of numerical predictions causing over-prediction of the pressure decrease and the size of the flow separation region. This accuracy is related to the level of governing equations (RANS or hybrid RANS-LES or LES), numerical treatments (low or high schemes) and other models (e.g., turbulence models). The investigation of 3D model prediction using the URANS turbulence model (i.e., SST turbulence model) shows that the 3D model with SST turbulence model still over-predicts the C_{p-ave} from the experimental result with a lower discrepancy, i.e., 1.16629%. Consequently, the SST turbulence model is capable of C_{p-ave} prediction of the 3D CFD model in $TSR = 2.64$. Note that, the 3D model with SST turbulence model still inherits the inability of the SST turbulence model to predict dynamic stall, trailing-edge roll up, and secondary vortices in the 2D model.

4) ***What kind of blade modifications and flow augmentation devices can effectively increase the inflow wind profile and improve the turbine's self-starting behaviour and efficiency in all TSR regimes?***

Based on the discussion in Chapter 2, Section 2.5.1, it is noticeable that using the Gurney flap or the straight upstream deflector is the best choice for the performance enhancement device of lift-driven VAWTs in all *TSR* regimes. Nevertheless, several research gaps need to be investigated in designing these two performance enhancement devices of VAWTs (see Chapter 2, Section 2.5.1). Therefore, this study investigates the design optimisation and performance evaluation of the GF and the SUD in each *TSR* regime using SBES with transitional SST turbulence models. The design optimisation is performed for a VAWT configuration to accommodate the effect of rotational flow and blade-to-blade interaction. In addition, this study also evaluates the combination of GF and SUD as performance enhancement devices of lift-driven VAWTs. 3D modifications of GFs in order to further improve the performance enhancement of lift-driven VAWT is also investigated. The detailed results can be found in Chapters 5, 6, 7 and 9. The main results of these investigations are:

- The stand-alone GF, stand-alone SUD and the combination of GF and SUD can improve the C_{p-ave} of lift-driven VAWT in all *TSR* regimes. The procedure of how the GF and the SUD improve the C_{p-ave} of lift-driven VAWT is different in each *TSR* regime. In low regime of *TSRs*, The GF increases the C_{p-ave} of the turbine by improving the positive moment production and reducing the moment fluctuation due to its ability to ease the dynamic stall of the turbine. Meanwhile, the SUD improves the average power coefficient of VAWT in this regime of *TSRs* by decreasing the negative moment production of VAWT due to higher rotational speed. In medium regime of *TSRs*, both the GF and the SUD increase the C_{p-ave} of the turbine by completely removing the negative moment production due to lift generation increase by easing the dynamic stall and increasing the rotational speed, respectively. In high regime of *TSRs*, the GF completely removes the negative moment production of the VAWT to increase the C_{p-ave} of the turbine. On the other hand, the SUD reduces the negative moment production of the turbine and increases the optimum moment production of the turbine.

- All performance enhancement devices experience a decrease in the rate of C_{p-ave} improvement as the TSR regime increases. As the TSR regime decreases, the AoA_D beyond the static stall AoA works on the blade of the VAWT becoming higher. Hence, the GF benefit of increasing the maximum lift and delaying the stall can be utilised effectively in low regime of $TSRs$ compared to medium and high regimes of $TSRs$. Meanwhile, in the case of the SUD, in low regime of $TSRs$, the enhancement of the rotational speed as a result of incoming wind speed increase has great benefit in helping the turbine to reduce high negative moment production, which leads to the improvement of the self-starting ability of the turbine and obviously, power generation increase. However, the higher rotational speed can also introduce a blockage effect and higher vibration in medium and high regimes of $TSRs$, resulting in less improvement in the C_{p-ave} of the turbine.
- The GF has the highest loss in its ability to enhance the C_{p-ave} of the turbine when used in high regime of $TSRs$ (e.g., compared to medium regime of $TSRs$, the VAWT with GF loses this ability by about 28% whilst a VAWT with SUD only loses by around 0.3% in high regime of $TSRs$). Hence, the GF is more suitable as a performance enhancement device of lift-driven VAWT in low and medium regimes of $TSRs$. In these two TSR regimes, the dynamic stall is stronger than in high regime of $TSRs$. Therefore, the ability of the GF to control dynamic stalls can be utilised effectively. In high regime of $TSRs$, the SUD is a better choice for performance enhancement of the VAWT. The flow is relatively stable in this regime of $TSRs$, so the dynamic stall control device is inappropriate. Therefore, to improve the performance enhancement of a VAWT, it is more relevant to increase the incoming wind speed and guide the wind to the rotor area of VAWT to improve the rotational speed of the turbine.
- Combining an optimised GF and an optimised SUD cannot enhance the improvement of C_{p-ave} caused by a stand-alone optimised GF or a stand-alone optimised SUD in all TSR regimes. In all TSR regimes, combining the GF and SUD will only introduce higher vortex generation as the flow characteristics are changed mainly by the SUD and GF losing their abilities to ease the dynamic stall of the VAWT as higher drag and vibration production are induced.

- Introducing 3D modifications of the GF (i.e., slits or holes) in the blades of the VAWT with GF further improves the power coefficient of lift-driven VAWTs. These modifications are the application of a flow control device called riblets (for the GF with slits) to the blades of the VAWT. The existence of slits and holes can reduce the drag generation of the VAWT with GF by 8% and 0.29%, respectively. VAWT with slit GF and VAWT with holed GF can produce smaller vortices with an irregular orientation that for VAWT with slit GF tends to interact and dissipate faster than VAWT with clean GF. However, the slits and holes can also decrease the lift generation of VAWT with GF by 2% and 0.01%, respectively. It is because the air flow through the slits and the air flow inside the holes reduces the effective surface of GF. The modification of GF by adding slits can improve the power coefficient of VAWT with GF by 6.5%, whilst the holes can only enhance the power coefficient of VAWT with GF by 0.28%. Noting that, the improvement of C_{p-ave} in VAWT with holed GF compared to VAWT with clean GF is still questionable as the percentage of the improvement is still under the range of the numerical accuracy of CFD simulation. Hence, experimental study is necessary to confirm the ability of both of VAWT with slit GF and VAWT with holed GF to improve the performance of VAWT with clean GF.

5) ***What is the optimisation method used to perform design optimisation? What is the optimum design of each enhancement device that can give an optimum improvement of VAWT performance in all TSR regimes?***

Most previous studies performed the design optimisation at a single stationary aerofoil rather than a turbine configuration. It can lead to wrong optimum design as lift-driven VAWT is highly affected by rotating flow and blade-to-blade interaction. Furthermore, due to the different behaviour of flow around a lift-driven VAWT in different *TSR* regimes, it is also essential to perform design optimisation in each *TSR* regime. Therefore, this study evaluates the design optimisation of a GF and a SUD in a VAWT configuration and each *TSR* regime. To improve the design optimisation of GF, this study performs the design evaluation in simultaneous optimisation of three parameters (height, mounting angle and position from trailing-edge) using Taguchi's method rather

than single parameter variation at a time used in previous studies of GF application in VAWT. Evaluation of GF shape modification's effect (i.e., wedged and curved GFs) to increment the turbine's C_{p-ave} enhancement rate is also performed. Regarding the design optimisation of SUD, this study uses a different approach to decide the position of the deflector upstream of the turbine. Instead of directly deciding the deflector's position upstream of the turbine, this study evaluates the location of the deflector upstream of the turbine so the optimum position of the deflector can be obtained. After that, the optimisations of the width and inclination angle are performed. The findings of this design optimisation of GF and SUD can be summarised as follows:

- GF geometries optimisation needs to be done in a VAWT configuration (i.e., including rotational effects and blade-to-blade interactions) rather than a single stationary aerofoil. For example, in the optimum height case, whilst single stationary GF usually has optimum height at $H = 2\% c$, the VAWT with GF has the optimum height at $H = 3\% c$. It is probably because of the rotational effects, there is no vortex generation upstream of the flap (see Figure 5.31), whilst for single stationary aerofoil, there is vortex generation upstream of the flap (see Figure A.14 in Appendix).
- It is crucial to evaluate the geometries optimisation in all TSR regimes. GF has the same optimum height and mounting angle ($H = 3\% c$ and $\theta_{GF} = 90^\circ$) in all TSR regimes. There is a difference in optimum position from trailing-edge between low regime of $TSRs$ and medium and high regimes of $TSRs$. In low regime of $TSRs$, the C_{p-ave} value reaches its optimum value when the location of GF is at $s = 4\% c$. Meanwhile, changing the position of GF toward the leading-edge of the blade only reduces the C_{p-ave} generation in medium and high regimes of $TSRs$. In these two TSR regimes, the optimum position of the GF is at the trailing-edge of the blade ($s = 0\% c$).
- Modifying the shape of original GF to wedge and curve generally cannot further improve the performance enhancement of VAWT with GF in all TSR regimes. The exception is only for wedged GF, which, in low regime of $TSRs$, it can slightly improve the C_{p-ave} value by about 3% compared to the original GF shape. The wedged and curved GFs cannot increase the improvement of C_{p-ave} value due to the height of GF is already relatively high and the advantages of the wedged and curved GFs to remove the vortex

generation upstream of the flap on the isolated (stationary) aerofoil is no longer applicable at a turbine configuration as VAWT with original GF does not induce this type of vortex. It shows the importance to evaluate the performance enhancement device of VAWT in a VAWT configuration rather than in a single stationary aerofoil.

- It is better to choose GF with a height of 3% c , a mounting angle of 90° and mounted at the trailing-edge of the blades of VAWTs to generate relatively higher average performance enhancement in all TSR regimes. GF with this geometry can produce optimum C_{p-ave} enhancement in medium and high regimes of $TSRs$ with still relatively great C_{p-ave} improvement in low regime of $TSRs$.
- Placing deflectors both at the upward and downward of the upstream of VAWT can generate the best improvement of power generation in all TSR regimes compared to other configurations (upward, downward and middle SUD). The gap between two deflectors in both configurations introduces the converged duct/nozzle effect to the flow, further enhancing the incoming wind speed. Adding a deflector at both upward and downward can also direct the wind both at the upward and downward of VAWT, resulting in larger wind directed to the rotor area of the turbine. Moreover, compared to other configurations, the blades of VAWT with both upward and downward SUD are mostly in avoided near-wake regions of the deflector when they rotate.
- In all TSR regimes, the increment of the width has a slightly positive effect on the increment of C_{p-ave} value of VAWT as long as the positive influence of narrower gap between two deflectors can surpass the disadvantage of larger wake region caused by the wider deflector. Meanwhile, adding inclination angle to the SUD generates worse C_{p-ave} improvement than SUD without inclination angle in all TSR regimes. Surprisingly, whilst tilting deflector indeed can reduce the vortices generation behind the deflector to reduce flow unsteadiness, the decrease in effective width only decreases the C_{p-ave} value of VAWT.
- Both configuration (i.e., placing deflector at both upward and downward of the upstream of VAWT) with original geometry (see Table 6.1) is

acceptable as SUD design to improve the performance of VAWT in all *TSR* regimes.

10.2 Recommendations and Future Works

In this study, a numerical method using high-fidelity CFD is applied to evaluate the design of the performance enhancement device of lift-driven VAWT. Hence, an experimental study is necessary to confirm the results of this study. Broader flow parameters investigation is also desired to achieve a better design of performance enhancement devices of lift-driven VAWT that can be applied in any operation condition. In addition, deeper analysis of turbulence model choice for CFD simulation of lift-driven VAWT is still essential to explore a better choice of turbulence model with better accuracy and lower computational costs. Therefore, the recommendation and future works of this study are presented below.

- It is recommended to perform an experimental study of the optimum design of GF and SUD to validate the rate of C_{p-ave} improvement of the CFD modelling.
- It is recommended to perform the experimental study of the validated model of Castelli, Englaro and Benini (2011) to enhance the available experimental data (for example, pressure distribution and flow-field visualisation) of this type of VAWT.
- This study has investigated the effect of the *TSR* variation on the performance of VAWT. It is worthy of studying the effect of the incoming wind speed with the same *TSR* regime to investigate the effect of the change of the rotational speed due to the change of incoming wind speed on the performance of VAWT.
- Hybrid RANS-LES has several options of sub-grid-scale models. It is worthy of investigating this sub-grid models effect on the accuracy and simulation cost of CFD modelling of VAWT.
- Although a representative *TSR* is sufficient enough to perform design optimisation for each *TSR* regime, due to similar flow behaviour in the same *TSR* regime, it is recommended to perform design optimisation in more than one *TSR* value in each regime.
- The evaluation of the combination of dynamic stall control and flow augmentation devices as the performance enhancement of VAWT in this present study is based on the optimum geometry of stand-alone GF and stand-alone SUD. Therefore, it is interesting to evaluate the effect of the combination of these two devices to the

performance enhancement of VAWT in non-optimum geometry of stand-alone GF and stand-alone SUD.

- As the arrangement of holes in the holed GF in the present study has only a low impact on the improvement of C_{p-ave} of VAWT with clean GF, it is recommended to investigate other holes arrangement of holed GF in the future by considering the creation of holes in the direction of the incoming wind.

References

- Abdelghany, E. S., Khalil, E. E., Abdellatif, O. E. and Elhariry, G. (2016) Air craft winglet design and performance: Cant angle effect. *Journal of Robotics and Mechanical Engineering Research*, 1(3), pp. 28-34.
- Acarer, S. (2020) Peak lift-to-drag ratio enhancement of the DU12W262 airfoil by passive flow control and its impact on horizontal and vertical axis wind turbines. *Energy*, 201, Paper ID 117659.
- Ahmed, N. A. and Cameron, M. (2014) The challenges and possible solutions of horizontal axis wind turbines as a clean energy solution for the future. *Renewable and Sustainable Energy Reviews*, 38, pp. 439-460.
- Akour, S. N., Al-Heydari, M., Ahmed, T. and Khalil, K. A. (2018) Experimental and theoretical investigation of micro wind turbine for low wind speed regions. *Renewable Energy*, 116(A), pp. 215-223.
- Alam, M. F., Thompson, D. and Walters, D. K. (2017) *Critical assessment of hybrid RANS-LES modeling for attached and separated flows*. In: *Turbulence Modelling Approaches - Current State, Development Prospects, Applications*. IntechOpen. Available from: <https://www.intechopen.com/chapters/56282> [Accessed 02 November 2021].
- Almohammadi, K., Ingham, D., Ma, L. and Pourkashanian, M. (2015) Modeling dynamic stall of a straight blade vertical axis wind turbine. *Journal of Fluids and Structures*, 57, pp. 144-158.
- Anon. (2017) Wind Turbines. [Online] Available from: <https://pursuitengineering.blogspot.co.uk/2017/02/wind-turbines.html> [Accessed 21 February 2018].
- ANSYS Inc., 2010. ANSYS Meshing User's Guide. Canonsburg.
- Ansys (2020) Ansys Fluent User's Guide. [Online] Available from: https://ansyshelp.ansys.com/account/secured?returnurl=/Views/Secured/corp/v194/flu_ug/flu_ug.html [Accessed 02 11 2020].
- Arab, A., Javadi, M., Anbarsooz, M. and Moghiman, M. (2017) A numerical study on the aerodynamic performance and the self-starting characteristics of a Darrieus wind turbine considering its moment of inertia. *Renewable Energy*, 107, pp. 298-311.
- Arpino, F., Cortellessa, G., Scungio, M., Fresilli, G., Facci, A. and Frattolillo, A. (2021) PIV measurements over a double bladed Darrieus-type vertical axis wind turbine: A validation benchmark. *Flow Measurement and Instrumentation*, 82, Paper ID 102064
- Bakırcı, M. and Yılmaz, S. (2018) Theoretical and computational investigations of the optimal tip-speed ratio of horizontal-axis wind turbines. *Engineering Science and Technology, an International Journal*, 21(6), pp. 1128-1142.
- Balduzzi, F., Bianchini A., Maleci R., Ferrara G. and Ferrari, L. (2016) Critical issues in the CFD simulation of Darrieus wind turbines. *Renewable Energy*, 85, pp. 419-435.

- Bangga, G. et al. (2017) Improving a two-equation eddy-viscosity turbulence model to predict the aerodynamic performance of thick wind turbine airfoils. *Journal of Physics: Conference Series*, 974, Paper ID 012019
- Bangga, G., Weihing, P., Lutz, T. and Krämer, E. (2017) Effect of computational grid on accurate prediction of a wind turbine rotor using delayed detached-eddy simulations. *Journal of Mechanical Science and Technology*, 31(5), pp. 2359-2364.
- Belamadi, R., Djemili, A., Ilinca, A. and Mdouki, R., 2016. Aerodynamic performance analysis of slotted airfoils for application to wind turbine blades. *Journal of Wind Engineering and Industrial Aerodynamics*, 151, pp. 79-99.
- Bhargav, M., Kishore, V. R. and Laxman, V. (2016) Influence of fluctuating wind conditions on vertical axis wind turbine using a three dimensional CFD model. *Journal of Wind Engineering and Industrial Aerodynamics*, 158, pp. 98-108.
- Bianchini, A., Balduzzi, F., Rosa, D. D. and Ferrara, G. (2019) On the use of Gurney Flaps for the aerodynamic performance augmentation of Darrieus wind turbines. *Energy Conversion and Management*, 184, pp. 402-415.
- Bianchini, A., Ferrara, G. and Ferrari, L. (2015) Design guidelines for H-Darrieus wind turbines: Optimization of the annual energy yield. *Energy Conversion and Management*, 89, pp. 690-707.
- BP PLC (2017) *BP statistical review of world energy 2017*. London: BP.
- Cai, W., Li, Y. and Liu, C. (2019) Comparative study of scale-resolving simulations for marine-propeller unsteady flows. *International Communications in Heat and Mass Transfer*, 100, pp. 1-11.
- Calarese, W., Crisler, W. P. and Gustafson, G. L., 1985. Afterbody drag reduction by vortex generators. *AIAA 23rd Aerospace Sciences Meeting*. Reno, Nevada, 14-17 January 1985. AIAA, Paper ID 85-0354.
- Castelli, M. R., Ardizzon, G., Battisti, L., Benini, E. and Pavesi, G. (2010) Modeling strategy and numerical validation for a Darrieus vertical axis micro-wind turbine. *ASME 2010 International Mechanical Engineering Congress & Exposition*. Vancouver, 12-18 November 2010. ASME Proceedings, pp. 409-418.
- Castelli, M. R., Englaro, A. and Benini, E. (2011) The Darrieus wind turbine: Proposal for a new performance prediction model based on CFD. *Energy*, 36, pp. 4919-4934.
- Cavazzuti, M. (2012) *Optimization methods: from theory to design scientific and technological aspects in mechanics*. Berlin: Springer Science & Business Media.
- Chamorro, L. P., Arndt, R. E. A. and Sotiropoulos, F. (2013) Drag reduction of large wind turbine blades through riblets: evaluation of riblet geometry and application strategies. *Renewable Energy*, 50, pp. 1095-1105.
- Chen, J., Yang, H., Yang, M. and Xu, H. (2015) The effect of the opening ratio and location on the performance of a novel vertical axis Darrieus turbine. *Energy*, 89, pp. 819-834.

- Childs, P. R. (2011) *Rotating cylinders, annuli, and spheres*. In: Rotating Flow. Oxford: Elsevier, pp. 177-247.
- Chong, W., Fazlizan, A., Poh, S. C., Pan, K. C., Hew, W. P. and Hsiao, F. B. (2013) The design, simulation and testing of an urban vertical axis wind turbine with the omnidirection-guide-vane. *Applied Energy*, 112, pp. 601-609.
- Choudhry, A., Arjomandi, M. and Kelso, R. (2016) Methods to control dynamic stall for wind turbine applications. *Renewable Energy*, 86, pp. 26-37.
- Chougule, P. D., Rosendahl, L. and Nielsen, S. R. (2015) Experimental study of the effect of a slat angle on double-element airfoil and application in vertical axis wind turbine. *Ships and Offshore Structures*, 10(2), pp. 176-182.
- Chougule, P. and Nielsen, S. R. (2014) Simulation of flow over double-element airfoil and wind tunnel test for use in vertical axis wind turbine. *Journal of Physics: Conference Series: The Science of Making Torque from Wind 2014 (TORQUE 2014)*. Copenhagen, 18-20 June 2014. IOPScience, Paper ID 012009.
- Claessens, M. (2006) *The design and testing of airfoils for application in small vertical*. Master Thesis. Delft: Delft University of Technology.
- Crawford, M. (2012) *Vertical-axis wind turbines: time for a comeback?*. [Online] Available from: <https://www.asme.org/engineering-topics/articles/turbines/vertical-axis-wind-turbines-time-for-a-comeback> [Accessed 15 February 2018].
- D'Ambrosio, M. and Medaglia, M. (2010) *Vertical axis wind turbines: History, technology and applications*. Master Thesis. Halmstad: Halmstad University.
- Delafin, P. L., Nishino, T., Kolios, A. and Wang, L. (2017) Comparison of low-order aerodynamic models and RANS CFD for full scale 3D vertical axis wind turbines. *Renewable Energy*, 109, pp. 564-575.
- Dixon, K. (2008) *The near wake structure of a vertical axis wind turbine*. Master Thesis. Delft: Delft University of Technology.
- Elkhoury, M., Kiwata, T. and Aoun, E. (2015) Experimental and numerical investigation of a three-dimensional vertical-axis wind turbine with variable-pitch. *Journal of Wind Engineering & Industrial Aerodynamics*, 139, pp. 111–123.
- Elkhoury, M., Kiwata, T., Nagao, K., Kono, T. and Elhajj, F. (2019) Wind tunnel experiments and Delayed Detached Eddy Simulation of a three-bladed micro vertical axis wind turbine. *Renewable Energy*, 128, pp. 63-74.
- Elsakka, M. (2020) *The aerodynamics of fixed and variable pitch vertical axis wind turbine*. PhD Thesis. Sheffield: University of Sheffield.
- Ferreira, C. J. S., van Kuik, G., van Bussel, G. and Scarano, F. (2009) Visualization by PIV of dynamic stall on a vertical axis wind turbine. *Experiments in Fluids*, 46, pp. 97-108.

- Ferreira, C. J. S., van Zuijlen, A., Bijl, H., van Bussel, G. and van Kuik, G. (2010) Simulating dynamic stall in a two-dimensional vertical-axis wind turbine: verification and validation with particle image velocimetry data. *Wind Energy*, 13(1), pp. 1-17.
- Fikadea, G., Bekeleb, A., Venkatachalam, C. and Parthiban, M. (2020) Effects of dimples on aerodynamic performance of horizontal axis wind turbine blades. *International Research Journal of Engineering and Technology (IRJET)*, 7(1), pp. 525-529.
- Frank, T. and Menter, F. (2017) Validation of URANS SST and SBES in ANSYS CFD for the turbulent mixing of two parallel planar water jets impinging on a stationary pool. *ASME 2017 Verification and Validation Symposium*, Las Vegas: 3-5 May 2017. ASME Proceedings, Paper ID VVS2017-4047.
- Ghasemian, M., Ashrafi, Z. N. and Sedaghat, A. (2017) A review on computational fluid dynamic simulation techniques for Darrieus vertical axis wind turbines. *Energy Conversion and Management*, 149, pp. 87-100.
- Ghasemian, M. and Nejat, A. (2015) Aero-acoustics prediction of a vertical axis wind turbine using Large Eddy Simulation and acoustic analogy. *Energy*, 88, pp. 711-717.
- Ghazalla, R. A., Mohamed, M. H. and Hafiz, A. A. (2019) Synergistic analysis of a Darrieus wind turbine using computational fluid dynamics. *Energy*, 189, Paper ID. 116214.
- Global Wind Energy Council (2018) *Global wind statistics 2017*. Belgium: Global Wind Energy Council.
- Han, M., Lim, H., Jang, Y. -G., Lee, S. and Lee, S. -J. (2003) Fabrication of a micro-riblet film and drag reduction effects on curved objects. *TRANSDUCERS '03, 12th International Conference on Solid-State Sensors, Actuators and Microsystems*. Boston: 8-12 June 2003. Digest of Technical Papers (Cat. No.03TH8664), 1, pp. 396-399.
- Heine, B., Mulleners, K., Joubert, G. and Raffel, M. (2013) Dynamic stall control by passive disturbance generators. *AIAA Journal*, 51(9), pp. 2086-2097.
- He, X., Wang, J., Yang, M., Ma, D., Yan, C. and Liu, P. (2016) Numerical simulation of Gurney flap on SFYT15thick airfoil. *Theoretical and Applied Mechanics Letters*, 6(6), pp. 286-292.
- Hirsch, H. and Mandal, A. (1987) A cascade theory for the aerodynamic performance of darrieus wind turbines. *Wind Engineering*, 11(3), pp. 164-175.
- Hofemann, C., Ferreira, C. S., Dixon, K., van Bussel, G., van Kuik, G. and Scarano, F. (2008) 3D stereo PIV study of tip vortex evolution on a VAWT. *Proceeding of European wind energy conference and exhibition European Wind Energy Association (EWEA)*. Brussels: 31 March-3 April 2008. pp. 1-8.
- Howell, R., Qin, N., Edwards, J. and Durrani, N., 2010. Wind tunnel and numerical study of a small vertical axis wind turbine. *Renewable Energy*, 35, pp. 412-422.

- Ishugah, T., Li, Y., Wang, R. and Kiplagat, J. (2014) Advances in wind energy resource exploitation in urban environment: A review. *Renewable and Sustainable Energy Reviews*, 37, pp. 613-626.
- Islam, M., Ting, D. S.-K. and Fartaj, A. (2008) Aerodynamic models for Darrieus-type straight-bladed vertical axis wind turbines. *Renewable and Sustainable Energy Reviews*, 12(4), pp. 1087-1109.
- Ismail, M. F. and Vijayaraghavan, K. (2015) The effects of aerofoil profile modification on a vertical axis wind turbine performance. *Energy*, 80, pp. 20-31.
- Jain, S., Sitaram, N. and Krishnaswamy, S. (2015) Computational investigations on the effects of Gurney Flap on airfoil aerodynamics. *International Scholarly Research Notice*, Paper ID 402358.
- Jin, X., Wang, Y., Ju, W., He, J. and Xie, S. (2018) Investigation into parameter influence of upstream deflector on vertical axis wind turbines output power via three-dimensional CFD simulation. *Renewable Energy*, 115, pp. 41-53.
- Jin, X., Zhao, G., Gao, K. J. and Ju, W. (2015) Darrieus vertical axis wind turbine: Basic research methods. *Renewable and Sustainable Energy Reviews*, 42, pp. 212-225.
- Johari, H., Henoch, C., Custodio, D. and Levshin, A. (2017) Effects of leading-edge protuberances on airfoil performance. *AIAA Journal*, 45(11), pp. 2634-2642.
- Kato, M. and Launder, B. E. (1993) The modelling of turbulent flow around stationary and vibrating square cylinders. *Ninth Symposium on "Turbulent Shear Flows*. Kyoto, 16-18 August 1993.
- Kemmler, S., Fuchs, A., Leopold, T. and Bertsche, B. (2015) Comparison of Taguchi method and robust design optimization (RDO) - by application of a functional adaptive simulation model for the robust product-optimization of an adjuster unit -. *Weimar Optimization and Stochastic Days*. Weimar: 5-6 November.
- Kim, D. and Gharib, M. (2013) Efficiency improvement of straight-bladed vertical-axis wind turbines with an upstream deflector. *Journal of Wind Engineering and Industrial Aerodynamics*, 115, pp. 48-52.
- Kim, D. and Gharib, M. (2014) Unsteady loading of a vertical-axis turbine in the interaction with an upstream deflector. *Experiments in Fluids*, 55, Paper ID 1658.
- Korprasertsak, N. and Leephakpreeda, T. (2016) Analysis and optimal design of wind boosters for Vertical Axis Wind Turbines at low wind speed. *Journal of Wind Engineering and Industrial Aerodynamics*, 159, pp. 9-18.
- Lam, H. and Peng, H. (2016) Study of wake characteristics of a vertical axis wind turbine by two- and three-dimensional computational fluid dynamics simulations. *Renewable Energy*, 90, pp. 386-398.
- Langtry, R. B., Gola, J. and Menter, F. (2006) Predicting 2D airfoil and 3D wind turbine rotor performance using a transition model for general CFD codes. *44th AIAA Aerospace*

Sciences Meeting and Exhibit. Reno, Nevada, 9-12 January 2006. AIAA, Paper ID 2006-0395.

Langtry, R. B., Menter, F. R., Likki, S. R., Suzen, Y. B., Huang, P. G. and Völker, S. (2006) A correlation-based transition model using local variables—Part II: Test cases and industrial applications. *Journal of Turbomachinery*, 128(3), pp. 423-434.

Langtry, R. and Menter, F. (2009) Correlation-based transition modeling for unstructured parallelized computational fluid dynamics codes. *AIAA Journal*, 47, pp. 2894-2906.

Lanzafame, R., Mauro, S. and Messina, M. (2013) 2D CFD modeling of H-Darrieus wind turbines using a transition turbulence model. *68th Conference of the Italian Thermal Machines Engineering Association, ATI2013*. Bologna, 11-13 September 2013.

Lanzafame, R., Mauro, S., Messina, M. and Brusca, S. (2020) Development and validation of CFD 2D models for the simulation of micro H-Darrieus turbines subjected to high boundary layer instabilities. *Energies*, 13, Paper ID 5564.

Larsen, H. C. (1975) Summary of a vortex theory of the Cyclogiro. *Second US National Conferences on Wind Engineering Research*. Colorado State University, 22-25 June 1975. Colorado: Colorado State University.

Launder, B. E. and Spalding, D. B. (1972) *Lectures in mathematical models of turbulence*, London, England: Academic Press.

Lee, Y.-T. and Lim, H.-C. (2015) Numerical study of the aerodynamic performance of a 500 W Darrieus-type vertical-axis wind turbine. *Renewable Energy*, 83, pp. 407-415.

Lei, H., Zhou, D., Bao, Y., Li, Y. and Han, Z. (2017) Three-dimensional Improved Delayed Detached Eddy Simulation of a two-bladed vertical axis wind turbine. *Energy Conversion and Management*, 133, pp. 235-248.

Letizia, S. and Zanforlin, S. (2016) Hybrid CFD-source terms modelling of a diffuser-augmented vertical axis wind turbine. *Energy Procedia*, 101, pp. 1280-1287.

Li, C., Zhu, S., Xu, Y. and Xiao, Y. (2013) 2.5D large eddy simulation of vertical axis wind turbine in consideration of high angle of attack flow. *Renewable Energy*, 51, pp. 317-330.

Liebeck, R. H. (1978) Design of subsonic airfoils for high lift. *Journal of Aircraft*, 15(9), pp. 547-561.

Liu, C., Bu, W., Xu, D., Lei, Y. and Li, X. (2017) Application of Hybrid RANS/LES turbulence models in rotor-stator fluid machinery: A comparative study. *International Journal of Numerical Methods For Heat & Fluid Flow*, 27(12), pp. 2717-2743.

Malael, I., Bogateanu, R. and Dumitrescu, H. (2012) Theoretical performances of double Gurney Flap equipped the VAWTs. *INCAS BULLETIN*, 4(4), pp. 93-99.

Malael, I., Dumitrescu, H. and Cardos, V. (2014) Numerical simulation of vertical axis wind turbine at low speed ratios. *Global Journal of Researches in Engineering: I Numerical Methods*, 14(1), pp. 9-20.

- Ma, N., Lei, H., Han, Z., Zhou, D., Bao, Y., Zhang, K., Zhou, L. and Chen, C. (2018) Airfoil optimization to improve power performance of a high-solidity vertical axis wind turbine at a moderate tip speed ratio. *Energy*, 150, pp. 236-252.
- Martin, S. and Bhushan, B. (2016a) Modeling and optimization of shark-inspired riblet geometries for low drag applications. *Journal of Colloid and Interface Science*, 474, pp. 206-215.
- Martin, S. and Bhushan, B. (2016b) Discovery of riblets in a bird beak (Rynchops) for low fluid drag. *Philosophical Transactions of the Royal Society A: Mathematical, Physical and Engineering Sciences*, Paper ID 20160134.
- McDonough, J. M. (2007) *Introductory lectures on turbulence physics, mathematics and modeling*, Kentucky, U.S: Departments of Mechanical Engineering and Mathematics, University of Kentucky.
- McLaren, K., Tullis, S. and Ziada, S. (2012) Measurement of high solidity vertical axis wind turbine aerodynamic loads under high vibration response conditions. *Journal of Fluids and Structures*, 32, pp. 12-26.
- Mcmullen, M., Jameson, A. and Alonso, J. J. (2001) Acceleration of convergence to a periodic steady state in turbomachinery flows. *39th AIAA aerospace sciences meeting & exhibit*. Nevada, 9-11 January 2001.
- Menter, F. (1994) Two-equation Eddy-viscosity turbulence models for engineering applications. *AIAA Journal*, 32(8), pp. 1598-1605.
- Menter, F. (2018) Stress-blended eddy simulation (SBES)-A new paradigm in hybrid RANS-LES modeling. *Notes on Numerical Fluid Mechanics and Multidisciplinary Design*, 137, pp. 27-37.
- Menter, F. and Kuntz, M. (2004) Adaptation of eddy-viscosity turbulence models to unsteady separated flow behind vehicles. In: F. B. J. R. R. McCallen, ed. *The Aerodynamics of Heavy Vehicles: Trucks, Buses, and Trains. Lecture Notes in Applied and Computational Mechanics*. Berlin, Germany: Springer, pp. 339-352.
- Menter, F., Langtry, R. and Volker, S. (2006) Transition modelling for general purpose CFD codes. *Flow Turbulence Combust*, 77, pp. 277-303.
- Meyer, R., Hage, W., Bechert, D. W., Schatz, M. and Thiele, F. (2006) Drag reduction on Gurney Flaps by three-dimensional modifications. *Journal of Aircraft*, 43, pp. 132-140.
- Mohamed, M. H., Ali, A. M. and Hafiz, A. A. (2015) CFD analysis for H-rotor Darrieus turbine as a low speed wind energy converter. *Engineering Science and Technology, an International Journal*, 18(1), pp. 1-13.
- Mohamed, O. S., Ibrahim, A. A., Etman, A. K., Abdelfatah, A. A. and Elbaz, A. M. R. (2020) Numerical investigation of Darrieus wind turbine with slotted airfoil blades. *Energy Conversion and Management X*, 5, Paper ID 100026.

- Mohammadi, M., Doosttalab, A. and Doosttalab, M. (2012) The effect of various Gurney flap shapes on the performance of wind turbine airfoils. *ASME Early Career Technical Conference*. Georgia, USA, 2-3 November 2012.
- Nedić J. and Vassilicos J.C. (2015) Vortex shedding and aerodynamic performance of an airfoil with multi-scale trailing edge modifications. *AIAA Journal*, 53(1), pp. 3240-3250.
- Newman, B. G. (1983) Actuator-disc theory for vertical-axis wind turbines. *Journal of Wind Engineering and Industrial Aerodynamics*, 15(1-3), pp. 347-355.
- Newman, B. G. (1986) Multiple actuator-disc theory for wind turbines. *Journal of Wind Engineering and Industrial Aerodynamics*, 24(3), pp. 215-225.
- Nobile, R., Vahdati, M., Barlow, J. F. and Mewburn-Crook, A. (2014) Unsteady flow simulation of a vertical axis augmented wind turbine: A two-dimensional study. *Journal of Wind Engineering and Industrial Aerodynamics*, 125, pp. 168-179.
- Paraschivoiu, I. and Delclaux, F. (1983) Double multiple streamtube model with recent improvements (for predicting aerodynamic loads and performance of Darrieus vertical axis wind turbines). *Journal of Energy*, 7 (3), pp. 250-255.
- Paraschivoiu, I. (1988) Double-multiple streamtube model for studying vertical-axis wind turbines. *Journal of Propulsion and Power*, 4(4), pp. 370-377.
- Peng, H. Y. and Lam, H. F. (2016) Turbulence effects on the wake characteristics and aerodynamic performance of a straight-bladed vertical axis wind turbine by wind tunnel tests and large eddy simulations. *Energy*, 109, pp. 557–568.
- Peyret, R. (1996) *Handbook of computational fluid mechanics*. Oxford: Academic Press Inc.
- Posa, A. and Balaras, E. (2018) Large Eddy Simulation of an isolated vertical axis wind turbine. *Journal of Wind Engineering and Industrial Aerodynamics*, 172, pp. 139-151.
- Qasemi, K. and Azadani, L. N. (2020) Optimization of the power output of a vertical axis wind turbine augmented with a flat plate deflector. *Energy*, 202, Paper ID 117745.
- Ragheb, M. and Ragheb, A. M. (2011) *Wind turbine theory-the Betz equation and optimum rotor tip speed ratio*. In: *Fundamental and Advanced Topics in Wind Power*. Rijeka, Croatia: IntechOpen, pp. 19-38.
- Ravelli, S. and Barigozzi, G. (2018) Stress-Blended Eddy Simulation of coherent unsteadiness in pressure side film cooling applied to a first stage turbine vane. *Journal of Heat Transfer*, 140(9), Paper ID 092201.
- Ravelli, S. and Barigozzi, G. (2019) Dynamics of coherent structures and random turbulence in pressure side film cooling on a first stage turbine vane. *Journal of Turbomachinery*, 141(1), Paper ID 011003.
- Rezaeiha, A., Kalkman, I. and Blocken, B. (2017) CFD simulation of a vertical axis wind turbine operating at a moderate tip speed ratio: Guidelines for minimum domain size and azimuthal increment. *Renewable Energy*, 107, pp. 373-385.

- Rezaeiha, A., Montazeri, H. and Blocken, B. (2018) Towards accurate CFD simulations of vertical axis wind turbines at different tip speed ratios and solidities: Guidelines for azimuthal increment, domain size and convergence. *Energy Conversion and Management*, 156, pp. 301-316.
- Rezaeiha, A., Montazeri, H. and Blocken, B. (2019) On the accuracy of turbulence models for CFD simulations of vertical axis wind turbines. *Energy*, 180, pp. 838-857.
- Roy, S. and Saha, U. K. (2013) Review on the numerical investigations into the design and development of Savonius wind rotors. *Renewable and Sustainable Energy Reviews*, 24, pp. 73-83.
- Rocchio, B., Chicchiero, C., Salvetti, M. V. and Zanforlin, S. (2020) A simple model for deep dynamic stall conditions. *Wind Energy*, 23, pp. 915-938.
- Saenz-Aguirre, A., Fernandez-Resines, S., Aramendia, I., Fernandez-Gamiz, U., Zulueta, E., Lopez-Guede J. M. and Sancho, J. (2018) 5 MW wind turbine annual energy production improvement by flow control devices. *2nd International Research Conference on Sustainable Energy, Engineering, Materials and Environment (IRCSEEME)*. Mieres, 25-27 July 2018.
- Salim, S. M., Ong, K. C. and Cheah, S. C. (2013) Comparison of RANS, URANS and LES in the prediction of airflow and pollutant dispersion. *Lecture Notes in Electrical Engineering*, 170, pp. 263-274.
- Santoli, L. d., Albo, A., Garcia, D. A., Bruschi, D. and Cumo, F. (2014) A preliminary energy and environmental assessment of a micro wind turbine prototype in natural protected areas. *Sustainable Energy Technologies and Assessments*, 8, pp. 42-56.
- Shih, T.-H., Liou, W. W., Shabbir, A., Yang, Z. and Zhu, J. (1995) A new-eddy-viscosity model for high Reynolds number turbulent flows-model development and validation. *Computers Fluids*, 24(3), pp. 227-238.
- Shih, T.-H., Zhua, J. and Lumley, J. L. (1995) A new Reynolds stress algebraic equation model. *Computer Methods in Applied Mechanics and Engineering*, 125, pp. 287-302.
- Shires, A. (2013) Design optimisation of an offshore vertical axis wind turbine. *Energy*, 166 (1), pp. 7-18.
- Shukla, V. and Kaviti, A. K. (2017) Performance evaluation of profile modifications on straight-bladed vertical axis wind turbine by energy and Spalart Allmaras models. *Energy*, 126, pp. 766-795.
- Shur, M. L., Spalart, P. R., Strelets, M. K. and Travin, A. K. (2008) A hybrid RANS-LES approach with delayed-DES and wall-modelled LES capabilities. *International Journal of Heat and Fluid Flow*, 29, pp. 1638-1649.
- Sobhani, E., Ghaffari, M. and Maghrebi, M. J. (2017) Numerical investigation of dimple effects on darrieus vertical axis wind turbine. *Energy*, 133, pp. 231-241.
- Sørensen, J. N. (2012) Aerodynamic analysis of wind turbines. *Comprehensive Renewable Energy*, 2, pp. 225-241.

- Spalart, P.R. and McLean, J. D. (2011) Drag reduction: Enticing turbulence, and then an industry. *Philosophical Transactions of The Royal Society A Mathematical Physical and Engineering Sciences*, 369, pp. 1556-1569.
- Spalart, P. R., Deck, S., Shur, M. L., Squires, K. D., Strelets, M. Kh. and Travin, A. (2006) A new version of Detached-Eddy Simulation, resistant to ambiguous grid densities. *Theoretical and Computational Fluid Dynamics*, 20, pp. 181-195.
- Sranpat, C., Unsakui, S., Choljararux, P. and Leephakpreeda, T. (2017) CFD-based performance analysis on design factors of vertical axis wind turbines at low wind speeds. *Energy Procedia*, 138, pp. 500-505.
- Srihari, P. S. V. V., Narayana, P. S. V. V. S., Rao, K. L., Venkatesh, J. D. and Rajesh, P. (2019) Influence of slat and flaps arrangement on the performance of modified Darrieus wind turbine. *AIP Conference Proceedings*, 2200, Paper ID 020012.
- Srivastav, D. and Ponnani, K. N. (2011) Surface modifications for improved maneuverability and performance of an aircraft. *ASME International Mechanical Engineering Congress and Exposition Denver, Colorado, 11-17 January 2011*. ASME Proceedings Series, Volume 1: Advances in Aerospace Technology; Energy Water Nexus; Globalization of Engineering; Posters, pp. 121-127.
- Stout, C., Islam, S., White, A., Arnott, S., Kollovozi, E., Shaw, M., Droubi, G., Sinha, Y. and Bird, B. (2017) Efficiency improvement of vertical axis wind turbines with an upstream deflector. *Energy Procedia*, 118, pp. 141-148.
- Strickland, J., Webster, B. and Nguyen, T. (1979) A vortex model of the Darrieus turbine: an analytical and experimental study. *Journal of Fluids Engineering*, 101, pp. 500-505.
- Su, J., Lei H., Zhou, D., Han, Z., Bao, Y., Zhu, H. and Zhou, L. (2019) Aerodynamic noise assessment for a vertical axis wind turbine using Improved Delayed Detached Eddy Simulation. *Renewable Energy*, 141, pp. 559-569.
- Sundaram, S., Viswanath, P. R. and Rudrakumar, S. (1996) Viscous drag reduction using riblets on NACA 0012 airfoil to moderate incidence. *AIAA Journal*, 34, pp. 676-682.
- Sutherland, H. J., Berg, D. E. and Ashwill, T. D. (2012) *A retrospective of VAWT technology*. Albuquerque, New Mexico: Sandia National Laboratories.
- Takao, M., Kuma, H., Maeda, T., Kamada, Y., Oki, M. and Minoda, A. (2009) A straight-bladed vertical axis wind turbine with a directed guide vane row-Effect of guide vane geometry on the performance-. *Journal of Thermal Science*, 18(1), pp. 54-57.
- Tchakoua, P., Wamkeue, R., Ouhrouche, M., Tameghe, T. A. and Ekemb, G. (2015) A new approach for modeling Darrieus-type vertical axis wind turbine rotors using electrical equivalent circuit analogy: Basis of theoretical formulations and model development. *Energies*, 8, pp. 10684-10717.
- Templin, R. (1974) *The elements of airfoil and airscrew theory*. Cambridge: Cambridge University Press, second edition.

- Trivellato, F. and Castelli, M. R. (2014) On the Courant–Friedrichs–Lewy criterion of rotating grids in 2D vertical-axis wind turbine analysis. *Renewable Energy*, 62, pp. 53-62.
- Tu, J., Yeoh, G.-H. and Liu, C. (2013) *Practical guidelines for CFD simulation and analysis*. In: *Computational Fluid Dynamics: A practical approach*. Second ed. Oxford: Butterworth-Heinemann, pp. 219-273.
- Vijgen, P. M. H. W., Dam, C. P. V., Holmes, B. J. and Howard, F. G. (1989) *Wind-tunnel investigations of wings with serrated sharp trailing edges*. In: *low Reynolds number aerodynamics. Lecture Notes in Engineering*. Berlin, Heidelberg: Springer, pp. 295-313.
- Wang, S., Ingham, D. B., Ma, L., Pourkashanian, M. and Tao, Z. (2010) Numerical investigations on dynamic stall of low Reynolds number flow around oscillating airfoils. *Computers & Fluids*, 39(9), pp. 1529-1541.
- Wang, Y., Li, G., Shen, S., Huang, D. and Zheng, Z. (2018) Investigation on aerodynamic performance of horizontal axis wind turbine by setting micro-cylinder in front of the blade leading edge. *Energy*, 143, pp. 1107-1124.
- Wang, Y., Shen, S., Li, G., Huang, D. and Zheng, Z. (2018) Investigation on aerodynamic performance of vertical axis wind turbine with different series airfoil shapes. *Renewable Energy*, 126, pp. 801-818.
- Wang, Z., Wang, Y. and Zhuang, M. (2018) Improvement of the aerodynamic performance of vertical axis wind turbines with leading-edge serrations and helical blades using CFD and Taguchi method. *Energy Conversion and Management*, 177, pp. 107-121.
- Wang, Z. and Zhuang, M. (2017) Leading-edge serrations for performance improvement on a vertical-axis wind turbine at low tip-speed-ratios. *Applied Energy*, 208, pp. 1184-1197.
- Warhaft, Z. (2000) Passive scalars in turbulent flows. *Annual Review of Fluid Mechanics*, 32, pp. 203-240.
- Watanabe, K., Takahashi, S. and Ohya, Y. (2016) Application of a diffuser structure to vertical-axis wind turbines. *Energies*, 9(6), Paper ID 406.
- Wei, Z., New, T. and Cui, Y. (2015) An experimental study on flow separation control of hydrofoils with leading-edge tubercles at low Reynolds number. *Ocean Engineering*, 108, pp. 336-349.
- Wernert, P., Geissler, W., Raffel, M. and Kompenhans, J. (1996) Experimental and numerical investigations of dynamic stall on a pitching airfoil. *AIAA Journal*, 34(5), pp. 982-989.
- Wilcox, D. C. (2006) *Turbulence modelling for CFD*. California, USA: DWC Industries.
- Wilson, R. E. and Lissaman, P. B. S. (1974) *Applied aerodynamics of wind power machines*. Oregon, USA: Oregon State University.

- Wong, K., Chong, W. T., Yap, H. T., Fazlizan, A., Omar, W. Z. W., Poh, S. C. and Hsiao, F. B. (2014) The design and flow simulation of a power-augmented shroud for urban wind turbine system. *Energy Procedia*, 61, pp. 1275-1278.
- Wong, K. H., Chong, W. T., Poh, S. C., Shiah, Y. -C., Sukiman, N. L. and Wang, C. -T. (2018a) 3D CFD simulation and parametric study of a flat plate deflector for vertical axis wind turbine. *Renewable Energy*, 129(A), pp. 32-55.
- Wong, K. H., Chong, W. T., Sukiman, N. L., Shiah, Y. -C., Poh, S. C., Sopian, K. and Wang, W. -C. (2018b). Experimental and simulation investigation into the effects of a flat plate deflector on vertical axis wind turbine. *Energy Conversion and Management*, 160, pp. 109-125.
- Wong, K. H., Chong, W. T., Sukiman, N. L., Poh, S. C., Shiah, Y. -C. and Wang, C. -T. (2017) Performance enhancements on vertical axis wind turbines using flow augmentation systems: A review. *Renewable and Sustainable Energy Reviews*, 73, pp. 904-921.
- Xu, H., Qiao, C. and Ye, Z. (2016) Dynamic stall control on the wind turbine airfoil via a co-flow jet. *Energies*, 9(6), Paper ID 429.
- Yang, Y., Li, C., Zhang, W., Guo, X. and Yuan, Q. (2017) Investigation on aerodynamics and active flow control of a vertical axis wind turbine with flapped airfoil. *Journal of Mechanical Science and Technology*, 31(4), pp. 1645-1655.
- Yan, Y., Avital, E. and Williams, J. (2019) CFD Analysis for the performance of Gurney Flap on aerofoil and vertical axis turbine. *International Journal of Mechanical Engineering and Robotics Research*, 8, no. 3, pp. 385-392.
- Yan, Y., Avital, E., Williams, J. and Cui, J. (2019) CFD analysis for the performance of micro-vortex generator on aerofoil and vertical axis turbine. *Journal of Renewable and Sustainable Energy*, 11(4), Paper ID 043302.
- Yan, Y., Avital, E., Williams, J. and Cui, J., 2020. Performance improvements for a vertical axis wind turbine by means of Gurney Flap. *Journal of Fluids Engineering*, 142(2), Paper ID 021205.
- Yen, J. and Ahmed, N. A. (2014) Enhancing vertical axis wind turbine by dynamic stall control using synthetic jets. *Journal of Wind Engineering and Industrial Aerodynamics*, 114, pp. 12-17.
- Zamani, M., Maghrebi, M. J. and Moshizi, S. A. (2016a) Numerical study of airfoil thickness effects on the performance of J-shaped straight blade vertical axis wind turbine. *Wind and Structures*, 22(5), pp. 595-616.
- Zamani, M., Maghrebi, M. J. and Varedi, S. R. (2016b) Starting torque improvement using J-shaped straight-bladed Darrieus vertical axis wind turbine by means of numerical simulation. *Renewable Energy*, 95, pp. 109-126.
- Zamani, M., Nazari, S., Moshizi, S. A. and Maghrebi, M. J. (2016c) Three dimensional simulation of J-shaped Darrieus vertical axis wind turbine. *Energy*, 116, pp. 1243-1255.

- Zanforlin, S. and Deluca, S. (2018) Effects of the Reynolds number and the tip losses on the optimal aspect ratio of straight-bladed Vertical Axis Wind Turbines. *Energy*, 148, pp. 179-195.
- Zhang, T.-t., Elsakka, M., Huang, W., Wang, Z.-g., Ingham, D. B., Ma, L. and Pourkashian, M. (2019) Winglet design for vertical axis wind turbines based on a design of experiment and CFD approach. *Energy Conversion and Management*, 135, pp. 712-726.
- Zhu, H., Hao, W., Li, C. and Ding, Q. (2018) Simulation on flow control strategy of synthetic jet in a vertical axis wind turbine. *Aerospace Science and Technology*, 77, pp. 439-448.
- Zhu, H., Hao, W., Li, C. and Ding, Q. (2019) Numerical study of effect of solidity on vertical axis wind turbine with Gurney flap. *Journal of Wind Engineering and Industrial Aerodynamics*, 186, pp. 17-31.
- Zou, T., Li, H., Wu, H., Hu, L. and Cai, M. (2019) Design of experiment in analysing uncertainty of simulation results in accident reconstruction. *Proceedings of the Institution of Mechanical Engineers, Part D: Journal of Automobile Engineering*, 233(4), pp. 836-850.

APPENDICES

APPENDIX A

(Linked to Chapter 2, Section 2.2.1)

Blade Shape Modification Devices Implemented in Lift-Driven VAWTs

A.1 Inward Dimple (Cavity)

A dimple can act as a vortex generator (VG) to enhance the aerofoil's lift coefficient, especially in high AoA . It can also reduce the drag coefficient due to the increase of the flow turbulence to resist flow separation and the decrease of the size and strength of the wake (Srivastav and Ponnani, 2011). A 2D numerical study by Sobhani, Ghaffari and Maghrebi (2017) found that inward dimple (cavity) introduced on a NACA 0021 aerofoil applied in a three-straight-bladed lift-driven VAWT has indeed improved the output torque of the turbine. They stated that whilst applying a cavity on the pressure side of the aerofoil could improve the torque generation in all TSR regimes, the existence of a cavity on the suction side of the aerofoil did not have a significant effect in low regime of $TSRs$. It was also found that an aerofoil can achieve an optimum power improvement of about 20% with a circular shaped cavity at 25% chord location from the leading-edge on the pressure side and with the largest cavity diameter of 0.08% chord (see Figure A.1). They further argued that the cavity can reduce local flow velocity on the pressure side of the aerofoil. Therefore, the lift force can be increased considerably due to the increment of the pressure. Moreover, a circular cavity with a larger diameter will create a larger gap near the leading-edge, and thus it has a larger trapped air surface area. It can lead to higher lift force increment due to more significant flow velocity reduction and higher pressure force. This study can be further extended by modifying the aerofoil shape by introducing an array of multiple cavities or different cavity shapes through a position optimisation process instead of just using a single large cavity. The application of an outward dimple for VAWT could be a perspective area to explore, as this technology has already been proven and successfully used in the power production improvement of HAWTs (Fikadea et al., 2020).

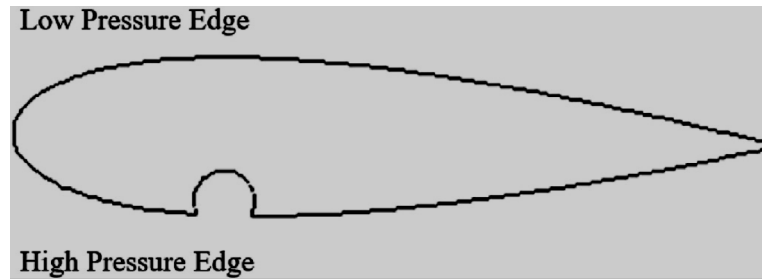


Figure A.1 NACA 0021 with optimum dimple location (Sobhani, Ghaffari and Maghrebi, 2017).

Ismail and Vijayaraghavan (2015) and Shukla and Kaviti (2017) further performed numerical studies by introducing an inward dimple (cavity) together with a Gurney flap near the trailing-edge on the pressure side of the aerofoil that is usually used for the blade profile of VAWT, as shown in Figure A.2. They found that using a cavity alone near the trailing-edge of the aerofoil on the pressure side, the lift coefficient (C_l) of such an aerofoil was lower than a clean aerofoil. This finding agrees well with a previous study (Sobhani, Ghaffari and Maghrebi, 2017) in which a cavity near the trailing-edge gave poor results compared with a cavity near the leading-edge. These two studies (Shukla and Kaviti, 2017; Ismail and Vijayaraghavan, 2015) included a GF in addition to a cavity near the aerofoil's trailing-edge to improve the C_l of an aerofoil with a cavity. Using a cavity and a GF near the trailing-edge of aerofoil on the pressure side can improve the lift-to-drag ratio (C_l/C_d) and lift and drag forces acting on the aerofoil compared to a clean aerofoil. For example, the optimum average tangential force of an aerofoil with a cavity and GF modified shape was almost 35% higher than a clean aerofoil. However, these studies only evaluated the performance of a geometrically modified single aerofoil in a stationary status and, in the case of rotation, only in one TSR operational point. Later, they introduced dynamic modelling for a pitching aerofoil (Ismail and Vijayaraghavan, 2015) so as to consider the impact of dynamic stall on simulation. However, these studies used only an optimum geometry obtained from an optimisation study of a single stationary aerofoil with a cavity and GF. Hence, the results obtained by this kind of study need to be further validated for a VAWT configuration (e.g., considering the rotational effects and blade-to-blade interactions) in all TSR regimes.

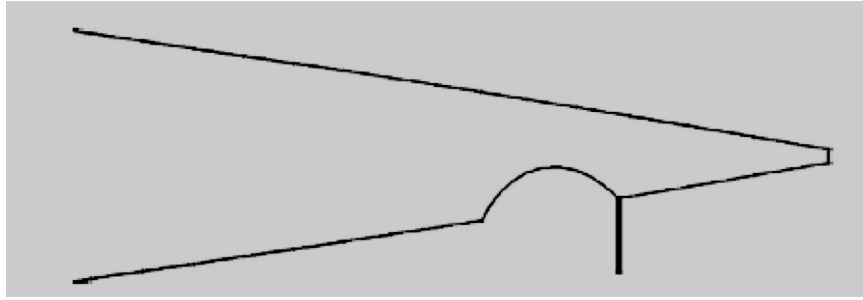


Figure A.2 Aerofoil with GF (i.e., downward straight plate) and inward dimple on the pressure side near the trailing-edge (Shukla and Kaviti, 2017; Ismail and Vijayaraghavan, 2015).

A.2 *Vortex Generator (VG)*

A VG is a type of passive flow control device, which has been widely applied in controlling dynamic stalls of 2D aerofoil and 3D wings. It has advantages of zero ‘net’ mass flux and, therefore, is easier to implement. A VG can suppress slight flow separation due to its ability to transport higher momentum fluids from the mainstream to lower momentum fluids inside the boundary layer. It can also improve lift generation and reduce the noise caused by flow separation (Calarese, Crisler and Gustafson, 1985). The implementation of a VG on the VAWT blades has been studied experimentally in the past (Yan et al., 2019; Choudhry, Arjomandi and Kelso, 2016). In the study of Choudhry, Arjomandi and Kelso (2016), several VGs that can produce counter-rotating stream-wise vortices were mounted along the entire span of a NACA 0021 wing leading-edge (see Figure A.3 (a)). These configurations were considered due to a dynamic stall being likely linked with a strong leading-edge vortex shedding at high AoA . Hence, these VGs were utilised as they can produce higher flow entrainments than other VGs that can only produce counter-rotating stream-wise vortices (Heine et al., 2013). VGs can eliminate the lift coefficient fluctuations often caused by leading-edge laminar bubble (LB) of a clean aerofoil. Nevertheless, VGs can substantially decrease the strength of the dynamic stall vortex (DSV), as shown in Figure A.4, due to the reduction of the maximum lift and drag forces associated with DSV. Reducing the gap between VG pairs can further avoid this DSV. Compared with a clean aerofoil, VGs can also reduce the drag increment by about 11% whilst improving the lift decrease by about 25%, leading to a lift-to-drag ratio increment of 41%. There was also approximately 10% delay in the stall AoA closely associated with large-scale unsteady flow separation. All these have confirmed the effectiveness of VGs for preventing the trailing-edge flow separation by migration and

propagation disturbances to the upstream. As this study only evaluated a single aerofoil at a constant pitching rate to introduce the dynamic stall, it is difficult to argue that those aforementioned improvements can significantly enhance the performance of VAWTs. Hence, further analysis of a VAWT configuration is necessary.

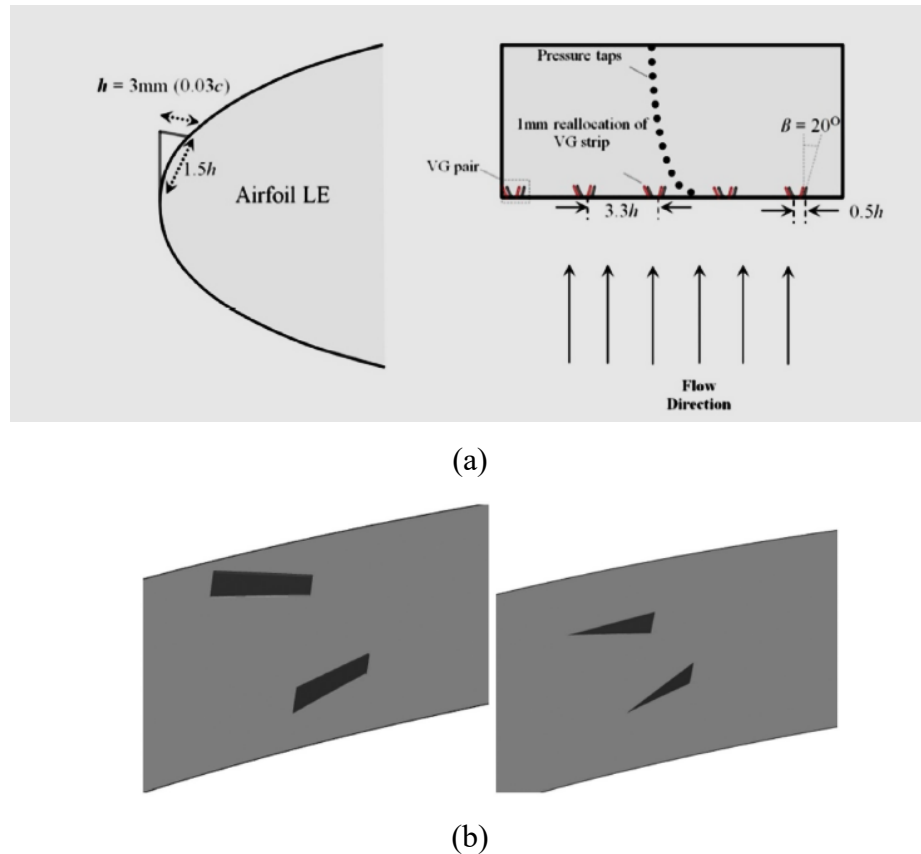


Figure A.3 (a) Multiple counter-rotating vortex generators (Choudhry, Arjomandi and Kelso, 2016) and (b) Single counter-rotating micro vortex generator (Yan et al., 2019), deployed at the leading-edge of an aerofoil.

On another front, Yan et al. (2019) numerically evaluated a single micro-VG on the NACA 0018 blades of a three-straight-bladed lift-driven VAWT (see Figure A.3 (b)). They have performed geometric optimisation (e.g., VG location, angle, shape and length) using a 2D single stationary aerofoil instead of a rotating blade. Then, a modified aerofoil with a VG was used for a three-dimensional (3D) VAWT configuration. Their study concluded that the presence of a VG can improve the power generation of a VAWT in the high regime of $TSRs$ with an optimum power coefficient (C_p) improvement of about 78% achieved in $TSR = 3$. Whilst the VG addition can improve the power efficiency of the turbines, it cannot strengthen the self-starting ability of VAWT (i.e., the ability of

VAWT to start rotating by itself without any assistance from external power) as it did not perform well in low regime of $TSRs$.

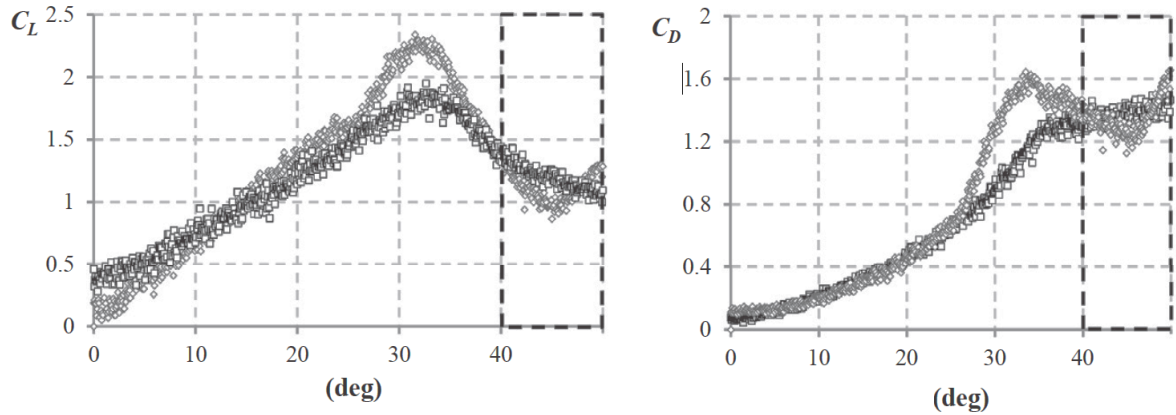


Figure A.4 Drag coefficient and lift coefficient distributions of a NACA 0021 aerofoil with counter-rotating VGs at a pitching rate of 320 degree/s over evaluated $AoAs$. The darker dashed lines, after $AoA = 40^\circ$, shows the lift and drag behaviour of the aerofoil after the pitching process has stopped (Choudhry, Arjomandi and Kelso, 2016).

A.3 Opening at Aerofoil Trailing-edge

In order to achieve a Darrieus VAWT which has an excellent self-starting ability with less power loss, Chen et al. (2015) proposed a new aerofoil profile design with an opening at the suction and pressure sides of the aerofoil trailing-edge. Their results have shown that the aerofoil openings can increase the torque production in lower incoming wind speed and lower TSR regimes. There were seven openings proposed on the suction and pressure sides of the aerofoil, and all have been investigated and evaluated numerically (see, e.g., Figure A.5 for aerofoil opening at the pressure side) by employing a VAWT configuration. Their results suggested that an opening on the blade at the suction side will give better improvement than an opening on the blade at the pressure side due to being less sensitive to flow separation and dynamic stall for the suction side opening. Moreover, an aerofoil with an opening can increase the self-starting ability due to the significant increment of instantaneous torque coefficient in low regime of $TSRs$ (where the self-starting ability is much needed). However, this improvement cannot be maintained in higher regimes of $TSRs$ as the C_p reduces with the increment of the opening ratio.

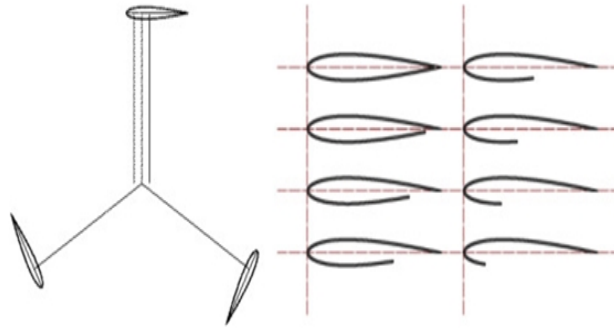


Figure A.5 Blades with opening modification at the pressure side (Chen et al., 2015).

Similar approaches were performed in other studies (Zamani, Maghrebi and Moshizi, 2016; Zamani, Maghrebi and Varedi, 2016; Zamani et al., 2016). In order to improve the self-starting ability of a VAWT, they removed the pressure side of the blade profile for a three-straight-bladed Darrieus VAWT so as to have a J-shaped blade (see Figure A.6). They argued that the J-shaped blade can utilise both lift and drag forces simultaneously, whilst usually, a VAWT can only generate power by generating either a lift or drag force. These studies adopted a 2D single stationary airfoil for geometrical optimisation simulation (Zamani, Maghrebi and Moshizi, 2016a) and performed 3D simulations (Zamani et al., 2016) to confirm the advantage of the J-shaped airfoil on a VAWT configuration. The results of these studies are similar to that of Chen et al. (2015). The J-shaped blade can decrease the negative torque and increase the positive torque production only in low to medium regimes of *TSRs*, but not in high regime of *TSRs*. Their numerical predictions showed that the modified blade could improve the average power production up to twice larger than the original blade in low regime of *TSRs*. This result suggested that a J-shaped blade indeed can increase the self-starting ability of a Darrieus VAWT. However, the C_p improvement gradually reduced with the increase of *TSR* regime, and it dropped to only a 5% improvement compared to an original blade in optimum *TSR* value. This J-shaped blade performance can drop further and be lower than the original blade at high regime of *TSRs* (i.e., 0.4% of C_p decrease compared to the original blade). Hence, a future study of an opening J-shaped blade is needed to evaluate how much percentage of enhancement of the power coefficient is needed to make a Darrieus VAWT self-starting. Further evaluations of the optimum opening ratio are necessary to improve self-starting without losing too much power efficiency. In addition, the development of adaptive blade walls that can be opened in low regime of *TSRs* and

closed in high regime of $TSRs$ might be desirable, though this will make the design, manufacturing, and operation more complicated.

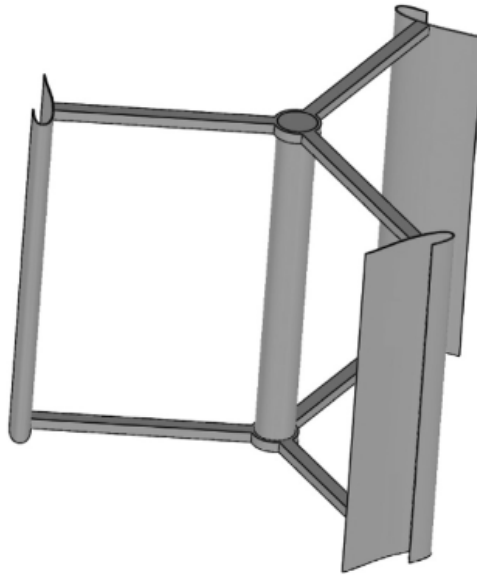


Figure A.6 Three-straight-bladed Darrieus VAWT with J-shaped blade (Zamani et al., 2016).

A.4 Multi-element Aerofoil

A.4.1 Slotted Aerofoil

Another method to control flow around VAWTs is to use a slotted aerofoil, as shown in Figure A.7. This approach can delay or even eliminate boundary layer separation due to the ability to enhance the low momentum fluids near the aerofoil surface. The slotted aerofoil has been applied in HAWT (Belamadi et al., 2016). This application found that aerodynamic performance can be improved if the slot is located just upstream of the separation point for each AoA . Moreover, a slot with a converging shape (from the pressure side to the suction side) can improve aerodynamic performance by accelerating the flow through the slot (Belamadi et al., 2016). This finding still needs to be confirmed for a VAWT configuration as the previous study only evaluated a single stationary aerofoil case.

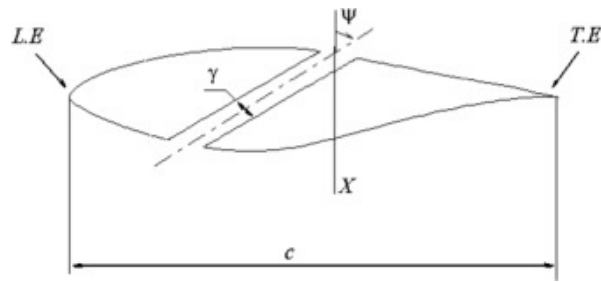


Figure A.7 Aerofoil with a slot (Belamadi et al., 2016).

Mohamed et al. modified the NACA 0018 aerofoil to be a slotted aerofoil and utilised it in constructing a three-straight-bladed VAWT configuration to evaluate the ability of a slotted aerofoil for the performance improvement of VAWT (Mohamed et al., 2020). This study performed geometric optimisation using a 2D single stationary aerofoil simulation. Then, the simulation of an optimum slotted NACA 0018 aerofoil for a 2D three-straight-bladed VAWT configuration was performed to investigate the blade rotational effects. Their results indicated that a VAWT with slotted aerofoil can produce higher torque in both low regime of *TSRs* and medium regime of *TSRs* (up to the optimum *TSR* value), compared to a clean aerofoil, and this can result in better self-starting ability. However, in high regime of *TSRs*, the torque production of a VAWT with slotted aerofoil was found less than that of the original clean aerofoil. The maximum increment of torque production was up to two times higher than a clean aerofoil in $TSR = 2$. Moreover, the optimum performance of a VAWT with slotted aerofoil can be achieved in a lower *TSR* value compared to a VAWT with a clean aerofoil. Hence, a VAWT with slotted aerofoil could have optimum performance at lower rotation speed (assuming the same incoming wind speed), thus reducing the turbine's possible vibration and noise production.

Acarer (2020) suggested further modification of a slotted aerofoil for VAWT. Instead of introducing a slot in the middle of the original aerofoil in the *y*-direction, a lambda (λ) shape slot is introduced along the *x*-direction of the aerofoil (see Figure A.8). The study first investigated a single stationary slotted aerofoil for geometric optimisation. For the optimum configuration (see Figure A.9), the C_l/C_d was higher in all *AoA* values investigated than for the original aerofoil. In $AoA = 0^\circ$, this study found a maximum C_l/C_d increment is about 45%, whilst in $AoA = 20^\circ$, the minimum increment of slightly under 5% is obtained. Overall, the optimum value of the C_l/C_d ratio is increased by about 16.5%, compared to the original aerofoil. The results indicated that the design could increase the lift generation (i.e., up to 50% in $AoA = 0^\circ$ and about 5% in $AoA = 20^\circ$)

with a very small drag increment (e.g., no drag increment up to AoA about $10\text{-}15^\circ$ and about 8.3% at the maximum $AoA = 20^\circ$).

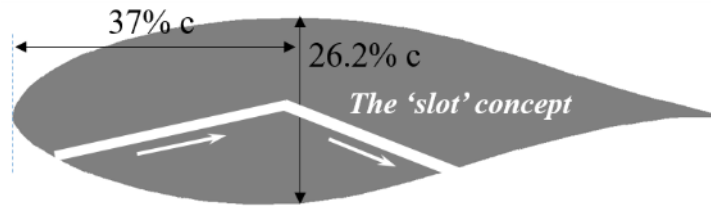
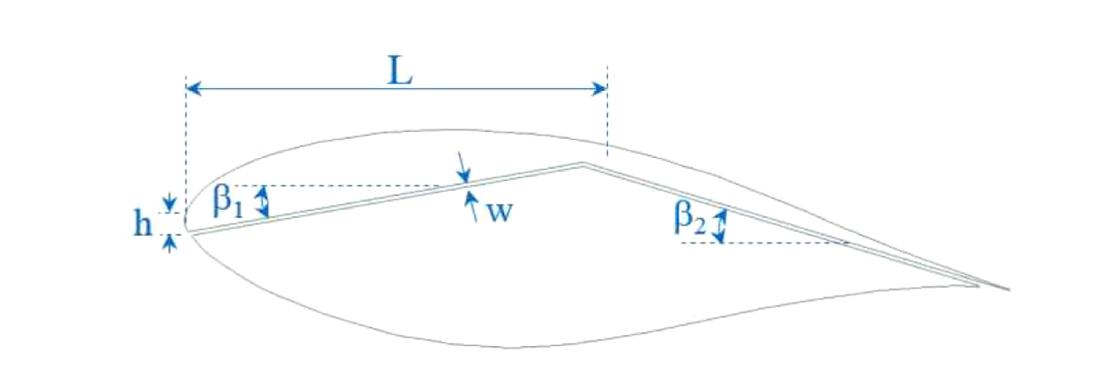


Figure A.8 Aerofoil with λ slot along x -direction (Acarer, 2020).



β_1	10°
β_2	16.8°
L	$48\% c$
h	$1.6\% c$
w	$0.5\% c$

Figure A.9 The optimum geometric parameters of a slotted aerofoil (Acarer, 2020).

Based on this new λ slot design evaluation on a single stationary aerofoil, Acarer applied it to a three-straight-bladed VAWT configuration (Acarer, 2020). In contrast to the previously slotted aerofoil by Mohamed et al., (2020) (see Figure A.7), a VAWT with a new λ slot aerofoil design produced better power coefficient values in medium to high regimes of $TSRs$ (e.g., with the optimum improvement of around 9.6% in $TSR = 10$), whilst in low regime of $TSRs$, the C_p was lower compared to the original VAWT. It was possibly due to the fall in the lift-to-drag ratio in low regime of $TSRs$ as the VAWT may experience higher $AoAs$ (i.e., a positive AoA at the upwind phase, $0^\circ < \text{azimuthal position } (\theta) < 180^\circ$, and negative AoA at the downwind phase, $180^\circ < \theta < 360$, respectively). This result is in good agreement with a single stationary aerofoil, as this slotted single stationary aerofoil cannot improve the lift-to-drag ratio in negative $AoAs$.

The result further implies that this new slotted aerofoil design was not suitable for improving the self-starting ability of VAWT. In addition, the VAWT equipped with the new slotted design aerofoil had a slightly higher optimum TSR than the original VAWT (about an 8.3% increment). If the blade's rotational speed remains the same, the higher optimum TSR means the new VAWT design can generate optimum power in lower incoming wind speeds. It indicates that the new VAWT design could be suitable for urban environment applications, where high turbulence levels and low-speed wind conditions co-exist. Nonetheless, both slotted aerofoil concepts described above can be further improved by performing the geometric optimisation using a VAWT configuration to include the effect of blade rotation and blade-to-blade interaction. A complete 3D study is also needed to quantify the support system for blades with slotted aerofoils and their effectiveness on the performance of a VAWT.

A.4.2 *Leading-edge Slat Aerofoil*

This passive flow control device modifies the flow around the leading-edge by dividing a single aerofoil into a two-element aerofoil (i.e., a main aerofoil and a slat aerofoil) as shown in Figure A.10. The existence of the slat at the leading-edge of a main aerofoil can accelerate the flow between the slat and main aerofoil, which can increase the kinetic energy of the flow and its momentum transfer into the boundary layer. As a result, the lift force can be improved and the stall phenomenon in high AoA can be delayed.

The two-element aerofoil modification for VAWT application has been studied experimentally and numerically by Chougule and Nielsen (2014) using the S1210 aerofoil in low Reynolds numbers (Re) from 40000 to 200000. The original single element aerofoil was modified to be a two-element aerofoil, as illustrated in Figure A.10 (a). This study found that the two-element aerofoil could increase the stall angle about 1.5 times higher than the original single aerofoil in lower Re ($Re = 50000$). By increasing Re to 100000, a maximum stall angle has been reached, and further increment of Re did not significantly impact the stall angle. The stall angle increment indicated that the two-element aerofoil can delay the stall phenomenon. Compared to HAWTs, this characteristic is fundamental for VAWTs to improve the power production due to its higher AoA value during the operation. As the stall is delayed, the maximum lift coefficient of a two-element aerofoil can also be improved by up to 40%, compared to a single element aerofoil at the same low wind speed.

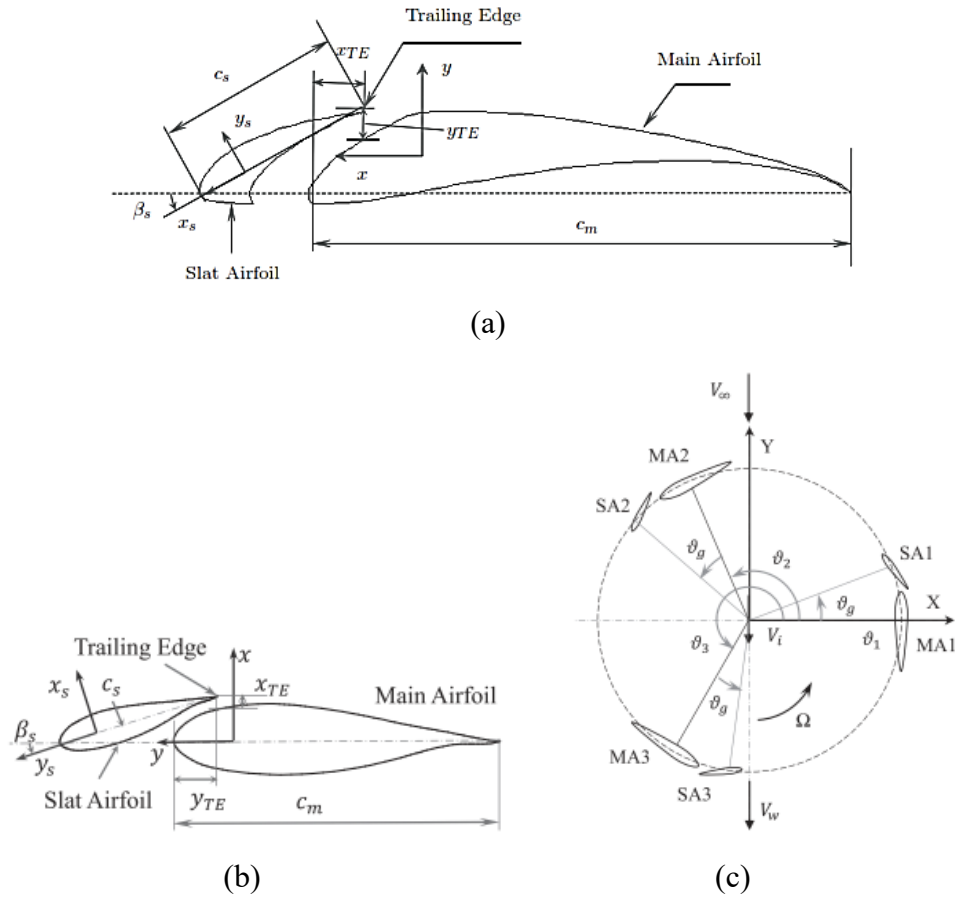


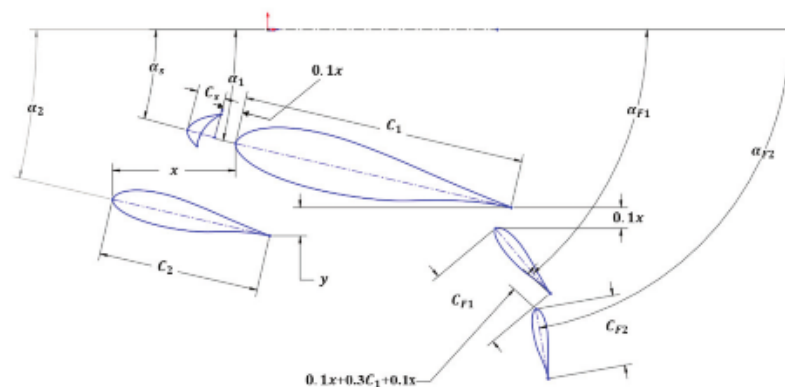
Figure A.10 Two-element aerofoil configuration, (a) S1210 two-element aerofoil (Chougule and Nielsen, 2014); (b) DU06-W200 two-element aerofoil (Chougule, Rosendahl and Nielsen, 2015) and (c) VAWT configuration with two-element aerofoil (Chougule, Rosendahl and Nielsen, 2015).

By confirming the ability of two-element aerofoil in low Re condition, Chougule, Rosendahl and Nielsen (2015) have performed further numerical studies to evaluate the 2D geometric optimisation of the DU06-W200 two-element aerofoil of a three-straight-bladed VAWT configuration (see Figure A.10 (b) and A.10 (c)). The momentum and blade element theories incorporated in the Double Multiple Stream Tube method (DMST) were used, and the results suggested that blades with a two-element aerofoil profile could enhance the maximum C_p by up to 90%, compared to a single aerofoil blade at low to medium wind speeds (from 0.3 m/s up to 11 m/s). Furthermore, there was a big decrease of C_p at high wind speeds (from 11 m/s up to 14 m/s), showing that this two-element aerofoil cannot improve the power generation of VAWT for higher wind speeds. Further study is needed to confirm this by running high-fidelity CFD simulations or experiments. In addition, a complete 3D study is crucial to design and

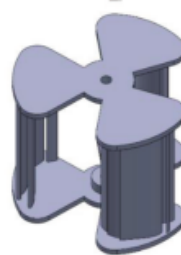
quantify the support system for two-element blades and their effect on the performance of a VAWT.

A.4.3 Five-element Aerofoil

Other multi-element aerofoils that have been adopted to improve the performance of a VAWT include a five-element aerofoil, as depicted in Figure A.11 (Srihari et al., 2019). This aerofoil is created by dividing the original aerofoil into two slats at the leading-edge, one main aerofoil and two flaps at the trailing-edge (see Figure A.11 (a)). By implementing this aerofoil for a three-straight-bladed VAWT (see Figure A.11 (b)), the turbine could produce positive torque at low wind speed (4 m/s in this case) whilst the turbine with a single element aerofoil configuration could not produce positive torque (i.e., experiencing the so-called dead band zone where a VAWT cannot produce any power). Hence, this modification improved the self-starting ability of the VAWT. In addition, the optimum C_p of this modified turbine blade was quite similar to the original turbine blade (only 0.6% in difference). This result indicates that, unlike the two-element aerofoil, this five-element modification does not adversely affect the performance of VAWT after the so-called dead band zone.



(a)



(b)

Figure A.11 (a) Five-element aerofoil and (b) 3D isometric view of VAWT with five-element aerofoil (Srihari et al., 2019).

A.5 *Leading-edge Serrations*

The morphology of humpback whales inspired this modification. Counter-rotating vortex pairs in each serration can modify the flow pattern near the blade surface and thus ease flow separation (Wei, New and Cui, 2015). Moreover, the leading-edge serrations decreased the maximum lift coefficient at the pre-stall condition whilst increasing it at the post-stall condition (Johari et al., 2017). The investigation of sinusoidal wave serrations on a two-straight-bladed NACA 0018 VAWT (see Figure A.12) revealed that these serrations could suppress the flow separation whilst the static stall occurred (Wang and Zhuang, 2017). During the dynamic stall phase, high separation was induced by the leading-edge on the blades so that in high AoA , flow separation could be eased due to the presence of counter-rotating vortex pairs induced by the serration pattern of geometry, leading to the delay of dynamic stall. Regarding the performance enhancement, the leading-edge serration can increase the maximum lift coefficient by 25% compared to a clean blade, and no significant increment on drag coefficient was observed. The power performance could be improved by approximately 50.1% in low wind speed ($U_\infty = 3 \text{ m/s}$), confirming that this configuration could also enhance the self-starting ability of a lift-driven VAWT. As wind speed increases, this ability decreases gradually (C_p improvement decreased to 14.8% compared to a clean blade in $U_\infty = 12 \text{ m/s}$), implying that this modification would probably not significantly impact the high regime of $TSRs$.

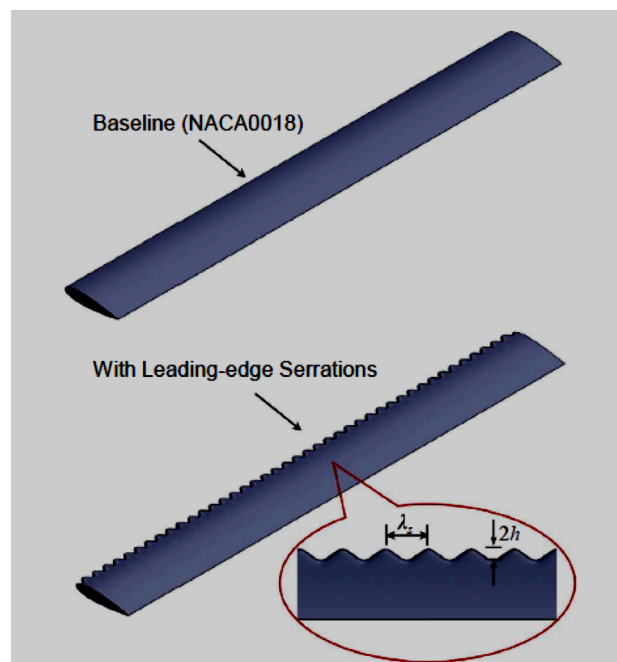


Figure A.12 Blade of VAWT with leading-edge serrations (Wang and Zhuang, 2017).

A.7 Trailing-edge Modifications

A.7.1 Winglet

The winglet has been used widely in most long-range commercial aeroplanes. It can reduce lift-induced drag by isolating the suction and pressure sides of the wing, thus resulting in the decrease in strength of tip vortices and enhancing the wing's performance (Abdelghany et al., 2016). In the case of a VAWT, a study has been done to evaluate the effect of winglets on the performance of a two-straight-bladed VAWT (Zhang et al., 2019). The presence of a winglet (see Figure A.13) can weaken the tip vortex as it can prevent flow mixing between the pressure and the suction sides of the blade in the tip region. The winglet can also eliminate the secondary flow effect called "blade tip leakage flow", resulting in radial load jump in the near tip region. Overall, C_p enhancement reached between 6.7% and 10.5% in the optimum design of the winglet in medium regime of $TSRs$. However, this optimum design was obtained only by evaluating a single isolated blade. A two-straight-bladed VAWT configuration was adopted in simulation and results were compared to a single blade case. The C_p enhancement of this VAWT configuration could only reach 6.7% in $TSR = 2.29$. This C_p enhancement is significantly reduced compared to a single blade case which could improve C_p of clean blade by around 31.6%). Hence, it is desirable to perform winglet optimisation in the presence of rotor wake effects and blade-to-blade interactions to evaluate these designs in a VAWT configuration model in different TSR regimes.

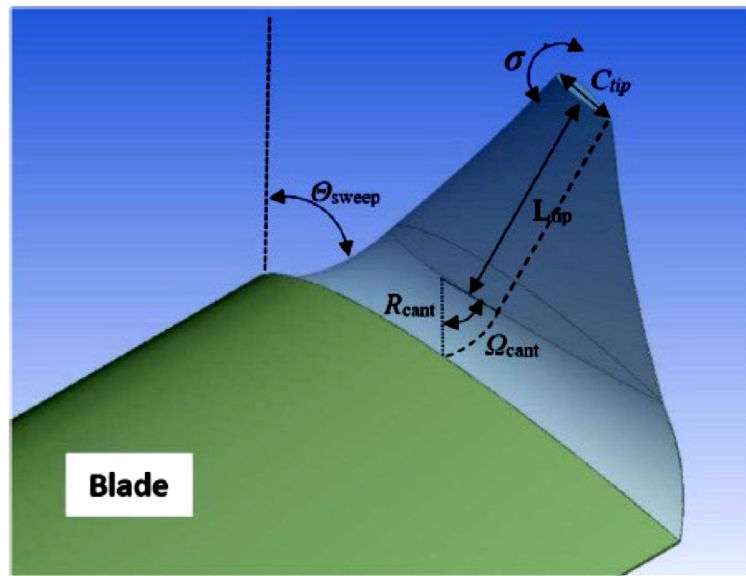


Figure A.13 VAWT blade with a winglet at the tip (Zhang et al., 2019).

A.7.2 Gurney flap (GF)

A Gurney flap is a passive flow control device that enhances lift force by exerting a small plate at the trailing-edge of aerofoil. It is gaining popularity due to its simplicity, low cost and reasonably good performance enhancement (Saenz-Aguirre et al., 2018). Based on a successful application on a racing car by Dan Gurney, a GF has been widely applied to aircraft wings as it is beneficial during the taking-off and landing stages (He et al., 2016). For a single stationary aerofoil, the existence of a GF will generate counter-rotating vortex pairs downstream, accompanied by a significant flow turning over the leeward side of the flap, leading to the decrease in wake momentum deficit and an increase in lift force (see Figure A.14) (Liebeck, 1978). Recently, a GF with a small fraction of blade chord length has been applied in HAWTs to improve the performance of turbine blades (Saenz-Aguirre et al., 2018; He et al., 2016). Results showed that blades with GFs indeed can increase the power generation of the wind turbine compared to those without GFs. In the case of the VAWTs, there are few studies on the GF applications. Most applications are for straight-bladed lift-driven VAWTs (Yan et al., 2020; Bianchini et al., 2019; Zhu et al., 2019; Malael, Bogateanu and Dumitrescu, 2012). They found that the GF could significantly improve the lift coefficient whilst having a minor effect on the drag coefficient, resulting in the C_p improvement of VAWTs. The C_p improvement could reach 116% in low TSR regime, whilst in medium and high regimes of $TSRs$, this improvement reduced to 28% and 18.18% respectively (Zhu et al., 2019).

Whilst some studies argued that the performance enhancement could be achieved in all TSR regimes (even though the increment would be decreased after the optimum value of TSR) (Bianchini et al., 2019; Zhu et al., 2019), there was a study stating that a GF could not improve the power coefficient in high regime of $TSRs$ (Yan et al., 2020). Those two contradicting conclusions can be due to the use of different types of aerofoil in their studies. Hence, it turns out that using a GF on different types of aerofoil can generate different or even contradicting results. Nevertheless, some results showed that a GF can be used for self-starting ability improvement and power coefficient enhancement (Bianchini et al., 2019).

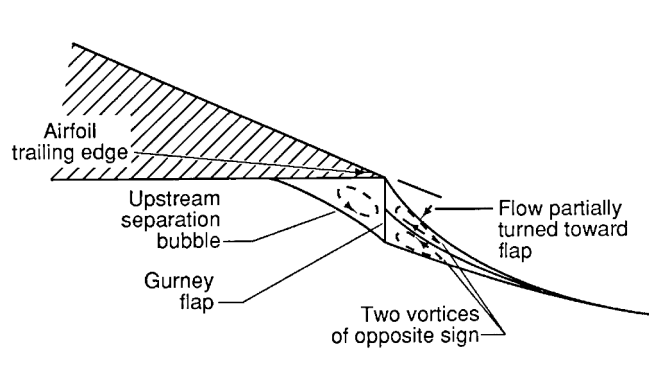


Figure A.14 Illustration of flow behaviour around trailing-edge of aerofoil with GF (Liebeck, 1978).

A.8 *Leading-edge Micro-cylinders*

This passive flow control approach modifies the local flow by adding a relatively small (micron size) cylinder upstream of the leading-edge of the aerofoil (or blade), usually near the suction side. Such a micro-cylinder could suppress the flow separation that occurred in large AoA , resulting in the improvement of lift coefficient and reduction of drag coefficient (Wang et al., 2018) values. Application of a leading-edge micro-cylinder on a NACA 0021 VAWT has been studied experimentally by Choudhry, Arjomandi and Kelso (2016) (see Figure A.15). The effect of the rotating motion of the VAWT was created by introducing a pitching motion to the aerofoil. This study indicated that the micro-cylinder could delay dynamic flow separation and suppress the dynamic stall vortex and unsteady flow separation was also delayed by approximately 25% in terms of stall angle in a lower pitching rate. However, this delay could only be up to 5% in the higher pitching rate. These results imply that the passive flow control is only effective in low regime of $TSRs$ rather than high regime of $TSRs$. In addition, a micro-cylinder could reduce the drag generation compared to the original aerofoil due to the lessened pressure drag associated with a DSV caused by the reduction of the apparent thickness of the aerofoil in the presence of the leading-edge micro-cylinder. Hence, this characteristic can benefit lift-driven VAWTs as it can improve the lift force without increasing the drag force. Nevertheless, further analysis of a VAWT configuration is still needed to confirm the ability of a leading-edge micro-cylinder on the improvement of a VAWT and its capability in each TSR regime also needs to be investigated.

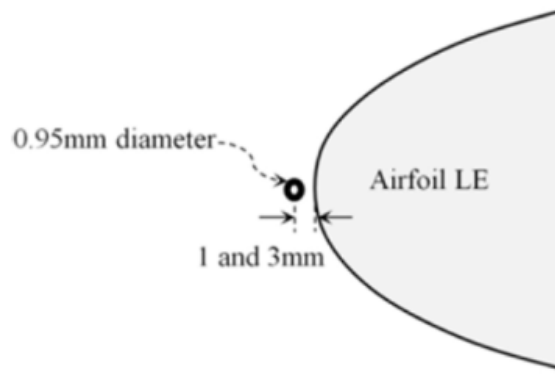


Figure A.15 Leading-edge micro-cylinder passive flow control (Choudhry, Arjomandi and Kelso, 2016).

APPENDIX B

(Linked to Chapter 2, Section 2.2.2)

Flow Augmentation Devices Implemented in Lift-Driven VAWTs

B.1 Single Directional Flow

B.1.1 Guide Vane Row and Tail Vane

Takao et al. (2009) placed a guide vane row with three arc plates upstream and tail vanes as the yaw mechanism downstream of three-straight-bladed H-type VAWT as illustrated in Figure B.1. The results found that the maximum C_p of the turbine rose 1.5 times compared with the bare turbine. However, this device generated lower power than the original turbine in low regime of $TSRs$ due to the radical change of the angle of airflow inlet caused by the guide vane row. Hence, this device could only provide power enhancement in medium and high regimes of $TSRs$ and could not enhance the self-starting ability of VAWTs as it did not perform well in low regime of $TSRs$.

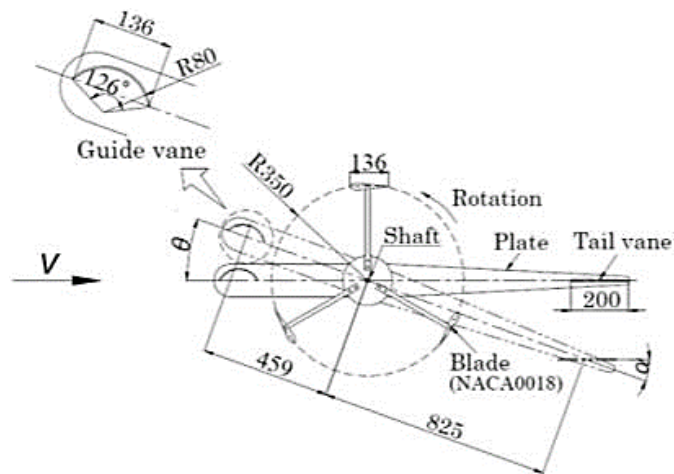


Figure B.1 Guide vane row with three arc plates (Takao et al., 2009).

B.1.2 Convergent Duct

Santoli et al. (2014) covered a commercial three-straight-bladed H-type VAWT with convergent duct (see Figure B.2) and studied its effect on the turbine's performance experimentally and numerically. This study claimed that a venturi in the convergent duct configuration could increase the wind speed and direct the wind to the turbine. This device could improve the power generation of the turbine by around 125% in low wind speed and 30% in high wind speed, indicating that the power improvement will decrease as the

wind speed increases. Nevertheless, this device is complicated to apply in practice as the large duct size will need a strong support structure, increasing the manufacturing and maintenance cost.

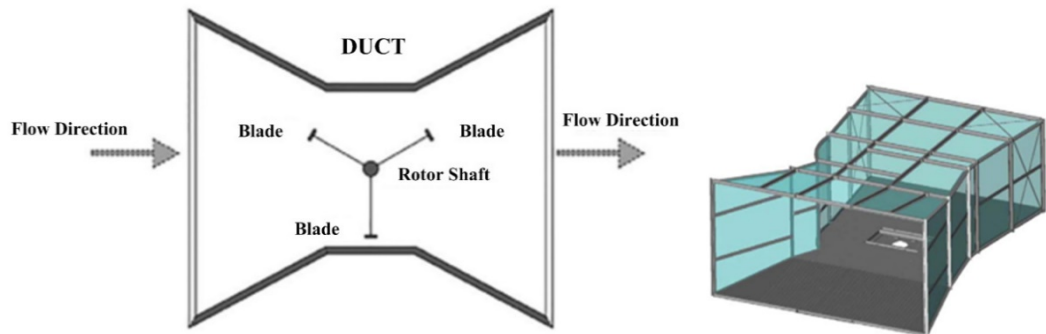
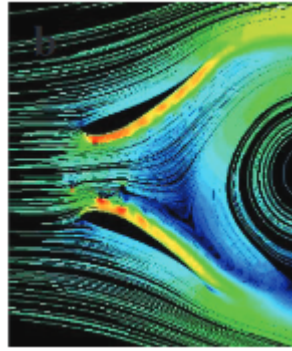


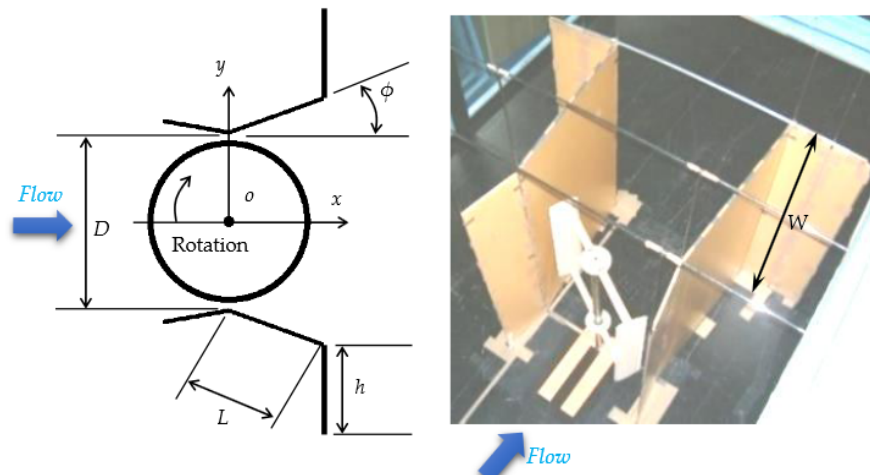
Figure B.2 Convergent duct configuration to increase wind velocity and direct the wind into the VAWT (Santoli et al., 2014).

B.1.3 Diffuser

Several studies have investigated the use of a diffuser as a flow augmentation device in lift-driven VAWTs. Letizia and Zanforlin (2016) applied a diffuser formed by two Selig 1223 wings with a zero AoA (see Figure B.3 (a)) around the rotor hub of three-straight-blades of a VAWT with the purpose of power enhancement. The results showed that the diffuser could improve the C_p by almost four times higher than the bare turbine. Moreover, another study investigated the effect of the shape of the diffuser (see Figure B.3 (b)) on the improvement of the performance of the VAWT (Watanabe, Takahashi and Ohya, 2016). The curved-surface-type diffuser generated a higher power augmentation than the flat-panel-type diffuser, improving the power generation by 2.1 times that of the bare turbine. The diffuser also can improve the power production in all TSR regimes. Regardless of this improvement, the same concerns as for a convergent duct application also arose in this device implementation in the VAWT.



(a)



(b)

Figure B.3 Diffuser application in lift-driven VAWTs, (a) two Selig 1223 wings diffuser (Letizia and Zanforlin, 2016) and (b) wind lens diffuser (Watanabe, Takahashi and Ohya, 2016).

B.1.4 Curve Plate

Stout et al. (2017) investigated the effect of adding a curved plate (see Figure B.4) upstream of a three-straight-bladed H-type VAWT on the turbine's performance numerically and experimentally. The curved plate did not always enhance the VAWT's performance, which depends on its location upstream of the turbine. When the curved plate is located at downward areas which are upstream of the turbine, the VAWT's performance could be improved by around 2.2% for the optimum design. However, the power production was worse than the bare turbine when the curved plate was placed at the upward areas as the presence of the plate induced a sudden flow velocity increment behind the plate, resulting in pressure difference drops of blade (i.e., the one that is at the position behind the plate) due to the change of the flow direction to the blade.

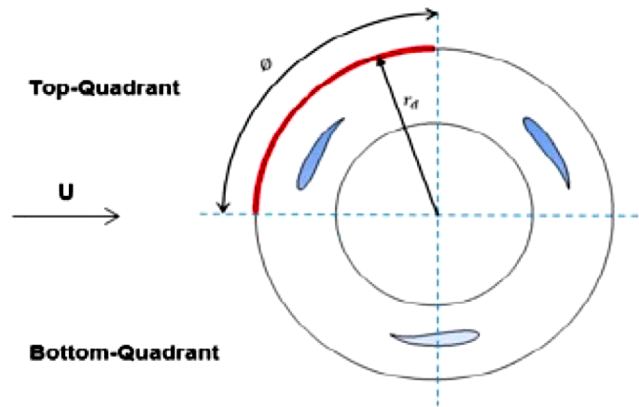


Figure B.4 VAWT model with curved plate (Stout et al., 2017).

B.1.5 Straight Plate

The use of a flat plate as an upstream deflector has shown that it can improve a VAWT's performance, mainly in drag-driven VAWTs. If the plate's location is correct, it can be used as an obstacle for returning blade flow, generating negative torque. Nonetheless, the investigations of the use of this plate as a flow augmentation device in lift-driven VAWTs are still limited. Kim and Gharib (2013) and Kim and Gharib (2014) put a straight plate deflector (see Figure B.5 (a)) upstream at the middle of two five-straight-bladed VAWTs that have different rotation directions. It was discovered that the performance of the turbines improved due to the increment of local wind velocity caused by the proper position of the deflector. However, the deflector caused a worse performance than the original turbine if it is sited inside the streamline of the wake occurring downstream of the deflector. This deflector increased the maximum C_p by approximately three times and improved the TSR operation values by 26% higher compared to bare turbines. Nevertheless, this study was limited to a VAWT with high solidity and operated in low power coefficient and low Reynolds number regime (low regime of $TSRs$). Hence, further study is still needed to investigate whether this deflector can improve general lift-driven VAWTs and in all TSR operational regimes.

A similar study was performed by Jin et al. (2018), which positioned a straight plate deflector in the middle of the upstream of two counter-rotating three-straight-bladed VAWTs, as shown in Figure B.5 (b). This study showed that a VAWT's performance improvement caused by the deflector, depends on the deflector's geometry and location. The deflector can also improve a VAWT's performance with lower solidity and a higher TSR regime. Due to the lack of investigation on the use of a straight plate as an improvement performance device for single lift-driven VAWTs, Wong et al. (2018a) and

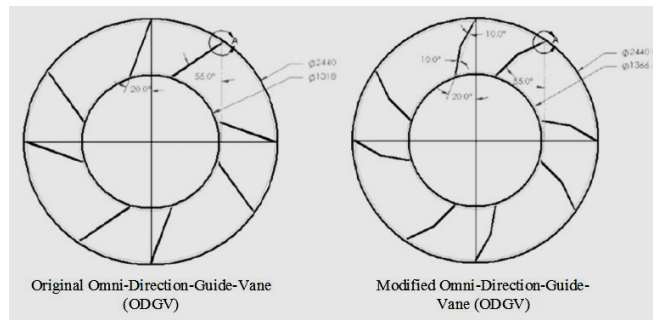
B.2 Omnidirectional Flow

B.2.1 Omnidirectional Guide Vane (ODGV)

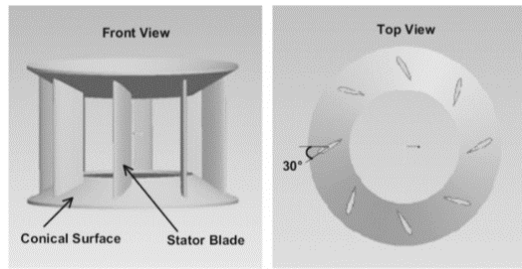
For improving the performance of a VAWT, Chong et al. (2013) placed an omnidirectional guide vane (ODGV) surrounding an H-type VAWT. Figure B.6 (a) shows that this mechanism has upper and lower ducts with four pairs of straight plate guide vanes surrounding the VAWT. Each pair of guide vanes has a tilt angle of 20° and 55° . The results indicated that the self-starting behaviour of the turbine improved due to the presence of ODGV which increases the inlet wind velocity and directs the wind to an optimum AoA . The rotational speed of the turbine was enhanced by around 182% of the original value. Moreover, the ODGV decreased the turbine's negative torque and the turbulence and rotational speed fluctuation. It improved the power generation by 3.48 times higher than the bare turbine in its optimum TSR . This ODGV was improved by Wong et al. (2014) by dividing each guide vane into two segments and bending it at a 10° angle (see Figure B.6 (a)). The improved design could enhance the C_p by around 31.65% and 147.1% compared to the original design of ODGV and bare VAWT, respectively. An ODGV can direct the flow in any direction as the vane surrounds the turbine. Nevertheless, the vast capital cost and potential of huge weight addition make this device unsuitable for commercial application on the VAWT.

B.2.2 Omnidirectional Stator

Nobile et al. (2014) designed a similar flow augmentation device like the ODGV by putting a stator around a H-type VAWT. The top and the bottom of the stator have a conical surface profile with eight straight vertical blades with a NACA0018 aerofoil profile in the middle (see Figure B.6 (b)). The conical surface profile can boost turbulence mixing and decrease the back pressure inside the stator whilst the presence of the blades concentrates the mass flow rate of the wind. Furthermore, the stator design can increase and decrease the airflow at specific areas and help the turbine improve its positive torque because it can produce shaded regions upstream which can decrease the drag force downstream. The average power coefficient and torque coefficient improved by 30-35% in the presence of this stator. However, this device has similar problems to the ODGV.



(a)



(b)

Figure B.6 A few omnidirectional-flow-augmentation devices to enhance the performance of lift-driven VAWTs, (a) Omni-Directional-Guide-Vane by Chong et al. (2013) (original) and Wong et al. (2014) (modified) and (b) Omnidirectional stator with NACA 0018 aerofoil profile by Nobile et al. (2014).

APPENDIX C

(Linked to Chapter 2, Section 2.4.2.3)

Previous Studies of VAWTs using CFD Simulations

C.1 *RANS and URANS*

These models solve the ensemble-averaged (or time-averaged) Navier-Stokes (NS) equations. They model all turbulent length scales and are the most widely used approach for calculating industrial flows. There are several types of these models depending on how many equations which involved in these models. The majority of these turbulence models can capture the time-averaged mean flow properties with a steady RANS approach, whilst the large-scale flow unsteadiness can be reproduced using URANS simulations. Both are sufficient for most engineering applications. However, the RANS model cannot capture the small-scale turbulence fluctuations, which are important for understanding the underlying flow physics. This could affect the accuracy of CFD predictions for VAWT performance.

Most CFD studies of VAWTs have utilised the two-equation turbulence models such as the $k-\varepsilon$ model and its variants, in particular the realisable $k-\varepsilon$ model. Compared to the standard $k-\varepsilon$ model, the turbulence viscosity formulation ($C\mu$) is a variable rather than a constant in the realisable $k-\varepsilon$ model. The dissipation rate (ε) is derived from an exact equation for the transport of the mean-square vorticity fluctuation. The realisable $k-\varepsilon$ model is commonly used as it can produce reasonably good results for swirling flows, rotating and separating flows, boundary layers under strong adverse pressure gradients, and separated and recirculated flows, compared to the standard $k-\varepsilon$ model (Mohamed, Ali and Hafiz, 2015; Trivello and Castelli, 2014; Castelli, Englaro and Benini (2011); Castelli et al., 2010). For example, the results by Castelli, Englaro and Benini (2011) demonstrated that the realisable $k-\varepsilon$ model can predict the C_p and the optimum TSR , in good agreement with the experimental data, even though it overestimated the power coefficient in the lower TSR regime by a factor of two compared to test data. The simulation of Ferreira et al. (2010) also showed that the standard $k-\varepsilon$ turbulence model was able to predict the time-averaged vertical velocity distributions and the roll-up of the trailing-edge vortex shedding at the correct phase angle (at around 120° azimuthal position), compared to that produced by the one-equation Spalart-Allmaras (SA) turbulence model.

Another two-equation turbulence model often utilised in VAWT simulation is the $k-\omega$ shear stress transport ($k-\omega$ SST) model. For example, the study by Wang et al. (2018) showed that the $k-\omega$ SST model could produce the C_p curve in alignment with the experimental results. Compared to the realisable $k-\varepsilon$ model, the $k-\omega$ SST results had improved prediction errors by about 50% in low regime of $TSRs$ and about 35% at high regime of $TSRs$ values, respectively. Other researchers also obtained similar results using the $k-\omega$ SST turbulence model (Arab et al., 2017; Lam and Peng, 2016; Almohammadi et al., 2015). In addition, a few studies have applied the Transitional SST turbulence model (Rezaeiha, Montazeri and Blocken, 2018; Bangga et al., 2017; Lanzafame, Mauro and Messina, 2013). The Transitional SST turbulence model is preferable for VAWT simulation as it can predict the laminar-to-turbulent transition, which can occur on the VAWT blade surfaces (Rezaeiha, Montazeri and Blocken, 2018). Compared to two-equation models, the prediction accuracy of the Transitional SST turbulence model was generally improved. Whilst the predicted power coefficients were close to the experimental data in the low TSR regime, the Transitional SST turbulence model still overestimated the C_p value in the high TSR regime. The cause of this discrepancy has not been fully understood yet. Most CFD studies of a VAWT using URANS turbulence models are performed on 2D configurations, especially for validation studies, turbulence model comparison and design optimisation due to high computational costs. q3D or 3D configurations are mostly used to verify the performance enhancement of the optimum design of the turbine.

C.2 Large Eddy Simulation (LES)

More advanced turbulence models, such as LES, have to be used in VAWT simulations to improve the prediction accuracy. The LES model is based on spatially filtered equations. Thus, it is time-accurate. It explicitly calculates the large-scale eddies that contain most of the energy spectrum, affecting the main flow. For small-scale eddies, their effects on the flow are considered using a Sub-grid Scale (SGS) model due to the universal behaviour of turbulence (i.e., Kolmogorov hypothesis). This feature makes the LES model more suitable for predicting the vortices' behaviour associated with the large flow separation and the dynamic stall in VAWTs.

Previous studies found that compared to the experiment data, LES can reduce the discrepancy between the C_p and C_m prediction using RANS and URANS simulations in all TSR regimes. Furthermore, when the flow is still attached to the blade, URANS and

LES have similar predictions to vortex generation and pressure field. However, when the flow starts to enter the stall condition, contrary to URANS which failed to capture dynamic stall vortices in high AoA , LES can produce a clear phenomenon of shedding vortices that develop along the inner surface of the blade from the trailing-edge. It is similar to the results of the PIV in experimental studies. Although LES shows better capability to predict the flow characteristics around rotating bodies such as VAWT blades; LES studies on VAWTs applications are still very limited, mainly due to its expensive computational cost (Posa and Balaras, 2013; Elkhoury, Kiwata and Aoun, 2015; Ghasemian and Nejat, 2015; Li et al., 2013). In addition, most of these studies are based on a q3D CFD study due to the increased computational cost of a complete 3D CFD study. Rather than simulate the turbine at its actual height, these studies extended the 2D model by about two to four times the blade's chord in the span-wise direction. The grids along the length of the blade in the span-wise direction are about 40 to 80 elements.

C.3 Hybrid RANS-LES

A hybrid RANS-LES model like the Detached Eddy Simulation (DES), Delayed-Detached Eddy Simulation (DDES), Improved-Delayed-Detached Eddy Simulation (IDDES), and Wall-Modelled LES (WMLES) are developed and utilised by many researchers in VAWT applications to overcome the expensive computational cost (Lei et al., 2017; Lam and Peng, 2016; Peng and Lam, 2016). These models still utilise the RANS turbulence model in the near-wall region to model small eddies whilst switching to LES to more accurately simulate large eddies in the intermediate and the far flow-fields, including the separated shear layer and wake regions (Liu et al., 2017). Most CFD studies using hybrid RANS-LES turbulence models were performed in 2D or q3D configurations. 3D complete configurations are very rare as they also significantly increase computational cost.

Based on previous studies (Lei et al., 2017; Lam and Peng, 2016; Peng and Lam, 2016), the hybrid RANS-LES model indeed can decrease the error of the CFD prediction of the experimental result for the power coefficient compared to URANS turbulence models. However, the computational cost is lower compared to LES. For example, IDDES could generate better accuracy of C_p prediction, especially in medium and high regimes of $TSRs$ compared to the $k-\omega$ SST turbulence model (Lei et al., 2017). IDDES can reduce the discrepancy of C_p prediction up to around 16% in high regime of $TSRs$. Meanwhile, this discrepancy is less than 10% in low and medium regimes of $TSRs$.

Similar to LES, IDDES also predicts richer vortex structures than the $k-\omega$ SST turbulence model at a higher azimuthal position when dynamic stall happens. This difference is noticeable, especially in low regime of $TSRs$ when the dynamic stall occurs. Furthermore, IDDES also generates more abundant 3D vortex structures around the blades than the $k-\omega$ SST turbulence model in low $TSRs$. IDDES produced columnar vortex shedding at a high azimuthal position, whilst the $k-\omega$ SST turbulence model did not generate this vortex shedding. Note that hybrid RANS-LES turbulence models are very sensitive to the grid resolution as the function used to change the solver from URANS to LES depends on the grid resolution. It is essential, especially for a VAWT mesh that usually has unequal mesh sizes in the x , y and z directions with unstructured or hybrid meshes. Hence, grid generation needs to be performed carefully to avoid the famous grid-induced separation that usually happens in hybrid RANS-LES simulation (Menter and Kuntz, 2004).

APPENDIX D

(Linked to Chapter 3, Section 3.2.2)

Details of Implemented Turbulence Models in the 2D CFD Validation Study

D.1 URANS Turbulence Models

This study considers two two-equation models and one four-equation model with a transition model to accommodate the laminar-to-turbulent transition process.

D.1.1 Two-equation k - ε realisable with enhanced wall treatment (RKE)

This model has proven to have better performance for flow prediction than the standard k - ε model, especially for flow with primary separation and secondary flow features, due to its greater ability to capture the mean flow. This is mainly due to the use of non-constants in the turbulent viscosity (μ_t) formulation. Equations (D.1) and (D.2) show the formulation of turbulent viscosity in this model. The C_μ is no longer a constant but a variable and the turbulence kinetic energy dissipation rate, ε (m^2/s^3), is derived from an exact equation for the transport of the mean-square vorticity fluctuation (Shih et al., 1995).

$$\mu_t = \rho C_\mu \frac{k^2}{\varepsilon}, \quad (\text{D.1})$$

$$C_\mu = \frac{1}{A_0 + A_s \frac{kU^*}{\varepsilon}}, \quad (\text{D.2})$$

where k is turbulence kinetic energy (m^2/s^2), A_0 is a constant equal to 4.04 and $A_s = \sqrt{6} \cos \varphi$ where φ is the rotation angle ($^\circ$). In Equation (D.2), $U^* \equiv \sqrt{S_{ij}S_{ij} + \widetilde{\Omega}_{ij}\widetilde{\Omega}_{ij}}$ is the modified stream-wise mean velocity where $S_{ij} = \frac{1}{2} \left[\frac{\partial U_i}{\partial x_j} + \frac{\partial U_j}{\partial x_i} \right]$ is the strain rate and $\widetilde{\Omega}_{ij}$ is the modified vorticity tensor as explained by Shih, Zhua and Lumley (1995).

This model is preferred over other k - ε models on single moving reference frame systems associated with a computational domain containing both rotating and stationary fluid zones. However, as the RKE model sometimes generates non-physical turbulent viscosities in this computational domain, its application on multiple reference frame systems like the VAWT model needs to be considered carefully. In addition, this model

also inherits the poor performance of any $k-\varepsilon$ based model for flows with low Re (Wilcox, 2006). In this study, the enhanced wall treatment for near-wall modelling is also included to ensure that the flow in the viscous sublayer can be captured.

D.1.2 Two-equation Shear-Stress Transport $k-\omega$ (SST)

This model combines some key features of $k-\varepsilon$ and standard $k-\omega$ models. It applies the $k-\omega$ formulation (Menter, 1994) in the inner parts of the boundary layer and switches to $k-\varepsilon$ formulation (Launder and Spalding, 1972) in the region away from the wall. Hence, this turbulence model can predict flow at low Re without using any extra functions and thus can avoid the common problem of high sensitivity to the inlet freestream turbulence in a standard $k-\omega$ model. The turbulent viscosity equation is modified by adding a limiter to avoid over-prediction of the eddy-viscosity (see Equations (D.3) and (D.4)).

$$\mu_t = \frac{\rho k}{\omega} \frac{1}{\max\left[\frac{1}{\alpha^*} + \frac{SF_2}{a_1\omega}\right]}, \quad (D.3)$$

$$\alpha^* = \alpha_\infty^* \left[\frac{\alpha_0^* + Re_t/R_k}{1 + Re_t/R_k} \right], \quad (D.4)$$

where ω is the specific dissipation rate ($1/s$), α^* is low Re correction parameter, $S = \sqrt{2S_{ij}S_{ij}}$ is shear strain rate, $\alpha_1 = 0.31$, $\alpha_\infty^* = 1$, $\alpha_0^* = \frac{\beta_i}{3}$, $\beta_i = 0.072$, $Re_t = \frac{\rho k}{\mu\omega}$ is the viscosity ratio, $R_k = 6$. Note that, for high Re number flows, $\alpha^* = \alpha_\infty^* = 1$. Furthermore, $F_2 = \tanh(\Phi_2^2)$ is the blending function and Φ_2 is the set of constants in the transformed $k-\varepsilon$ model, which is defined as $\Phi_2 = \max\left[2 \frac{\sqrt{k}}{0.09\omega y_w}, \frac{500\mu}{\rho y_w^2 \omega}\right]$ where y_w is the distance to the next wall surface (m) and μ is the dynamic viscosity ($Pa.s$).

Moreover, the transport of the turbulent shear stress in the turbulent viscosity equation (see Equation (D.4)) makes this model have better performance for flow with adverse pressure gradient and separation, such as an aerofoil flown in high AoA . As the Reynolds number in this study is relatively low, low Re corrections model can be activated.

In addition, Menter (1994) and Kato and Launder (1993) production limiters are also activated to prevent enormous turbulence energy production in the stagnation region. Menter's production limiter introduces a parameter C_{lim} (i.e., coefficient of limit) in the

equation of turbulence energy generation (G_k) of the model (see Equations (D.5) and (D.6)). Thus, the model will choose the minimal value between the calculated turbulence energy and a prescribed limit value to avoid excessive turbulence kinetic energy production.

$$G_k = \min[G_{k,cal}, C_{lim}\rho\varepsilon], \quad (D.5)$$

$$G_{k,cal} = \mu_t S^2, \quad (D.6)$$

where coefficient C_{lim} has a default value of 10. There is no effect of this limiter on the shear layer performance of the model, but it avoids the ‘artificial’ stagnation point in aerodynamic simulations (Menter, 1994; Kato and Launder, 1993).

Alternatively, Kato and Launder (1993) modified the equation of turbulence kinetic energy generation by replacing the shear strain rate with the vorticity rate, as shown in Equation (D.7). This modification is based on the observation that the excessive turbulence kinetic energy production level is caused by a very high level of shear strain rate in the stagnation regions (Kato and Launder, 1993). This enormous level of shear strain rate is mainly induced by quasi-irrotational flow with a very low vorticity rate in the flow-field near the stagnation point.

$$G_{k,cal} = \mu_t S \Omega, \quad (D.7)$$

where $\Omega = \sqrt{\Omega_{ij}\Omega_{ij}}$ is the magnitude of the vorticity tensor.

D.1.3 Four-equation transition SST (TSST)

This model is based on the SST k - ω transport equations with the addition of two other transport equations: intermittency (γ) (see Equation (D.8)) and transition onset criteria in term of momentum-thickness Reynolds number (Re_θ) (see Equations (D.9) to (D.12)). The intermittency can trigger local transition whilst the transition onset Re_θ will enable the model to capture the non-local influence of the change of turbulence intensity due to the decay of the turbulence kinetic energy in the free stream and free stream velocity variation outside of the wall boundary layer (Menter, Langtry and Volker, 2006). Due to these two additional equations, the prediction of the transition onset and its length can be dealt with by the SST k - ω model. Based on previous works (Langtry et al., 2006;

Langtry, Gola and Menter, 2006; Menter, Langtry and Volker, 2006), this model was proven to accurately predict natural and/or induced separation and bypass transitions for wall-bounded flows. In this study, the turbulence production limiters proposed by Menter (1994) and Kato and Launder (1993) are activated to avoid the excessive turbulence energy generation and a very high shear strain rate in the stagnation region.

$$\frac{\partial(\rho\gamma)}{\partial y} + \frac{\partial(\rho U_j \gamma)}{\partial x_j} = P_{\gamma 1} - E_{\gamma 1} + P_{\gamma 2} - E_{\gamma 2} + \frac{\partial}{\partial x_j} \left[\left(\mu + \frac{\mu_t}{\sigma_\gamma} \right) \frac{\partial \gamma}{\partial x_j} \right], \quad (\text{D.8})$$

In Equation (D.8), $P_{\gamma 1} = C_{a1} F_{length} \rho S [\gamma F_{onset}]^{C_{\gamma 3}}$ and $E_{\gamma 1} = C_{e1} P_{\gamma 1} \gamma$ are the transition sources with $C_{a1} = 2$. F_{length} is an empirical correlation that controls the length of the transition region, F_{onset} is a function used to trigger the intermittency production, $C_{\gamma 3} = 0.5$, and $C_{e1} = 1$. $P_{\gamma 2} = C_{a2} \rho \Omega F_{turb}$ and $E_{\gamma 2} = C_{e2} P_{\gamma 2} \gamma$ are destruction/relaminarisation relationships with $F_{turb} = e^{-\left(\frac{R_t}{4}\right)^4}$ as the function to control the length of the turbulent region.

$$\frac{\partial(\rho \overline{Re_{\theta t}})}{\partial y} + \frac{\partial(\rho U_j \overline{Re_{\theta t}})}{\partial x_j} = P_{\theta t} + \frac{\partial}{\partial x_j} \left[\sigma_{\theta t} (\mu + \mu_t) \frac{\partial \overline{Re_{\theta t}}}{\partial x_j} \right], \quad (\text{D.9})$$

$$P_{\theta t} = C_{\theta t}^t \frac{\rho}{t} (Re_{\theta t} - \overline{Re_{\theta t}}) (1.0 - F_{\theta t}), \quad (\text{D.10})$$

$$F_{\theta t} = \min \left(\max \left(F_{wake} e^{\left(\frac{-y_w}{\delta}\right)^4}, 1.0 - \left(\frac{\gamma-1}{1.0-1/50}\right)^2 \right), 1.0 \right), \quad (\text{D.11})$$

$$F_{wake} = e^{-\left(\frac{Re_\omega}{1E+5}\right)^2}, \quad (\text{D.12})$$

where $Re_{\theta t}$ is the transition onset momentum thickness Reynolds number, $\overline{Re_{\theta t}}$ is the local transition onset momentum thickness Reynolds number, $P_{\theta t}$ is the source term, $\sigma_{\theta t} = 2.0$, $t = \frac{500\mu}{\rho U^2}$ is a time scale that is present for dimensional reasons and $C_{\theta t} = 0.03$. $F_{\theta t}$ in Equation (D.10) is a blending function used to turn off the source term in the boundary layer. F_{wake} is a function to ensures that the blending function is not active in the wake regions downstream of the body. $\delta = \frac{50\Omega y_w}{U} \delta_{BL}$ is the boundary layer thickness (m), $\delta_{BL} = \frac{15}{2} \theta_{BL}$ is the boundary layer transition thickness (m), $\theta_{BL} = \frac{\overline{Re_{\theta t}} \mu}{\rho U}$ is the

momentum thickness in boundary layer transition (m) and $Re_\omega = \frac{\rho\omega y_w^2}{\mu}$ is the dissipation Reynolds number.

D.2 Hybrid-RANS turbulence models

Three types of hybrid RANS-LES turbulence models are applied in this study, of which the first is based on delayed-detached eddy simulation (DDES) model, the second is based on improved-detached-delayed eddy simulations (IDDES), and the third is a relatively new model called stress-blended eddy simulation (SBES).

D.2.1 Delayed-Detached Eddy Simulation (DDES)

This model is based on the DES model, which treats the attached boundary layer using RANS, while LES is implemented in the separated flow regions. DDES is designed to solve some weaknesses in the standard DES model, such as high grid-size sensitivity leading to grid induced separation (GIS) due to a "grey area" where the models vary from URANS to LES and possible delay in the formation of instabilities in the mixing layers (Menter and Kuntz, 2004). This model has successfully overcome some drawbacks in the DES model, but at an extra computational cost due to extreme grids used in the model (Spalart et al., 2006). This study chooses the SST $k-\omega$ model for URANS simulation. Therefore, this model applies the DES equations proposed by Menter and Kuntz (2004), which modified the dissipation term of the turbulence kinetic energy by

$$Y_k = \rho\beta^*k\omega F_{DES}, \quad (D.13)$$

where β^* is a model constant = 0.09 and the blending function, F_{DES} , is expressed as

$$F_{DES} = \max\left(\frac{L_t}{C_{DES}\Delta_{max}}, 1\right), \quad (D.14)$$

where C_{DES} is a calibration constant used in the DES model and has a value of 0.61, Δ_{max} is the maximum grid spacing inside the boundary layer thickness (m) and L_t is turbulence length scale (m) which is calculated by

$$L_t = \frac{\sqrt{k}}{\beta^*\omega}, \quad (D.15)$$

A function (known as a shielded function) is added into the equation of the blending function of DES to protect the boundary layer from GIS. Therefore, it becomes

$$F_{DES} = \max\left(\frac{L_t}{C_{DES}\Delta_{max}}(1 - f_{DDES}), 1\right), \quad (D.16)$$

where f_{DDES} is the blending function used in the DDES model and is expressed by

$$f_{DDES} = \tanh[(C_{d1}r_d)^{C_{d2}}], \quad (D.17)$$

where $C_{d1} = 20$ and $C_{d2} = 3$ and

$$r_d = \frac{v_t + v_l}{\kappa^2 y^2 \sqrt{0.5(S^2 + \Omega^2)}}, \quad (D.18)$$

where v_t is turbulent kinematic viscosity (m^2/s), v_l is laminar kinematic viscosity (m^2/s), and the Karman constant $\kappa = 0.41$.

This model has been proven to produce reasonable predictions (the discrepancies between CFD prediction and experimental results of VAWT's power coefficient were about 20%) in rotating flows with separation and flow around an aerofoil with stall condition (Elkhoury et al., 2019). Nevertheless, as this is a DES-type turbulence model, refined grids are still needed both in the near wall and far-field regions. In this study, the DDES model is adopted with the SST $k-\omega$ representation for the RANS model with the activation of the low Reynolds number correction model.

D.2.2 Improved-Detached-Delayed Eddy Simulations (IDDES)

DES and DDES address two parts of the entire logarithmic layer (denote 'log-layer' thereafter) in a separate manner, i.e., the "inner" log-layer part is covered by the RANS model and the "outer" log-layer part by the LES model. The LES function will only be activated in regions with local grid sizes that are much smaller than the distance of this region to the wall. However, these two layers are usually mismatched in DES and DDES models causing under-prediction of the skin friction coefficient by 15-20% compared to the experimental results (Shur et al., 2008). Therefore, IDDES is proposed to address this problem by including a non-zonal hybrid RANS-LES model called wall-modelled LES (WMLES). It has a new definition of the sub-grid length-scale which includes an explicit wall-distance dependence. This addition allows the DES-based model

to respond differently depending on the grid resolution and inflow turbulence content. WMLES will be activated if the grid resolution is satisfactory enough and inflow turbulence exists in the simulation, otherwise it will operate the DDES model (Shur et al., 2008). IDDES model has demonstrated good ability in predicting massive flow separation and vortex shedding, such as in flow around an aerofoil at a high angle of attack.

D.2.3 Stress-Blended Eddy Simulation (SBES)

DES-based hybrid RANS-LES models, including DDES and IDDES, have shown several shortcomings for industrial application. Whilst the mesh is refined in the boundary layer region, an issue of so-called GIS may appear due to the LES grid limiter influence on the RANS model, causing improper balancing between RANS and LES turbulence content (even when using DDES). Moreover, there is a tendency towards slow "transition" from the RANS to the LES zones in separating shear layers (SSL) (Frank and Menter, 2017) with no clear differentiator between the RANS and LES regions. Hence, Menter (2018) has proposed an upgraded version of the DES model called SBES. This model revises the shielding function of the shielded DES (SDES) SST model to protect the RANS boundary layers and automatically switches to an existing algebraic LES model in the LES zone. Whilst the blending function remains the same as that of the shielding function SDES (f_{SDES}), in the LES zone where $f_{SDES} = 0$, SBES introduces an explicit model to switch to an algebraic LES. This modification changes the turbulence stress tensor and eddy viscosity equations as

$$\tau_{i,j}^{SBES} = f_{SDES}\tau_{i,j}^{RANS} + (1 - f_{SDES})\tau_{i,j}^{LES}, \quad (D.19)$$

$$\nu_t^{SBES} = f_{SDES}\nu_t^{RANS} + (1 - f_{SDES})\nu_t^{LES}, \quad (D.20)$$

where $\tau_{i,j}^{SBES}$, $\tau_{i,j}^{RANS}$ and $\tau_{i,j}^{LES}$ are turbulence stress tensors and ν_t^{SBES} , ν_t^{RANS} and ν_t^{LES} are turbulent kinematic viscosities.

As a result, the RANS and the LES zones can be clearly distinguished by visualising the shielding function. Moreover, due to the lower turbulence stress level enforced by the LES model, the SBES model can change rapidly from the RANS to the LES function in SSL, producing better, realistic, and consistent solutions. Furthermore, this turbulence model allows a RANS-LES "switch" to be predicted even on a coarser grid that other DES models cannot do. This model has been applied in the CFD

simulations of rotating devices (Cai, Li and Liu, 2019; Ravelli and Barigozzi, 2019; Ravelli and Barigozzi, 2018). This model can generate better predictions compared to RANS and other hybrid RANS-LES models. For example, the SBES can generate closer trend of the experimental results of averaged adiabatic effectiveness compared to RANS and DDES turbulence models. It can also produce a better prediction of the experimental results of coolant-to-mainstream mass flow rate compared RANS and DDES turbulence models (about 2.94% discrepancy compared to the experimental result). SBES can produce more refined turbulence structures and ordered, and abundant vortex structures compared to RANS models. Meanwhile, it offers faster development of turbulence and clearer and ordered turbulent structures compared to other hybrid RANS-LES models.

APPENDIX E

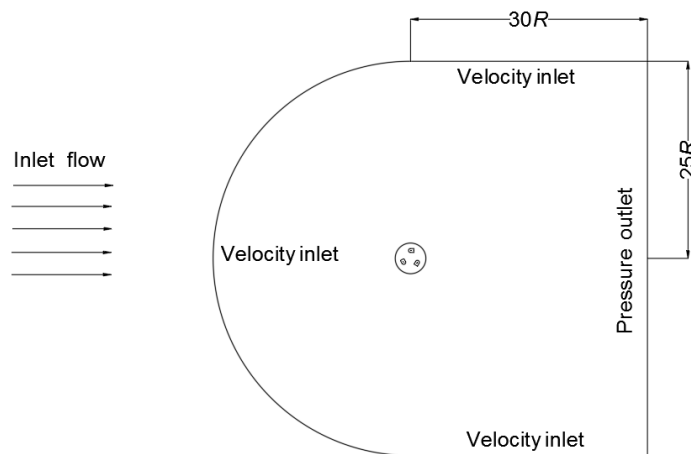
(Linked to Chapter 5, Section 5. 2; Chapter 6, Section 6.2 and Chapter 7, Section 7.2.1)

SBES Transitional SST Sensitivity to Grid Topology

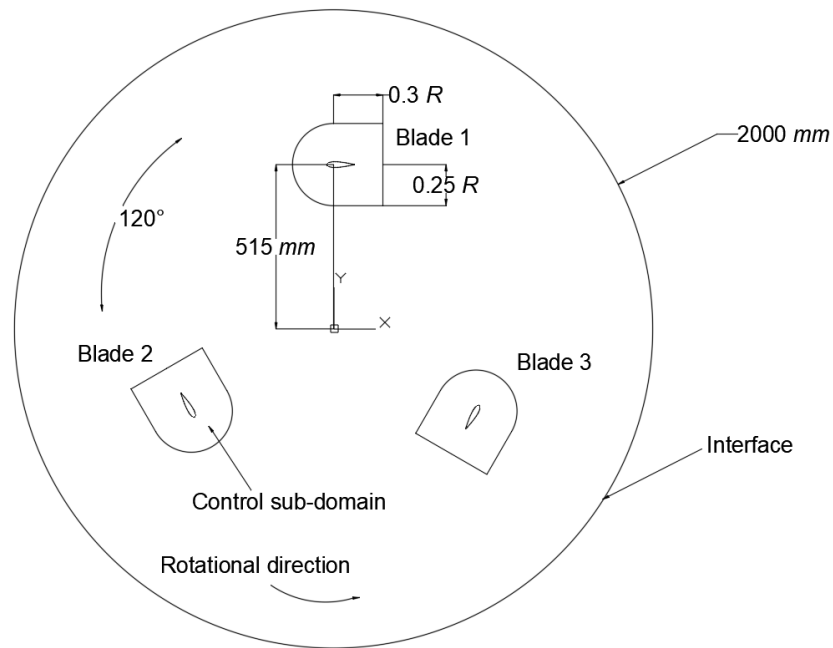
This appendix presents the investigation of the SBES Transitional SST model sensitivity to grid topology changes. The aim is to identify an appropriate grid topology and resolution for the primary VAWT simulation using the SBES turbulence model. This study considers two types of grids, i.e., O-grid and C-grid. Note that, all computational settings remain the same as in the turbulence model study.

E.1 Computational domain and grid discretisation of C-grid

For the O-grid, the computational domain and grid discretisation are the same as those used to evaluate the turbulence models' accuracies (see Chapter 4, Section 4.2). Table E.1 lists the details of the grid discretisation for these two grids. Figure E.1 shows the computational domain, consisting of three sub-domains, namely far-field, rotating core and control sub-domains for C-grid. The specifications of the domain and the grid generation are described below.



(a) Overview of the computational domain



(b) Rotating core sub-domain

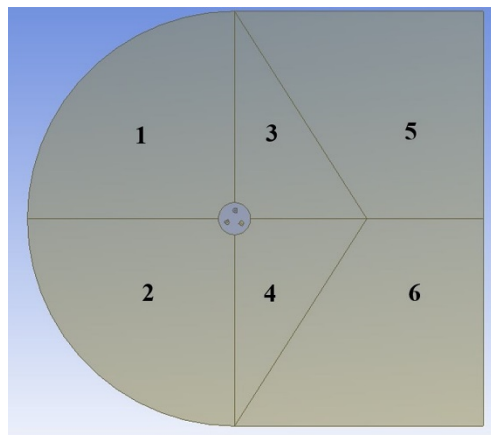
Figure E.1 Detailed computational domain and sub-domains of C-grid.

Table E.1 Detail of grid discretisation.

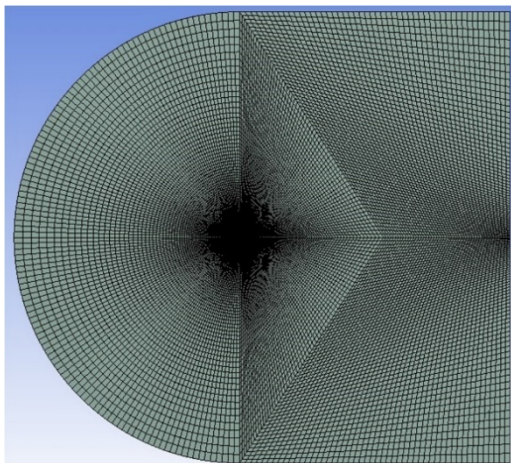
	O-grid	C-grid
<i>Type of Shape</i>		
Far-field	Rectangular	C combined with rectangular
Rotating Core	Circle	Circle
Control Circle	Circle	C combined with rectangular
<i>Type of Grid</i>		
Far-field	Quadrilateral structured grid	Quadrilateral structured grid
Rotating Core	Quadrilateral dominant grid	Quadrilateral dominant grid
Control Circle	Quadrilateral structured grid	Quadrilateral structured grid
<i>Total number of cells</i>		
Far-field	34200	18240
Rotating Core	22527	22527
Control Circle	20880	49680
<i>Growth Rate</i>	1.2	1.2
<i>Element around body</i>	174	174
<i>Element around trailing-edge</i>	14	14
<i>Body sizing for rotating core</i>	12 mm	12 mm

E.1.1 Far-field sub-domain

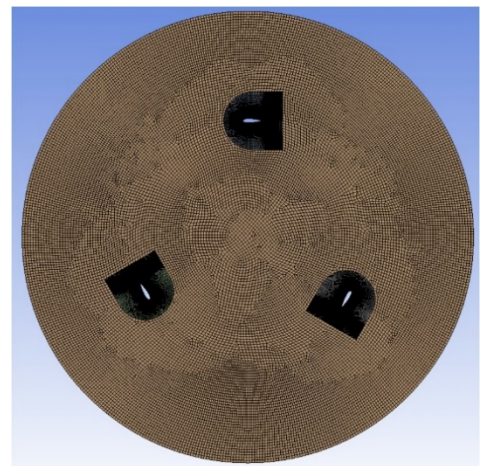
It is a non-rotating sub-domain surrounding the rotating core sub-domain. The C-grid together with a rectangular enclosure is used for the far-field sub-domain. The C-grid is $25R$ in radius and the rectangular enclosure is $30R$ in the stream-wise distance from the centre of the turbine's rotating axis to the exit, as suggested by Zhu et al. (2018). Figure E.2 (a) has shown that this sub-domain is divided into six regions to facilitate smooth grid discretisation. Similar to the O-grid, a structured grid with quadrilateral cells is generated within this sub-domain (see Figure E.2 (b)).



(a) Partition of far-field sub-domain



(b) Far-field sub-domain



(c) Control sub-domain

Figure E.2 Grid details in two sub-domains of C-grid.

E.1.2 Rotating core sub-domain

This sub-domain is a fluid region and utilised to implement the revolution of the rotor blade. It has a 2000 mm diameter and rotates in an anti-clockwise direction around the turbine's rotating axis at a given angular velocity. A 'fluid-fluid' interface is set up at the boundary intersection of these two sub-domains to ensure the continuity of fluid flow across the far-field and the rotating core sub-domains. This domain utilises quadrilateral elements (see Figure E.2 (c)).

E.1.3 Control sub-domain

This sub-domain is adopted to generate meshes around the blades. Three control domains with inserted blades are located inside the rotating core and separated by 120° angular distance between the adjacent blades. The boundary is also interpreted as “interior” to ensure the continuity of the fluid flow. The C-shape in the C-grid has 0.25r in radius and 0.3r in length from the centre of the blade. It uses the C-grid around the blade with gradually increasing grid-cell size.

The structured quadrilateral cells are generated in this sub-domain, with fine grids in the near-wall region (see Figure E.3) and coarser grids away from the wall. When the transitional SST turbulence model is applied, it is necessary to generate the first layer height to satisfy the criteria of non-dimensional wall distance $y^+ < 1$.

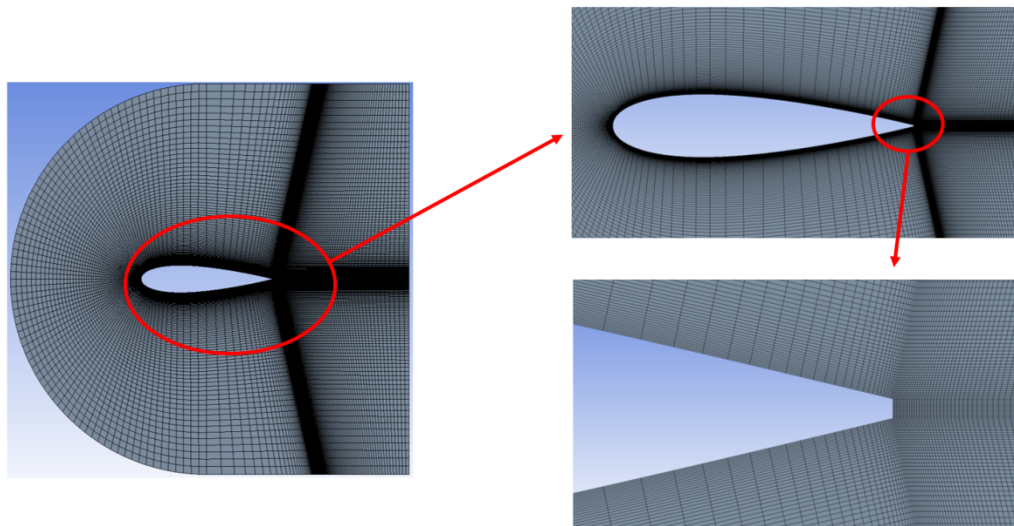


Figure E.3 Grid around the blade wall in the C-grid.

E.2 Grid convergence study

The grid convergence study is conducted for simulations in $TSR = 3.09$. At first, the O-grid is considered with three grid resolutions from coarse, medium to fine meshes, each having 87, 174 and 348 cells around the blade. Then, the C-grid is tested using three grid resolutions with the same number of cells around the blade as for the O-grid. Figures E.4 and E.5 compare instantaneous moment coefficients over one revolution for both O-grid and C-grid results, respectively. Both figures show that the moment coefficient changes with azimuthal position with little difference between the medium and the fine grids, whilst the coarse grid generates largest difference of instantaneous moment coefficients compared to the medium and fine grids. For both the O-grid and the C-grid, the average power coefficients of medium and fine grids are in good agreement (i.e., about 1.23% difference in average) with the experimental results of Castelli, Englaro and Benini (2011). Moreover, the relative error of average power coefficients between the medium and the fine grids is less than 4%; therefore, the medium grid has been selected for the rest of simulations.

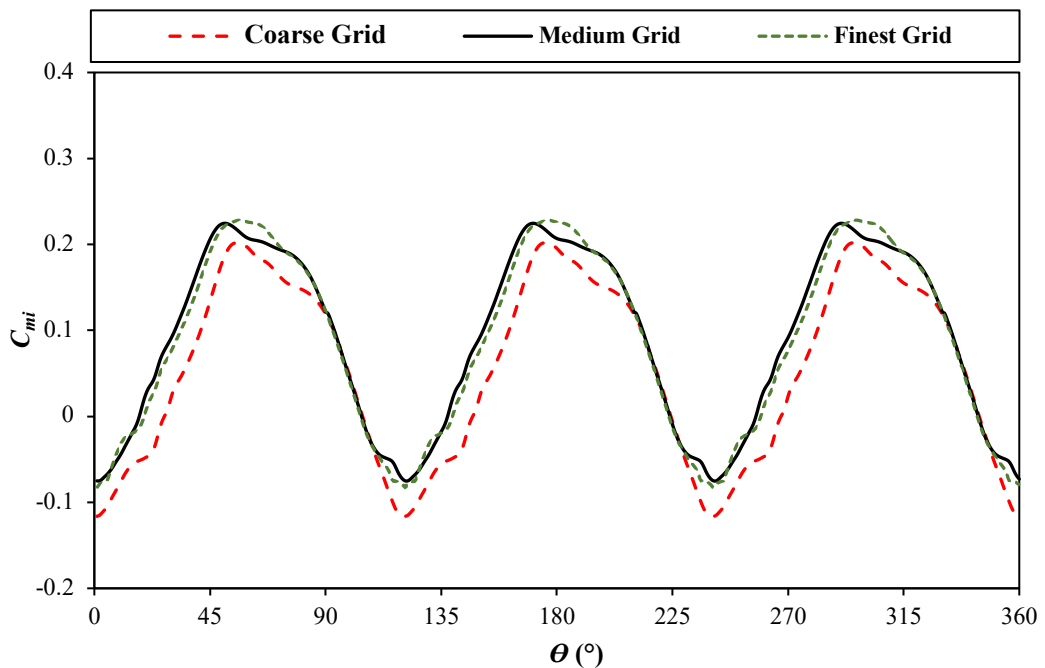


Figure E.4 C_{mi} comparison of VAWT with various grid resolutions for O-grids.

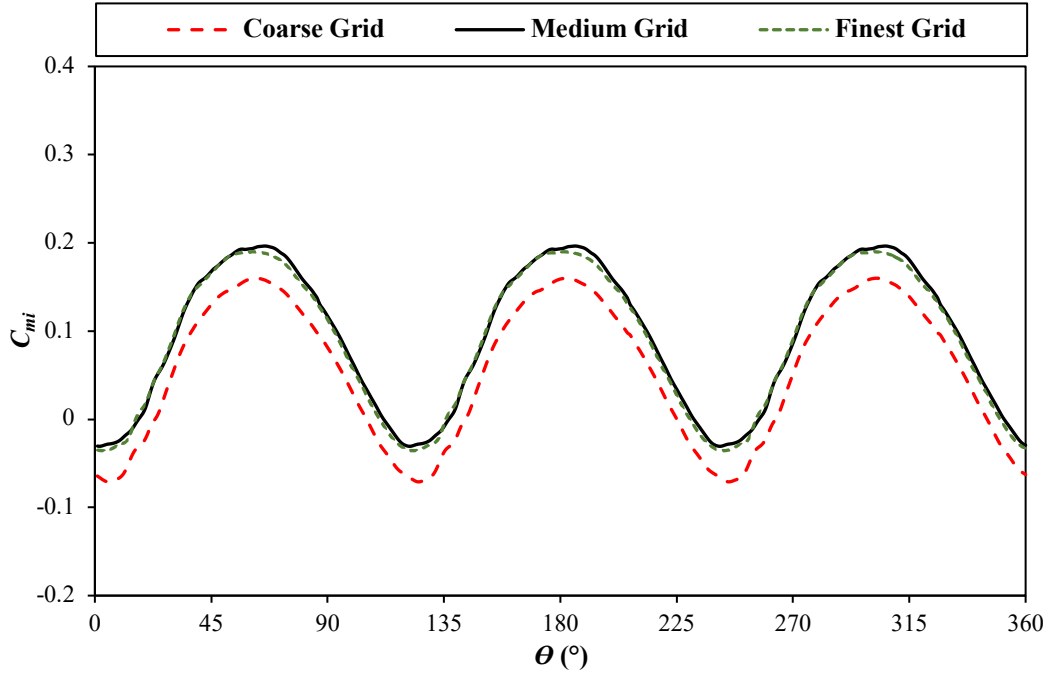


Figure E.5 C_{mi} comparison of VAWT with various grid resolutions for C-grids.

E.3 Grid topology study

As depicted in Figures E.6 and E.7, there are clear differences in the C_{p-ave} distribution between C-grid and O-grid meshes, despite that the general behaviour of C_{p-ave} distribution is predicted consistently by two grid topologies. Overall, the discrepancy between the O-grid and C-grid topologies is relatively minor if the time step is small enough (see Figures E.6 and E.7, respectively).

For all three TSR regimes, the simulations using the C-grid mesh produce smaller errors than that from using the O-grid, when compared to experiment. It is probably due to the effect of grid density in the close region of the blade (i.e., control sub-domain) rather than the grid topology. The C-grid control sub-domain contains more cells than O-grid (see Table E.1), even though they have the same number of cells around the blade. Furthermore, the DES turbulence model family (including SBES) is relatively sensitive to the near-wall and far-field grid resolutions. As a result, simulations using the C-grid gives better predictions than from the O-grid. This observation agrees with a previous study of the HAWT blade using DDES (Bangga et al., 2017).

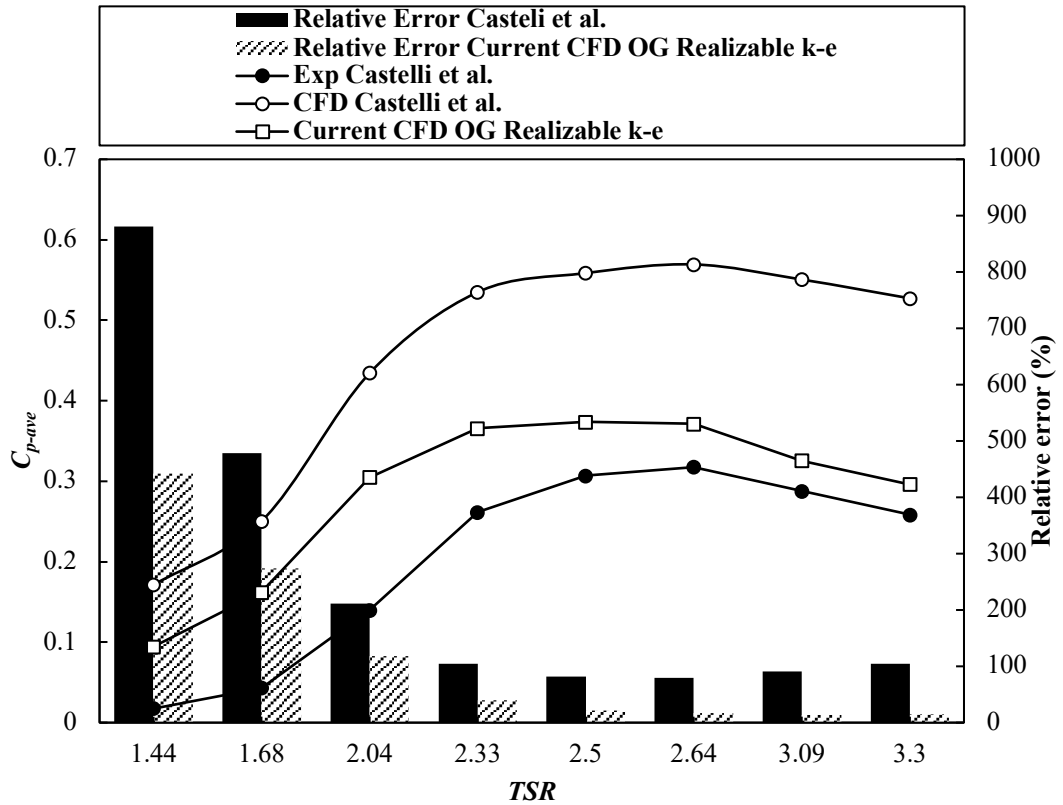


Figure E.6 C_{p-ave} comparison between the experiment, simulation of Castelli, Englaro and Benini (2011) and current CFD simulations (RKE) as well as relative errors in percentage (compared to experiment).

Instantaneous moment coefficients of one representative blade (i.e., blade 1) over one revolution are plotted in Figure E.8 for O-grid and C-grid in $TSR = 3.09$. Simulation using the O-grid predicts earlier separation than with the C-grid, exhibited by the earlier drop of C_{mi} value below zero at around 130° azimuthal position, whilst simulations with the C-grid starts to have a negative C_{mi} value later at about 150° azimuthal position (see a dashed circle in Figure E.8). It means that the starting point of no torque production (i.e., no power generation) predicted by simulations using O-grid is earlier than that of using the C-grid. However, the predicted recovery points (i.e., starting to produce positive torque again) are similar (around 190° azimuthal position) and their behaviours after that point are almost identical. In addition, both simulations produce almost the same maximum C_{mi} values at the same azimuthal position. Due to these differences in prediction, the predicted power generation with an O-grid is slightly lower than both using the C-grid and from the experimental measurements. Hence, this study will use the C-type grid for the rest of the simulations.

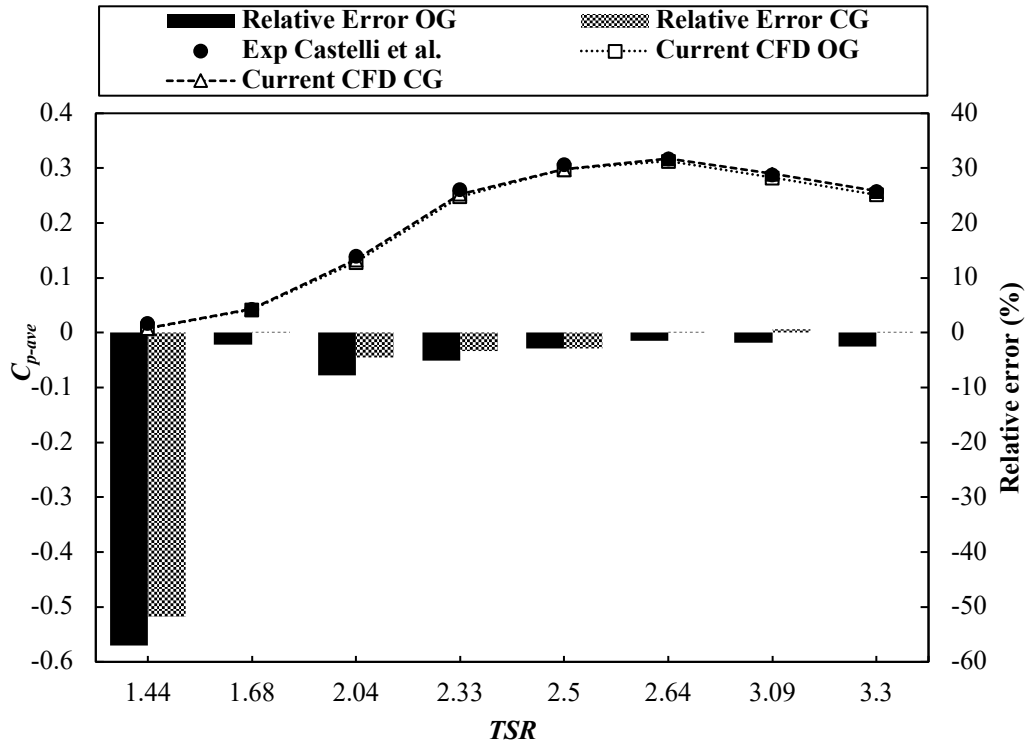


Figure E.7 C_{p-ave} comparison between the experiment of Castelli, Englaro and Benini (2011) and current CFD simulation (SBES with TSST) as well as relative errors in percentage (compared to experiment).

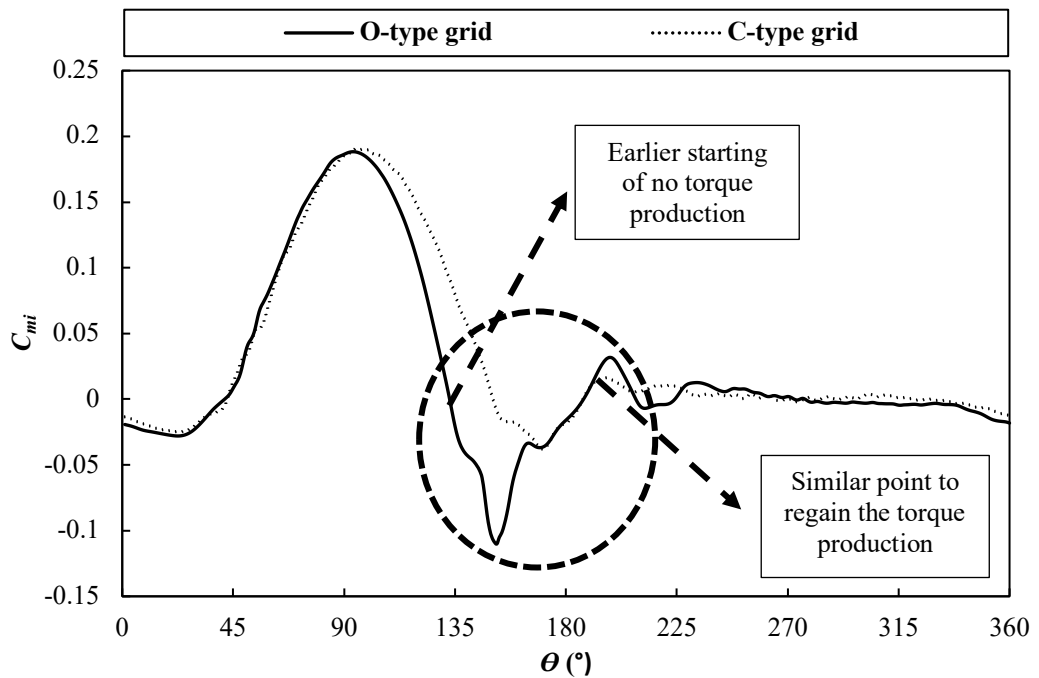


Figure E.8 C_{mi} comparison of blade 1 for one turbine revolution between O-grid and C-grid simulations.

APPENDIX F

(Linked to Chapter 5, Section 5.3)

Evaluation of Regime Values of the Height, Mounting Angle and Position from the Trailing-edge of the GF

F.1 Regime values of the height of the GF

Pre-evaluation is conducted by varying the GF height from 1% c to 4% c with a fixed mounting angle of 90° and a fixed position at 0% c from trailing-edge to determine the regime of GF height for the optimisation. Figure F.1 shows the effect of GF height with regard to the averaged power coefficient over a one blade revolution for all three regimes of $TSRs$. The C_{p-ave} increases with the increase of GF height until reaching an optimum value at $H = 3\% c$ in all three TSR regimes. After that, the C_{p-ave} decreases, indicating that GF height larger than 3% c will not further improve the VAWT performance. Hence, further study (see the detail in Chapter 5, Section 5.4.2) only evaluates three GF heights for optimisation, i.e., $H = 2\%$, 3% and 4% c .

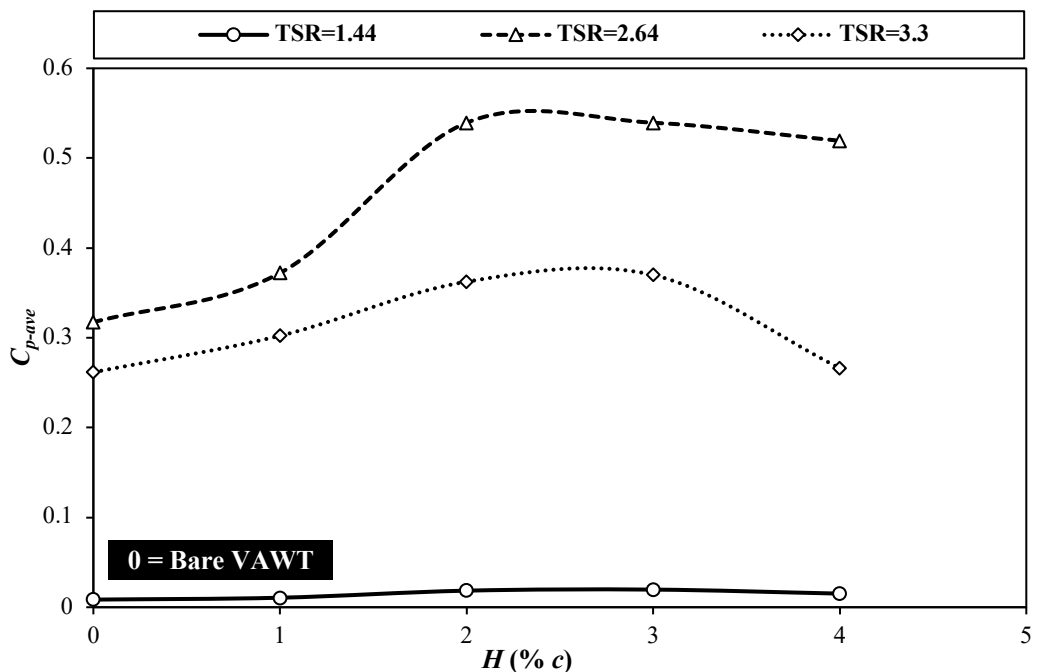


Figure F.1 C_{p-ave} comparison between VAWT with and without GF in various GF heights in all three regimes of $TSRs$.

F.2 Regime values of the mounting angle of GF

In order to determine the regime of GF mounting angle, the mounting angle is varied from 30° to 135° . The GF height and trailing-edge position are fixed at $3\% c$ and $0\% c$, respectively. As illustrated in Figure F.2, the C_{p-ave} enhances in all three regimes of $TSRs$ as the mounting angle increases. The maximum improvement is achieved for a mounting angle of 90° . Further increase of mounting angle does not enhance the C_{p-ave} . Therefore, three mounting angles of $\theta_{GF} = 60^\circ, 90^\circ$ and 135° are chosen for GF geometry optimisation.

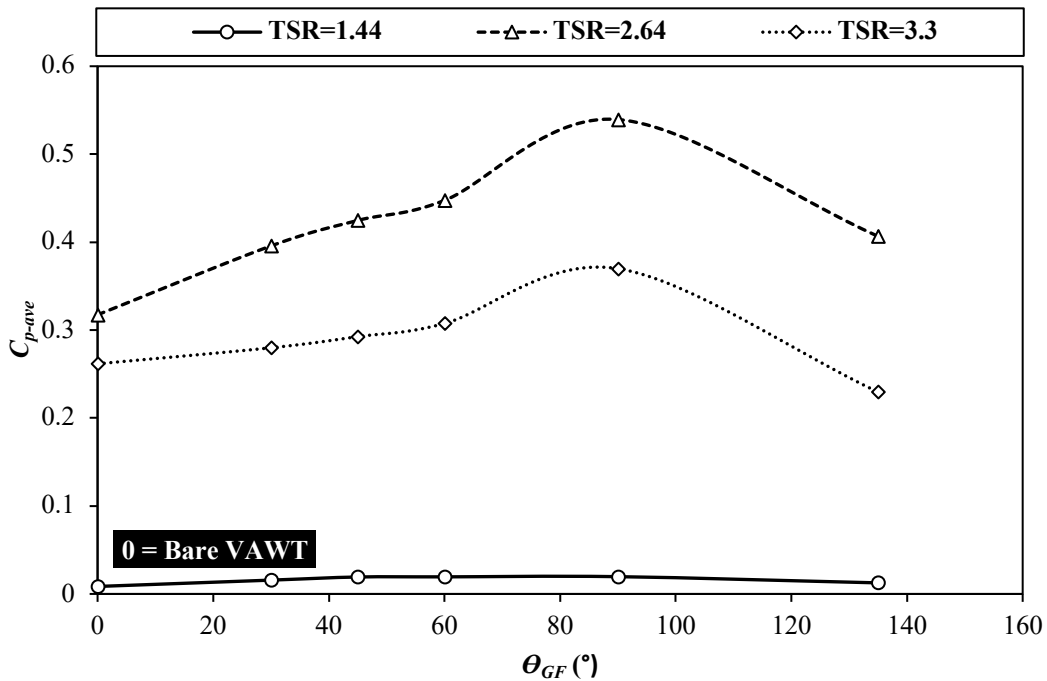


Figure F.2 C_{p-ave} comparison between VAWT with and without a GF for various GF mounting angles in all three regimes of $TSRs$.

F.3 Regime values of the position from trailing-edge of GF

In this pre-evaluation, the position from trailing-edge of the GF is varied from 0% to $7\% c$ with fixed height and mounting angle of $3\% c$ and 90° , respectively. Figure F.3 shows that the maximum performance comes from a GF positioned at the trailing-edge, i.e., $s = 0\% c$, in medium and high regimes of $TSRs$. Whilst the GF at all tested positions can enhance the C_{p-ave} compared to the bare VAWT, the increase of the distance between GF and trailing-edge will produce slightly decreased C_{p-ave} in these TSR regimes (see Figure F.3). However, different behaviours happened in low regime of $TSRs$. As the GF position moves away from the trailing-edge, the C_{p-ave} increases compared to the GF

at the trailing-edge until it reaches its optimum value at 4% c from the trailing-edge. After this position, the C_{p-ave} decreases. Further explanation about this behaviour is discussed in Chapter 5, Section 5.4.4. Based on these pre-evaluations, three distances to trailing-edge are chosen as 0%, 4% c and 7% c to include all the influential positions in all TSR regimes.

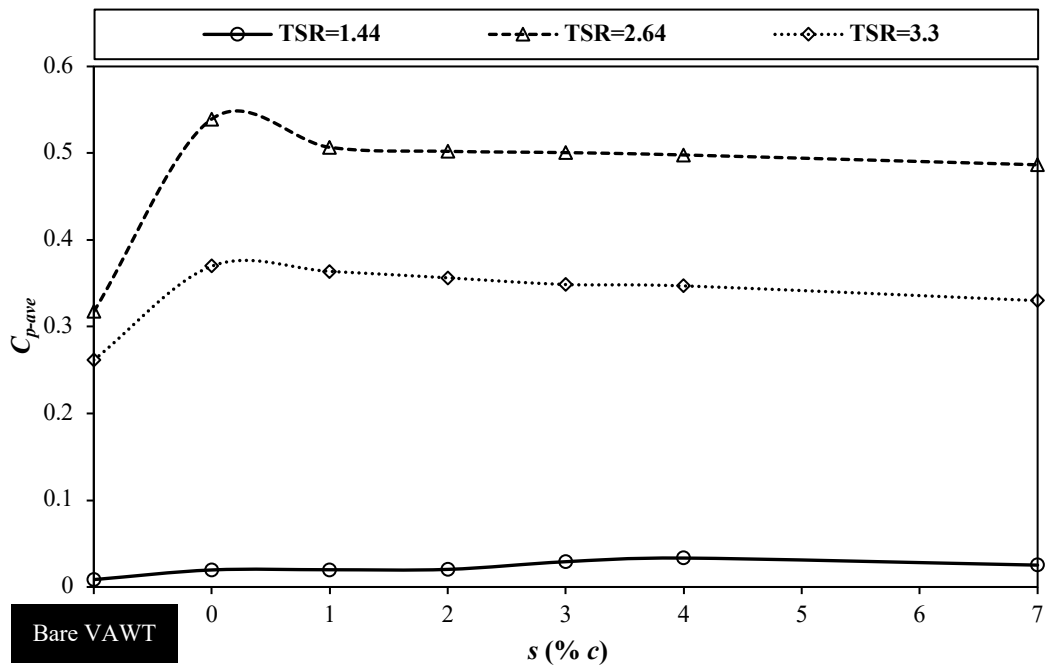


Figure F.3 C_{p-ave} comparison between VAWT with and without the GF in various GF positions from trailing-edge in all three regimes of $TSRs$.